Imperial College
London

MATERIAL PROPERTIES AND FRACTURE MECHANISMS OF EPOXY NANO-COMPOSITES

by

Reza Dave Mohammed

A thesis submitted for the degree of
Doctor of Philosophy of the University of London and for
the Diploma of Imperial College London

Department of Mechanical Engineering
Imperial College London

March 2007

ABSTRACT

Thermosetting polymers such as epoxies are widely used in their bulk form for their favourable structural engineering properties such as: a high modulus and failure strength, low creep, and good performance at elevated temperatures. They are also used as the matrices for fibre reinforced polymers (FRPs). The main drawback of using thermosetting polymers however, is their brittleness. Indeed, the addition of other phases such as soft rubbery particles and nano-sized (20nm diameter) silica particles can improve the toughness, without compromising any of the other major thermo-mechanical properties which would render the epoxies unsuitable for engineering applications.

The present work describes the material properties and fracture of epoxy polymers and their corresponding FRPs when CTBN rubber and nano-silica particles are used as toughening agents. Three systems were examined for this work - an amine-cured DGEBA-based, an amine-cured TGMDA-based, and an anhydride-cured DGEBA-based system.

Considering the bulk epoxies, it was found that there was good dispersion of rubber particles in all the systems, which led to an increase in toughness (mainly because of rubber cavitation, plastic hole growth of the epoxy, shear yielding, and epoxy plasticisation), but a decrease in glass transition temperature (T_g) and stiffness. Nano-silica on its own improved the toughness and a detailed investigation into the nano-toughening mechanisms of the anhydride-cured DGEBA-based system, showed that the increase in toughness occurred due to the debonding of the nano-silica particles and the subsequent plastic void growth in the epoxy around the nano-silica particles. Nano-silica on its own also improved the stiffness, but had no effect on the T_g. In bulk epoxy samples containing both rubber and nano-silica (ie. hybrids), it was found that the stiffness was improved, and the toughness increased (ie. a synergy between the tougheners was observed) if the nano-silica remained well dispersed or formed three-dimensional necklace-like chains.

The FRPs from the amine-cured DGEBA-based system had a poor transfer of toughness from the bulk epoxy to the FRPs, possibly because of the poor adhesion strength between the fibres and the matrix. However, the other two systems showed a good transfer of toughness, and in these systems, it was found that hybrid FRPs had the best combination of both high stiffness and high interlaminar fracture energy.

ACKNOWLEDGEMENTS

How does one go about acknowledging a lifetime's worth of friends, family, colleagues, and acquaintances, in the space confines of a single page? Should one thank them chronologically? Or maybe in terms of the quantity of funding they supplied? In order of importance even? But then, how does one define 'importance'? Indeed, by any method, there will be some who would be inadvertently omitted, and for this, I apologise in advance. In an attempt to circumvent any ranking technique, I shall just list people as I remember them.

I would like to thank my parents, Farouk and Farida, and my family for the support and encouragement they gave me from day one. My sincerest appreciations go out to my friends, not limited to the likes of: Idris (my brother and friend), Valissa, Neil, Ryan, Clint, Mark, Alan, Amir, and Shareef. The importance of my online friends on MSN and the Guardian Online Forum cannot be underscored, for they have all helped me through many a depressing time.

I could not have studied at one of the greatest institutions in the world, were it not for the funding of the Government of the Republic of Trinidad and Tobago. The further assistance given to me by organisations such as Imperial College London, the US Army ERO, hanse chemie, and the University of Trinidad and Tobago was heartily welcomed.

I would like to thank some of my colleagues who morphed into close friends over the years: Dr Bernt Johnsen, Dr Carlos Martinez-Baca, Dr Peter Lee and Mr Gordon McGourty. I would also like to collectively thank all the lecturers, technicians and ancillary staff for their assistance over the last seven and a half years.

I cannot begin to express my sincerest gratitude to my supervisors: Dr Ambrose Taylor and Professor Anthony 'Tony' Kinloch. Both Ambrose and Tony have helped me through some of the darker moments, both academically and personally, over the course of my PhD. Indeed, I never could have asked for better mentors.

The usual caveat applies: all errors in this thesis are my own. Enjoy!

For those who had no faith

CONTENTS

ABSTRACT..... 2
ACKNOWLEDGEMENTS..... 3
DEDICATION..... 4
CONTENTS..... 5
LIST OF FIGURES..... 11
LIST OF TABLES..... 30
NOMENCLATURE..... 32
ABBREVIATIONS..... 35

INTRODUCTION..... 36
1 BACKGROUND..... 36
1.1 AIMS AND OBJECTIVES..... 37
1.2 THESIS OUTLINE..... 38

LITERATURE REVIEW..... 40
2 INTRODUCTION..... 40
2.1 EPOXY POLYMERS..... 41
2.1.1 Curing..... 43
2.2 FRACTURE MECHANICS..... 44
2.2.1 Energy Balance Approach..... 45
2.2.2 Stress Intensity Factor Approach..... 46
2.2.3 Relationship between G_{Ic} and K_{Ic}..... 47
2.2.4 Crack Tip Plasticity..... 48
2.3 DEFORMATION BEHAVIOUR OF POLYMERS..... 50
2.3.1 Definition of Yielding..... 51
2.3.2 Theoretical Models for Predicting Young's Modulus... 52
2.4 TOUGHENED EPOXY POLYMERS..... 54
2.5 RUBBER TOUGHENING..... 55

2.5.1 Chemical and Physical Properties of Rubber..... 55
2.5.2 Rubber Toughening Mechanisms..... 56
2.5.3 Microstructure-Property Relationship..... 63
2.6 RIGID PARTICLE TOUGHENED EPOXY POLYMERS..... 68
2.6.1 Toughening Mechanisms..... 69
2.6.2 Effect of Volume Fraction and Particle Size..... 75
2.6.3 Hybrid (Rubber & Rigid Particle Toughened) Epoxy Polymers..... 77
2.6.4 Nano-scale Particle Toughened Polymers..... 79
2.7 FIBRE REINFORCED POLYMERS (FRPS)..... 81
2.7.1 Reinforcements..... 81
2.7.2 Manufacture..... 82
2.7.3 FRP Fracture Mechanisms..... 84
2.8 CHAPTER SUMMARY..... 87

MATERIALS AND EXPERIMENTAL PROCEDURE..... 88
3 BACKGROUND..... 88
3.1 MATERIALS..... 88
3.1.1 Amine-cured DGEBA-based..... 88
3.1.2 Amine-cured TGMDA-based..... 90
3.1.3 Anhydride-cured DGEBA-based..... 91
3.2 MICROSCOPY..... 92
3.2.1 Scanning Electron Microscopy..... 92
3.2.2 Microtoming..... 93
3.2.3 Transmission Electron Microscopy..... 93
3.2.4 Atomic Force Microscopy..... 93
3.3 BULK THERMAL AND MECHANICAL TESTS..... 93
3.3.1 Glass Transition Temperature..... 94
3.3.2 Tensile Tests..... 94
3.3.3 Single Edge Notch Bend Tests..... 95
3.4 FRP TESTS..... 96

3.4.1 Mode I Fracture Tests 97
3.4.2 Flexural Modulus Tests 99
3.4.3 Fibre Volume Fraction Tests 100
3.5 CHAPTER SUMMARY 101

RESULTS AND DISCUSSION: THE AMINE-CURED DGEBA-BASED SYSTEM.. 103
4 INTRODUCTION 103
4.1 BULK EPOXY POLYMER RESULTS 104
4.1.1 Microstructure 105
4.1.2 Thermal and Mechanical Properties 117
4.1.3 Bulk Fracture Surfaces 125
4.2 GLASS FIBRE REINFORCED POLYMER RESULTS 142
4.2.1 Mode I Fracture Results 142
4.2.2 Mode I GFRP Fracture Surfaces 144
4.3 CHAPTER DISCUSSION 163
4.4 CONCLUSIONS 166

RESULTS AND DISCUSSION: THE AMINE-CURED TGMDA-BASED SYSTEM.. 167
5 INTRODUCTION 167
5.1 BULK EPOXY POLYMER RESULTS 168
5.1.1 Microstructure 169
5.1.2 Thermal and Mechanical Properties 175
5.1.3 Bulk Fracture Surfaces 181
5.2 CARBON FIBRE REINFORCED POLYMER RESULTS 191
5.2.1 Mode I Fracture Results 191
5.2.2 Flexural Modulus 194
5.2.3 Mode I CFRP Fracture Surfaces 197
5.3 CHAPTER DISCUSSION 208
5.4 CONCLUSIONS 210

RESULTS AND DISCUSSION: THE ANHYDRIDE-CURED DGEBA-BASED SYSTEM..... 211

6 INTRODUCTION..... 211

6.1 BULK EPOXY POLYMER RESULTS..... 212

6.1.1 Microstructure..... 213

6.1.2 Thermal and Mechanical Properties..... 226

6.1.3 Bulk Fracture Surfaces..... 235

6.2 CARBON FIBRE REINFORCED POLYMER RESULTS..... 249

6.2.1 Mode I Fracture Results..... 249

6.2.2 Mode I CFRP Fracture Surfaces..... 251

6.2.3 Flexural Modulus..... 260

6.3 CHAPTER DISCUSSION..... 264

6.3.1 Bulk Epoxy Polymers..... 265

6.3.2 CFRP Laminates..... 267

6.4 CONCLUSIONS..... 268

SYSTEM COMPARISONS AND TOUGHENING MECHANISMS: BULK EPOXY.. 269

7 INTRODUCTION..... 269

7.1 MICROSTRUCTURAL ASPECTS..... 270

7.1.1 Unmodified Epoxies..... 270

7.1.2 Rubber Modified Epoxies..... 271

7.1.3 Nano-silica Modified Epoxies..... 274

7.1.4 Hybrid Modified Epoxies..... 276

7.1.5 Summary..... 281

7.2 THERMAL AND MECHANICAL PROPERTIES..... 280

7.2.1 Glass Transition Temperature..... 281

7.2.2 Young's Modulus..... 284

7.2.3 Fracture Toughness..... 287

7.3 BULK EPOXY TOUGHENING MECHANISMS..... 291

7.3.1 Rubber Toughening..... 291

7.3.2 Nano-silica Toughening..... 295

7.3.3 Hybrid Toughening..... 307
7.4 CHAPTER SUMMARY..... 311

SYSTEM COMPARISONS AND TOUGHENING MECHANISMS: FRPS..... 312
8 INTRODUCTION..... 312
8.1 MODE I FRACTURE ENERGY..... 313
8.2 FRP FRACTURE COMPARISONS AND TOUGHENING MECHANISMS..... 317
8.2.1 Unmodified Epoxy Matrices..... 317
8.2.2 Nano-silica Modified Matrices..... 318
8.2.3 Rubber Modified Matrices..... 319
8.2.4 Hybrid Modified Matrices..... 321
8.2.5 Summary..... 323
8.3 FLEXURAL MODULUS..... 323
8.4 CHAPTER SUMMARY..... 325

CONCLUSIONS AND FUTURE WORK..... 327
9 BACKGROUND..... 327
9.1 MATERIAL PROPERTIES OF THE EPOXY-BASED SYSTEMS..... 327
9.1.1 Amine-cured DGEBA-based System..... 327
9.1.2 Amine-cured TGMDA-based System..... 329
9.1.3 Anhydride-cured DGEBA-based System..... 330
9.2 TOUGHENING MICROMECHANISMS..... 331
9.2.1 Toughening Micromechanisms in the Bulk Epoxy Polymers..... 332
9.2.2 Toughening Micromechanisms in the FRPs..... 332
9.3 CONCLUDING REMARKS..... 333
9.4 FUTURE WORK..... 334

REFERENCES..... 337

APPENDIX..... 347

LIST OF FIGURES

Figure 2.1.1. Classification of polymers [22]. 41
Figure 2.1.2. General formula of DGEBA resins. When n=0 the molecular weight is 340, when n = 10 the molecular weight is 3000. Commercial resins seldom have average molecular weights exceeding 4000 [25]. 42
Figure 2.1.3. Chemical formula of tetraglycidyl methylenedianaline (TGMDA) [27]. . 43
Figure 2.2.1. Modes of loading: (a) Mode I, cleavage or tensile-opening mode; (b) Mode II, in-plane shear mode; (c) Mode III, anti-plane shear mode [21] 47
Figure 2.2.2. Irwin's model of the plastic zone at crack tip [34]. 48
Figure 2.2.3. Schematic variation of elastic/plastic stresses ahead of a crack as a function of distance, r: (a) In plane stress ($\sigma_3 = 0$); and (b) in plane strain ($e_3 = 0$) [36]. 49
Figure 2.2.4. Dugdale's line plastic-zone model [37] 50
Figure 2.3.1. Schematic of a typical stress-strain curve for glassy polymers [39]. 52
Figure 2.5.1. Transmission electron microscope image of a thin section of a CTBN rubber toughened epoxy polymer [52] (Red arrows point to some rubber particles). 56
Figure 2.5.2. Schematic showing the stages of the rubber-bridging mechanism [53].... 58
Figure 2.5.3. Illustration of the deformation mechanisms in rubber toughened epoxy polymers; (a) before rubber particle cavitation, and (b) after rubber particle cavitation [54]. 59
Figure 2.5.4. Distribution of the von Mises stress around rubber particles in a unit cell under triaxial loading: (a) before cavitation and (b) after cavitation [62]. 60
Figure 2.5.5. Distribution of the von Mises stress around rubber particles [57]. 61
Figure 2.5.6. Schematic representation of the different toughening mechanisms involved in the fracture of rubber toughened epoxy polymers. The diameter of the plastic, or process, zone is $2r_y$ [63]. 63
Figure 2.5.7. Variation of fracture toughness, K_{Ic}, as a function of molecular weight between cross-links, M_c [68]. 65

Figure 2.6.1. (a) Schematic representation of the crack pinning mechanism for increasing the toughness when rigid particles are present in a brittle adhesive. (b) Optical micrograph of the fracture surface of a glass particle toughened epoxy polymer showing the crack front pinned between glass particles [63]..... 70
Figure 2.6.2. Scanning electron microscope image of a fracture surface of an epoxy polymer containing spherical glass particles showing the 'tails' behind the particles [21]. 71
Figure 2.6.3. Schematic of the path of a crack around a particle in rigid particle toughened polymers under stress. (a) Crack approaching particle. (b) Crack moving around the equator of a poorly bonded particle. (c) Crack attracted to poles of a well-bonded particle [12]..... 72
Figure 2.6.4. Scanning electron microscope images of fracture surfaces of (a) sPS spheres and (b) hollow glass spheres toughened polymers [82,83] (The pink circles illustrates debonding and void growth)..... 74
Figure 2.6.5. Fluorescent microscopy images of glass sphere toughened epoxy polymers in (a) crack tip and (b) crack wake region. Note the presence of microcracks at the crack tip and in the crack wake. Arrows indicate direction of crack growth [89]..... 74
Figure 2.6.6. (a) Relationship between fracture energy, G_{Ic}, and volume fraction, V_{fr}, of rigid particle toughened epoxy polymers; (b) Relationship between K_{Ic}/K_{Ic}(matrix) and the ratio of the particle radius to inter-particle distance, r_{pa}/ID, for a glass bead toughened epoxy polymers. Δ, r_{pa}=2.5μm; , r_{pa}=31μm. Theoretical curves from (i) Evan's theory and (ii & iii) modification of Green et al. [21]..... 76
Figure 2.6.7. Fracture toughness, K_{Ic}, versus volume fraction of tougheners showing synergistic toughening [96]..... 79
Figure 2.7.1. Schematic showing VARTM process [110]..... 83
Figure 2.7.2. Schematic showing fibres debonding from an epoxy matrix [113]..... 85
Figure 2.7.3. Schematic showing fibre pull-out [113]..... 86
Figure 2.7.4. Schematic of the fibre bridging mechanism [113]..... 86

Figure 3.1.1. Transmission electron micrograph of epoxy with 5 wt. % nano-silica, showing excellent dispersion [116]. 89
Figure 3.1.2. Graph showing particle size distribution of nano-silica particles, determined by small angle neutron scattering (SANS) [116]. 89
Figure 3.3.1. Schematic of a tensile specimen. 94
Figure 3.3.2. Schematic of an SENB specimen. 96
Figure 3.4.1. Schematic of a DCB specimen. 98
Figure 3.4.2. Schematic of a specimen used to test flexural modulus. 99

Figure 4.1.1. Transmission electron micrograph of a sample containing unmodifed epoxy. 105
Figure 4.1.2. AFM images of the amine-cured DGEBA-based samples containing: (a,b) 4.6 wt. % CTBN, (c,d) 6.9 wt. % CTBN, and (e,f) 10.9 wt. % CTBN. (White arrows point to some rubber particles) 107
Figure 4.1.3. AFM image of a sample containing 4.1 wt. % CTBN and 2 wt. % nano-silica. (White arrows point to some rubber particles and blue arrows point to some nano particles) 108
Figure 4.1.4. Transmission electron micrograph of a sample containing 4.1 wt. % CTBN and 2 wt. % nano-silica. (White arrows point to some rubber particles and blue arrows point to some nano particles) 109
Figure 4.1.5. Transmission electron micrograph of a sample containing 4.1 wt. % CTBN and 4.1 wt. % nano-silica. (White arrows point to some rubber particles and blue arrows point to some nano particles) 110
Figure 4.1.6. AFM image of a sample containing 4.1 wt. % CTBN and 4.1 wt. % nano-silica. (White arrows point to some rubber particles and blue arrows point to some nano particles) 110
Figure 4.1.7. Transmission electron micrograph of a sample containing 6.9 wt. % CTBN and 3.5 wt. % nano-silica. (White arrows point to some rubber particles and blue arrows point to some nano particles) 111

Figure 4.1.8. (a) Transmission electron micrograph of a sample containing 7 wt. % CTBN and 7 wt. % nano-silica. (b) at higher magnification. (White arrow points to rubber particles, blue arrows point to some nano particles, green arrows point to some three dimensional necklace-like structures and pink arrows point to super-clumps) ... 113
Figure 4.1.9. Transmission electron micrograph of a sample containing 11.3 wt. % CTBN and 5.7 wt. % nano-silica. (White arrows point to some rubber particles and pink arrows point to some three dimensional necklace-like structures of nano-silica) 114
Figure 4.1.10. Transmission electron micrograph of a sample containing 11.6 wt. % CTBN and 11.6 wt. % nano-silica. (White arrows point to some rubber particles and pink arrows point to some super-clumps) 115
Figure 4.1.11. AFM image of a sample containing 11.6 wt. % CTBN and 11.6 wt. %. (White arrows point to some rubber particles and pink arrows point to some super-clumps) 115
Figure 4.1.12. (a) Sample DMTA traces performed at 1Hz for a sample containing 7 wt. % CTBN and 7 wt. % nano-silica, showing the loss modulus and *tan δ* values. (b) Trace of the same sample with adjusted Y-axis showing the rubber peak more clearly. 118
Figure 4.1.13. Glass transition temperatures for the amine-cured DGEBA-based bulk epoxy composites at a test frequency of 1Hz. The dashed lines separate the samples into sub-systems of similar CTBN content. 118
Figure 4.1.14. Young's moduli for all the amine-cured DGEBA-based bulk epoxy composites. (error bars are ± one standard deviation) 120
Figure 4.1.15. Comparison of Young's moduli of the hybrid versus nano-silica content. (error bars are ± one standard deviation) 122
Figure 4.1.16. Fracture energy results for all the amine-cured DGEBA-based bulk epoxy composites. (error bars are ± one standard deviation) 123
Figure 4.1.17. Fracture surface of pure epoxy (crack propagation from left to right).. 126
Figure 4.1.18. Fracture surface of pure epoxy at higher magnification (crack propagation from left to right). 126
Figure 4.1.19. Fracture surface of a sample containing 4.6 wt. % CTBN (crack propagation from left to right). 127

Figure 4.1.20. Fracture surface of a sample containing 4.6 wt. % CTBN at higher magnification (crack propagation from left to right, and red arrows point to some cavitated rubber particles). 128
Figure 4.1.21. Fracture surface of a sample containing 6.9 wt. % CTBN (crack propagation from left to right). 129
Figure 4.1.22. Fracture surface of a sample containing 6.9 wt. % CTBN at higher magnification (crack propagation from left to right and red arrows point to some cavitated rubber particles). 129
Figure 4.1.23. Fracture surface of a sample containing 10.9 wt. % CTBN (crack propagation from left to right). 130
Figure 4.1.24. Fracture surface of a sample containing 10.9 wt. % CTBN at higher magnification (crack propagation from left to right and red arrows point to some cavitated rubber particles). 131
Figure 4.1.25. Fracture surface of a sample containing 4.1 wt. % CTBN and 2 wt. % nano-silica (crack propagation from left to right). 132
Figure 4.1.26. Fracture surface of a sample containing 4.1 wt. % CTBN and 2 wt. % nano-silica at higher magnification(crack propagation from left to right and red arrows point to some cavitated rubber particles). 132
Figure 4.1.27. Fracture surface of a sample containing 4.1 wt. % CTBN and 4.1 wt. % nano-silica (crack propagation from left to right). 133
Figure 4.1.28. Fracture surface of a sample containing 4.1 wt. % CTBN and 4.1 wt. % nano-silica at higher magnification (crack propagation from left to right). 134
Figure 4.1.29. Fracture surface of a sample containing 6.9 wt. % CTBN and 3.5 wt. % nano-silica (crack propagation from left to right). 135
Figure 4.1.30. Fracture surface of a sample containing 6.9 wt. % CTBN and 3.5 wt. % nano-silica at higher magnification (crack propagation from left to right and the red arrows point to some cavitated rubber particles). 135
Figure 4.1.31. Fracture surface of a sample containing 7 wt. % CTBN and 7 wt. % nano-silica (crack propagation from left to right). 136
Figure 4.1.32. Fracture surface of a sample containing 7 wt. % CTBN and 7 wt. % nano-silica at higher magnification (crack propagation from left to right).137

Figure 4.1.33. Fracture surface of a sample containing 7 wt. % CTBN and 7 wt. % nano-silica at higher magnification (crack propagation from left to right. Pink circles around super-clumps)..... 137
Figure 4.1.34. Fracture surface of a sample containing 7 wt. % CTBN and 7 wt. % nano-silica at higher magnification (crack propagation from left to right)..... 138
Figure 4.1.35. Fracture surface of a sample containing 11.3 wt. % CTBN and 5.7 wt. % nano-silica (crack propagation from left to right)..... 139
Figure 4.1.36. Fracture surface of a sample containing 11.3 wt. % CTBN and 5.7 wt. % nano-silica at higher magnification (crack propagation from left to right). 139
Figure 4.1.37. Fracture surface of a sample containing 11.6 wt. % CTBN and 11.6 wt. % nano-silica (crack propagation from left to right)..... 140
Figure 4.1.38. Fracture surface of a sample containing 11.6 wt. % CTBN and 11.6 wt. % nano-silica at higher magnification (crack propagation from left to right. Pink circles around super-clumps)..... 141
Figure 4.2.1. Mode I interlaminar fracture energy for GFRPs with an amine-cured DGEBA matrix. (error bars are ± one standard deviation) 143
Figure 4.2.2. Fracture surface of a GFRP sample with an unmodified amine-cured epoxy matrix (crack propagation from right to left)..... 145
Figure 4.2.3. Fracture surface of a GFRP sample with an unmodified amine-cured epoxy matrix at higher magnification (crack propagation from right to left)..... 146
Figure 4.2.4. Fracture surface of a GFRP sample with an unmodified amine-cured epoxy matrix at higher magnification showing clean fibres (crack propagation from right to left)..... 146
Figure 4.2.5. Fracture surface of a GFRP sample with an amine-cured epoxy matrix containing 4.6 wt. % CTBN (crack propagation from right to left). 147
Figure 4.2.6. Fracture surface of a GFRP sample with an amine-cured epoxy matrix containing 4.6 wt. % CTBN at higher magnification (crack propagation from right to left)..... 148
Figure 4.2.7. Fracture surface of a GFRP sample with an amine-cured epoxy matrix containing 4.6 wt. % CTBN at higher magnification showing debonding at fibre-matrix interface (crack propagation from right to left). 148

Figure 4.2.8. Fracture surface of a GFRP sample with an amine-cured epoxy matrix containing 6.9 wt. % CTBN (crack propagation from right to left). 149
Figure 4.2.9. Fracture surface of a GFRP sample with an amine-cured epoxy matrix containing 6.9 wt. % CTBN at higher magnification (crack propagation from right to left). 150
Figure 4.2.10. Fracture surface of a GFRP sample with an amine-cured epoxy matrix containing 6.9 wt. % CTBN at higher magnification (crack propagation from right to left). 150
Figure 4.2.11. Fracture surface of a GFRP sample with an amine-cured epoxy matrix containing 10.9 wt. % CTBN (crack propagation from right to left). 151
Figure 4.2.12. Fracture surface of a GFRP sample with an amine-cured epoxy matrix containing 10.9 wt. % CTBN at higher magnification (crack propagation from right to left). 152
Figure 4.2.13. Fracture surface of a GFRP sample with an amine-cured epoxy matrix containing 10.9 wt. % CTBN at higher magnification (crack propagation from right to left). 152
Figure 4.2.14. Fracture surface of a GFRP sample with an amine-cured epoxy matrix containing 4.1 wt. % CTBN and 2 wt. % nano-silica (crack propagation from right to left). 153
Figure 4.2.15. Fracture surface of a GFRP sample with an amine-cured epoxy matrix containing 4.1 wt. % CTBN and 2 wt. % nano-silica at higher magnification with the evidence of fibre bridging circled in pink (crack propagation from right to left). 154
Figure 4.2.16. Fracture surface of a GFRP sample with an amine-cured epoxy matrix containing 4.1 wt. % CTBN and 2 wt. % nano-silica at higher magnification (crack propagation from right to left). 154
Figure 4.2.17. Fracture surface of a GFRP sample with an amine-cured epoxy matrix containing 6.9 wt. % CTBN and 3.5 wt. % nano-silica (crack propagation from right to left). 155
Figure 4.2.18. Fracture surface of a GFRP sample with an amine-cured epoxy matrix containing 6.9 wt. % CTBN and 3.5 wt. % nano-silica at higher magnification (crack propagation from right to left). 156

Figure 4.2.19. Fracture surface of a GFRP sample with an amine-cured epoxy matrix containing 6.9 wt. % CTBN and 3.5 wt. % nano-silica at higher magnification (crack propagation from right to left). 156
Figure 4.2.20. Fracture surface of a GFRP sample with an amine-cured epoxy matrix containing 7 wt. % CTBN and 7 wt. % nano-silica (crack propagation from right to left). 157
Figure 4.2.21. Fracture surface of a GFRP sample with an amine-cured epoxy matrix containing 7 wt. % CTBN and 7 wt. % nano-silica at higher magnification (crack propagation from right to left). 158
Figure 4.2.22. Fracture surface of a GFRP sample with an amine-cured epoxy matrix containing 7 wt. % CTBN and 7 wt. % nano-silica at higher magnification (crack propagation from right to left). 158
Figure 4.2.23. Fracture surface of a GFRP sample with an amine-cured epoxy matrix containing 11.3 wt. % CTBN and 5.7 wt. % nano-silica (crack propagation from right to left). 159
Figure 4.2.24. Fracture surface of a GFRP sample with an amine-cured epoxy matrix containing 11.3 wt. % CTBN and 5.7 wt. % nano-silica at higher magnification (crack propagation from right to left). 160
Figure 4.2.25. Fracture surface of a GFRP sample with an amine-cured epoxy matrix containing 11.3 wt. % CTBN and 5.7 wt. % nano-silica at higher magnification showing possibly un-cavitated rubber particles (crack propagation from right to left). 160
Figure 4.2.26. Fracture surface of a GFRP sample with an amine-cured epoxy matrix containing 11.6 wt. % CTBN and 11.6 wt. % nano-silica (crack propagation from right to left). 161
Figure 4.2.27. Fracture surface of a GFRP sample with an amine-cured epoxy matrix containing 11.6 wt. % CTBN and 11.6 wt. % nano-silica at higher magnification (crack propagation from right to left). 162
Figure 4.2.28. Fracture surface of a GFRP sample with an amine-cured epoxy matrix containing 11.6 wt. % CTBN and 11.6 wt. % nano-silica at higher magnification (crack propagation from right to left). 162

Figure 4.3.1. Comparison between the mean GFRP and bulk fracture energies of the amine-cured DGEBA-based system. (Dashed line indicates the 1:1 relationship between the fracture energies of the GFRPs and the bulk epoxy composites [ie. the matrices]) 165

Figure 5.1.1. AFM image of a sample containing unmodified epoxy (black arrows point to some knife marks) 169
Figure 5.1.2. AFM image of a sample containing 5 wt. % nano-silica. (Dark blue arrows point to some nano particles and light blue arrows point to some agglomerates) 170
Figure 5.1.3. AFM image of a sample containing 10 wt. % nano-silica. (Dark blue arrows point to some nano particles and light blue arrows point to some agglomerates) 171
Figure 5.1.4. AFM images of a sample containing 19.5 wt. % nano-silica. (Light blue arrows point to some agglomerates) 172
Figure 5.1.5. AFM image of a sample containing 8 wt. % CTBN. (White arrows point to some rubber particles) 173
Figure 5.1.6. AFM image of a sample containing 8 wt. % CTBN and 10 wt. % nano-silica. (White arrows point to some rubber particles and blue arrows point to some nano particles) 174
Figure 5.1.7. Glass transition temperatures for the amine-cured TGMDA-based bulk epoxy composites at a test frequency of 1Hz 175
Figure 5.1.8. Young's moduli for the amine-cured TGMDA-based bulk epoxy composites. (error bars are ± one standard deviation) 177
Figure 5.1.9. Graph showing linear increase in Young's modulus with increasing nano-silica content (error bars are ± one standard deviation). 178
Figure 5.1.10. Fracture energy results for the amine-cured TGMDA-based bulk epoxy composites (error bars are ± one standard deviation) 179
Figure 5.1.11. Fracture surface of pure epoxy (crack propagation from left to right).. 182
Figure 5.1.12. Fracture surface of pure epoxy at higher magnification (crack propagation from left to right). 182
Figure 5.1.13. Fracture surface of a sample containing 5 wt. % nano-silica (crack propagation from left to right). 183

Figure 5.1.14. Fracture surface of a sample containing 5 wt. % nano-silica at higher magnification (crack propagation from left to right). 184
Figure 5.1.15. Fracture surface of a sample containing 10 wt. % nano-silica (crack propagation from left to right). 185
Figure 5.1.16. Fracture surface of a sample containing 10 wt. % nano-silica at higher magnification (crack propagation from left to right. Blue arrows point to some nano-silica particles)..... 185
Figure 5.1.17. Fracture surface of a sample containing 19.5 wt. % nano-silica (crack propagation from left to right). 186
Figure 5.1.18. Fracture surface of a sample containing 19.5 wt. % nano-silica at higher magnification in the fast-fracture region (crack propagation from left to right). 187
Figure 5.1.19. Fracture surface of a sample containing 8 wt. % CTBN (crack propagation from left to right). 188
Figure 5.1.20. Fracture surface of a sample containing 8 wt. % CTBN at higher magnification (crack propagation from left to right and the red arrow points to a cavitated rubber particle)..... 188
Figure 5.1.21. Fracture surface of a sample containing 8 wt. % CTBN and 10 wt. % nano-silica (crack propagation from left to right)..... 189
Figure 5.1.22. Fracture surface of a sample containing 8 wt. % CTBN and 10 wt. % nano-silica at higher magnification (crack propagation from left to right)..... 190
Figure 5.2.1. Critical Mode I interlaminar fracture energy for amine-cured CFRPs with a TGMDA matrix. (error bars are ± one standard deviation)..... 192
Figure 5.2.2. Graph showing the variation in the initiation and arrest values of fracture energy with crack length for a sample containing 19.5 wt. % nano-silica. 192
Figure 5.2.3. Flexural modulus results for CFRPs with an amine-cured TGMDA-based matrix (error bars are ± one standard deviation). 194
Figure 5.2.4. Flexural modulus results for amine-cured CFRPs with a TGMDA matrix, toughened with nano-silica only (error bars are ± one standard deviation. Note: y-axis does not start at zero). 195
Figure 5.2.5. Fracture surface of a CFRP sample with an unmodified tetrafunctional epoxy matrix (crack propagation from *bottom to top*)..... 197

Figure 5.2.6. Fracture surface of a CFRP sample with an unmodified tetrafunctional epoxy matrix at higher magnification (crack propagation from *bottom to top*). 198
Figure 5.2.7. Fracture surface of a CFRP sample with a tetrafunctional epoxy matrix containing 5 wt. % nano-silica (crack propagation from *right to left*)..... 199
Figure 5.2.8. Fracture surface of a CFRP sample with a tetrafunctional epoxy matrix containing 5 wt. % nano-silica at higher magnification (crack propagation from *right to left*). 199
Figure 5.2.9. Fracture surface of a CFRP sample with a tetrafunctional epoxy matrix containing 10 wt. % nano-silica (crack propagation from *right to left*)..... 200
Figure 5.2.10. Fracture surface of a CFRP sample with a tetrafunctional epoxy matrix containing 10 wt. % nano-silica at higher magnification (crack propagation from *right to left*. Fibre bridging circled in pink). 201
Figure 5.2.11. Fracture surface of a CFRP sample with a tetrafunctional epoxy matrix containing 19.5 wt. % nano-silica (crack propagation from *right to left*)..... 202
Figure 5.2.12. Fracture surface of a CFRP sample with a tetrafunctional epoxy matrix containing 19.5 wt. % nano-silica at higher magnification (crack propagation from *right to left*. Fibre bridging circled in pink)..... 202
Figure 5.2.13. Fracture surface of a CFRP sample with a tetrafunctional epoxy matrix containing 8 wt. % CTBN (crack propagation from *right to left*). 203
Figure 5.2.14. Fracture surface of a CFRP sample with a tetrafunctional epoxy matrix containing 8 wt. % CTBN at higher magnification (crack propagation from *right to left*). 204
Figure 5.2.15. Fracture surface of a CFRP sample with a tetrafunctional epoxy matrix containing 8 wt. % CTBN at higher magnification (crack propagation from *right to left*. Cavitated rubber particles circled in pink)..... 204
Figure 5.2.16. Fracture surface of a CFRP sample with a tetrafunctional epoxy matrix containing 8 wt. % CTBN and 10 wt. % nano-silica (crack propagation from *right to left*). 205
Figure 5.2.17. Fracture surface of a CFRP sample with a tetrafunctional epoxy matrix containing 8 wt. % CTBN and 10 wt. % nano-silica at higher magnification (crack propagation from *right to left*). 206

Figure 5.2.18. Fracture surface of a CFRP sample with a tetrafunctional epoxy matrix containing 8 wt. % CTBN and 10 wt. % nano-silica at higher magnification (crack propagation from *right to left*. White arrows point to some cavitated rubber particles).206
Figure 5.3.1. Comparison between the FRP and bulk fracture energies of the amine-cured TGMDA-based system. (Dashed line indicates the 1:1 relationship between the fracture energies of the CFRPs and bulk epoxy composites [ie. the matrices]) 210

Figure 6.1.1. (a) Transmission electron micrograph of a sample containing unmodified epoxy (b) AFM image of a sample containing unmodified epoxy. 213
Figure 6.1.2. Transmission electron micrograph of a sample containing 5 wt. % nano-silica. (Blue arrows point to some nano particles) 214
Figure 6.1.3. Transmission electron micrograph of a sample containing 14.8 wt. % nano-silica. (Blue arrows point to some nano particles) 215
Figure 6.1.4. AFM image of a sample containing 14.8 wt. % nano-silica. (Blue arrows point to some nano particles) 215
Figure 6.1.5. Transmission electron micrograph of a stained sample containing 9 wt. % CTBN. (White arrows point to some rubber particles. Ignore circular grid) 216
Figure 6.1.6. AFM image of a sample containing 9 wt. % CTBN. (White arrows point to some rubber particles) 217
Figure 6.1.7. Transmission electron micrograph of a sample containing 18 wt. % CTBN. (White arrows point to some rubber particles) 218
Figure 6.1.8. Transmission electron micrograph of a sample containing 5.03 wt. % CTBN and 5.03 wt. % nano-silica. (White arrows point to some rubber particles and blue arrows point to some nano particles) 219
Figure 6.1.9. Transmission electron micrographs of a sample containing 9 wt. % CTBN and 2.3 wt. % nano-silica. (White arrows point to some rubber particles and blue arrows point to some nano-silica agglomerates) 220
Figure 6.1.10. AFM image of a sample containing 9 wt. % CTBN and 10.5 wt. % nano-silica. (White arrows point to some rubber particles and blue arrows point to some nano-silica agglomerates) 220

Figure 6.1.11. Transmission electron micrograph of a sample containing 9 wt. % CTBN and 15.4 wt. % nano-silica. (White arrows point to some rubber particles, blue arrows point to some nano-silica agglomerates and green arrows point to scanning artefacts)221
Figure 6.1.12. AFM image of a sample containing 9 wt. % CTBN and 15.4 wt. % nano-silica. (White arrows point to some rubber particles, blue arrows point to some nano-silica agglomerates) 222
Figure 6.1.13. Transmission electron micrograph for a sample containing 12 wt. % CTBN and 12 wt. % nano-silica. (White arrows point to some rubber particles, blue arrows point to some nano-silica agglomerates) 223
Figure 6.1.14. Transmission electron micrograph for a sample containing 18 wt. % CTBN and 9 wt. % nano-silica. (Blue arrows point to some nano-silica agglomerates) 224
Figure 6.1.15. Transmission electron micrograph for a sample containing 18 wt. % CTBN and 18 wt. % nano-silica. (Blue arrows point to some nano-silica agglomerates) 224
Figure 6.1.16. AFM image for a sample containing 18 wt. % CTBN and 18 wt. % nano-silica. (Blue arrows point to some nano-silica agglomerates, white arrows point to possible CTBN particles) 225
Figure 6.1.17. (a) Sample DMTA trace performed at 1Hz for a sample containing 9 wt. % CTBN and 10.5 wt. % nano-silica. (b) Trace of same sample with adjusted Y-axis showing the rubber peak more clearly. 227
Figure 6.1.18. Glass transition temperatures for the anhydride-cured DGEBA-based bulk epoxy composites at a test frequency of 1Hz. The dashed lines separate the samples into sub-systems of similar CTBN content. 228
Figure 6.1.19. Young's moduli for samples containing 0% and 9% CTBN. (error bars are ± one standard deviation) 231
Figure 6.1.20. Fracture energy versus nano-silica content, for samples containing 0 and 9 wt. % CTBN 233
Figure 6.1.21. Fracture energy versus CTBN content for samples containing 0 and 9 wt. % nano-silica content. 233
Figure 6.1.22. Fracture surface of pure epoxy (crack propagation from left to right).. 237
Figure 6.1.23. Fracture surface of a pure epoxy sample (crack propagation from *right* to *left*). 237

Figure 6.1.24. Fracture surface of a sample containing 4.1 wt. % nano-silica only (crack propagation from left to right). 238
Figure 6.1.25. Fracture surface of a sample containing 20.2 wt. % nano-silica only (crack propagation from left to right). 239
Figure 6.1.26. Fracture surface of a sample containing 14.8 wt. % nano-silica only. Blue arrows point to some nano particles. Box indicates area to be enlarged in the following figure. (crack propagation from *top right to bottom left*) 240
Figure 6.1.27. Enlargement of boxed area in previous Figure. Blue arrows point to some nano particles and voids around them 240
Figure 6.1.28. Fracture surface of a sample containing 6 wt. % CTBN. (crack propagation from left to right). 241
Figure 6.1.29. Fracture surface of a sample containing 6 wt. % CTBN. Cavitated rubber particles are indicated by white arrows (crack propagation from left to right). 241
Figure 6.1.30. Fracture surface of a sample containing 9 wt. % CTBN. (crack propagation from left to right). 242
Figure 6.1.31. Fracture surface of a sample containing 9 wt. % CTBN. Cavitated rubber particles are indicated by white arrows (crack propagation from left to right). 242
Figure 6.1.32. Fracture surface of a sample containing 18 wt. % CTBN. (crack propagation from left to right). 243
Figure 6.1.33. Fracture surface of a sample containing 18 wt. % CTBN at higher magnification. (crack propagation from left to right). 244
Figure 6.1.34. Fracture surface of a sample containing 9 wt. % CTBN and 2.3 wt. % nano-silica. (crack propagation from left to right) 245
Figure 6.1.35. Fracture surface of a sample containing 9 wt. % CTBN and 10.5 wt. % nano-silica. (crack propagation from left to right) 246
Figure 6.1.36. Fracture surface of a sample containing 9 wt. % CTBN and 10.5 wt. % nano-silica at higher magnification. Cavitated rubber particles are indicated by white arrows. (crack propagation from left to right). 246

Figure 6.1.37. FEG-SEM image of the fracture surface of a sample containing 9 wt. % CTBN and 10.5 wt. % nano-silica. A possible rubber cavity is indicated by the white arrow. Agglomerates of nano-silica are indicated by the dark blue arrows, and voids by light blue arrows. (crack propagation from left to right). 247
Figure 6.1.38. Fracture surfaces of hybrid samples containing: (a) 12 wt. % CTBN and 6 wt. % nano-silica, (b) 12 wt. % CTBN and 12 wt. % nano-silica, (c) 18 wt. % CTBN and 9 wt. % nano-silica, and (d) 18 wt. % CTBN and 18 wt. % nano-silica (crack propagation from left to right). 248
Figure 6.2.1. Sample graph showing the Mode I fracture energy (initiation and arrest) versus the crack length for a sample containing 9 wt. % CTBN and 10.5 wt. % nano-silica. 249
Figure 6.2.2. Mode I interlaminar fracture energy for CFRPs with an anhydride-cured DGEBA matrix. (error bars are ± one standard deviation) 250
Figure 6.2.3. Fracture surface of a CFRP sample with an unmodified anhydride-cured epoxy matrix (crack propagation from right to left). 252
Figure 6.2.4. Fracture surface of a CFRP sample with an unmodified anhydride-cured epoxy matrix at higher magnification (crack propagation from right to left). 252
Figure 6.2.5. Fracture surface of a CFRP sample with an anhydride-cured epoxy matrix containing 11.9 wt. % nano-silica only (crack propagation from right to left). 253
Figure 6.2.6. Fracture surface of a CFRP sample with an anhydride-cured epoxy matrix containing 11.9 wt. % nano-silica only at higher magnification (crack propagation from right to left). 254
Figure 6.2.7. Fracture surface of a CFRP sample with an anhydride-cured epoxy matrix containing 9 wt. % CTBN (crack propagation from right to left). 255
Figure 6.2.8. Fracture surface of a CFRP sample with an anhydride-cured epoxy matrix containing 9 wt. % CTBN at higher magnification (crack propagation from right to left). 255
Figure 6.2.9. Fracture surface of a CFRP sample with an anhydride-cured epoxy matrix containing 9 wt. % CTBN only at higher magnification. White arrows point to some cavitated rubber particles (crack propagation from right to left). 256

Figure 6.2.10. Fracture surface of a CFRP sample with an anhydride-cured epoxy matrix containing 9 wt. % CTBN and 2.3 wt. % nano-silica (crack propagation from right to left). 257
Figure 6.2.11. Fracture surface of a CFRP sample with an anhydride-cured epoxy matrix containing 9 wt. % CTBN and 2.3 wt. % nano-silica at higher magnification (crack propagation from right to left). 257
Figure 6.2.12. Fracture surface of a CFRP sample with an anhydride-cured epoxy matrix containing 9 wt. % CTBN and 2.3 wt. % nano-silica at higher magnification (crack propagation from right to left). 258
Figure 6.2.13. Fracture surface of a CFRP sample with an anhydride-cured epoxy matrix containing 9 wt. % CTBN and 10.5 wt. % nano-silica (crack propagation from right to left). 259
Figure 6.2.14. Fracture surface of a CFRP sample with an anhydride-cured epoxy matrix containing 9 wt. % CTBN and 10.5 wt. % nano-silica at higher magnification (crack propagation from right to left). 259
Figure 6.2.15. Flexural modulus results for CFRPs with an anhydride-cured DGEBA matrix. (error bars are ± one standard deviation) 260
Figure 6.2.16. Fibre volume fraction for CFRPs with an anhydride-cured DGEBA based matrix. (error bars are ± one standard deviation) 261
Figure 6.2.17. A comparison of the flexural moduli, with the fibre volume fractions for the CFRPs. 262
Figure 6.2.18. Comparison of calculated and measured moduli for the CFRPs..... 262
Figure 6.3.1. Comparison of bulk and CFRP fracture energies..... 268

Figure 7.1.1. Microscopy images showing the microstructure of the unmodified epoxies of the: (a) amine-cured DGEBA-based system, (b) amine-cured TGMDA-based system and (c) anhydride-cured DGEBA-based system (ignore arc-like feature)..... 271
Figure 7.1.2. AFM images of (a) an amine-cured DGEBA-based sample with 6.9 wt. % CTBN, (b) an amine-cured TGMDA-based sample with 8 wt. % CTBN, and (c) an anhydride-cured DGEBA-based sample with 9 wt. % CTBN. 272

Figure 7.1.3. Micrographs of (a) an amine-cured TGMDA-based sample with 5 wt. % nano-silica, and (b) an anhydride-cured DGEBA-based sample with 5 wt. % nano-silica [38]. 275
Figure 7.1.4. TEM images of amine-cured DGEBA-based samples containing: (a) 4.1 wt. % CTBN and 2 wt. % nano-silica, (b) 11.3 wt. % CTBN and 5.7 wt. % nano-silica, (c) 7 wt. % CTBN and 7 wt. % nano-silica, and (d) 11.6 wt. % CTBN and 11.6 wt. % nano-silica. (White arrow points to some rubber particles, blue arrows point to some nano particles, green arrows point to some three dimensional necklace-like structures and pink arrows point to super-clumps.) 277
Figure 7.1.5. AFM image of an amine-cured TGMDA-based samples with (a) 8 wt. % CTBN-only, and (b) 8 wt. % CTBN and 10 wt. % nano-silica. 278
Figure 7.1.6. TEM micrographs of anhydride-cured DGEBA-based samples containing: (a) 5.03 wt. % CTBN and 5.03 wt. % nano-silica, (b) 9 wt. % CTBN and 2.3 wt. % nano-silica, (c) 9 wt. % CTBN and 15.4 wt. % nano-silica, and (d) 18 wt. % CTBN and 18 wt. % nano-silica 279
Figure 7.2.1. Graphs showing the glass transition temperature at 1Hz for the: (a) amine-cured DGEBA-based system, (b) amine-cured TGMDA-based system, and (c) anhydride-cured DGEBA-based system. 282
Figure 7.2.2. Graphs comparing the Young's moduli for all three systems containing: (a) nano-silica only, and (b) CTBN only. The points are the experimental data, and the lines are a linear best-fit to the data. 285
Figure 7.2.3. Comparison of predicted tensile modulus with experimental results of samples with only nano-silica from the: (a) amine-cured TGMDA-based system, and (b) anhydride-cured DGEBA-based system. 286
Figure 7.2.4. Comparison of predicted tensile modulus with experimental results of samples with CTBN-only from the amine-cured DGEBA-based system. 287
Figure 7.2.5. Graph showing the relative fracture energy results of the nano-only samples for the amine-cured TGMDA-based system and the anhydride-cured DGEBA-based system. The lines are the polynomial best-fit lines to the data. 288
Figure 7.2.6. Graph showing the relative fracture energy results of the CTBN-only samples for all three systems. The lines are the polynomial best-fit lines to the data.. 289

Figure 7.2.7. Graph showing the relative fracture energy results of the hybrid samples containing ~8 wt. % CTBN relative to their respective ~8 wt. % CTBN-only fracture energies for all three systems. The lines are the polynomial best-fit lines to the data.. 291
Figure 7.3.1. SEM micrographs of the fracture surfaces of samples from: (a) the amine-cured DGEBA-based system containing 6.9 wt. % CTBN (the stress-whitened region is indicated by the pink parenthesis), (b) the amine-cured TGMDA-based system containing 8 wt. % CTBN, and (c) the anhydride-cured DGEBA-based system containing 6 wt. % CTBN. 293
Figure 7.3.2. Higher magnification SEM micrographs of the fracture surfaces of samples from: (a) the amine-cured DGEBA-based system containing 6.9 wt. % CTBN, (b) the amine-cured TGMDA-based system containing 8 wt. % CTBN, and (c) the anhydride-cured DGEBA-based system containing 6 wt. % CTBN. 294
Figure 7.3.3. Schematic showing the crack tip, with the calculated crack opening displacement and nano particles for the epoxy polymer containing approximately 4.1 wt. % nano-silica 296
Figure 7.3.4. Mean roughness of the fracture surfaces versus measured toughening increment, Ψ. The wt. % of nano-silica is shown in brackets 298
Figure 7.3.5. FEG-SEM micrographs of the fracture surface of a sample containing 14.8 wt. % nano-silica. (Voids with nano-silica particles are circled in the middle and last image.) 300
Figure 7.3.6. FEG-SEM micrograph of the fracture surface of the pure epoxy. 301
Figure 7.3.7. AFM height image of a fracture surface of the epoxy polymer containing 14.8 wt. % nano-silica 302
Figure 7.3.8. Surface profile of the dashed line drawn across the nano-silica particle and void in the previous Figure. 302
Figure 7.3.9. FEG-SEM micrograph of the fracture surface of an amine-cured TGMDA-based sample with 10 wt. % nano-silica. 308

Figure 8.1.1. Mode I (initiation) interlaminar fracture energies calculated using the CBT method for laminates with matrices of: (a) amine-cured DGEBA, (b) amine-cured TGMDA, and (c) anhydride-cured DGEBA. (The 'control' employs the appropriate unmodified epoxy as the matrix for the FRP.) 314
Figure 8.1.2. Comparison between the interlaminar FRP and bulk epoxy fracture energies for the: (a) amine-cured DGEBA-based system, (b) amine-cured TGMDA-based system, and (c) anhydride-cured DGEBA-based system (Note: the hybrid toughened systems are circled in pink in Figure 8.1.2 (c)). 316
Figure 8.2.1. Micrographs of the fracture surface of laminates with unmodified matrices from the: (a) amine-cured DGEBA-based system, (b) amine-cured TGMDA-based system, and (c) anhydride-cured DGEBA-based system 317
Figure 8.2.2. Micrographs of the fracture surface of laminates with the following matrices: (a) 5 wt. % nano-silica in an amine-cured TGMDA-based system, (b) 10 wt. % nano-silica in an amine-cured TGMDA-based system, (c) 19.5 wt. % nano-silica in an amine-cured TGMDA-based system, and (d) 11.5 wt. % nano-silica in an anhydride-cured DGEBA-based system. 319
Figure 8.2.3. Micrographs of the fracture surface of laminates with the following matrices: (a) 6.9 wt. % CTBN in an amine-cured DGEBA-based system, (b) 8 wt. % CTBN in an amine-cured TGMDA-based system, and (c) 9 wt. % CTBN in an anhydride-cured DGEBA-based system. 320
Figure 8.2.4. Micrographs of the fracture surface of laminates with the following matrices: (a) 8 wt. % CTBN and 10 wt. % nano-silica in an amine-cured TGMDA-based system, and (b) 9 wt. % CTBN and 2.3 wt. % nano-silica in an anhydride-cured DGEBA-based system. 322
Figure 8.3.1. Flexural modulus results for laminates with the following matrices: (a) amine-cured TGMDA, and (b) anhydride-cured DGEBA. 325

LIST OF TABLES

Table 4.1.1. Summary of all the amine-cured DGEBA-based bulk epoxy composites investigated. 104
Table 4.1.2. Summary of the microstructure of samples from the amine-cured DGEBA-based bulk epoxy composites. (NA = Not Applicable) 116
Table 4.1.3. Summary of the glass transition temperatures of the epoxy for all the amine-cured DGEBA-based bulk epoxy composites, tested at a frequency of 1 Hz. 119
Table 4.1.4. Summary of Young's Moduli for all the amine-cured DGEBA-based bulk epoxy composites (± one standard deviation). 121
Table 4.1.5. Summary of fracture results for all the amine-cured DGEBA-based bulk epoxy composites (± one standard deviation). 123
Table 4.2.1. Summary of the Mode I interlaminar fracture energies for GFRPs with an amine-cured DGEBA matrix. (*only one sample tested for this formulation) 143

Table 5.1.1. Summary of all amine-cured TGMDA-based bulk epoxy composites investigated. 168
Table 5.1.2. Summary of the microstructure of samples from the amine-cured TGMDA-based bulk epoxy composites. (NA = Not Applicable) 174
Table 5.1.3. Summary of glass transition temperatures for the amine-cured TGMDA bulk epoxy composites tested at a frequency of 1Hz. 176
Table 5.1.4. Summary of the Young's moduli for the amine-cured TGMDA-based bulk epoxy composites (± one standard deviation). 177
Table 5.1.5. Summary of fracture toughness and energies for the amine-cured TGMDA-based bulk epoxy composites (± one standard deviation). 179
Table 5.2.1 Summary of the Mode I interlaminar fracture energies for amine-cured CFRPs with a TGMDA matrix. (± one standard deviation) 193
Table 5.2.2. Summary of flexural moduli for CFRPs with an amine-cured TGMDA-based matrix. (± one standard deviation) 194

Table 5.3.1. Summary of all mean values for the material properties (bulk composite and CFRPs) of the amine-cured TGMDA-based system. 208

Table 6.1.1. Summary of all the anhydride-cured DGEBA-based samples investigated.212
Table 6.1.2. Summary of the rubber and nano-silica morphology in the anhydride-cured DGEBA-based bulk epoxy composites. (NA = Not Applicable) 226
Table 6.1.3. Summary of the glass transition temperatures of the epoxy for all the anhydride-cured DGEBA-based bulk epoxy composites, tested at a frequency of 1Hz.229
Table 6.1.4. Summary of Young's moduli for the anhydride-cured DGEBA-based bulk epoxy composites (± one standard deviation). 231
Table 6.1.5. Summary of fracture toughness and energies for all bulk anhydride-cured samples (± one standard deviation)..... 234
Table 6.2.1. Summary of the Mode I interlaminar fracture energy for CFRPs with an anhydride-cured DGEBA matrix. (± one standard deviation)..... 250
Table 6.2.2. Summary of the calculated flexural moduli of the CFRPs. 263
Table 6.3.1. Summary of the mean values of the material properties for the anhydride-cured DGEBA-based bulk samples. ('ND' means No Data)..... 265

Table 7.1.1. Summary of the rubber morphology. (*ND* – No Data) 273
Table 7.1.2. Summary of the nano-silica morphology..... 275
Table 7.1.3. Summary of the rubber and nano-silica morphology of the hybrid samples.280
Table 7.3.1. Material properties of the unmodified epoxy, and constants used for calculation of the fracture energy, G_{Ic}, and for the contribution to the increase in fracture energy from the plastic void growth mechanism, ΔG_v. (Ref. 1 - measured in present work) 304
Table 7.3.2. Measured and predicted toughening increments. Predicted values calculated assuming that $\Psi = \Delta G_v$. (Note $G_{Icu} = 103 J/m^2$.)..... 305
Table 7.3.3. Summary of fracture energy results showing synergy for epoxies based upon the anhydride-cured DGEBA-based system. The blue cells denote the hybrids. The fourth column, ΔG, denotes the difference in measured fracture energy for rubber-only, nano-only and hybrid samples compared to the unmodified epoxy. (*NA* – Not applicable) 310

NOMENCLATURE

English Alphabet

a	crack length
A	cross sectional area of the sample in the gauge region
B	width of specimen (plate thickness)
d_p	2nd phase particle diameter
e	extension of the gauge length
e_1, e_2, e_3	plane strains
E	modulus
E_f	Young's modulus
E_c	Young's modulus of composite
E_m	Young's modulus of matrix
F	large displacement correction
G_c	critical energy required for crack growth
G_{Ic}	Mode I critical fracture energy
G_{Icu}	Mode I critical fracture energy for unmodified epoxy polymer
K	stress intensity factor
k_E	generalised Einstein coefficient
K_c	critical stress intensity factor
K_{Ic}	Mode I critical stress intensity factor
l_1	centre of the loading pin to the midplane of the specimen
l_2	distance from the loading pin centre to the edge of the end block
L	specimen length
L_0	gauge length
L_s	support span
m_p	plastic constraint factor
M_c	average molecular weight between cross-links
M_f	mass of fibres
M_{FRP}	mass of the FRP laminate sample

N	the end block correction factor
P	load
P_{Ic}	critical Mode I load
P_c	critical load
r, θ	polar coordinates
r_{pa}	particle radius
r_y	plastic zone radius
R	length of plastic zone
R_{cr}	rate of crosshead motion in mm/min
s	slope of the tangent
T_g	glass transition temperature
T_{gc}	glass transition temperature of composite
T_{ge}	glass transition temperature of pure epoxy
T_{gr}	glass transition temperature of rubber
U	potential energy
V_f	volume fraction
V_{max}	maximum volume fraction of particles
w	aspect ratio

Greek Alphabet

γ	surface free energy
δ	displacement
δ_{tc}	crack-opening displacement
Δ_I	Mode I crack length correction
ΔG_s	increase in fracture energy due to shear yielding
ΔG_v	increase in fracture energy due to plastic void growth
ΔG_y	increase in fracture energy due to rubber-bridging
ν	Poisson's ratio
ρ_{FRP}	density of the FRP laminate sample
ρ_f	density of the fibres
$\sigma_1, \sigma_2, \sigma_3$	plane stresses
σ_{ij}	components of stress tensor
σ_y	uniaxial tensile yield stress
Ψ	overall toughening contribution
ζ	shape factor

ABBREVIATIONS

AFM	atomic force microscope
CBT	corrected beam theory
CTBN	carboxy-terminated butadiene-acrylonitrile
DCB	double cantilever beam
DMTA	dynamic mechanical thermal analysis
DGEBA	diglycidyl ether of bisphenol-A
EEW	epoxy equivalent weight
ETBN	epoxy-terminated butadiene-acrylonitrile
FEG-SEM	scanning electron microscope with a field emission gun attached
FRP	fibre reinforced polymer
HTBN	hydroxyl-terminated butadiene-acrylonitrile
ID	inter-particle distance
LEFM	linear elastic fracture mechanics
PAN	polyacrylonitrile
PTFE	polytetrafluoroethylene
SANS	small angle neutron scattering
SENB	single edge notch bend specimen
SEM	scanning electron microscope
sPS	syndiotactic polystyrene
SiO_2	silica
TEM	transmission electron microscope
TGMDA	tetraglycidyl methylenedianaline
UD	uni-directional
VARTM	vacuum assisted resin transfer moulding
VTBN	vinyl-terminated butadiene-acrylonitrile

CHAPTER 1

INTRODUCTION

1 Background

Composites have been used in different forms and in a variety of applications since the dawn of civilisation itself. Indeed, a crude composite of tar and straw was used to join bricks in Babylon more than four thousand years ago [1].

A composite material may be defined as being made up of two or more components, and consisting of two or more phases [2]. Whilst this definition holds true even for Babylonian construction techniques, the materials used today are much more advanced.

Epoxy polymers are widely used for the matrices of FRPs and as adhesives. When cured, epoxies are amorphous and highly-crosslinked (i.e. thermosetting) polymers. This microstructure results in many useful properties for structural engineering applications, such as a high modulus and failure strength, low creep, and good performance at elevated temperatures [113].

However, these benefits come at a price, since the structure of such thermosetting polymers also leads to a highly undesirable property: they are relatively brittle materials, with a poor resistance to crack initiation and crack growth. Nevertheless, it has been well established for many years that the addition of a second micro-phase of a dispersed rubber [3-7], or a thermoplastic polymer [8-10] into the epoxy can increase its toughness. The phase-separated rubber particles or thermoplastic particles are usually between 0.1 to 5μm in diameter with a volume fraction of about 5-20%. Again, there is

a price to pay because the presence of the rubbery phase typically increases the viscosity of the epoxy monomer mixture and reduces the modulus of the cured epoxy polymer.

As a result, inorganic particles have also been used, as these can increase the toughness and stiffness without affecting the glass transition temperature of the epoxy. In this case glass beads or ceramic (e.g. silica or alumina) particles with a diameter of between 4 and 100μm are typically used [11-16]. However, these relatively large particles also significantly increase the viscosity of the resin, reducing the ease of processing. In addition, due to the relatively large size of these particles they are unsuitable for use with infusion processes for the production of FRPs as they are strained out due to the small gaps between the fibres.

More recently, a new technology has emerged which holds promise for increasing the mechanical performance of such thermosetting polymers. This is via the addition of a nano-phase structure in the polymer, where the nano-phase consists of small rigid particles of silica [17-20] where all three dimensions are in the nanometre range (diameter of ~20nm). Due to the very small size of the silica particles and its non-agglomeration, there is no significant increase in the viscosity of the epoxy monomer. The very small size of the nano-silica particles (and the low resin viscosity) have made the addition of nano-silica attractive for use with infusion processes for producing FRPs, since the particles would not be strained out by the fibres.

1.1 Aims and Objectives

The overall aim of the present work is to investigate the mechanical properties and fracture of epoxy-based polymers and FRPs that have been modified with CTBN and nano-silica. The objectives can be broken down as follows:

- To investigate the thermo-mechanical properties and fracture of different epoxy polymers:
  - cured with different hardeners,
  - modified with nano-silica particles and/or rubber.
- To relate the thermo-mechanical properties to their microstructure.

- To determine the fracture mechanisms occurring in the modified and unmodified bulk epoxy polymers, and in particular, to explain the fracture mechanisms caused by the nano-silica particles.

- To evaluate the transfer of properties from the bulk epoxy polymers, to its use as a matrix in FRPs.

- To determine the fracture mechanisms occurring in the FRPs.

1.2 Thesis Outline

The structure of the thesis is organised as follows:

- Chapter 2 reviews literature pertaining to the subject being studied, and introduces the reader to the various terms that will be used in the course of the thesis. It discusses the fracture mechanics of materials, as well as the fracture mechanisms responsible for toughening epoxies and FRPs.

- Chapter 3 details the materials used in this study, as well as the experimental methods and conditions used to obtain the results in the subsequent Chapters.

- Chapter 4 presents and discusses the results obtained from testing an amine-cured diglycidyl ether of bis-phenol A (DGEBA)-based system (bulk epoxy polymer and FRP).

- Chapter 5 presents and discusses the results obtained from testing an amine-cured tetraglycidyl methylene dianiline (TGMDA)-based system (bulk epoxy polymer and FRP).

- Chapter 6 presents and discusses the results obtained from testing an anhydride-cured DGEBA-based system (bulk epoxy polymer and FRP).

- Chapter 7 compares and contrasts the results of the three bulk epoxy-based systems that were investigated. It also details the possible rubber and nano-silica toughening mechanisms observed.

- Chapter 8 compares and contrasts the results of the FRPs of the three epoxy-based systems that were investigated. It also details possible FRP toughening mechanisms observed.

- Chapter 9 states the conclusions of the research and recommends future work to add to the field of study.

CHAPTER 2

LITERATURE REVIEW

2 Introduction

This Chapter introduces the reader to some of the terms that will be used in the rest of the Thesis and reviews some of the important theories and previous work carried out in the field.

The reader will see the gaps in the present knowledge and progress in the subjects, and will therefore see the justification in carrying out these investigations to add to the field.

The present study involves epoxies that have been toughened with rubber and rigid nano-silica, and their subsequent use as the matrix in fibre reinforced polymers (FRPs). As a result, this chapter will discuss epoxy polymers and FRPs and give a brief introduction to the fracture mechanics applicable to this study. It also explores various toughening agents used, and their toughening mechanisms in both epoxy and fibre composite. This will focus on the use of rubber and silica particles, as well as the motivation for using nano-sized silica particles.

2.1 Epoxy Polymers

A polymer can be defined as a long molecule containing atoms held together by primary covalent bonds along the molecule [21]. The word 'polymer' describes a wide family of different polymeric materials with a wide range of properties and chemical structures. The most common way of classifying polymers is outlined in Figure 2.1.1, where they can be subdivided into three main categories:

- *Thermoplastics* - linear or branched polymers which consist of individual long chain molecules. In principle, any thermoplastic can melt upon heating
- *Elastomers* - lightly cross-linked polymers which contain looser three dimensional networks. They are often used interchangeably with the term 'rubbers' [22,23].
- *Thermosets* - rigid, highly cross-linked polymers which contain an infinite three dimensional network. They degrade rather than melt upon the application of heat

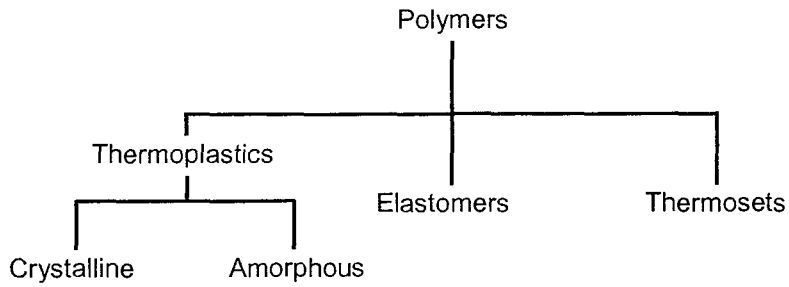


Figure 2.1.1. Classification of polymers [22].

Thermoplastics can be separated into two subgroups, *crystalline* and *amorphous*. However, thermoplastics do not crystallise easily upon cooling to the solid state, as crystallisation requires substantial ordering of the highly coiled and entangled macromolecules present in the liquid state. Thus crystalline thermoplastics do not form perfectly crystalline material but instead are *semi-crystalline*, with both crystalline and amorphous regions. Nevertheless, many thermoplastics are completely amorphous and incapable of crystallisation [22]. Some common examples of thermoplastics are polyethylene and polypropylene.

Elastomers include natural rubber, polysiloxane and acrylonitrile butadiene copolymer (as used in this study). They have the ability to be deformed to quite large deformations

and then elastically spring back to their original form [28]. Elastomers are lightly crosslinked, and for natural rubber this is achieved by a non-reversible process called *vulcanisation*, which involves adding sulphur to the heated elastomer.

Epoxy polymers are thermosets which have been widely used as adhesives, bulk composites and as matrices for FRPs due to the cross-linking reaction (which occurs in the production of thermosets) which can be used to give good adhesion to other materials [23]. The final products generally exhibit advantages such as excellent electrical insulation properties, high modulus, low shrinkage, and good moisture resistance [24].

Epoxy resins refer to a family of molecules containing more than one epoxide group which may lie within the body of the molecule, but is usually terminal [6]. The most commonly used epoxy resin is the diglycidyl ether of bisphenol-A (DGEBA), the chemical formula of which is shown in Figure 2.1.2. It is made from epichlorohydrin and the disodium salt of bisphenol-A and is one of the most common resins used in industrial applications.

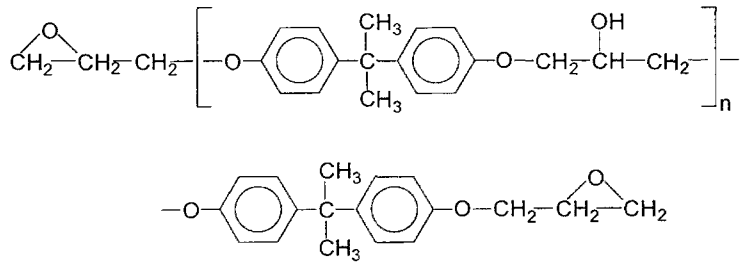


Figure 2.1.2. General formula of DGEBA resins. When n=0 the molecular weight is 340, when n=10 the molecular weight is 3000. Commercial resins seldom have average molecular weights exceeding 4000 [25].

Another epoxy resin (used in this study) is tetraglycidyl methylenedianaline (TGMDA), and its chemical formula can be seen in Figure 2.1.3. This epoxy resin is used when operational requirements call for high service temperature and the best attainable mechanical properties, particularly in carbon-fibre-reinforced systems [26].

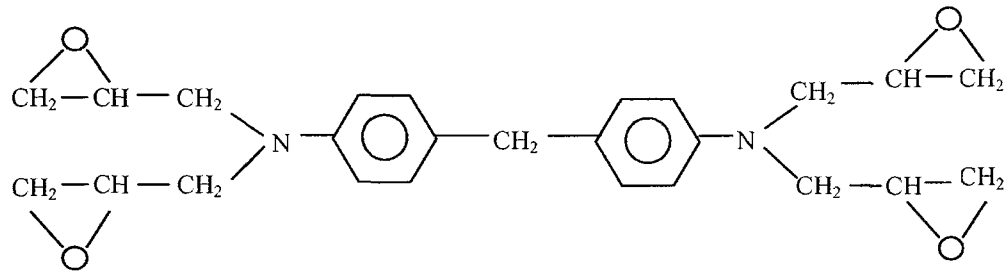


Figure 2.1.3. Chemical formula of tetraglycidyl methylenedianaline (TGMDA) [27].

2.1.1 Curing

The chemical chosen to react with these epoxides to cross-link the polymer is referred to as the curing agent (or hardener), and it typically has active hydrogen attached to nitrogen, oxygen, or sulphur [24]. The selection of the curing agent depends on many parameters and determines to a large extent, the cross-link density, glass transition temperature and modulus. Furthermore, some systems use several additives other than curing agents to improve processing properties (such as viscosity, shrinkage, curing temperature and storage life). Ultimately, the cure conditions (i.e. duration and temperature) will also affect the kinetics and extent of each of the above processes, and hence have a profound effect on the subsequent microstructure [29].

The most common curing agents used with epoxy resins are based upon amines [22]. Primary aliphatic amines react with epoxy resins at room temperature without the presence of a catalyst. A number of aromatic amines also react with epoxy resins at room temperature and the final products have significantly higher heat distortion temperatures than products obtained with aliphatic amines. These room temperature curing adhesives are delivered as two component pastes.

Anhydrides are also used as curing agents with epoxy resins, and give lower exotherms on cure when compared with amine cured systems [25]. Moreover, some systems provide cured resins with very high heat distortion temperatures and with generally good physical, electrical and chemical properties. In this study, both amine and anhydride curing agents are used.

In addition to the amine and anhydride curing agents, many other curing agents have been made available. These include a number of amides that contain amine groups [25].

Among them are polyamides which form the basis of some domestic adhesives. One of the main advantages of the system is that roughly similar quantities of curing agent and resin are required and since this is not too critical, adequate metering can be done visually. Dicyandiamide is also used with epoxy resins for adhesives which is insoluble in common resins at room temperature but dissolves at elevated temperatures [25]. Hence the package of epoxy resin and dicyandiamide is available as single component paste or film adhesives.

2.2 Fracture Mechanics

For centuries, structures have been known to fail in a brittle manner. The failures have occurred for many reasons, including uncertainties in the loading or environment, defects in the materials, inadequate design, and deficiencies in construction and maintenance. The main difficulty in designing against fracture in high-strength materials is that the presence of cracks can modify the local stresses to such an extent, that they can propagate catastrophically through the structure [30]. Thermosetting polymers are very brittle, and before discussing some of the ways in which they can be made tougher, it is imperative to discuss some of the fracture mechanics behind how they fracture.

The basic tenet of fracture mechanics theory is that the strength of most real solids is governed by the presence of flaws. Since the theory enables the manner in which cracks propagate under stress to be analysed mathematically, the application of fracture mechanics to crack growth in polymers has received considerable attention [31]. It has proven to be particularly useful for such aspects as characterising the toughness of epoxies and identifying the mechanisms of failure. Only by identifying the mechanisms of failure can methods of toughening the composites be proposed.

The concepts of linear elastic fracture mechanics (LEFM) may strictly only be applied macroscopically to those materials which obey Hooke's law. However, the basic LEFM analyses may be applied to materials which exhibit inelastic deformations around the crack tip provided that such deformations are confined to the immediate vicinity of the crack tip [21]. Hence, the bulk of the body will still exhibit linear elastic properties.

The first milestone of fracture mechanics was conceived by Griffith [32] who developed a relationship between the flaw size and the fracture stresses. His hypothesis explained why the measured fracture strengths of materials were much lower than the theoretical values, and laid down the foundations for the later developments of fracture mechanics.

2.2.1 Energy Balance Approach

According to Griffith's hypothesis [32], for fracture to take place a system must meet the criterion such that the energy available for crack growth should be equal to, or exceed, the energy required to produce new crack surfaces, ∂A, associated with an increment of crack growth, ∂a. It may be written as:

$$\frac{\partial(W-U)}{\partial a} \geq \gamma \frac{\partial A}{\partial a} \qquad \textbf{Equation 2.1}$$

where W is the work done by the external force and U is the available elastic energy stored in the bulk of the specimen and γ is the surface free energy of the specimen. For a crack propagating in a lamina of thickness, B, the criterion becomes:

$$\frac{1}{B} \cdot \frac{\partial(W-U)}{\partial a} \geq 2\gamma \qquad \textbf{Equation 2.2}$$

However, Griffith's approach was too primitive for engineering applications, as it was only true for perfectly brittle materials. Consequently, Orowan [33] and Irwin [34] independently modified the Griffith theory and showed that the energy to create the new crack surfaces was substantially greater than the theoretical values. This is due to the irreversible energy dissipated during plastic deformation at the crack tip. If the energy dissipation around the crack tip is taken into the consideration, the criterion becomes:

$$\frac{1}{B} \cdot \frac{\partial(W-U)}{\partial a} \geq G_c \qquad \textbf{Equation 2.3}$$

where G_c is the critical energy required for crack growth which includes the increase of surface energy and the plastic energy dissipation at the crack tip. This is termed the fracture energy.

For structures exhibiting bulk linear-elastic behaviour, Equation 2.3 may be expressed as:

$$G_c = \frac{P_c^2}{2B} \cdot \frac{\partial C}{\partial a} \qquad \textbf{Equation 2.4}$$

where P_c is the critical load at the onset of crack propagation and C is the compliance of the structure and is given by displacement/load (δ/P) [21]. This equation is the foundation for many calculations of G_c since if C is determined as a function of the crack length, and a is determined either analytically or experimentally, then $\partial C/\partial a$ may be found. Thus, if P_c is measured, then the value of G_c may be deduced [21].

2.2.2 Stress Intensity Factor Approach

Irwin [34] proposed an alternative method to the energy balance approach and introduced a new parameter called the stress intensity factor, K. This approach examines the stresses near the tip of a sharp crack directly and has been more useful in engineering practice. He modified Westergaard [35] stress functions which relate the local concentration of stresses at the crack tip to the applied stress, and the equation may be expressed as:

$$\sigma_{ij} = \frac{K}{(2\pi r)^{1/2}} f_{ij}(\theta) \qquad \textbf{Equation 2.5}$$

where σ_{ij} are the components of the stress tensor at a point, r and θ are the polar coordinates of the point, and $f_{ij}(\theta)$ is the trigonometric function. This equation for crack growth was based on K, and K_c is a critical value required for the crack growth (critical stress intensity factor) and is often referred to as the fracture toughness of the material.

A crack in a solid may be stressed in three different modes, denoted mode I, II and III, as depicted in Figure 2.2.1. However, mode I loading is the most commonly encountered in practice (and is employed in this study), and as fracture occurs at the lowest energy, hence mode I is the most important when designing structures. This loading mode was applied to all the fracture tests performed in the current investigations.

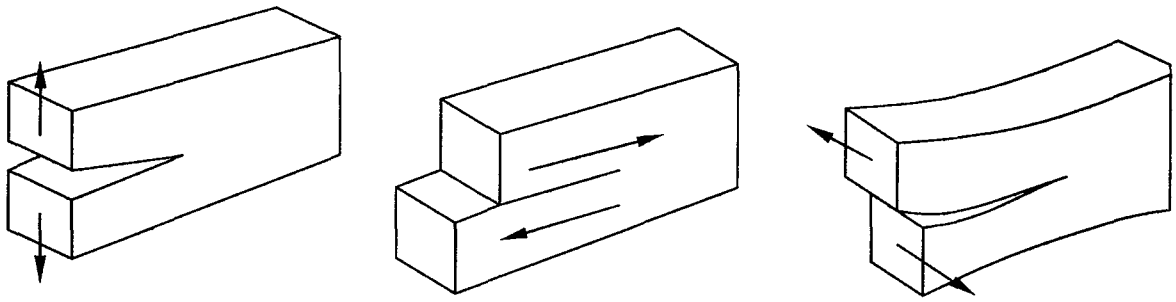


Figure 2.2.1. Modes of loading: (a) Mode I, cleavage or tensile-opening mode; (b) Mode II, in-plane shear mode; (c) Mode III, anti-plane shear mode [21].

2.2.3 Relationship between G_{Ic} and K_{Ic}

From the above analysis, a simple relationship exists between G and K, and for a crack propagating in a homogenous material, under plane-strain conditions, this relationship is given by:

$$G_c = \left(\frac{1-\nu^2}{E}\right) K_{Ic}{}^2 + \left(\frac{1-\nu^2}{E}\right) K_{IIc}{}^2 + \left(\frac{1-\nu}{E}\right) K_{IIIc}{}^2 \qquad \textbf{Equation 2.6}$$

where for Mode I

$$G_{Ic} = \frac{1}{E} K_{Ic}{}^2 \qquad \text{for plane stress} \qquad \textbf{Equation 2.7}$$

$$G_{Ic} = \left(\frac{1-\nu^2}{E}\right) K_{Ic}{}^2 \qquad \text{for plane strain} \qquad \textbf{Equation 2.8}$$

where ν is the Poisson's ratio and E is the modulus [21]. Plane strain and plane stress conditions are defined by the thickness of the sample being tested. The minimum thickness required to satisfy plane strain conditions can be seen below [28], and a smaller thickness implies plane stress conditions:

$$B \geq 2.5\left(\frac{K_{Ic}}{\sigma_y}\right)^2 \qquad \textbf{Equation 2.9}$$

Where B is the specimen thickness and σ_y is the uniaxial tensile yield stress. It should be noted that the fracture tests in this study were performed under *plane strain* conditions. It was necessary to convert the fracture toughness values to fracture energy values (using Equation 2.8) to compare the bulk fracture resistance to the FRP fracture resistance.

2.2.4 Crack Tip Plasticity

Under the assumption of LEFM, where plastic yielding is confined to the immediate vicinity of a crack tip, the size of the plastic zone at the tip can be deduced from the elastic stresses. According to Irwin's model [34] of the plastic zone at a crack tip (see Figure 2.2.2) the radius of the plastic zone, r_y, is given by

$$r_y = \frac{1}{2\pi}\left(\frac{K_I}{m_p \sigma_y}\right)^2 \qquad \textbf{Equation 2.10}$$

Where m_p is the plastic constraint factor (effective yield stress/σ_y). An effective crack length ($a+r_y$) is used instead of the initial crack length a, and the elastic stress field ahead of the crack is regarded as identical to the stress distribution of a real crack of length a with the extent of the plastic zone $2r_y$.

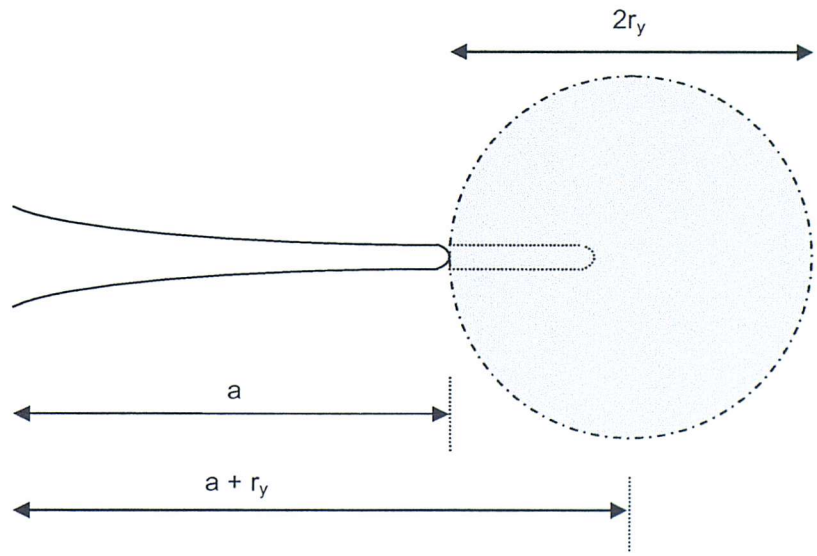


Figure 2.2.2. Irwin's model of the plastic zone at crack tip [34].

The plastic constraint factor, m_p, is dependant upon the stress state around the crack tip. Knott [36] has considered the stress distribution ahead of a crack around which localised plastic yielding has occurred. Figure 2.2.3 shows the stress distribution obtained for plane stress (σ_3=0) and plane strain (e_3=0) conditions. Although it is only approximate and semi-quantitative, it is a useful model for illustrating the effect of plastic constraint. In plane stress, the plastic constraint factor has a value of unity, and in plane strain, the value can be assumed to be $\sqrt{3}$. Hence, from Equation 2.10, the expressions for the radius of the plastic zone are given by:

$$r_y = \frac{1}{2\pi}\left(\frac{K_I}{\sigma_y}\right)^2 \qquad \text{for plane stress} \qquad \textbf{Equation 2.11}$$

And

$$r_y = \frac{1}{6\pi}\left(\frac{K_I}{\sigma_y}\right)^2 \qquad \text{for plane strain} \qquad \textbf{Equation 2.12}$$

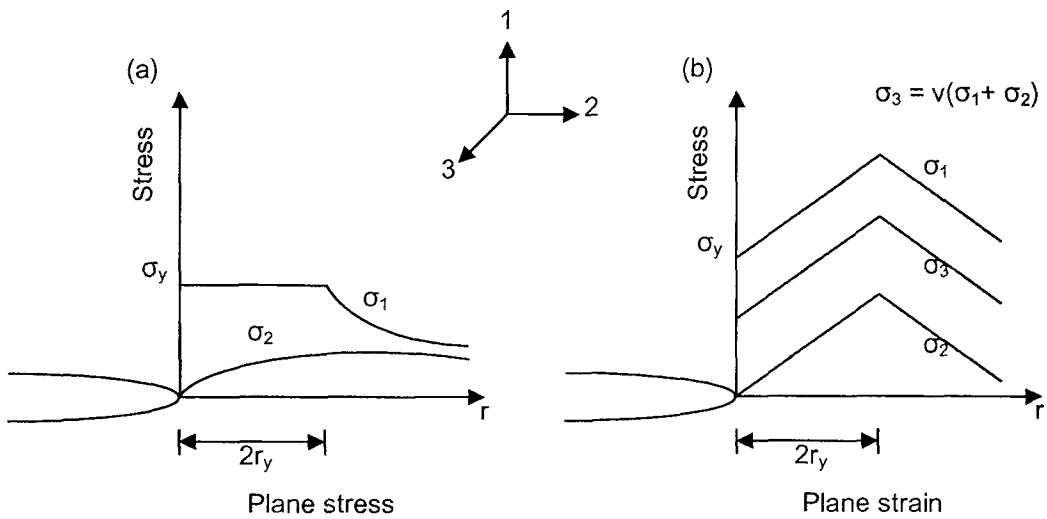


Figure 2.2.3. Schematic variation of elastic/plastic stresses ahead of a crack as a function of distance, r: (a) In plane stress ($\sigma_3 = 0$); and (b) in plane strain ($e_3 = 0$) [36].

Alternatively, the Dugdale analysis [37] could be employed for the estimation of the plastic zone size, as illustrated in Figure 2.2.4. It is assumed that yielding of the material at the crack tip makes the crack longer by the length of the plastic zone, R. This model

is particularly applicable to the plasticity ahead of a crack tip which is not circular but rather like a line in shape. The length of the plastic zone ahead of the crack is given by:

$$R = \frac{\pi}{8}\left(\frac{K_I}{\sigma_y}\right)^2 \qquad \textbf{Equation 2.13}$$

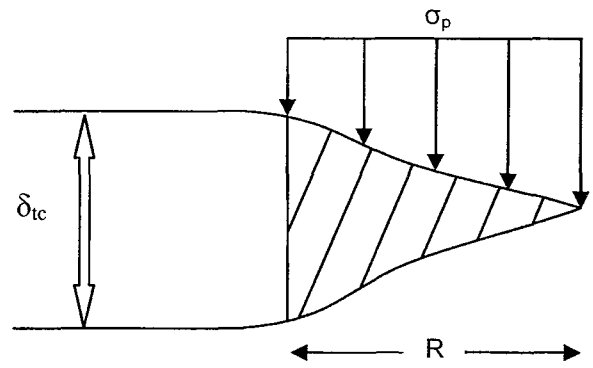


Figure 2.2.4. Dugdale's line plastic-zone model [37].

Under plane-strain conditions, the crack opening displacement, δ_{tc}, can be calculated using the relationship [21]:

$$\delta_{tc} = \frac{K_{Ic}^2}{E.\sigma_y}(1-\nu^2) = \frac{G_{Ic}}{\sigma_y} \qquad \textbf{Equation 2.14}$$

2.3 Deformation Behaviour of Polymers

The deformation of materials can be distinguished as elastic or elastic-plastic, if there is no time dependence. The simplest deformation is a linear elastic one, which does not involve any energy dissipation and can be described by Hooke's law. However, for most polymers, this linear elastic relationship applies only within a very small strain range. Thereafter, irreversible plastic deformation and subsequent energy dissipation upon unloading occurs. Note that rubbery polymers are one exception, and these behave in a non-linear way. This section will briefly review some general aspects of the yield behaviour of polymers according to several detailed reviews already available [21,38].

2.3.1 Definition of Yielding

The yield strength, or the yield point, is defined as the stress that a material can undergo before moving from elastic deformation into plastic deformation. Therefore, when a material is said to have yielded, the applied stress has reached a level to initiate permanent strain in the material. However, this concept is rather more complicated for polymers. Experimentally, the distinction between elastic (recoverable) and plastic (permanent) deformation is not clear-cut and there may be no sharp distinction in mechanisms. For example, almost all the plastic deformation is recoverable in glassy polymers when the material is heated above glass transition temperature, T_g [21].

A typical stress-strain curve for a glassy polymer is shown in Figure 2.3.1. There are two different yield points shown: the intrinsic and the extrinsic. The intrinsic yield point is a material property and can be defined as the maximum point in the stress-strain curve. The extrinsic yield point is defined by Considère's construction as shown in Figure 2.3.1, where a tangent to the curve through the point on the abscissa of nominal strain equals -1. In the case where a sample is tested in tension, the deformation becomes unstable at this point and a neck develops. The point is referred to as the extrinsic yield point because of its geometry dependency, and this is the one which is often used to define the yield stress. Most thermosets (like the epoxies used in this study), because of their brittleness, will usually fail at this point. Subsequently, strain-softening occurs after yielding, and then strain-hardening follows. As opposed to most other materials, such softening is often considered as an intrinsic material property for polymers, which can be defined as a fall in the true stress as deformation takes place at yield. The strain-hardening refers to a region where the true stress rises after yield and after any strain-softening has occurred.

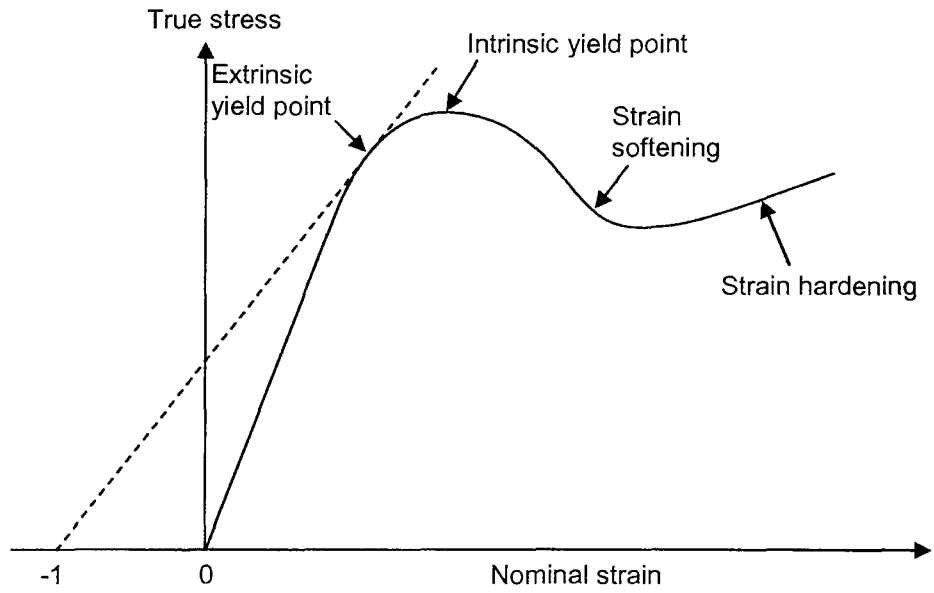


Figure 2.3.1. Schematic of a typical stress-strain curve for glassy polymers [39].

The Young's modulus is the ratio of the true stress to the nominal strain in the linear-elastic region (straight-line part of Figure 2.3.1) [30] and is a measurement of how stiff a material is.

2.3.2 Theoretical Models for Predicting Young's Modulus

Over the years of research into polymer-based composites, many models have been developed to predict the Young's modulus of a sample. For brevity, only the three models used in this study will be reviewed.

2.3.2.1 The Rule of Mixtures

This is one of the simplest models used to predict the modulus of a composite. It assumes equal strain in all components, that each component of the polymer is linearly elastic, and that the particles (rubber and/or nano-silica in this study) are homogenously distributed throughout the polymer matrix. The equation used [30] is given by:

$$E_c = V_f E_f + (1 - V_f) E_m \qquad \textbf{Equation 2.15}$$

Where V_f and E_f are the toughening agent's volume fraction and Young's modulus respectively. E_c and E_m are the Young's modulus of the composite and matrix (unmodified epoxy in this study) respectively.

2.3.2.2 The Halpin-Tsai Model

A shape factor, ζ, is included in this model to enable it to predict the Young's modulus of a composite not only as a function of the polymer and toughening agents' moduli and volume fraction, but also in terms of aspect ratio. The Halpin-Tsai equations [40] are given by:

$$\frac{E_c}{E_m} = \frac{1+\zeta\eta V_f}{1-\eta V_f} \qquad \textbf{Equation 2.16}$$

Where

$$\eta = \left(\frac{E_f}{E_m} - 1\right) \Big/ \left(\frac{E_f}{E_m} - \zeta\right) \qquad \textbf{Equation 2.17}$$

Halpin and Tsai recommend that $\zeta = 2w/t$ where w/t is the aspect ratio. The aspect ratio of spherical particles like those encountered in this study is unity. However, van Es [41] has shown that this is too large for most particulate composites, and recommends $\zeta = 2w3/t = 2/3$ for spherical particles.

2.3.2.3 The Lewis-Nielsen and McGee-McCullough Models

The previous model assumes that there is perfect bonding between the particles and the matrix, which is normally not the case. This effect can be considered further using the Lewis-Nielsen model [42] and the work of McGee & McCullough [43]. The authors showed that the composite modulus can be predicted using [43]:

$$E_c = \frac{1+(k_E-1)\beta V_f}{1-\beta\mu V_f} E_m \qquad \textbf{Equation 2.18}$$

where k_E is the generalised Einstein coefficient, and β and μ are constants. The constant β takes into account the relative modulus of the particles and the matrix, and is given by:

2.3.2.4 Other Models

Whilst only three predictive models were used in the present work, there are a number of other models that have been used in similar studies of particle-reinforced epoxies. Brief mention of some of these models will be made, but more details can be found in their respective references.

Guild and Kinloch [184] used spherical and cylindrical finite element models of rubber particles to predict the modulus of rubber toughened epoxies. Their model showed a decrease in epoxy modulus with increasing rubber content, which agrees well with the results obtained in this study (see Chapter 7). Chen and Mai [185] used a 3-D periodic micromechanical finite element model that had a face centred cubic (ie. an f.c.c.) structure, using rubber particles instead of atoms. Their predicted moduli were in good agreement with their experimental data, and agreed much better than Guild and Kinloch's [184] spherical model agreed with their (Chen and Mai's) experimental data.

Many models predicting the modulus of rigid particle-reinforced epoxies have been developed. Guild and Young [186] were some of the first researchers to try to model the modulus of epoxies that were toughened with rigid particles. Theirs was a finite element 2-D square model with one quarter of a glass sphere surrounded by epoxy. The predicted moduli obtained, showed an increase in stiffness with increasing particle volume fraction %, and were in good agreement with experimental results obtained from other researchers. Wu *et al.* [187] also used a 2-D finite element model with a composite spherical cell that consisted of a glass sphere, surrounded by an annulus of resin. Their model assumed that there was an imperfect interface between the particle and the epoxy, as compared to the previous models which assumed that there was perfect adhesion between the particle and epoxy. Their predicted modulus values showed good agreement with their experimental results.

Chawla and Chawla's [188] 2-D and 3-D models used the true microstructure of the materials to predict the stiffness (as compared to many of the previous models, which have assumed a regular distribution of particles). They compared their results to many other finite element models (including the Halpin-Tsai model), and all the models gave very similar results, which shows that the predicted modulus values are relatively insensitive to the model used.

$$\beta = \left(\frac{E_f}{E_m} - 1\right) \Big/ \left(\frac{E_f}{E_m} + (k_E - 1)\right) \qquad \textbf{Equation 2.19}$$

The value of μ depends on the maximum volume fraction of particles, V_{max}, and can be calculated from [2]:

$$\mu = 1 + \frac{(1 - V_f)}{V_{\max}}\left[V_{\max} V_f + (1 - V_{\max})(1 - V_f)\right] \qquad \textbf{Equation 2.20}$$

Values of V_{max} have been tabulated by Nielsen & Landel [2] for a range of particle shapes and types of packing. For random close packing, non-agglomerated spheres, Nielsen & Landel quote a value of V_{max} = 0.632. This value was used in the modulus predictions in this study.

The value of k_E varies with the degree of matrix to particle adhesion. For a matrix with a Poisson's ratio of 0.5 containing dispersed spheres, k_E = 2.5 if there is no slippage at the interface, and k_E = 1.0 if there is slippage [2]. Nielsen [44] has shown that the value of k_E is reduced when the Poisson's ratio of the matrix is lower then 0.5. In the present work v = 0.35, so values of k_E are reduced by a factor of 0.867. Hence, k_E = 2.167 if there is no slippage and k_E = 0.867 if there is slippage.

2.4 Toughened Epoxy Polymers

It has been reiterated in previous sections that thermosetting epoxy polymers are brittle materials with poor resistance to crack initiation and growth. However, they have many attractive properties for engineering applications, such as in the electronic industry (as bulk resin) and as matrix resins for composites, due to their amorphous and highly cross-linked microstructure. Therefore, a lot of attention has been given to improving their fracture properties by the incorporation of various toughening without significantly impairing the other desirable engineering properties. Possible toughening agents include aluminium and titanium oxide, but this section will focus only on the toughening agents used in this study: rubber and silica.

2.5 Rubber Toughening

McGarry and Sultan [45,46] were among the first researchers to show that the fracture toughness of brittle epoxy polymers could be improved by the incorporation of a rubbery phase. They prepared their rubber toughened epoxy polymers by mixing the liquid rubber and epoxy together and allowed in-situ phase separation to occur during cure to form the second rubbery phase. The final product showed a significant improvement in toughness. Since then, there have been extensive studies on toughening epoxy resins by utilising suitable liquid rubber copolymers of butadiene-acrylonitrile with various functional end-groups.

2.5.1 Chemical and Physical Properties of Rubber

The main factors which affect the microstructure of a rubber toughened epoxy polymer are the chemical and physical properties of the rubber and resin/curing agent, and the cure conditions. Subsequently, the microstructure controls the mechanical behaviour of the cured epoxy polymers [29].

There are two main requirements to determine the optimum molecular structure of the rubber [29]. The first important requirement is that the rubber should be miscible with epoxy prior to the cure and should be able to form a well-dispersed separate phase during the curing process. Miscibility and phase separation are governed by the thermodynamics of the rubber/epoxy system. The fundamental aim is to match the respective solubility parameters of the rubber and the epoxy. Hence, the rubber will dissolve in the resin when the free energy of the system is negative. During the cure, however, with increasing molar mass, the free energy should become positive to ensure phase separation. The second condition is that the spherical rubbery particles that phase separate need to be well bonded to the epoxy matrix to be able to cavitate (this toughening mechanism will be discussed later). To ensure this condition, rubbers with reactive end-groups can be employed.

These rubbers are usually liquid rubber copolymers of butadiene-acrylonitrile with various functional end-groups such as carboxy-terminated (CTBN), amine-terminated (ATBN), vinyl-terminated (VTBN) [47], hydroxyl-terminated (HTBN) [48], and epoxy-terminated (ETBN) [49]. However, CTBN and ATBN rubbers are the most frequently

and successfully used rubbers for the toughening of epoxy polymers, and in this study, CTBN was employed. As can be seen from Figure 2.5.1, CTBN rubber particles usually have sharp interfacial boundaries [50]. (This section was exposed to osmium tetroxide prior to examination to increase the contrast between the rubber particles and the epoxy matrix, and the wavy lines are artefacts due to the cutting of a very thin section of material.) On the other hand, ATBN rubber particles have less well defined interfacial boundaries [51].

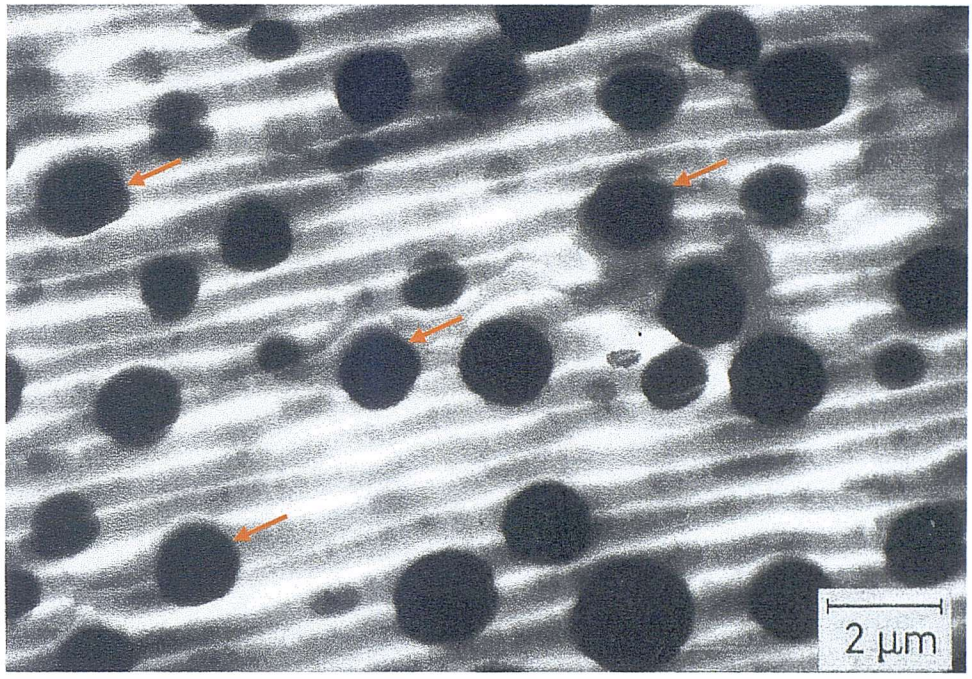


Figure 2.5.1. Transmission electron microscope image of a thin section of a CTBN rubber toughened epoxy polymer [52] (Red arrows point to some rubber particles).

2.5.2 Rubber Toughening Mechanisms

In recent years, the theoretical explanation of toughening mechanisms has been advanced and several reviews [3-7,53-58] have given detailed descriptions of the theory behind rubber toughening mechanisms. In this section, some important aspects of these toughening mechanisms are summarised.

2.5.2.1 Crazing

Crazing was proposed by McGarry and Sultan [45,46] as a major toughening mechanism. They suggested that the observed stress whitening near the crack tip region

was due to crazing in the matrix. Since then, additional support for crazing as a major mechanism was suggested by several other researchers [59,60]. Bucknall [61] suggested that crazing is the principal mechanism of toughening, but shear yielding also contributes in some rubber toughened plastics. Nevertheless, no conclusive evidence of crazing being the principal mechanism of rubber toughening has been provided by these authors. Alternatively, later authors suggested that the observed stress whitening near the crack tip was caused by the cavitation of rubber particles, and claimed cavitation and shear yielding as the main toughening mechanisms [4,7].

2.5.2.2 Rubber-Bridging

Kunz-Douglass *et al.* [53] concentrated their work on the rubber particle bridging mechanism, and observed rubber particles stretching between the two crack surfaces prior to failure. A schematic diagram of this mechanism is shown in Figure 2.5.2. A crack was propagated in samples of the rubber toughened epoxy polymer by driving a wedge into a pre-cut notch, and the crack tip region was studied by optical microscopy. The results revealed that the brittle epoxy matrix cracks, and leaves ligaments of rubber attached to the two crack surfaces. The authors calculated the increase in toughness of the rubber toughened epoxy polymer and compared it to the untoughened epoxy polymer. Direct measurements of the tearing strains of rubber particles, and toughness data obtained from the composites were in good agreement with the model. Overall, they claimed that the rubber-bridging mechanism (tearing of stretched rubber particles) is the major source of energy absorption in rubber toughened epoxy polymers.

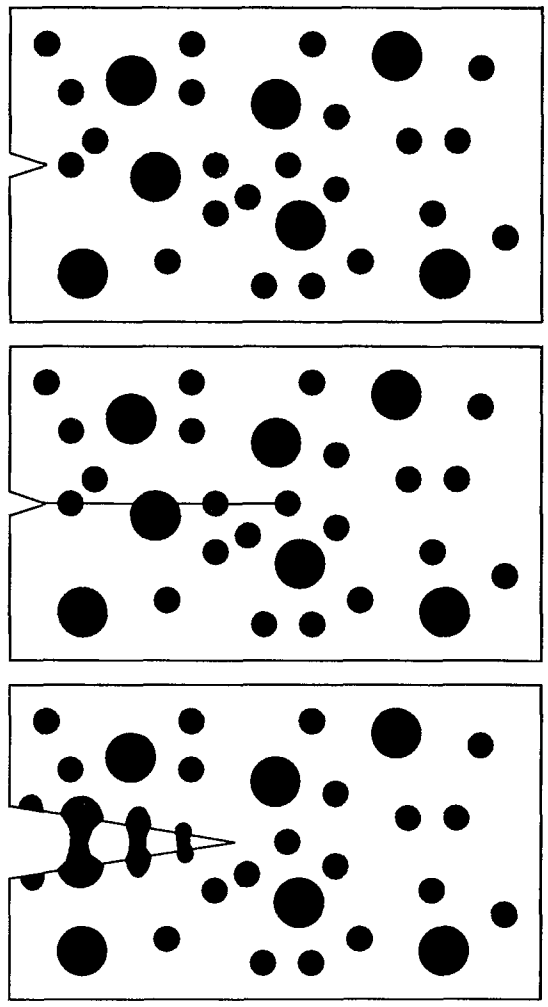


Figure 2.5.2. Schematic showing the stages of the rubber-bridging mechanism [53].

However, this mechanism cannot be taken as the major toughening mechanism since it does not take the role of the matrix into account, and cannot explain other experimental observations such as the stress whitening which is present in most rubber toughened epoxy polymers. Moreover, Huang and Kinloch [56] reported that the contribution of rubber-bridging to the fracture energy is less than 10% at room temperature. Generally, rubber-bridging is now only accepted as a secondary toughening mechanism for rubber toughened epoxy polymers.

2.5.2.3 Cavitation and Void Growth

Kinloch *et al.* [4] suggested that the toughening mechanism in the fracture of rubber toughened epoxy polymers arises from shear yielding in the epoxy matrix and cavitation inside the rubber particles or at the particle/matrix interface. The authors argued that

shear yielding is the main source of energy dissipation and occurs to a far greater degree in the matrix of the rubber toughened epoxy polymer, due to interactions between the stress field ahead of the crack and the rubbery particles.

Yee and Pearson [7] also investigated the cavitation of rubber particles in rubber toughened epoxy polymers. They provided fractographic evidence of cavitation occurring within rubber particles, and suggested that cavitation of the rubber particles was a major deformation mechanism. Yee and his colleagues [36] extended their work on the cavitation of rubber particles, and reported that the rubber cavitation causes local constraint relief in the material. As a result, the crack initiation process in the epoxy matrix is delayed, and the surrounding epoxy matrix can undergo more plastic deformation and absorb more plastic energy. Figure 2.5.3 shows their illustration of the cavitation process where: (a) before rubber particle cavitation, the material behaves like unmodified epoxy, and (b) after rubber particle cavitation, the constraints in the transverse directions are relieved, and the matrix epoxy deforms in the plane stress state if the rubber concentration is sufficiently high.

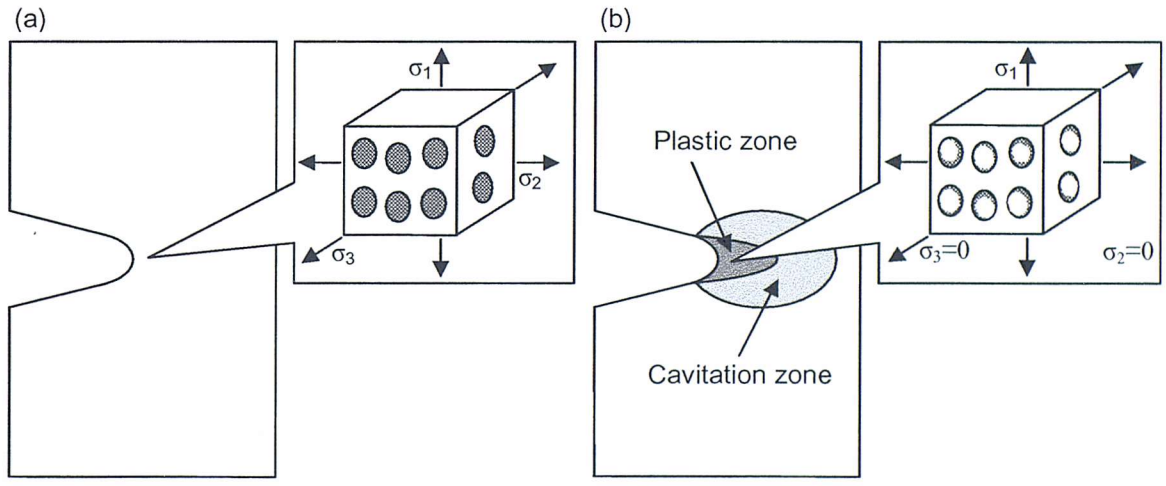
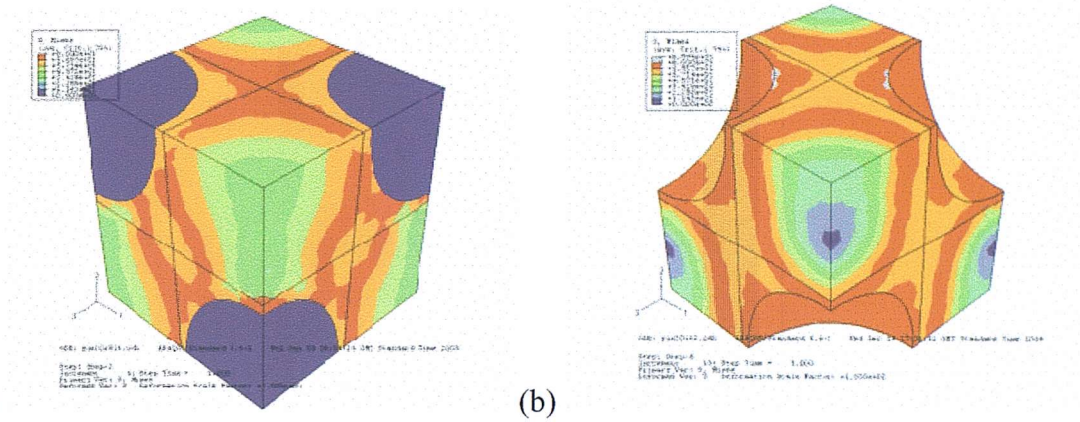


Figure 2.5.3. Illustration of the deformation mechanisms in rubber toughened epoxy polymers; (a) before rubber particle cavitation, and (b) after rubber particle cavitation [54].

Bagheri and Pearson [58] studied the role of particle cavitation in rubber toughened epoxy polymers. They reported that the cavitation resistance of the rubbery phase does not directly contribute to toughness, but instead simply allows the matrix to deform by

shear. They also suggested the possible importance of inter-particle distance in toughening of epoxy polymers with rubber particles.

3-D finite element modelling of the cavitation process by Wang and Guild *et al.* [62] confirm their (Wang and Guild's) experimental observations that cavitation leads to both plastic hole growth and increased growth of shear bands. This is illustrated in Figure 2.5.4 which shows the distribution of the von Mises stress in a unit cell under triaxial loading, before and after cavitation. The rubber particles are in blue in the diagram on the left.



(a) (b)

Figure 2.5.4. Distribution of the von Mises stress around rubber particles in a unit cell under triaxial loading: (a) before cavitation and (b) after cavitation [62].

2.5.2.4 Shear Yielding

Shear yielding is one of the main energy dissipating mechanisms of rubber toughened epoxy polymers [4,7]. This toughening mechanism was particularly clarified by Huang and Kinloch [56,57]. Figure 2.5.5 shows the calculated stress distribution between the rubber particles using a 2-D finite element analysis method. They suggested that there is clearly a high stress region between the rubber particles, which corresponds to a shear band.

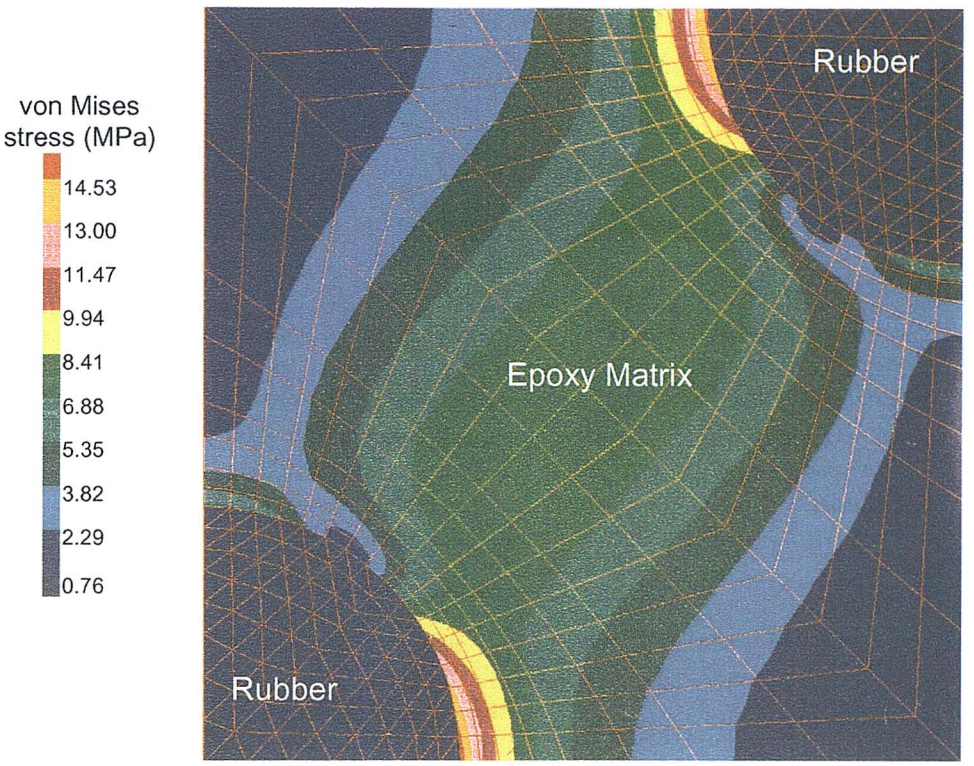


Figure 2.5.5. Distribution of the von Mises stress around rubber particles [57].

They reported that the contribution of shear yielding to the fracture energy depends on the temperature and decreases with increasing temperature. The plastic void growth mechanism becomes the dominant proportion of the energy dissipation when the temperature is relatively high, at about 40°C.

2.5.2.5 Combination of Toughening Mechanisms

Generally, the addition of rubber particles can toughen epoxy polymers by promoting many different mechanisms such as shear yielding, plastic void growth and rubber-bridging.

Indeed, Huang and Kinloch [56,57] developed a mathematical model to quantify the toughening mechanisms of rubber toughened epoxy polymers using three different toughening mechanisms, which is given by:

$$\Psi = \Delta G_s + \Delta G_v + \Delta G_r \qquad \textbf{Equation 2.21}$$

where Ψ represents the overall toughening contribution, and ΔG_s, ΔG_v, and ΔG_r represent the increase in fracture energy due to shear yielding, plastic void growth and rubber-bridging respectively. The overall fracture energy of the rubber toughened epoxy is expressed by:

$$G_{Ic} = G_{Icu} + \Psi \qquad \textbf{Equation 2.22}$$

Where G_{Icu} represents the fracture energy of the unmodified epoxy polymer. The mathematical model states that the overall toughness is the sum of the individual contributions. Figure 2.5.6 is a classic diagram from Kinloch, Maxwell, and Young [63] showing the different toughening mechanisms of rubber toughened epoxy polymers. Experimentally measured fracture energy values of the rubber toughened epoxy polymers were compared to the theoretical predictions and were shown to be in good agreement. Moreover, the calculations showed that localised shear yielding is the main source of the increased toughness, and constitutes more than 50% of the total dissipated energy. They also pointed out the importance of plastic void growth around the cavitated particles as an energy absorbing process second to the shear yielding.

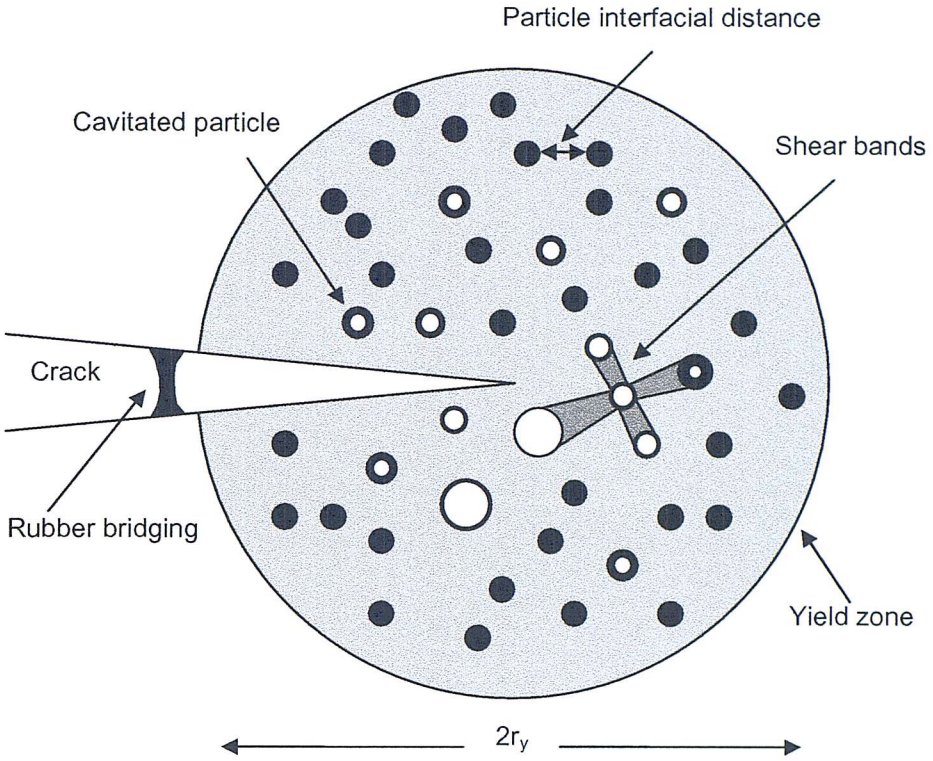


Figure 2.5.6. Schematic representation of the different toughening mechanisms involved in the fracture of rubber toughened epoxy polymers. The diameter of the plastic, or process, zone is $2r_y$ [63].

2.5.3 Microstructure-Property Relationship

The relationships between the microstructure and fracture properties in rubber toughened epoxy polymers have been described by several researchers [52,4,7]. This section will briefly review the effect of various parameters, such as cross-link density and rubber volume fraction, on the structure-property relationships in rubber toughened epoxy polymers.

2.5.3.1 Effect of Cross-Link Density

The cross-link density of the epoxy matrix can be characterised by the average molecular weight between cross-links, M_c. A high cross-link density will result in a low M_c value, and a low cross-link density will result in a high M_c value. This is an important parameter for the structure-property relationship of pure epoxy resins [64], and is also expected to play an important role in rubber toughened epoxy polymers. Several studies have investigated the effect of cross-link density by changing the degree

of cross-linking in rubber toughened epoxy polymers. This has been achieved by altering the curing conditions [65], by employing resins with different monomer molecular weights [7,66] or by using different amounts of curing agents [67]. According to these reports, an increase in the M_c value will result in a small increase in the fracture energy of unmodified epoxy polymers but a significant increase in the fracture energy of rubber toughened epoxy polymers.

Pearson and Yee [68] also investigated the effect of cross-link density on fracture toughness in rubber toughened epoxy polymers. They reported that rubber toughened epoxy polymers with a low cross-link density exhibit greater facture toughness and suggested a linear relationship between the critical stress intensity factor (fracture toughness), K_{Ic}, and $M_c^{1/2}$, which is shown in Figure 2.5.7.

In general, it has been found that lowering the cross-link density values should result in an increase of fracture toughness (or fracture energy) of the rubber toughened epoxy polymers. Nevertheless, more research is required to establish a detailed relationship between the toughness and the cross-link density.

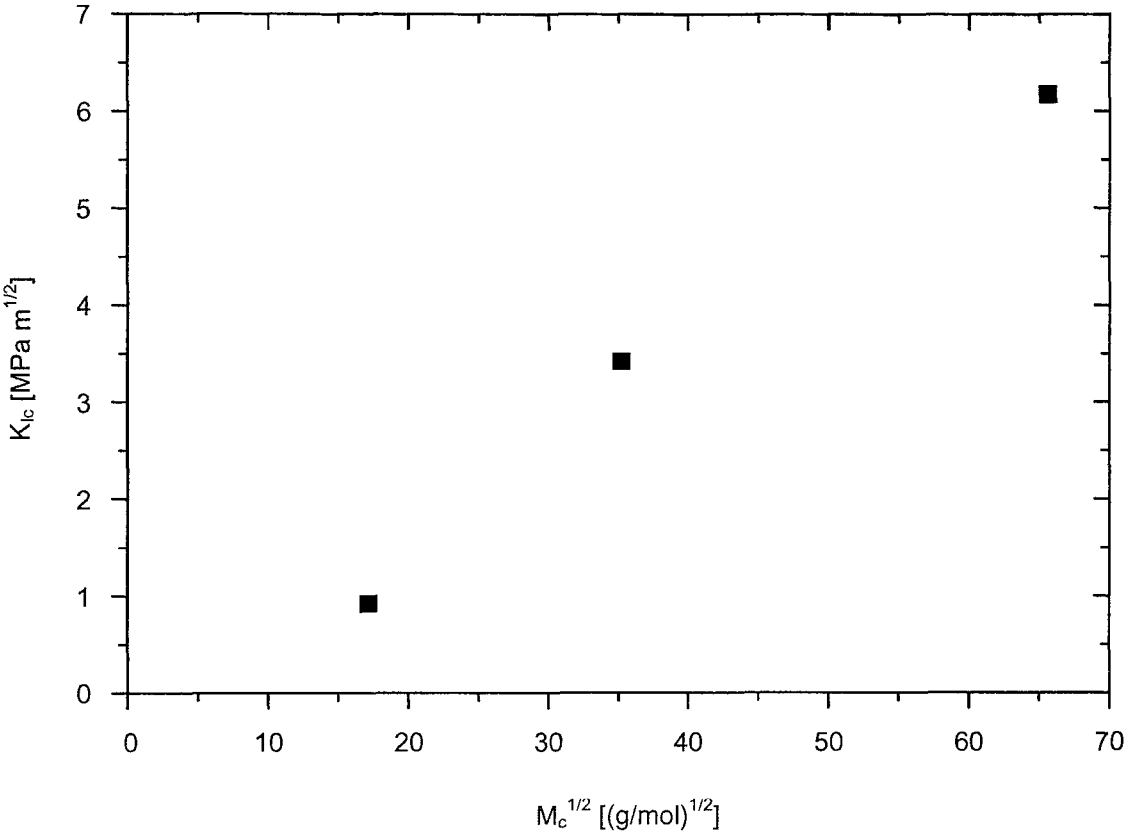


Figure 2.5.7. Variation of fracture toughness, K_{Ic}, as a function of molecular weight between cross-links, M_c [68].

2.5.3.2 Effect of Volume Fraction of Rubber

According to several researchers [7,57,69-72], the fracture energy generally increases with increasing volume fraction of rubber. However, it is still unclear whether the relationship between fracture energy and volume fraction of rubber is linear or not.

Bucknall and Yoshii [69] investigated the structure-property relationship of CTBN rubber toughened epoxy polymers and claimed that there is a linear relationship between the fracture energy, G_{Ic}, and the volume fraction of rubber, V_f. Karger-Kocsis and Friedrich [70] also supported the linear relationship but they used the rubber content which was initially added instead of the volume fraction of phase-separated particles.

Conversely, Kinloch and Hunston [71] studied the effect of the volume fraction of rubber with varying test temperature and rate, and reported that there is no one unique relationship between G_{Ic} and V_f. According to their results, when tests were performed

at high temperatures or low rates, the fracture energy increases steadily with an increasing volume fraction of rubber, and the relationship between G_{Ic} and V_f is almost linear. However, at low test temperatures or high test rates, the relationship between G_{Ic} and V_f deviates somewhat from a linear relationship.

It is important to note that the initially added rubber content is not necessarily equivalent to the volume fraction of rubber particles which is measured after the cure. During the curing process, all the rubber may not have been phase separated and some might still remain in solution in the epoxy matrix. One indication of not all the rubber phase separating, is a decrease in the glass transition temperature, T_g, of the epoxy. The amount of phase separation depends on many factors such as the curing agent and cure conditions. Usually, there is a limit to the amount of rubber that can precipitate out as particles by the in-situ phase separation. Beyond this limit, phase inversion occurs and the material becomes a rubbery matrix with epoxy particles within it [72].

One way of calculating the amount of rubber that remains in the epoxy phase, is using the Fox-Flory equation. This equation as reported by Couchman [177] is given by:

$$\frac{1}{T_{gc}} = \frac{1-w_r}{T_{ge}} + \frac{w_r}{T_{gr}} \qquad \textbf{Equation 2.23}$$

Where T_{gc}, T_{ge} and T_{gr} are the glass transition temperatures of the composite, unmodified epoxy and rubber respectively and w_r is the weight fraction of the rubber that remains in solution in the epoxy phase.

2.5.3.3 Effect of Particle Size

Initially, it was thought that larger rubber particles promote crazing and hence were more effective than small rubber particles which cause shear yielding. Sultan and McGarry [46] have shown that 1μm particles are more efficient than smaller, 40nm particles for rubber toughened epoxy polymers. However, later studies reported that crazing is not a major toughening mechanism in rubber toughened epoxy polymers [4,7,53]. Kunz-Douglas *et al.* [53] reported that large, 40μm particles are not as efficient in providing an increase in fracture toughness as smaller, 1μm particles. Moreover, Wu and Margolina [73,74] developed a correlation which predicts that smaller particles should be better toughening agents.

More recently, Pearson and Yee [75] investigated the influence of particle size and particle distribution in rubber toughened epoxy polymers. Various rubber particle sizes from 0.2 to 200μm were incorporated with a constant rubber content of 10phr (parts per hundred resin by weight). They reported that smaller rubber particles provide a significant increase in toughness by cavitation-induced shear bands, whereas large rubber particles provide only a moderate increase in fracture toughness by the rubber-bridging mechanism. They also stated that larger rubber particles cannot be cavitated, because they lie outside the plastic zone, where the large hydrostatic stress exists.

It should be noted that particle size cannot be adjusted independently without changing other parameters such as the properties of the rubber particles, volume content of the rubber particles, and adhesion strength between the matrix and the rubber particles. Indeed, the rubber is usually in liquid form until cured. Thus, Kim *et al.* [76] employed synthesized core-shell rubber particles as a toughening agent for investigating the effect of rubber particle size. According to their study, more shear deformation can be obtained with smaller rubber particles, since the stress field is superimposed owing to shorter inter-particle distances, and transition from plane strain to plane stress occurs. However, they also mentioned that rubber particles should be larger than 0.2μm in diameter for effective toughening, since cavitation is difficult with rubber particles less than 0.2μm. Similarly, Lazzeri and Bucknall [77] proposed a theoretical model for rubber particle cavitation showing that cavitation in the rubber particles cannot occur for particles less than 0.25μm in diameter. This theoretical calculation agrees with the experimental result by Kim *et al.* [76].

In summary, the literature suggests that small rubber particles are more efficient in producing a toughening effect than large rubber particles. However, rubber particles smaller than 0.2-0.3μm in diameter may not be as efficient, due to the difficulty in cavitation with such small rubber particles.

2.5.3.4 Effect of Interfacial Adhesion

Generally, most of the rubber employed in the rubber toughened epoxy polymers has reactive end-groups, and good adhesion is usually found between the epoxy matrix and the rubber particles. Chan *et al.* [51] employed an unreactive rubber to investigate the

effect of interfacial adhesion and suggested that poor interfacial adhesion results in no toughness increase, since poorly bonded particles do not have a load bearing capacity.

However, Huang *et al.* [57,78] reported that once phase separation has been achieved, the interfacial bonding between the rubber particle and the epoxy matrix has only a minor effect on the fracture properties of the rubber toughened epoxy polymers. They suggested that there is a competition, which depends on the interfacial adhesion strength, between internal cavitation of the rubber particle and debonding of the interface during fracture. Good interfacial adhesion results in internally cavitated rubber particles but poor adhesion results in the debonding of the rubber particles. They claimed that the occurrence of either event is a necessary condition of further plastic deformation in the matrix via plastic void growth mechanism.

Alternatively, Huang and Kinloch [79] investigated the toughness of epoxy polymers containing microvoids and reported that voids themselves can significantly increase the toughness of epoxy polymers. This work strongly supports their previous work on the effect of interfacial adhesion, which demonstrates that the interfacial adhesion strength has a small effect on the toughness. Nevertheless, they mentioned that the maximum toughness values are invariably observed when rubber particles are chemically bonded to the matrix (ie. high interfacial adhesion strength).

More recently, Bagheri and Pearson [58] examined the role of particle cavitation in rubber toughened epoxy polymers through comparative examination of epoxy polymers toughened by conventional rubber particles and hollow plastic particles. The results of their study showed that rubber particles with different cavitation resistance and pre-existing microvoids toughen the epoxy matrix in the same manner.

2.6 Rigid Particle Toughened Epoxy Polymers

Epoxy polymers can be toughened by other substances apart from rubber particles. The tougheners of interest in the present work are rigid inorganic spherical particles such as glass beads, alumina or silica particles. They have some advantages over rubber toughened epoxy polymers such as improved stiffness, reduced shrinkage, increased modulus and enhanced toughness without any loss in thermo-mechanical properties

[64]. However, the improvement in toughness is far less significant compared with rubber toughened epoxy polymers.

2.6.1 Toughening Mechanisms

Rigid inorganic spherical particles may toughen epoxy through crack pinning [80], crack deflection [81,82], debonding and void growth [82,83], and microcracking [84], which are notably different mechanisms from those present in rubber toughened epoxy polymers. Micro-shear banding has also been proposed for epoxy polymers toughened with glass spheres [85,86]. This section will briefly discuss some of the aforementioned toughening mechanisms.

2.6.1.1 Crack Pinning

Although the use of inorganic particles as toughеners in many polymers is widespread, their fracture behaviour and toughening mechanisms are less well understood compared with those toughened by rubber particles. Nevertheless, for rigid spherical particles, one of the most widely accepted toughening mechanisms is the crack pinning mechanism, which was originally suggested by Lange [80] and later analysed further by Evans [87] and Green *et al.* [88]. In crack pinning, when the crack begins to propagate through the rigid particle toughened epoxy polymer, it becomes pinned and tends to bow out between the toughening particles. This is illustrated schematically in Figure 2.6.1(a) and by direct observation using optical microscopy in Figure 2.6.1(b).

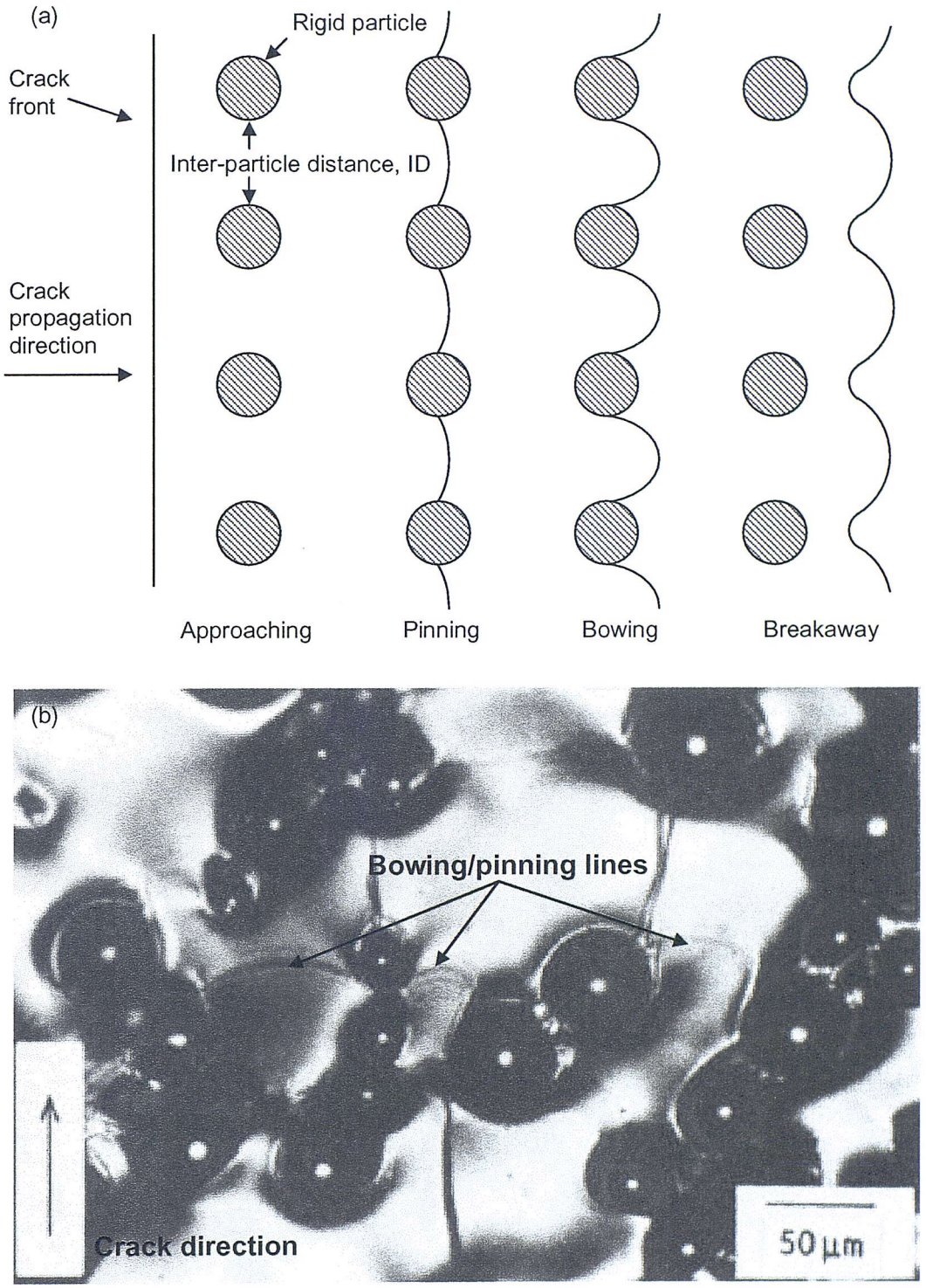


Figure 2.6.1. (a) Schematic representation of the crack pinning mechanism for increasing the toughness when rigid particles are present in a brittle adhesive. (b) Optical micrograph of the fracture surface of a glass particle toughened epoxy polymer showing the crack front pinned between glass particles [63].

Alternatively, some researchers [21] claimed that the evidence of crack pinning mechanism may be observed, as shown in Figure 2.6.2, where tails or steps are formed

at the rear of the inclusion due to the meeting of the two arms of the crack front from different fracture planes.

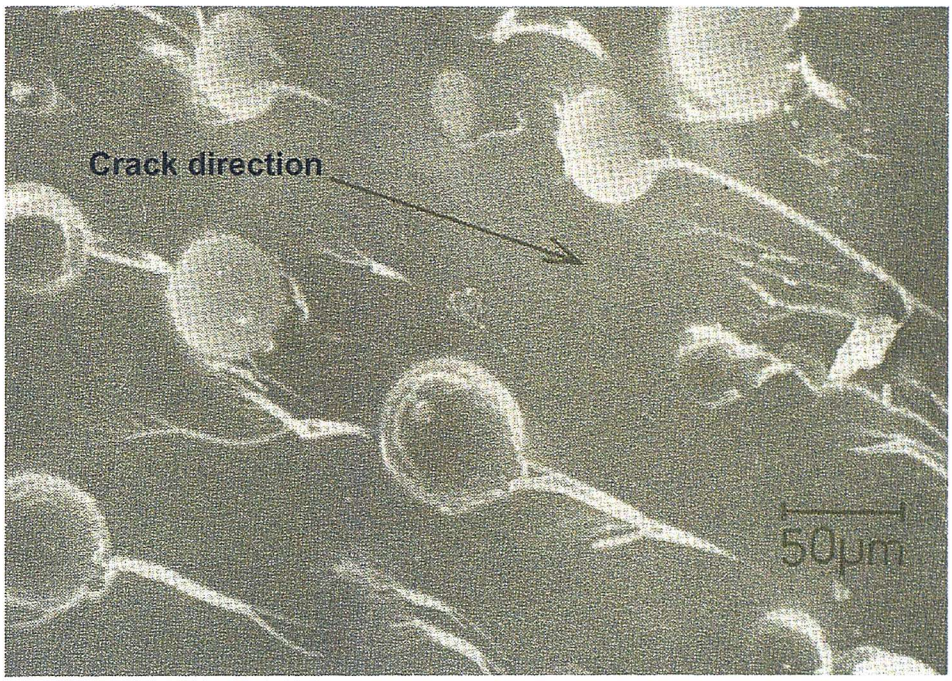


Figure 2.6.2. Scanning electron microscope image of a fracture surface of an epoxy polymer containing spherical glass particles showing the 'tails' behind the particles [21].

2.6.1.2 Crack Deflection

The crack deflection mechanism arises whenever interaction between the crack front and the particulate phase produces a non-planar crack, subject to a stress intensity lower than that experienced by the corresponding planar crack [81]. The tilting and twisting of the crack front is as a result of mixed mode loading and due to the high fracture energy required for mixed mode failure as compared to mode I, the fracture toughness is increased.

Figure 2.6.3 shows the effect of interfacial strength on the crack path when rigid particles are encountered. It can be seen that for a poorly-bonded particle, the crack will move around the equator of the particle as shown in Figure 2.6.3 (b). With good interfacial adhesion between the matrix and the particle as in Figure 2.6.3 (c), the crack is attracted to the poles of the particle which is desirable as a larger fracture area is created.

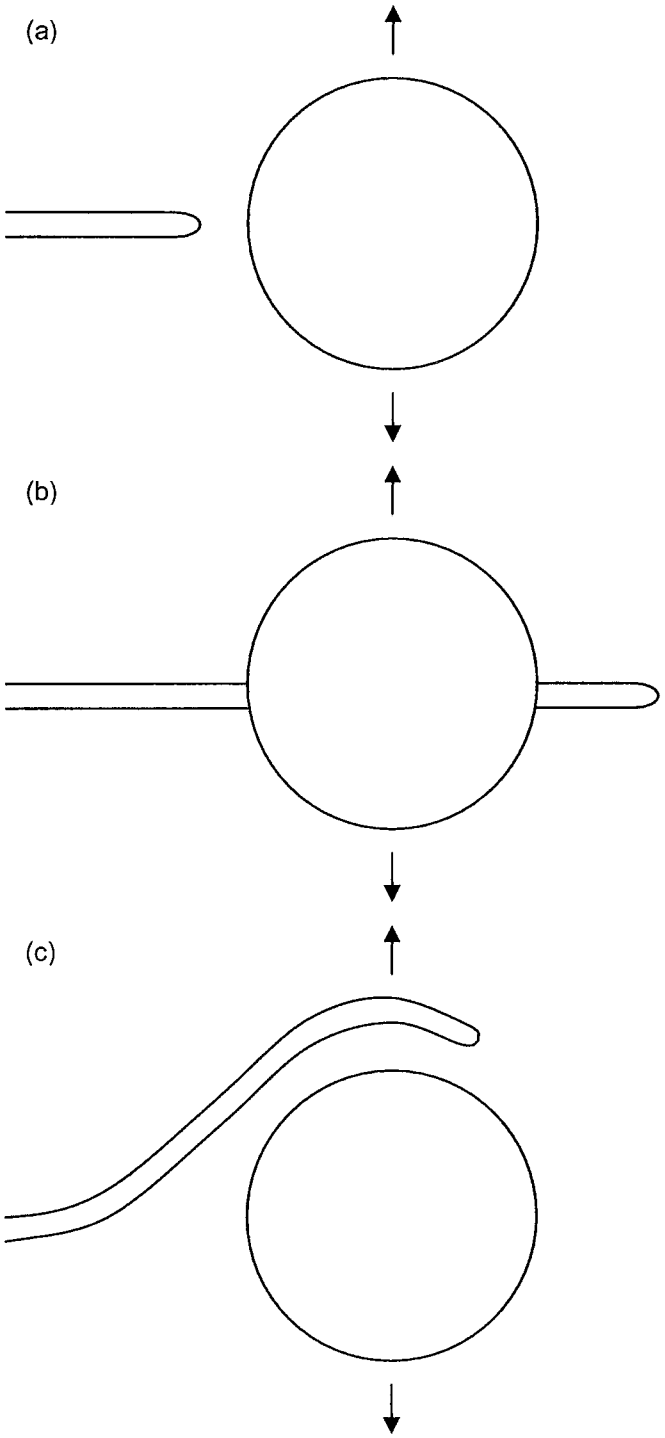


Figure 2.6.3. Schematic of the path of a crack around a particle in rigid particle toughened polymers under stress. (a) Crack approaching particle. (b) Crack moving around the equator of a poorly bonded particle. (c) Crack attracted to poles of a well-bonded particle [12].

A fracture mechanics approach has been used to predict fracture toughness increases due to crack deflection around second phase particles by Faber and Evans [81]. According to their report, the crack pinning and crack deflection processes occur simultaneously.

2.6.1.3 Debonding and Void Growth

The toughening mechanisms associated with micrometre-sized particles have frequently been shown to be due to debonding of the particles followed by plastic void growth [14,15,83]. Indeed, Kinloch and Taylor [83] have also demonstrated that the voids around particles closed-up when the epoxy polymer was heated above its T_g and allowed to relax. The debonding process is generally considered to absorb little energy compared to the plastic deformation of the matrix. However, debonding is essential because this reduces the constraint at the crack tip and hence allows the matrix to deform plastically via a void growth mechanism.

More recently, Johnsen *et al.* [82] investigated thermoplastic/epoxy blends, which were formed using a semi-crystalline thermoplastic, syndiotactic polystyrene (sPS), as the toughening phase. Phase separation of dissolved sPS from the epoxy occurs upon curing of the resin. The phase-separated particles were in the form of spheres, depending on the phase separation method. They reported that debonding of the sPS and epoxy phases and plastic void growth of the epoxy matrix were observed for the thermoplastic/epoxy blend containing the sPS spheres, as shown in Figure 2.6.4 (a). The evidence of these mechanisms was also observed by Kinloch and Taylor [83], where cavities were observed around the particles, as shown in Figure 2.6.4 (b).

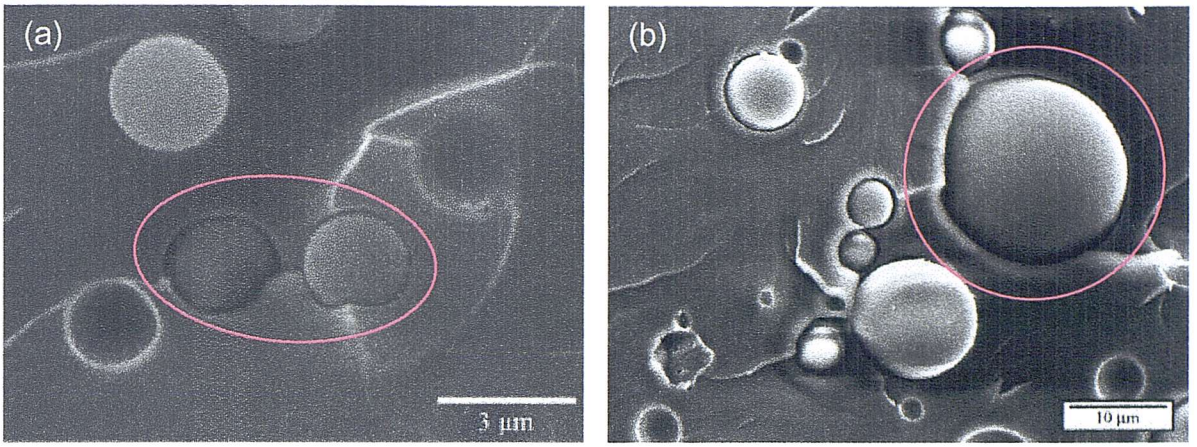


Figure 2.6.4. Scanning electron microscope images of fracture surfaces of (a) sPS spheres and (b) hollow glass spheres toughened polymers [82,83]. (The pink circles illustrate debonding and void growth.)

2.6.1.4 Microcracking

Evans *et al.* [84] proposed microcracking of the matrix as an alternative deformation mechanism. They reported that the residual misfit strain due to differential shrinkage between the matrix and the particles results in residual tangential stresses. Consequently, the applied load imposes additional tangential tensile stresses, which may cause microcracking of the matrix. The micrographs in Figure 2.6.5 clearly show evidence of microcracking.

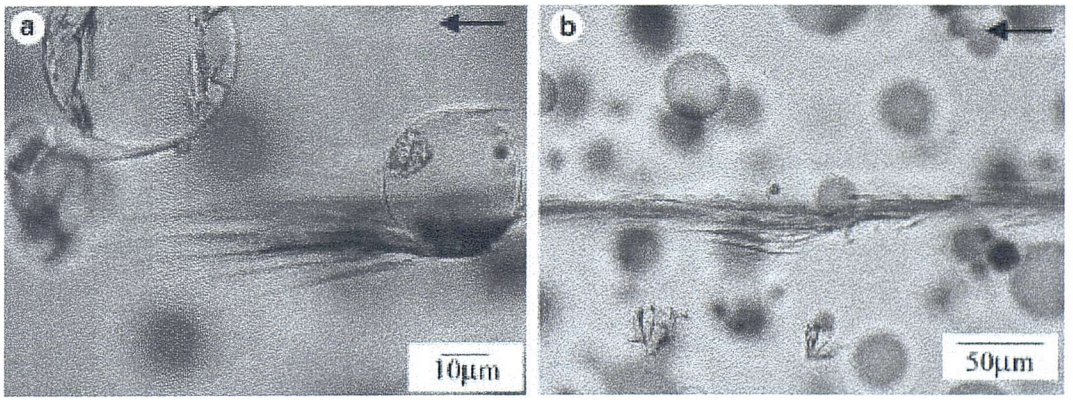


Figure 2.6.5. Fluorescent microscopy images of glass sphere toughened epoxy polymers in (a) crack tip and (b) crack wake region. Note the presence of microcracks at the crack tip and in the crack wake. Arrows indicate direction of crack growth [89].

2.6.2 Effect of Volume Fraction and Particle Size

According to several researchers [12,90-92], the fracture energy of a rigid particle toughened epoxy polymer passes through a maximum at a given volume fraction, V_f, but the position of the maximum depends upon the particle size as illustrated in Figure 2.6.6 (a). However, the fracture toughness, K_{Ic}, may increase steadily with increasing volume fraction due to the continuous increase in modulus, E, with V_f as may be seen from Equation 2.8 and 2.9. Spanoudakis and Young [12,93] investigated the effect of particle volume fraction and size on the fracture behaviour of spherical glass bead toughened epoxy polymers in terms of Evans' [87] theory. Figure 2.6.6 (b) shows some of the results where the ratio of K_{Ic} for the toughened polymer to K_{Ic} for the untoughened matrix is plotted against the ratio of the particle radius to inter-particle distance, r_{pa}/ID. The inter-particle distance was calculated [58] from the following relationship:

$$ID = 2r_{pa}\left[\left(\frac{\pi}{6V_f}\right)^{1/3} - 1\right] \qquad \textbf{Equation 2.24}$$

The data in Figure 2.6.6 (b) are from experimental results with two different particle sizes, Δ, r_{pa}=2.5μm, , r_{pa}=31μm, theoretical curves from the Evans' theory (i) [87] and modification to it calculated by Green *et al.* (ii,iii) [88]. There is a reasonable agreement between the theory and experimental data. However, at higher values of r_{pa}/ID, some experimental points fall below the lower theoretical curve. The authors suggested that the difference between these values as being due to a change in toughening mechanism from crack pinning to interfacial breakdown at the particle/matrix boundary, which makes pinning more difficult. Moreover, this change in mechanism coincides approximately with the maximum fracture energy value for the toughened epoxy polymers.

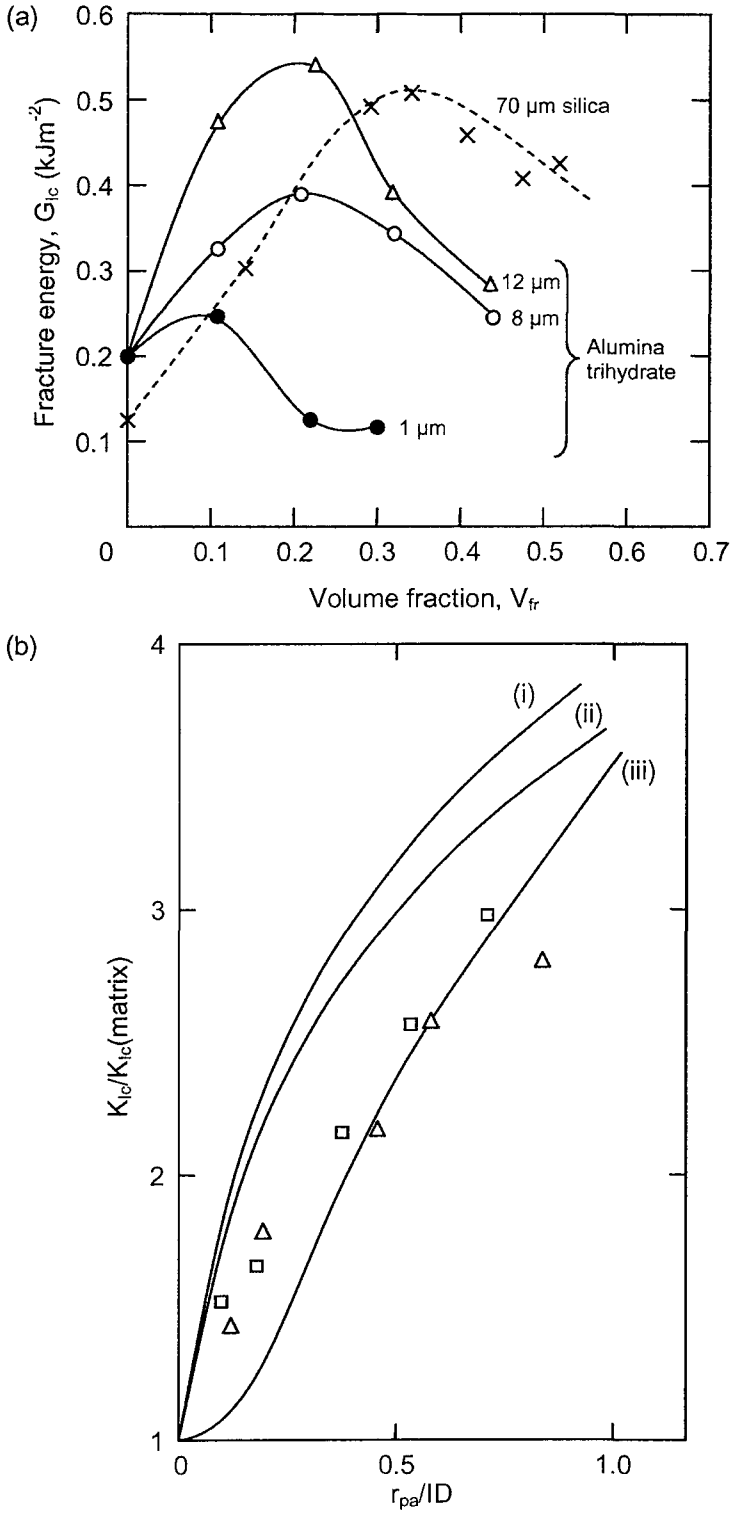


Figure 2.6.6. (a) Relationship between fracture energy, G_{Ic}, and volume fraction, V_{fr}, of rigid particle toughened epoxy polymers; (b) Relationship between K_{Ic}/K_{Ic}(matrix) and the ratio of the particle radius to inter-particle distance, r_{pa}/ID, for a glass bead toughened epoxy polymers. Δ, r_{pa}=2.5μm; , r_{pa}=31μm. Theoretical curves from (i) Evan's theory and (ii & iii) modification of Green et al. [21].

Recently, Lee and Yee [85] investigated the fracture behaviour of rigid particle toughened epoxy polymers employing glass beads with two different diameters of 3.3 and 24.4μm. They reported that the fracture toughness and modulus of the toughened epoxy polymer generally increases with the increasing volume fraction of glass beads. The increase would not occur indefinitely because of the reduced inter-particle distance, and the reduced amount of epoxy available for deformation. However, they mentioned that the effect of glass bead size on the fracture toughness and modulus is not significant.

Generally, according to previous studies reviewed here, the fracture toughness, K_{Ic}, of rigid particle toughened epoxy polymer increases as the volume fraction of the rigid particles increases. However, the fracture energy, G_{Ic}, reaches a peak at a certain volume fraction and the toughening effect diminishes after the peak (due to the increasing Young's modulus). Moreover, epoxy polymers toughened with larger rigid particles (>2μm) are slightly tougher than those with smaller rigid particles.

2.6.3 Hybrid (Rubber & Rigid Particle Toughened) Epoxy Polymers

In order to obtain optimum properties from toughened epoxy polymers, hybrid epoxy polymers, which contain both rubber and rigid particles, have been investigated. Kinloch *et al.* [63] incorporated CTBN rubber and glass beads with epoxy polymers to investigate their fracture behaviour. They employed a fixed amount of rubber with varying volume fractions of untreated and silane-treated glass beads. According to their results, the fracture toughness of the hybrid epoxy polymer was higher than either of the formulations containing only the individual tougheners. The authors indicated that the increase in toughness seems to be a result of both crack pinning and plastic shear yielding. Moreover, formulations containing silane-treated glass beads showed higher fracture toughness values than untreated beads, which may indicate that increasing interfacial adhesion strength also improves the efficiency of the crack-pinning mechanism. Furthermore, a maximum fracture toughness value was observed with a glass bead volume fraction of 0.1. Vallo *et al.* [94] investigated the influence of rubber-phase morphology on the mechanical properties of hybrid epoxy polymers by employing various rubber contents (epoxy-terminated acrylonitrile-butadiene random copolymer (ETBN)) while maintaining the volume fraction of glass beads. The authors

observed different morphologies depending on the rubber content. The classic random dispersion of rubber particles was seen up to 10 wt. % of rubber, which showed the highest fracture toughness value. At 15 wt. % rubber, large and irregular domains were present, and a co-continuous structure was generated at 20 wt. %. They suggested that the increase in the fracture toughness is a synergistic effect of the different toughening mechanisms.

Alternatively, Low *et al.* [95] employed zirconia particles, short alumina fibres or glassy-metal ribbons ($Fe_{60}Ni_{20}B_{10}Si_{10}$) with a fixed amount of epoxy polymer and CTBN rubber. The diameter of the zirconia particles was less than 1μm, and the alumina fibres were about 5μm thick and 2mm in length. Short glassy-metal ribbons were 0.75mm wide by 39.5μm thick with an average length of 6mm. They reported that the hybrid epoxy polymers with glassy-metal ribbons exhibited the highest fracture energy value. The authors claimed that their formulation with glass-metal ribbons possessed the highest toughness values to date (K_{Ic} of 4.2MPa $m^{1/2}$ and G_{Ic} of 5.4kJ/m^2). However, the hybrid epoxy polymers containing zirconia particles and alumina fibres resulted in less significant increases of toughness compared to the glass-metal ribbons, even though their toughness values were around 50-80% higher than the simple rubber toughened epoxy polymers. By microscopic observations, they proposed that the toughening effect of the glassy-metal ribbons is due to rubber particle cavitation and matrix shear yielding, plus ribbon interfacial debonding, pull-out and bridging mechanisms.

Azimi *et al.* [96] investigated the effect of varying the volume fraction of rubber and glass particles while maintaining the total volume fraction of toughenners. According to their results, a synergistic effect is found for the rubber/glass formulation of 7.5%/2.5%, which is shown in Figure 2.6.7. Increasing the glass sphere content to 7.5% and decreasing the rubber content to 2.5% resulted in a reduction of toughness to lower than that of the rubber-only toughened polymer. This suggests that the volume fraction of rubber should not be less than the rigid particle content to obtain good toughness in hybrid polymers. The authors observed the crack pinning mechanism associated with glass spheres, which is in agreement with Kinloch's observation [63]. However, they also mentioned that the synergy of hybrid epoxy polymer is found to be stretching of the plastic zone due to the presence of the glass particles. In other words, the driving force

for glass particle debonding is reduced, following the cavitation of the rubber particles, which increases the pinning/bridging efficiency of the glass particles in the hybrid system.

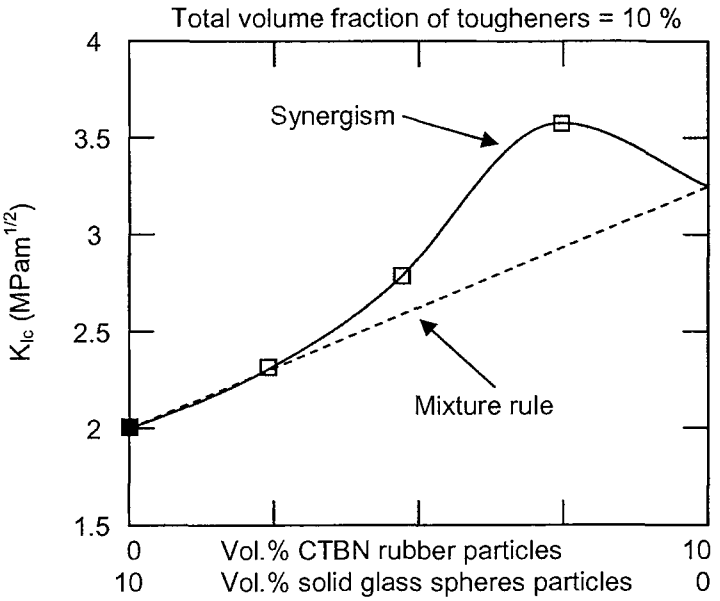


Figure 2.6.7. Fracture toughness, K_{Ic}, versus volume fraction of tougheners showing synergistic toughening [96].

Generally, the addition of a rubbery phase can toughen the epoxy polymers by promoting mechanisms such as shear yielding and plastic void growth. However, there is often a decrease in yield strength and stiffness associated with incorporation of rubber particles. Incorporating rigid particles can enhance the toughening mechanisms, even though the efficiency is not comparable to that of the rubber toughened epoxy. Nevertheless, the use of rigid particles may provide desirable engineering properties such as thermal and electrical properties. Unifying both mechanisms showed further toughening effects at certain content ratios. Hybrid epoxy polymers showed the potential to provide additional properties along with the toughening effect, and hence further investigation of hybrid materials and the toughening mechanisms associated with rubber particles and rigid particles are required.

2.6.4 Nano-scale Particle Toughened Polymers

There is a new technology which has emerged and holds a promising future in many engineering fields. This is known as 'nano-technology' which refers to any technology

which deals with the manipulation of materials in the nano-metre range (nm). A nano particle may be defined as any particle that has at least one dimension in the nano-metre range. Particles such as nano-clays [97] are plate-like in shape and have their thickness in the nano range. Carbon nano-tubes and nano-fibres [98] are strand-like in shape and have both their thickness and width in the nano-metre range. Nano-silica spheres (as used in this study) have all three dimensions in the nano-metre range.

Nanotechnology affords unique opportunities to create revolutionary material combinations. These new materials will enable the circumvention of classic material performance by accessing new properties and exploiting synergism. The uniform dispersion of nano-sized particles produces a large interfacial area per unit volume compared to large particles. These characteristics imply the overall performance of polymer nano-composites may not be fully understood by simple scaling arguments that may apply to traditional polymer composites. Overall, the advance and application of nanotechnology could lead polymer composites to be even more attractive materials.

2.6.4.1 Nano-Silicate Toughened Polymers

The development of inorganic reinforced polymers has received considerable attention. Recent research shows the potential of these composites, for example using surface-treated silicates or organoclays to produce layered-silicate nano-composites [99,100]. Currently, the layered silicates are the most commonly used inorganic nano-materials in polymer nano-composites. Each silicate layer is around 1nm thick, and the lateral dimensions of these layers may vary from 30nm to several microns and even larger depending on the particular silicates. These layers are organised in stacks with a regular Van der Waals gap in between them called the interlayer or the gallery [101]. These stacks can be used to form polymer layered-silicate nano-composites using various approaches. The effects of these materials are to increase the tensile modulus and strength, without sacrificing other polymeric properties, even when small amounts are employed (as little as 2% by volume).

Alternatively, silica (SiO_2) nano particles can be surface modified and cross-linked into the resin during the cure. This technique enables modified nano-silica to mix with a variety of matrix resins without agglomeration. The particles are created during a sol-

gel process and their size remains unchanged during further processing steps. A hybrid epoxy polymer can be formulated by incorporating the nano-silica particles with a rubbery phase and epoxy resin. Most of the literature that has been published at the time this Thesis was being written, on the use of nano-silica in epoxies and moreover, in FRPs, stems from the work done in this study. Accordingly, these results will be discussed later in the Thesis instead of in the literature review, but for reference purposes, the literature can be found in the following publications: [102-108].

2.7 Fibre reinforced polymers (FRPs)

Fibres can be added to an epoxy to enhance its properties, and the most common fibres are made from organic fibre or glass, and both are investigated in this thesis. Rigid micron-sized particles cannot be used in the matrix, since the fibres act as a sieve due to their micron-sized diameters and even smaller inter-fibre separation [106]. This makes the use of nano-silica particles attractive as a toughener in the matrix, since they are so small and can penetrate between fibres during the manufacturing and curing process. It should be reiterated that the rubber remains dissolved in the epoxy phase during laminate manufacture, and only phase separates as rubbery particles on curing.

2.7.1 Reinforcements

There are a number of different types of reinforcement available today, some of which are designed for particular matrices. However, all have relatively high stiffness and low density [109].

2.7.1.1 Aramid fibres

These were first developed by Du Pont under the trade name *Kevlar* and are made from aromatic polyamides by extrusion and spinning. They have a Young's modulus of ~130GPa parallel to the chain axis and a much lower modulus (~10GPa) perpendicular to the fibre axis. They have a very high tensile strength of up to 3GPa, are highly anisotropic and because of the weak inter-chain bonding, they readily split into much finer fibrils and microfibrils [109]. Aramid fibres are used in the laminates to make bullet-proof vests, but have not been used in this study.

2.7.1.2 Glass fibres

Most glass fibres are based on silica (SiO_2) and there are three types of glass that are commonly used in composites:

- E-glass (E for electrical) – good strength (3.5GPa), stiffness (76GPa), electrical and weathering properties
- C-glass (C for corrosion) – better corrosion resistance than E-glass, but lower strength (3.3GPa) and stiffness (69GPa)
- S-glass (S for strength) – highest strength (4.6GPa), stiffness (86GPa) and cost

Glass fibres, unlike carbon and aramid fibres, are isotropic, and have the same axial and transverse modulus [109]. In this study, E-glass fibres were used.

2.7.1.3 Carbon fibres

Carbon fibres consist of small crystallites of turbostratic graphite – one of the allotropic forms of carbon. There are three main routes for producing carbon fibres:

- From polyacrylonitrile (PAN) fibres – method to produce most high modulus fibres (up to 500GPa and a tensile strength of 2.5GPa). PAN is drawn down to a fibre, stretched, heated in oxygen, reduced and converted to turbostratic graphite by heating at elevated temperatures.
- From mesophase pitch – heated and then rapidly extruded and oxidised. Graphite fibres form when cooled.
- From pyrolytic deposition – formed by pyrolytic deposition from the gases such as methane and benzene. Turbostratic carbon fibres are formed with poor control over fibre diameter. Little use in industry so far [109].

The fibres used in this study were made from PAN.

2.7.2 Manufacture

The method of manufacturing the FRPs in this study was by vacuum assisted resin transfer moulding (VARTM), which is used for woven fibres, and not uni-directional (UD) fibres. It is not applicable to making UD laminates, since the vacuum would cause

the fibres to become very close to each other, and would not allow the flow of resin between fibres.

In this process, a stack of fibres is laid up and then covered with peel ply and a knitted type of non-structural fabric. The whole dry stack is then vacuum-bagged, and when the bag-leaks have been eliminated, resin is allowed to flow at an elevated temperature (to reduce viscosity) into the laminate from one end. The resin distribution over the whole laminate is aided by a vacuum at the other end, as illustrated in Figure 2.7.1.

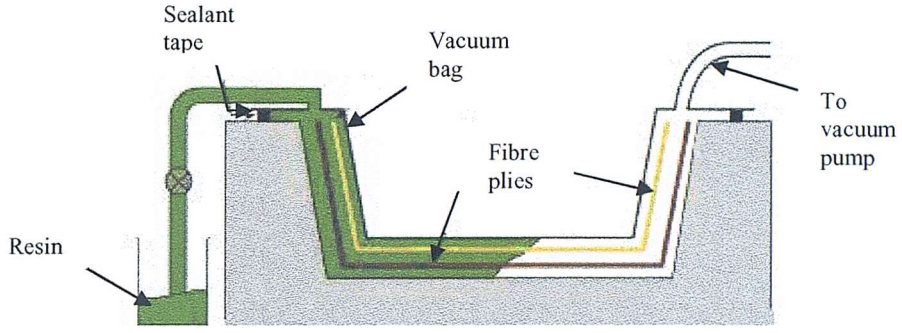


Figure 2.7.1. Schematic showing VARTM process [110].

To achieve optimal and reproducible laminate quality, the processing of VARTM parts demands a lot of experience and great operator skill. The impregnation of the fibre reinforcements inside the mould is one of the most important VARTM processing steps to influence the final part quality. Local deviations of the permeability inside the preform prevent a homogeneous flow front and wet-out of the fibres. Typical appearances are the channelling effect, deviations in compression characteristics of fibre layers and shear deformations during preforming. Additional restrictions, such as high fibre volume fraction, integrated inserts and thick part areas, are demands of VARTM parts which also make reproducible quality difficult. The consequences are pores or dry spots on the surface and inside the laminate which can be avoided by flushing the laminate with excess resin. Another process step which is important for the laminate quality is the curing phase, which can last from several minutes to several hours and dominates the cycle time [111]. The laminates used in this study were cured for several hours at a temperature above room temperature, and laminate quality was an issue in only one of the three different systems of laminates researched.

2.7.3 FRP Fracture Mechanisms

In a given FRP, more than one toughening mechanism may be at work, even though one particular mechanism may dominate. The effectiveness of these toughening mechanisms depends to varying degrees on a number of factors, such as [109]:

- Size, morphology and volume fraction of the reinforcement fibres
- Interfacial bonding between the fibre and the matrix
- Thermal and mechanical properties of the matrix and the reinforcement fibres

The general physics of fracture mechanics described in previous Sections, still apply to FRPs, but this Section will briefly describe some of the additional toughening mechanisms at work in FRP laminates.

2.7.3.1 Matrix Deformation

The extent of matrix deformation during laminate fracture may differ appreciably from that of the bulk resin. The main effect is one of increased constraint, so that the matrix is unable to deform freely because it is surrounded by stiff and strong fibres. There is thus a tendency for triaxial stress states to be set up which inhibit plastic flow of the matrix. Indeed, the deformation of the matrix between fibres may be thought of as an adhesive joint, where the matrix is the adhesive, and the fibres are the substrates. The radius of the crack tip can be larger than the distance between fibres (which is analogous to an adhesive joint where the epoxy is the adhesive, and the fibres are the substrates), and this may limit matrix deformation [112]. Theory suggests, therefore, that the presence of fibres limits the plastic deformation of the matrix [109]. It should be noted that the toughening mechanisms described in preceding Sections for rubber and rigid particles, are also present when a toughened laminate deforms. For example, if the matrix of a laminate is toughened with CTBN, then there may be cavitation of the rubber particles when the laminate undergoes loading.

2.7.3.2 Fibre Fracture

Depending on the fibre architecture and the loading configuration, component failure usually involves the fracture of fibres. In general, the contribution this makes to the fracture energy of the laminate is small for most fibres. In particular, typical fracture

energies for fibres of glass and carbon (as have been used in this study) are only a few tens of J/m^2 [109].

2.7.3.3 Crack Bowing and Deflection

Crack bowing (crack pinning) is also present in fibre composites, and has been discussed in a previous section (see Figure 2.6.1). The increase in fracture energy from crack bowing increases with the volume fraction of reinforcement fibres, and is dependent on the size (diameter and length) of the reinforcement [113].

The interaction between the crack front and the reinforcement can cause the crack to deflect, and to become non-planar. Indeed, this crack deflection may be a twisting or tilting motion around the fibre, which alters the mode of cracking. Tilting produces a mixture of modes I (tensile) and II (in-plane shear), whereas twisting produces a mixture of modes I and III (anti-plane shear) [81,114,115].

In both cases, crack propagation is hindered, although it is believed that crack deflection toughening arises mainly from twisting rather than tilting of the crack [113].

2.7.3.4 Fibre Debonding and Pull-out

Sometimes, the fibre can start to debond from the epoxy matrix, as shown in Figure 2.7.2. New surfaces are created during this process, which leads to an increase in the fracture energy.

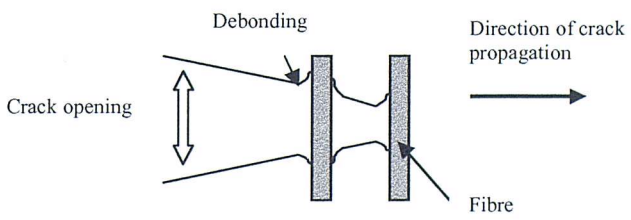


Figure 2.7.2. Schematic showing fibres debonding from an epoxy matrix [113].

Sometimes, the fibre debonds almost completely from the epoxy matrix, in a process called 'pull-out' as shown in

Figure 2.7.3. A force is required to pull out the fibre as normal frictional forces need to be overcome. Pull-out can also occur in continuous FRPs, as variations in strength along the length of the fibres allow fracture to occur. If fibre fracture precedes pull-out there will be an additional contribution to toughness, since a loaded debonded fibre dissipates energy when it fractures. This pull-out mechanism is potentially the most significant contributor to the fracture energy of a laminate [109].

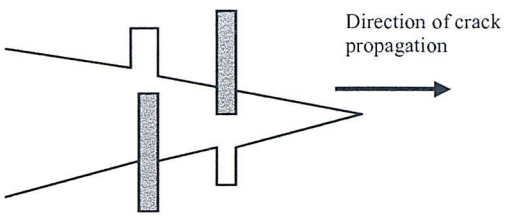


Figure 2.7.3. Schematic showing fibre pull-out [113].

2.7.3.5 Fibre Bridging

Another common type of toughening mechanism is fibre bridging. In this scenario debonding takes place, but not all the fibres in the wake of the crack have fractured, and some bridge the 'crack gap'. This is illustrated in Figure 2.7.4.

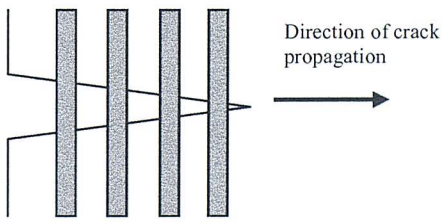


Figure 2.7.4. Schematic of the fibre bridging mechanism [113].

As the crack opens under the applied force, some of the stress will be transmitted to the fibres, which will deform elastically. There is a corresponding reduction in the K values at the crack tip, and therefore, crack progression is hindered. This toughening mechanism occurs not at the crack tip, but in the crack wake. As the crack extends, the wake region increases in size, and the toughness contribution from fibre bridging increases as a consequence, until a steady-state toughness value is reached (R-curve

behaviour is displayed where the fracture energy increases with increasing crack length).

The toughness of a material can also be enhanced by the presence of microcracks. The strain energy of the primary crack is lowered, since the microcracks enter the stress field at the crack tip, and the ensuing interactions cause crack blunting, branching and deflection.

2.8 Chapter Summary

This Chapter has reviewed epoxy polymers, the basic principles of fracture mechanics, the deformation behaviour of polymers and the toughening mechanisms of rubber and rigid particle toughened epoxy polymers. It has also discussed FRP constituents, manufacture and toughening mechanisms. The next Chapter will review the materials and the experimental techniques which have been used in the present study.

CHAPTER 3

MATERIALS AND EXPERIMENTAL PROCEDURE

3 Background

This Chapter will describe the materials used in this study, as well as the experimental and data analysis methods employed in characterising the material properties and fracture of the epoxy nano-composites.

3.1 Materials

It was stated in Chapter 1 that three epoxy-based systems were investigated in the present study, and each system shall be described individually, in the order in which their 'Results Chapters' appear subsequently in the thesis. It should be noted that the formulations were supplied ready-made in the form of bulk epoxy polymer and FRP laminate plates, by *hanse chemie (Geesthacht, Germany)*. The term 'wt. %' refers to the percentage by weight of a cured sample that contains that constituent. For example: '9 wt. % CTBN and 11 wt. % nano-silica' means that in a cured sample weighing 100g, there would be 9g of CTBN, 11g of nano-silica, and 80g of epoxy and hardener.

3.1.1 Amine-cured DGEBA-based

The amine-cured DGEBA-based system used an epoxy polymer made from epichlorohydrin and the disodium salt of bisphenol-A, to give diglycidylether of

bisphenol-A (DGEBA). The rubber used was a low molecular weight copolymer of butadiene and acrylonitrile with a carboxy-terminated (CTBN) end-group and was 'Hycar 1300x8', produced by *Emerald Inc., (Cleveland, USA)*. This was pre-reacted with the DEGBA resin to give a 40 wt. % CTBN-epoxy adduct: 'Albipox 1000' from *hanse chemie (Geesthacht, Germany)*. The nano-silica particles that were added to the epoxy are initially well dispersed, have a narrow particle-size distribution and an average particle size of about 20nm, as shown in Figure 3.1.1 and Figure 3.1.2 respectively. The particular grade of nano-silica used was 'Nanopox F400' and was produced by *hanse chemie* as an epoxy resin with 40 wt. % of nano-silica particles.

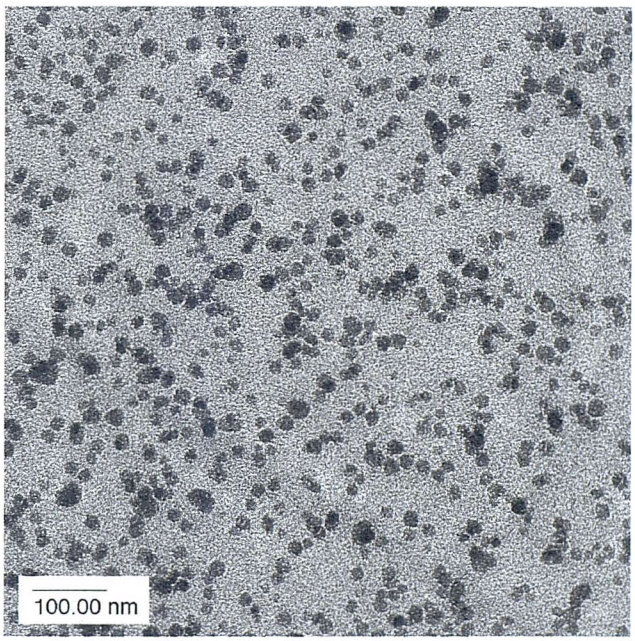


Figure 3.1.1. Transmission electron micrograph of epoxy with 5 wt. % nano-silica, showing excellent dispersion [116].

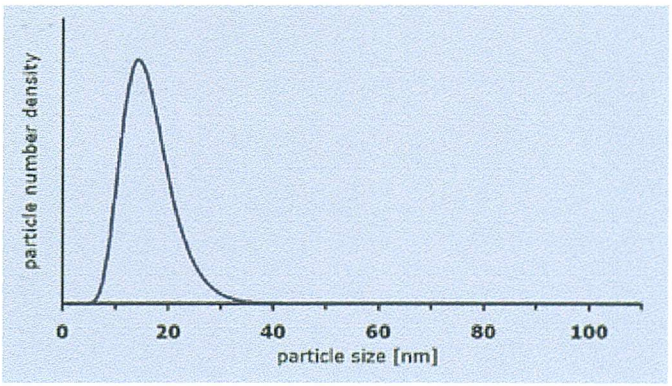


Figure 3.1.2. Graph showing particle size distribution of nano-silica particles, determined by small angle neutron scattering (SANS) [116].

The bulk samples were cured by firstly mixing together the DGEBA epoxy with the given amounts of the nano-silica epoxy and the CTBN-epoxy adduct, to give the required levels of added nano-silica and CTBN rubber. The value of the epoxy equivalent weight (EEW) of the blend was then calculated and the stoichiometric amount of the cycloaliphatic amine hardener ('Hardener 286' from *MGS/Hexion, Germany*) was added to the mixture, which was then cured for 2 hours at 80°C. Bulk epoxy polymers from this system are used as adhesives and for marine coatings.

E-Glass fibres were used to reinforce laminates using the bulk epoxies as the matrix. The glass fibres used were in the form of an isotropic linen-weave (ie. plain weave) fibre fabric, provided by *Lange-Ritter (Gerlingen, Germany)*. The glass fibres had a density of 200g/m^2, and were arranged in a 0/90° pattern. Eight plies of the fabric were used to manufacture the fibre reinforced polymers (FRPs) by vacuum-assisted resin transfer moulding (VARTM) at an injection temperature of 60°C, and then cured for 2 hours at 80°C. The fibre:resin ratio was 3:2. (Note that a thin film of polytetrafluoroethylene (PTFE) was inserted 30mm into the fabric along one edge prior to resin infusion to act as a starter crack for the fracture specimens.) FRPs based upon this system are used in windmill blades, sporting goods and racing boats.

3.1.2 Amine-cured TGMDA-based

The amine-cured TGMDA-based system used an epoxy of tetraglycidyl methylene dianiline (TGMDA). The reactive liquid rubber used was 'Hycar CTBN 1300x8' and was provided by *Emerald Inc., (Cleveland, USA)*. This was pre-reacted with the epoxy resin to give a 26 wt. % CTBN-epoxy adduct, supplied by *hanse chemie, (Geesthacht, Germany)*. The nano-silica was obtained at a master-batch concentration of 30 wt. % in this epoxy polymer and was produced as 'Epikote 486' from *Hexion, (Duisburg, Germany)*. The nano-silica particles in this system had the same size and distribution as in the amine-cured DGEBA-based system. The samples were cured by firstly mixing together the TGMDA epoxy with given amounts of the nano-silica epoxy and the CTBN-epoxy adduct, to give the required levels of added nano-silica and CTBN rubber. The value of the EEW of the blend was then measured via titration, and the stoichiometric amount of the hardener (a mixture of two sterically-hindered aromatic-

amines, supplied by *POLYNT, SpA, (Scanzorosciate, Italy)*) was added to the mixture, which was then cured for 2 hours at 180°C.

Eight plies of a 0/90° isotropic linen-weave of carbon fibre-fabric ('Style 439 T') was used to make FRP laminates by VARTM using the bulk epoxies as the matrices. The carbon fibres used ('Tenax HTA 5131') had a density of 370g/m^2 and were supplied by *ECC, (Germany)*. The fibre:resin ratio was 3:2 and the injection temperature was 120°C followed by a cure cycle of 2 hours at 180°C. (Note that a thin film of polytetrafluoroethylene (PTFE) was inserted 30mm into the fabric along one edge prior to resin infusion to act as a starter crack for the fracture specimens.) FRPs based upon this system are used in aerospace applications and Formula 1 cars.

3.1.3 Anhydride-cured DGEBA-based

The anhydride-cured DGEBA-based system used a DGEBA epoxy, and the curing agent was an accelerated methylhexahydrophthalic acid anhydride, ('Albidur HE 600') supplied by *hanse chemie, (Geesthacht, Germany)*. The CTBN used ('Hycar 1300x8') was produced by *Emerald Inc., (Cleveland, USA)* which was pre-reacted with the DEGBA epoxy to give a 40 wt. % CTBN-epoxy adduct: 'Albipox 1000' from *hanse chemie (Geesthacht, Germany)*. The nano-silica used was 'Nanopox F400' from *hanse chemie*, and was produced as an epoxy resin with 40 wt. % of nano-silica particles. The bulk samples were cured by firstly mixing together the DGEBA epoxy with given amounts of the nano-silica epoxy and the CTBN-epoxy adduct, to give the required levels of added nano-silica and CTBN rubber. The value of the EEW of the blend was then calculated and the stoichiometric amount of the accelerated methylhexahydrophthalic acid anhydride hardener ('Albidur HE 600' supplied by *hanse chemie, (Geesthacht, Germany)*) was added. The samples were cured for 1 hour at 90°C, followed by 2 hours at 160°C. Bulk epoxy polymers from this system are used as casts and on circuit boards.

Six plies of isotropic linen-weave carbon fibre fabric arranged in a 0/90° pattern with a density of 168g/m^2 and supplied by *Lange-Ritter, (Gerlingen, Germany)*, were used to make laminates by VARTM using the bulk epoxy as matrices. The fibre:resin ratio was 3:2, the injection temperature was 70°C, and the samples were cured for 1 hour at 90°C,

followed by a post-cure of 2 hours at 160°C. (Note that a thin film of polytetrafluoroethylene (PTFE) was inserted 30mm into the fabric along one edge prior to resin infusion to act as a starter crack for the fracture specimens.) FRPs based upon this system are used in sporting equipment such as ski poles, tennis racquets, hockey sticks, and surf board masts.

3.2 Microscopy

This section will discuss the various methods of microscopic analysis used to characterise the microstructure and fracture of both the bulk epoxies and the FRPs.

3.2.1 Scanning Electron Microscopy

A 'JEOL JSM 5300' scanning electron microscope (SEM) was used to investigate the fracture surfaces of both the FRPs and the bulk epoxies, with a typical acceleration voltage of 20kV. Small square pieces of side 2cm were cut from each FRP sample (or in the case of the bulk fracture surface, a shortened fracture sample was used), and adhered to an aluminium disk. A very thin coating of gold was sputtered over the sample to make it more conductive, and to avoid electrically charging the specimen. In general, the entire surface was scanned and images of striking and indicative surface features were saved. High resolution electron microscopy was performed on the fracture surfaces with an electron microscope equipped with a field emission gun (FEG-SEM). The instrument used was a 'Leo 1525' from *Carl Zeiss (Hertfordshire, UK)* equipped with a Gemini column. Typically, the acceleration voltage was set at 5kV. All specimens were coated with an approximately 5nm thick layer of gold or platinum before analysis.

3.2.1.1 Surface Roughness Measurements

Surface roughness measurements of the fracture surfaces were performed using a Form Talysurf series 2 from *Taylor Hobson (Pennsylvania, USA)*. A sharp stylus with a tip radius of 2.5mm, attached to a cantilever, was drawn across the surface at a constant speed for a set distance. Five measurements with a traverse length of 4mm were performed perpendicular to the direction of the crack growth. The average roughness, R_a, of the line profiles was calculated.

3.2.2 Microtoming

A 'PowerTome XL' ultramicrotome from *RMC Products (Arizona, USA)* was used to cut slices of specimens for the transmission electron microscope (TEM), and to prepare flat surfaces to be viewed under the atomic force microscope (AFM).

TEM slices of between 60-100nm were prepared by cryo-ultramicrotomy at a temperature of -65°C to reduce the compression of the rubber particles in particular. Since cryo-ultramicrotomy does not affect the microstructure of unmodified epoxy, or samples with nano-silica only, it was decided to microtome all samples at this temperature (ie. -65°C) for convenience. The TEM slices were then placed on a carbon-filmed copper grid, and the samples containing CTBN were stained with a solution of 2 wt. % osmium tetroxide in a 50:50 mixture (by volume) of water and tetrahydrofuran, for twenty four hours to improve the contrast of the rubber particles under the TEM.

The AFM samples just needed to have a very smooth surface, so the sample that provided the TEM slices, was subsequently used for AFM investigations.

3.2.3 Transmission Electron Microscopy

The microtomed slices were viewed using a 'JEOL JEM-2000FX II' transmission electron microscope (TEM) at an acceleration voltage of 200kV. This microscopy method was used to determine the microstructure of the samples.

3.2.4 Atomic Force Microscopy

Atomic force microscopy studies were undertaken on a MultiMode scanning probe microscope from *Veeco (California, USA)* equipped with a 'J' scanner and a 'NanoScope IV' controller. The scans were performed in tapping mode using silicon probes with a tip radius of ~10nm and both height and phase images were recorded. The imaging software used to perform volume fraction analyses on the micrographs, was the *Global Lab Image/2* from *Data Translation (Massachusetts, USA)*.

3.3 Bulk Thermal and Mechanical Tests

This Section reviews the preparation and methods used for determining the thermal, mechanical, and fracture properties of the bulk epoxy polymers.

3.3.1 Glass Transition Temperature

Dynamic mechanical thermal analysis (DMTA) was performed by testing bars 48×3×2mm in size in the three-point-bending mode at 1Hz, at a rate of 4°C per minute from -80 to 180°C, using a 'Tritec 2000 DMTA' from Triton Technology (*Nottinghampshire, UK*). The storage modulus, loss modulus and loss factor, *tan* δ, were calculated as a function of temperature. The glass transition temperature, T_g, was taken to be the temperature at which the peak value of *tan* δ occurred.

3.3.2 Tensile Tests

Tensile dumbbells were machined from the bulk plates with the profile shown in Figure 3.3.1. The Young's Modulus, E, of the bulk samples for the various blend compositions were measured in accordance with the relevant standards [117,118].

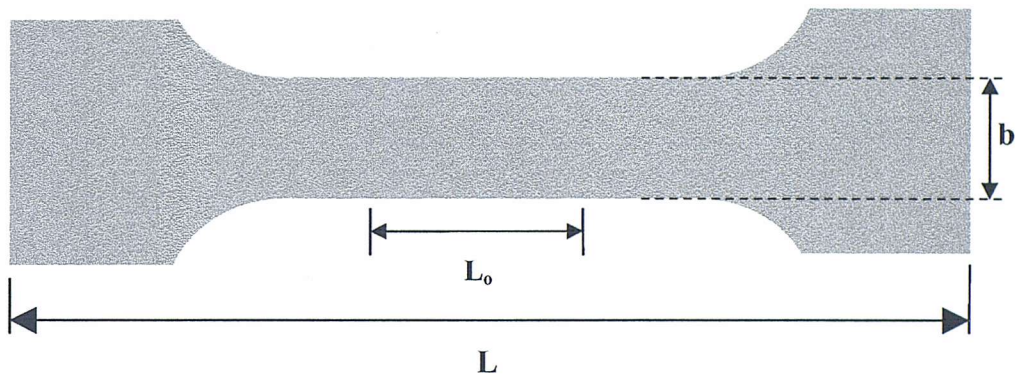


Figure 3.3.1. Schematic of a tensile specimen.

Typical measurements for the tensile specimens used were as follows:

L_0 = gauge length = 20mm

b = 3.8mm

B (not shown in this schematic) = plate thickness ~ 4mm

L = 75mm

After clamping in the testing machine, the specimens were pulled apart at a rate of 1mm/min, and at 20°C. The Young's Modulus was calculated from the elastic (straight line) portion of the load-displacement graphs recorded. The straight line portion of the graph was divided into a number of segments and the modulus was calculated for each

segment. The Young's modulus of the sample was taken as the largest modulus of all the line-segments. The following simple equations were used to determine the Young's Modulus:

$$\sigma = \frac{P}{A} \qquad \textbf{Equation 3.1}$$

$$\varepsilon = \frac{e}{L_0} \qquad \textbf{Equation 3.2}$$

$$E = \frac{\sigma}{\varepsilon} \qquad \textbf{Equation 3.3}$$

where σ is the stress, P is the applied load, A is the cross sectional area of the sample in the gauge region, ε is the strain, L_0 is the gauge length and e is the extension of the gauge length (measured by a clip-on extensometer).

3.3.3 Single Edge Notch Bend Tests

To ascertain the fracture toughness of the bulk materials, single edge notch bend specimens (SENBs) were machined from plates of the bulk epoxies, and tested in accordance with the relevant standard [119]. A pre-crack was inserted in each specimen to increase constraint at the crack tip, by drawing a razorblade through the notch. Figure 3.3.2 shows the dimensions of the specimens machined.

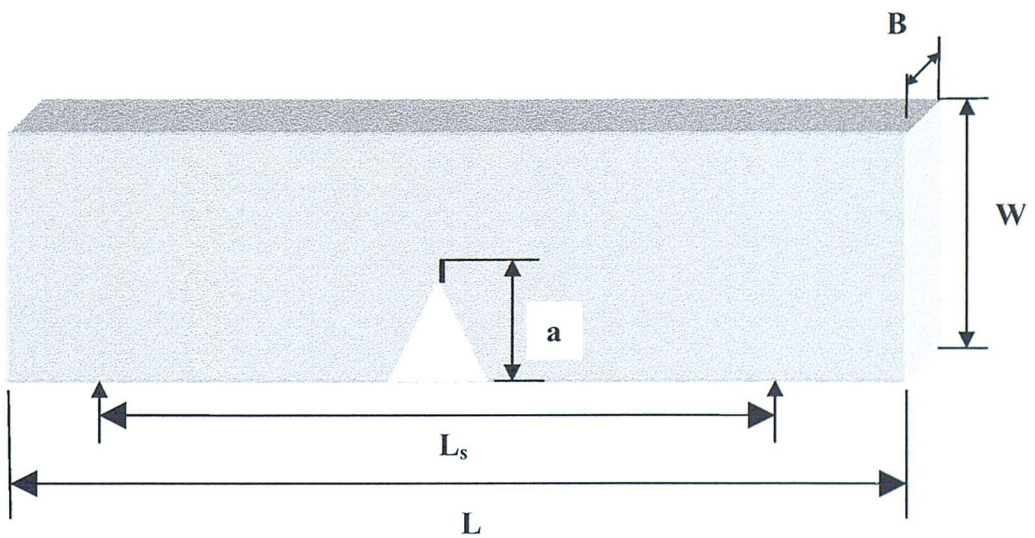


Figure 3.3.2. Schematic of an SENB specimen.

Typical measurements for the SENB specimens used were as follows:

W = 12mm

B = plate thickness ~ 4mm

a = 5.6mm (razor blade notch ~0.1mm in length)

L = 52.8mm

$L_s = 4W = 48mm$

During testing, the specimen was loaded at the centre of the specimen in line with the notch, and supported on the two outer loading points. For each blend composition, at least three replicate specimens were tested, at a test rate of 1mm/min at 20°C. Load-displacement graphs were recorded, and these were used to calculate the fracture toughness according to the standard [119].

The aim was to quantify the critical stress-intensity factor, K_{Ic}, for the various bulk specimens. Plane strain conditions were satisfied since the samples were sufficiently thick (see Equation 2.9 in the Literature Review Chapter).

The toughness was calculated from [119]:

$$K_{Ic} = (P_{Ic} B W^{\frac{1}{2}}) f(x) \qquad \textbf{Equation 3.4}$$

Where P_{Ic} is the maximum load and $f(x)$ is:

$$f(x) = 6x^{\frac{1}{2}} \frac{\left[1.99 - x(1-x)(2.15 - 3.93x + 2.7x^2)\right]}{(1+2x)(1-x)^{\frac{3}{2}}} \qquad \textbf{Equation 3.5}$$

and $0<x<1$, where $x = a/W$.

During post-experiment analysis, the fracture toughness values were converted to fracture energy values, to compare to those of the FRPs (see Equation 2.8 in the Literature Review Chapter).

3.4 FRP Tests

This Section reviews the preparation and methods used for determining the mechanical properties of the FRP samples. The specimens were all cut from the laminates using a circular saw lubricated with cutting fluid, and each DCB sample was cut from the end of the laminate that had a pre-inserted starter film during manufacture.

3.4.1 Mode I Fracture Tests

Double cantilever beam (DCB) specimens with a pre-inserted starter crack were used to measure the interlaminar fracture energy, G_{Ic}, of the laminates under mode I loading conditions. Aluminium-alloy end-blocks were grit-blasted and wiped with acetone to improve adhesion-integrity during testing. They were then bonded on either side of the sample (which was also grit-blasted and acetone-wiped) with a two-part rubber toughened epoxy, and placed in jigs to cure at 60°C for 1 hour. White, water-soluble 'Tippex' was applied to the side of each sample, and graduated in millimetres. The sample was then positioned in the testing machine and secured by pins through the holes of the two end-blocks. A travelling microscope was placed in line with the graduations on the side of the sample to observe crack progress. During testing of some of the laminates, there was a large radius of curvature of the laminate-arm or the specimen broke near the pre-crack. It was decided that backing beams were needed for the repeat tests. Uni-directional, 1mm-thick carbon fibre composite beams were adhered to the DCBs to improve stiffness and to promote stable crack growth. The same preparation, adhesive and curing regime that was used for adhering the end-blocks, were used to attach the backing beams to the FRPs. The tests were performed according to the relevant standard [120] and a schematic of a DCB sample is shown in Figure 3.4.1.

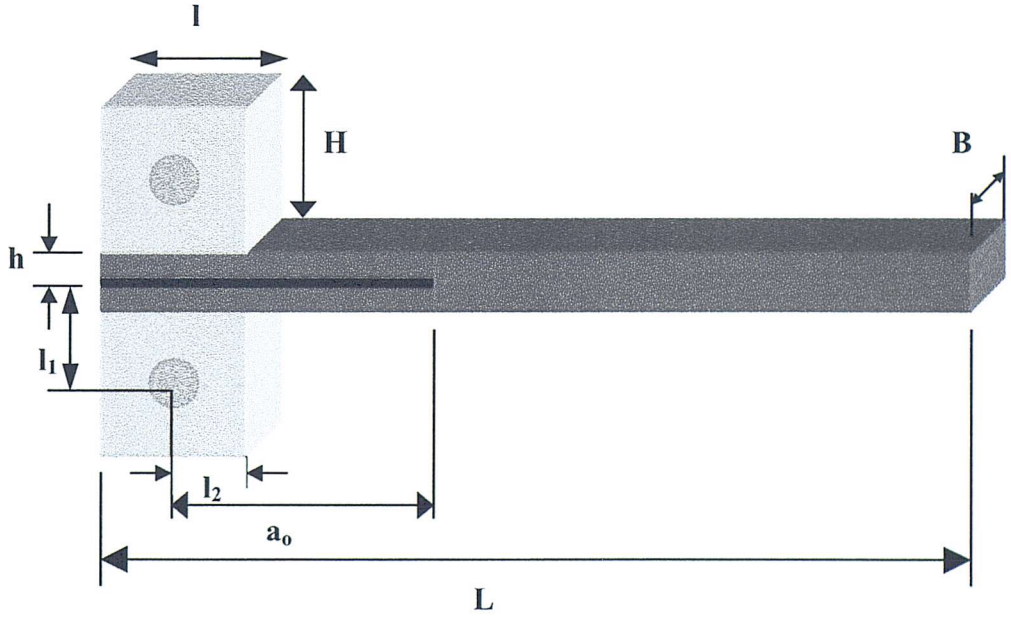


Figure 3.4.1. Schematic of a DCB specimen.

Typical measurements for the DCB specimens were as follows:

L = 145mm

a_o = 20mm

h = half thickness of laminate ~ 1.5mm

H = 12.5mm

l = 20mm

B = 20mm

Each specimen was loaded at a cross-head speed of 1mm/min at 20°C under tensile conditions for the crack to propagate ~5mm beyond the pre-inserted starter crack, and then unloaded at a rate of 5mm/min. The specimen was loaded again at 1mm/min until the crack progressed to at least 80% along the length of the sample, and then unloaded at 5mm/min. The crack lengths were recorded at the initiation and arrest points on the load-displacement traces and the value of the interlaminar fracture energy was calculated at each point. For each formulation, at least three samples were tested.

The critical mode I interlaminar fracture energy was calculated using the corrected beam theory (CBT) method for DCBs [120]:

$$G_{Ic} = \frac{3P\delta}{2B(a+|\Delta_I|)}\frac{F}{N} \qquad \textbf{Equation 3.6}$$

where P is the load at the onset of crack propagation, δ is the displacement, a is the crack length and Δ_I is the mode I crack length correction for a beam that is not perfectly built-in [121].

F, the large displacement correction, is given by:

$$F = 1 - \frac{3}{10}\left(\frac{\delta}{a}\right)^2 - \frac{2}{3}\left(\frac{\delta \cdot l_1}{a^2}\right) \qquad \textbf{Equation 3.7}$$

And N, the end block correction factor, is given by:

$$F = 1 - \left(\frac{l_2}{a}\right)^3 - \frac{9}{8}\left[1 - \left(\frac{l_2}{a}\right)^2\right]\frac{\delta \cdot l_1}{a^2} - \frac{9}{35}\left(\frac{\delta}{a}\right)^2 \qquad \textbf{Equation 3.8}$$

Where l_1 is the distance from the centre of the loading pin to the midplane of the specimen, and l_2 is the distance from the loading pin centre to the edge of the end block (see the DCB schematic in Figure 3.4.1).

3.4.2 Flexural Modulus Tests

At least three specimens were cut from each FRP laminate plate in a direction parallel to the starter crack, and three more in a perpendicular direction, to investigate whether the orientation of the specimens affected the modulus (a check for isotropy). The specimens had the same rectangular shape as the DCB samples, but the test required no end-blocks or starter cracks, as shown in Figure 3.4.2.

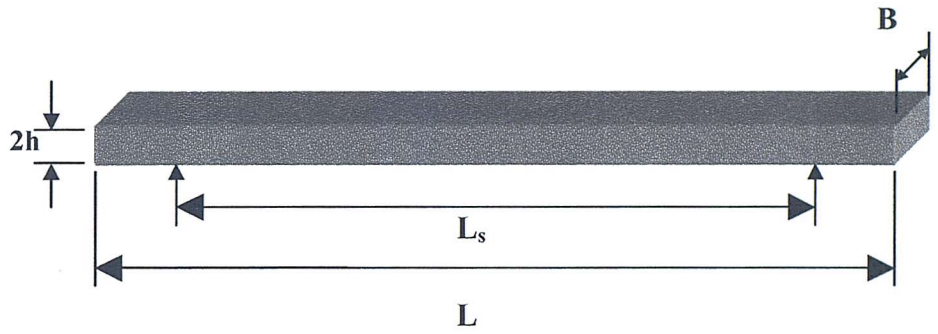


Figure 3.4.2. Schematic of a specimen used to test flexural modulus.

Typical specimen dimensions were:

L = 140mm

B = 25mm

2h = 3mm

L_s = support span = 40(2h) = 120mm

For each individual specimen, four tests were performed according to the relevant standard [122]: two repeat tests on each face of the sample, to check if the modulus was affected by which side of the specimen faced upwards.

The test rate was dependent on the specimen dimensions, as stipulated by the standard:

$$R_{cr} = 0.01\frac{L_s^{\ 2}}{6(2h)}$$ **Equation 3.9**

where R_{cr} is the rate of crosshead motion in mm/min, L_s is the support span.
Typical crosshead speeds were between 1 and 2mm/min. This varying test speed ensured a constant strain rate of 0.01/min and the samples were supported on two outer loading points, at 20°C. This test was conducted elastically, to a preset displacement limit of 5mm. Load-displacement graphs were recorded, and the flexural modulus was calculated, utilising the following equation [122]:

$$E_B = \frac{L^3 s}{4B(2h)^3}$$ **Equation 3.10**

where s is the slope of the tangent to the initial straight-line portion of the load deflection curve, and B is the width of the beam.

3.4.3 Fibre Volume Fraction Tests

After examining the initially puzzling results from the flexural modulus tests performed on the anhydride-cured DGEBA-based FRPs, it was hypothesised that the variability in the results was probably due to varying fibre volume fractions. Thus, it was decided to perform volume fraction analyses on this system's FRPs. The relevant standard was consulted [123], as well as an in-house industry test method [124]. Whilst measuring the fibre volume percentage using acid digestion is not terribly difficult, it is very time consuming, and extra care needs to be taken, due to the use of hazardous chemicals.

For each formulation, two FRP samples were cut, each having dimensions of about 15x20mm. Each sample was first weighed to four decimal places, and an Accupyc machine was used to measure the dry density of each sample, by measuring the volume of helium gas displaced by the sample.

The next stage of the process involved the digestion of the FRP in the confines of a fume cupboard. 25ml of 98% sulphuric acid were used to digest each sample, at a temperature of about 140°C on a hot plate. The flask was stirred constantly with a glass rod that was also used to ensure that the matrix had dissolved and that the fibres had all separated into individual strands. The acid digested the matrix (including the rubber particles), but left the fibres and nano-silica particles intact.

Once the matrix was dissolved, the flasks were taken off the hot-plate and hydrogen peroxide was carefully added, one drop at a time, since the reaction is very violent. The hydrogen peroxide was added until the liquid became clear – indicating that the reaction stopped and the acid was neutralised.

The mixture was then carefully filtered using glass crucibles and a water-pump, whilst being doused with copious amounts of distilled water. The nano-silica particles were small enough to pass through the filters, so only the fibres were left in the crucible. The crucible with wet fibres was then placed in an oven at 120°C and dried overnight.

The following day, the dried fibres were weighed and by comparing the masses and densities of the FRP and the fibres, the fibre volume fraction was calculated according to:

$$V_f = \frac{100 M_f \rho_{FRP}}{M_{FRP} \rho_f} \qquad \textbf{Equation 3.11}$$

Where M_f is the mass of fibres, ρ_{FRP} is the density of the FRP laminate sample, M_{FRP} is the mass of the FRP laminate sample, and ρ_f is the density of the fibres.

3.5 Chapter Summary

This Chapter stated the materials used in this study, and the companies that provided them. It also stated how the bulk and FRP plates were manufactured, and how the test samples were prepared. Additionally, the test conditions and the way in which the data was analysed, was also discussed.

The next three Chapters present and discuss the results from tests performed (as described in this Chapter) on the three epoxy-based systems.

CHAPTER 4

RESULTS AND DISCUSSION: THE AMINE-CURED DGEBA-BASED SYSTEM

4 Introduction

This Chapter investigates the microstructure, material properties and fracture of a DGEBA-based epoxy system that was cured using formulated isophoronediamine with a cure cycle of 2 hours at 80°C, and has had combinations of both rubber and nano-silica particles added to improve the resistance to fracture.

The results have been divided into those obtained from testing the bulk epoxy polymer, and the results obtained from testing the glass fibre reinforced polymers (GFRPs) which have used said bulk epoxy polymers as their matrices.

The section that discusses the bulk epoxy polymer has been divided into subsections which discuss the microstructure, thermal and mechanical properties, and fracture surfaces. Each has a summary at the end, and there is a general discussion at the end of the section which reviews all the results and examines how each material property affects the others. A similar format is followed for the GFRP results, with a Chapter Discussion at the very end.

4.1 Bulk Epoxy Polymer Results

The bulk epoxies investigated are summarised in Table 4.1.1 and it may be seen that an unmodified sample (the control) was compared to samples toughened with varying amounts of CTBN rubber (between 0 and ~11 wt. %), and hybrid samples toughened with varying amounts of rubber and nano-silica (between 0 and ~11 wt. %). The microstructure was studied to see how the rubber and nano-silica particles were distributed, and a number of tests were performed on the samples to determine the thermal and mechanical properties of the bulk material. The fracture surfaces were then investigated to ascertain the fracture mechanisms. It should be noted that all tests were performed on cured samples. Formulations with larger amounts of CTBN were not tested, since samples with large CTBN contents would have low glass transition temperatures and higher viscosities, which would make processing more difficult. Additionally, low rubber contents reduce the amount of water absorption, which is especially valid for its use in FRP applications. No nano-only samples were supplied by *hanse chemie*, due to time constraints.

Table 4.1.1. Summary of all the amine-cured DGEBA-based bulk epoxy polymers investigated.

wt. % CTBN	wt. % nano-silica
0	0
4.6	0
6.9	0
10.9	0
4.1	2
4.1	4.1
6.9	3.5
7	7
11.3	5.7
11.6	11.6

4.1.1 Microstructure

A transmission electron microscope (TEM) was used to view thin microtomed slices of the cured bulk samples under high magnification. The aim was to observe how the nano-silica and rubber particles were dispersed in the epoxy, as well as relative to each other. An atomic force microscope (AFM) was used to give further information about the microstructure.

4.1.1.1 Unmodified Epoxy

The transmission electron micrograph in Figure 4.1.1 is for a control sample of unmodified epoxy. The epoxy matrix is featureless, which is expected for a homogenous thermosetting polymer.

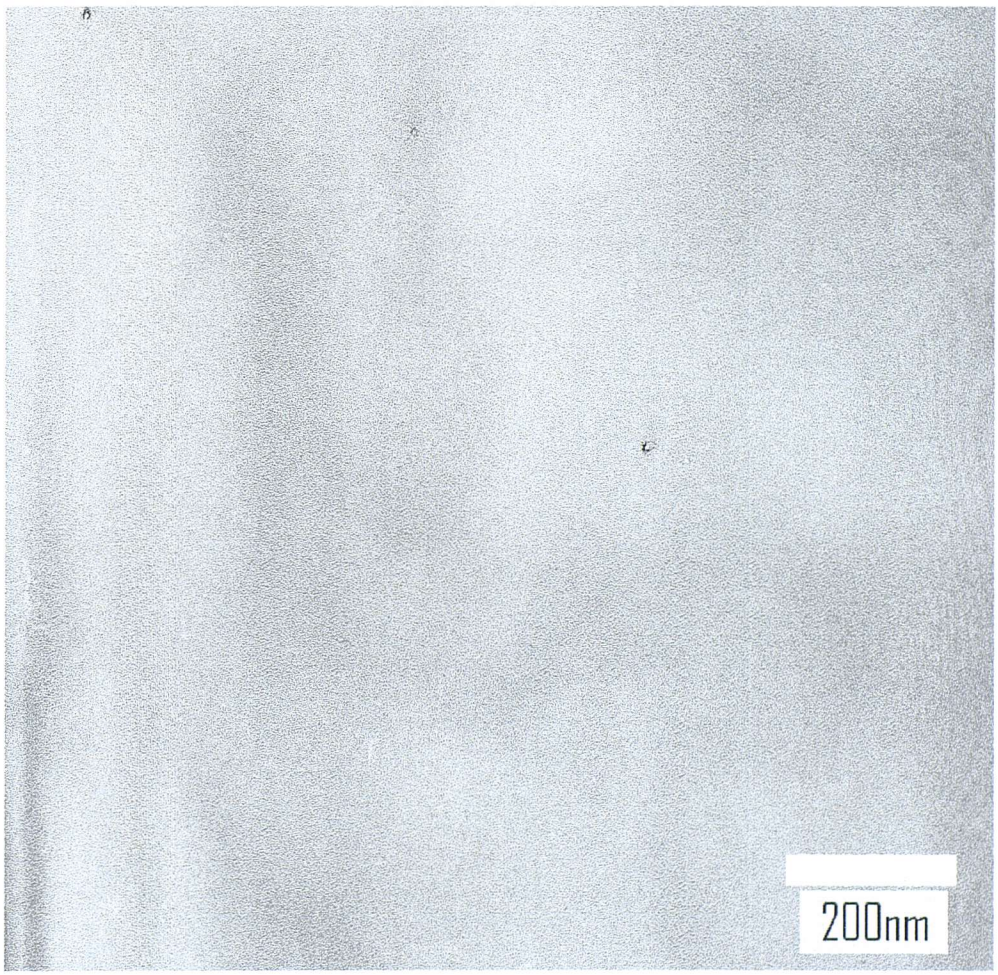


Figure 4.1.1. Transmission electron micrograph of a sample containing unmodifed epoxy.

4.1.1.2 Rubber Modified Epoxies

Figure 4.1.2 shows AFM images of the surfaces of microtomed samples with 4.6, 6.9 and 10.9 wt. % CTBN. The well dispersed, phase-separated spherical rubber particles are clearly visible in all images, and some of them are highlighted by the white arrows. The series of images for increasing CTBN content shows that the rubber particles are between 0.1 and 0.5μm in diameter, which falls in the typical range of particle diameters (ie. 0.1-5μm) for phase separated CTBN [75,125]. Volume fraction analysis of the images suggests that ~3.5, 6 and 9 wt. % of CTBN phase separates from the 4.6, 6.9 and 10.9 wt. % CTBN samples respectively. Therefore more than 80% of the rubber phase separates, and a similar percentage has been previously reported [126].

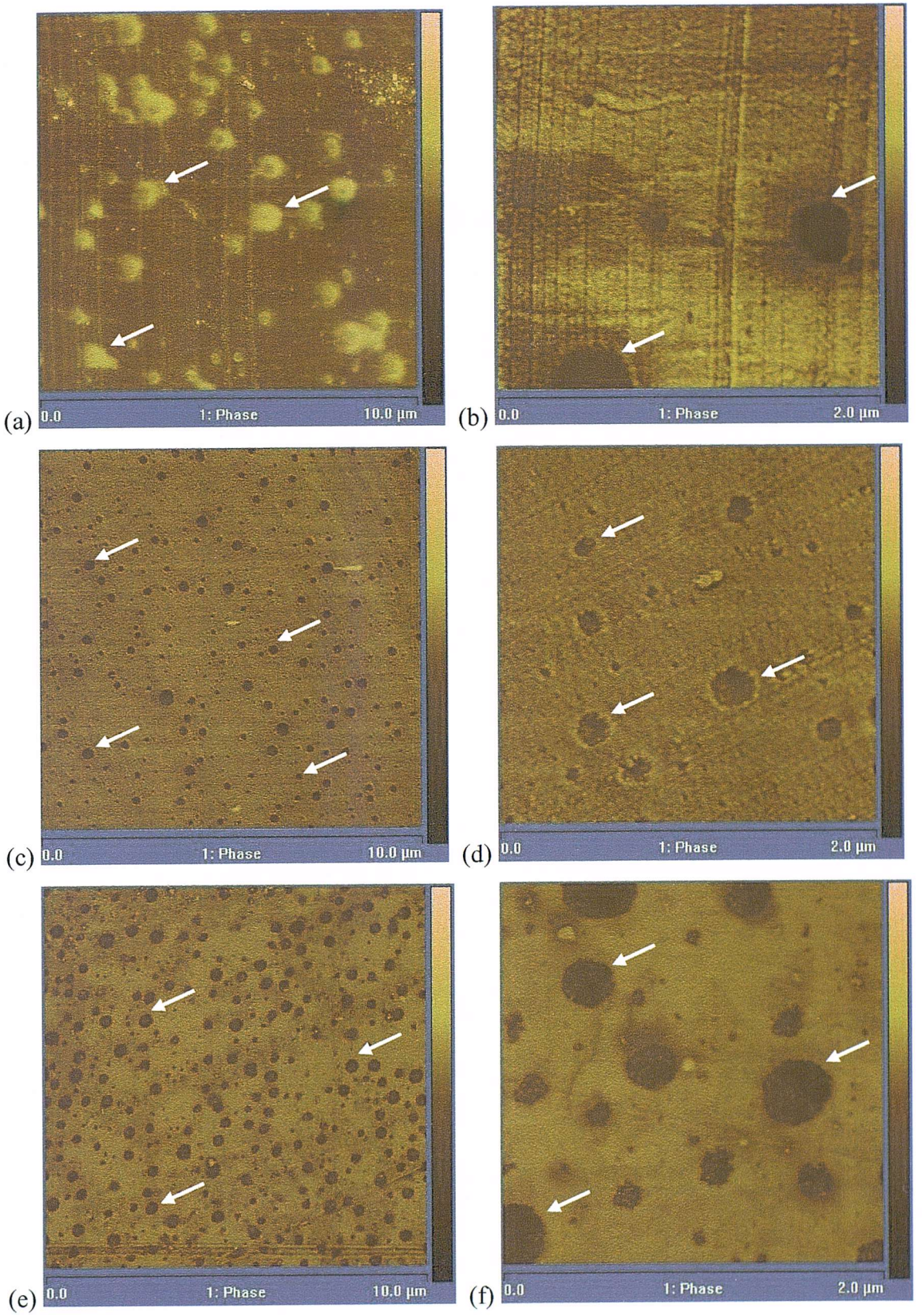


Figure 4.1.2. AFM images of the amine-cured DGEBA-based samples containing: (a,b) 4.6 wt. % CTBN, (c,d) 6.9 wt. % CTBN, and (e,f) 10.9 wt. % CTBN. (White arrows point to some rubber particles.)

4.1.1.3 Hybrid Modified Epoxies

The AFM image in Figure 4.1.3 is of a sample that contained 4.1 wt. % CTBN and 2 wt. % nano-silica. The phase-separated rubber particles and nano-silica particles are highlighted by the white and blue arrows respectively. The rubber particles in the AFM image are lighter in colour than the previous AFM images because of the tapping force used (ie. in these images, the tapping force was less). The rubber particles are oval-shaped in the TEM image because the rubber particles were compressed during microtoming due to an insufficiently low microtoming temperature. However, it can still be seen that the rubber particles are of a similar size and shape (ie. spherical and up to 0.5μm in diameter) as in the CTBN-only samples. The nano particles are not in the rubber domains and remain well dispersed throughout the epoxy matrix, with their diameters remaining constant at about 20nm.

The TEM image in Figure 4.1.4 shows a similar microstructure to the AFM image. Indeed, these two methods are interchangeable when characterising the microstructure of an epoxy [127,128]. Volume fraction analysis showed that ~3 wt. % of the CTBN phase separated into rubber particles.

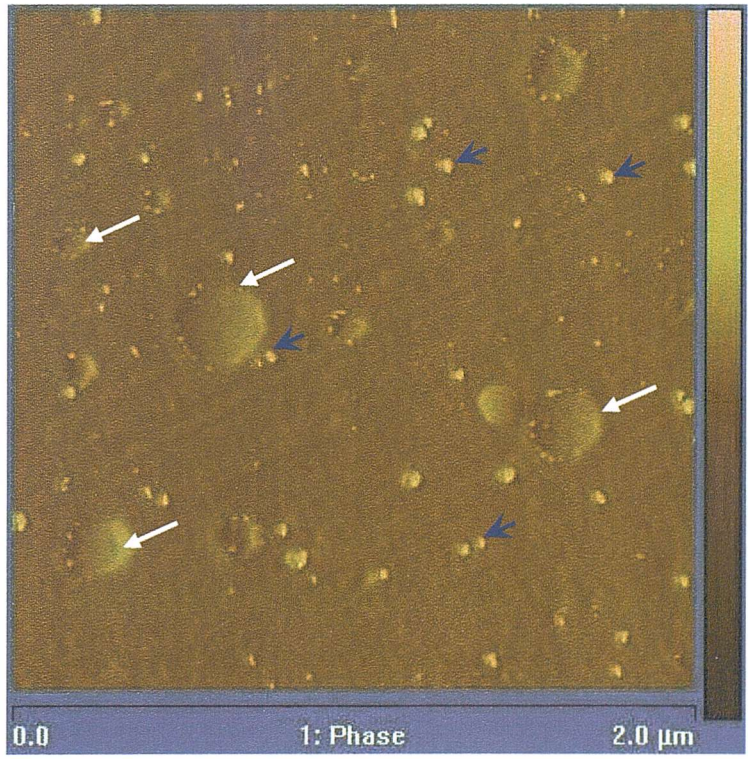


Figure 4.1.3. AFM image of a sample containing 4.1 wt. % CTBN and 2 wt. % nano-silica. (White arrows point to some rubber particles and blue arrows point to some nano particles.)

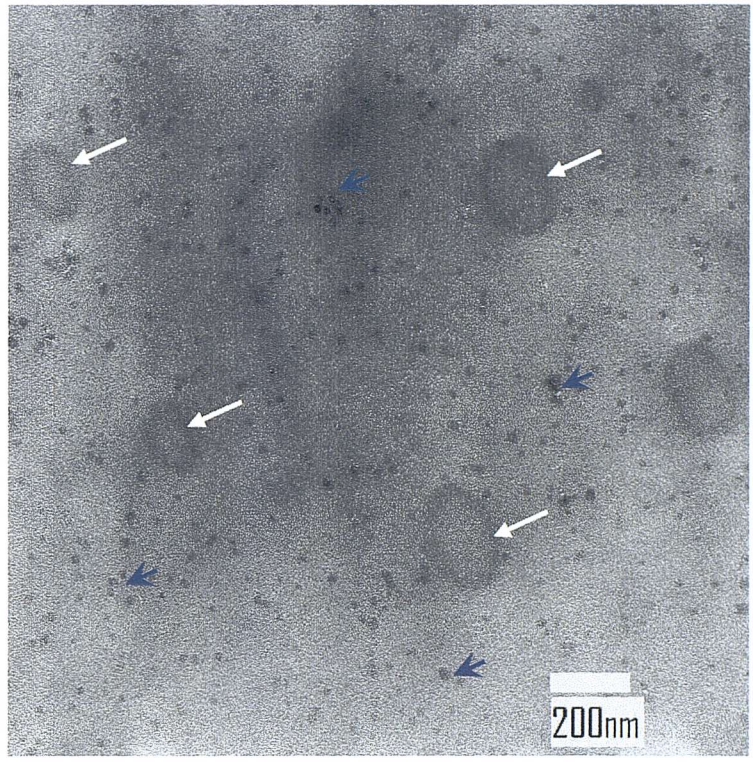


Figure 4.1.4. Transmission electron micrograph of a sample containing 4.1 wt. % CTBN and 2 wt. % nano-silica. (White arrows point to some rubber particles and blue arrows point to some nano particles.)

The micrograph in Figure 4.1.5 is of a sample containing 4.1 wt. % CTBN and 4.1 wt. % nano-silica. The nano-silica particles are well distributed throughout the epoxy matrix, as are the rubber particles. The rubber particles should appear as dark shapes, due to the osmium tetroxide staining. However, in this image they are light coloured, which suggests that the rubber particles were not stained for a long enough period. Also, the rubber particles are oval-shaped in this image because the sample was not cooled to a low enough temperature, so that they were still compliant during microtoming and were slightly compressed. However, the AFM sample used to obtain the image in Figure 4.1.6 was prepared at a lower temperature, and shows that the rubber particles are spheres of up to 0.5μm in diameter. A height image mode was used instead of a phase image mode, because this gave a crisper image. The very small dark circles are the holes left by nano-silica particles that were removed during microtoming. However, this image confirms that the nano-silica particles are well dispersed. Volume fraction analysis of the both the TEM and AFM images suggests that ~3 wt. % CTBN phase separated into rubber particles.

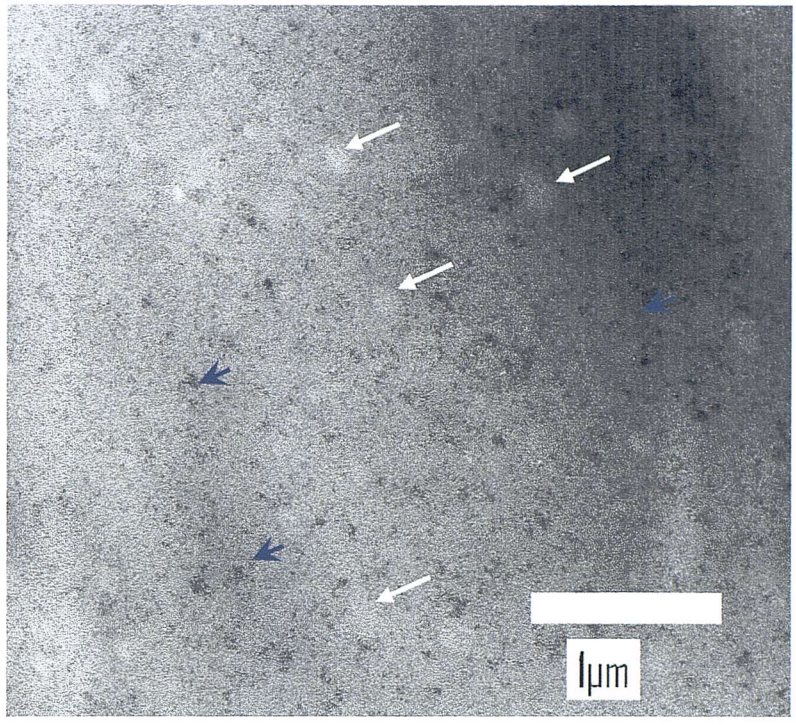


Figure 4.1.5. Transmission electron micrograph of a sample containing 4.1 wt. % CTBN and 4.1 wt. % nano-silica. (White arrows point to some rubber particles and blue arrows point to some nano particles.)

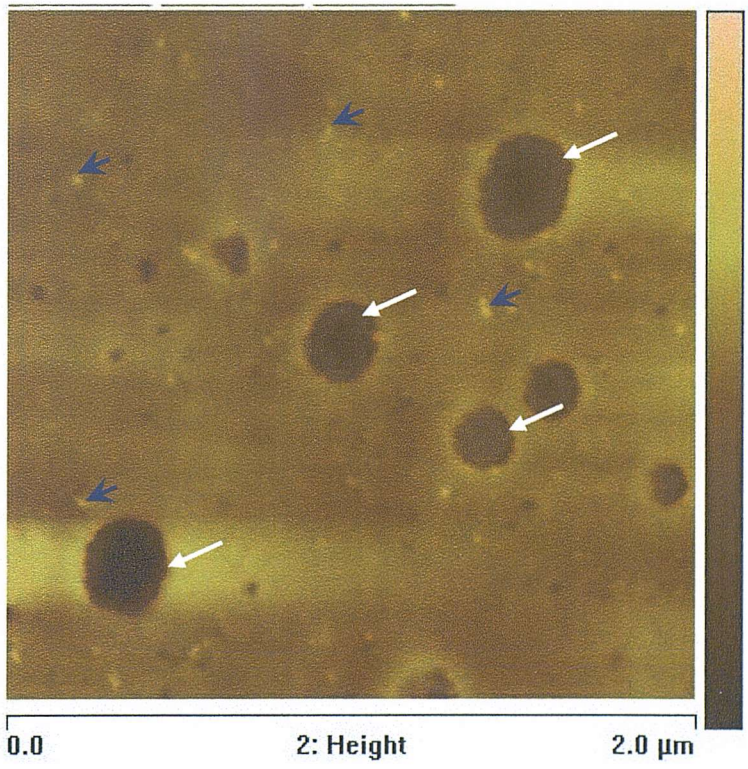


Figure 4.1.6. AFM image of a sample containing 4.1 wt. % CTBN and 4.1 wt. % nano-silica. (White arrows point to some rubber particles and blue arrows point to some nano particles.)

Figure 4.1.7 is a transmission electron micrograph for a sample containing 6.9 wt. % CTBN and 3.5 wt. % nano-silica. The microstructure is very similar to that of the previous sample. The light areas are (up to) 0.5μm-diameter rubber particles that were not stained sufficiently. The nano-silica remains well dispersed and non-agglomerated. Volume fraction analysis suggests that ~5 wt. % of the CTBN phase separated into rubber particles.

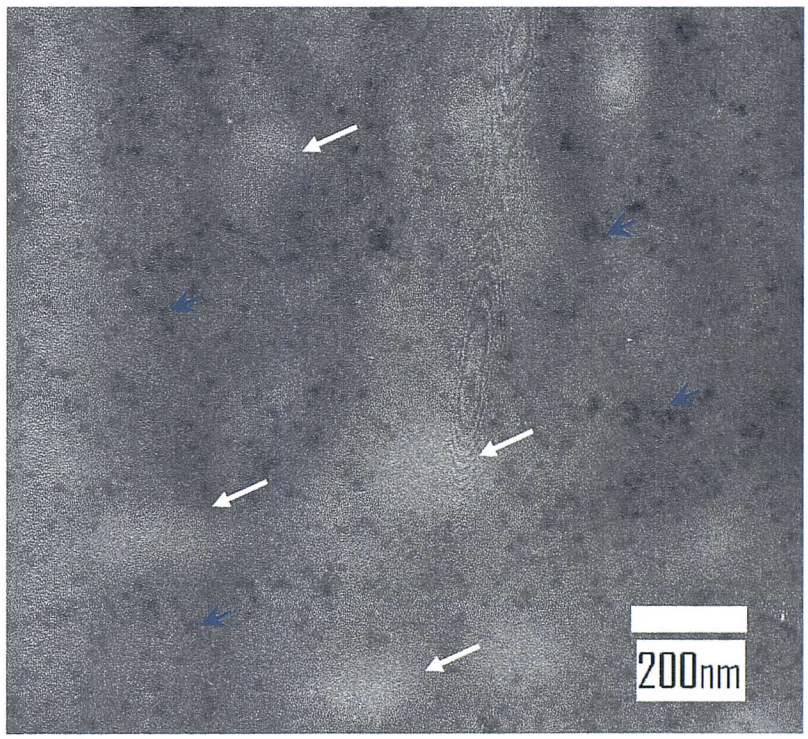


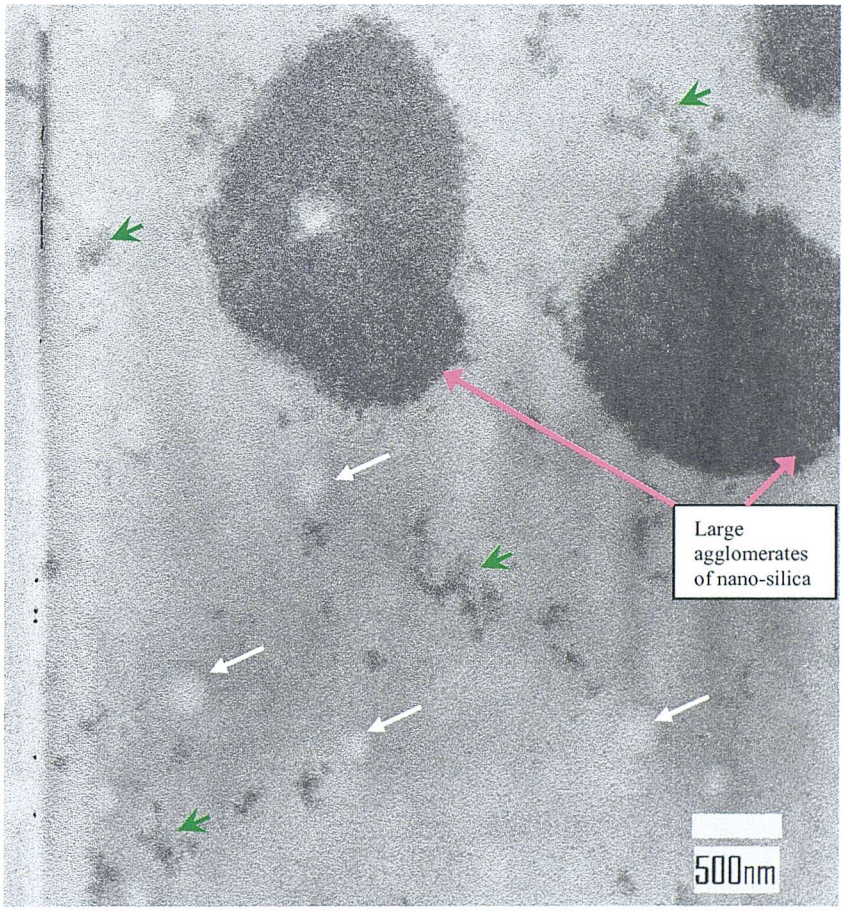
Figure 4.1.7. Transmission electron micrograph of a sample containing 6.9 wt. % CTBN and 3.5 wt. % nano-silica. (White arrows point to some rubber particles and blue arrows point to some nano particles.)

It is interesting to note at this point, that the nano-silica particles did not agglomerate in any of the previous samples. Hybrid samples containing less than ~4.5 wt. % nano-silica have shown good nano particle dispersion, regardless of CTBN content.

However, a different microstructure is revealed from the micrograph of a sample containing 7 wt. % CTBN and 7 wt. % nano-silica in Figure 4.1.8. Whilst the rubber particles are well distributed and are of a similar size to those in the previous samples, the same cannot be said of the nano-silica. (Note that volume fraction analysis of the images suggests that ~5 wt. % CTBN phase separated into rubber particles) Indeed, most of the nano-silica particles agglomerate into 'super-clumps' of more than 3μm in

diameter. Although, some particles agglomerate to form smaller, three dimensional necklace-like structures of about 0.5μm in length, and 0.1μm in width. The micrograph at higher magnification in Figure 4.1.8 (b) shows that some of the nano particles remain well dispersed as single particles. A comparison with the previous sample (containing 6.9 wt. % CTBN and 3.5 wt. % nano-silica) which has a similar CTBN content, suggests that it is the amount of *nano-silica* present that determines whether agglomeration occurs or not. (It should be reiterated that the nano-silica was surface modified for *all* samples in the same way, and cured using the same hardener and cure cycle.)

(a)



(b)

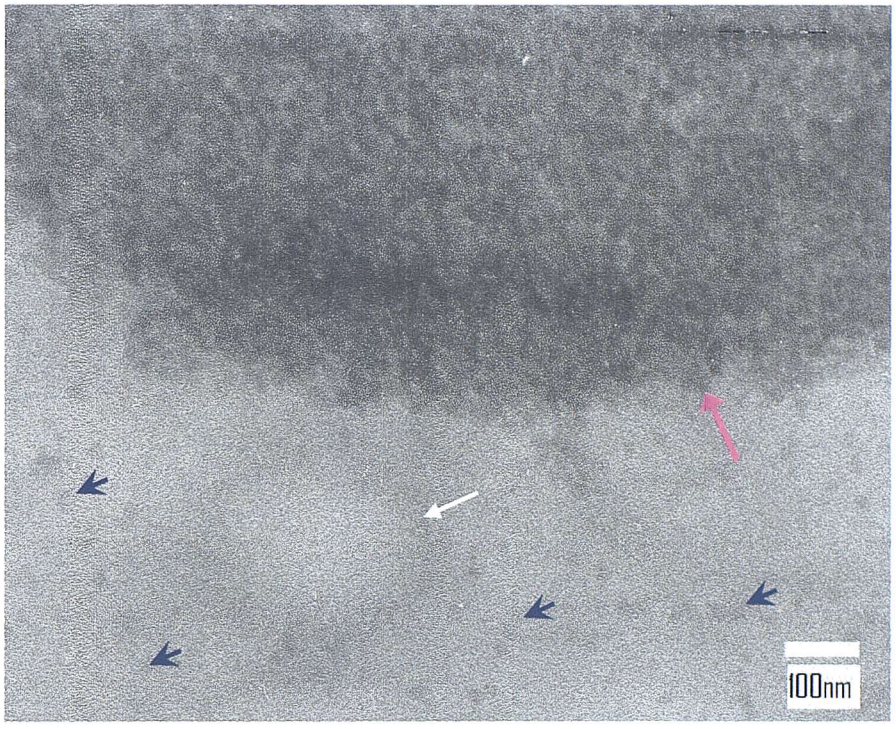


Figure 4.1.8. (a) Transmission electron micrograph of a sample containing 7 wt. % CTBN and 7 wt. % nano-silica. (b) at higher magnification. (White arrow points to rubber particles, blue arrows point to some nano particles, green arrows point to some three dimensional necklace-like structures and pink arrows point to super-clumps.)

A different microstructure is revealed in the micrograph in Figure 4.1.9 for a sample containing 11.3 wt. % CTBN and 5.7 wt. % nano-silica. The rubber particles are well distributed, oval-shaped (compressed during microtoming) particles but they are larger than in the previous samples with a diameter of almost 1μm. Indeed, an increase in the size of phase separated rubber particles with increasing CTBN content in a DGEBA-based epoxy has been reported before [129]. Volume fraction analysis suggests that ~8 wt. % of the CTBN phase separated into rubber particles. The nano-silica coalesce into well distributed three dimensional necklace-like structures of about 1μm in length and 0.2μm in width.

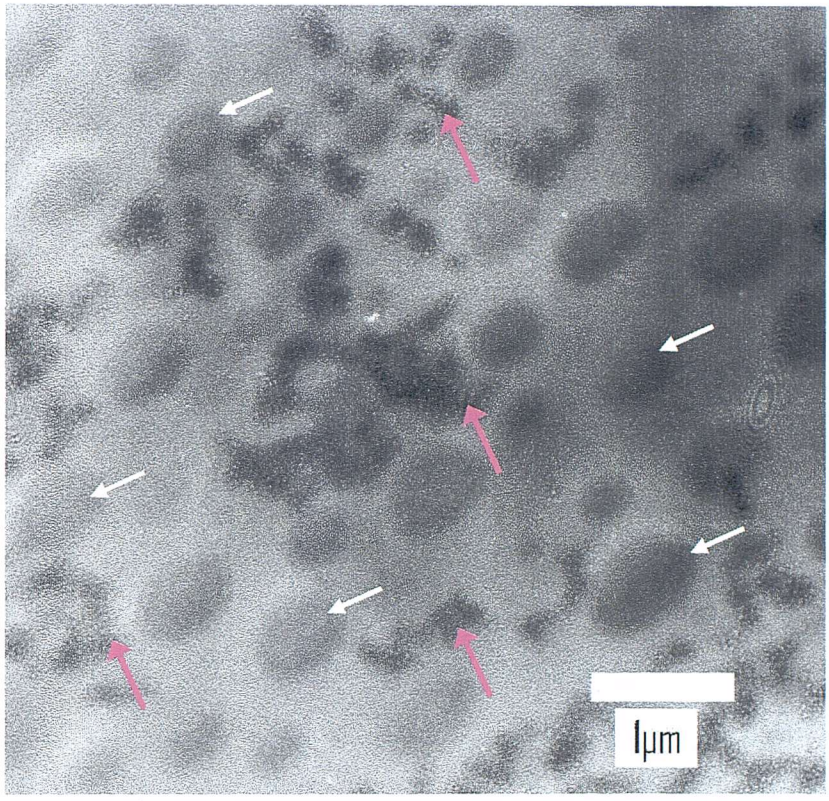


Figure 4.1.9. Transmission electron micrograph of a sample containing 11.3 wt. % CTBN and 5.7 wt. % nano-silica. (White arrows point to some rubber particles and pink arrows point to some three dimensional necklace-like structures of nano-silica.)

The micrograph in Figure 4.1.10 is for a sample containing 11.6 wt. % CTBN and 11.6 wt. % nano-silica and clearly shows the agglomeration of nano-silica into super-clumps of about 3μm in diameter. The AFM image in Figure 4.1.10 shows the rubber particles more clearly than the TEM image, and they are seen to be about 1μm in diameter. Volume fraction analysis of the images suggests that ~8.5 wt. % of the CTBN phase separated into rubber particles. This sample contains a comparable amount of CTBN to the previous sample, but twice as much nano-silica. This confirms that it is the *nano-silica content* that determines the degree of agglomeration (or lack thereof) that occurs for the nano-silica particles.

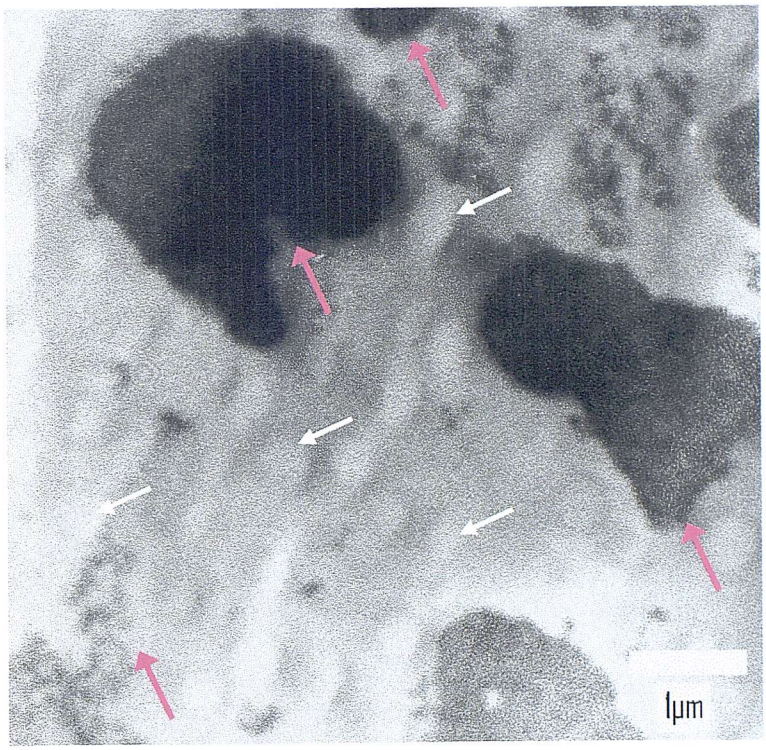


Figure 4.1.10. Transmission electron micrograph of a sample containing 11.6 wt. % CTBN and 11.6 wt. % nano-silica. (White arrows point to some rubber particles and pink arrows point to some super-clumps.)

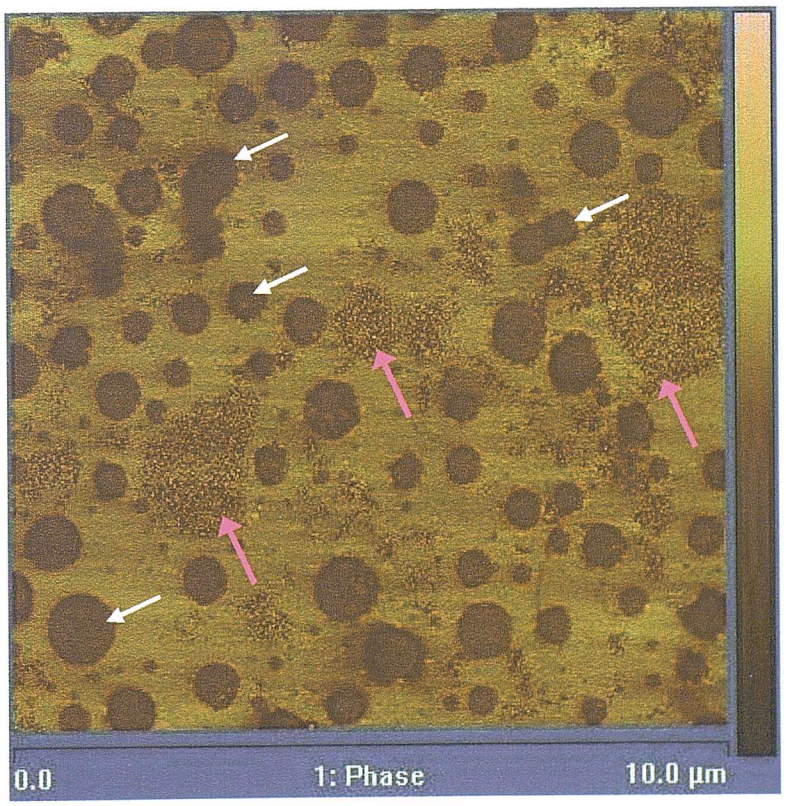


Figure 4.1.11. AFM image of a sample containing 11.6 wt. % CTBN and 11.6 wt. %. (White arrows point to some rubber particles and pink arrows point to some super-clumps.)

4.1.1.4 Summary

AFM and TEM images were both used to investigate the microstructure of the amine-cured DGEBA bulk epoxy polymer samples, and both gave excellent images. The microstructure of the different samples is summarised in Table 4.1.2. It should be noted that for hybrid samples in this system, it was found that the degree of dispersion of the nano particles in the epoxy matrix *is* dependant on the wt. % of nano-silica, but the wt. % of the nano-silica phase only marginally affects the amount of rubber that phase separates.

Table 4.1.2. Summary of the microstructure of samples from the amine-cured DGEBA-based bulk epoxy polymers. (NA = Not Applicable)

wt. % CTBN	wt. % nano-silica	Rubber Microstructure	Visual wt. % CTBN phase separated	Nano-silica Microstructure
0	0	NA	NA	NA
4.6	0	Well dispersed rubber spheres, 0.1-0.5μm diameter	3.5	NA
6.9	0	Well dispersed rubber spheres, 0.1-0.5μm diameter	6	NA
10.9	0	Well dispersed rubber spheres, 0.1-0.5μm diameter	9	NA
4.1	2	Well dispersed rubber spheres, 0.1-0.5μm diameter	3	Well dispersed 20nm spheres
4.1	4.1	Well dispersed rubber spheres, 0.1-0.5μm diameter	3	Well dispersed 20nm spheres
6.9	3.5	Well dispersed rubber spheres, 0.1-0.5μm diameter	5	Well dispersed 20nm spheres
7	7	Well dispersed rubber spheres, 0.1-0.5μm diameter	5	Super-clumps 4μm in diameter, as well as necklace-like structures
11.3	5.7	Well dispersed rubber spheres, up to 1μm diameter	8	Necklace-like structures 1μm in length, 0.2μm in width. Well dispersed
11.6	11.6	Well dispersed rubber spheres, up to 1μm diameter	8.5	Super-clumps 4μm in diameter, as well as necklace-like structures

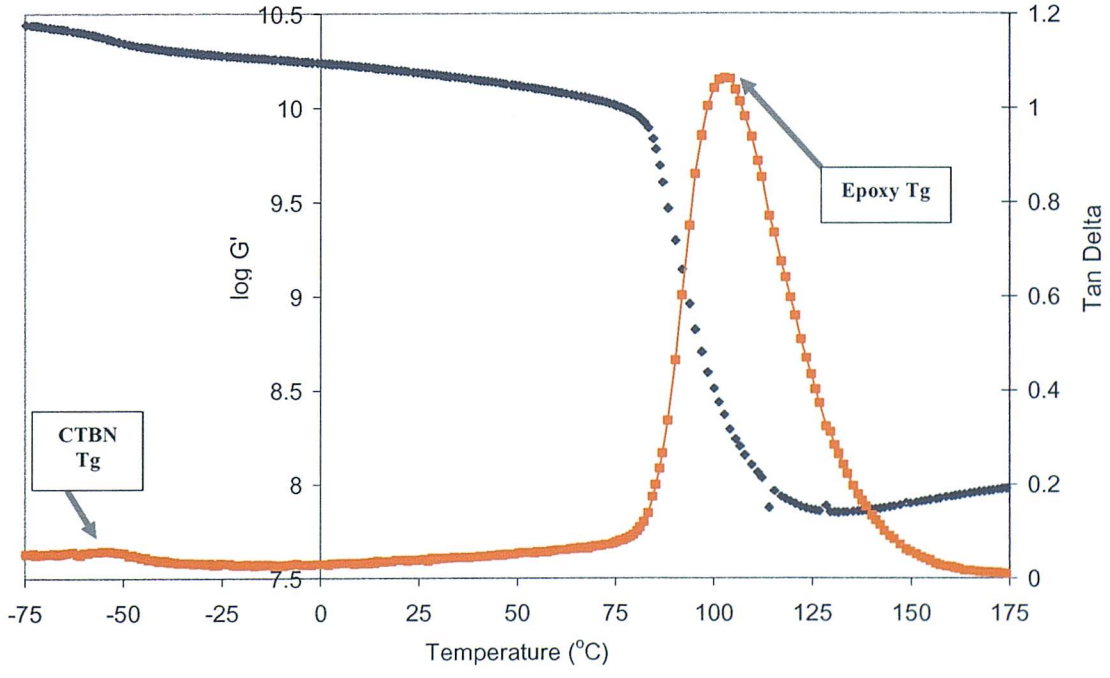
4.1.2 Thermal and Mechanical Properties

This section investigates the thermal and mechanical properties of the bulk epoxy polymers where the results from dynamic mechanical thermal analysis (DMTA), tensile tests and single edge notch bend tests are presented.

4.1.2.1 Glass transition temperature test results

The glass transition temperature (T_g) values were determined by performing dynamic mechanical thermal analysis (DMTA). A sample DMTA trace of a hybrid specimen is shown in Figure 4.1.12, with the loss modulus, G', and *tan* δ data for a test frequency of 1Hz. The graph clearly shows the epoxy peak (indicating the T_g of the epoxy) and the smaller peak indicating the T_g of the CTBN. The smaller peak becomes more defined when the Y-axis scale is adjusted, as shown in Figure 4.1.12 (b). It should be noted that the DMTA trace for the unmodified epoxy did *not* show a smaller peak, which confirms that the smaller peak observed in the hybrid sample traces indicated the T_g of the CTBN. The loss modulus decreased with increasing temperature, which is expected, since the sample was becoming more compliant. Table 4.1.3 summarises all the epoxy glass transition temperatures at a frequency of 1Hz, and the error for each value is ±2°C.

(a)



(b)

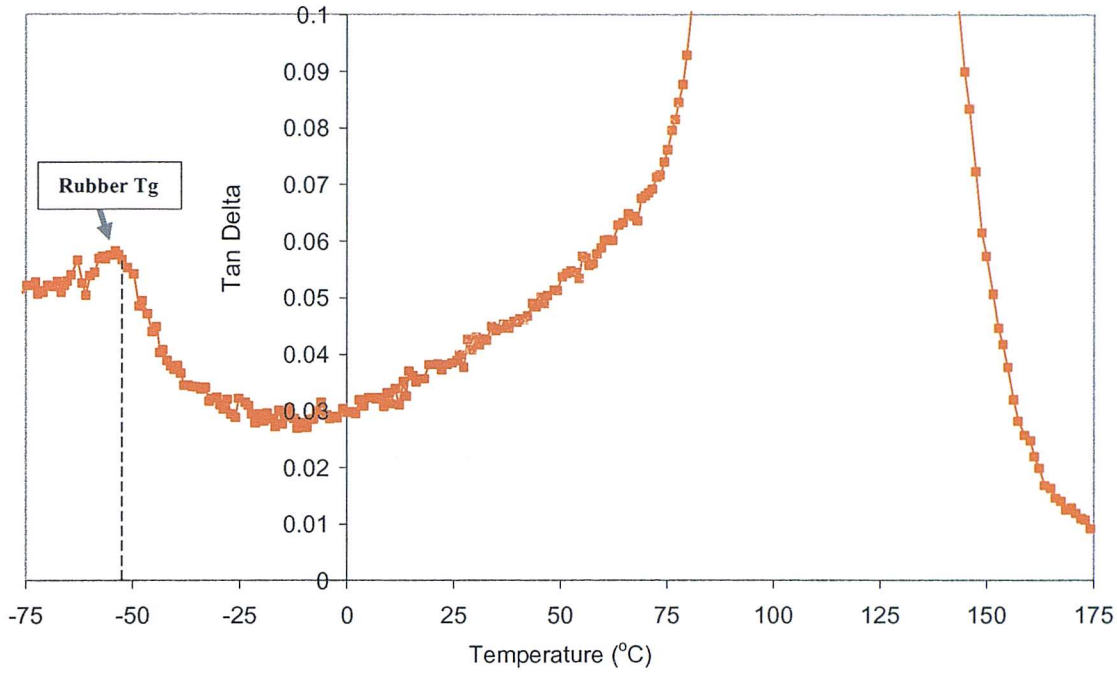


Figure 4.1.12. (a) Sample DMTA traces performed at 1Hz for a sample containing 7 wt. % CTBN and 7 wt. % nano-silica, showing the loss modulus and *tan δ* values. (b) Trace of the same sample with adjusted Y-axis showing the rubber peak more clearly.

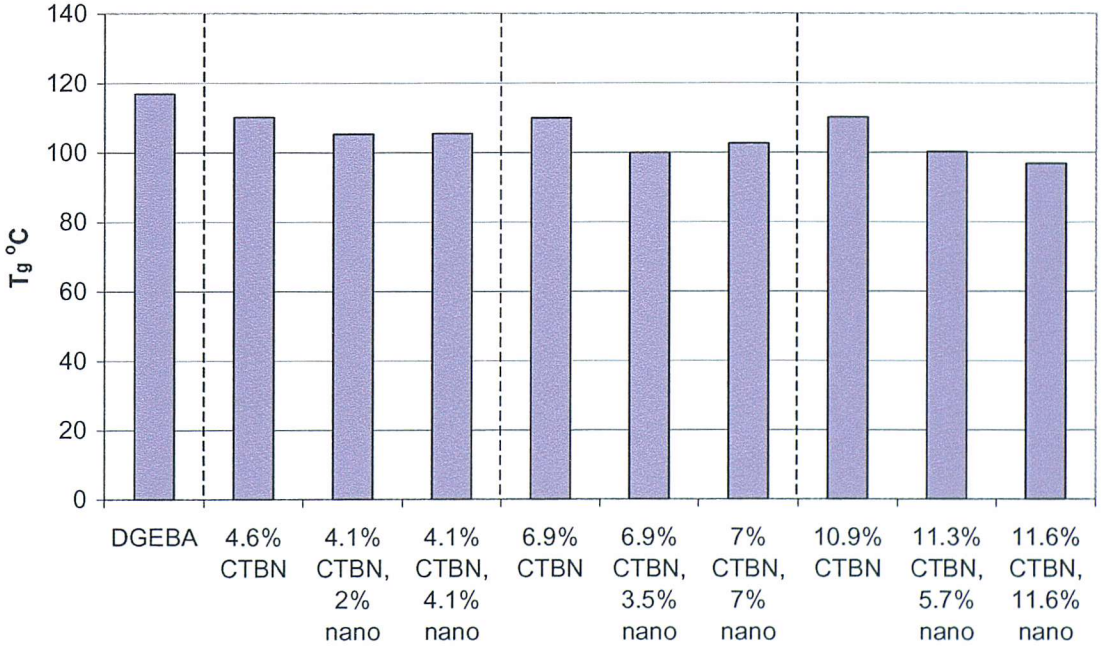


Figure 4.1.13. Glass transition temperatures for the amine-cured DGEBA-based bulk epoxy polymers at a test frequency of 1Hz. The dashed lines separate the samples into sub-systems of similar CTBN content.

Table 4.1.3. Summary of the glass transition temperatures of the epoxy for all the amine-cured DGEBA-based bulk epoxy polymers, tested at a frequency of 1Hz.

wt. % CTBN	wt. % nano-silica	T_g (°C)
0	0	117
4.6	0	110
6.9	0	110
10.9	0	110
4.1	2	105
4.1	4.1	105
6.9	3.5	100
7	7	103
11.3	5.7	102
11.6	11.6	97

Other studies of amine-cured DGEBA have shown similar values for the glass transition temperature of the unmodified epoxy [131-133]. The glass transition temperature of the CTBN rubbery phase was about the same in all samples, at -50°C, which is a similar temperature reported in other work for this grade of CTBN (ie. Hycar 1300x8) [134,135].

A review of Table 4.1.3 shows that the glass transition temperature of the epoxy matrix drops from 117°C for the unmodified epoxy to 110°C for the rubber-only modified epoxies. This suggests that some of the rubber remains dissolved in the epoxy phase and plasticises the epoxy, which is not unusual [134]. In addition, this suggests that the same amount of rubber remains in solution regardless of CTBN content. Calculations using the Fox-Flory equation (see Equation 2.23 in Chapter 2) show that ~2.5 wt. % of CTBN (ie. 50% at most) would have to remain in the epoxy phase to produce a 7°C reduction in glass transition temperature. This does not correlate very well with the volume fraction image analysis, which indicated that 80% of the rubber remained in the epoxy phase. The Fox-Flory equation is not totally accurate, and is only meant to be used as an approximate guide to rubber phase separation and, in addition, the microstructure

images were limited in number, so it is possible that the images were from a CTBN-rich region.

When both CTBN and nano-silica are used as toughening agents, it can be seen that the glass transition temperature is lowered even more than when only CTBN is present. This could be interpreted to mean that, as more nano particles are added, more of the long, flexible rubber molecules are being crosslinked into the resin matrix instead of participating in the phase separation of rubber particles [102,134]. Again, Fox-Flory equation calculations and the volume fraction image analyses do not agree. Indeed, a 20°C reduction in glass transition temperature (as in the sample with 11.6 wt. % CTBN and 11.6 wt. % nano-silica) would necessitate ~7 wt. % CTBN to remain in the epoxy phase. This contradicts the image analysis which suggests that only ~2 wt. % remains in solution. This discrepancy will be the source of future investigations, but it should be noted however that the images *do* show a slight decrease in the amount of rubber that phase separates (compared to their CTBN-only counterparts), and this is reflected in the T_g data which also shows a reduction in glass transition temperature.

4.1.2.2 Tensile test results

Tensile tests were performed using dumbbell specimens at a rate of 1mm/min at 20°C, to determine the Young's modulus of the different compositions. The main results are illustrated in Figure 4.1.14 and the numerical results can be found in Table 4.1.4.

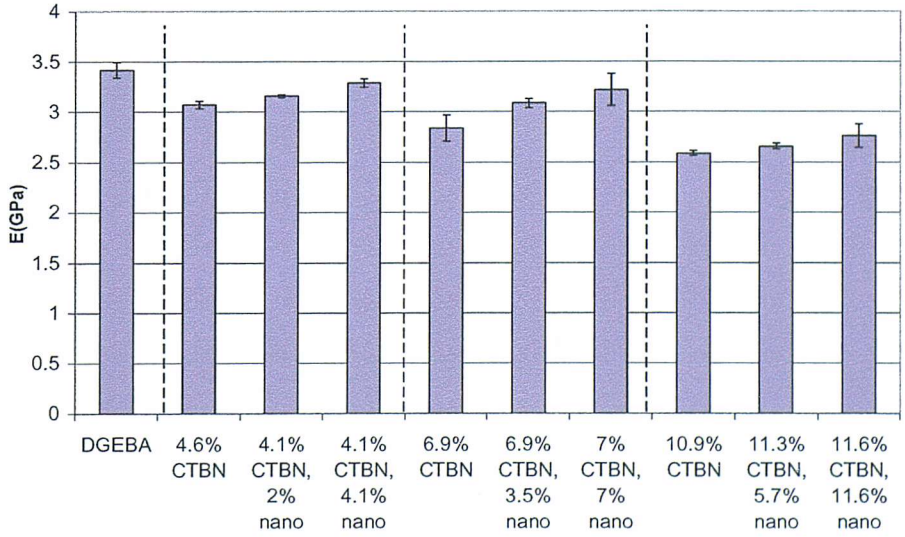


Figure 4.1.14. Young's moduli for all the amine-cured DGEBA-based bulk epoxy polymers. (error bars are ± one standard deviation)

Table 4.1.4. Summary of Young's Moduli for all the amine-cured DGEBA-based bulk epoxy polymers (± one standard deviation).

wt. % CTBN	wt. % nano-silica	Young's Modulus, *E (GPa)*
0	0	3.42 ± 0.08
4.6	0	3.07 ± 0.04
6.9	0	2.84 ± 0.13
10.9	0	2.59 ± 0.03
4.1	2	3.16 ± 0.02
4.1	4.1	3.29 ± 0.05
6.9	3.5	3.09 ± 0.05
7	7	3.22 ± 0.16
11.3	5.7	2.66 ± 0.03
11.6	11.6	2.76 ± 0.11

Amine-cured epoxies have been shown to have tensile moduli of ~3.5GPa [136], which agrees well with the modulus obtained here for the unmodified epoxy sample.

Table 4.1.4 shows that the Young's modulus decreases (ie. from 3.42GPa for unmodified epoxy, to 2.59GPa for a sample with 10.9 wt. % CTBN) as the amount of CTBN increases, which is expected because the CTBN rubber has a much lower stiffness than that of the epoxy [129]. A comparison with analytical models was performed and this can be found in Chapter 7.

The hybrid samples all showed an increase in modulus when nano-silica was added. Examining the group of samples containing ~7 wt. % CTBN shows that the modulus increases from 2.84GPa to 3.09GPa with the addition of 3.5 wt. % nano-silica, and to 3.22GPa with the addition of 7 wt. % nano-silica. This is not unexpected, since silica particles are known to have a much higher modulus (ie. ~70GPa) [137,138] than the epoxy, so even a small increase in silica content increases the matrix modulus. The tensile results for a given CTBN content with increasing nano-silica content for the three subsystems are shown in Figure 4.1.15. Recalling the microstructure of the

samples, the graphs show that super-clumps of nano-silica particles do not greatly improve the Young's modulus, as compared to the samples with well-dispersed particles or chains of nano-silica. The ~11 wt. % CTBN subsystem shows a gentle increase in modulus with increasing nano-silica content.

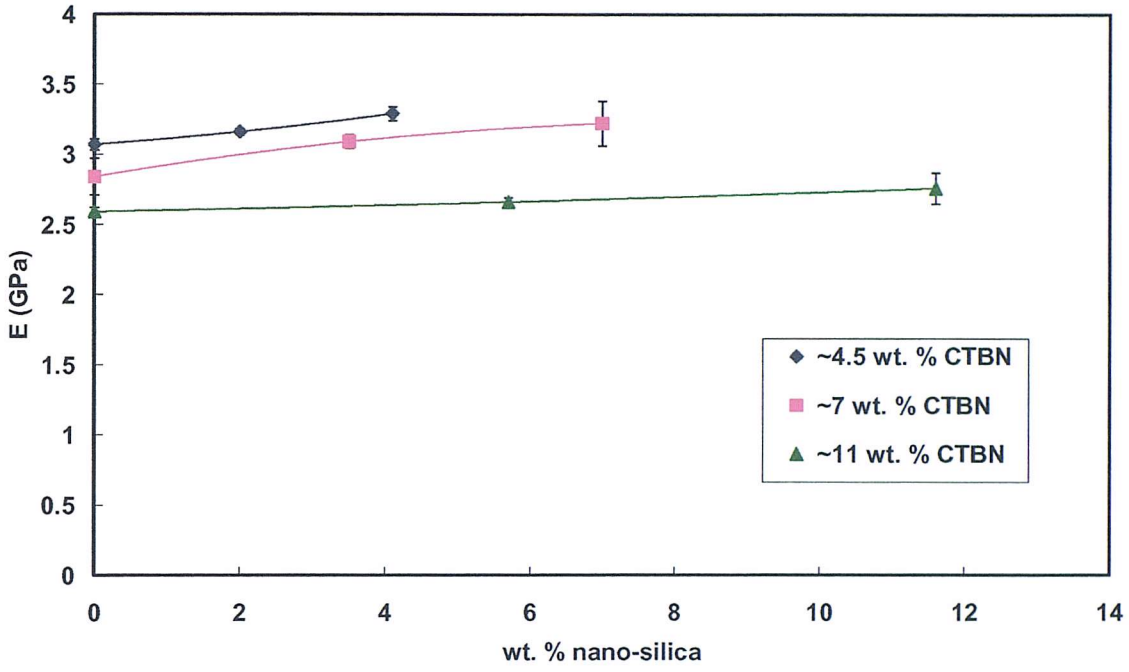


Figure 4.1.15. Comparison of Young's moduli of the hybrid versus nano-silica content. (error bars are ± one standard deviation)

4.1.2.3 Fracture Test Results

At least triplicate three-point bend tests were performed at a rate of 1mm/min at 20°C, to ascertain the critical mode I stress intensity factor (K_{Ic}). This fracture toughness value was then converted to the fracture energy using Equation 2.8 in Chapter 2.

The pre-crack was formed by drawing a new razor blade through the notch tip. The fracture energy results are illustrated in Figure 4.1.16 and the numerical values can be found in Table 4.1.5.

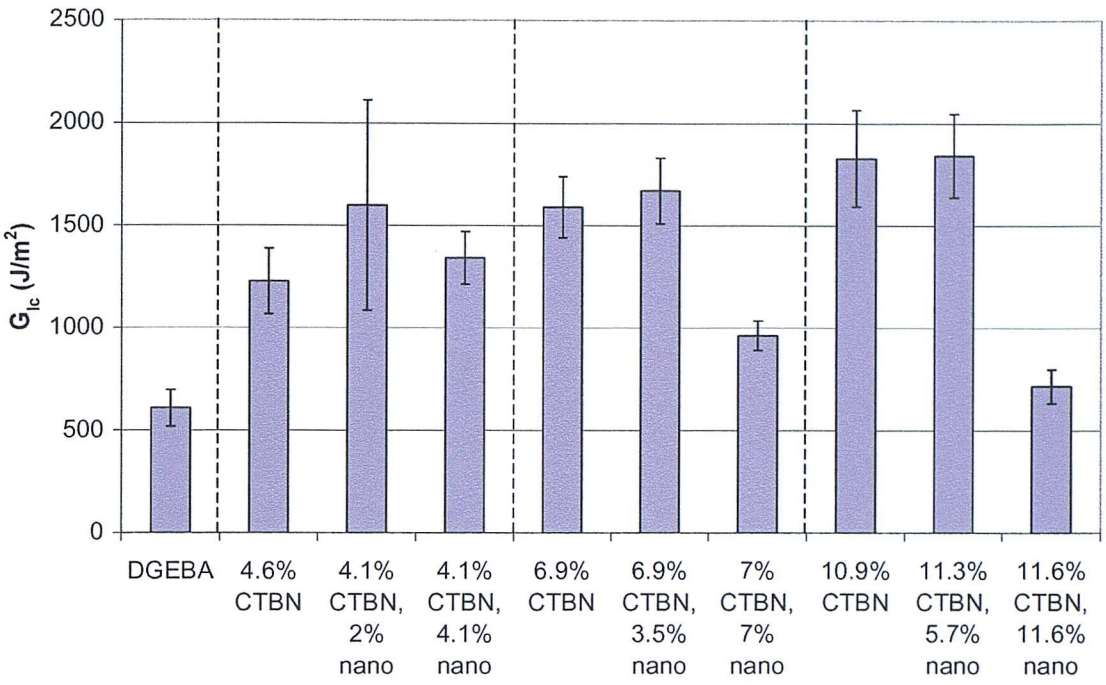


Figure 4.1.16. Fracture energy results for all the amine-cured DGEBA-based bulk epoxy polymers. (error bars are ± one standard deviation)

Table 4.1.5. Summary of fracture results for all the amine-cured DGEBA-based bulk epoxy polymers (± one standard deviation).

wt. % CTBN	wt. % nano-silica	K_{Ic} *(MPa m$^{1/2}$)*	G_{Ic} *(J/m^2)*
0	0	1.54 ± 0.12	612 ± 90
4.6	0	2.07 ± 0.13	1234 ± 160
6.9	0	2.27 ± 0.11	1595 ± 149
10.9	0	2.32 ± 0.15	1835 ± 235
4.1	2	2.40 ± 0.37	1599 ± 512
4.1	4.1	2.25 ± 0.11	1346 ± 128
6.9	3.5	2.43 ± 0.12	1674 ± 160
7	7	1.88 ± 0.07	967 ± 72
11.3	5.7	2.36 ± 0.13	1847 ± 205
11.6	11.6	1.50 ± 0.09	719 ± 82

Previous work by Zhang *et al.* [139] and Park *et al.* [140] involving amine-cured DGEBA, have shown similar toughness values for the unmodified epoxy. However, the cured epoxies in those studies had a much lower glass transition temperature. In contrast, the work of Jin *et al.* [141] where the cured epoxy had a similar modulus and glass transition temperature, the epoxy showed toughness values of half of what was obtained in the present work. Mezzenga *et al.* [142] used the same curing agent and epoxy as used in this study, but obtained a fracture toughness of less than half of that which was observed here. However, they did not state their cure conditions.

Compared with the control which has a fracture energy of 612J/m^2, the addition of CTBN rubber greatly enhances the resistance to fracture of the specimens. Adding 4.6 wt. % CTBN doubles the fracture energy to 1234J/m^2 and 10.9 wt. % triples the fracture energy 1835J/m^2. Similar increases in toughness have been reported by Russell *et al.* for amine-cured DGEBA with Hycar 1300x8 [126]. The rubbery particles greatly increase the toughness of the material via interactions of the stress field ahead of the crack tip and lead to greatly enhanced plastic deformation of the epoxy matrix [4,5,7]. The actual toughening mechanisms are discussed in greater detail in Chapter 7.

On examining the graph in Figure 4.1.16, it can be seen that the samples may be grouped into three distinct sets containing either: ~4, 7 or 11 wt. % CTBN. In each case, the CTBN on its own produces a spectacular increase in toughness, and a small amount of nano-silica produces no significant change in fracture energy. However, in each set, the toughness decreased dramatically if a relatively large amount of nano-silica was added. Possible explanations for this behaviour are discussed in Section 4.1.3, as well as in Chapter 7.

4.1.2.4 Summary

The glass transition temperature of the unmodified epoxy was 117°C and even a small addition of CTBN (4.6 wt. %) reduced the T_g to 110°C. However, increased amounts of CTBN did not reduce the glass transition temperature further. The samples containing CTBN have a lower T_g than the unmodified epoxy because some of the CTBN remains in the epoxy phase. The tensile modulus decreases with increasing CTBN content (ie. from 3.42GPa for unmodified epoxy, to 2.59GPa for a sample with 10.9 wt. % CTBN)

but increasing the CTBN content produces a steady increase in the fracture energy from 612J/m^2 for the unmodified epoxy to 1835J/m^2 for a sample with 10.9 wt. % CTBN.

The hybrid samples (ie. containing both CTBN and nano-silica) exhibited a further decrease in the glass transition temperature, to a minimum of 97°C for a sample containing 11.6 wt. % CTBN and 11.6 wt. % nano-silica. This suggests that the presence of nano-silica inhibits the phase separation of rubber particles. For each group of samples containing ~4, 7 and 11 wt. % CTBN, it was found that the tensile modulus increased with increasing nano-silica content. However, the fracture toughness results were not as straight-forward. In each group of samples, it was found that a relatively small amount of nano-silica did not affect the toughness. However, larger amounts of nano-silica had a detrimental effect on the toughness, and in the case of the formulation with 11.6 wt. % CTBN and 11.6 wt. % nano-silica, the toughness was reduced to that of the unmodified epoxy.

4.1.3 Bulk Fracture Surfaces

Scanning electron microscopy was performed on some of the fracture surfaces of the SENB samples to investigate the fracture mechanisms responsible for the change in toughness that was observed. It should be noted that the pre-crack was formed by drawing a new razor blade through the notch tip, and this pre-crack is visible in the low magnification images as a vertical line to the far left of the micrograph.

4.1.3.1 Unmodified Epoxy

The fracture surface of the unmodified epoxy polymer is shown in Figure 4.1.17 and Figure 4.1.18, where the direction of crack propagation is from left to right. The fracture surface is relatively smooth and glassy, which is typical of a brittle thermosetting polymer [83], and reveals that no large-scale plastic deformation has occurred during fracture. These observations agree well with the comparatively low measured toughness of the material, where K_{Ic}=1.54MPa m$^{1/2}$. In addition, there are apparent steps and changes in the level of the crack which can be observed in Figure 4.1.17. These features are feather markings, which are caused by the crack forking due to the excess of energy associated with the relatively fast crack growth. This repeated forking and the multi-

planar nature of the surface are ways of absorbing this excess energy in a very brittle material [145]. No stress-whitening was observed in this sample.

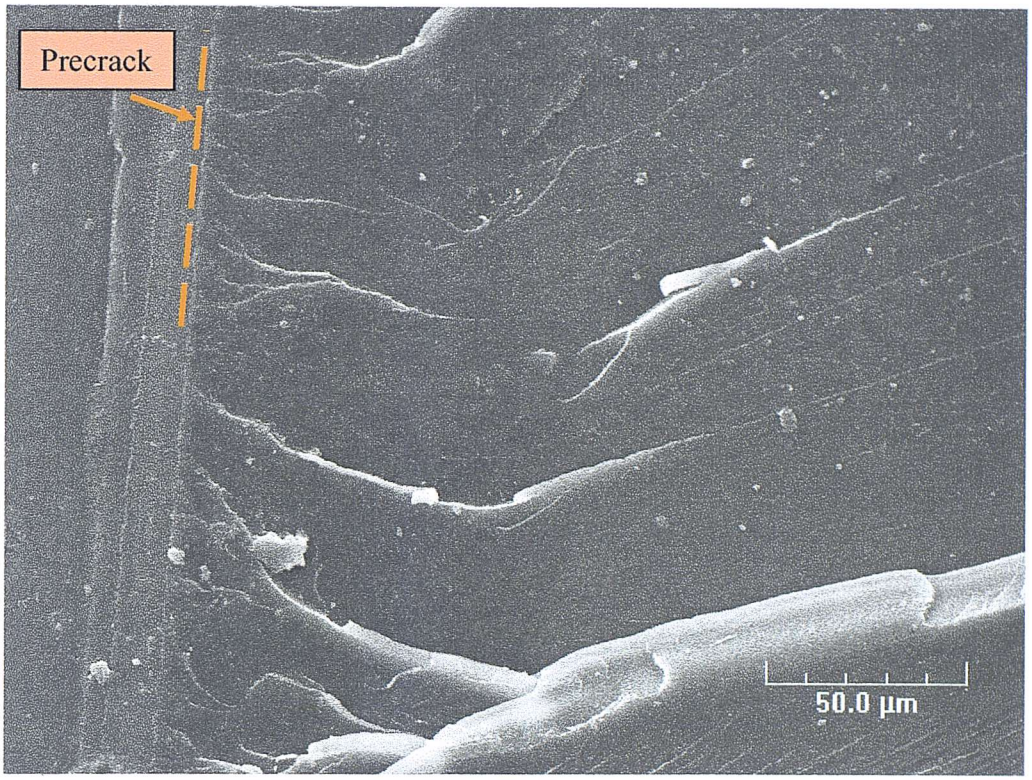


Figure 4.1.17. Fracture surface of unmodified epoxy (crack propagation from left to right).

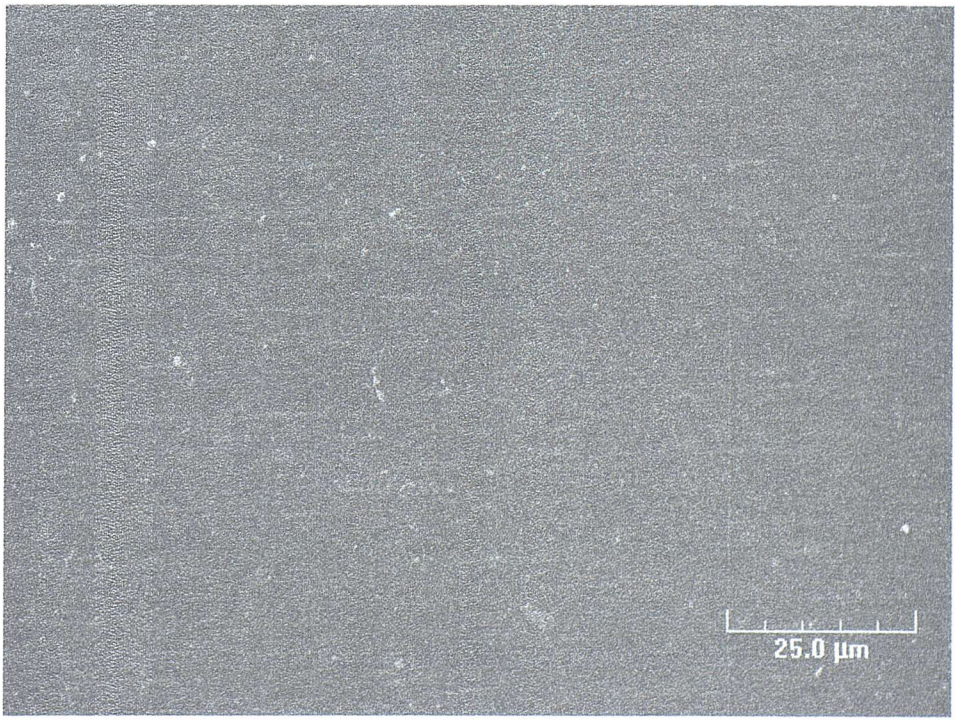


Figure 4.1.18. Fracture surface of unmodified epoxy at higher magnification (crack propagation from left to right).

4.1.3.2 Rubber Modified Epoxies

The micrograph in Figure 4.1.19 is of a sample containing 4.6 wt. % CTBN. A stress-whitened region of ~200μm was observed just after the precrack in the direction of crack growth.

The higher magnification image in Figure 4.1.20, which was taken near the start of the stress-whitened region, clearly shows that cavitation of the rubber particles [125,147] has occurred, which leads to the increased toughness of 2.07MPa $m^{1/2}$ observed. The cavitated rubber particles are responsible for scattering the light which gives rise to the stress-whitened region. The size of the cavities (~0.5 μm) is similar to the size of the rubber particles observed in the microstructure images, and the volume fraction of cavitated rubber particles also correlates well with the AFM images. This shows that the majority of rubber particles that phase separated, did indeed cavitate during fracture.

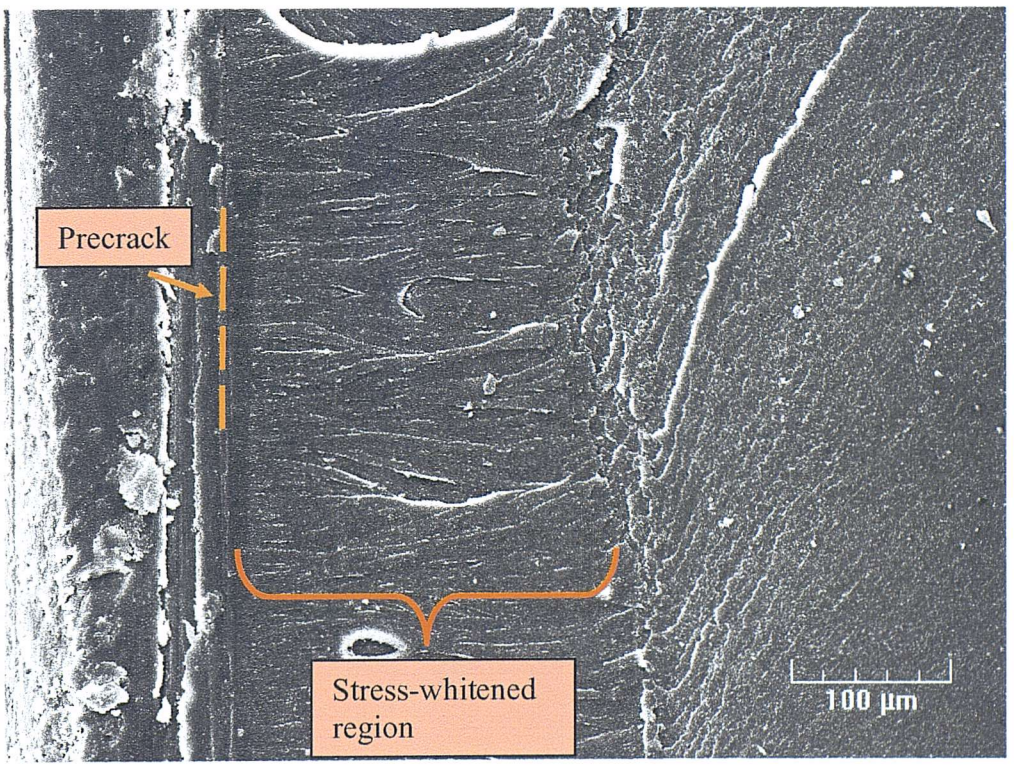


Figure 4.1.19. Fracture surface of a sample containing 4.6 wt. % CTBN (crack propagation from left to right).

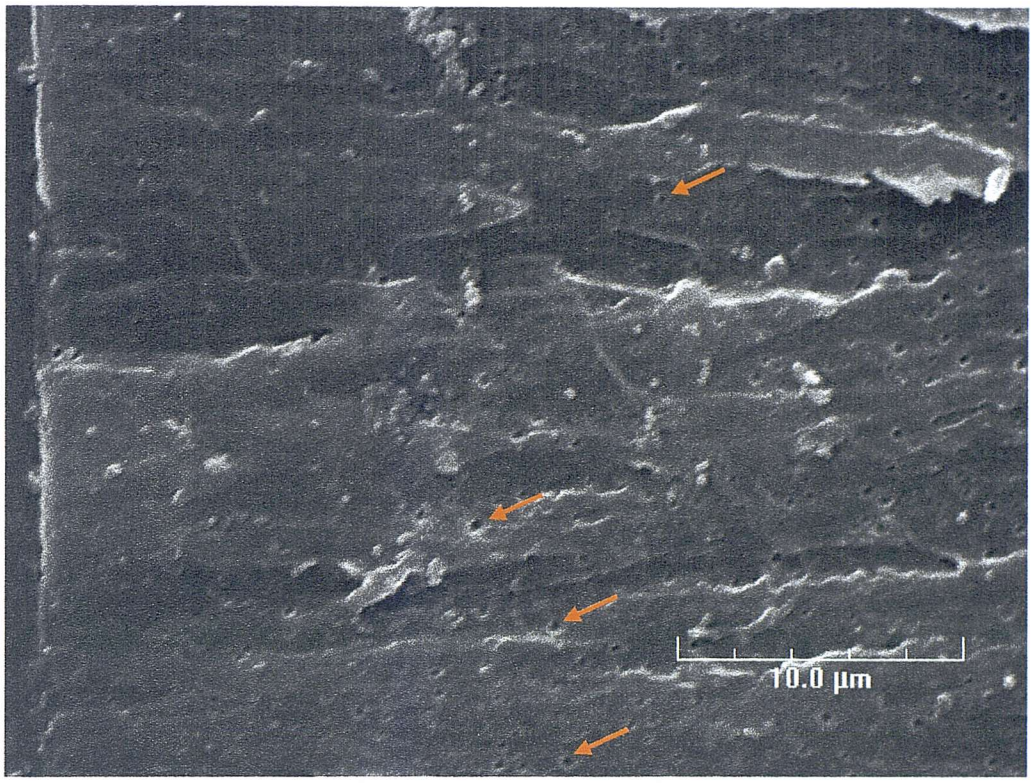


Figure 4.1.20. Fracture surface of a sample containing 4.6 wt. % CTBN at higher magnification (crack propagation from left to right, and red arrows point to some cavitated rubber particles).

The micrograph in Figure 4.1.21 is for a sample containing 6.9 wt. % CTBN. The region of stress-whitening is larger (~500µm) than in the previous sample containing 4.6 wt. % CTBN, and this corresponds to the increase in fracture toughness to 2.27MPa $m^{1/2}$.

The micrograph in Figure 4.1.22 is at higher magnification and shows more cavitated rubber particles (correlating with the higher CTBN content) than the previous sample. The cavities themselves are of a similar diameter to the previous sample containing 4.6 wt. % CTBN. The increase in toughness can be attributed to the higher CTBN content leading to more rubber cavitation, which then enables plastic void growth and shear bands to develop in the matrix. These mechanisms will be discussed in greater detail in Chapter 7.

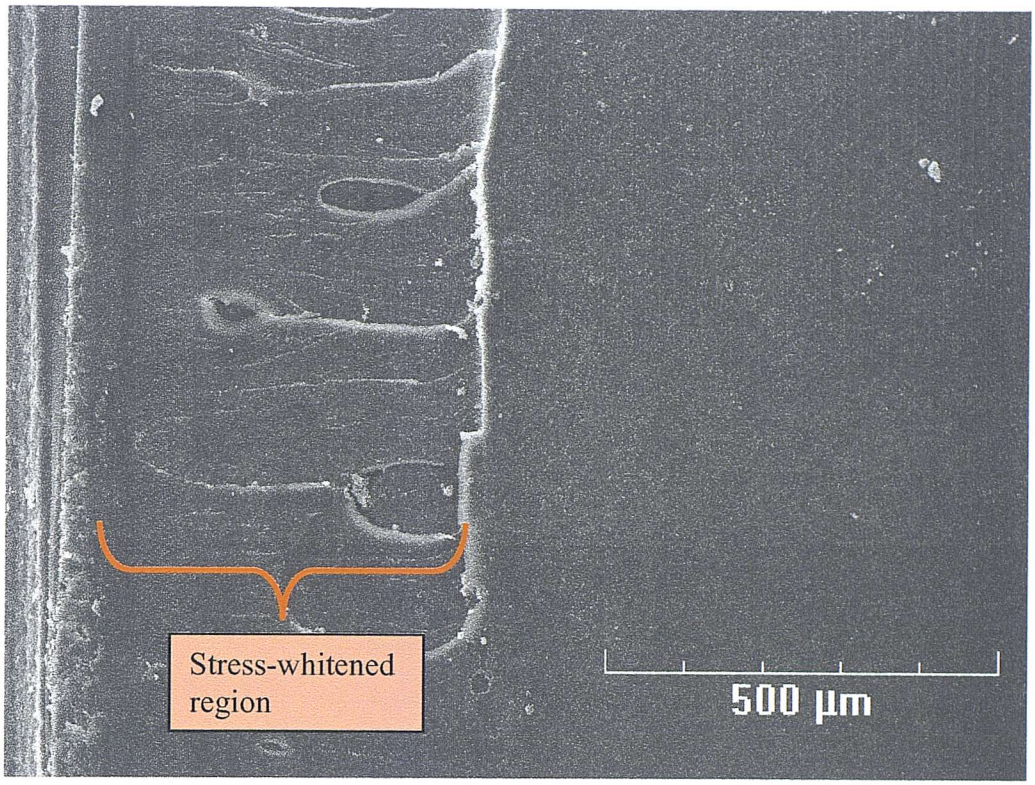


Figure 4.1.21. Fracture surface of a sample containing 6.9 wt. % CTBN (crack propagation from left to right).

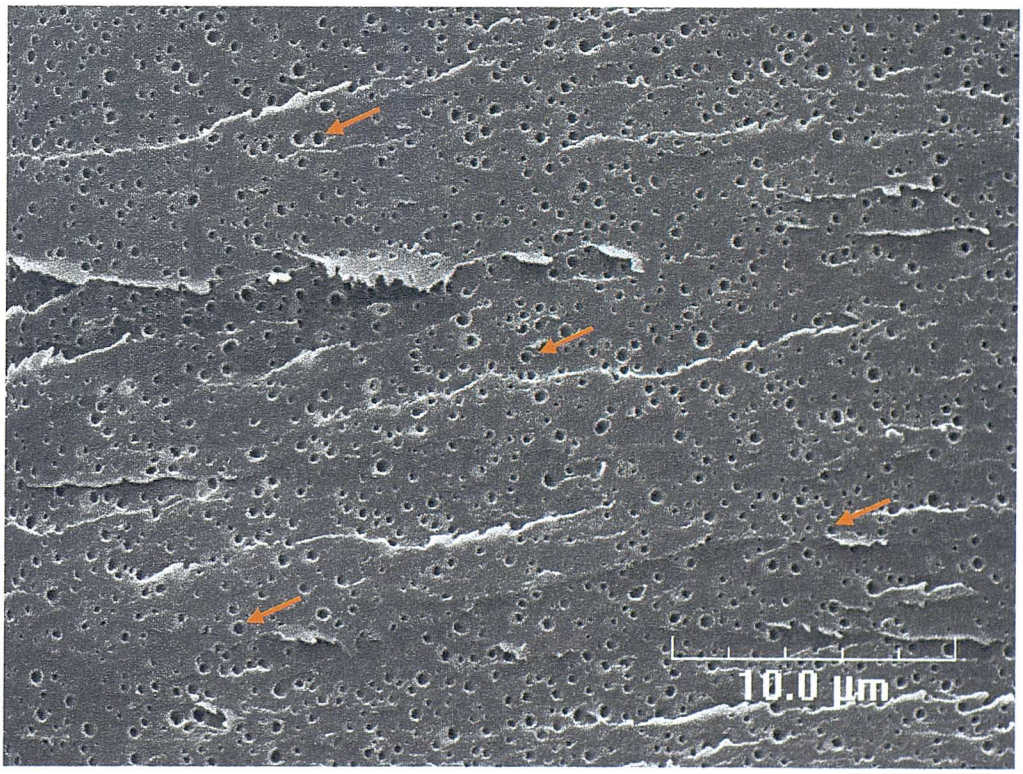


Figure 4.1.22. Fracture surface of a sample containing 6.9 wt. % CTBN at higher magnification (crack propagation from left to right and red arrows point to some cavitated rubber particles).

The micrograph in Figure 4.1.23 is for a sample containing 10.9 wt. % CTBN. The region of stress-whitening is even larger (~1100μm) than in the previous samples, which corresponds to the increase in fracture toughness 2.32MPa $m^{1/2}$. Kim *et al.* [148] performed a study which showed that there was a correlation between the increase in length of the stress-whitened region and an increase in fracture toughness, which has been confirmed in this present study. This increase in toughness manifests itself as cavitated rubber particles, and more of these can be seen in Figure 4.1.24 than the previous samples, because of the increased CTBN content. The size of the cavities in these three samples is about the same. The increasing extent of rubber cavitation with increasing rubber content in these three samples, agrees well with the microstructure and glass transition data, which showed that increasing the amount of CTBN in a sample increased the amount of rubbery particles that phase separated.

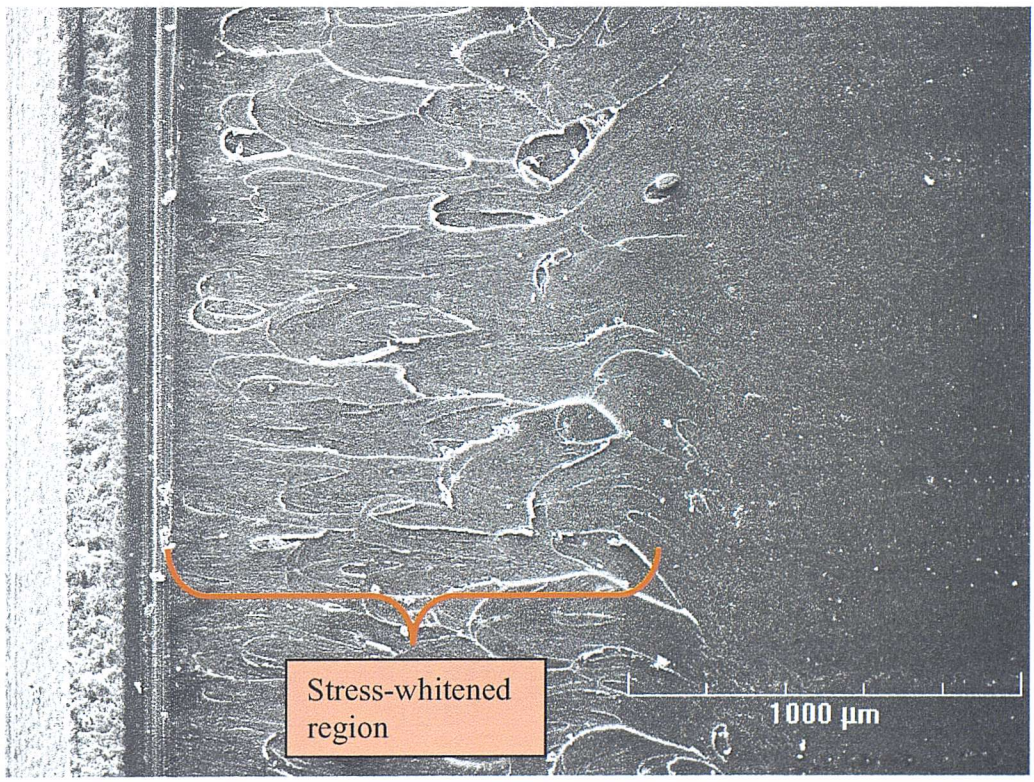


Figure 4.1.23. Fracture surface of a sample containing 10.9 wt. % CTBN (crack propagation from left to right).

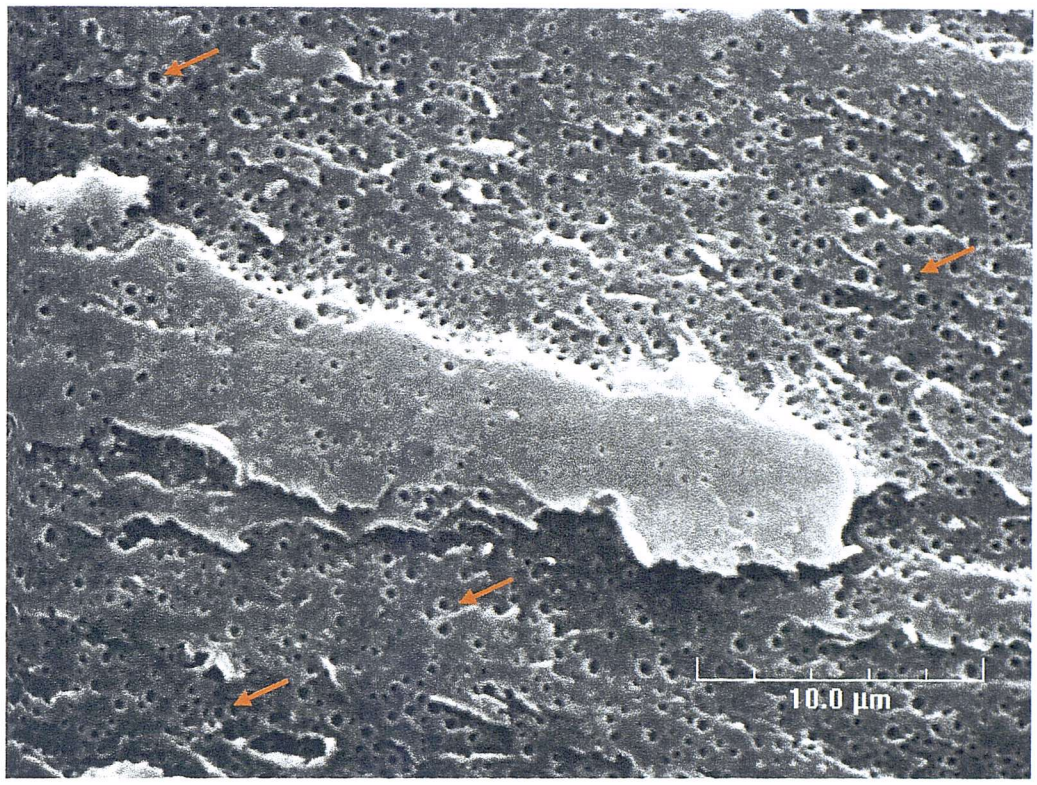


Figure 4.1.24. Fracture surface of a sample containing 10.9 wt. % CTBN at higher magnification (crack propagation from left to right and red arrows point to some cavitated rubber particles).

4.1.3.3 Hybrid Modified Epoxies

The micrograph in Figure 4.1.25 is for a hybrid sample containing 4.1 wt. % CTBN and 2 wt. % nano-silica. The stress-whitened region is slightly smaller (~175µm) than those of the samples containing only CTBN (~200µm), but this is because the CTBN-only sample had a slightly higher rubber content (4.6 wt. % CTBN). However, the fracture surface in Figure 4.1.26 shows no significant difference to the CTBN-only fracture surface in Figure 4.1.20. Indeed, there is evidence of rubber cavitation of the same size and extent as the CTBN-only sample. This explains why the toughness is statistically the same as for the CTBN-only sample. (It should be noted that the nano-silica particles are not visible at this magnification due to their small size.)

In addition, the discussion above suggests that the nano-silica particles do not restrict the macroscopic plastic deformation of the epoxy resin because the nano-scale size (20nm) of the nano particles means that the yielding of the epoxy network in front of the crack tip is not significantly limited [149]. There is no evidence from these SEM micrographs (due to the low magnification) that shows how well-distributed nano-silica

particles (see Figure 4.1.3) alter the fracture surface, and indeed, this is confirmed by the fact that the toughness remains statistically unaltered.

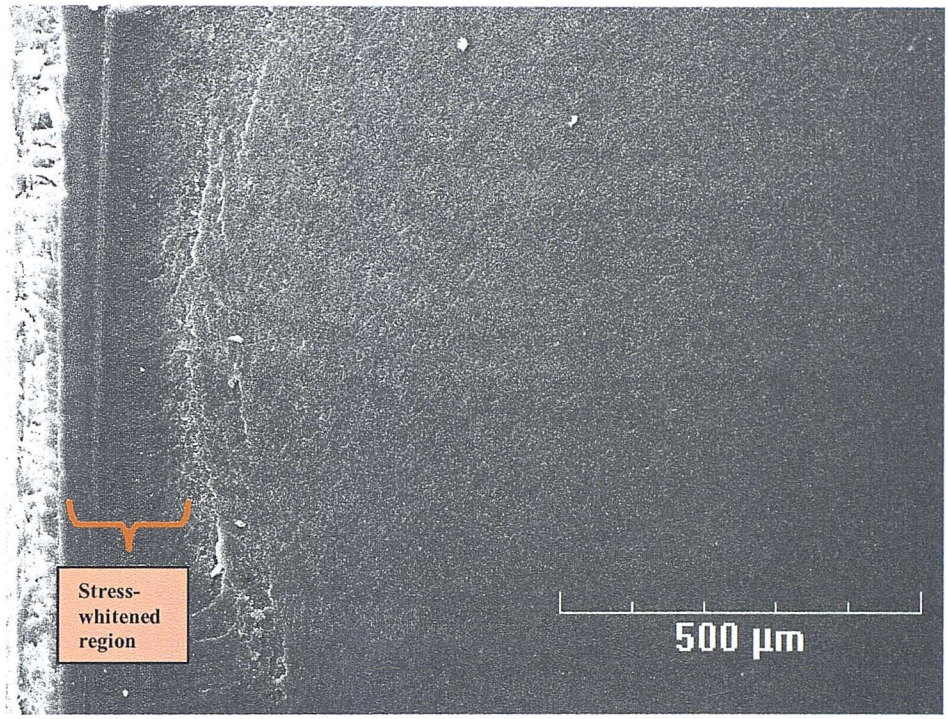


Figure 4.1.25. Fracture surface of a sample containing 4.1 wt. % CTBN and 2 wt. % nano-silica (crack propagation from left to right).

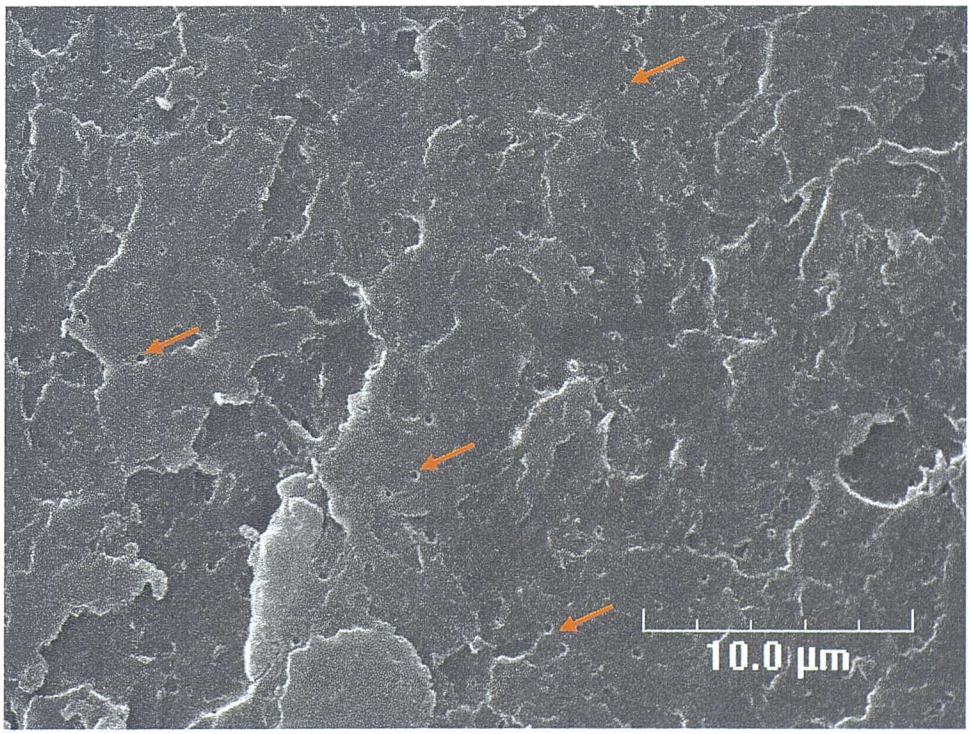


Figure 4.1.26. Fracture surface of a sample containing 4.1 wt. % CTBN and 2 wt. % nano-silica at higher magnification(crack propagation from left to right and red arrows point to some cavitated rubber particles).

The micrograph in Figure 4.1.27 shows a stress-whitened region of between 150 and 250μm for a sample containing 4.1 wt. % CTBN and 4.1 wt. % nano-silica, which is comparable to the previous hybrid sample containing 4.1 wt. % CTBN and 2 wt. % nano-silica, and its 4.6 wt. % CTBN-only counterpart. The stress-whitened region had a similar appearance to that of the previous hybrid sample containing 4.1 wt. % CTBN and 2 wt. % nano-silica, with a similar amount of rubber cavitation and cavity diameters. This correlates well with the statistical similarity in toughness values, and the fact that the increase in toughness is due to the cavitation of the rubber particles. (It should be noted that the higher magnification micrograph in Figure 4.1.28 shows a smoother surface, and less rubber cavitation than the previous sample hybrid sample containing 4.1 wt. % CTBN and 2 wt. % nano-silica but this is because this image was taken in the region of fast fracture.) It is known from the AFM and TEM images that the nano-silica particles are well dispersed in the epoxy matrix, but the lack of change in toughness in this sample, and the previous sample, show that the nano-silica does nothing to improve the toughness. A more positive affirmation can be made: the addition of up to 4.1 wt. % nano-silica *does not decrease* the toughness of a hybrid with 4.1 wt. % CTBN.

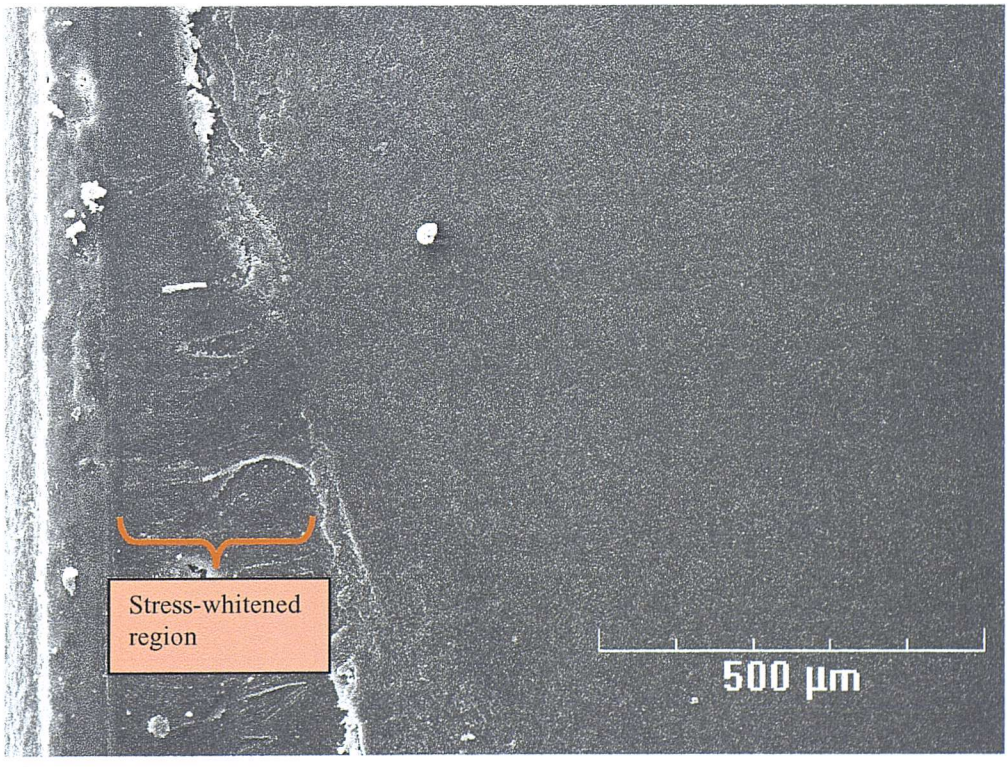


Figure 4.1.27. Fracture surface of a sample containing 4.1 wt. % CTBN and 4.1 wt. % nano-silica (crack propagation from left to right).

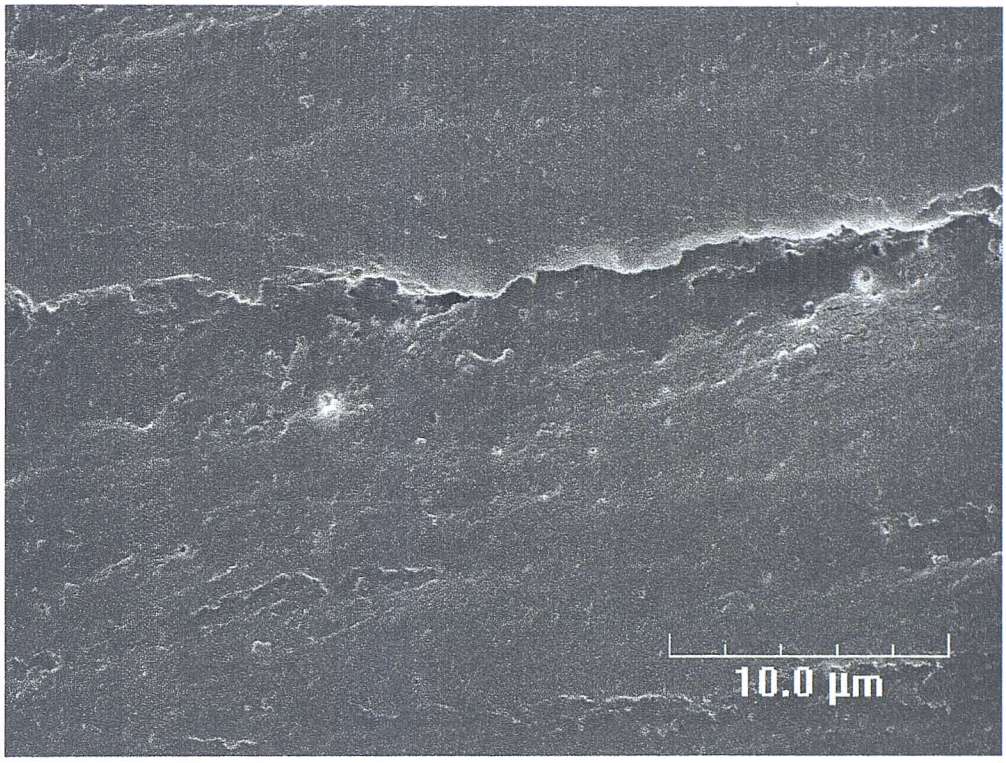


Figure 4.1.28. Fracture surface of a sample containing 4.1 wt. % CTBN and 4.1 wt. % nano-silica at higher magnification (crack propagation from left to right).

The micrograph in Figure 4.1.29 clearly shows the stress-whitened region of a sample containing 6.9 wt. % CTBN and 3.5 wt. % nano-silica. This area is ~500µm wide, which is similar to that of its CTBN-only counterpart (see Figure 4.1.21), and the cavitated rubber particles are easily seen in Figure 4.1.30. The size and distribution of the cavitated rubber particles are the same as in the CTBN-only micrograph. At this magnification, the nano-silica particles are not visible, but there is no apparent difference in the appearance of the fracture surface compared to the CTBN-only sample. This correlates well with the statistical similarity in their toughness. This confirms the claim made earlier that well-distributed nano-silica particles do not decrease the toughness of a hybrid sample from this system.

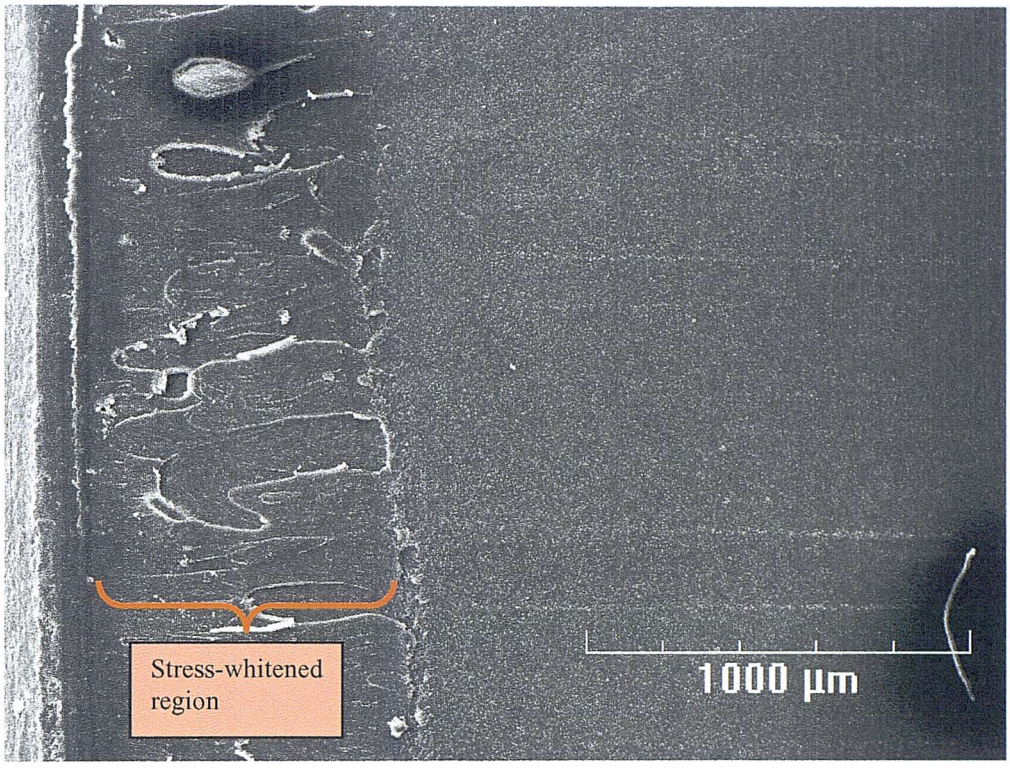


Figure 4.1.29. Fracture surface of a sample containing 6.9 wt. % CTBN and 3.5 wt. % nano-silica (crack propagation from left to right).

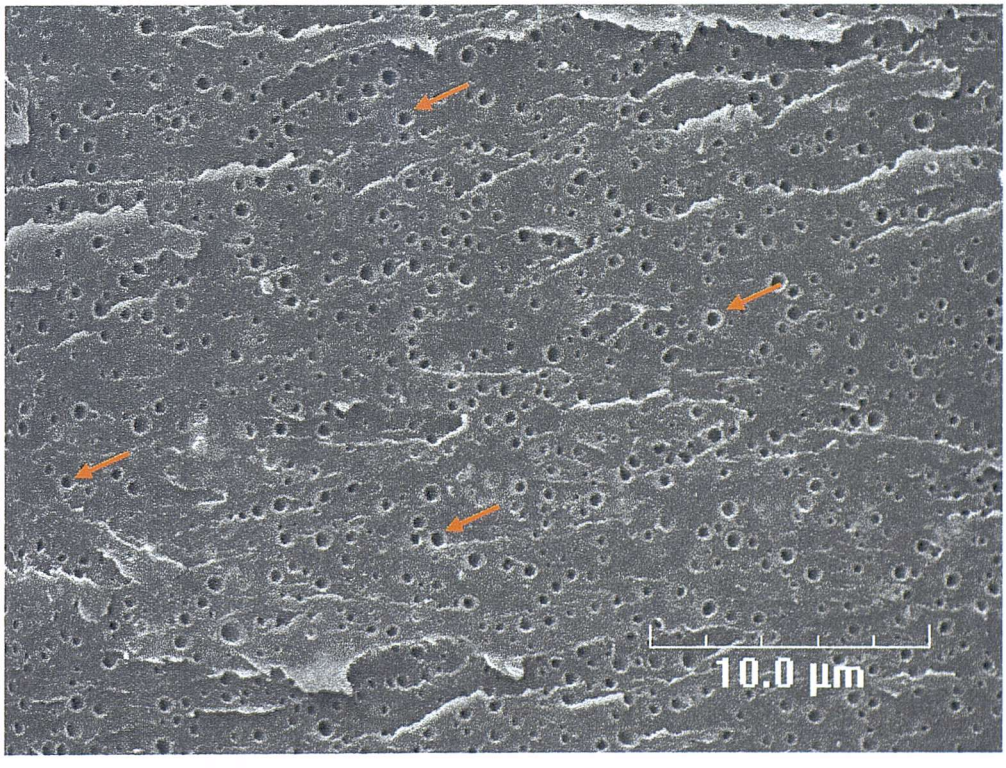


Figure 4.1.30. Fracture surface of a sample containing 6.9 wt. % CTBN and 3.5 wt. % nano-silica at higher magnification (crack propagation from left to right and the red arrows point to some cavitated rubber particles).

The fracture surface of a sample containing 7 wt. % CTBN and 7 wt. % nano-silica can be seen in Figure 4.1.31 and Figure 4.1.32. Although the fracture surface appears to be rougher than the previous sample, and there is cavitation of rubber particles occurring, this formulation has a statistically lower toughness (of 1.88MPa $m^{1/2}$) compared to its CTBN-only counterpart (2.27MPa $m^{1/2}$). On reviewing the TEM image in Figure 4.1.8, the microstructure shows the formation of super-clumps of agglomerated nano-silica of ~4μm in diameter. Indeed, at higher magnification, these large agglomerates are visible on the fracture surface in Figure 4.1.32 and Figure 4.1.33. This suggests that super-clumps have a detrimental effect on the fracture toughness. This is because the large agglomerates act like very brittle defects, and also reduce the amount of epoxy between particles that is available for deformation, due to the very small inter-particle within the agglomerates [85]. This would suggest that the toughness should be less than that of the unmodified epoxy, but some fracture resistance is provided by the cavitation of the rubber particles [112,150].

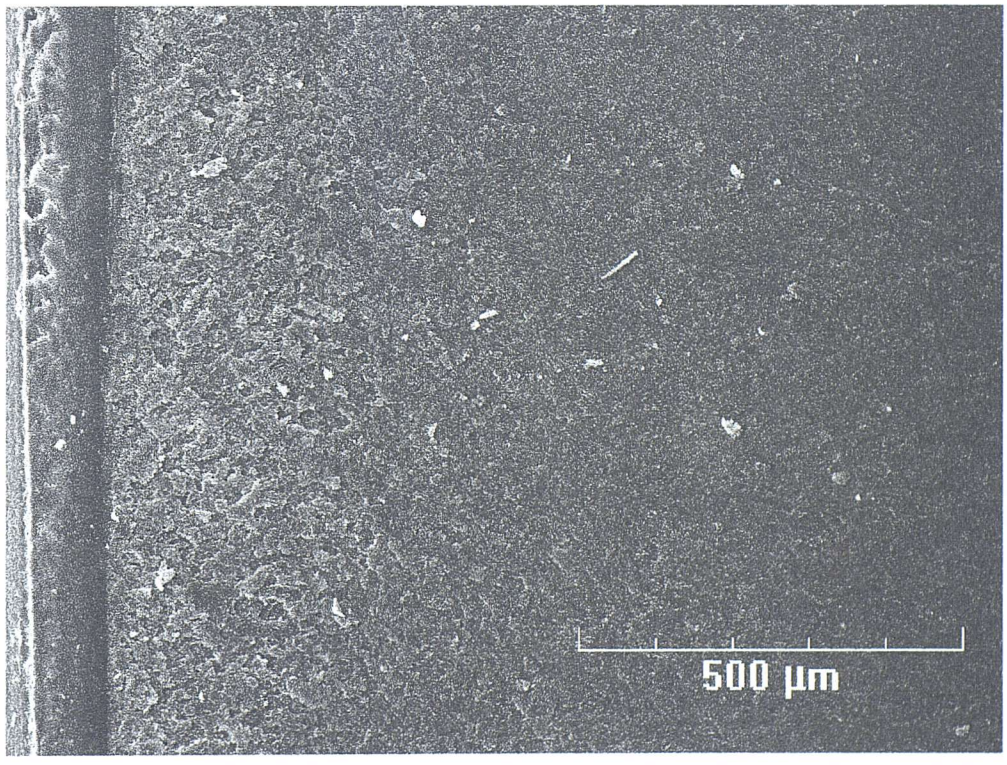


Figure 4.1.31. Fracture surface of a sample containing 7 wt. % CTBN and 7 wt. % nano-silica (crack propagation from left to right).

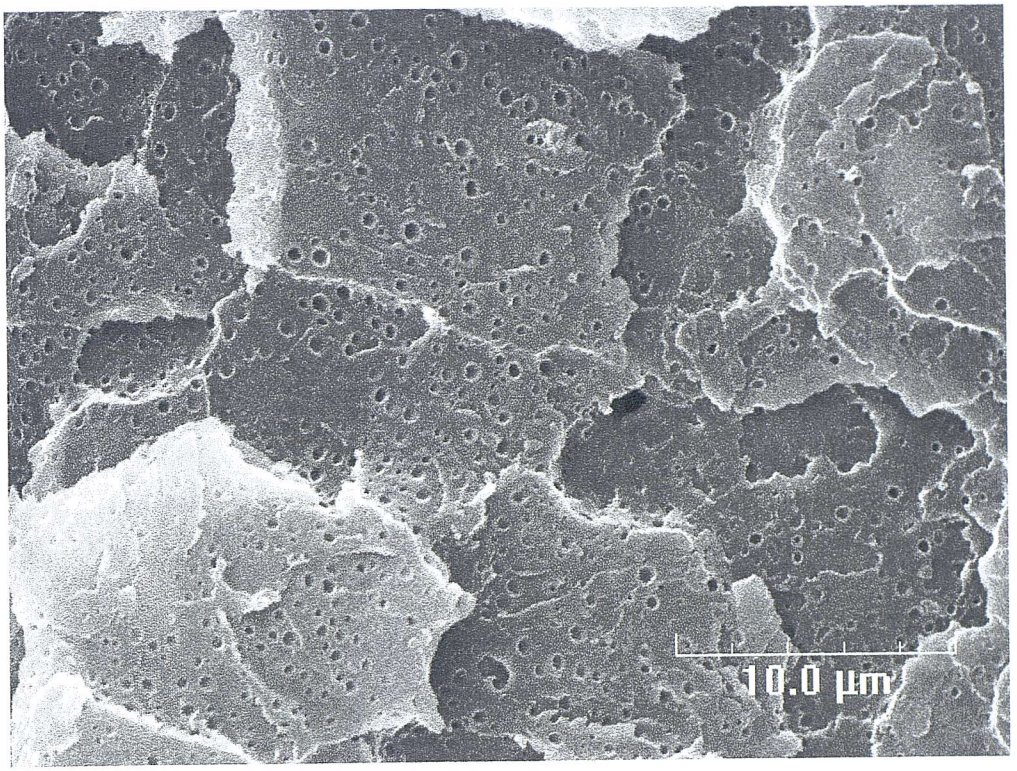


Figure 4.1.32. Fracture surface of a sample containing 7 wt. % CTBN and 7 wt. % nano-silica at higher magnification (crack propagation from left to right).

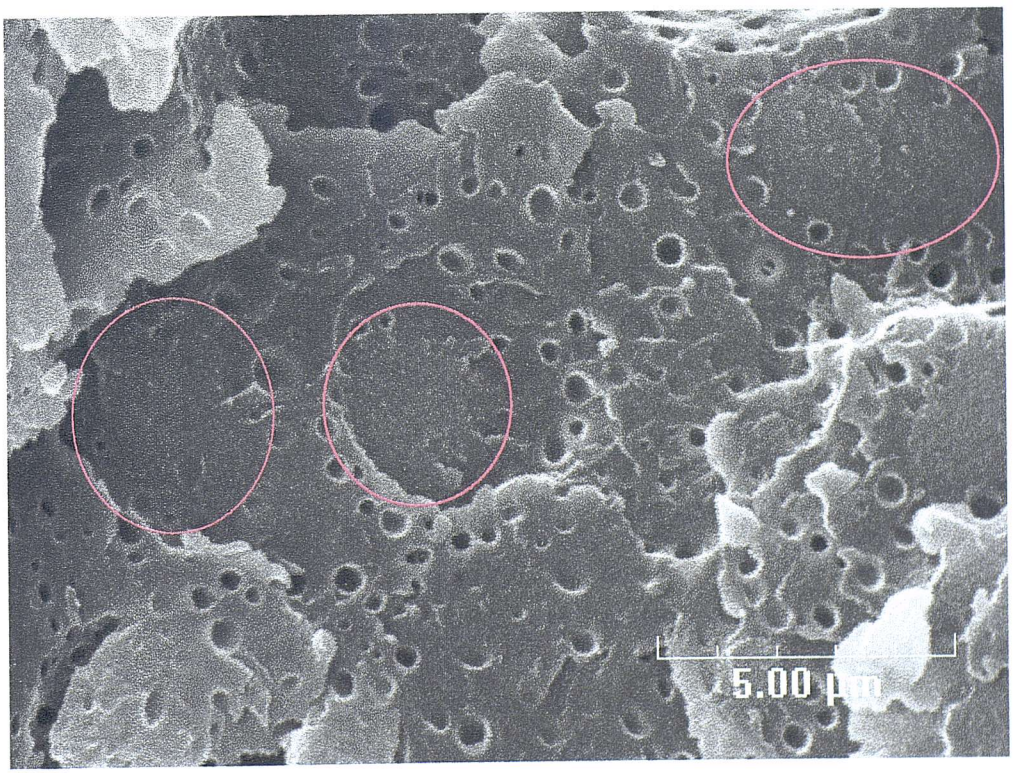


Figure 4.1.33. Fracture surface of a sample containing 7 wt. % CTBN and 7 wt. % nano-silica at higher magnification (crack propagation from left to right. Pink circles around super-clumps).

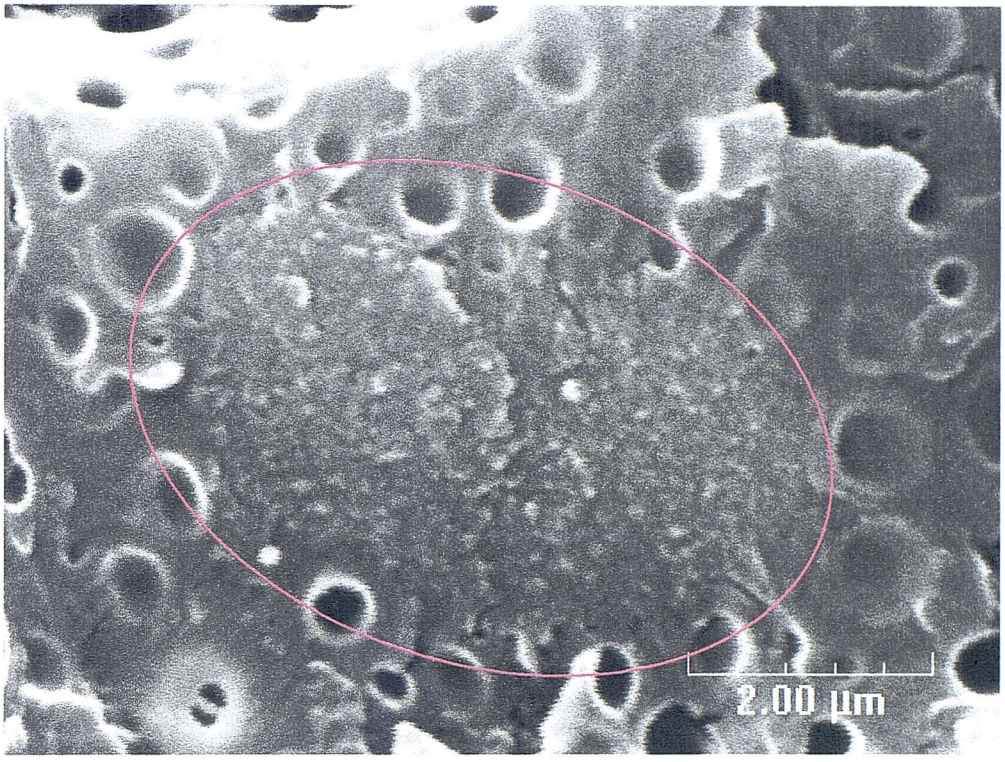


Figure 4.1.34. Fracture surface of a sample containing 7 wt. % CTBN and 7 wt. % nano-silica at higher magnification (crack propagation from left to right).

The micrographs in Figure 4.1.35 and Figure 4.1.36 are for a sample containing 11.3 wt. % CTBN and 5.7 wt. % nano-silica. A very large stress-whitened region is observed (due to the large CTBN content), as well as widespread cavitation of the rubber particles. The cavitated rubber particles in this sample are larger than other samples, because the microstructure images show that the particles are larger (~1µm). This leads to the high toughness of 2.36MPa $m^{1/2}$. It should be noted that this is statistically the same as that of the corresponding CTBN-only sample, which had a toughness of 2.32MPa $m^{1/2}$. This shows that the three-dimensional necklace-like nano-silica features have not altered the toughness of this formulation.

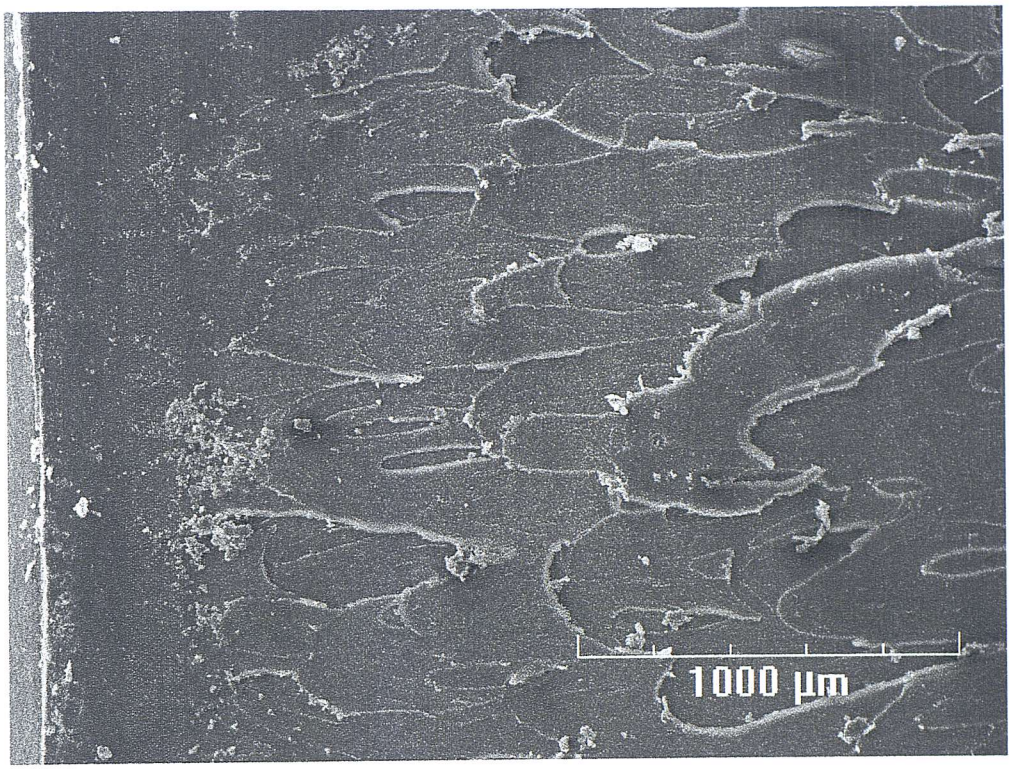


Figure 4.1.35. Fracture surface of a sample containing 11.3 wt. % CTBN and 5.7 wt. % nano-silica (crack propagation from left to right).

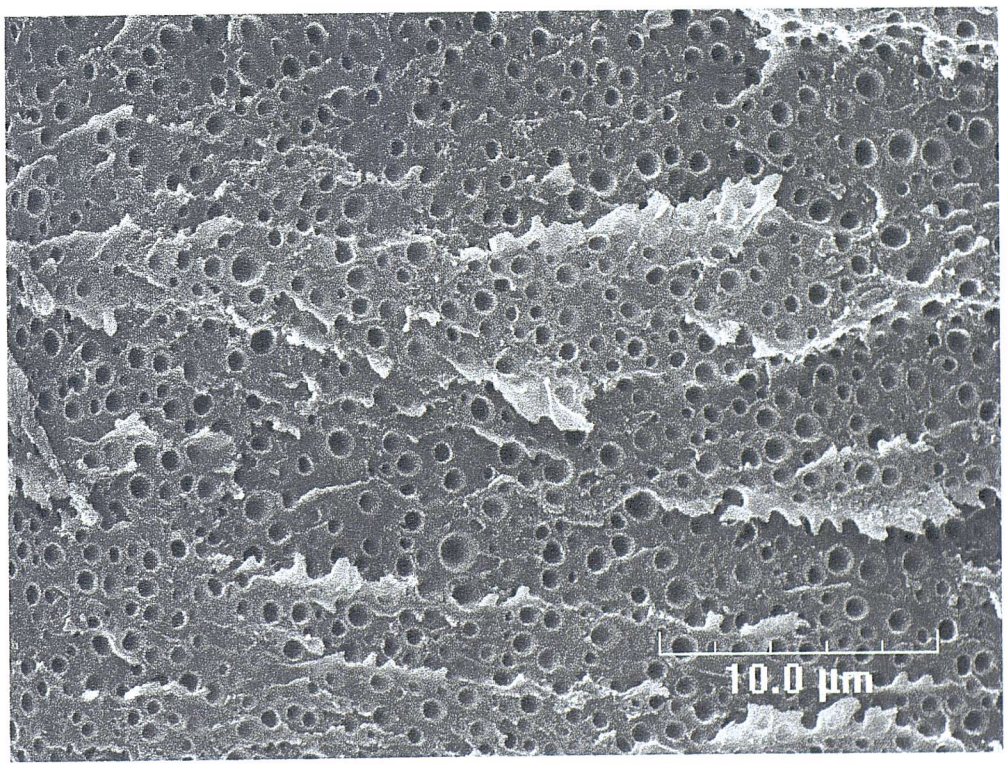


Figure 4.1.36. Fracture surface of a sample containing 11.3 wt. % CTBN and 5.7 wt. % nano-silica at higher magnification (crack propagation from left to right).

The fracture surface of a sample containing 11.6 wt. % CTBN and 11.6 wt. % nano-silica can be seen in the micrographs in Figure 4.1.37 and Figure 4.1.38. It is interesting to note that the surface appears to be very similar to that of the sample containing 7 wt. % CTBN and 7 wt. % nano-silica because both are very rough, both show high amounts of cavitation, and both have large agglomerates of nano-silica (see Figure 4.1.10 and Figure 4.1.11 for microstructure details). These super-clumps are easily visible in the higher magnification image. This sample has a very low toughness of 1.50MPa $m^{1/2}$, which is comparable to the unmodified epoxy. This confirms that large amounts of nano-silica lead to agglomeration which has a detrimental effect on the fracture toughness because the large agglomerates act like very brittle defects, and also reduce the amount of epoxy available for plastic deformation [85,112,150].

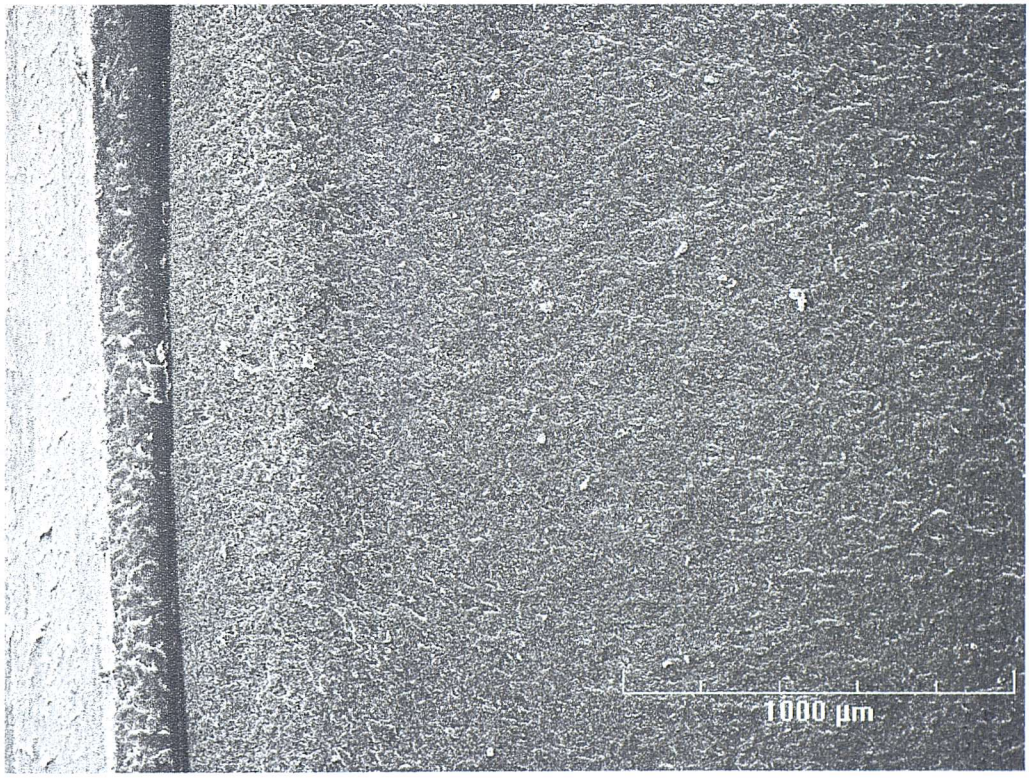


Figure 4.1.37. Fracture surface of a sample containing 11.6 wt. % CTBN and 11.6 wt. % nano-silica (crack propagation from left to right).

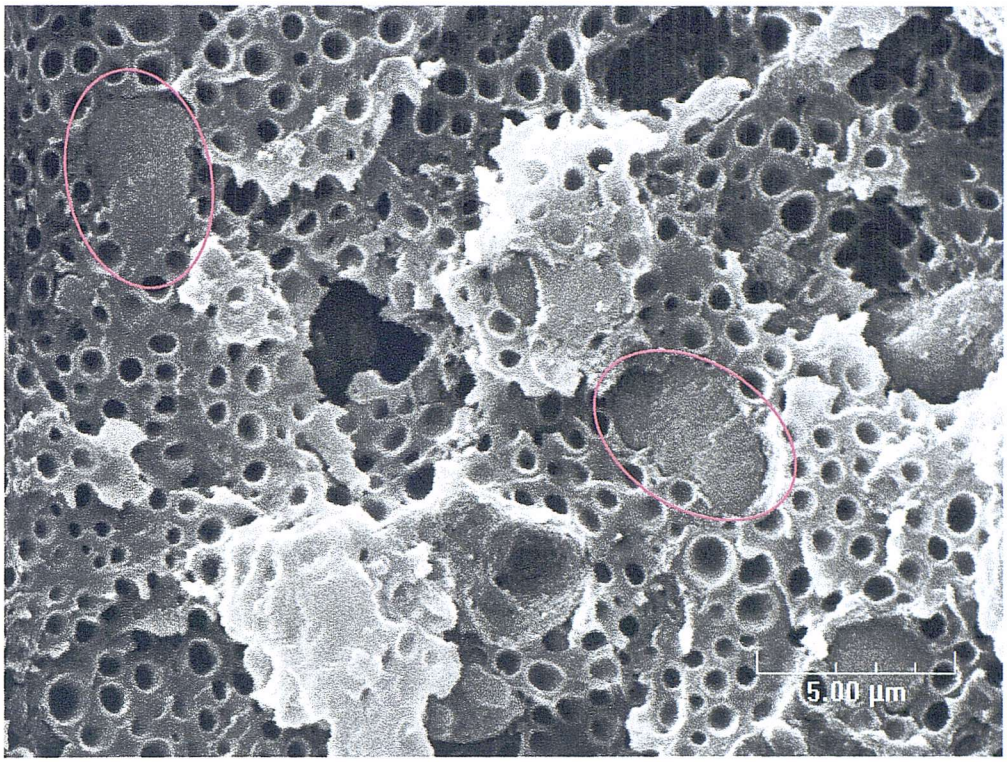


Figure 4.1.38. Fracture surface of a sample containing 11.6 wt. % CTBN and 11.6 wt. % nano-silica at higher magnification (crack propagation from left to right. Pink circles around super-clumps).

4.1.3.4 Summary

All the fracture surfaces of samples containing CTBN, as well as CTBN and nano-silica, were much rougher than the smooth, barren surface of the unmodified epoxy. The formulations with CTBN-only showed increasing amounts of rubber cavitation, which correlates well with the increase in toughness observed.

The hybrid fracture surfaces with small amounts of nano-silica appeared to be very similar to the corresponding CTBN-only samples, as were their fracture toughness values. Small amounts of nano-silica, when well-dispersed and coalesced into three-dimensional necklace-like features, do not decrease the toughness. When 7 wt. % or more of nano-silica was added, the fracture surfaces became very rough, with high amounts of rubber cavitation. The drastically reduced fracture toughness prompted a closer inspection of the fracture surfaces, and it was found that the super-clumps of nano-silica particles were visible. These super-clumps which are formed at high nano-silica contents, lead to reduced toughness because the large agglomerates act like very brittle defects, and also reduce the amount of epoxy available for plastic deformation.

4.2 Glass Fibre Reinforced Polymer Results

Glass fibres were used to reinforce matrices of the same formulations as described in the previous Bulk Epoxy Polymer Results Section. Mode I tests were performed and the fracture surfaces were investigated. It should be noted that the laminates were of rather poor quality because the resin and hardener blend was too viscous and had to be injected at a relatively high temperature. The elevated injection temperature speeded up the curing of the epoxy, which affected the flow into the mould. Thus the laminates were of uneven thickness and surface finish, were epoxy-rich in some laminates, and some even had the starter films in a thick epoxy layer. As a result, only Mode I tests were performed, since flexural modulus results would have been severely compromised due to the large amounts of epoxy reducing the measured moduli. Indeed, due to the difficulty in doing Mode I tests, such as a large deformation of the arms, and samples breaking due to crack growth perpendicular to the starter film, stiff uni-directional CFRP backing beams were adhered to the surface to counteract this.

4.2.1 Mode I Fracture Results

The graph in Figure 4.2.1 illustrates the interlaminar fracture energy results obtained using double cantilever beam (DCB) samples. A summary of all the fracture energies, including whether any R-curve behaviour was observed for each sample, can be found in Table 4.2.1. It should be noted that where R-curve behaviour was observed, the R-curve was very small, which is expected for woven FRPs [152], since the fibres cannot bridge along the entire length of the sample like in a unidirectional laminate. Two samples were tested for all but one formulation (the second sample failed at the bond-line between the backing beam and the laminate, due to the very uneven surface finish), and the mean fracture energy calculated from the corrected beam theory (CBT) method is quoted. All samples failed in a stick-slip manner (initiation-arrest) and the values quoted are the mean values of the initiation interlaminar fracture energy. The error bars are the standard deviation of these mean values.

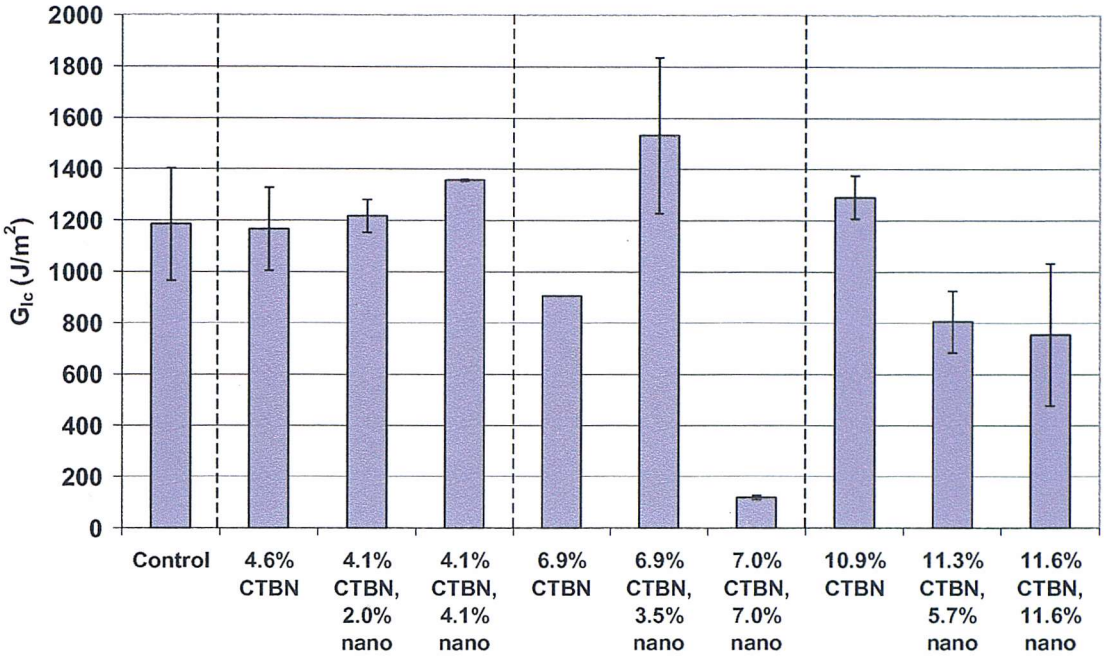


Figure 4.2.1. Mode I interlaminar fracture energy for GFRPs with an amine-cured DGEBA matrix. (error bars are ± one standard deviation)

Table 4.2.1. Summary of the mode I interlaminar fracture energies for GFRPs with an amine-cured DGEBA matrix. (*only one sample tested for this formulation)

wt. % CTBN	wt. % nano-silica	GFRP Mode I fracture energy, G_{Ic} (J/m^2)	R-curve? (2 samples tested)
0	0	1185 ± 219	Yes and Yes
4.6	0	1167 ± 162	Yes and No
6.9	0	906 *	Yes*
10.9	0	1291 ± 85	Yes and No
4.1	2	1217 ± 64	Yes and Yes
4.1	4.1	1357 ± 4	Yes and Yes
6.9	3.5	1532 ± 304	Yes and No
7	7	120 ± 8.5	No and No
11.3	5.7	806 ± 120	Yes and No
11.6	11.6	755 ± 276	Yes and No

The results show that no laminate with a toughened matrix is statistically more fracture resistant than the laminate with the unmodified epoxy matrix, which had a fracture energy of 1185J/m^2. Research into FRPs with an amine-cured DGEBA-based matrix, performed by Velmuragan *et al.* [152] showed unmodified GFRPs with a fracture energy of 580J/m^2, and the work of Suppakul *et al.* [153] also showed unmodified GFRPs with a fracture energy of less than 600J/m^2. Indeed, compared to the literature, the untoughened laminate in this study is almost twice that of those in other work. However, it should be recalled that the fracture energy of the bulk epoxy was also much higher than that reported in previous work.

The GFRP sample with the 6.9 wt. % CTBN-only matrix is more brittle than the GFRP with an unmodified epoxy matrix, as were the hybrid GFRPs with an ~11 wt. % CTBN and nano-silica matrix. The one sample that had a very low fracture energy was the one with a matrix containing 7 wt. % CTBN and 7 wt. % nano-silica, but it had a low fibre volume fraction (confirmed by a visual inspection), and the crack propagated through an epoxy-rich region.

A more complete discussion about the fracture energy results can be found in the following section which examines the fractograpy of the samples. The micrographs offer explanations for the low fracture energies of the GFRP materials compared to that of the control GFRP based on the unmodified epoxy matrix.

4.2.2 Mode I GFRP Fracture Surfaces

Scanning electron microscopy was performed on some of the GFRP fracture surfaces to investigate the fracture mechanisms responsible for the changes in toughness that were observed. It should be noted that the microstructure of the bulk epoxy polymer, and the corresponding formulation used as the matrix for the GFRPs, was the same. The presence of the glass fibres did not alter the microstructure of the epoxy matrix, which can be observed by comparing the micrographs of the bulk epoxy polymer in Section 4.1.3 with their GFRP counterparts in this section (Section 4.2.2). A good example of this comparison can be found by contrasting the micrographs in Figure 4.1.30 (which shows the microstructure of the bulk epoxy polymer toughened with 6.9 wt. % CTBN

and 3.5 wt. % nano-silica) and Figure 4.2.19 (where said bulk epoxy polymer was used as the matrix for a GFRP laminate).

4.2.2.1 Unmodified Epoxy Matrix

The low magnification micrograph in Figure 4.2.2 is for a GFRP sample with an unmodified epoxy matrix. The small region of epoxy matrix that is visible, shows some plastic deformation, which contributes to the fracture energy of the sample. The higher magnification micrographs in Figure 4.2.3 and Figure 4.2.4 show the fibres in much more detail. It can be seen that fibre pull-out has occurred, and there is evidence of matrix failure (which contributed to the high fracture energy) [154] where the fibres cross. Some broken fibres and evidence of fibre bridging were visible which also contribute to toughening the laminate, and the small R-curve observed [113,155]. The plastic deformation of the epoxy matrix, in addition to the fibre toughening mechanisms, gave this laminate a fracture energy of 1185J/m^2 which is almost twice that of the bulk epoxy.

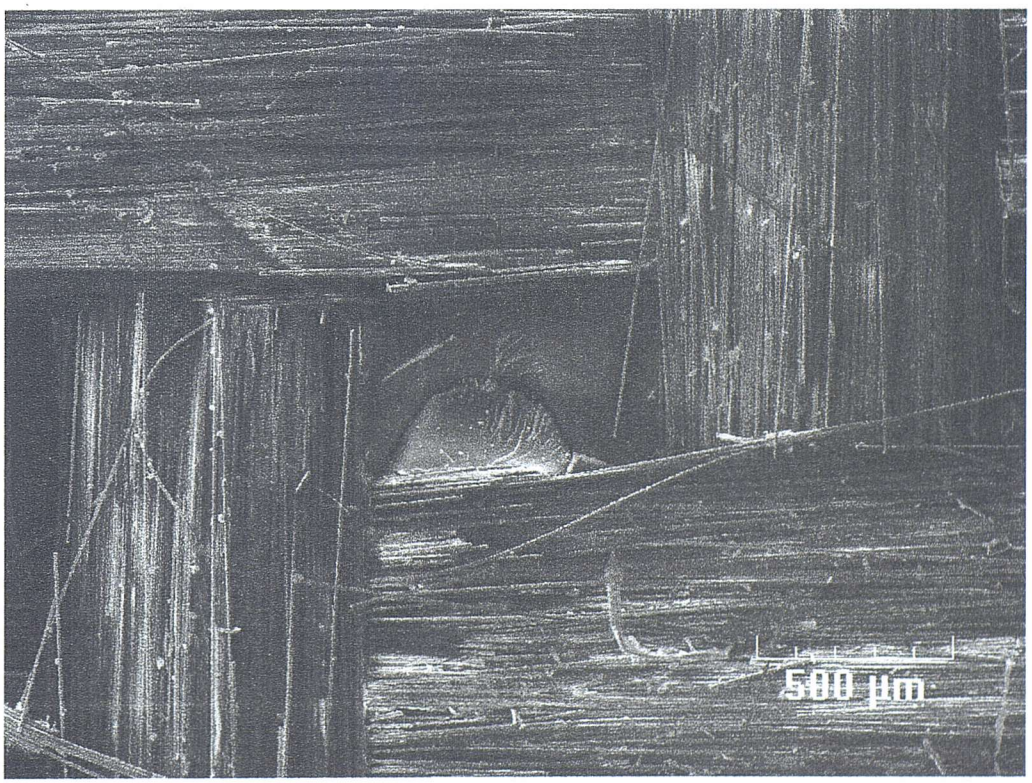


Figure 4.2.2. Fracture surface of a GFRP sample with an unmodified amine-cured epoxy matrix (crack propagation from right to left).

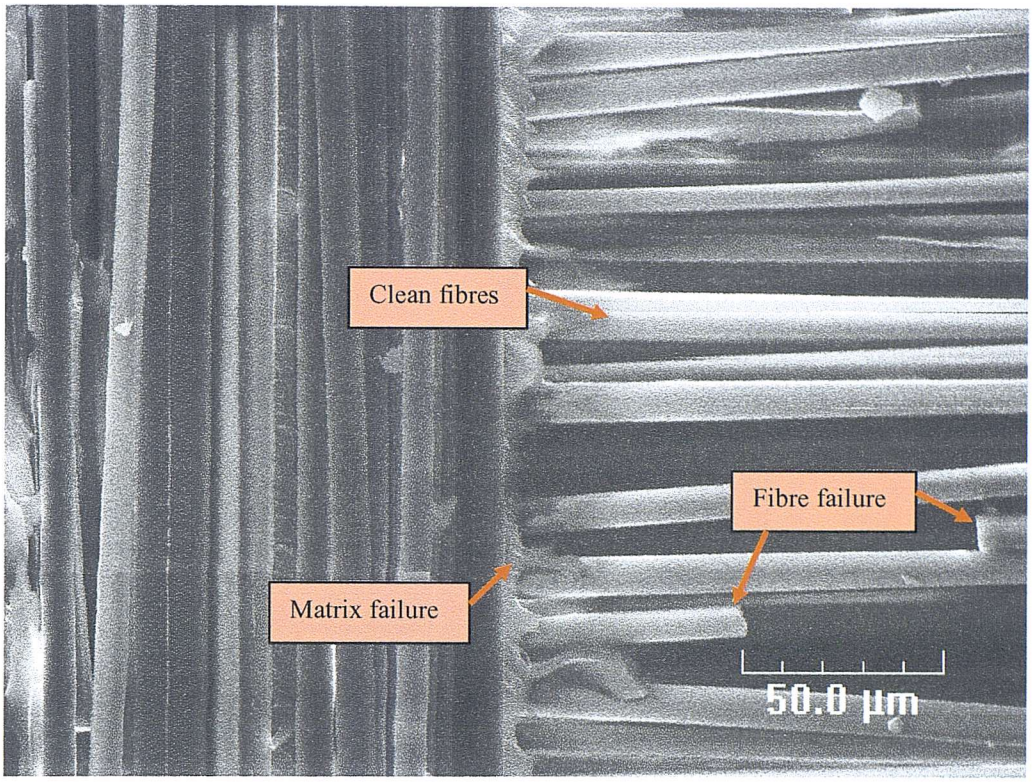


Figure 4.2.3. Fracture surface of a GFRP sample with an unmodified amine-cured epoxy matrix at higher magnification (crack propagation from right to left).

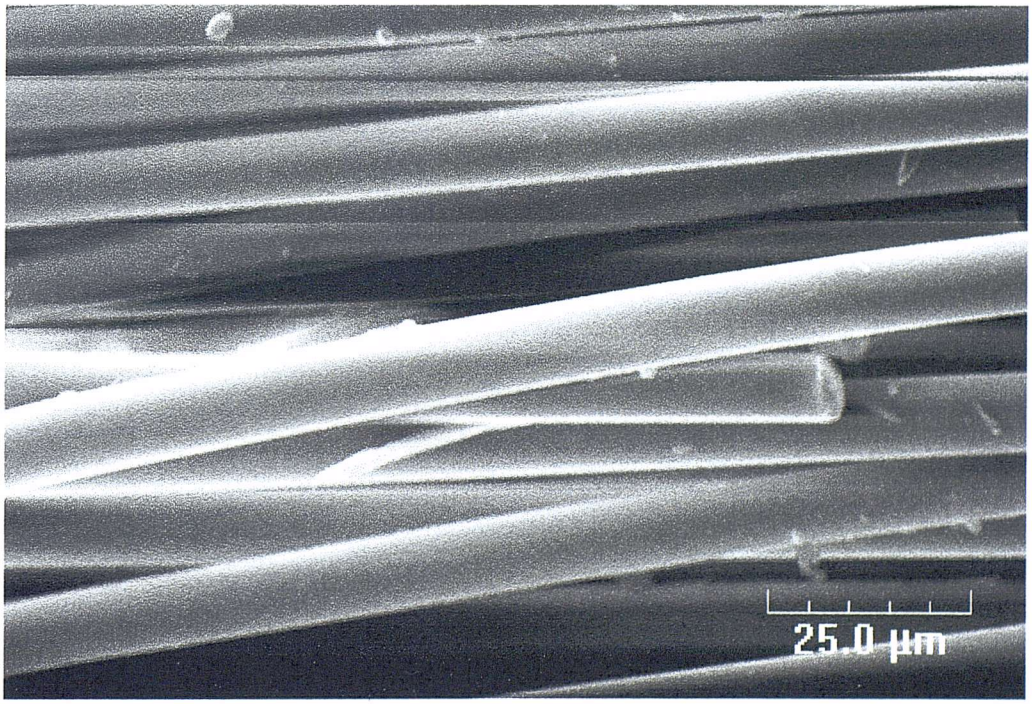


Figure 4.2.4. Fracture surface of a GFRP sample with an unmodified amine-cured epoxy matrix at higher magnification showing clean fibres (crack propagation from right to left).

4.2.2.2 Rubber Modified Epoxy Matrices

The micrograph in Figure 4.2.5 is the fracture surface of a GFRP sample with a matrix toughened with 4.6 wt. % CTBN. The fracture surface shows broken fibres, as well as some deformation of the epoxy matrix. The higher magnification micrograph in Figure 4.2.6 shows broken fibres and evidence of fibre pullout. The continuous channels [156] are the impressions left by the fibres that remain on the other half of the fracture surface. The debonding phenomena, as well as cavitation of the rubber particles in the epoxy matrix, can be seen clearly in Figure 4.2.7. The GFRP material formulation had a fracture energy of 1167J/m^2 whereas the bulk epoxy had a fracture energy of 1234J/m^2, suggesting that not much extra fracture resistance was provided by the fibres. The adhesion between the fibres and matrix in this sample is poor, which means that the fracture energy may have been higher if the adhesion was better. This means that the rubber cavitation was the major contributor to the fracture energy of this sample. Indeed, a comparison to the bulk fracture surface (see Figure 4.1.20) shows a similar extent of cavitated rubber particles.

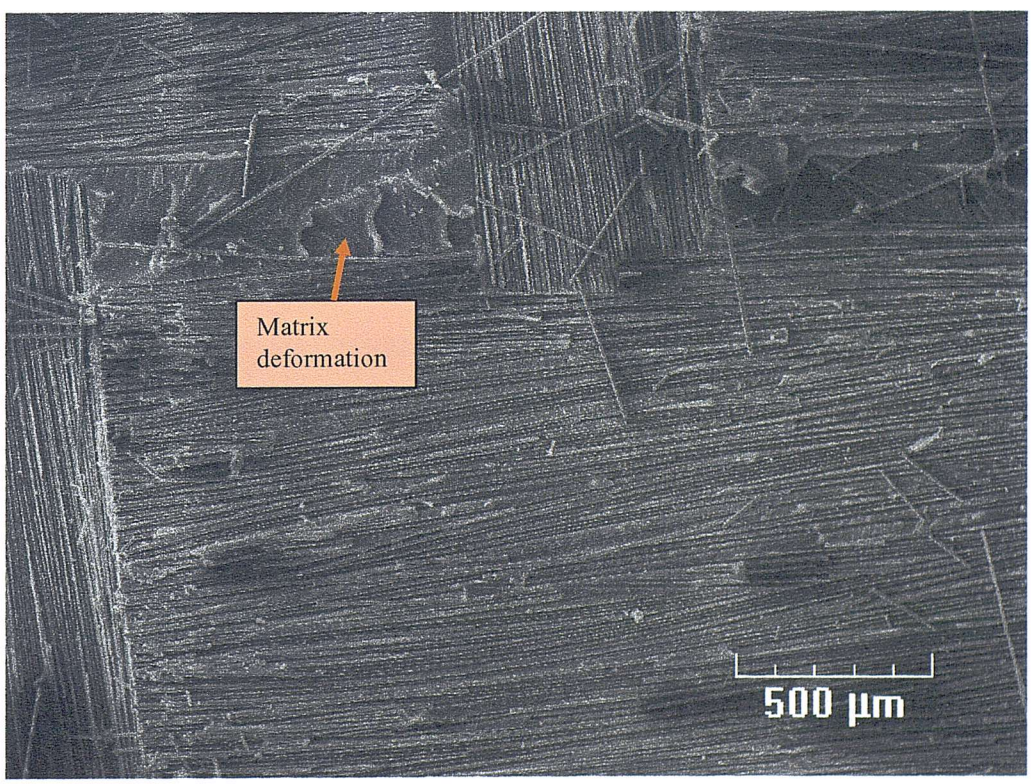


Figure 4.2.5. Fracture surface of a GFRP sample with an amine-cured epoxy matrix containing 4.6 wt. % CTBN (crack propagation from right to left).

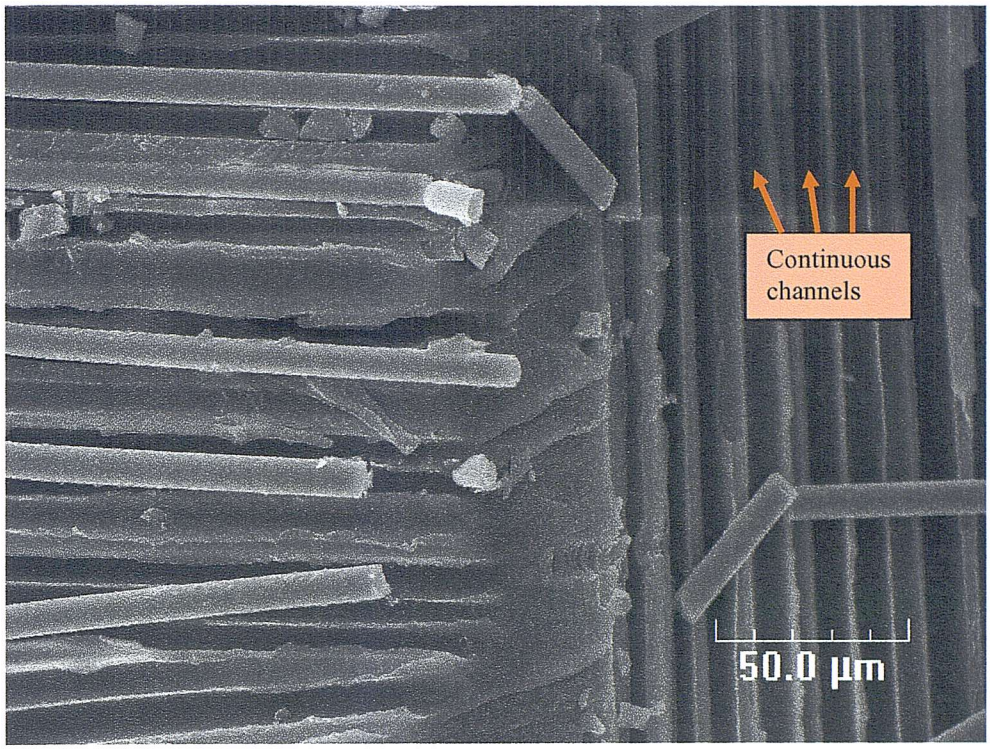


Figure 4.2.6. Fracture surface of a GFRP sample with an amine-cured epoxy matrix containing 4.6 wt. % CTBN at higher magnification (crack propagation from right to left).

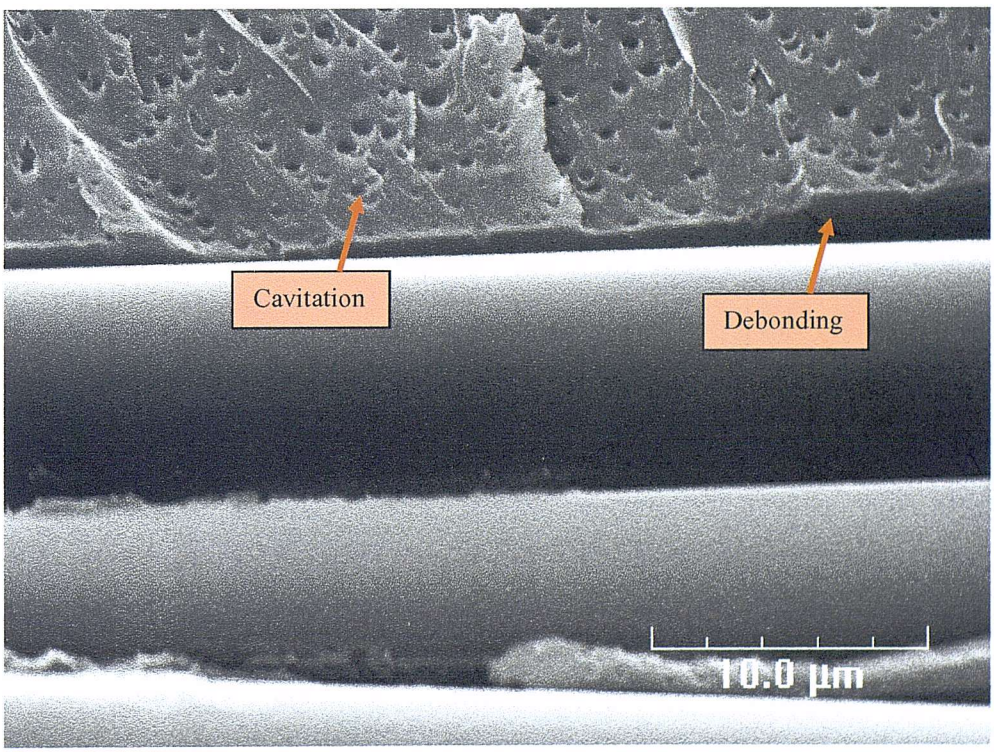


Figure 4.2.7. Fracture surface of a GFRP sample with an amine-cured epoxy matrix containing 4.6 wt. % CTBN at higher magnification showing debonding at fibre-matrix interface (crack propagation from right to left).

The micrographs in Figure 4.2.8, Figure 4.2.9 and Figure 4.2.10 are for a GFRP sample with an epoxy matrix toughened with 6.9 wt. % CTBN. Although the adhesion between the matrix and fibres appears to be better than the previous samples, many regions of the sample show pristine fibres. Cavitation of the rubber particles, fibre debonding and fibre pullout are evident. Yet, this formulation has a fracture energy of 906J/m^2, which is less than the previous samples, as well as the bulk fracture energy of the matrix. One possible reason for this is that there seems to be less cavitated rubber particles visible than in the corresponding bulk micrograph (see Figure 4.1.22). This is because the plastic-zone size is larger than the inter-fibre distance, which means that the crack tip is constrained by the fibres and full cavitation does not occur [112]. An inspection of the micrographs shows that the maximum inter-fibre distance is ~5μm. Using Equation 2.12 in Chapter 2 to calculate the radius of the plastic zone, it was found that $r_p \approx 70\mu m$, which is far greater than the inter-fibre distance. This confirms that the plastic zone would most probably *not* fully develop. Additionally, there is no rubber cavitation in the continuous channels left by the fibres that pull out. Indeed, the surfaces of these channels are smooth.

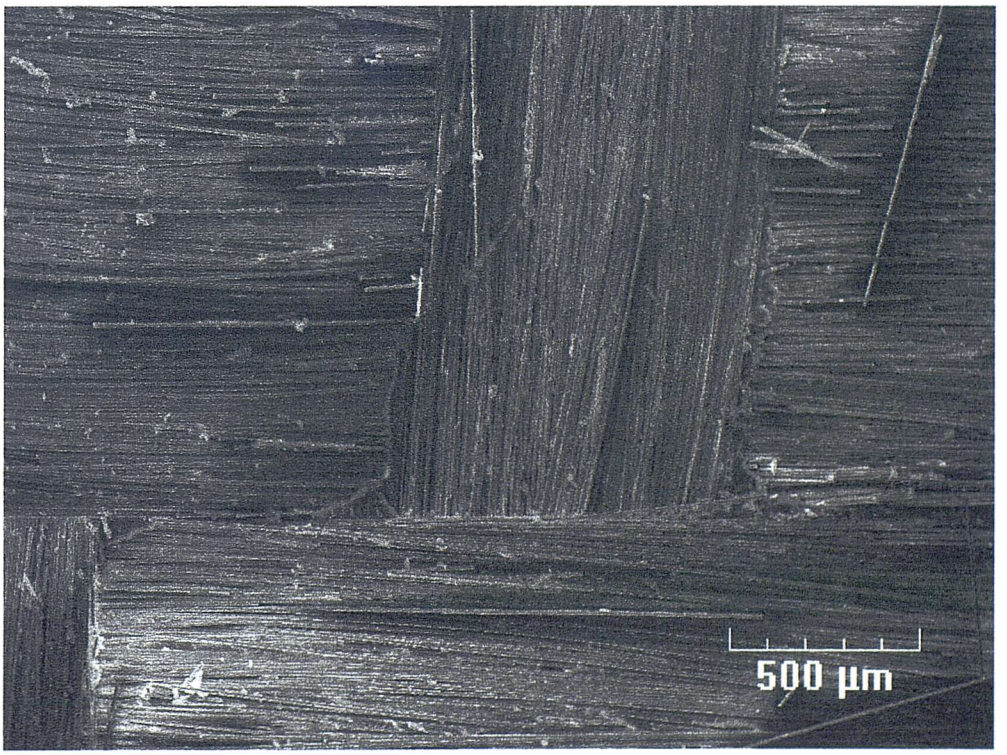


Figure 4.2.8. Fracture surface of a GFRP sample with an amine-cured epoxy matrix containing 6.9 wt. % CTBN (crack propagation from right to left).

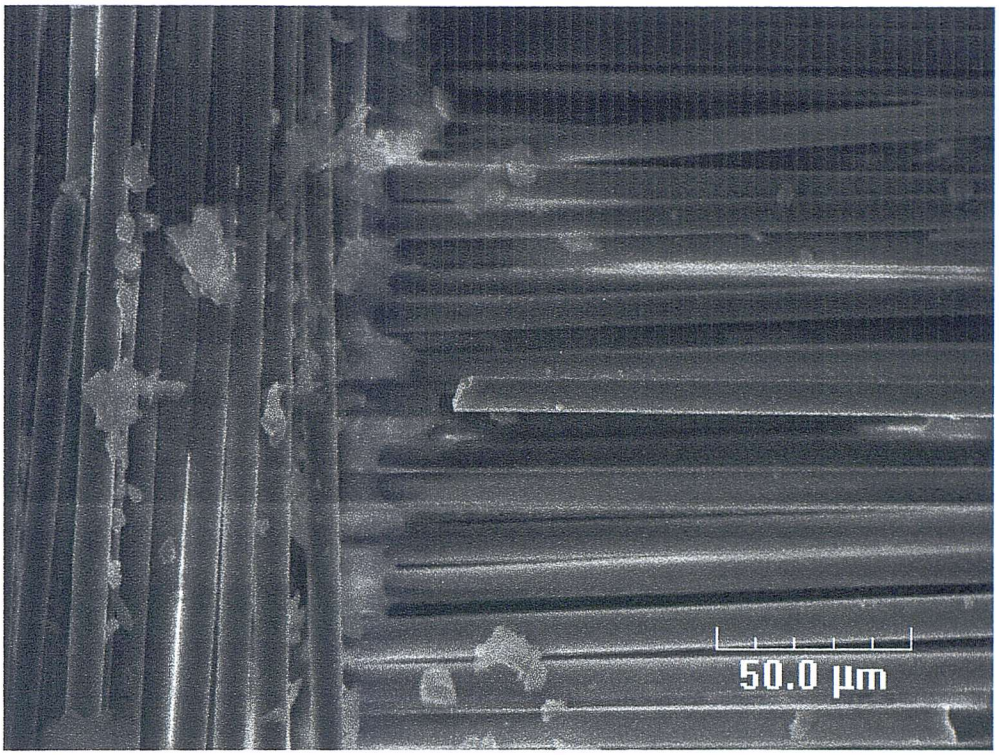


Figure 4.2.9. Fracture surface of a GFRP sample with an amine-cured epoxy matrix containing 6.9 wt. % CTBN at higher magnification (crack propagation from right to left).

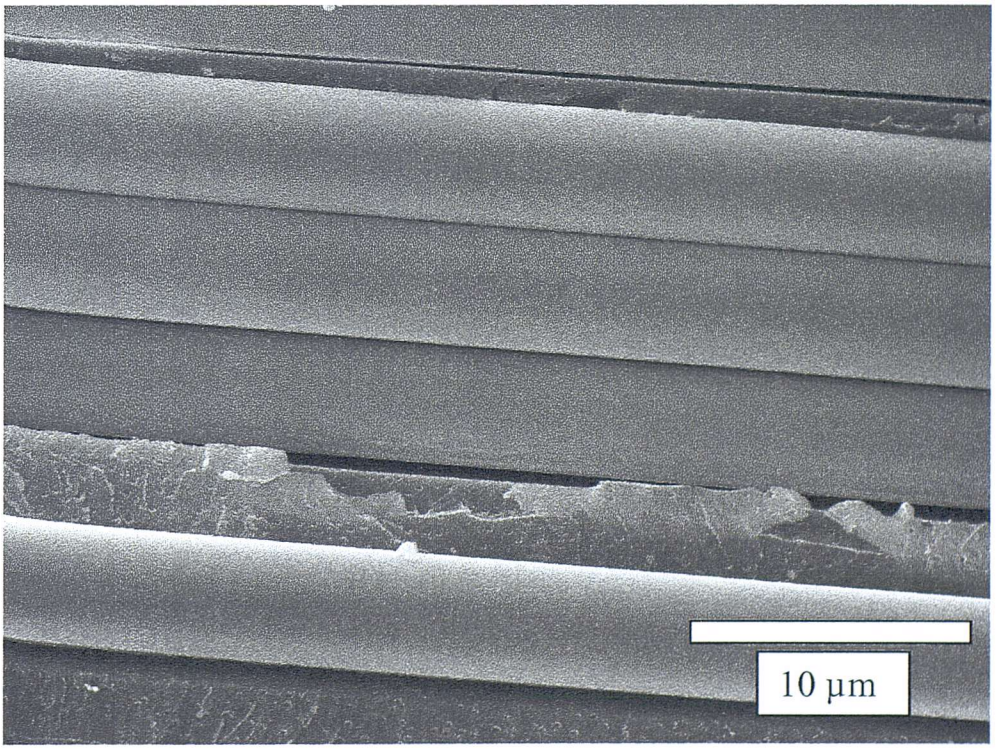


Figure 4.2.10. Fracture surface of a GFRP sample with an amine-cured epoxy matrix containing 6.9 wt. % CTBN at higher magnification (crack propagation from right to left).

The micrographs in Figure 4.2.11, Figure 4.2.12 and Figure 4.2.13 are of a GFRP sample with a matrix that has been toughened by the addition of 10.9 wt. % CTBN. This series of micrographs have been chosen because they show the matrix side of the interfacial failure between fibres and matrix. Cavitation of the rubber particles in the epoxy matrix is visible. In addition, the continuous channels left by the pulled-out fibres is very smooth. This is because there was poor adhesion between the fibres and the matrix (as observed in some of the previous samples examined in this section). The fracture energy of this formulation containing 10.9 wt. % CTBN was 1291J/m^2 whereas the bulk fracture energy was 1835J/m^2. Thus the laminate fracture energy is relatively low because of the poor adhesion between the matrix and the fibres, and the limited rubber cavitation that occurs due to the fibres constraining plastic deformation at the crack tip.

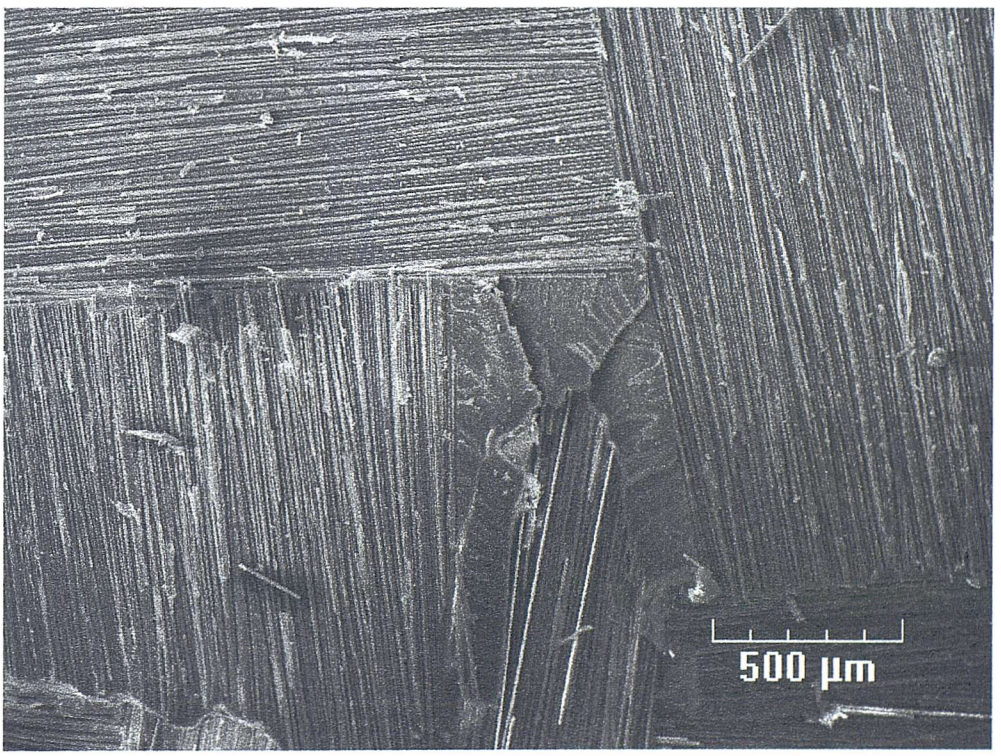


Figure 4.2.11. Fracture surface of a GFRP sample with an amine-cured epoxy matrix containing 10.9 wt. % CTBN (crack propagation from right to left).

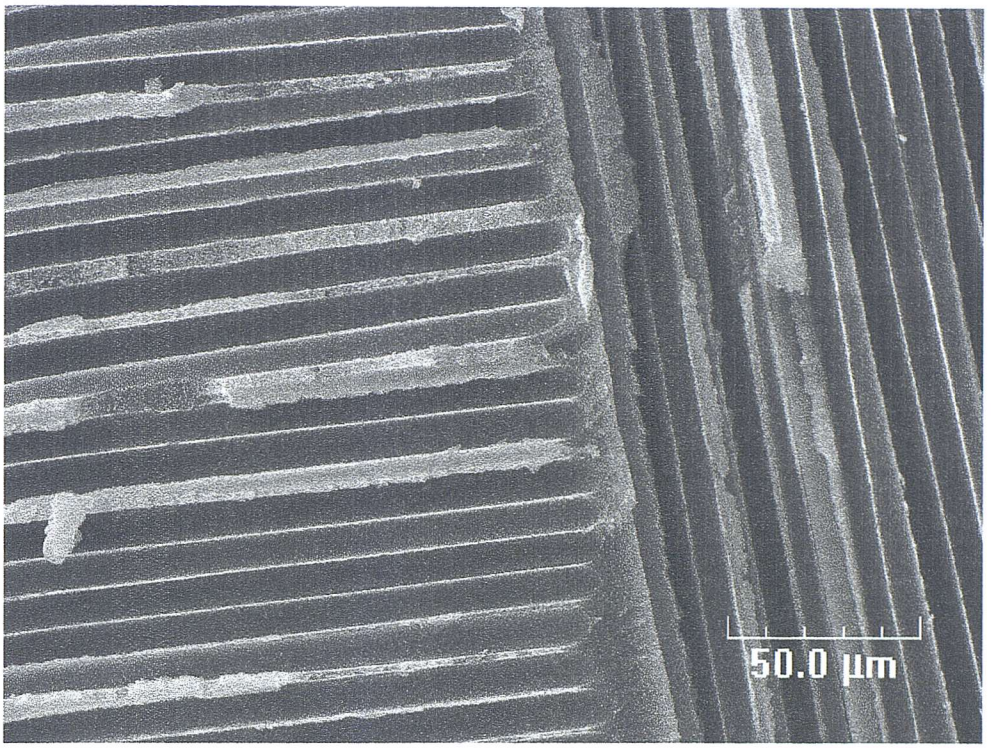


Figure 4.2.12. Fracture surface of a GFRP sample with an amine-cured epoxy matrix containing 10.9 wt. % CTBN at higher magnification (crack propagation from right to left).

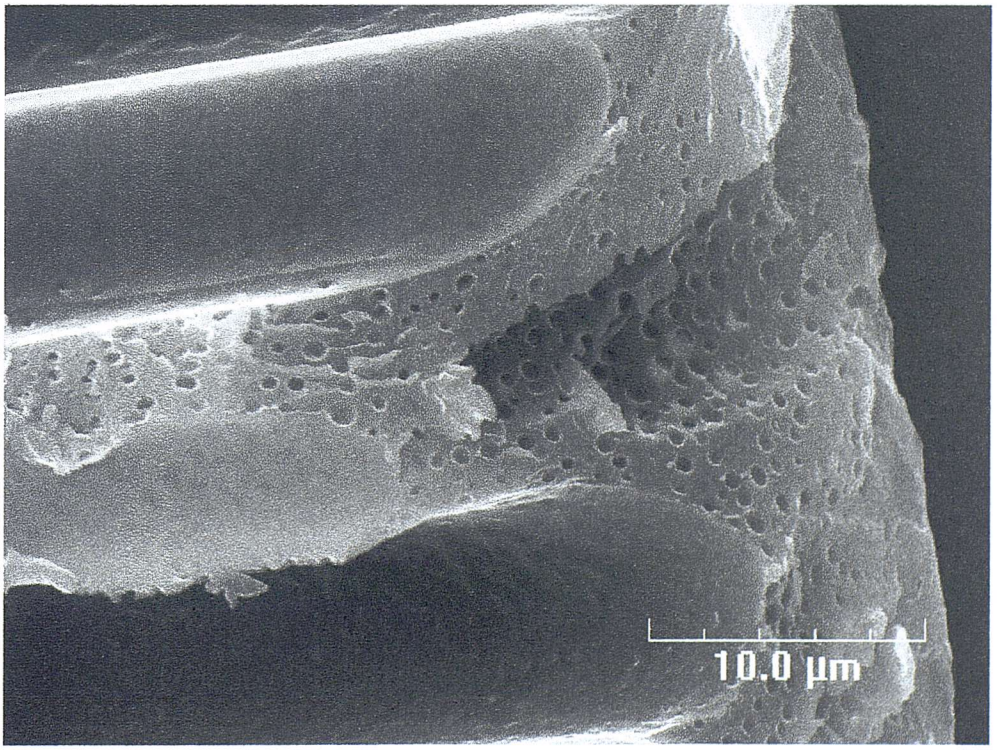


Figure 4.2.13. Fracture surface of a GFRP sample with an amine-cured epoxy matrix containing 10.9 wt. % CTBN at higher magnification (crack propagation from right to left).

4.2.2.3 Hybrid Modified Epoxy Matrix

The micrographs in Figure 4.2.14, Figure 4.2.15 and Figure 4.2.16 represent the fracture surface of a GFRP laminate that has a hybrid epoxy matrix modified with 4.1 wt. % CTBN and 2 wt. % nano-silica. The fibre weave is clearly visible, and there are small regions of exposed epoxy where cohesive failure occurred. The cavitated rubber particles are also visible and fibre bridging was observed which explains the small R-curve that was recorded. The fracture energy of this sample was 1217J/m^2 which is statistically the same as the CTBN-only laminate, and as the unmodified laminate. This is still less than that of the bulk hybrid epoxy (which had a toughness of 1600J/m^2) mainly because of the poor adhesion between the fibres and the matrix which led to interfacial failure and limited plastic deformation of the epoxy matrix.

It should be noted that the fracture surface of the laminate toughened with 4.1 wt. % CTBN and 4.1 wt. % nano-silica had a very similar appearance in every way to this (ie. 4.1 wt. % CTBN and 2 wt. % nano-silica). Indeed, this is reflected in the similar fracture energies of 1357J/m^2 and 1217J/m^2 respectively. The nano-silica particles are not visible at this magnification in any of the samples, but the fracture energies suggest that they do not play a role in improving the fracture energy of the laminates.

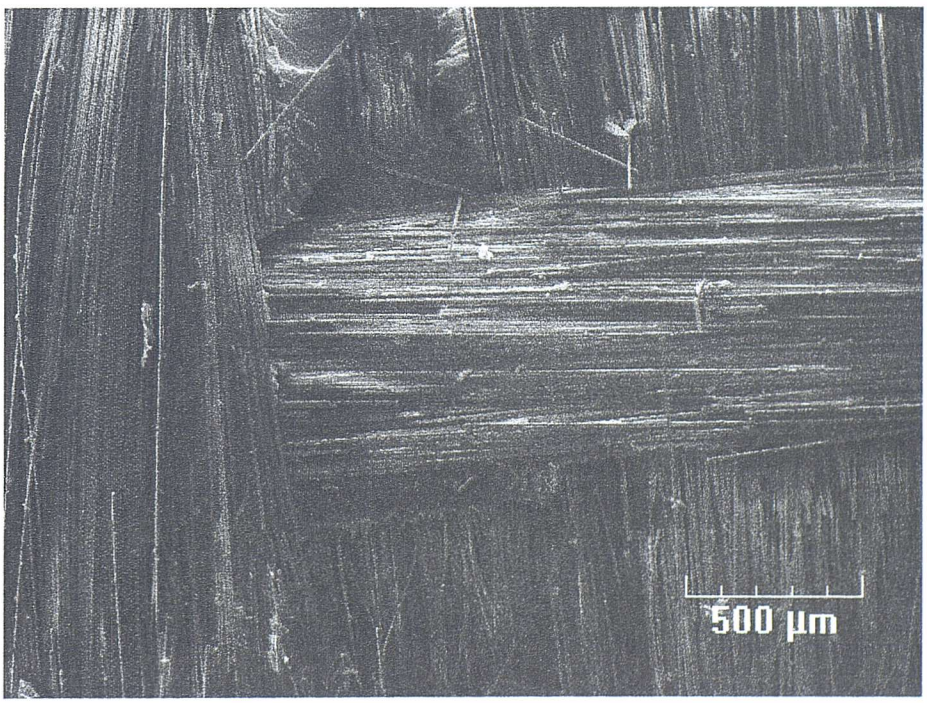


Figure 4.2.14. Fracture surface of a GFRP sample with an amine-cured epoxy matrix containing 4.1 wt. % CTBN and 2 wt. % nano-silica (crack propagation from right to left).

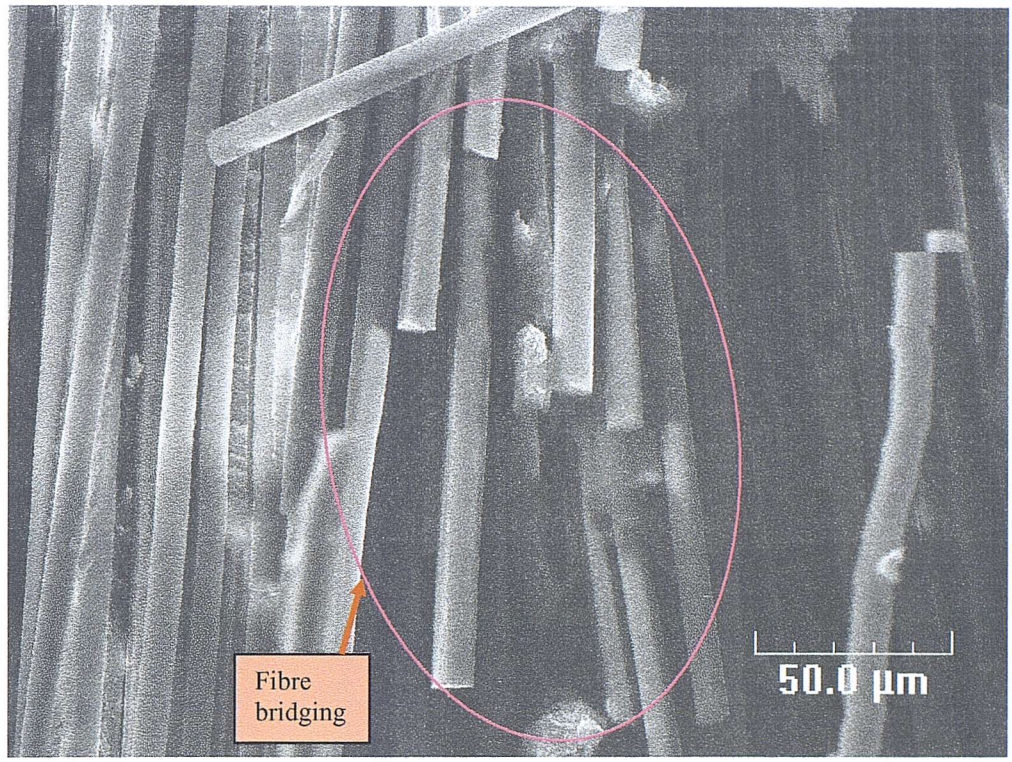


Figure 4.2.15. Fracture surface of a GFRP sample with an amine-cured epoxy matrix containing 4.1 wt. % CTBN and 2 wt. % nano-silica at higher magnification with the evidence of fibre bridging circled in pink (crack propagation from right to left).

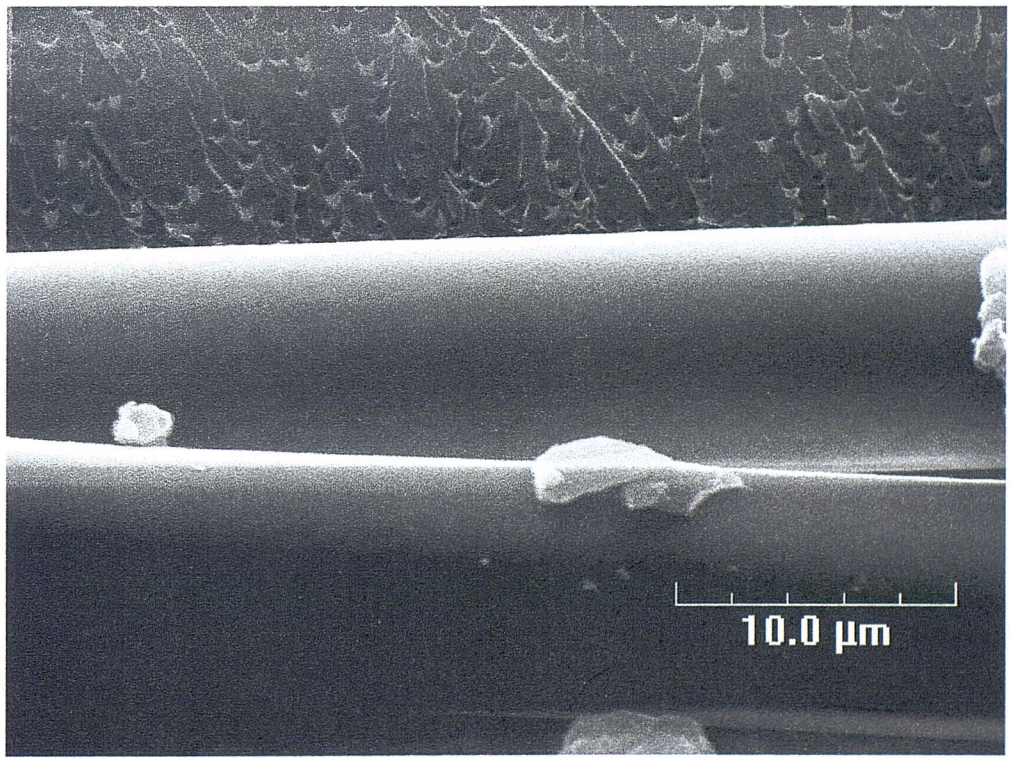


Figure 4.2.16. Fracture surface of a GFRP sample with an amine-cured epoxy matrix containing 4.1 wt. % CTBN and 2 wt. % nano-silica at higher magnification (crack propagation from right to left).

The micrographs in Figure 4.2.17, Figure 4.2.18 and Figure 4.2.19 are of a laminate with an epoxy matrix containing 6.9 wt. % CTBN and 3.5 wt. % nano-silica. Fibre debonding, fibre pullout and rubber cavitation in the matrix are some of the toughening mechanisms observed. Poor adhesion between the fibres and matrix was observed. The fracture energy of the laminate was 1532J/m^2 and that of the bulk resin was 1674J/m^2, which is slightly higher, but both values are comparable. Again, this is because the poor adhesion between the fibres and the matrix has the propensity to decrease the fracture energy, but cavitation of the rubber particles and subsequent plastic deformation of the matrix, increase the toughness. Indeed, the diameter and amount of cavitated rubber particles is similar to the CTBN-only laminate shown in Figure 4.2.10.

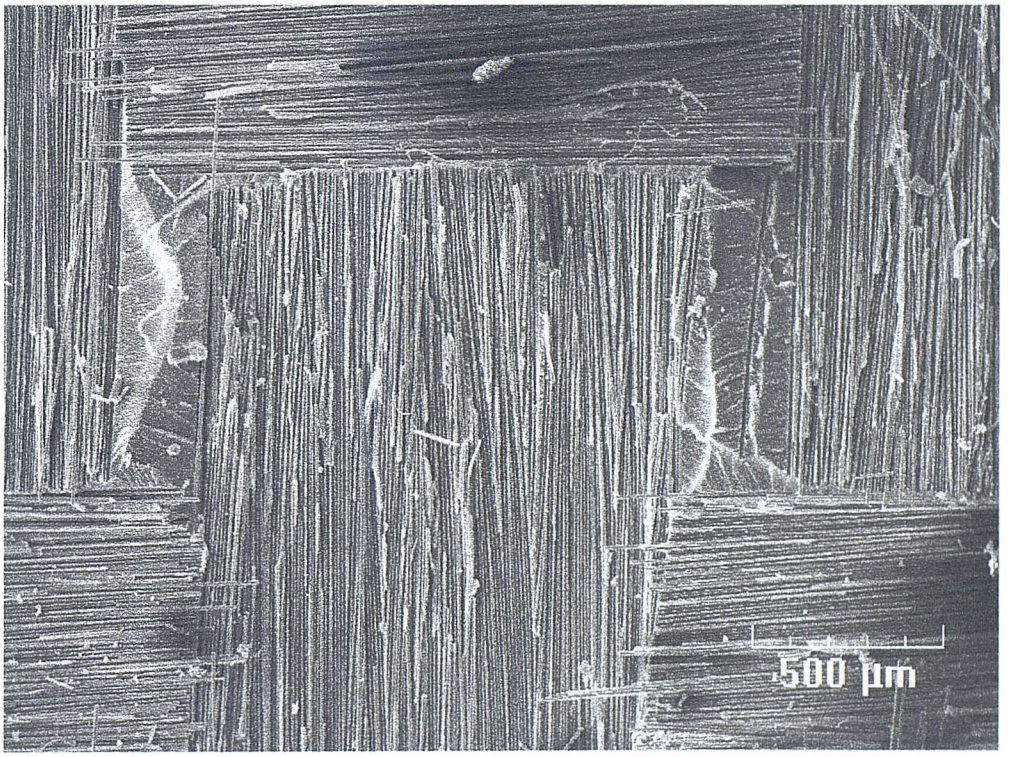


Figure 4.2.17. Fracture surface of a GFRP sample with an amine-cured epoxy matrix containing 6.9 wt. % CTBN and 3.5 wt. % nano-silica (crack propagation from right to left).

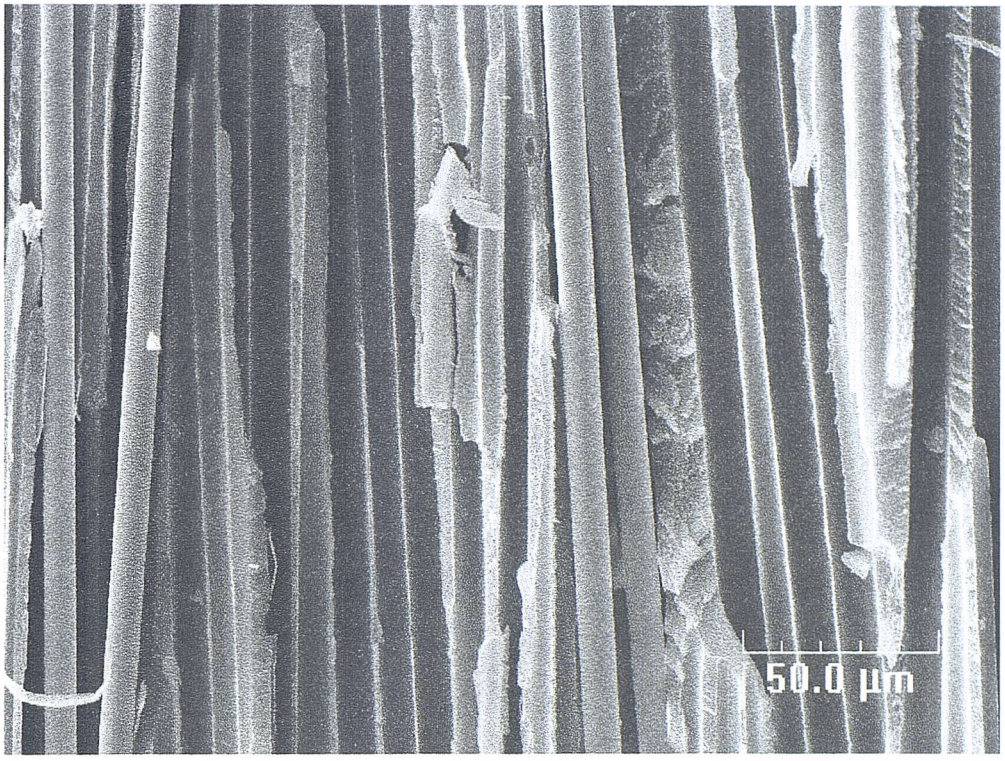


Figure 4.2.18. Fracture surface of a GFRP sample with an amine-cured epoxy matrix containing 6.9 wt. % CTBN and 3.5 wt. % nano-silica at higher magnification (crack propagation from right to left).

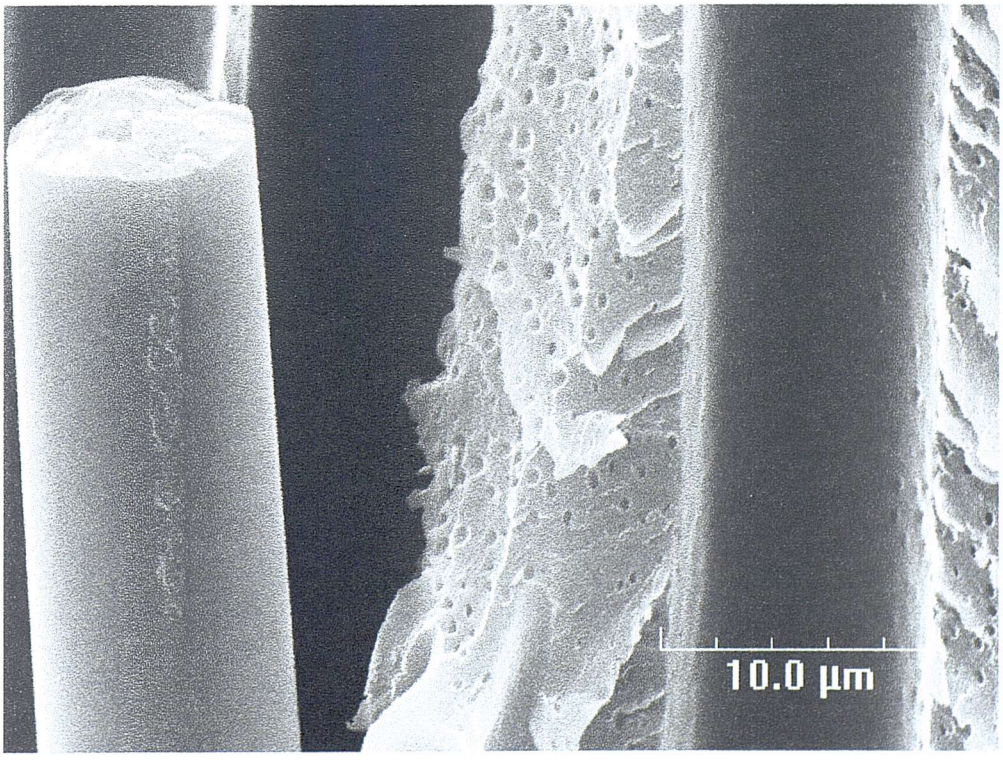


Figure 4.2.19. Fracture surface of a GFRP sample with an amine-cured epoxy matrix containing 6.9 wt. % CTBN and 3.5 wt. % nano-silica at higher magnification (crack propagation from right to left).

The laminate with a matrix toughened by 7 wt. % CTBN and 7 wt. % nano-silica had the lowest toughness, at 120J/m^2, which is less than one eighthof its corresponding bulk epoxy polymer fracture energy, and one fifth that of the unmodified epoxy bulk polymer. An investigation of the fracture surface, as shown in Figure 4.2.20, Figure 4.2.21 and Figure 4.2.22 suggest that the majority of failure occurs at the interfacial boundary between the fibre and matrix, due to poor adhesion. This, in tandem with the rubber cavitation, provided the small resistance to fracture that was recorded. Indeed, although there appears to be extensive cavitation of the rubber particles, it may be recalled that the microstructure showed the presence of super-clumps of nano-silica. These super-clumps act like defects and cancel out the contribution from the rubber particles.

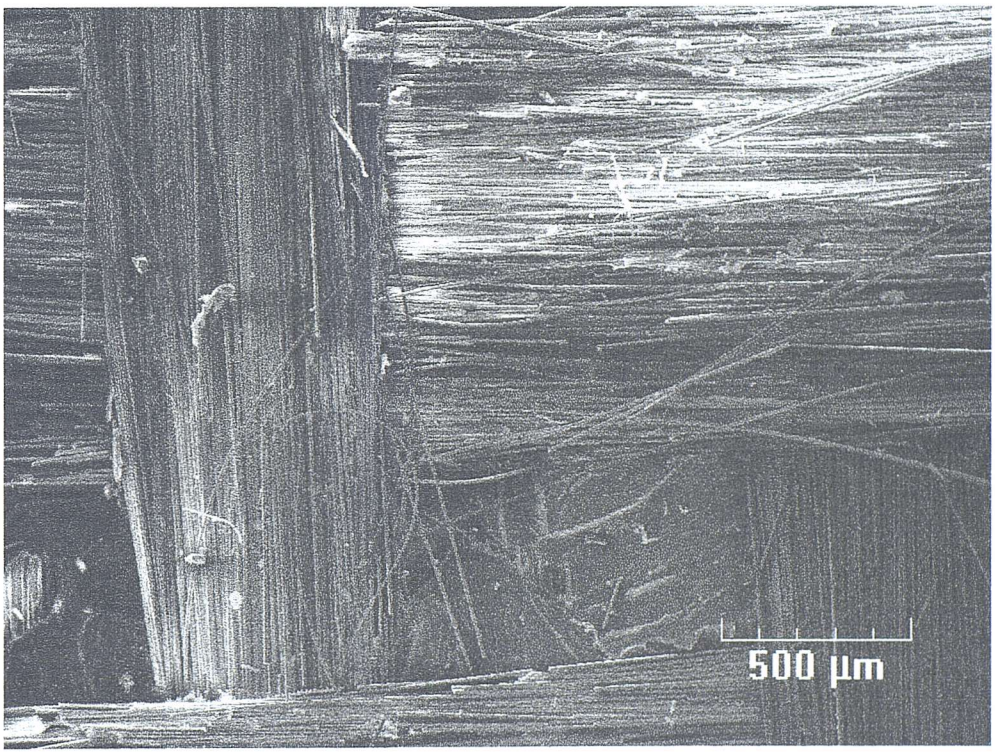


Figure 4.2.20. Fracture surface of a GFRP sample with an amine-cured epoxy matrix containing 7 wt. % CTBN and 7 wt. % nano-silica (crack propagation from right to left).

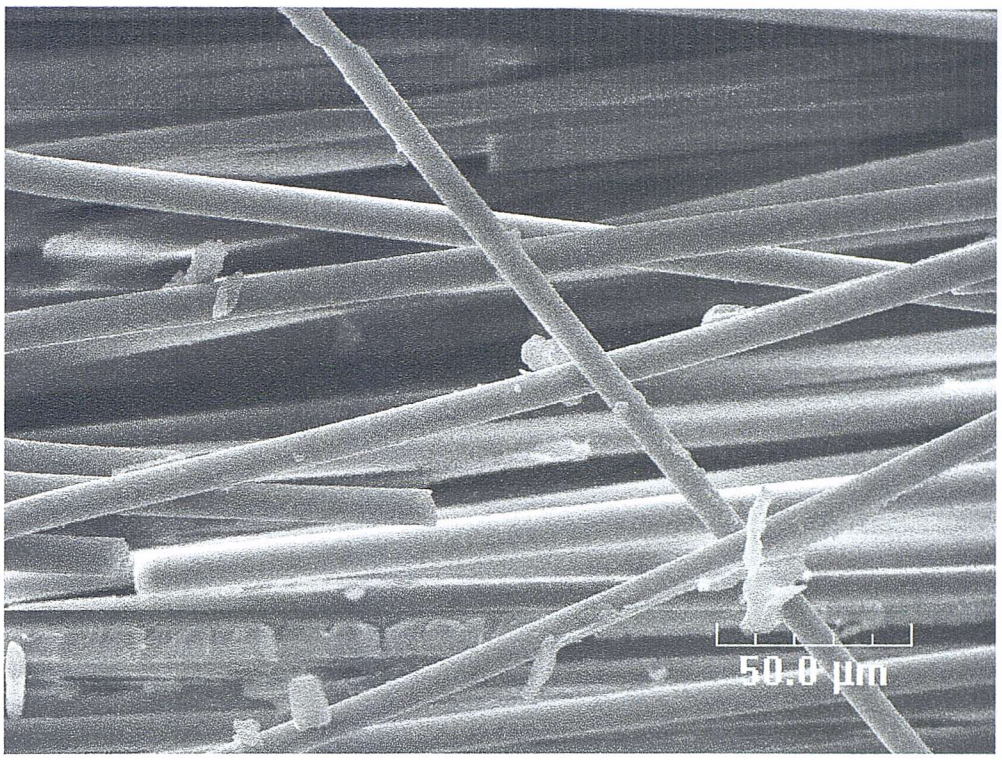


Figure 4.2.21. Fracture surface of a GFRP sample with an amine-cured epoxy matrix containing 7 wt. % CTBN and 7 wt. % nano-silica at higher magnification (crack propagation from right to left).

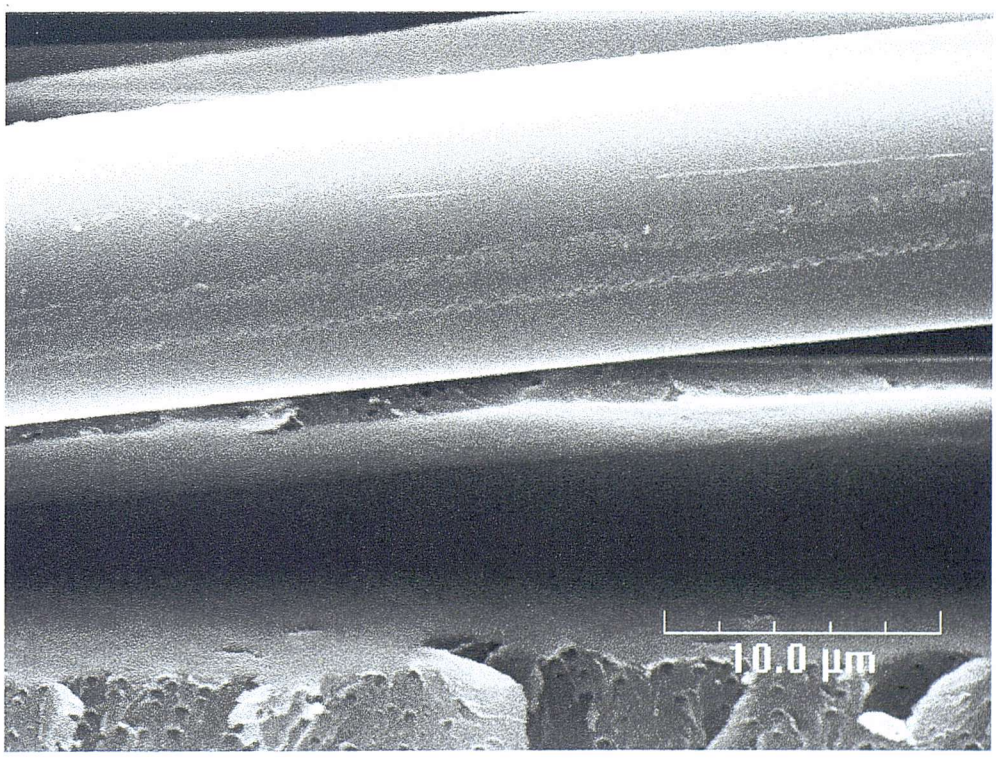


Figure 4.2.22. Fracture surface of a GFRP sample with an amine-cured epoxy matrix containing 7 wt. % CTBN and 7 wt. % nano-silica at higher magnification (crack propagation from right to left).

The micrographs in Figure 4.2.23 and Figure 4.2.24 are for a sample with a matrix containing 11.3 wt. % CTBN and 5.7 wt. % nano-silica. They show better adhesion between the matrix and the fibres, as well as what appear to be cavitated rubber particles. However, the fracture energy of the laminate is only 806J/m^2 whereas the bulk epoxy had a fracture energy of 1847J/m^2. There appears to be widespread cavitation of the rubber particles, so it is surprising that the laminates fracture energy is lower than some of the previous samples. The cavitated rubber particles are larger in this sample compared to the previous samples, but microstructural analysis showed that the rubber particles themselves are slightly larger in this hybrid. A higher magnification micrograph in Figure 4.1.29, however, shows what appear to be *un*-cavitated rubber particles, still embedded in the matrix. This raises the interesting possibility that not all the rubber particles cavitate: a phenomena described by Bucknall *et al.* [157]. Indeed, it is possible that a lower fraction of the rubber particles has cavitated in this formulation, which has resulted in the lower fracture energy.

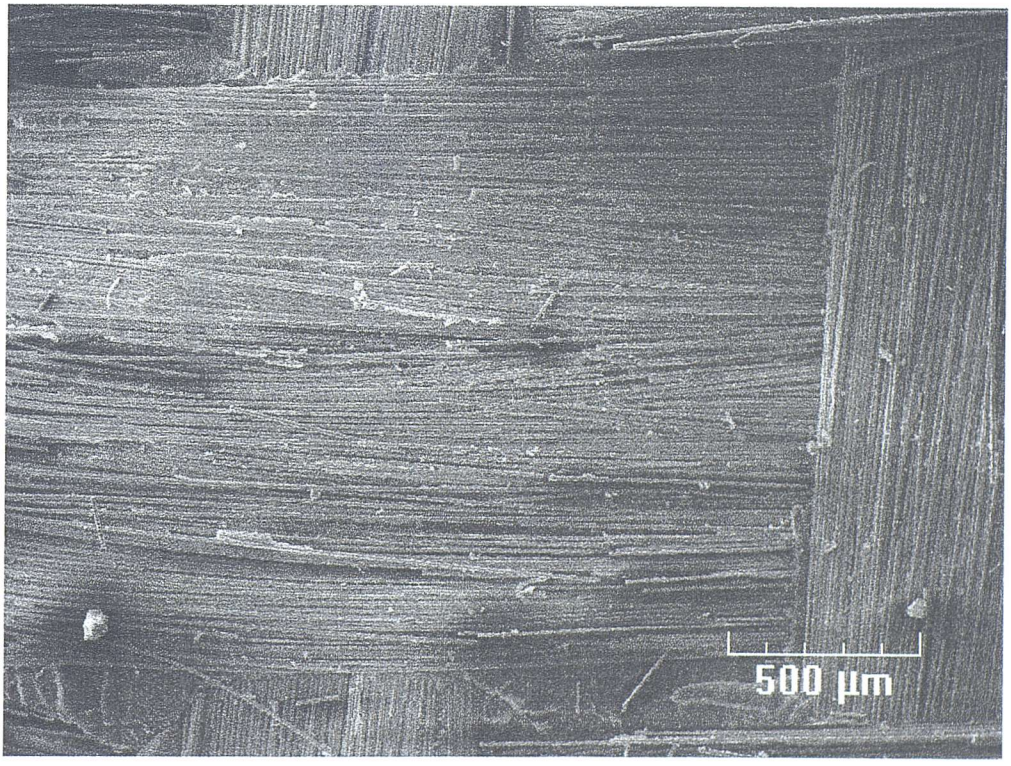


Figure 4.2.23. Fracture surface of a GFRP sample with an amine-cured epoxy matrix containing 11.3 wt. % CTBN and 5.7 wt. % nano-silica (crack propagation from right to left).

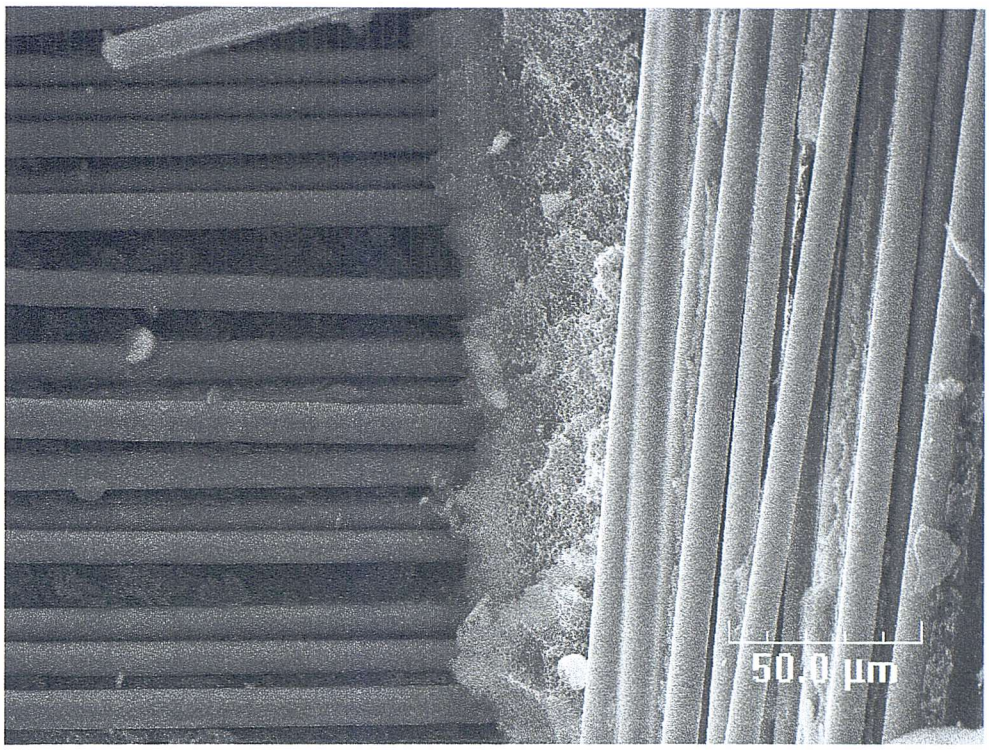


Figure 4.2.24. Fracture surface of a GFRP sample with an amine-cured epoxy matrix containing 11.3 wt. % CTBN and 5.7 wt. % nano-silica at higher magnification (crack propagation from right to left).

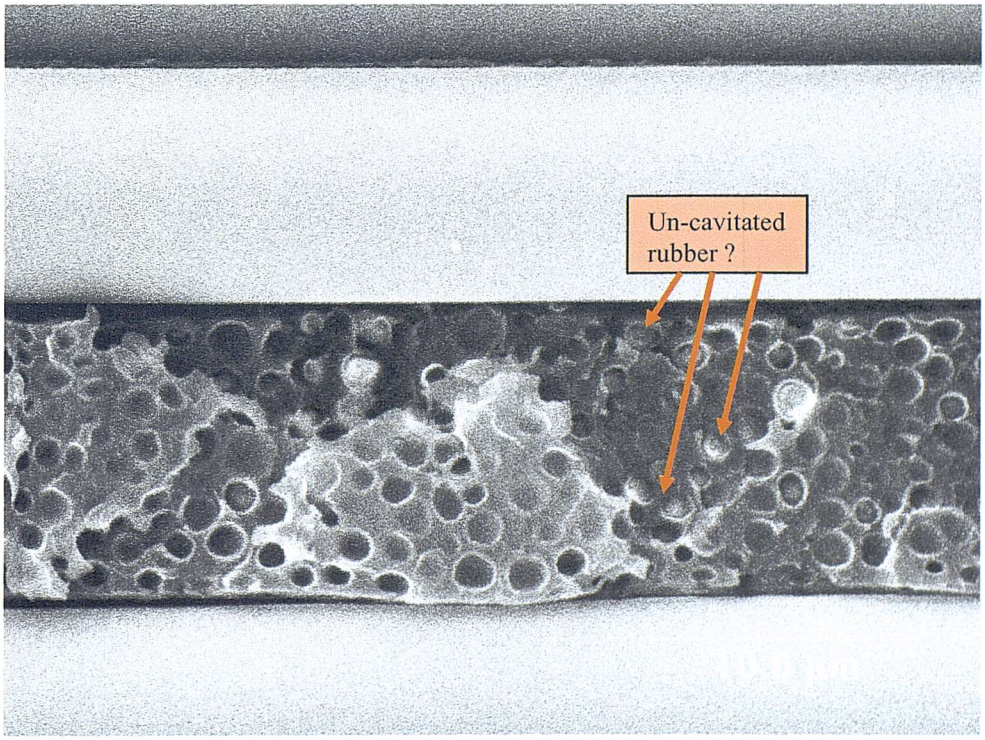


Figure 4.2.25. Fracture surface of a GFRP sample with an amine-cured epoxy matrix containing 11.3 wt. % CTBN and 5.7 wt. % nano-silica at higher magnification showing possibly un-cavitated rubber particles (crack propagation from right to left).

The micrographs in Figure 4.2.26, Figure 4.2.27 and Figure 4.2.28 are for a sample with a matrix that has been toughened with 11.6 wt. % CTBN and 11.6 wt. % nano-silica. This laminate shows the best adhesion between fibre and matrix, and it also shows extensive rubber cavitation in the epoxy matrix. The laminate fracture energy was 755J/m^2 and the bulk epoxy had a comparable fracture energy of 719J/m^2. This suggests that most of the toughness emanated from deformation of the epoxy matrix. The micrographs support this, since there was a paucity of broken fibres, and the plots of the crack growth versus crack length showed a very small R-curve in one sample and no R-curve in the other. The sample in this set of micrographs is the one that showed no R-curve.

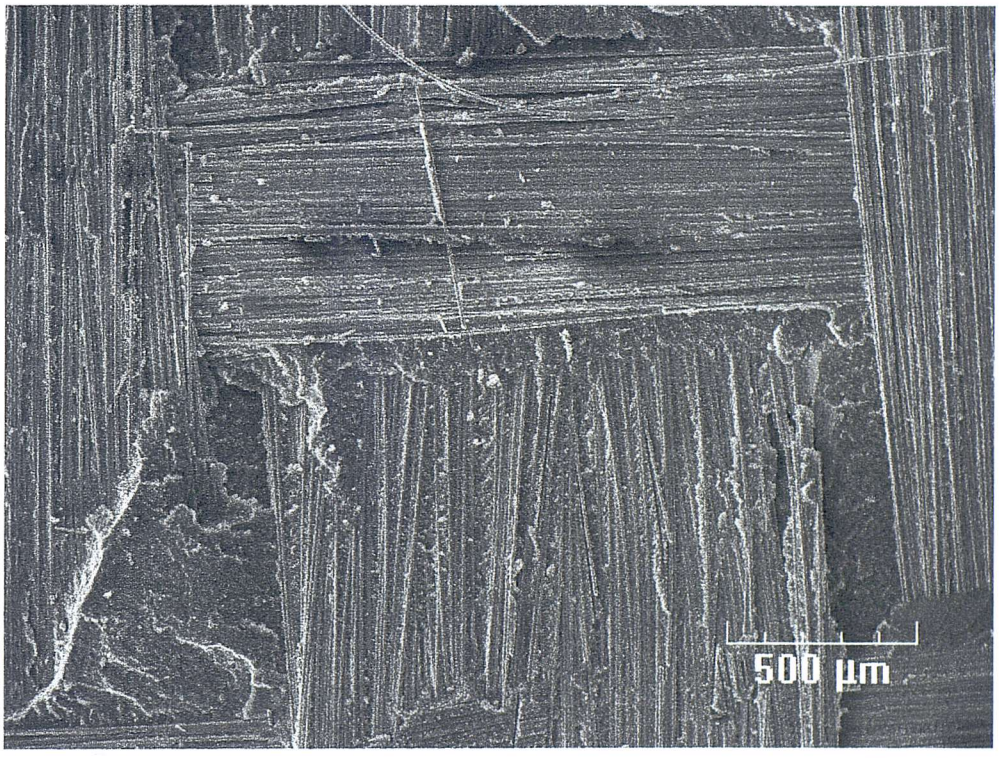


Figure 4.2.26. Fracture surface of a GFRP sample with an amine-cured epoxy matrix containing 11.6 wt. % CTBN and 11.6 wt. % nano-silica (crack propagation from right to left).

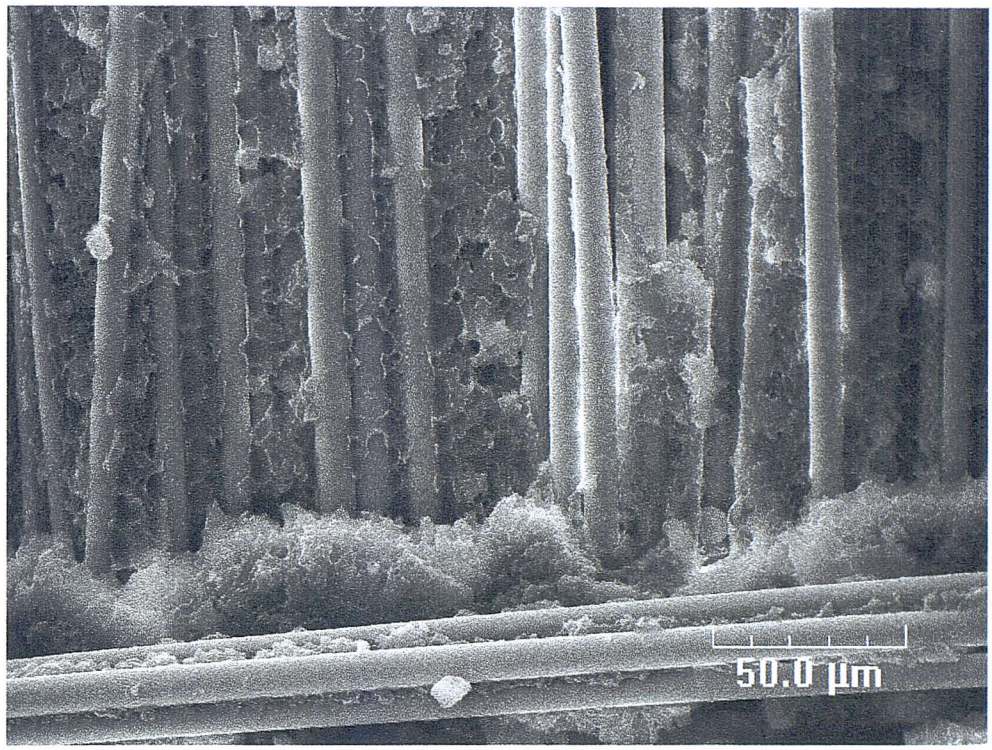


Figure 4.2.27. Fracture surface of a GFRP sample with an amine-cured epoxy matrix containing 11.6 wt. % CTBN and 11.6 wt. % nano-silica at higher magnification (crack propagation from right to left).

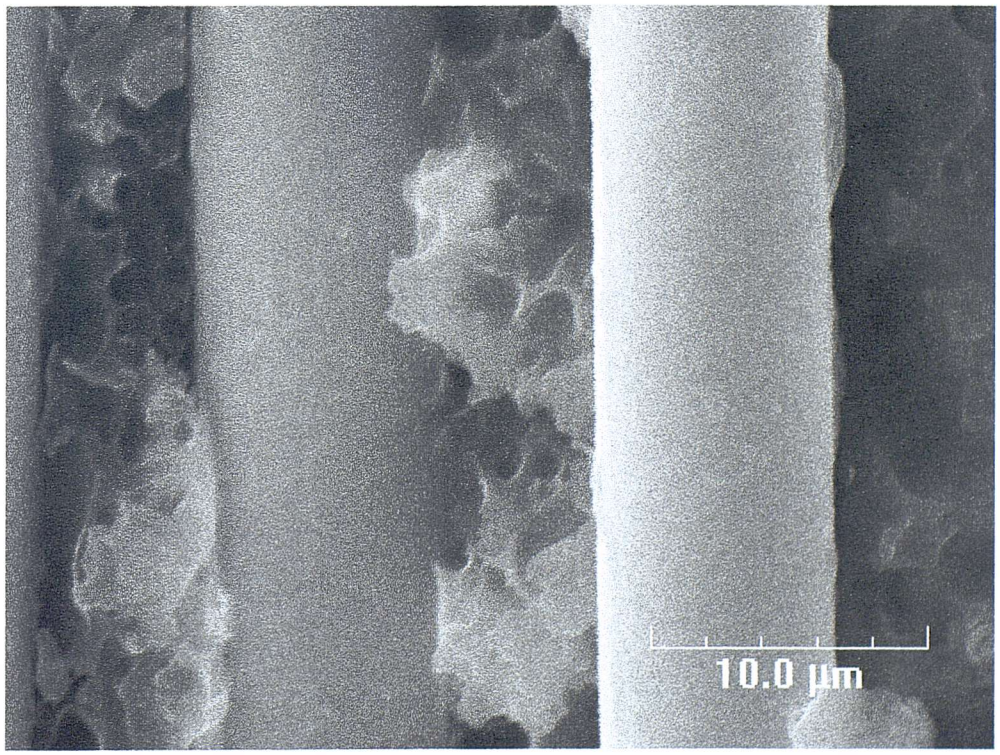


Figure 4.2.28. Fracture surface of a GFRP sample with an amine-cured epoxy matrix containing 11.6 wt. % CTBN and 11.6 wt. % nano-silica at higher magnification (crack propagation from right to left).

4.2.2.4 Summary

A common feature of the GFRP samples with an amine-cured DGEBA-based matrix, was the poor adhesion between the fibres and the matrix. This often lead to interfacial failure at a low fracture energy. Thus, in the majority of cases, the mode I bulk fracture energy was not transferred to the laminates. Another reason for the low toughness is the restriction of crack-tip deformation due to the comparatively small inter-fibre distance. The laminate toughened with 6.9 wt. % CTBN and 3.5 wt. % nano-silica had the highest toughness, at 1532J/m^2, but even this was not a statistical increase over a laminate with a unmodified epoxy matrix.

4.3 Chapter Discussion

This chapter has investigated the microstructure, mechanical properties and fracture of an amine-cured DGEBA-based bulk epoxy polymer that was toughened with CTBN rubber and nano-silica particles. It has also explored the toughness of laminates that were composed of glass fibres using these bulk epoxy polymers as the matrices.

Investigations into the microstructure showed that the unmodified epoxy polymer was a single-phase material, but which contained an increasing volume fraction of phase-separated spherical rubber particles of up to 0.5μm with increasing CTBN content. In the hybrid samples, the nano-silica particles remained well dispersed up to 4.1 wt. % nano-silica and formed three-dimensional necklace-like chains up to 5.7 wt. % nano-silica. At higher nano-silica contents, super-clumps formed. The propensity for agglomeration of the nano-silica particles is independent of the rubber content, and depends solely on the nano-silica content. Vega-Baudrit *et al.* [158] also showed agglomeration of nano-silica with increasing nano-silica content. Their argument was that a decreasing degree of silanol treatment led to an increase in the degree of agglomeration, and this is one avenue of further research that may be undertaken to ascertain why the nano-silica particles agglomerated in this system for the present work.

The glass transition temperature of the bulk epoxy polymer decreased from 117°C (unmodified epoxy) to 110°C when 4.6 wt. % of CTBN was added, but remained constant at 110°C when 6.9 and 10.9 wt. % of CTBN was added. The glass transition temperature decreased even more in the hybrid samples. This suggests that some of the

CTBN remains in the epoxy phase, and the presence of nano-silica inhibits rubber phase separation. The reduction in the epoxy T_g stems from the fact that CTBN has a much lower glass transition temperature than the epoxy.

Increasing CTBN content also reduces the tensile modulus of the formulations, but increasing amounts of nano-silica increase the tensile modulus since silica particles have a much higher modulus than epoxy [137,138]. Indeed, if one considers the hybrid sample with 4.1 wt. % CTBN, the addition of 4.1 wt. % nano-silica increases it to within 90% of the unmodified epoxy stiffness.

The bulk epoxy polymer was found to be relatively tough (612J/m^2) when unmodified, and increasingly tough as increasing amounts of CTBN were added (1835J/m^2 when 10.9 wt. % of CTBN was present). For the hybrid bulk epoxy polymers, the addition of up to 5.7 wt. % nano-silica did not decrease the toughness (compared to its CTBN-only counterpart), and this coincided with a microstructure that showed good dispersion of nano-silica particles or the formation of necklace-like chains. However, any further increase in nano-silica content led to the formation of large agglomerates of nano particles (super-clumps), which had a detrimental effect on the toughness (in the case of the sample containing 11.6 wt. % CTBN and 11.6 wt. % nano-silica, the fracture energy of 719J/m^2 was comparable to that of the unmodified bulk epoxy polymer). The micrographs showing the fracture surfaces, correlated well with the toughness results although the individual nano-silica particles were not visible because of their small size. The super-clumps were visible however, and it is believed that they cause a drastic reduction in toughness because they act like very brittle defects.

The graph in Figure 4.3.1 shows a comparison of the mean GFRP and bulk epoxy polymer fracture energies. It can be seen that the only sample which showed an improvement in laminate fracture energy compared to its bulk fracture energy, was that of the control (unmodified epoxy). An investigation of the fracture surface showed that this is because the control laminate had very good interfacial adhesion between the fibres and matrix and there was relatively extensive plastic deformation of the epoxy matrix. In general however, the fracture resistance of the bulk epoxy was not transferred to the GFRPs when used as the matrix. The main reasons for this were the poor

adhesion between the fibres and the matrix, which led to crack propagation at the fibre-matrix interface, and hence there was limited deformation of the epoxy matrix.

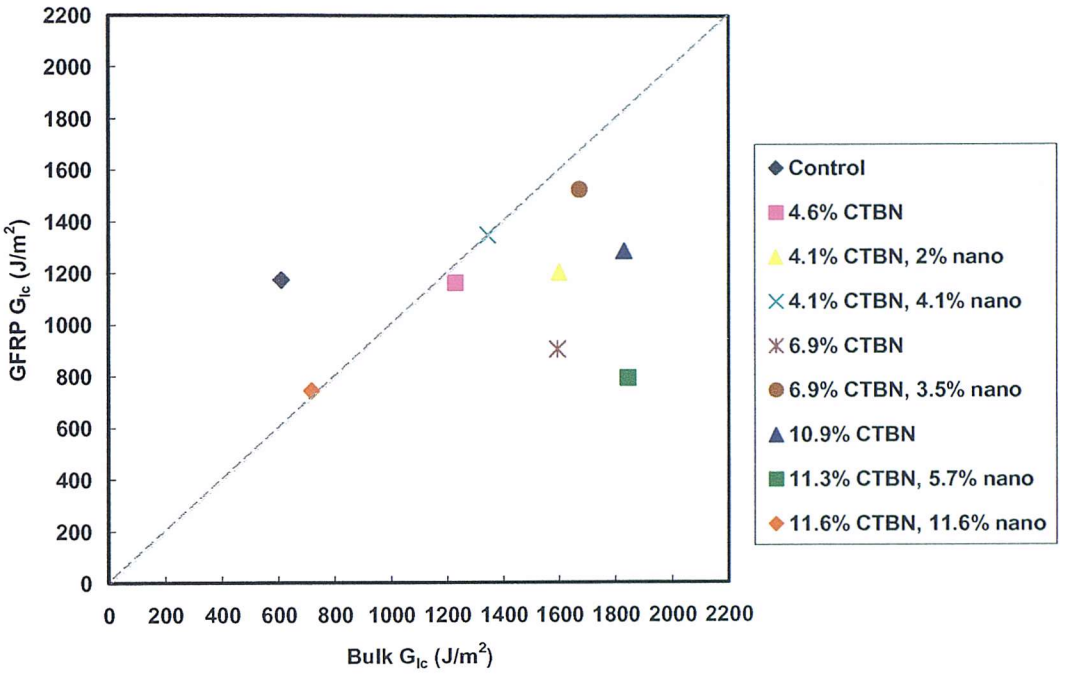


Figure 4.3.1. Comparison between the mean GFRP and bulk fracture energies of the amine-cured DGEBA-based system. (Dashed line indicates the 1:1 relationship between the fracture energies of the GFRPs and the bulk epoxy polymers [ie. the matrices])

4.4 Conclusions

This chapter has investigated the microstructure, mechanical properties and fracture of an amine-cured DGEBA-based bulk epoxy polymer that was toughened with CTBN rubber and nano-silica particles. It has also explored the toughness of laminates that were composed of glass fibres using these bulk epoxy polymers as the matrices.

It was found that for the bulk epoxy polymers, the addition of CTBN-only led to a decrease in stiffness and glass transition temperature, but an increase in fracture energy. Microstructural analysis showed that the rubber particles phase-separated in varying amounts as spherical particles (which accounted for the increase in toughness), whilst some rubber remained in solution in the epoxy phase (which accounted for the decrease in glass transition temperature). Hybrid bulk epoxy polymers containing both rubber and nano-silica showed a small change in T_g (because in some cases the nano-silica suppressed the phase separation of the rubber), an increase in stiffness (due to the higher

stiffness of silica particles) and no increase in toughness. In the samples that showed a decrease in toughness with increasing nano-silica content, microstructural analysis showed that this was because the nano-silica particles agglomerated into super-clumps that reduced the amount of epoxy available for plastic deformation, and acted like brittle defects.

There was a poor transfer of toughness from the bulk epoxy polymers to the GFRPs because of the poor adhesion at the fibre-matrix interface, which led to crack propagation along this interface, and limited plastic deformation of the epoxy matrix.

CHAPTER 5

RESULTS AND DISCUSSION: THE AMINE-CURED TGMDA-BASED SYSTEM

5 Introduction

This Chapter investigates the material properties of a tetraglycidyl methylene dianiline (TGMDA) based epoxy system that has been stoichiometrically cured for 2 hours at 180°C using a blend of two sterically hindered aromatic amines. CTBN rubber and nano-silica particles were added to improve the resistance to fracture.

The results have been divided into those obtained from testing the bulk epoxy polymer (ie. this amine-cured TGMDA-based epoxy containing combinations of rubber and nano-silica particles), and the results obtained from testing the carbon fibre reinforced polymers (CFRPs) which used said bulk epoxy polymers as their matrices.

The section that discusses the bulk epoxy polymer has been divided into subsections which discuss the microstructure, thermal and mechanical properties, and fracture surfaces. Each has a summary at the end, and there is a general discussion at the end of the section which reviews all the results and examines how each material property affects the others. A similar format is followed for the CFRP results, with a Chapter Discussion at the very end.

5.1 Bulk Epoxy Polymer Results

The bulk epoxies tested are summarised in Table 5.1.1 and it may be seen that an unmodified sample (the control) was compared to samples toughened with varying amounts of nano-silica, a sample toughened with CTBN rubber, and a hybrid sample toughened with both rubber and nano-silica. The microstructure was studied to see how the rubber and nano-silica particles were distributed in the cured samples, and a number of tests were performed on the samples to determine the thermal and mechanical properties of the bulk material. The fracture surfaces were then investigated to ascertain the fracture mechanisms. Formulations with larger amounts of CTBN were not tested, since samples with large CTBN contents would have low glass transition temperatures (which would make this particular epoxy unattractive for high temperature applications) and higher viscosities (which would make processing more difficult). Additionally, low rubber contents reduce the amount of water absorption, which is especially valid for its use in FRP applications.

Table 5.1.1. Summary of all amine-cured TGMDA-based bulk epoxy polymers investigated.

wt. % CTBN	wt. % nano-silica
0	0
0	5
0	10
0	19.5
8	0
8	10

5.1.1 Microstructure

An atomic force microscope (AFM) was used to observe how the nano-silica and rubber particles were dispersed in the epoxy, as well as relative to each other. No transmission electron microscopy was performed on these samples since it was shown in the previous Chapter that both methods correlate well and can be used interchangeably.

5.1.1.1 Unmodified Epoxy

The AFM image in Figure 5.1.1 is for a control sample of unmodified epoxy. The unmodified epoxy matrix is featureless, which is expected for a homogenous thermosetting polymer. The vertical lines are knife marks from the microtoming process.

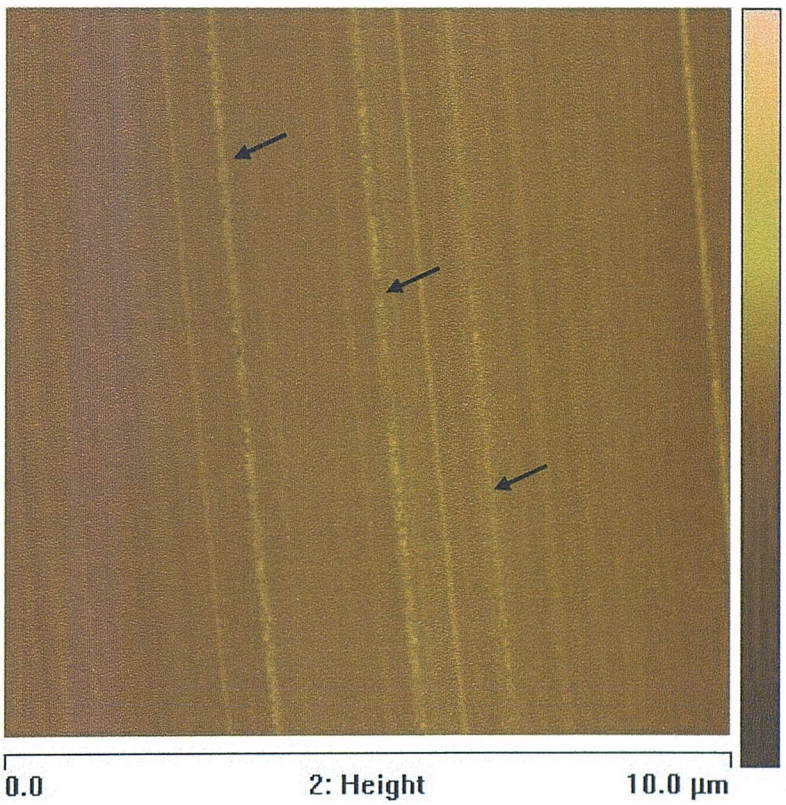


Figure 5.1.1. AFM image of a sample containing unmodified epoxy (black arrows point to some knife marks).

5.1.1.2 Nano-silica Modified Epoxies

The AFM image in Figure 5.1.2 is of a sample containing 5 wt. % nano-silica. The nano-particles are observed to be well-dispersed spheres with almost constant diameters of ~20nm. Other studies have also reported good dispersion in epoxy of nano-scale silica particles [102,103,105,106,108]. On close examination, however, it can be seen that some of the nano particles agglomerate in groups of two as indicated by the light blue arrows. These small agglomerates are themselves well dispersed throughout the epoxy matrix.

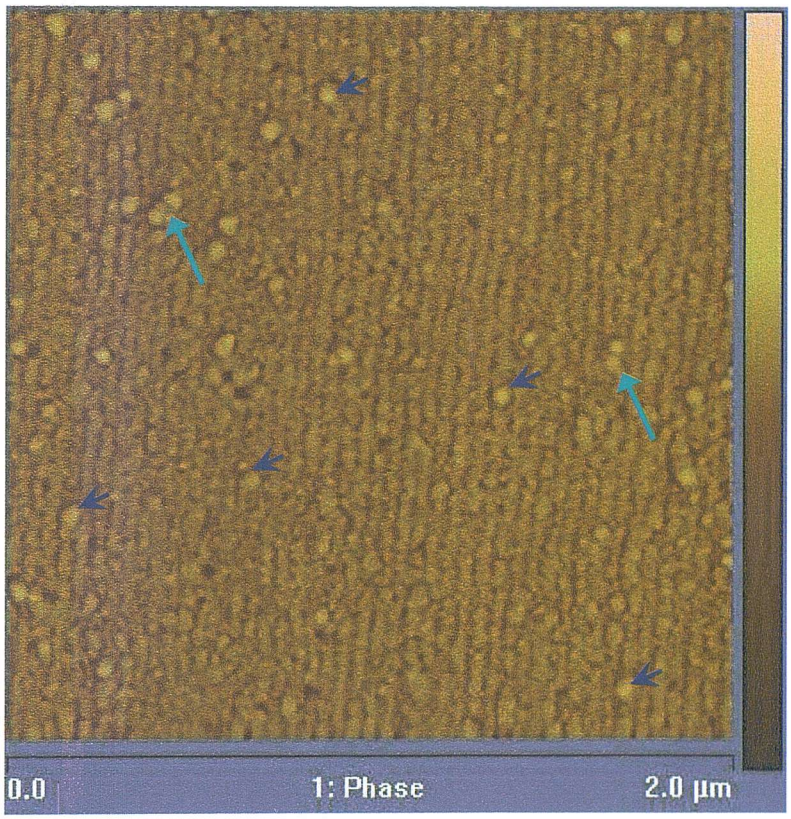


Figure 5.1.2. AFM image of a sample containing 5 wt. % nano-silica. (Dark blue arrows point to some nano particles and light blue arrows point to some agglomerates.)

Figure 5.1.3 is an AFM image of a sample containing 10 wt. % nano-silica. The nano-silica particles are easily discernible and appear to be mostly well-dispersed single particles. Some small agglomerates of five or six particle are visible and are indicated by the light blue arrows. As the nano-silica content increases, the number of agglomerates and the maximum number of particles per agglomerate increase.

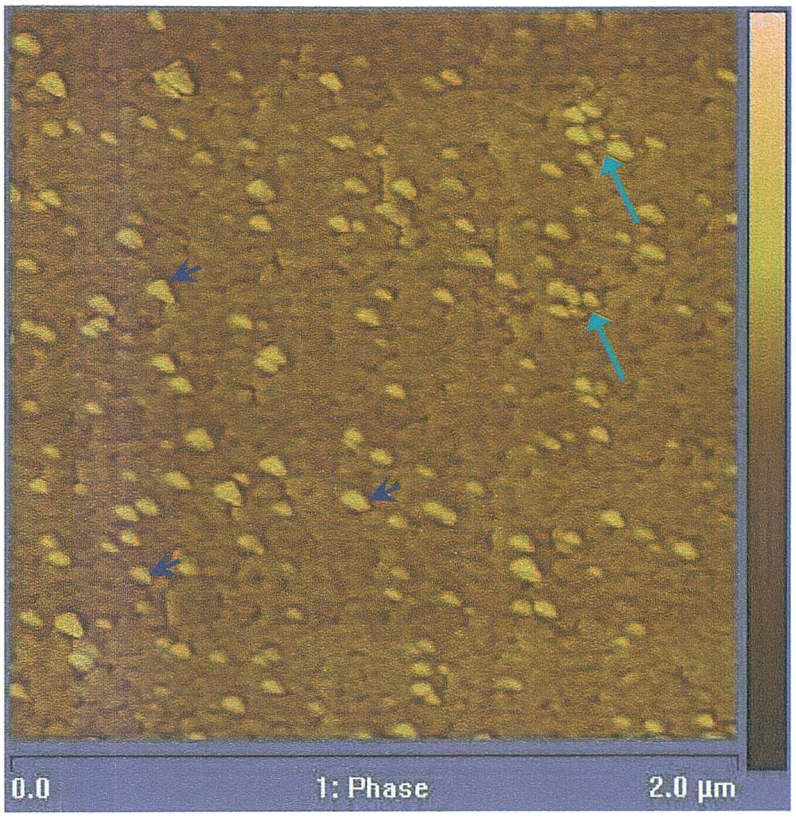


Figure 5.1.3. AFM image of a sample containing 10 wt. % nano-silica. (Dark blue arrows point to some nano particles and light blue arrows point to some agglomerates.)

The AFM phase and height images in Figure 5.1.4 show the microstructure of a sample containing 19.5 wt. % nano-silica. Although all samples were microtomed under the same conditions using a very sharp diamond cryo-knife at -65°C, the AFM image appears to be of poor quality. On closer examination, however, it would seem that the nano-silica particles have formed agglomerates of up to ten particles, and the agglomerates are more numerous. Indeed, it appears that most nano-silica particles are part of agglomerates and there are just a few single particles. This shows that when used in TGMDA epoxy, the nano particles tend to agglomerate, and the agglomerate size increases with increasing nano-silica content.

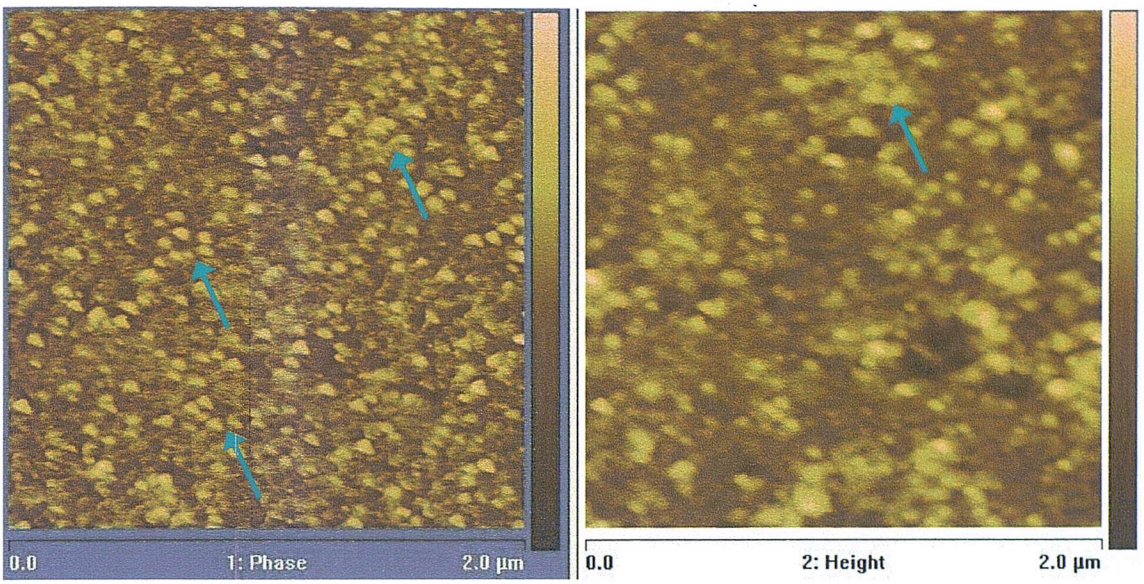


Figure 5.1.4. AFM images of a sample containing 19.5 wt. % nano-silica. (Light blue arrows point to some agglomerates.)

5.1.1.3 Rubber Modified Epoxies

Figure 5.1.5 is an image showing the microstructure of a sample containing 8 wt. % CTBN. The white arrows point to some of the well-dispersed phase-separated rubber particles, which vary in diameters between 0.1µm and 1µm, which is typical for phase-separated CTBN (which can be anywhere between 0.1µm and 5µm [75,125,126]). The size also appears to vary because the microtome may cut closer to or further away from the poles of the spheres. (Note that the rubber particles are actually spheres in three dimensions.)

Volume fraction analysis of the image showed that only ~2 wt. % (ie. ~25%) of the rubber phase separated. Indeed, this image only shows the microstructure of a very small region of the sample but it does indicate that some of the CTBN remains in solution in the epoxy phase.

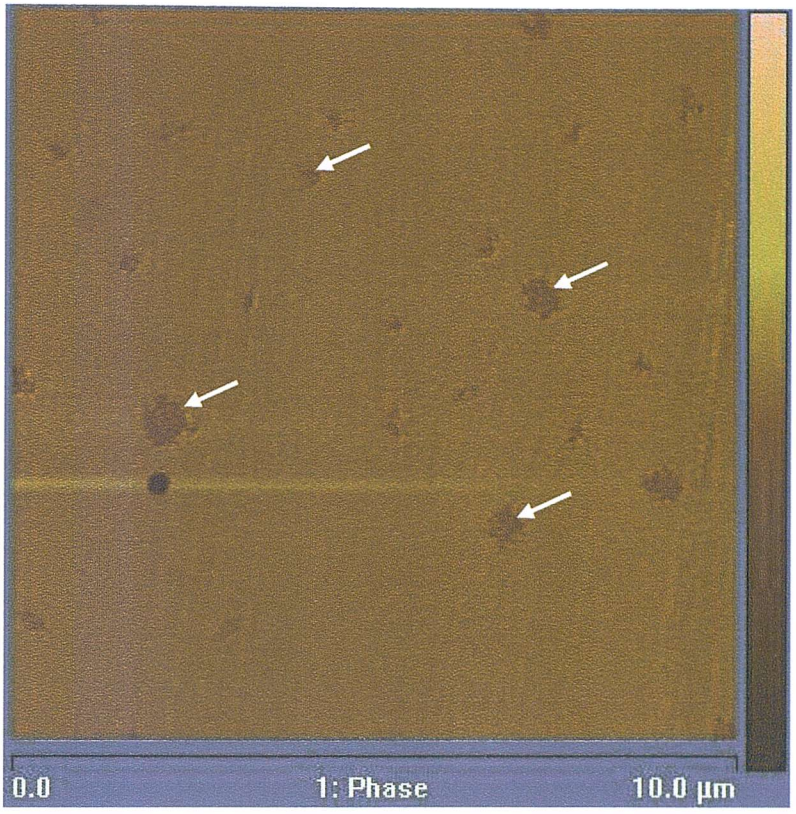


Figure 5.1.5. AFM image of a sample containing 8 wt. % CTBN. (White arrows point to some rubber particles.)

5.1.1.4 Hybrid Modified Epoxies

Figure 5.1.6 shows a micrograph for a sample containing 8 wt. % CTBN and 10 wt. % nano-silica. The phase-separated rubber particles are well distributed and have a maximum diameter of ~1µm, which is the same size as the rubber particles in the CTBN-only sample that was previously discussed. The nano-silica particles agglomerate into possible three-dimensional necklace-like structures (1.5µm in length and 0.5µm in width) that are themselves well-dispersed. (A similar structure was observed in the anhydride-cured DGEBA-based epoxy for samples containing nano-silica and 9 wt. % CTBN, and is discussed in the following Chapter). Volume fraction analysis of the image also showed that ~2 wt. % of the rubber phase-separated. Based on the analysis of this image, and the image containing only CTBN, the addition of nano-silica does not further inhibit CTBN phase separation.

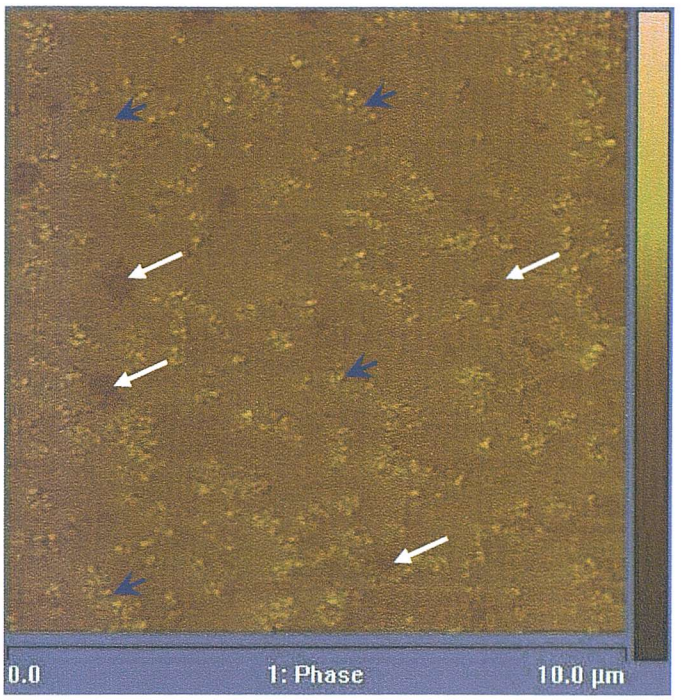


Figure 5.1.6. AFM image of a sample containing 8 wt. % CTBN and 10 wt. % nano-silica. (White arrows point to some rubber particles and blue arrows point to some nano particles.)

5.1.1.5 Summary

The microstructure of the amine-cured TGMDA-based bulk epoxy polymer samples is summarised in Table 5.1.2.

Table 5.1.2. Summary of the microstructure of samples from the amine-cured TGMDA-based bulk epoxy polymers. (NA = Not Applicable)

wt. % CTBN	wt. % nano-silica	Rubber Microstructure	Visual wt. % CTBN phase separated	Nano-silica Microstructure
0	0	NA	NA	NA
0	5	NA	NA	Single 20nm particles. Small agglomerates with up to two particles. Well dispersed
0	10	NA	NA	Single 20nm particles. Small agglomerates with up to six particles. Well dispersed
0	19.5	NA	NA	Few single 20nm particles. Small agglomerates with up to ten particles. Well dispersed
8	0	Well dispersed rubber spheres, 0.1-1µm diameter	2	NA
8	10	Well dispersed rubber spheres, 0.1-1µm diameter	2	3-D necklace like chains, 1.5µm long and 0.5µm wide

5.1.2 Thermal and Mechanical Properties

This section investigates the thermal and mechanical properties of the bulk epoxy polymers where the results from dynamic mechanical thermal analysis (DMTA), tensile tests and single edge notch bend tests are reported.

5.1.2.1 Glass transition temperature test results

The glass transition temperatures, T_g, of the various formulations were measured using bulk samples and tested by dynamic mechanical thermal analysis (DMTA) at a rate of 3K/minute and a frequency of 1Hz. These results were supplied by *hanse chemie AG (Geesthacht, Germany)* [104,107] and the DMTA trace had the same shape as those obtained from the amine-cured DGEBA-based system in the previous Chapter. However an inspection of the traces showed that all the samples were heated up to 300°C, *except* the sample containing 10 wt. % nano-silica. Indeed, this sample was inadvertently heated to only 250°C so its trace was truncated. The test was stopped prematurely before passing through the maximum *tan* δ and so a lower glass transition temperature was recorded. The results are displayed in Figure 5.1.7 and are summarised in Table 5.1.3.

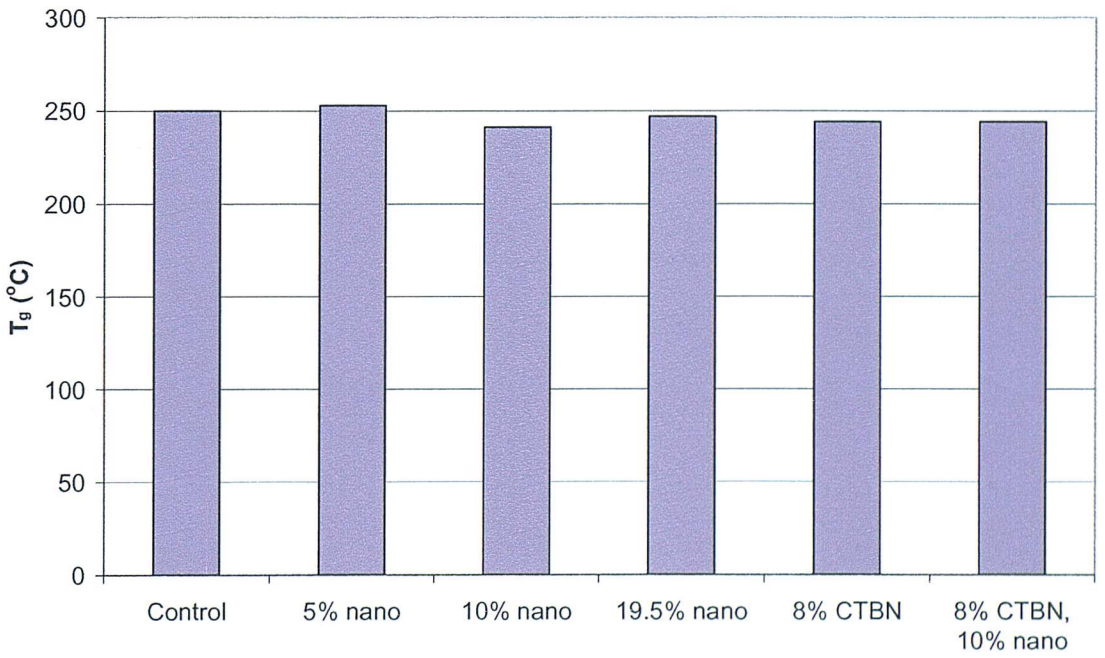


Figure 5.1.7. Glass transition temperatures for the amine-cured TGMDA-based bulk epoxy polymers at a test frequency of 1Hz.

Table 5.1.3. Summary of glass transition temperatures for the amine-cured TGMDA bulk epoxy polymers tested at a frequency of 1Hz.

wt. % CTBN	wt. % nano-silica	T_g *(°C)*
0	0	250
0	5	253
0	10	241
0	19.5	247
8	0	244
8	10	244

A glass transition temperature in the range of 250°C for unmodified tetrafunctional epoxies has been reported before [159,160], so the results obtained in this study agree well with the literature.

The quoted value of 241°C for the glass transition temperature of the sample with 10 wt. % nano-silica is lower than the actual value, as has been discussed earlier. Taking this into account, it can be seen that nano-silica does not affect the T_g of this system. This agrees well with the findings in other work [105,108].

The T_g of the samples containing CTBN are both 244°C showing that the same amount of rubber phase separates in both samples which agrees with volume fraction analysis of the AFM images. However, calculations using the Fox-Flory Equation (see Equation 2.23 in Chapter 2) suggest that ~2 wt. % of CTBN would have had to remain in solution in the epoxy phase to produce the small decrease observed, whereas volume fraction analysis showed that ~6 wt. % remained in the epoxy phase. It is believed that the AFM images represent a rubber-deficient area of the epoxy, and is not representative of the entire sample. At least twelve images from random areas of the sample would be needed to have a more statistically sound calculation [151], but time constraints did not permit this.

5.1.2.2 Tensile test results

Tensile tests were performed on dumbbell specimens at a rate of 1mm/min at 20°C, to determine the Young's modulus of the different formulations. The main results are illustrated in Figure 5.1.8 and the numerical results can be found in Table 5.1.4.

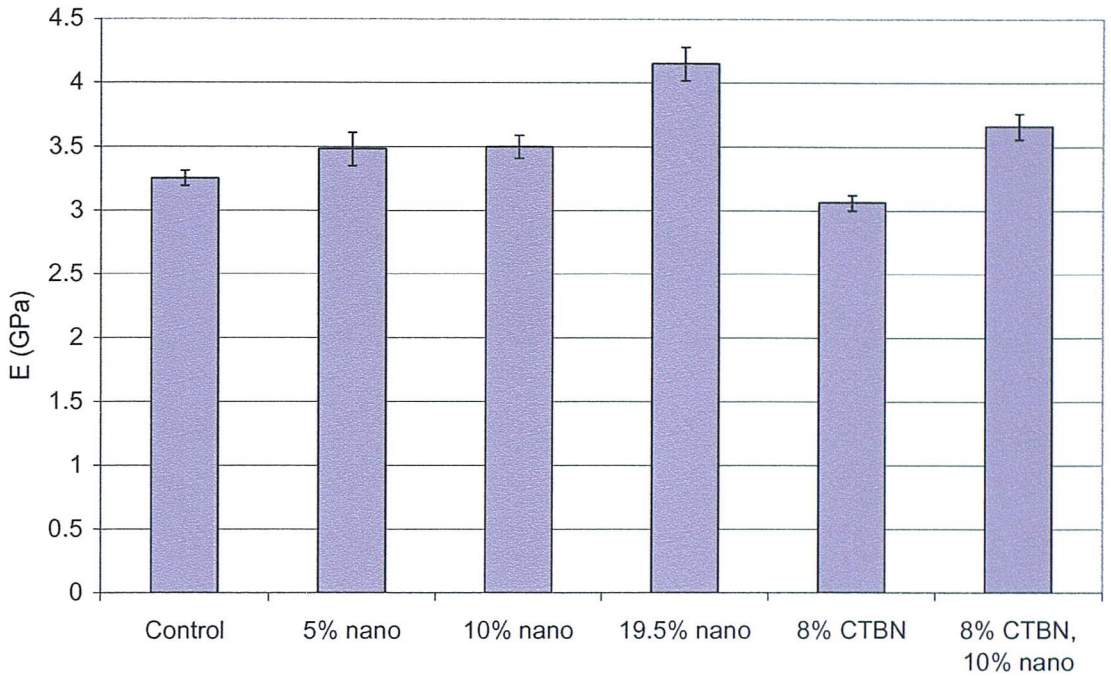


Figure 5.1.8. Young's moduli for the amine-cured TGMDA-based bulk epoxy polymers. (error bars are ± one standard deviation)

Table 5.1.4. Summary of the Young's moduli for the amine-cured TGMDA-based bulk epoxy polymers (± one standard deviation).

wt. % CTBN	wt. % nano-silica	E *(GPa)*
0	0	3.25 ± 0.06
0	5	3.48 ± 0.13
0	10	3.50 ± 0.09
0	19.5	4.15 ± 0.13
8	0	3.06 ± 0.06
8	10	3.37 ± 0.10

The Young's modulus of the unmodified epoxy was 3.25GPa, and other studies on tetrafunctional epoxies have obtained values between 2.5 and 3.5GPa [161,162], which correlates well with the value obtained in this study.

The modulus increases with increasing nano-silica content (up to 4.15GPa for the sample containing 19.5 wt. % nano-silica) which is expected because the nano particles have a much higher modulus (ie. ~70GPa) [137,138] than the epoxy.

The linear increase in stiffness (within statistical boundaries) with increasing nano-silica content is shown in Figure 5.1.9 and has been reported before [105,108]. The experimental data will be compared to predictive analytical models in Chapter 7.

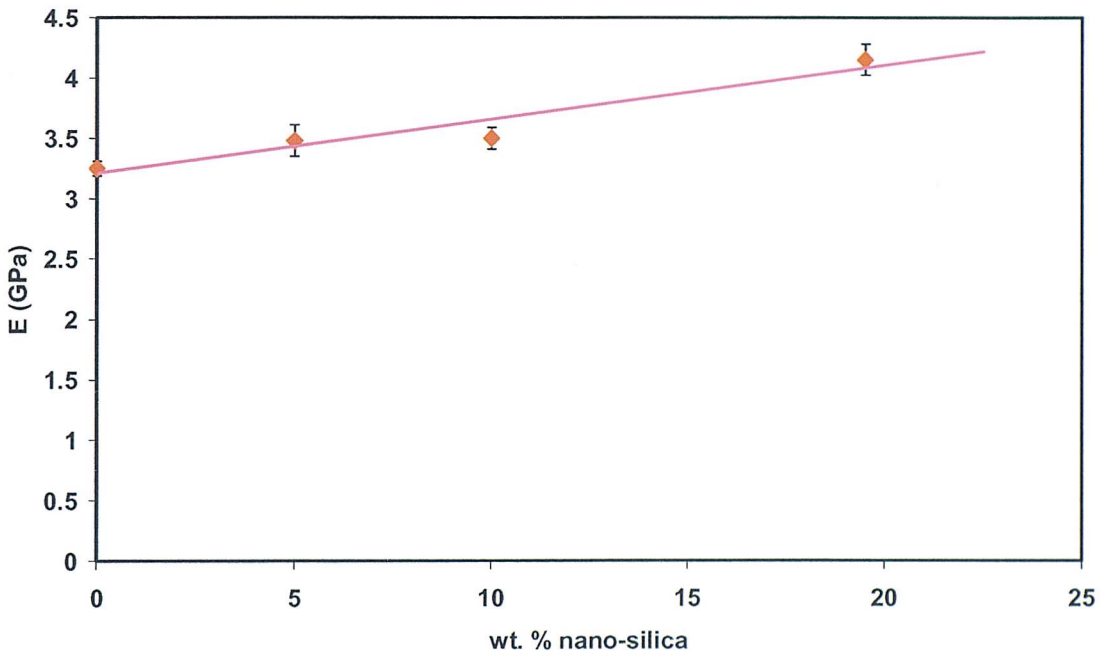


Figure 5.1.9. Graph showing linear increase in Young's modulus with increasing nano-silica content (error bars are $\pm$ one standard deviation).

The modulus decreases to 3.06GPa with the presence of 8 wt. % CTBN since rubber has a much lower modulus [126] than the epoxy, but a hybrid sample with 8 wt. % CTBN and 10 wt. % nano-silica had an increased modulus of 3.37GPa due to the presence of the much stiffer nano-silica particles.

5.1.2.3 Fracture Test Results

At least triplicate three-point bend tests were performed at a rate of 1mm/min at 20°C to ascertain the critical mode I stress intensity factor (K_{Ic}). This fracture toughness value was then converted to the mode I fracture energy (G_{Ic}) (to compare with the FRP interlaminar fracture energies) using Equation 2.8 in Chapter 2. The pre-crack was formed by drawing a new razor blade through the notch tip. The fracture energy results are illustrated in Figure 5.1.10 and the numerical values can be found in Table 5.1.5.

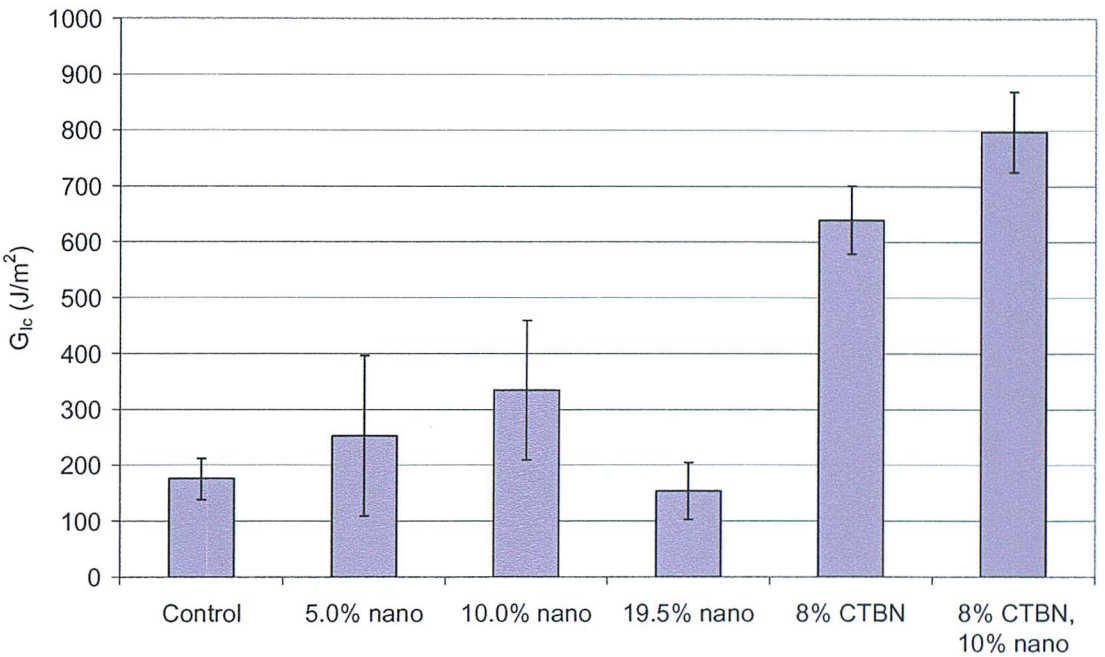


Figure 5.1.10. Fracture energy results for the amine-cured TGMDA-based bulk epoxy polymers (error bars are ± one standard deviation).

Table 5.1.5. Summary of fracture toughness and energies for the amine-cured TGMDA-based bulk epoxy polymers (± one standard deviation).

wt. % CTBN	wt. % nano-silica	K_{Ic} *(MPa m$^{1/2}$)*	G_{Ic} *(J/m^2)*
0	0	0.80 ± 0.08	176 ± 37
0	5	0.98 ± 0.26	253 ± 144
0	10	1.14 ± 0.22	336 ± 125
0	19.5	0.84 ± 0.15	154 ± 51
8	0	1.49 ± 0.07	640 ± 61
8	10	1.75 ± 0.08	798 ± 72

Other studies involving unmodified tetrafunctional epoxies showed toughness values of ~1MPa $m^{1/2}$ [160,161] which are comparable to the value recorded for the unmodified polymer in this study (ie. 0.80MPa $m^{1/2}$).

There is no statistical increase in toughness when nano-silica particles are added since the error bars overlap. If the mean values are examined, this would suggest that the toughness increases when up to 10 wt. % nano-silica is included, and decreases when 19.5 wt. % is present. The AFM images suggest that the nano particles agglomerate with increasing nano-silica content, and large amounts of agglomeration have a detrimental effect on the toughness. The reason for the decrease in toughness may be because the agglomerates reduce the amount of epoxy between particles within the agglomerate that is available to plastically deform [85,112,151].

The addition of 8 wt. % CTBN almost doubles the fracture toughness to 1.49MPa $m^{1/2}$. This increase is expected, and has been reported in other research on tetrafunctional epoxies, like Pearce *et al.* [26] who showed that CTBN could produce up to three times the toughness of an unmodified epoxy.

The addition of 10 wt. % nano-silica to a sample containing 8 wt. % CTBN produces a further increase in toughness to 1.75MPa $m^{1/2}$, which was the highest of all the tetrafunctional formulations used. This synergistic effect between CTBN and nano-silica, where necklace-like nano-silica agglomerates form, was also observed in the anhydride-cured DGEBA-based system. (See Chapter 6)

5.1.2.4 Summary

The glass transition temperature of the unmodified epoxy was 250°C and the addition of nano-silica did not vary the epoxy T_g. The Young's moduli increased with increasing nano-silica content since nano-silica particles have a much higher modulus than the epoxy. Nano-silica on its own did not statistically increase the toughness, but agglomeration of the nano-silica particles at 19.5 wt. % nano-silica, contributed to a decrease in toughness.

The samples containing 8 wt. % CTBN both had a reduced T_g of 244°C because some of the rubber remained in the epoxy phase. The AFM images show that ~6 wt. % CTBN remained in solution in the epoxy phase, but calculations using the Fox-Flory equation suggest that only ~2 wt. % CTBN would have to remain in the epoxy phase to produce the small decrease in T_g observed. Many more AFM images would be needed to test this hypothesis and time constraints did not permit this. The tensile modulus of the sample containing only 8 wt. % CTBN (ie. 3.06GPa) was lower than that of the unmodified epoxy since CTBN has a lower modulus than the unmodified epoxy, but adding 10 wt. % nano-silica increased the modulus to 3.37GPa. The CTBN-only sample had a toughness of 1.49MPa $m^{1/2}$, and the addition of 10 wt. % nano-silica increased this toughness to 1.75MPa $m^{1/2}$ giving the hybrid sample the highest toughness of all the formulations.

5.1.3 Bulk Fracture Surfaces

Scanning electron microscopy was performed on some of the fracture surfaces of the SENB samples to investigate the fracture mechanisms responsible for the toughness values observed. It should be noted that the pre-crack was formed by drawing a new razor blade through the notch tip, and this pre-crack is visible in the low magnification images as a vertical line to the far left of the micrograph.

5.1.3.1 Unmodified Epoxy

The micrographs in Figure 5.1.11 and Figure 5.1.12 are of the fracture surface of the unmodified TGMDA epoxy. The surface is flat, glass-like and barren because very little plastic deformation occurred, as expected for an unmodified, brittle thermosetting polymer.

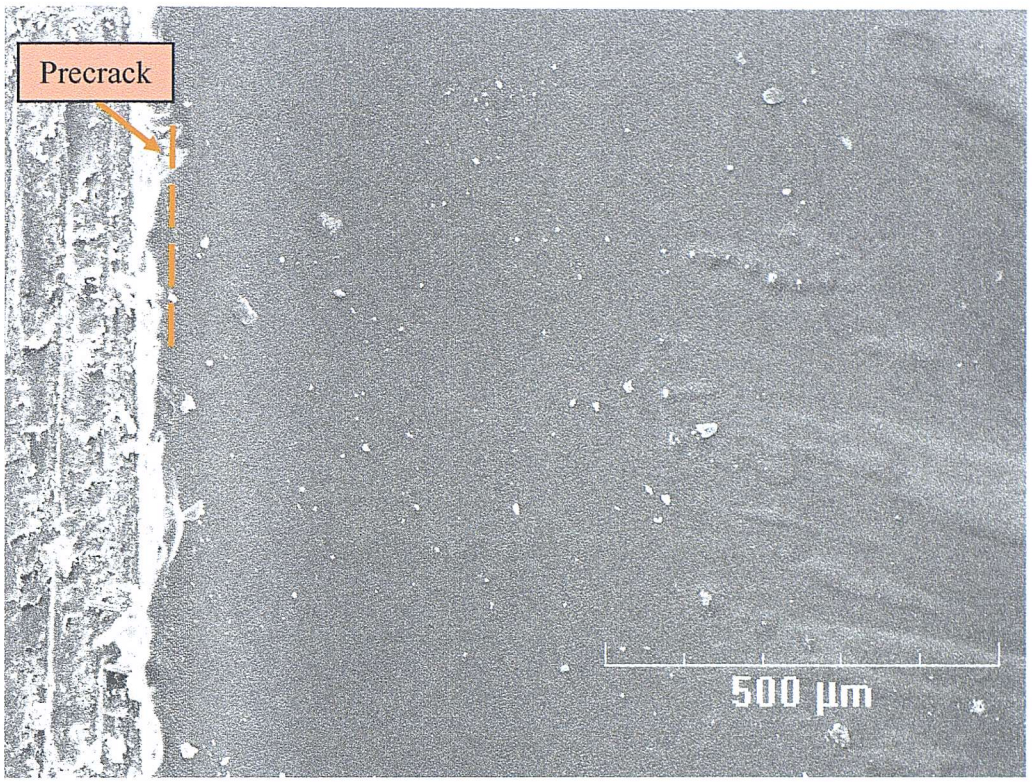


Figure 5.1.11. Fracture surface of unmodified epoxy (crack propagation from left to right).

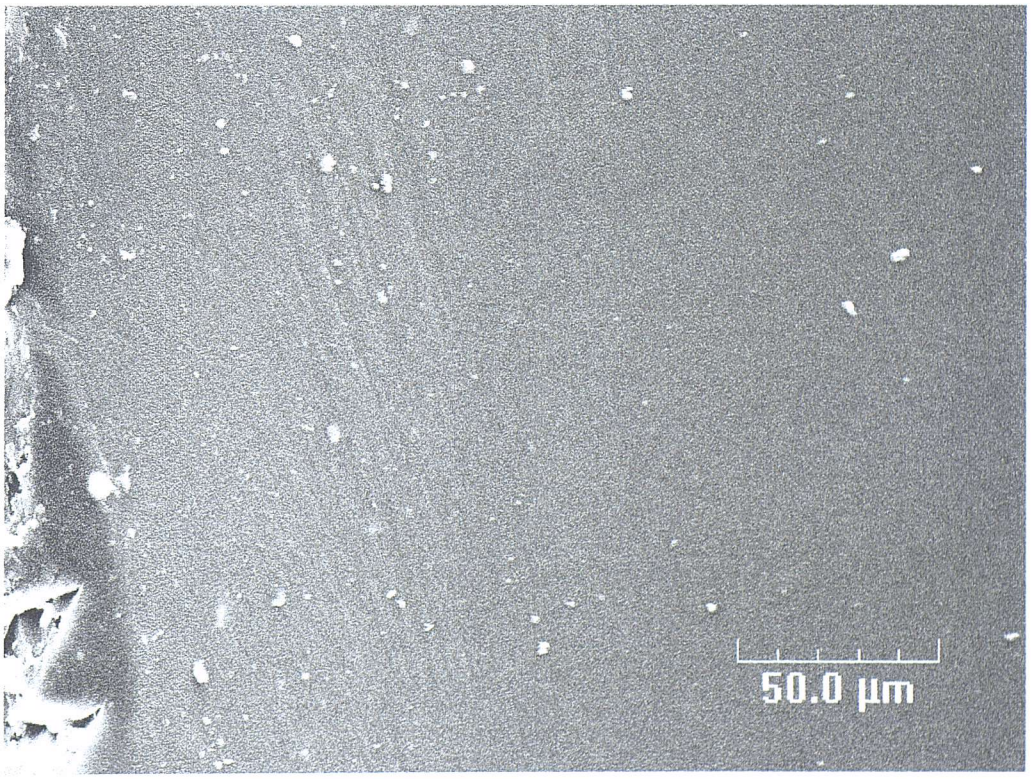


Figure 5.1.12. Fracture surface of unmodified epoxy at higher magnification (crack propagation from left to right).

5.1.3.2 Nano-silica Modified Epoxies

The micrographs in Figure 5.1.13 and Figure 5.1.14 show the relatively smooth fracture surface of a sample containing 5 wt. % nano-silica. Feather markings are visible and these absorb the excess energy associated with fast crack growth in a brittle manner [83,145]. This is why the toughness of 0.98MPa $m^{1/2}$ is so much lower than the formulations containing CTBN (see Section 5.1.3.3). The nano-silica particles are not visible at this magnification due to their very small particle diameters of 20nm.

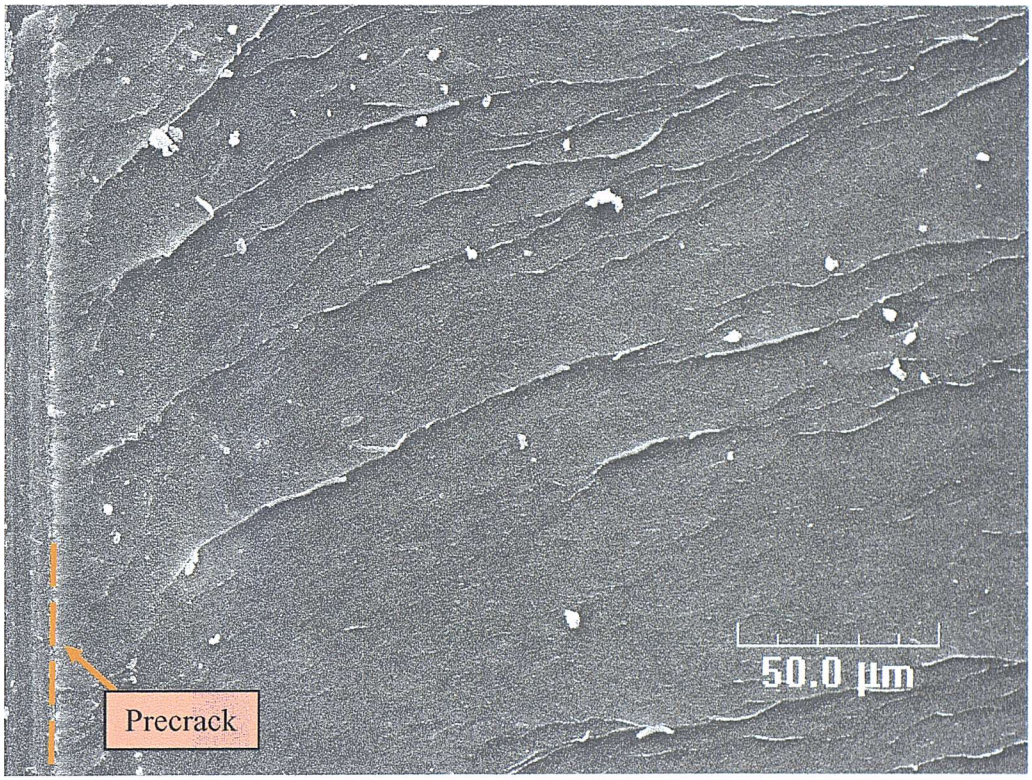


Figure 5.1.13. Fracture surface of a sample containing 5 wt. % nano-silica (crack propagation from left to right).

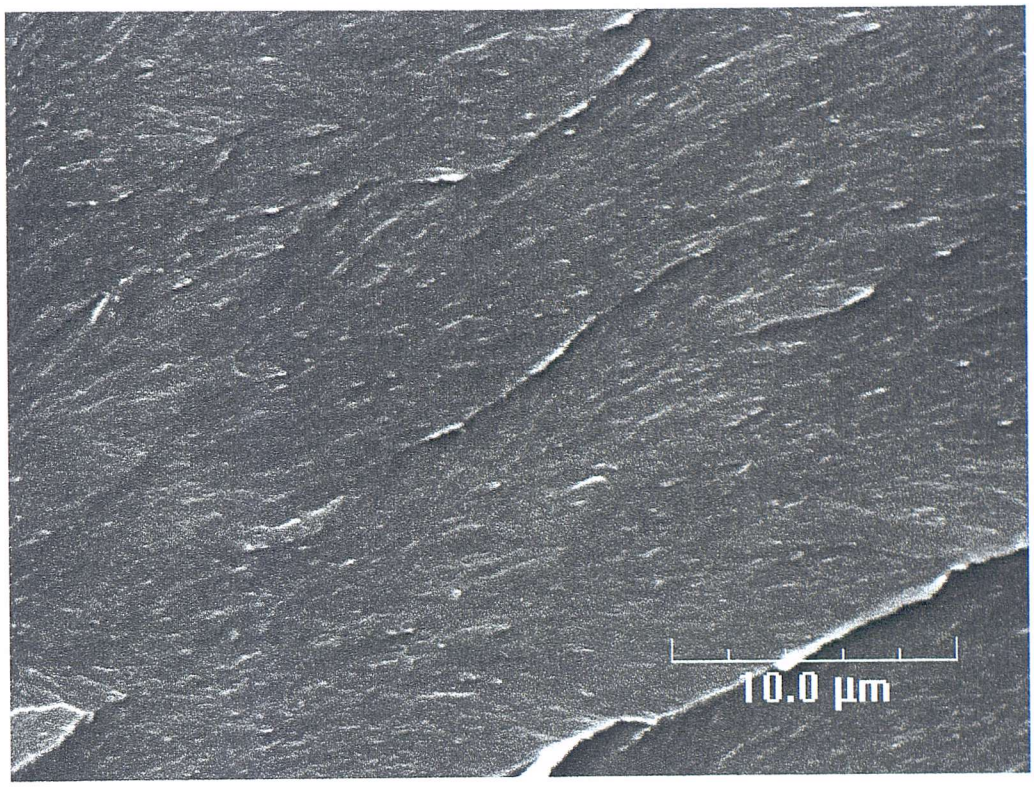


Figure 5.1.14. Fracture surface of a sample containing 5 wt. % nano-silica at higher magnification (crack propagation from left to right).

Figure 5.1.15 and Figure 5.1.16 are high magnification micrographs taken with FEG-SEM of a sample containing 10 wt. % nano-silica only. The lower magnification image shows a very rough surface with some flat, oval-shaped micron-sized regions. These features are believed to be localised concentrations of gold as a result of too much sputter coating. (Note that these features were not visible in the images taken with an SEM with no field emission gun attachment, because a different sputter coater was used.) In the higher magnification image in Figure 5.1.16, the nano particles are visible, and appear to be well bonded to the epoxy matrix. No void growth or any evidence of toughening from the nano-silica particles are visible in these images, and indeed, this correlates well with the lack of statistical improvement in toughness that was observed in this sample.

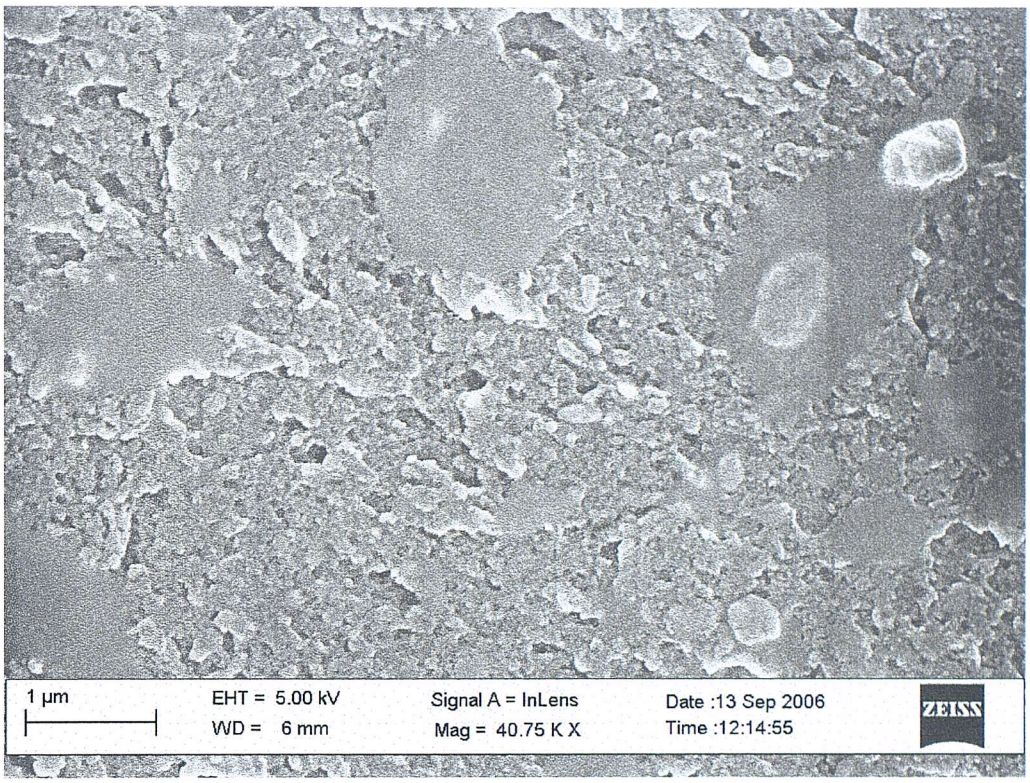


Figure 5.1.15. Fracture surface of a sample containing 10 wt. % nano-silica (crack propagation from left to right).

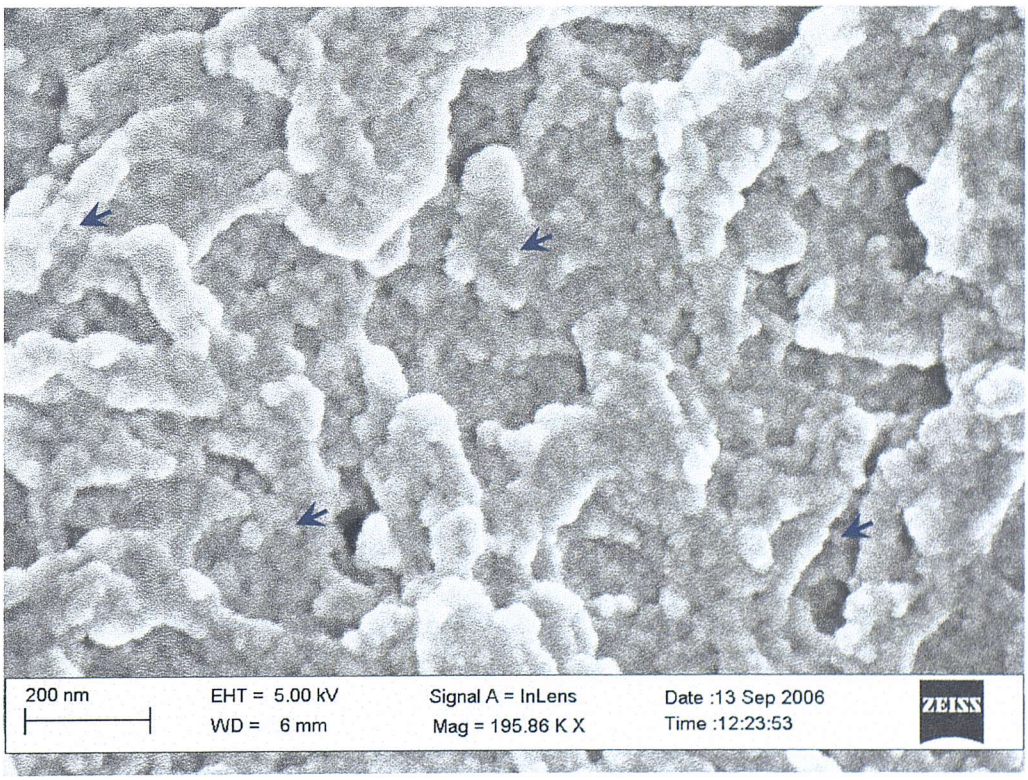


Figure 5.1.16. Fracture surface of a sample containing 10 wt. % nano-silica at higher magnification (crack propagation from left to right. Blue arrows point to some nano-silica particles).

The images in Figure 5.1.17 and Figure 5.1.18 are the fracture surfaces of a sample containing 19.5 wt. % nano-silica. The micrographs shows a mostly flat, plate-like surface in the fast fracture region due to the multiplanar nature of the crack progression. However, in the plastic zone near the precrack, it can be seen that the surface is flat, and there was little plastic deformation, which correlates well with its low fracture toughness.

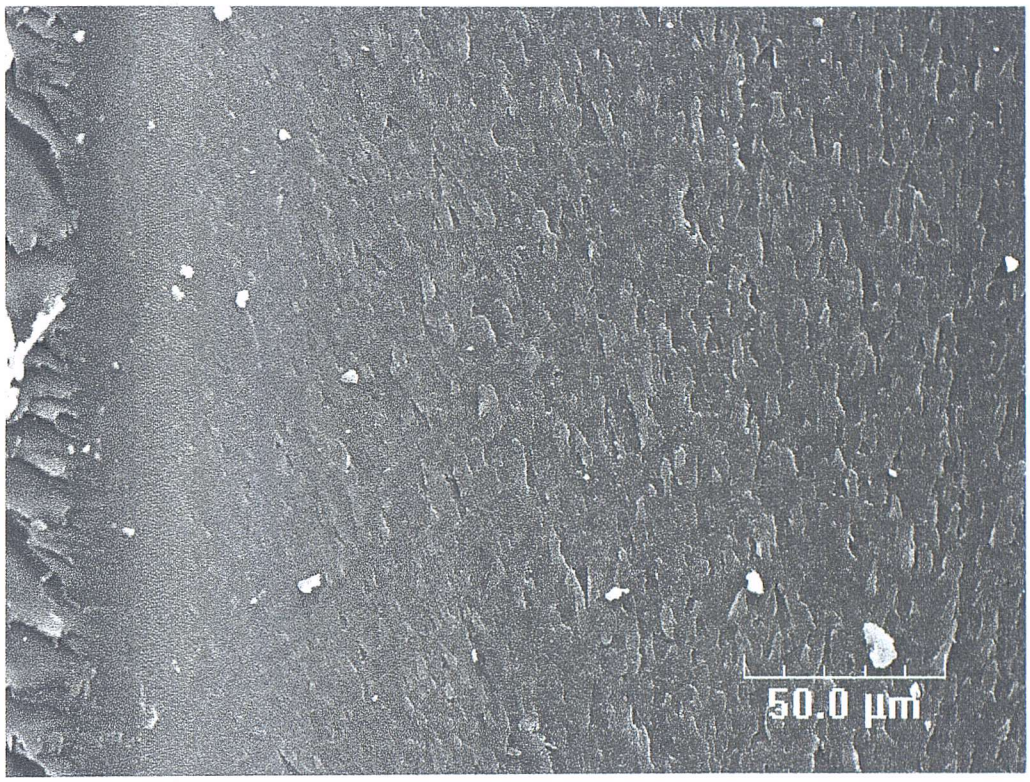


Figure 5.1.17. Fracture surface of a sample containing 19.5 wt. % nano-silica (crack propagation from left to right).

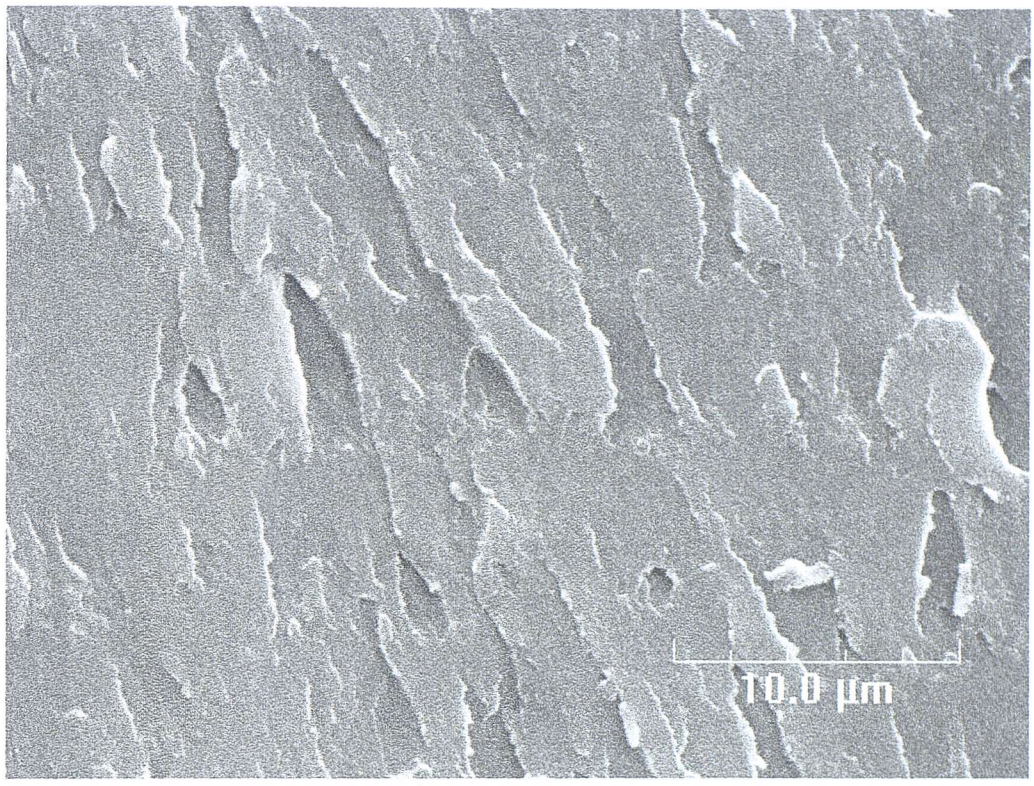


Figure 5.1.18. Fracture surface of a sample containing 19.5 wt. % nano-silica at higher magnification in the fast-fracture region (crack propagation from left to right).

5.1.3.3 Rubber Modified Epoxy

The micrographs in Figure 5.1.19 and Figure 5.1.20 are the fracture surfaces of a sample containing 8 wt. % CTBN. The surface is relatively flat and plate-like, but the toughness is almost twice as high as that of the unmodified epoxy. Some evidence of rubber cavitation is visible, but the dominant toughening mechanisms are believed to be from shear yielding of the epoxy between the phase separated rubber particles, and plasticization of the epoxy by the rubber that remains in solution in the epoxy phase [4,7].

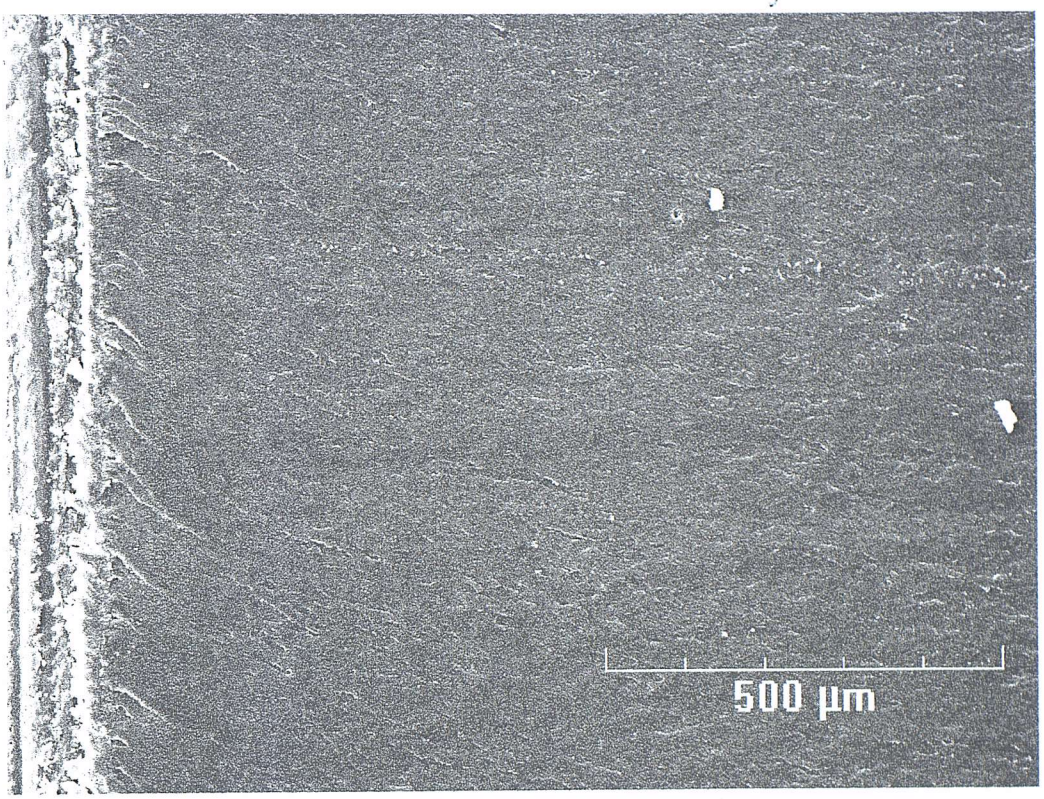


Figure 5.1.19. Fracture surface of a sample containing 8 wt. % CTBN (crack propagation from left to right).

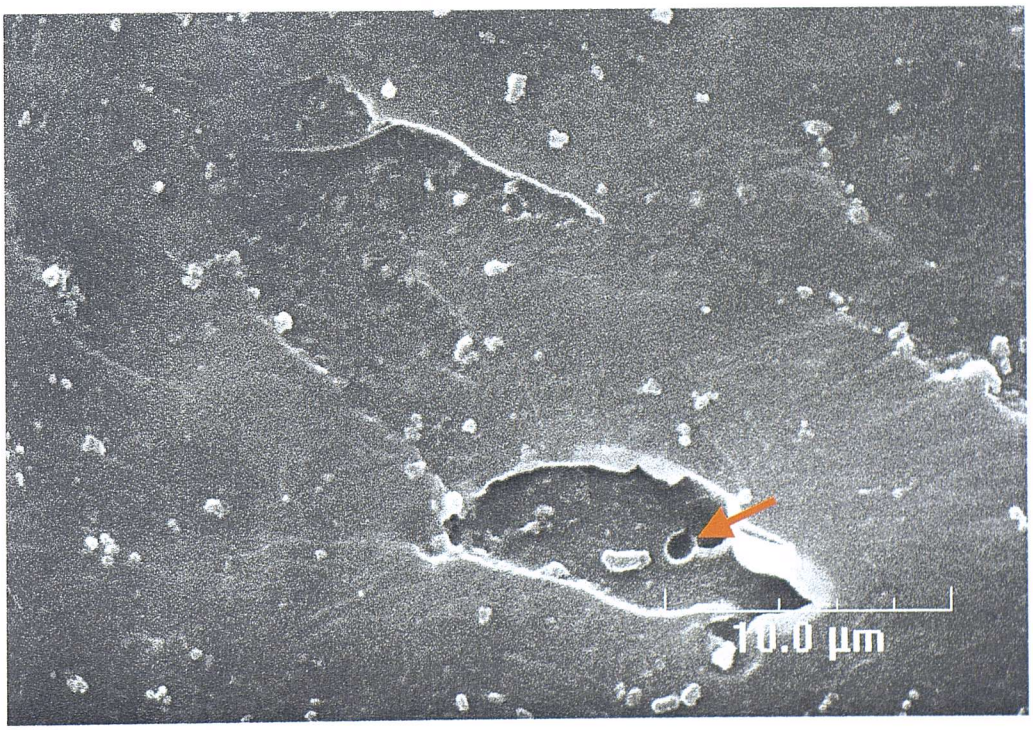


Figure 5.1.20. Fracture surface of a sample containing 8 wt. % CTBN at higher magnification (crack propagation from left to right and the red arrow points to a cavitated rubber particle).

5.1.3.4 Hybrid Modified Epoxies

The micrographs in Figure 5.1.21 and Figure 5.1.22 are for a hybrid sample toughened with 8 wt. % CTBN and 10 wt. % nano-silica. Large amounts of plastic deformation of the epoxy is visible, which confirms that the major toughening mechanisms are from shear yielding of the epoxy between the phase separated rubber particles, and plasticization of the epoxy by the rubber that remains in solution in the epoxy phase [4,7]. However, the nano-silica particles are not visible at this magnification, and it is unclear if and how they added any additional toughness. This remains subject to further investigations.

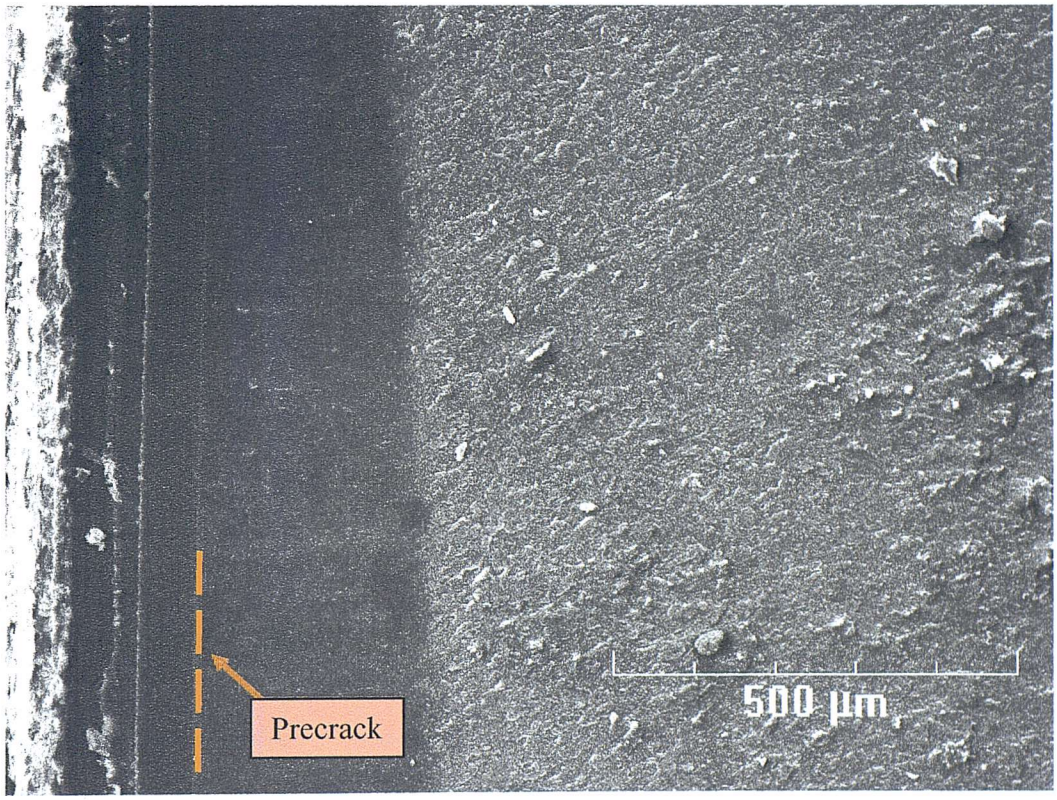


Figure 5.1.21. Fracture surface of a sample containing 8 wt. % CTBN and 10 wt. % nano-silica (crack propagation from left to right).

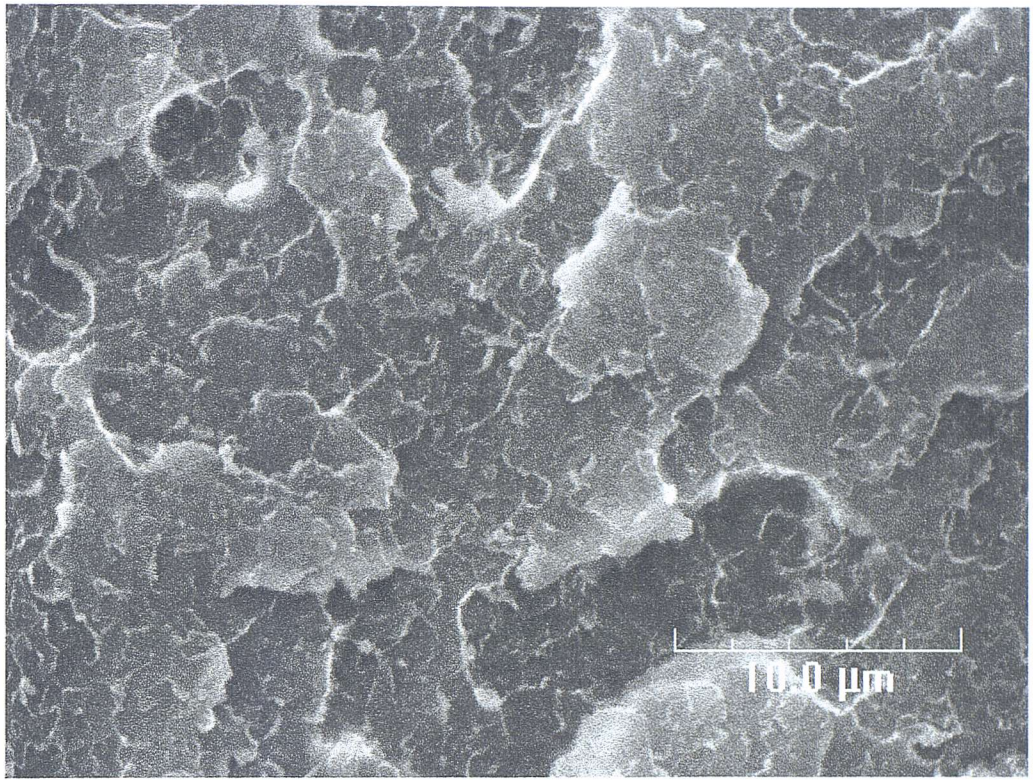


Figure 5.1.22. Fracture surface of a sample containing 8 wt. % CTBN and 10 wt. % nano-silica at higher magnification (crack propagation from left to right).

5.1.3.5 Summary

There was no statistical increase in the toughness of the bulk samples when nano-silica was used. This was correlated by the similarity of the fracture surfaces of the nano-only samples and the unmodified epoxy.

The samples containing 8 wt. % CTBN-only and both rubber and nano-silica, showed hardly any evidence of rubber cavitation. It is believed that the increases in toughness that was observed was from shear yielding of the epoxy between the phase separated rubber particles and plasticisation of the epoxy by the rubber that remained in solution in the epoxy phase.

5.2 Carbon Fibre Reinforced Polymer Results

The CFRP polymer panels (8 ply) were manufactured by vacuum assisted resin transfer moulding (VARTM). The polymer matrices used for the laminates were of the same composition as those described in the 'Bulk Epoxy Polymer Results' section of this Chapter. The average weight fraction of the fibres in the laminates was 60%.

Mode I tests and flexural modulus tests were performed on these samples and the results are presented in the following sections. Unlike the amine-cured DGEBA-based samples discussed in the previous Chapter, these laminates were manufactured with a much higher quality: the surfaces were smooth and the laminates were thick (so no backing beams were needed). The fracture surfaces of the Mode I samples are discussed, and there is a Chapter Discussion in the final section which discusses the nexus between the bulk epoxy polymers and the CFRPs.

5.2.1 Mode I Fracture Results

At least triplicate double cantilever beams (DCBs) were tested for each formulation at a cross-head speed of 1mm/min at 20°C under mode I conditions and all failed in a stick-slip (initiation-arrest) manner.

The graph in Figure 5.2.1 illustrates the initiation interlaminar fracture energies calculated by the corrected beam theory (CBT) method. Small R-curves were observed for all of the samples and an example curve for the initiation and arrest interlaminar fracture energy of a sample toughened with 19.5 wt. % nano-silica is shown in Figure 5.2.2. Table 5.2.1 contains the mean numerical values of the calculated initiation and arrest interlaminar fracture energies, but only the mean initiation interlaminar fracture energies will be quoted in all subsequent discussions.

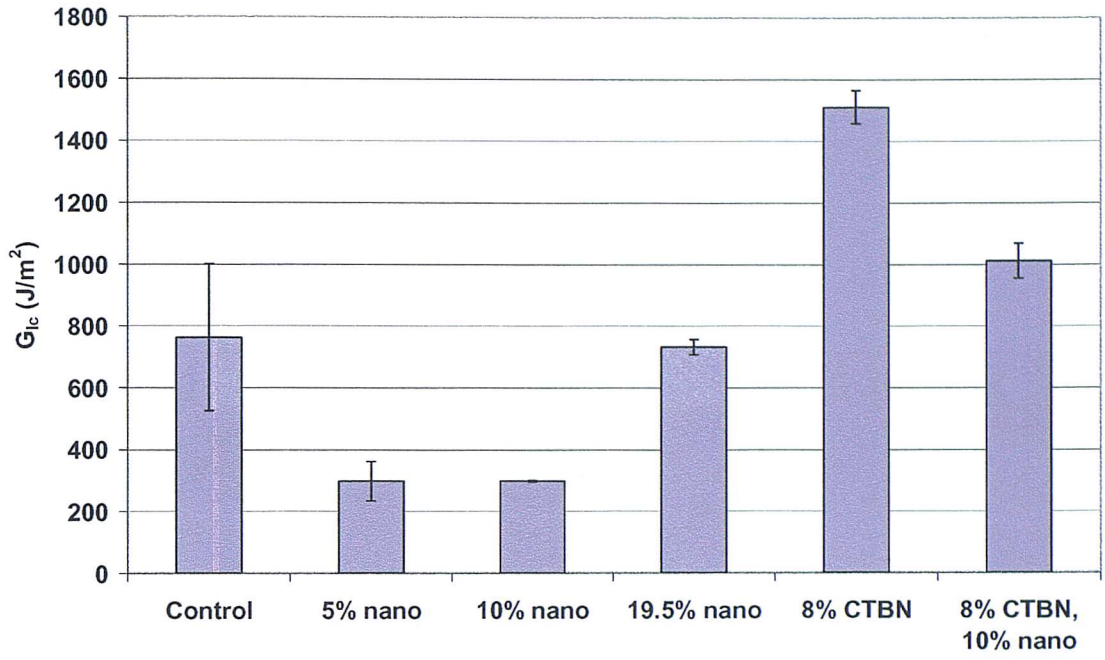


Figure 5.2.1. Critical mode I interlaminar fracture energy for amine-cured CFRPs with a TGMDA matrix. (error bars are ± one standard deviation)

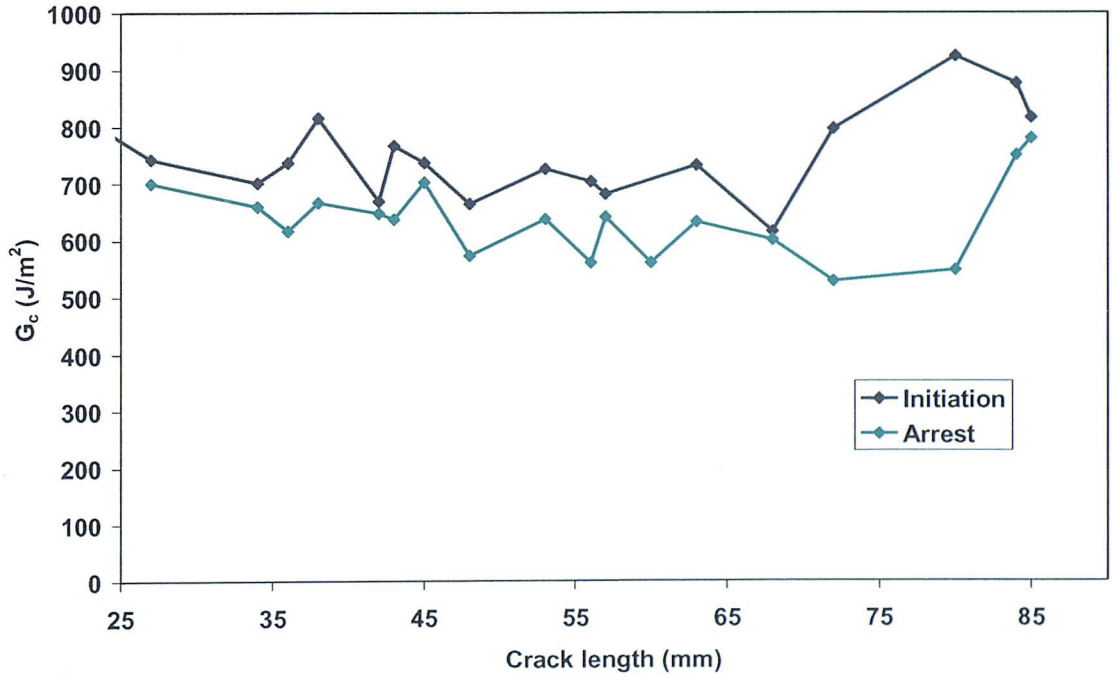


Figure 5.2.2. Graph showing the variation in the initiation and arrest values of the interlaminar fracture energy with crack length for a sample containing 19.5 wt. % nano-silica.

Table 5.2.1 Summary of the mode I interlaminar fracture energies for amine-cured CFRPs with a TGMDA matrix. (± one standard deviation)

wt. % CTBN	wt. % nano-silica	$G_{Ic\ Initiation}$ (J/m^2)	$G_{Ic\ Arrest}$ (J/m^2)
0	0	764 ± 237	661 ± 213
0	5	300 ± 64	235 ± 60
0	10	299 ± 2	247 ± 3
0	19.5	733 ± 24	614 ± 30
8	0	1511 ± 54	1203 ± 9
8	10	1012 ± 56	785 ± 56

The control FRP laminate had an interlaminar fracture energy of 764J/m^2 but the addition of 5 and 10 wt. % nano-silica lead to a *decrease* in fracture energy of the laminates of more than a half. This dramatic decrease in interlaminar fracture energy at such low amounts of silane-treated, 20nm diameter nano-silica particles, is contrary to what has been reported in other work [102,106]. Increasing the nano-silica content of the matrix to 19.5 wt. % increases the interlaminar fracture energy back to a level that is comparable with the control. It may be concluded that the addition of nano-silica alone does not produce an increase in the interlaminar fracture energy of the laminates in this system.

A matrix that was toughened with 8 wt. % CTBN gave a laminate that had twice the interlaminar fracture energy of the control CFRP. A large increase in the interlaminar fracture energy of laminates with rubber modified matrices, has been reported before [163].

Although the mean initiation interlaminar fracture energy of the hybrid CFRP (ie.1012J/m^2) is more than 250J/m^2 higher than the mean initiation interlaminar fracture energy of the control laminate, their error bars overlap. This suggests that there is no statistical difference in the interlaminar fracture energy between the hybrid and control laminates. The synergy observed between CTBN and nano-silica in other systems [106] is not present in this system.

5.2.2 Flexural Modulus

The laminates were tested at a constant strain rate of 0.01/min under three-point loading conditions at 20°C. This test was conducted elastically, to a preset centre-displacement limit of 3mm. Load-displacement graphs were recorded, and the flexural modulus was calculated. The graph in Figure 5.2.3 illustrates the results, and the numerical values can be found in Table 5.2.2.

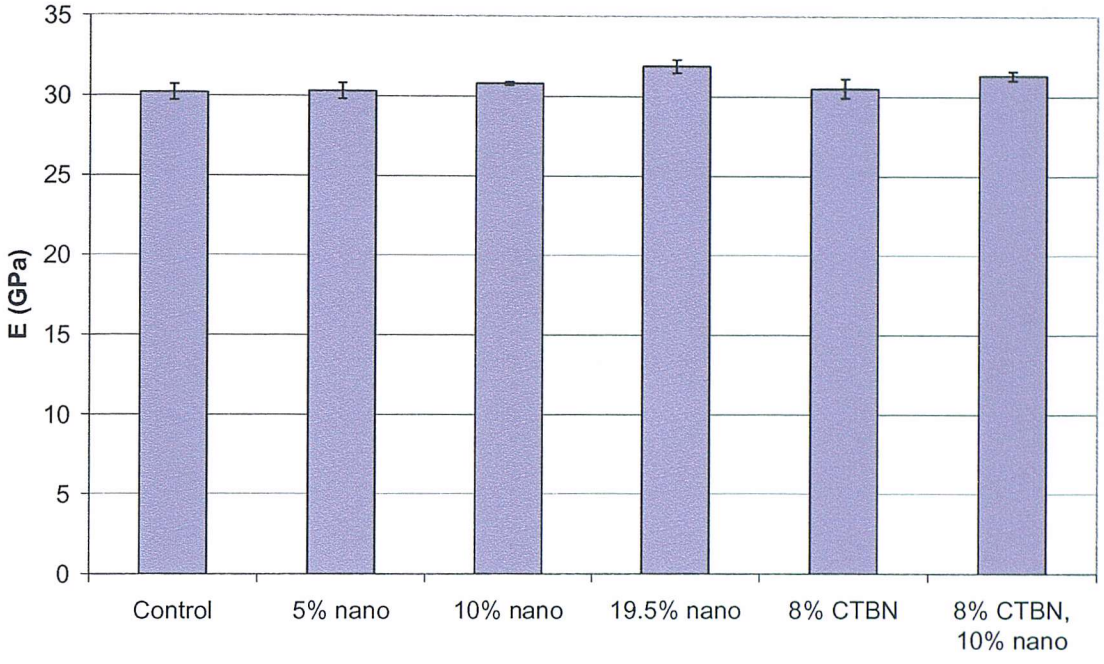


Figure 5.2.3. Flexural modulus results for CFRPs with an amine-cured TGMDA-based matrix (error bars are ± one standard deviation).

Table 5.2.2. Summary of flexural moduli for CFRPs with an amine-cured TGMDA-based matrix. (± one standard deviation)

wt. % CTBN	wt. % nano-silica	E *(GPa)*
0	0	30.2 ± 0.5
0	5	30.3 ± 0.5
0	10	30.8 ± 0.1
0	19.5	31.9 ± 0.4
8	0	30.5 ± 0.6
8	10	31.3 ± 0.3

The flexural modulus of the control laminate was 30.2GPa. The modulus increased linearly with increasing nano-silica content to a maximum of 31.9GPa for a laminate with a matrix toughened with 19.5 wt. % nano-silica, as shown in Figure 5.2.4. This small increase is expected since silica has a much higher stiffness than the epoxy [137,138], and only small amounts of nano-silica were added. (It should be noted that the fibre:matrix weight ratio was 60:40 and '19.5 wt. % nano-silica' refers to the wt. % of the *total epoxy matrix* and thus does not include the weight of the fibres.) The modulus of the woven fibres is ~100GPa [150], whereas the matrix moduli are ~3.5GPa (as presented earlier in this Chapter). As a result, the moduli of the laminates are fibre-dominated and such a relatively small wt. % of nano-silica only produces a 5% increase in modulus.

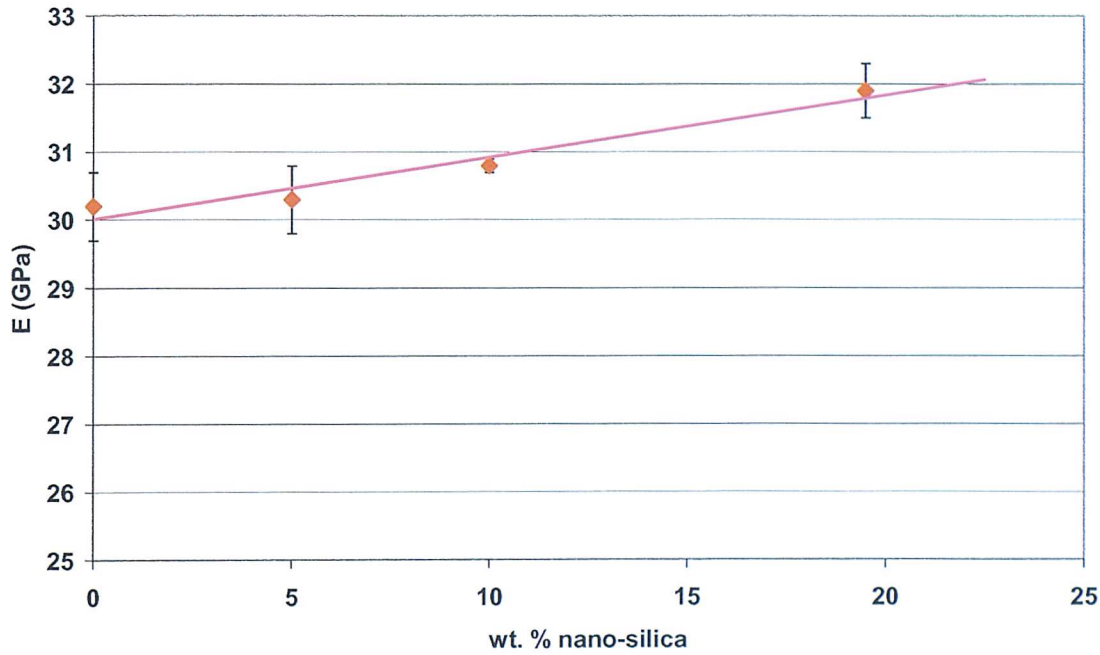


Figure 5.2.4. Flexural modulus results for amine-cured CFRPs with a TGMDA matrix, toughened with nano-silica only (error bars are ± one standard deviation. Note: y-axis does not start at zero).

Statistically, the flexural modulus of the laminate with 8 wt. % CTBN is similar to that of the control laminate. However, since rubber is so much more compliant than the epoxy matrix, the laminate would be expected to have a lower flexural modulus. This was not observed because this particular sample was slightly thinner than the others because there was less epoxy matrix. As a result, the 'extra' stiffness was provided by

the carbon fibres. Fibre volume fraction analysis would have been able to give a more accurate *corrected* flexural modulus (as was done for the anhydride-cured DGEBA-based CFRPs discussed in Chapter 6). This was not deemed necessary since there was only a 5% variation in thickness amongst the samples, and the flexural modulus results were within a reasonable range of 30-32GPa. This corresponds with the work of Mouritz [164] who performed flexural tests on a wide variety of laminates with woven fibres, including CFRPs with a fibre:matrix ratio of 64:36, and found values between 25GPa and 30GPa.

The hybrid sample with a matrix toughened with 8 wt. % CTBN and 10 wt. % nano-silica showed an increase in modulus to 31.3GPa. The addition of the rigid nano-silica particles reinstates some of the stiffness lost by the addition of the CTBN.

5.2.2.1 Summary

The addition of nano-silica to the matrix of laminates linearly increases the flexural modulus with increasing nano-silica content. This is expected due to the rigid silica particles having a higher stiffness than that of the epoxy. However, the relationship between nano-silica content and the interlaminar fracture energy is more tenuous. Indeed, the addition of 5 and 10 wt. % nano-silica leads to a dramatic decrease in interlaminar fracture energy, whereas the addition of 19.5 wt. % nano-silica increases the toughness back to that of the laminate with an unmodified matrix. Whilst nano-silica improves the laminate stiffness, it does not increase the interlaminar fracture energy.

The laminate with 8 wt. % CTBN had a slightly higher stiffness than the control because it was slightly thinner (less epoxy matrix), and was more fibre dominated. This laminate had a interlaminar fracture energy that was twice that of the control.

The hybrid laminate with 8 wt. % CTBN and 10 wt. % nano-silica had a higher stiffness than the CTBN-only sample because of the inclusion of the rigid nano particles. There was no synergy between rubber and nano-silica in terms of resistance to fracture. Indeed, the interlaminar fracture energy was comparable to that of the control laminate. It is believed that this reduction in interlaminar fracture energy may be due to the agglomeration of the nano-silica.

5.2.3 Mode I CFRP Fracture Surfaces

Scanning electron microscopy was performed on the fracture surfaces of the CFRP samples to investigate the fracture mechanisms responsible for the changes in toughness that were observed.

5.2.3.1 Unmodified Epoxy Matrix

The micrographs in Figure 5.2.5 and Figure 5.2.6 show the fracture surfaces of a CFRP laminate that had an unmodified matrix. The micrograph at lower magnification shows deformation of the epoxy matrix which contributed to its toughness. Although the fibres are not easily visible in the higher magnification micrograph there was good bonding between the matrix and the fibres. This can be deduced from the fact that the epoxy between the continuous channels (caused by fibre debonding and then eventual pullout) is deformed. This shows that because of the good adhesion between the fibres and the matrix, a lot of energy was needed for the fibres to debond and pull-out [83]. Additional evidence can be seen in the form of one fibre that is still embedded in the matrix, and is still covered in epoxy resin. The plastically deformed matrix, continuous channels and broken fibres correlate well with this laminate having a higher fracture energy (764J/m^2) than that of the *bulk* unmodified epoxy (176/m^2).

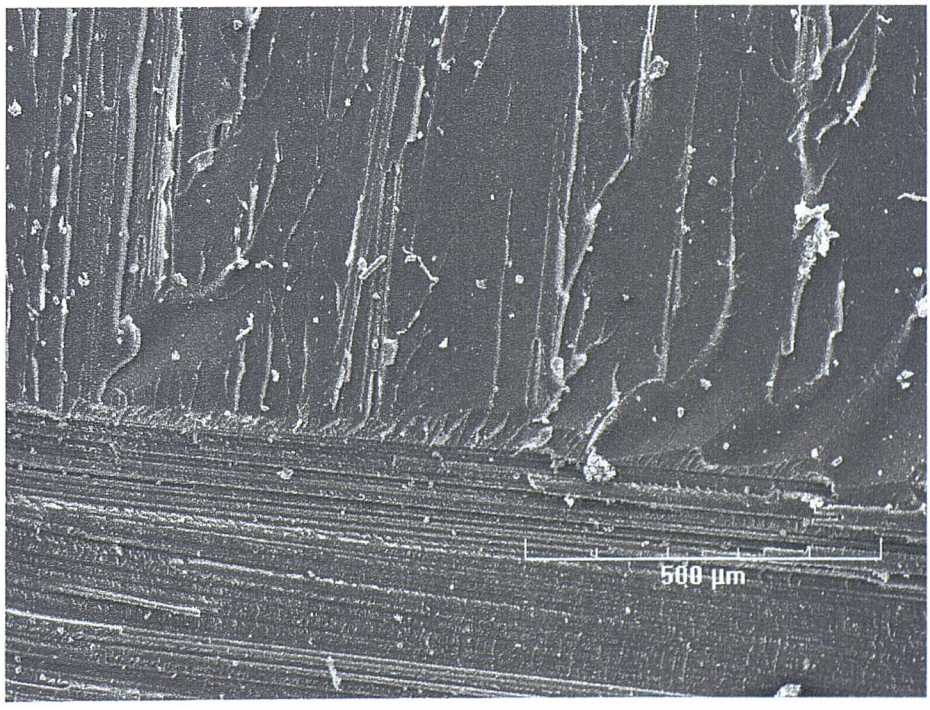


Figure 5.2.5. Fracture surface of a CFRP sample with an unmodified tetrafunctional epoxy matrix (crack propagation from *bottom to top*).

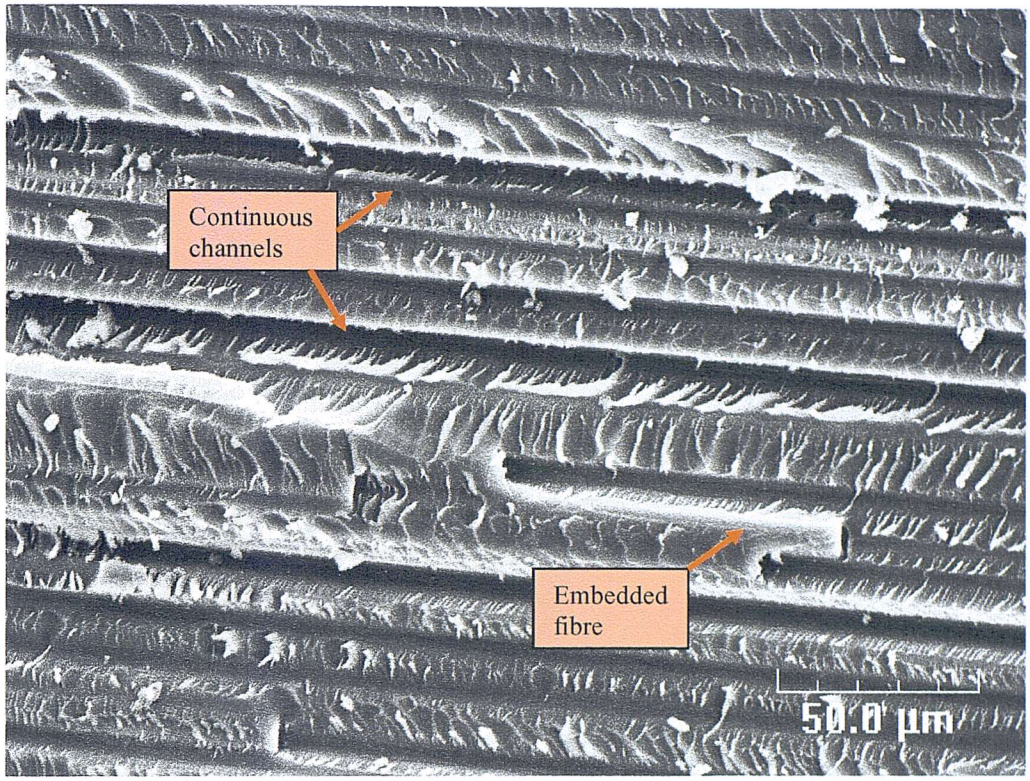


Figure 5.2.6. Fracture surface of a CFRP sample with an unmodified tetrafunctional epoxy matrix at higher magnification (crack propagation from *bottom to top*).

5.2.3.2 Nano-silica Modified Epoxy Matrices

The micrograph in Figure 5.2.7 and Figure 5.2.8 shows the fracture surface of a CFRP sample that has a matrix toughened with 5 wt. % nano-silica. The epoxy matrix is smoother than the previous sample (unmodified matrix), and the matrix between fibres is also less plastically deformed because not as much energy was absorbed. This correlates well with the low fracture energy of 300J/m^2 that was recorded. The fibres are also less well bonded to the matrix, which suggests that less energy would be needed to debond and pull-out the fibres. There is some evidence of fibre bridging, which led to a slight increase in fracture energy with increasing crack length (ie. a small R-curve).

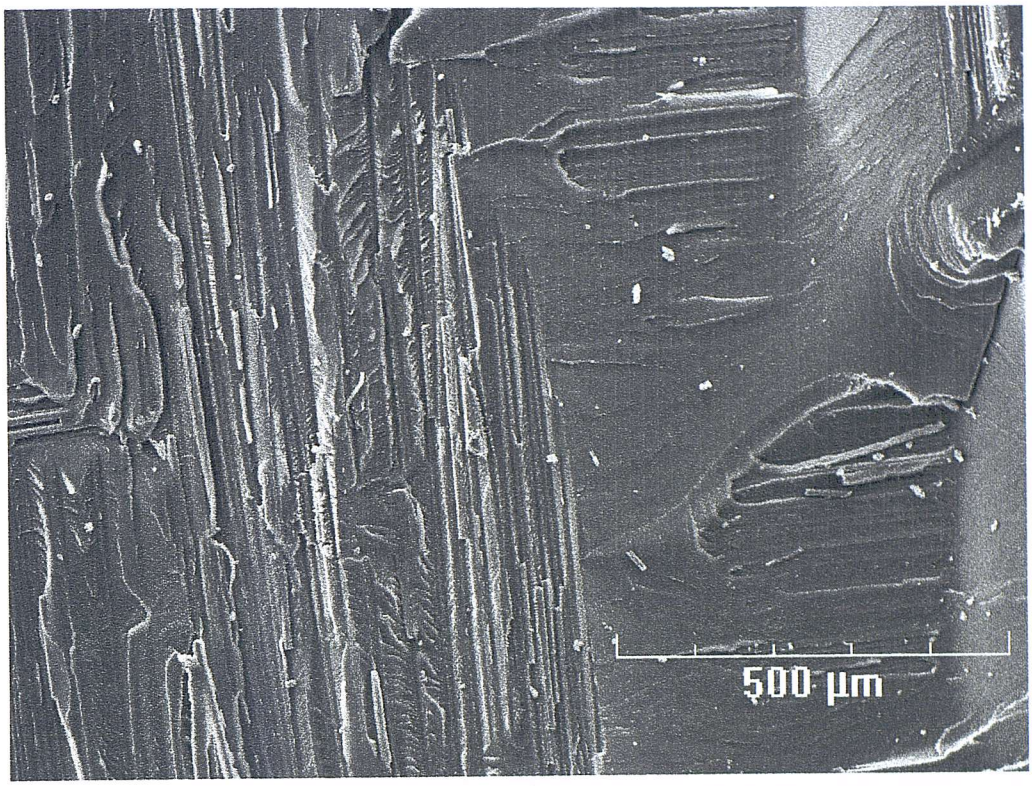


Figure 5.2.7. Fracture surface of a CFRP sample with a tetrafunctional epoxy matrix containing 5 wt. % nano-silica (crack propagation from *right to left*).

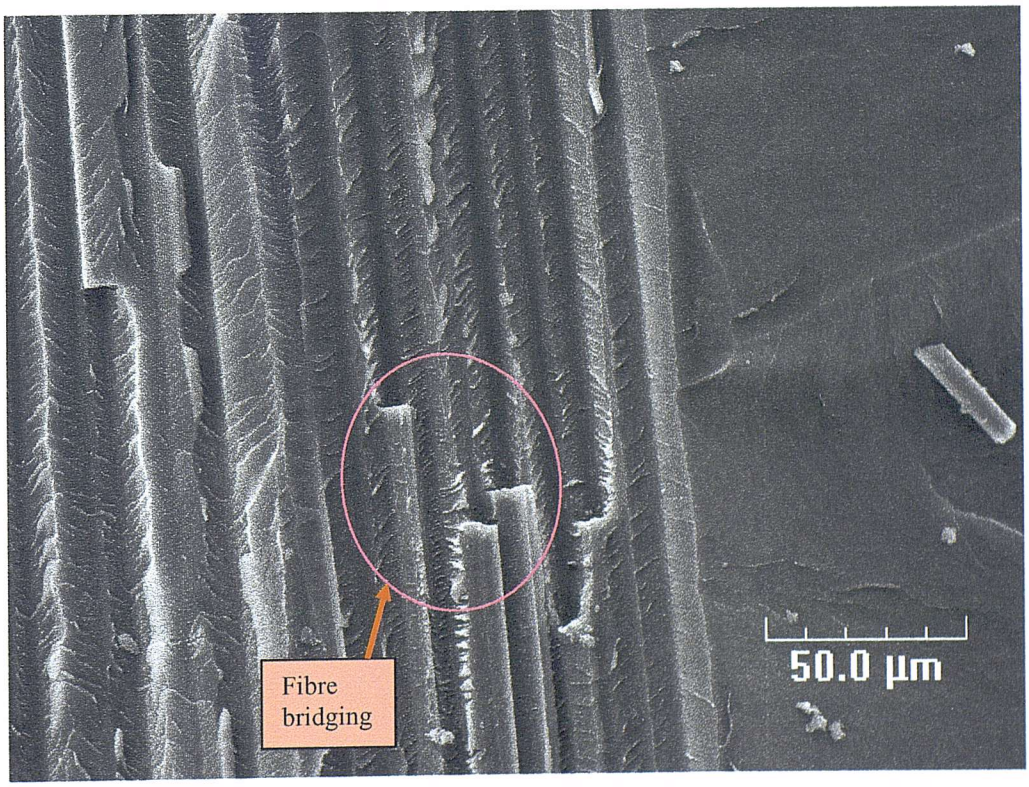


Figure 5.2.8. Fracture surface of a CFRP sample with a tetrafunctional epoxy matrix containing 5 wt. % nano-silica at higher magnification (crack propagation from *right to left*).

The micrograph in Figure 5.2.9 is the fracture surface of a sample with a matrix that was toughened with 10 wt. % nano-silica. A large area of epoxy is visible because there was a large amount of cohesive failure [165] between epoxy surfaces on both halves of the DCB specimen (in other words, the crack progressed through the epoxy matrix, with little toughening from the fibres). This is why the interlaminar fracture energy of this sample (299J/m^2) is comparable to that of the bulk epoxy polymer (336J/m^2). The micrograph in Figure 5.2.10 is at a higher magnification and shows evidence of fibre bridging (which resulted in a slight R-curve) and hardly any deformation of the epoxy matrix. So whilst the interlaminar fracture energy increased with increasing crack length, the mean interlaminar fracture energy was still quite low because of the brittle failure of the epoxy matrix.

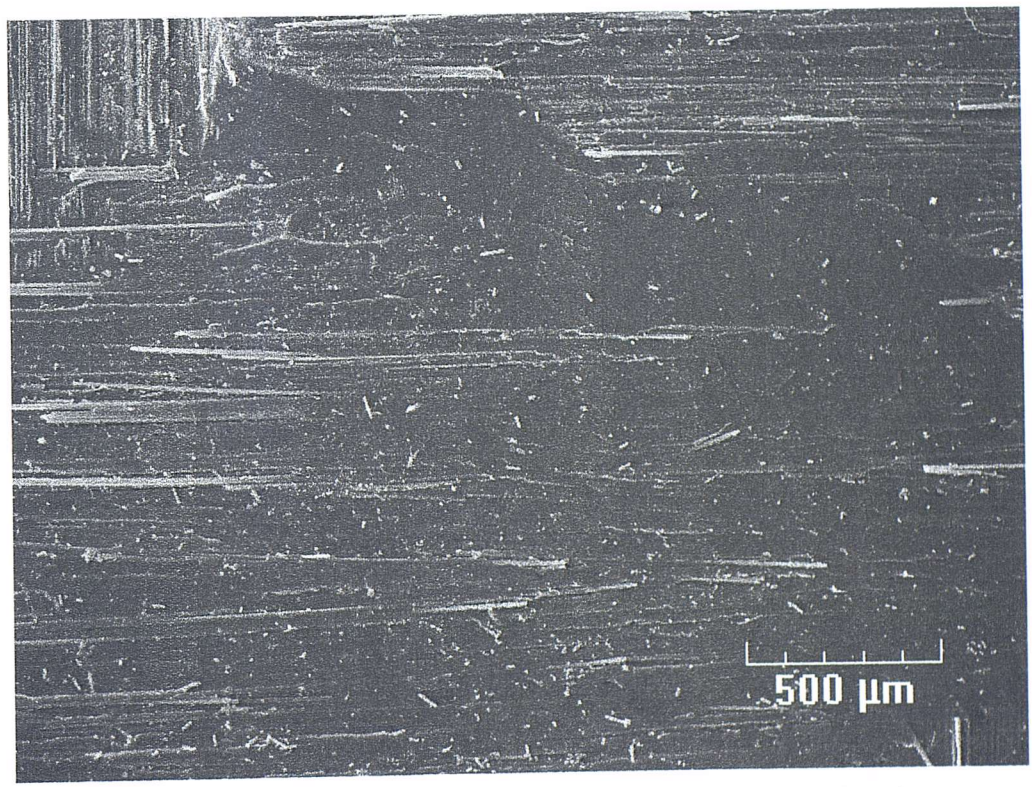


Figure 5.2.9. Fracture surface of a CFRP sample with a tetrafunctional epoxy matrix containing 10 wt. % nano-silica (crack propagation from *right to left*).

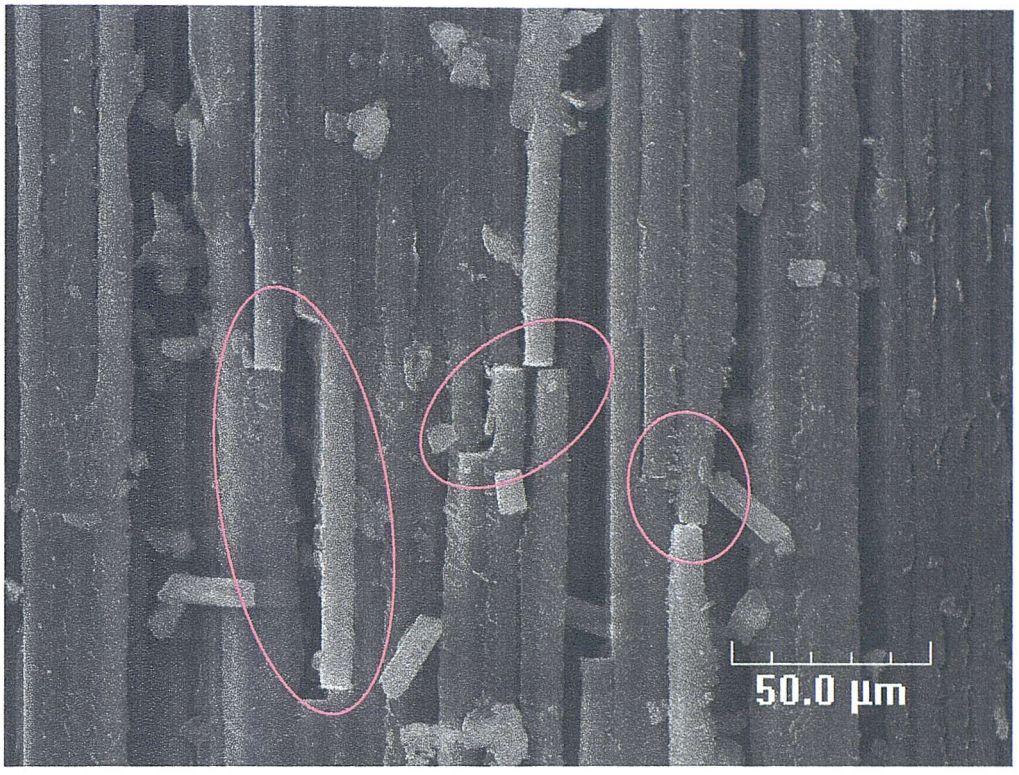


Figure 5.2.10. Fracture surface of a CFRP sample with a tetrafunctional epoxy matrix containing 10 wt. % nano-silica at higher magnification (crack propagation from *right to left*. Fibre bridging circled in pink).

The micrographs in Figure 5.2.11 and Figure 5.2.12 are the fracture surfaces of a laminate toughened with 19.5 wt. % nano-silica. What is immediately striking, is the difference in fracture appearance between this sample, and the previous samples containing nano-silica. Indeed, the surface is very similar to that of the CFRP with the unmodified matrix. The fibres are well bonded to the epoxy matrix, which led to an increase in toughness compared to the other nano-only samples. Also, the crack did not propagate through an epoxy-rich layer. There is some evidence of fibre bridging, which also contributed to the increase (relative to the other nano-only samples) in interlaminar fracture energy to 733J/m^2. This interlaminar fracture energy is comparable to that of the control laminate.

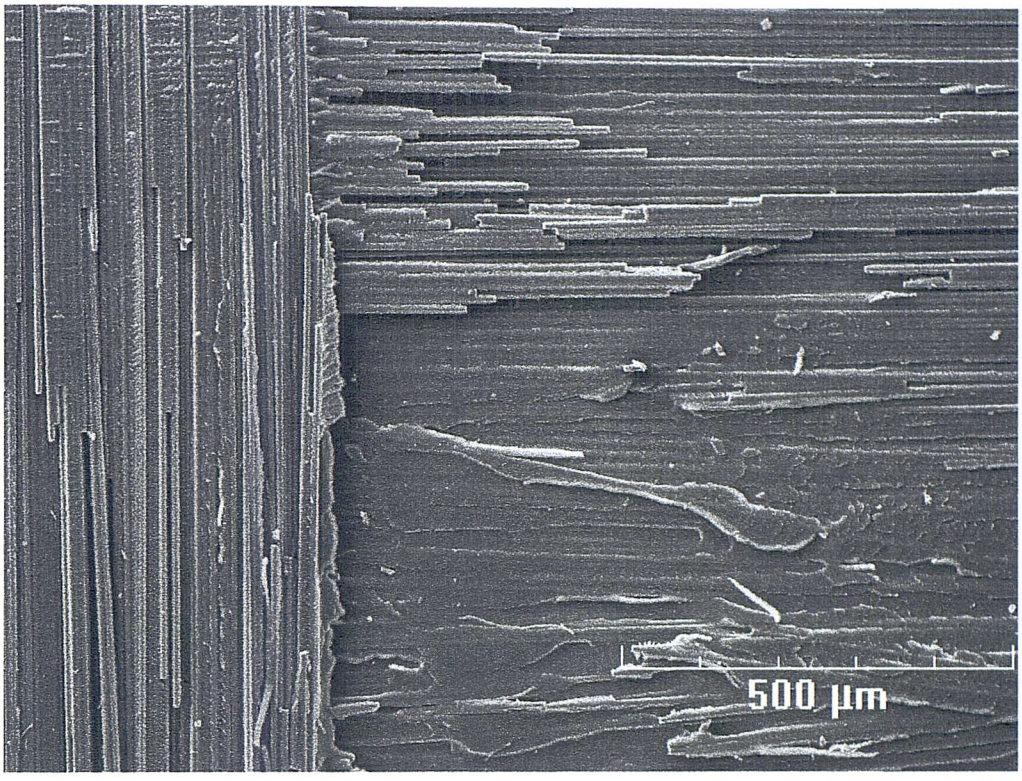


Figure 5.2.11. Fracture surface of a CFRP sample with a tetrafunctional epoxy matrix containing 19.5 wt. % nano-silica (crack propagation from *right to left*).

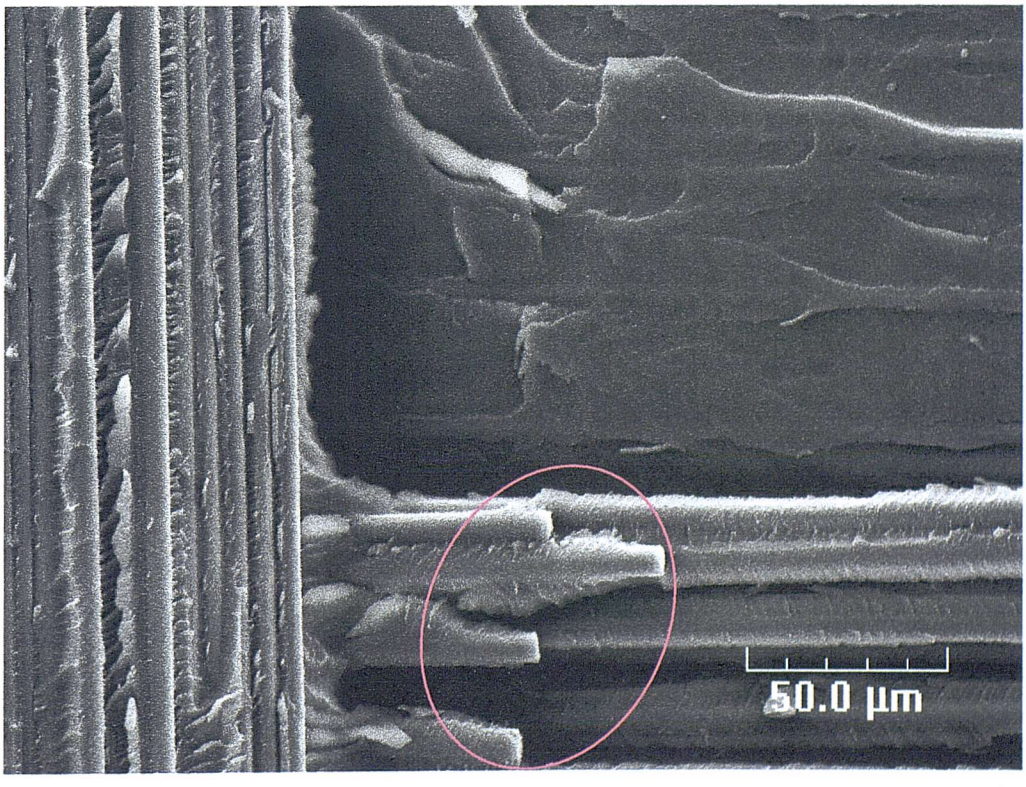


Figure 5.2.12. Fracture surface of a CFRP sample with a tetrafunctional epoxy matrix containing 19.5 wt. % nano-silica at higher magnification (crack propagation from *right to left*. Fibre bridging circled in pink).

5.2.3.3 Rubber Modified Epoxy

The micrographs in Figure 5.2.13 and Figure 5.2.14 are the fracture surfaces of a CFRP sample toughened with 8 wt. % CTBN. The visible matrix has a fairly flat, plate-like appearance which is similar to that of the bulk fracture surface. According to Kim *et al.* [166] the presence of resin-rich regions at the strand cross-over allows the possibility of full deformation of the tough matrix. Indeed, this sample has the highest toughness of all the laminates. This high toughness is a result of the good interfacial adhesion between fibre and matrix (so a large amount of energy would be needed for the fibres to debond and pull-out), the plastic deformation of the matrix, as well as some cavitation of the rubber particles. A few of these ~1μm diameter cavitated rubber particles are visible in Figure 5.2.15.

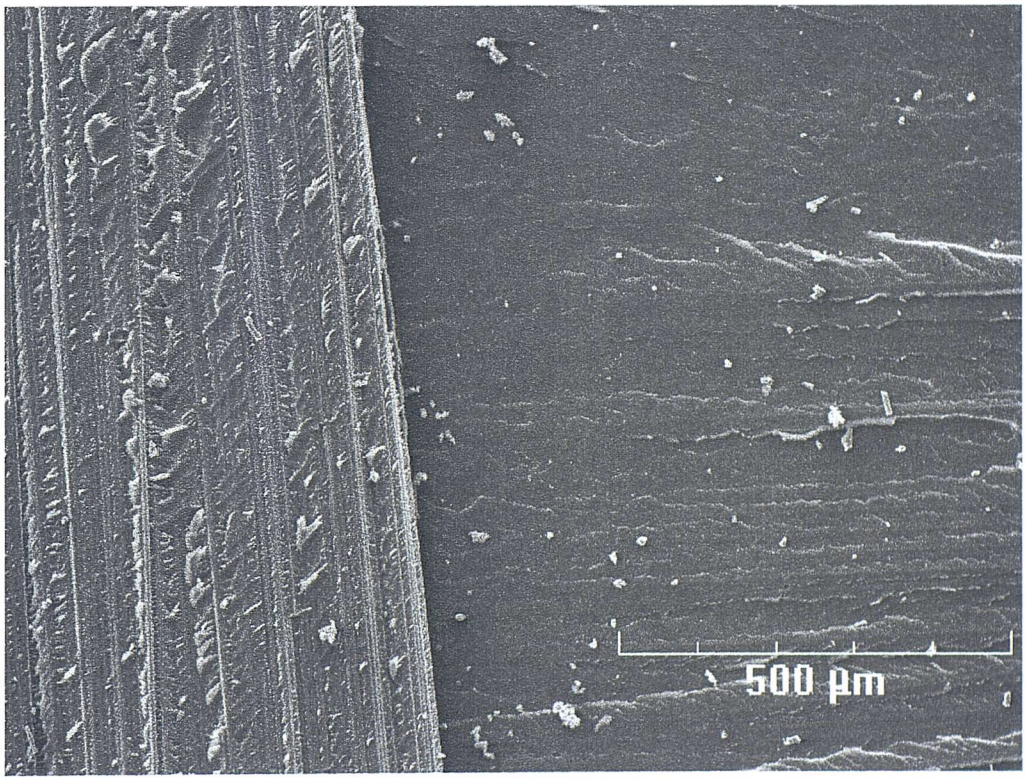


Figure 5.2.13. Fracture surface of a CFRP sample with a tetrafunctional epoxy matrix containing 8 wt. % CTBN (crack propagation from *right to left*).

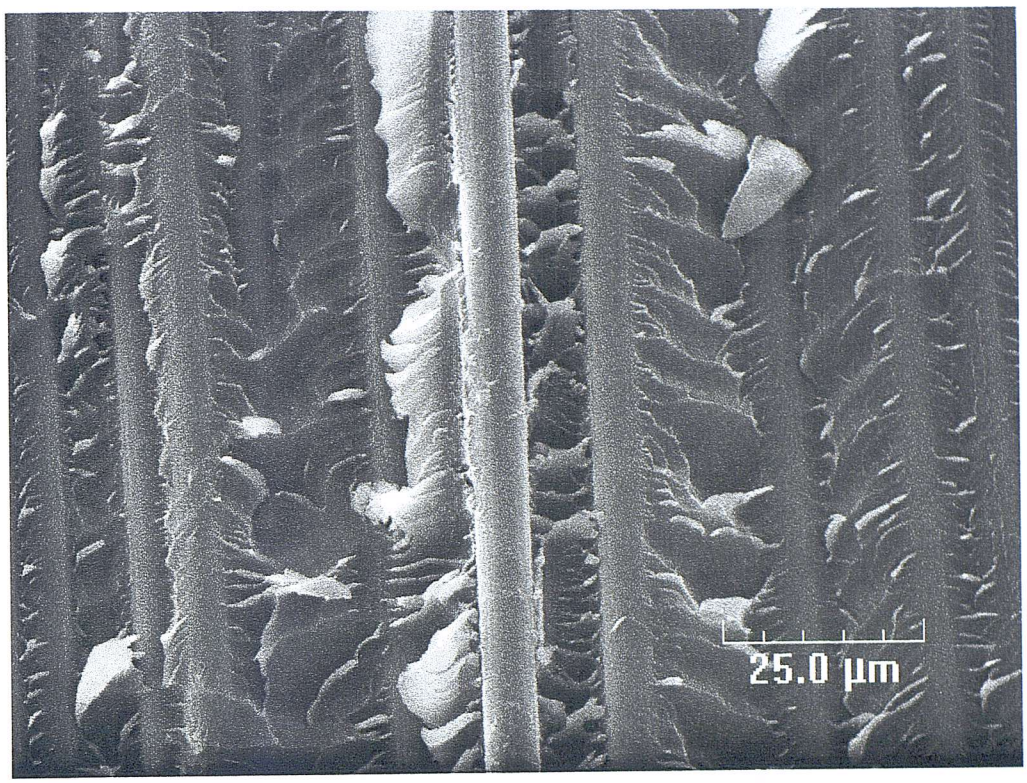


Figure 5.2.14. Fracture surface of a CFRP sample with a tetrafunctional epoxy matrix containing 8 wt. % CTBN at higher magnification (crack propagation from *right to left*).

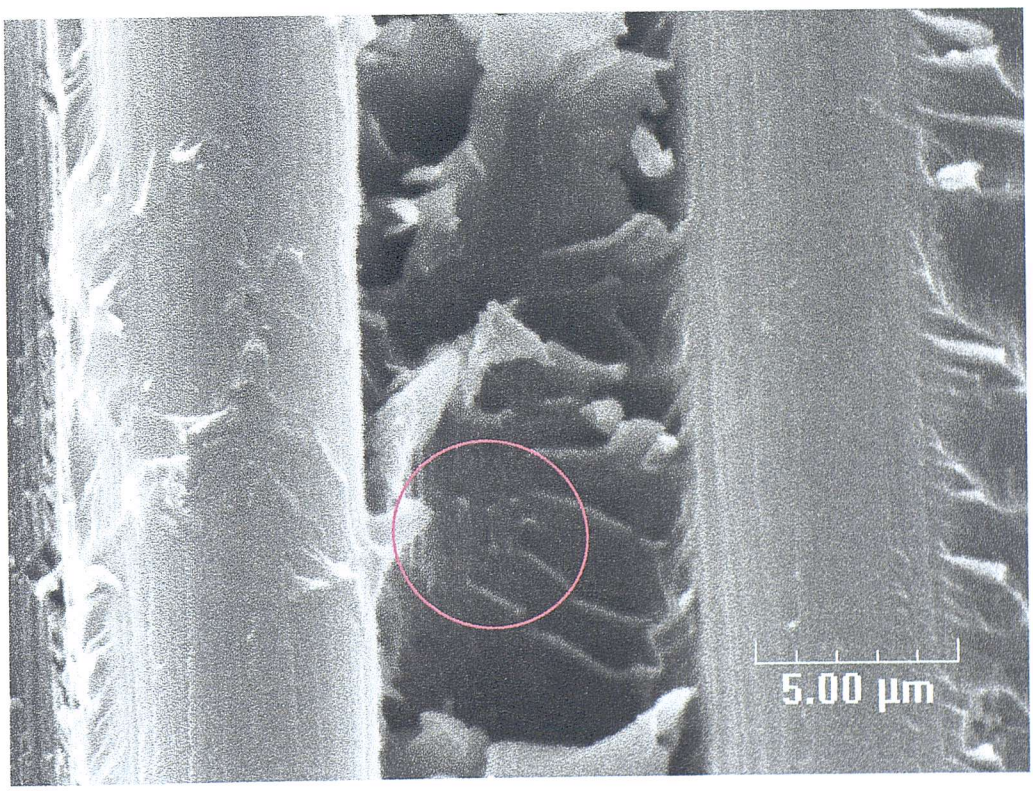


Figure 5.2.15. Fracture surface of a CFRP sample with a tetrafunctional epoxy matrix containing 8 wt. % CTBN at higher magnification (crack propagation from *right to left*. Cavitated rubber particles circled in pink).

5.2.3.4 Hybrid Modified Epoxies

The micrographs in Figure 5.2.16 and Figure 5.2.17 are of a laminate with a hybrid matrix toughened with 8 wt. % CTBN and 10 wt. % nano-silica. The fibres are well bonded to the matrix, but there is less plastic deformation of the matrix than the previous 8 wt. % CTBN-only sample. Figure 5.2.18 shows that some cavitation of the rubber particles occurs (they appear as small holes of ~0.5μm in diameter), but the nano-silica particles are not visible at this magnification. The reduction in interlaminar fracture energy (relative to the CTBN-only sample) is because of the reduced plastic deformation of the matrix. It can be concluded that nano-silica at any wt. % in an amine-cured TGDMA-based matrix, used to make laminates with carbon fibres, does not increase the interlaminar fracture energy of the laminate.

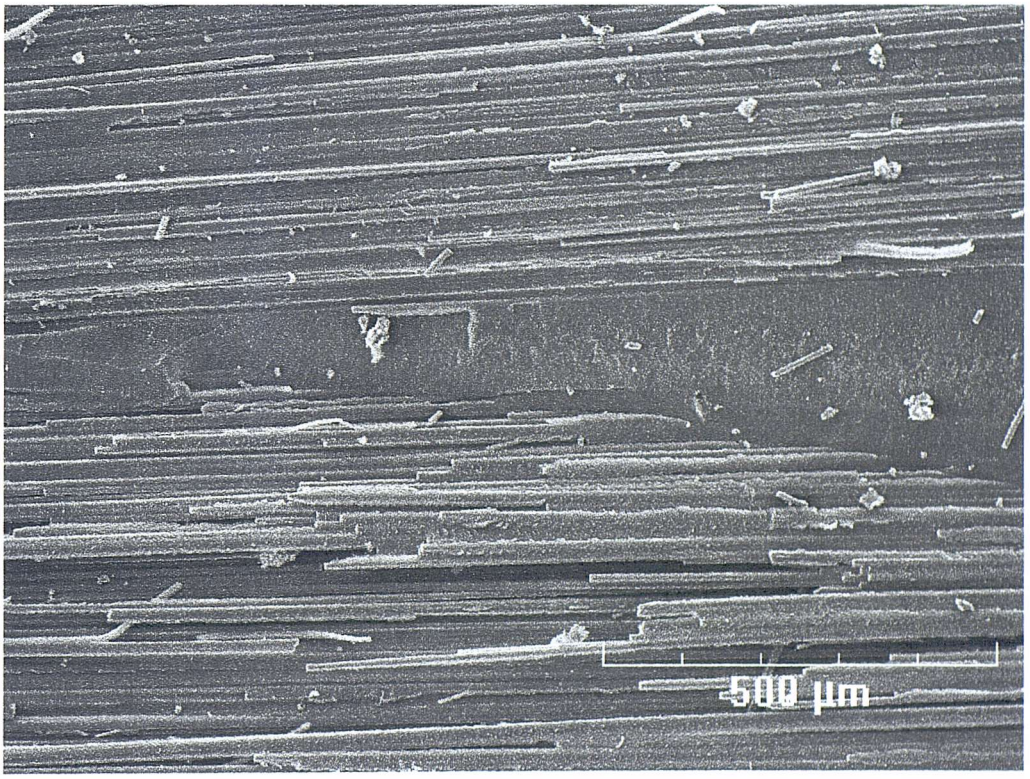


Figure 5.2.16. Fracture surface of a CFRP sample with a tetrafunctional epoxy matrix containing 8 wt. % CTBN and 10 wt. % nano-silica (crack propagation from *right to left*).

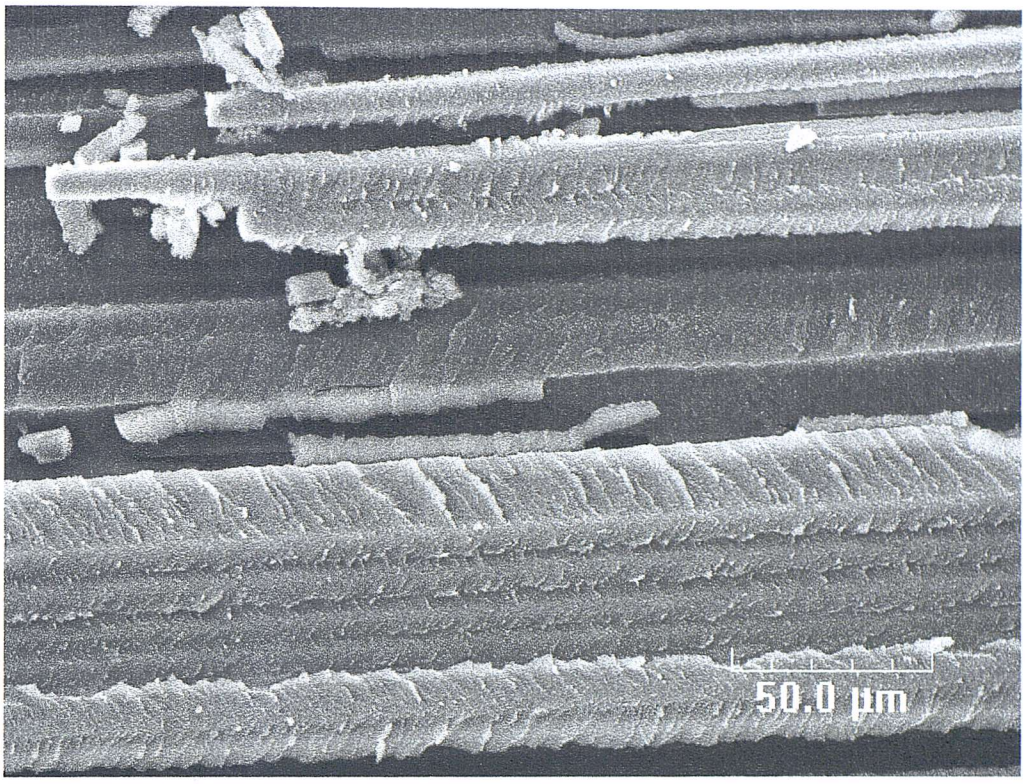


Figure 5.2.17. Fracture surface of a CFRP sample with a tetrafunctional epoxy matrix containing 8 wt. % CTBN and 10 wt. % nano-silica at higher magnification (crack propagation from *right to left*).

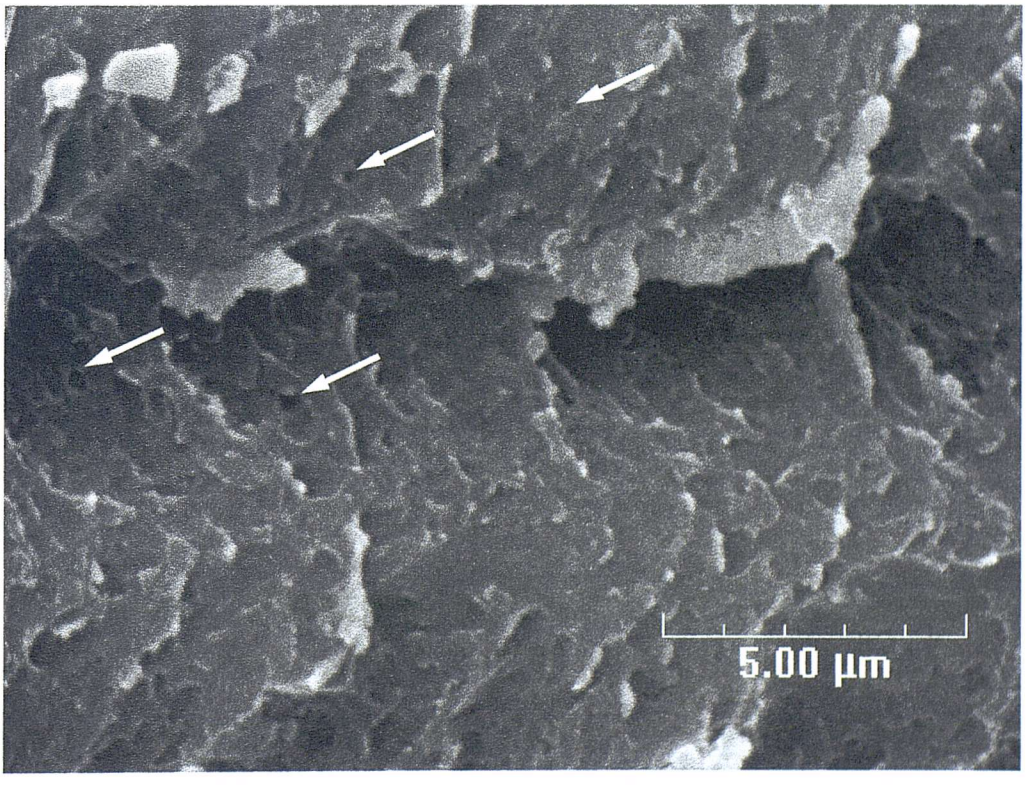


Figure 5.2.18. Fracture surface of a CFRP sample with a tetrafunctional epoxy matrix containing 8 wt. % CTBN and 10 wt. % nano-silica at higher magnification (crack propagation from *right to left*. White arrows point to some cavitated rubber particles).

5.2.3.5 Summary

It was found that the fracture surfaces of the CFRP laminates that were tested under Mode I conditions correlated well with the recorded interlaminar fracture energies. The laminates that had higher interlaminar fracture energies than the bulk epoxy were more fracture resistant because of the good adhesion between the fibres and the matrix requiring more energy for fibre debonding and pull-out. Conversely, even though some evidence of fibre-bridging was observed, the 5 and 10 wt. % nano-silica samples had very low interlaminar fracture energies because of the poor adhesion between the fibres and matrix, and the crack propagating through an epoxy rich layer. Generally however, there was good interfacial bonding between fibre and matrix, and cavitated rubber particles (which contributed to the relatively high interlaminar fracture energies of the samples containing CTBN) were visible in the micrographs.

5.3 Chapter Discussion

This Chapter has investigated the microstructure, mechanical properties and fracture of an amine-cured TGMDA-based bulk epoxy polymer that was toughened with both CTBN rubber and nano-silica particles. This bulk epoxy was used as the matrix for CFRP laminates reinforced with carbon fibres, and the material properties and fracture of these laminates were also explored.

Unlike both the amine-cured DGEBA-based system and the anhydride-cured DGEBA-based system, this TGMDA-based system is not normally used in its bulk form, but is usually used as a matrix in laminates [150,151]. Therefore it is of paramount importance to explore the nexus between the bulk and CFRP results. A summary of the mean values of all the material properties can be found in Table 5.3.1 for easy reference.

Table 5.3.1. Summary of all mean values for the material properties (bulk polymer and CFRPs) of the amine-cured TGMDA-based system.

wt. % CTBN	wt. % nano-silica	T_g (°C)	E_{bulk} (GPa)	K_{Ic} (MPa $m^{-1/2}$)	$G_{Ic\ bulk}$ (J/m^2)		$G_{Ic\ CFRP}$ (J/m^2)	E_{CFRP} (GPa)
0	0	250	3.25	0.80	176		764	30.2
0	5	253	3.48	0.98	253		300	30.3
0	10	241	3.50	1.14	336		299	30.8
0	19.5	247	4.15	0.84	154		733	31.9
8	0	244	3.06	1.49	640		1511	30.5
8	10	244	3.37	1.75	798		1012	31.3

The bulk epoxy polymer has a very high glass transition temperature, in the order of ~250°C. This high T_g makes it an attractive matrix for use in aerospace applications, since it can be used at higher working temperatures [104] than say, the amine or anhydride-cured DGEBA systems discussed in this Thesis. The addition of nano-silica to the epoxy did not alter the glass transition temperature. Even adding 8 wt. % CTBN only reduced the T_g to 244°C. It can be concluded that neither nano-silica nor CTBN has an adverse effect on the high-temperature application prospects of this system.

The addition of increasing amounts of rigid nano-silica particles linearly increased the stiffness of both the bulk and CFRP samples. The softer CTBN caused a reduction in stiffness, and this is the reason why rubber is not normally used in tetrafunctional systems [104]. However, the hybrid formulation had a higher bulk Young's modulus *and* a higher CFRP flexural modulus than the control samples. It can be concluded that the addition of nano-silica increases the stiffness of this system, and when used in conjunction with CTBN, restores any lost stiffness caused by the softer rubbery phase.

The fracture energy of the bulk epoxy polymer was statistically similar to that of the three formulations containing different nano-silica contents. The AFM images show that the samples containing 5 and 10 wt. % nano-silica have well dispersed nano-silica particles, whereas the sample with 19.5 wt. % nano-silica showed the particles to be agglomerated. These images agree well with the *mean* fracture energies because an increase in nano-silica up to 10 wt. % produced an increase in fracture energy, and the agglomeration of particles in the 19.5 wt. % sample had a smaller fracture energy (because the epoxy ligaments between particles were not large enough to plastically deform). This trend was not transferred to the CFRP laminates however, as can be seen in Figure 5.3.1. Indeed, CFRP laminates toughened with 5 and 10 wt. % nano-silica had a *lower* interlaminar fracture energy than the control, but was comparable to that of their respective bulk epoxy polymers, whereas the CFRP laminate with 19.5 wt. % had a comparable interlaminar fracture energy to that of the control laminate. The CFRP laminates with 5 and 10 wt. % nano-silica did not have very good fibre-matrix adhesion, and the crack propagated through an epoxy rich region. The sample with 19.5 wt. % nano-silica showed better fibre-matrix adhesion, and so more energy was needed for the fibres to debond and pull-out. This agrees well with the work of Kinloch and Taylor [83] who suggested that there was an optimum adhesion strength that would produce tough laminates.

The bulk epoxy polymer containing CTBN was four times as tough as the control, and this high toughness transferred well to its laminate (as shown in Figure 5.3.1), which had twice the interlaminar fracture energy of the control laminate. This was because of the good adhesion between the fibres and the matrix. When 10 wt. % nano-silica was added to the bulk sample with 8 wt. % CTBN, the toughness increased by 15%, but the interlaminar fracture energy of the laminate *decreased* by 30% due to limited plastic

deformation of the matrix. However, the mean fracture energy was still 50% *greater* than the control.

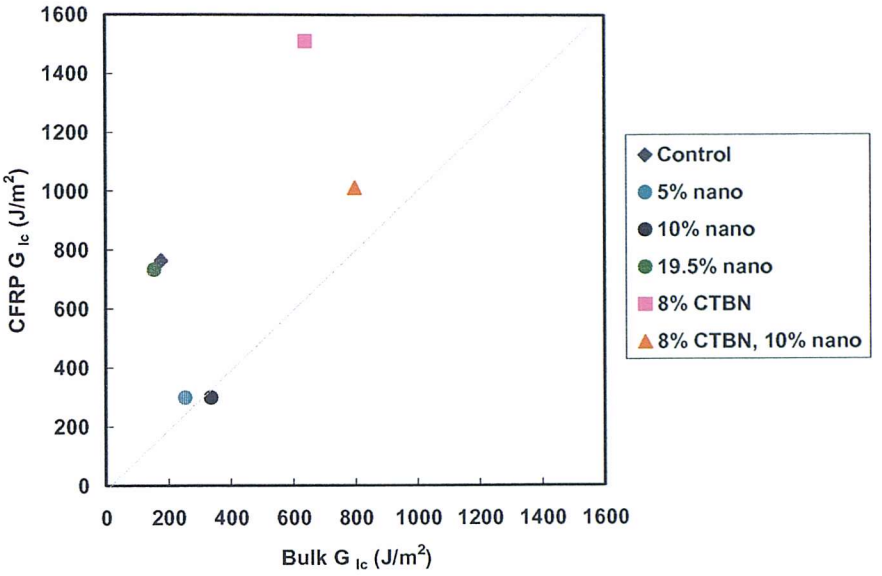


Figure 5.3.1. Comparison between the FRP and bulk fracture energies of the amine-cured TGMDA-based system. (Dashed line indicates the 1:1 relationship between the fracture energies of the CFRPs and bulk epoxy polymers [ie. the matrices])

5.4 Conclusions

This chapter has investigated the microstructure, mechanical properties and fracture of an amine-cured TGMDA-based bulk epoxy polymer that was toughened with CTBN rubber and nano-silica particles. It has also explored the toughness of laminates that were composed of carbon fibres using these bulk epoxy polymers as the matrices. Since bulk epoxies based upon this system is not presently being used commercially, only the main conclusions about the FRPs will be stated.

It can be concluded from this study that a hybrid laminate with 8 wt. % CTBN and 10 wt. % nano-silica has:

- a comparable glass transition temperature to the control (ie. the laminate with an unmodified epoxy matrix).
- a higher flexural modulus than the control.
- a higher fracture energy than the control.

This study has shown that whilst laminates based upon this system, toughened with CTBN rubber, have not previously been used commercially because of the reduction in stiffness, the addition of nano-silica (ie. to form a hybrid) can yield a laminate that has both high stiffness and very high fracture energy.

CHAPTER 6

RESULTS AND DISCUSSION: THE ANHYDRIDE-CURED DGEBA-BASED SYSTEM

6 Introduction

This Chapter investigates the microstructure, material properties and fracture of a DGEBA-based epoxy system that was cured using accelerated methyl hexahydropthalic acid anhydride, and has had combinations of both rubber and nano-silica particles added. The samples were cured for 1 hour at 90°C, followed by a post-cure of 2 hours at 160°C.

The results have been divided into those obtained from testing the bulk epoxy polymer (ie. this anhydride-cured DGEBA-based epoxy containing combinations of rubber and nano-silica particles), and the results obtained from testing the carbon fibre reinforced polymers (CFRPs) which used said bulk epoxy polymers as its matrix.

The section that discusses the bulk epoxy polymer has been divided into subsections which discuss the microstructure, the thermal and mechanical properties, and fracture surfaces. Each has a summary at the end, and there is a general discussion at the end of the section which reviews all the results and examines how each material property affects the others. A similar format is followed for the CFRP results, with a Chapter Discussion at the very end.

6.1 Bulk Epoxy Polymer Results

The samples investigated are summarised in Table 6.1.1 and it may be seen that an unmodified sample (the control) was compared to samples toughened with varying amounts of nano-silica (between 0 and ~20 wt. %), CTBN rubber (between 0 and 18 wt. %), and hybrid samples toughened with varying amounts of rubber and nano-silica. The microstructure was studied to see how the rubber and nano-silica particles were distributed, and a number of tests were performed on the samples to determine the thermal and mechanical properties of the bulk material. The fracture surfaces were then investigated to ascertain the fracture mechanisms. It should be noted that all tests were performed on cured samples.

Table 6.1.1. Summary of all the anhydride-cured DGEBA-based samples investigated.

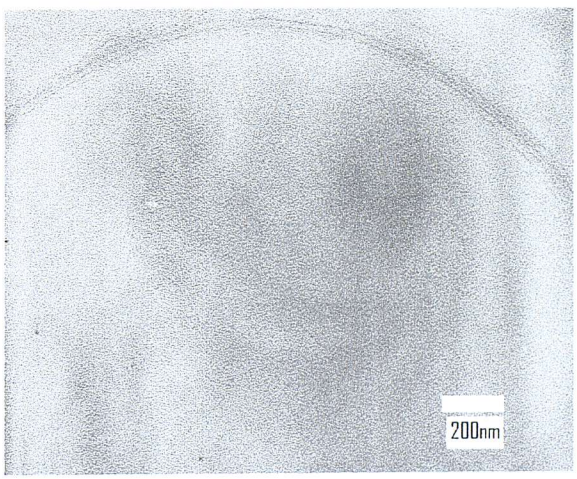
wt. % CTBN	wt. % nano-silica
0	0
0	4
0	7.8
0	11.1
0	14.8
0	20.2
6	0
5.17	2.59
5.03	5.03
9	0
9	2.3
9	4.5
9	9
9	10.5
9	15.4
12	6
12	12
18	0
18	9
18	18

6.1.1 Microstructure

A transmission electron microscope (TEM) was used to view microtomed slices of the cured bulk samples under high magnification. The aim was to observe how the nano-silica and rubber particles were dispersed in the epoxy, as well as relative to each other. An atomic force microscope (AFM) was used to give further information about the microstructure, including height and phase imaging. It has been shown that AFM and TEM images are interchangeable [127,128], so for some samples either type of image is shown.

6.1.1.1 Unmodified Epoxy

The transmission electron micrograph shown in Figure 6.1.1 (a) is for a control sample of unmodified epoxy. The arc-like feature is from the copper grid, and the swirl-like feature is an artefact, and both can be ignored. This control sample is featureless otherwise, which is expected for a homogenous thermosetting polymer. The AFM image in Figure 6.1.1 (b) also shows a barren surface.

(a) 

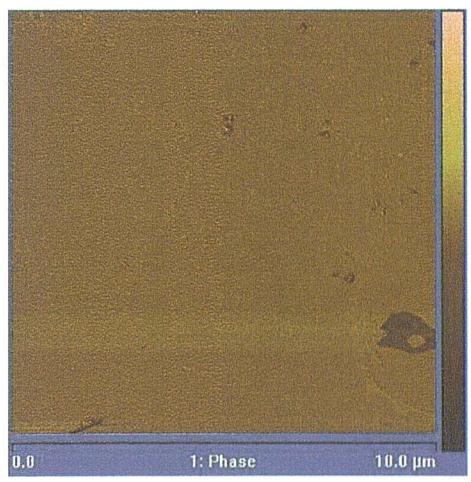
(b) 

Figure 6.1.1. (a) Transmission electron micrograph of a sample containing unmodified epoxy (b) AFM image of a sample containing unmodified epoxy.

6.1.1.2 Nano-silica Modified Epoxy

The TEM micrograph in Figure 6.1.2 is of a sample containing 5 wt. % nano-silica. It shows the silica particles being well-dispersed spheres of approximately 20nm in diameter.

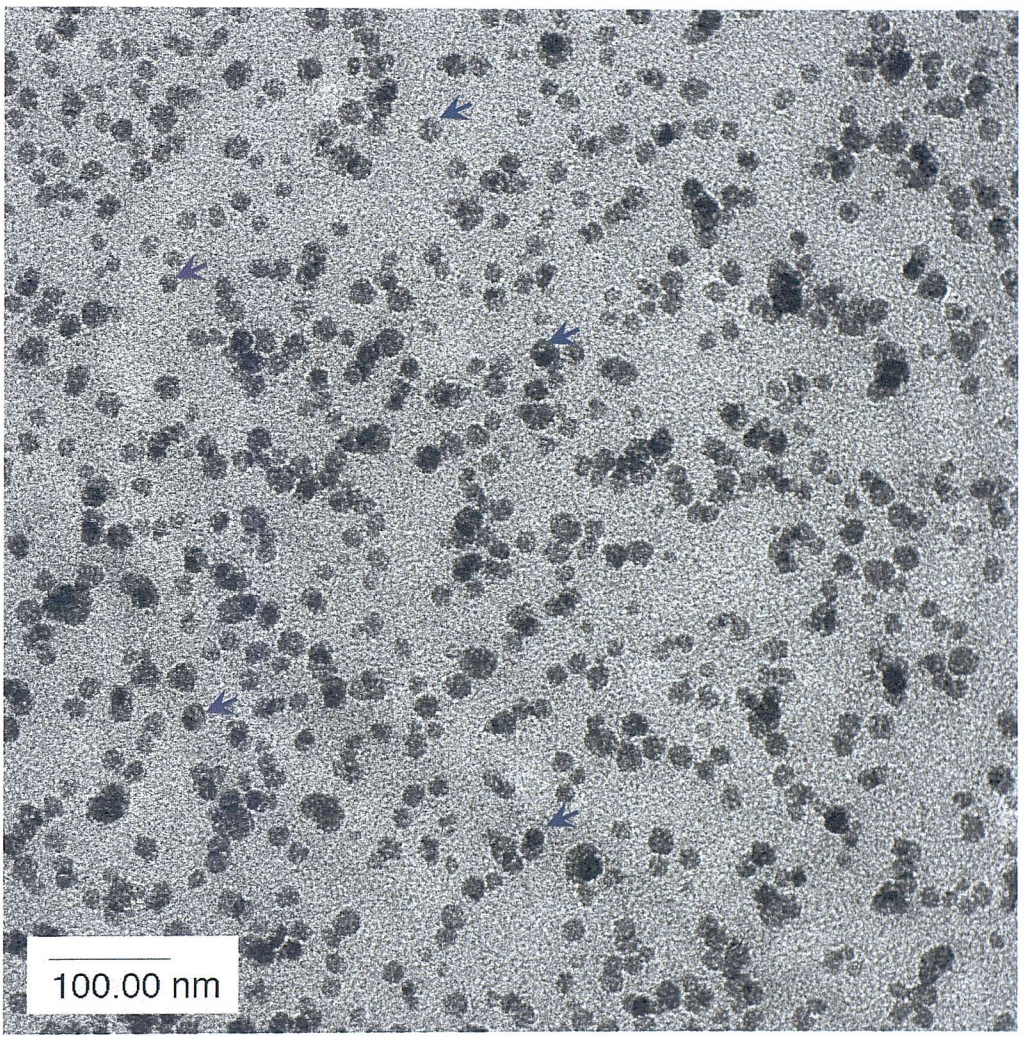


Figure 6.1.2. Transmission electron micrograph of a sample containing 5 wt. % nano-silica. (Blue arrows point to some nano particles)

The micrograph shown in Figure 6.1.3 is of a sample containing 14.8 wt. % nano-silica and clearly shows the nano-silica particles being well distributed throughout the epoxy as small clusters. The AFM image in Figure 6.1.4 shows the nano particles as being well-dispersed *single* particles. This is because the small clusters seen in the TEM image are nano-silica particles stacked on top each other in three dimensions, due to their diameters being 20nm and the microtomed slices being about 100nm thick. The AFM, however, only examines the surface. This shows that nano-silica remains well

dispersed in an anhydride-cured DGEBA epoxy, even when relatively high amounts of nano-silica are added. Good dispersion of nano-silica in anhydride-cured epoxies, even at high nano-silica contents, has been reported before [167].

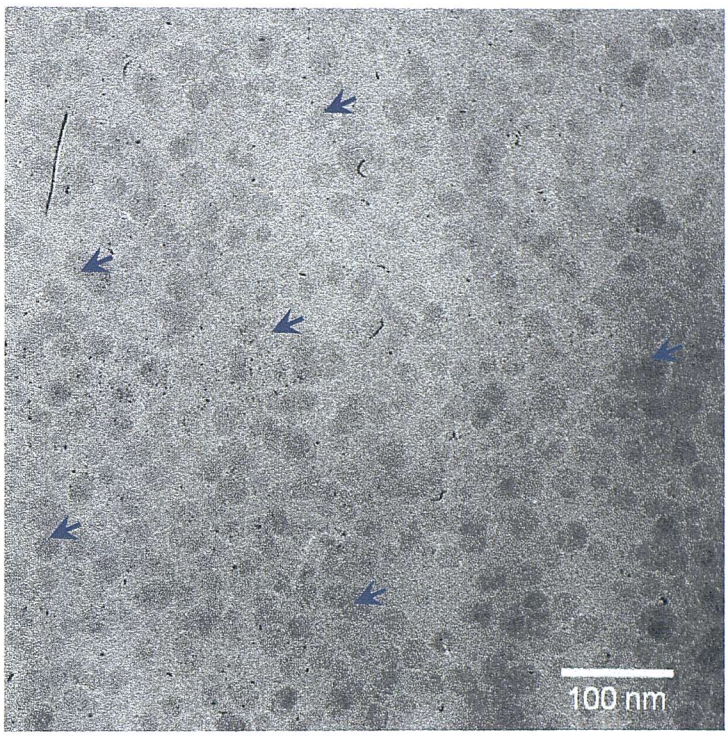


Figure 6.1.3. Transmission electron micrograph of a sample containing 14.8 wt. % nano-silica. (Blue arrows point to some nano particles.)

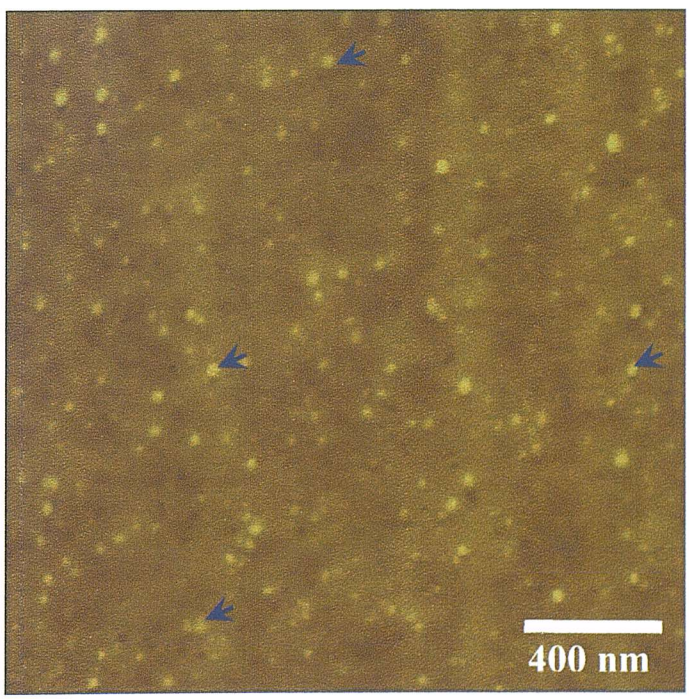


Figure 6.1.4. AFM image of a sample containing 14.8 wt. % nano-silica. (Blue arrows point to some nano particles.)

6.1.1.3 Rubber Modified Epoxy

The microtomed slices containing CTBN were stained with osmium tetroxide to make the CTBN particles visible (ie. under a TEM) as shown in the subsequent micrographs. The micrograph in Figure 6.1.5 is for a sample containing 9 wt. % CTBN and like the AFM image in Figure 6.1.6, clearly shows the phase separated rubber particles. The rubber particles are between 1 and 2μm in diameter. It has been shown in previous work that CTBN particles are between 0.1 to 5μm in diameter [75,125], so the particles in these samples compare well. The circles in the TEM micrograph are from the copper grid that the slices were placed on before being put into the microscope, and should be ignored. The rubber particles are oval-shaped in the TEM image, but are round in the AFM image. This is because the TEM slice was not microtomed at a sufficiently low temperature, and as a result the rubber particles were slightly compressed during cutting by the diamond knife of the microtome. Volume fraction analysis of these images show that ~4.5 wt. CTBN (ie. ~50%) phase separated into rubber particles.

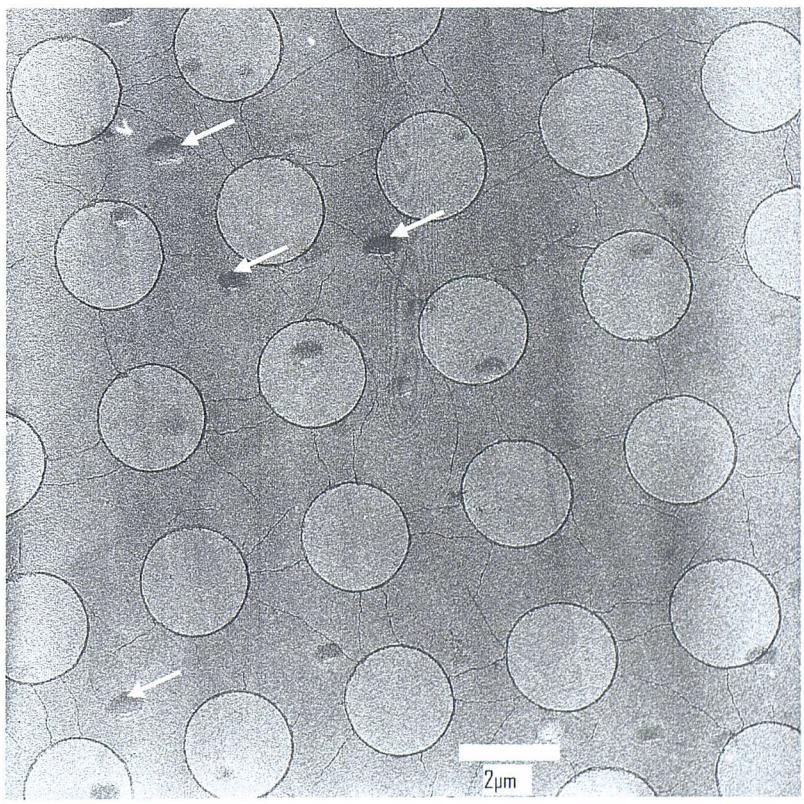


Figure 6.1.5. Transmission electron micrograph of a stained sample containing 9 wt. % CTBN. (White arrows point to some rubber particles. Ignore circular grid.)

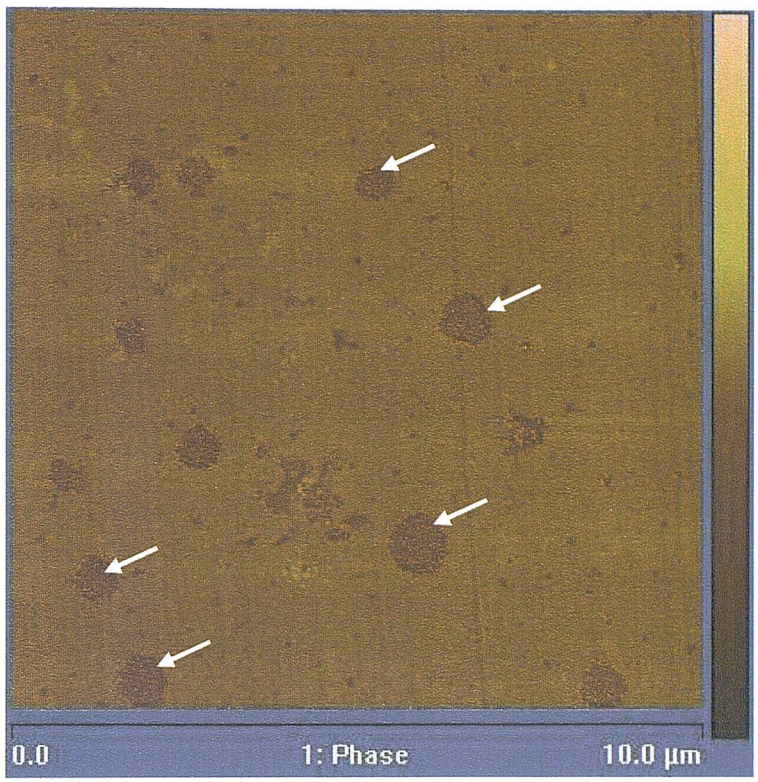


Figure 6.1.6. AFM image of a sample containing 9 wt. % CTBN. (White arrows point to some rubber particles.)

The micrograph in Figure 6.1.7 is of a stained sample containing 18 wt. % CTBN only. The well-dispersed phase separated rubber particles of up to 1µm are clearly visible. Volume fraction analysis showed that ~4.5 wt. % CTBN (ie. ~25%) phase separated into particles. It is evident that with increasing rubber contents, increasing amounts of rubber remained in solution in the epoxy phase.

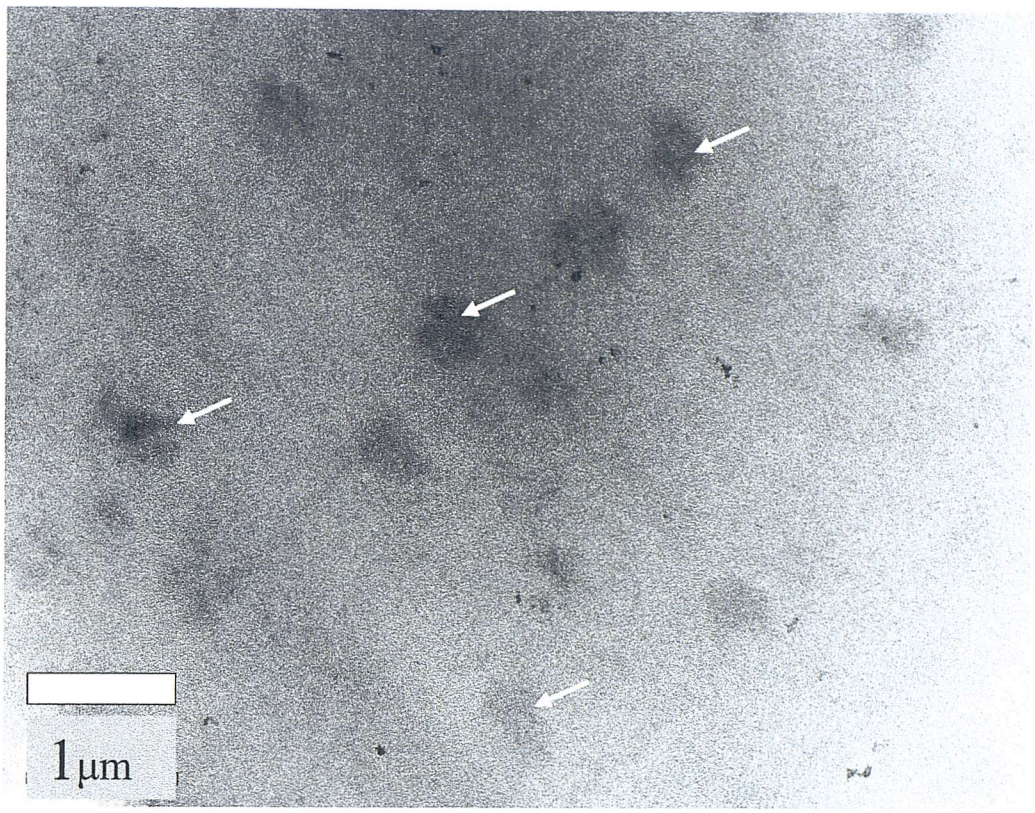


Figure 6.1.7. Transmission electron micrograph of a sample containing 18 wt. % CTBN. (White arrows point to some rubber particles.)

6.1.1.4 Hybrid Modified Epoxy

The micrograph in Figure 6.1.8 is of a sample containing 5.03 wt. % CTBN and 5.03 wt. % nano-silica. It was microtomed at room temperature which is why the CTBN was compressed during cutting, and appears to be oval-shaped. The bright white oval is a hole that was left when a rubber particle was removed during microtoming. It can be seen however, that the 20nm diameter nano-particles remain well dispersed in the epoxy and the rubber particles are well-dispersed and up to 1μm in diameter (ie. the same size as in the previous CTBN-only samples containing 9 and 18 wt. % CTBN). It should be noted that there was an insufficient number of microstructure images for any of the hybrid samples to perform accurate volume fraction analyses. Indeed, the only reliable indication of the extent of rubber phase separation is from the glass transition temperature data, which can be found in Section 6.1.2.1.

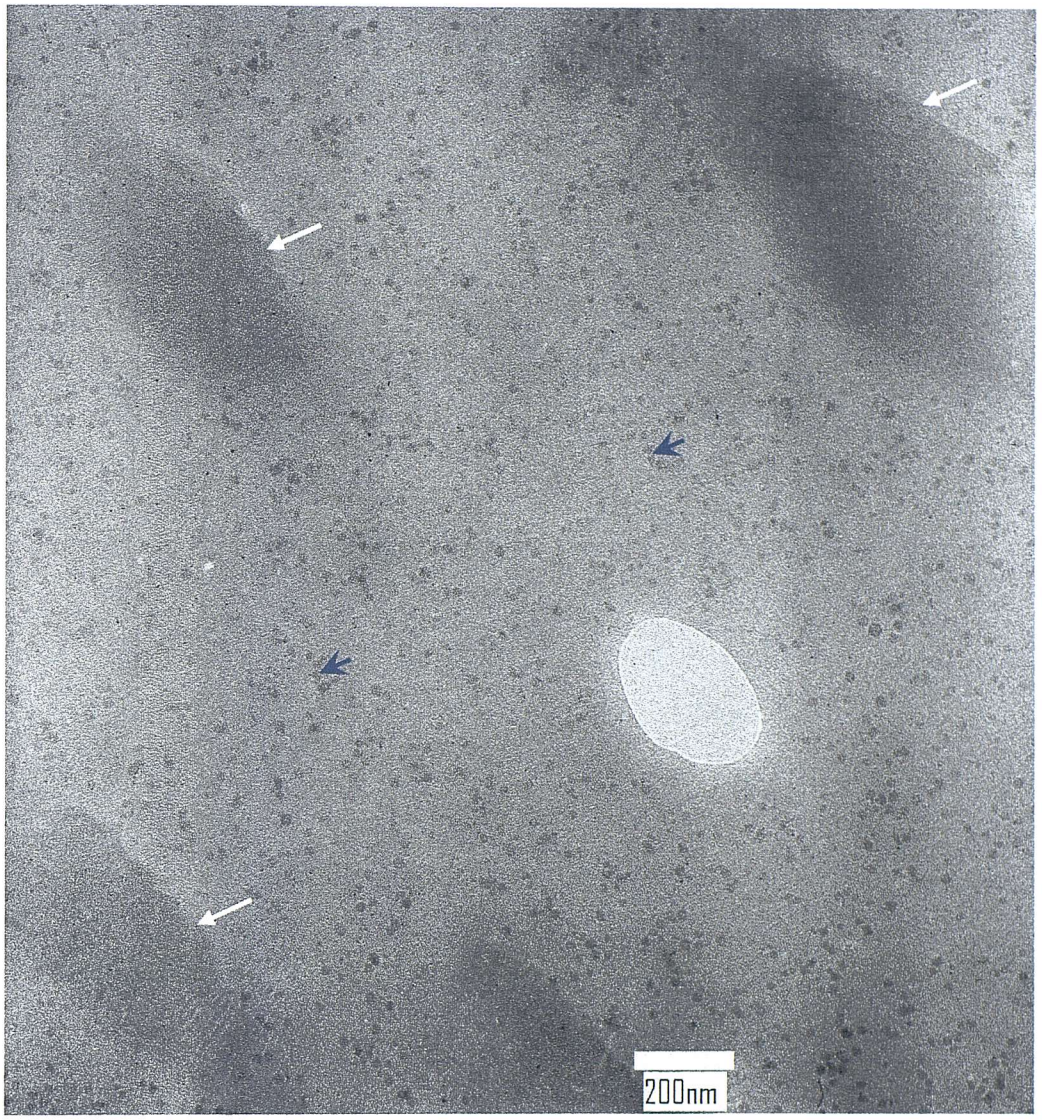


Figure 6.1.8. Transmission electron micrograph of a sample containing 5.03 wt. % CTBN and 5.03 wt. % nano-silica. (White arrows point to some rubber particles and blue arrows point to some nano particles.)

The micrographs in Figure 6.1.9 are for a sample containing 9 wt. % CTBN and 2.3 wt. % nano-silica. Unlike the previous hybrid sample (ie. containing 5.03 wt. % CTBN and 5.03 wt. % nano-silica), the nano-silica particles in this present sample are no longer well dispersed, single particles, but are agglomerated into three-dimensional necklace-like features of up to 2μm in length and 0.1μm in width. These features, however, are well dispersed throughout the sample. The rubber particle size, shape and distribution remain unchanged compared to all the previous samples.

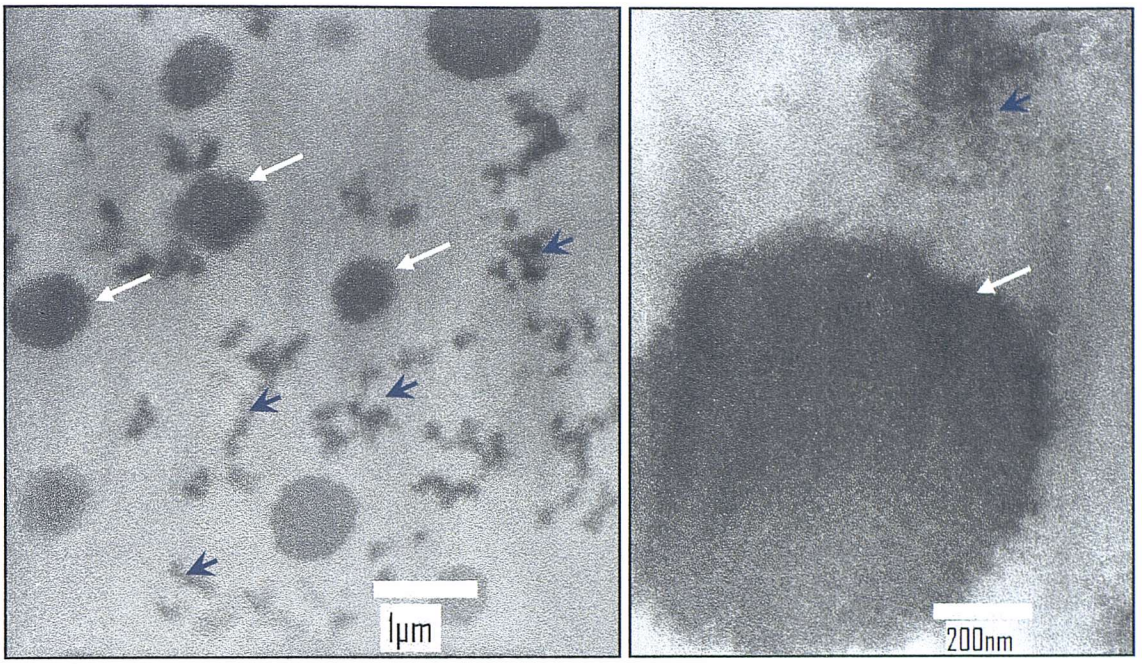


Figure 6.1.9. Transmission electron micrographs of a sample containing 9 wt. % CTBN and 2.3 wt. % nano-silica. (White arrows point to some rubber particles and blue arrows point to some nano-silica agglomerates.)

The AFM image in Figure 6.1.10 is of a sample containing 9 wt. % CTBN and 10.5 wt. % nano-silica. Both the phase and height images are shown, since neither image on its own was able to clearly show both the rubber and nano-silica morphology. The rubber particles are up to 1μm in diameter, and the nano-silica particles coalesce into well dispersed three-dimensional necklace-like features of up to 2μm in length and 0.1μm in width.

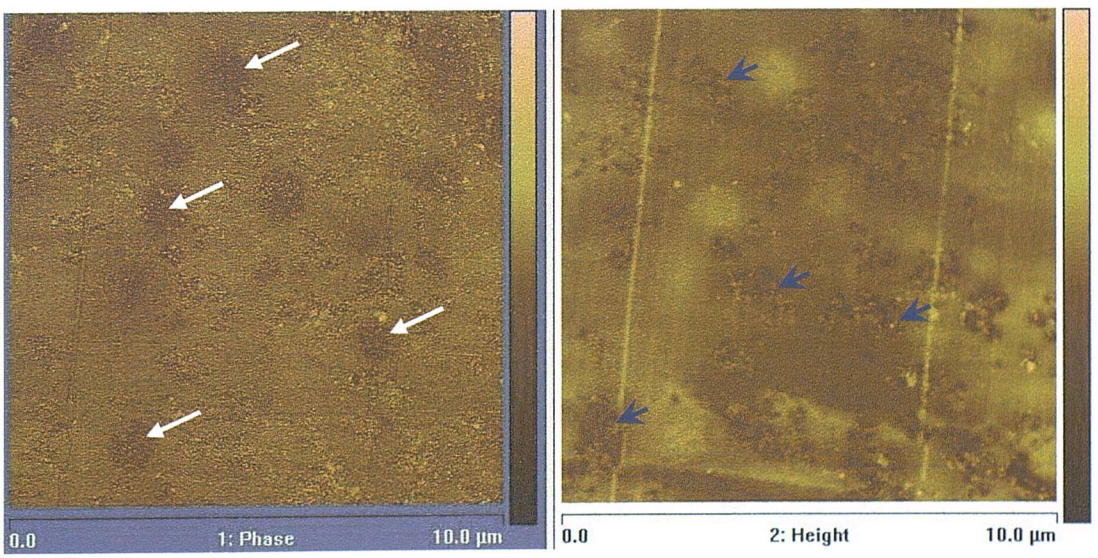


Figure 6.1.10. AFM image of a sample containing 9 wt. % CTBN and 10.5 wt. % nano-silica. (White arrows point to some rubber particles and blue arrows point to some nano-silica agglomerates.)

The micrograph in Figure 6.1.11 is for a sample containing 9 wt. % CTBN and 15.4 wt. % nano-silica. The nano particles coalesce into larger three-dimensional necklace-like structures than the previous sample by virtue of there being more nano particles present. The chains are up to 3μm in length and 0.5μm in width. The swirls indicated by the green arrows are artefacts that were acquired when scanning the TEM film-negative, and are to be ignored. The AFM image in Figure 6.1.12 confirms this microstructure.

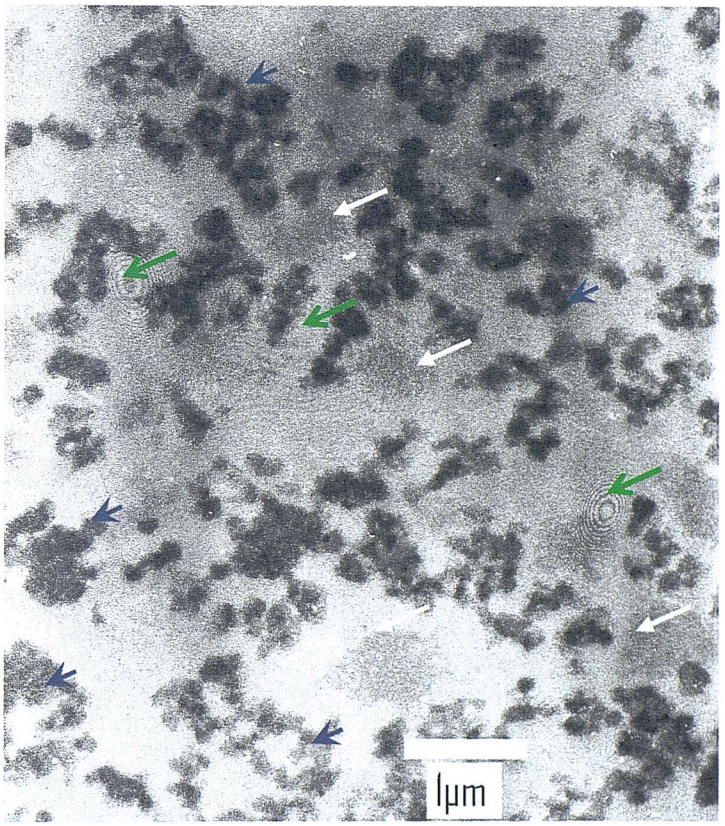


Figure 6.1.11. Transmission electron micrograph of a sample containing 9 wt. % CTBN and 15.4 wt. % nano-silica. (White arrows point to some rubber particles, blue arrows point to some nano-silica agglomerates and green arrows point to scanning artefacts.)

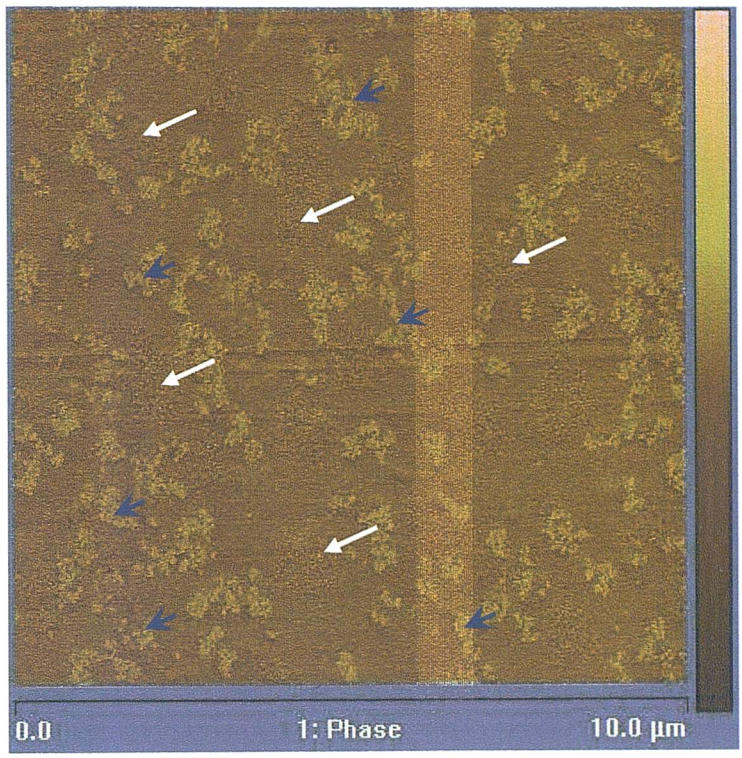


Figure 6.1.12. AFM image of a sample containing 9 wt. % CTBN and 15.4 wt. % nano-silica. (White arrows point to some rubber particles, blue arrows point to some nano-silica agglomerates.)

The following micrograph in Figure 6.1.13 is of a sample containing 12 wt. % CTBN and 12 wt. % nano-silica. A visual inspection suggests that whilst the rubber particles are about the same size as in the previous samples, less rubber particles have phase separated in this sample compared to the previous hybrid samples containing 9 wt. % CTBN. The nano particles are agglomerated and these well distributed agglomerates are ~2µm in length and ~0.4µm in width.

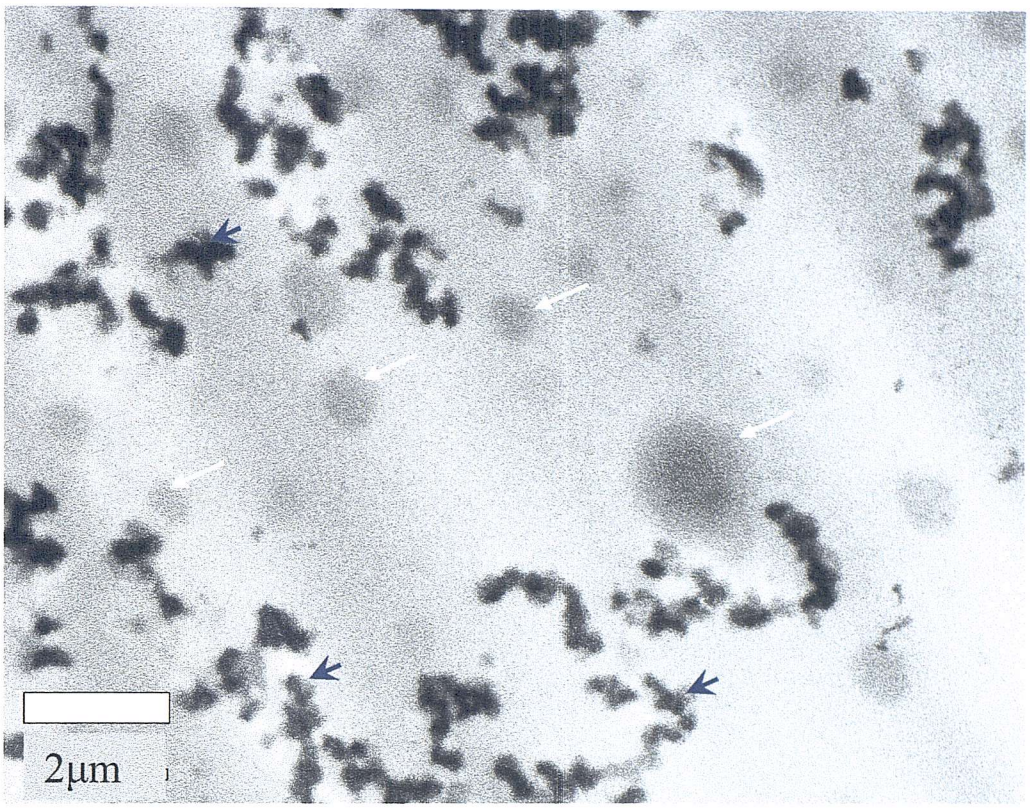


Figure 6.1.13. Transmission electron micrograph for a sample containing 12 wt. % CTBN and 12 wt. % nano-silica. (White arrows point to some rubber particles, blue arrows point to some nano-silica agglomerates.)

The following micrographs in Figure 6.1.14 and Figure 6.1.15 are for samples containing 18 wt. % CTBN and 9 and 18 wt. % nano-silica respectively. Both images show well distributed three-dimensional necklace-like chains of nano-silica up to 3μm in length and 0.5μm in width. Although these samples were stained using the same chemicals and staining regime as the previous samples, the rubber particles are imperceptible. The micrograph for the 18 wt. % CTBN-only sample in Figure 6.1.7 clearly shows the phase separated rubber particles. This suggests that the presence of nano particles in a sample containing 18 wt. % CTBN suppresses the phase separation of rubber particles from the epoxy, by changing the cure kinetics [134].

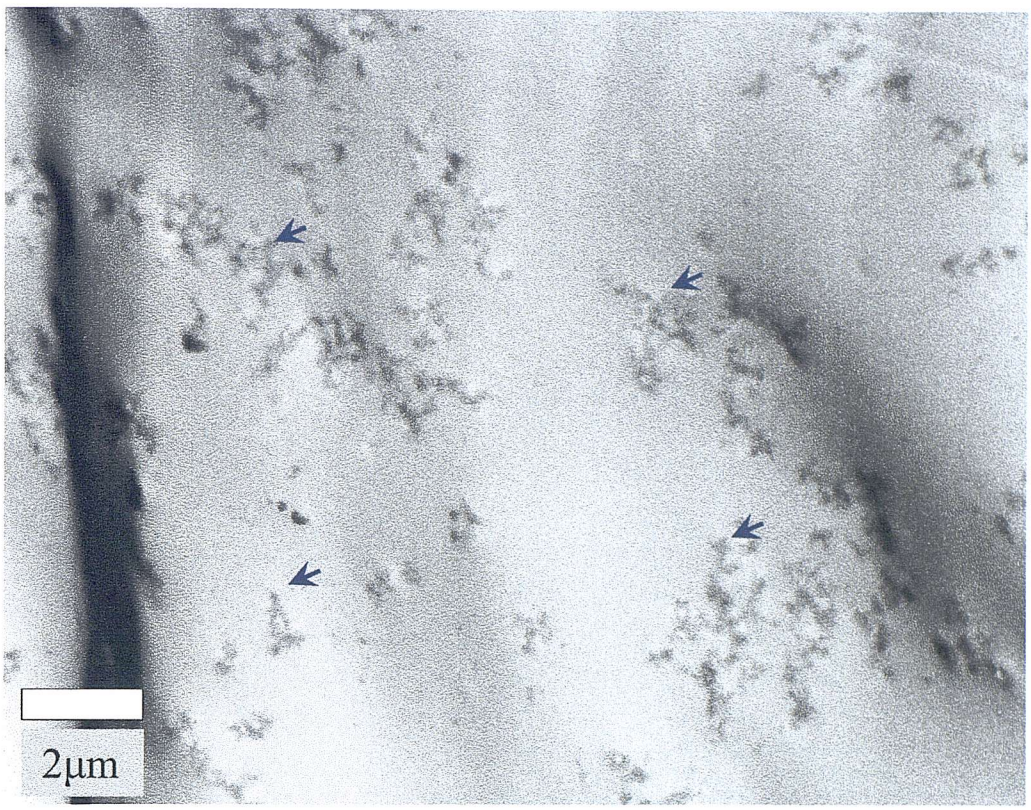


Figure 6.1.14. Transmission electron micrograph for a sample containing 18 wt. % CTBN and 9 wt. % nano-silica. (Blue arrows point to some nano-silica agglomerates.)

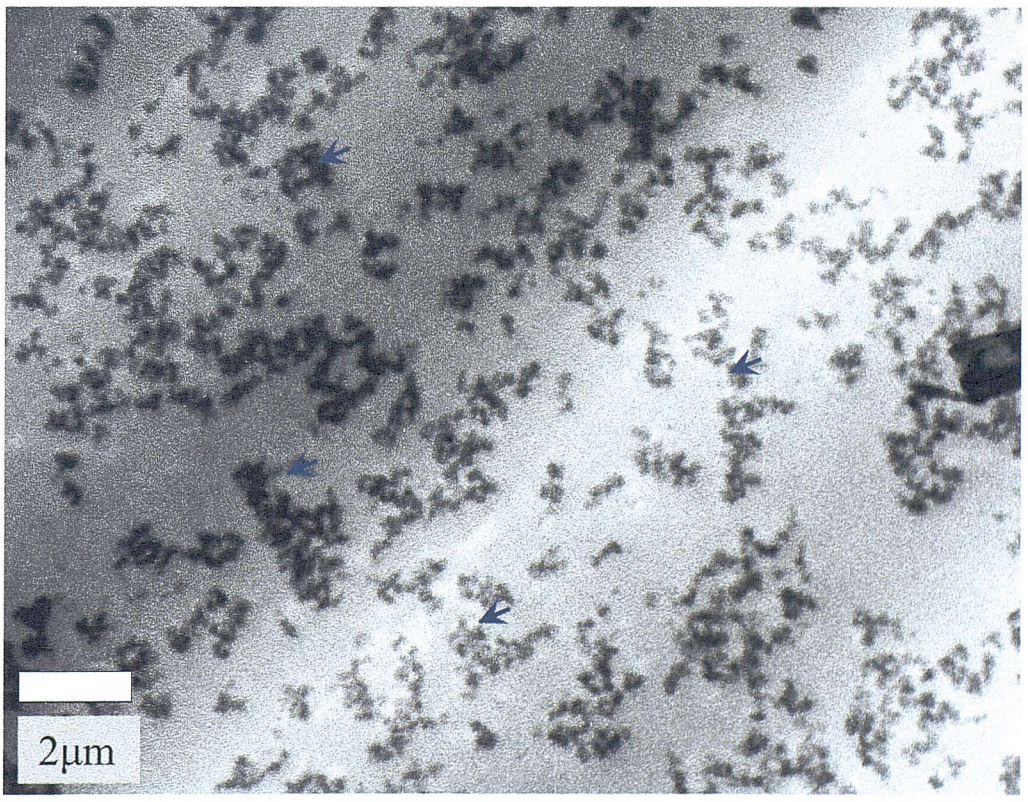


Figure 6.1.15. Transmission electron micrograph for a sample containing 18 wt. % CTBN and 18 wt. % nano-silica. (Blue arrows point to some nano-silica agglomerates.)

However, the AFM image for a sample containing 18 wt. % CTBN and 18 wt. % nano-silica in Figure 6.1.16 suggests that although the CTBN is well distributed in the epoxy, it has not phase separated into spherical rubber particles. It is possible that the rubber particles are undetectable in the stained TEM samples because the CTBN is evenly distributed in the epoxy at an insufficient localised concentration to appear as dark patches [168,169]. It has been reported by Lin *et al.* [169] that all the rubber can remain in the epoxy phase at high CTBN contents, which agrees well with what is observed in the hybrid samples with 18 wt. % CTBN. The nano-silica has changed the cure kinetics of this system [134].

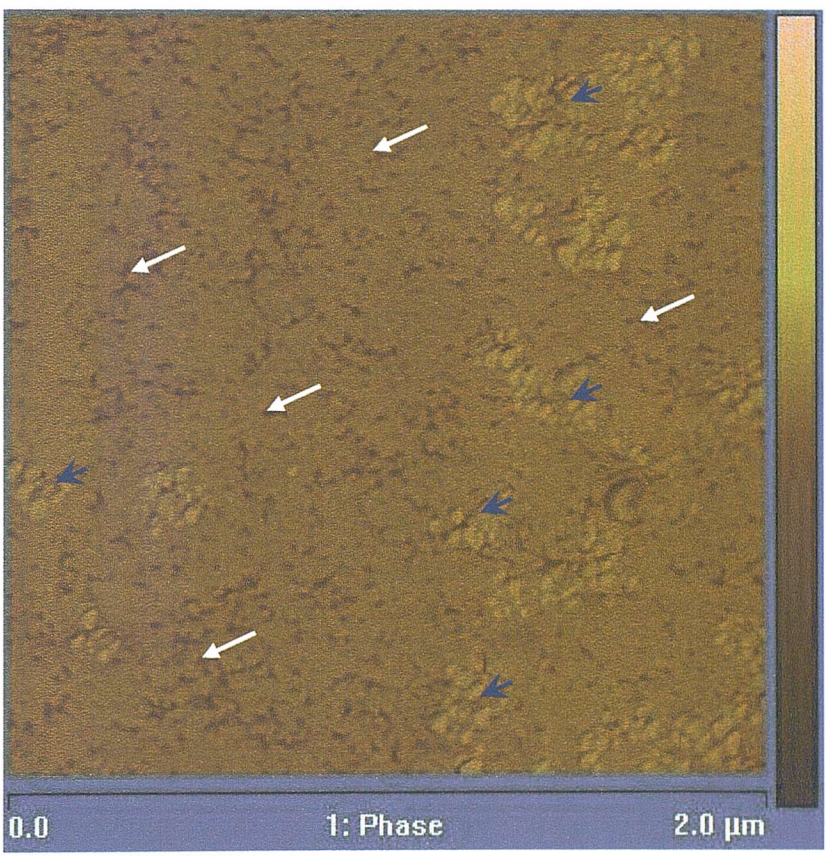


Figure 6.1.16. AFM image for a sample containing 18 wt. % CTBN and 18 wt. % nano-silica. (Blue arrows point to some nano-silica agglomerates, white arrows point to possible CTBN particles)

6.1.1.5 Summary

AFM and TEM images were both used to investigate the microstructure of the anhydride-cured DGEBA bulk epoxy polymer samples, and both gave excellent images. The microstructure of the different samples is summarised in Table 6.1.2.

Table 6.1.2. Summary of the rubber and nano-silica morphology in the anhydride-cured DGEBA-based bulk epoxy polymers. (NA = Not Applicable)

wt. % CTBN	wt. % nano-silica	Rubber Microstructure	Nano-silica Microstructure
0	0	NA	NA
0	5	NA	Well-dispersed spherical single particles, Ø20nm
0	14.8	NA	Well-dispersed spherical single particles, Ø20nm
5.03	5.03	Well dispersed rubber spheres, Ø 0.4-1μm	Well-dispersed spherical single particles, Ø20nm
9	0	Well dispersed rubber spheres, Ø 0.4-1μm	NA
9	2.3	Well dispersed rubber spheres, Ø 0.4-1μm	Necklace-like chains of up to 2μm x 0.1μm in size
9	10.5	Well dispersed rubber spheres, Ø 0.4-1μm	Necklace-like chains of up to 2μm x 0.1μm in size
9	15.4	Well dispersed rubber spheres, Ø 0.4-1μm	Necklace-like chains of up to 3μm x 0.5μm in size
12	12	Well dispersed rubber spheres, Ø 0.4-1μm	Necklace-like chains of up to 2μm x 0.4μm in size
18	0	Well dispersed rubber spheres, Ø 0.4-1μm	NA
18	9	Rubber remained in solution in the epoxy phase	Necklace-like chains of up to 3μm x 0.5μm in size
18	18	Rubber remained in solution in the epoxy phase	Necklace-like chains of up to 3μm x 0.5μm in size

6.1.2 Thermal and Mechanical Properties

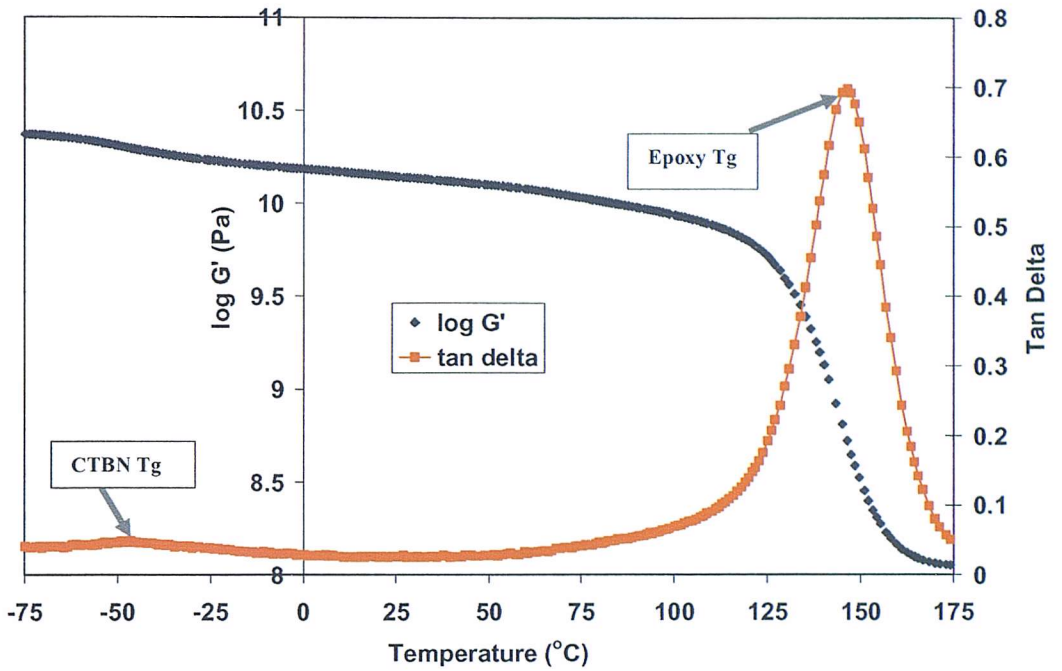
This section investigates the thermal and mechanical properties of the bulk epoxy polymers where the results from dynamic mechanical thermal analysis (DMTA), tensile tests and single edge notch bend tests are reported.

6.1.2.1 Glass transition temperature test results

The glass transition temperature (T_g) values were determined by performing dynamic mechanical thermal analysis (DMTA). A sample DMTA trace is shown in Figure 6.1.17 (a), with *tan* δ data for a test frequency of 1Hz, and the logarithm (base 10) of the loss

modulus, *G'*. The *tan δ* graph clearly shows the epoxy peak (indicating the T_g of the epoxy) and smaller peak indicating the T_g of the CTBN. The smaller peak becomes more defined when the Y-axis scale is adjusted as shown in Figure 6.1.17 (b).

(a)



(b)

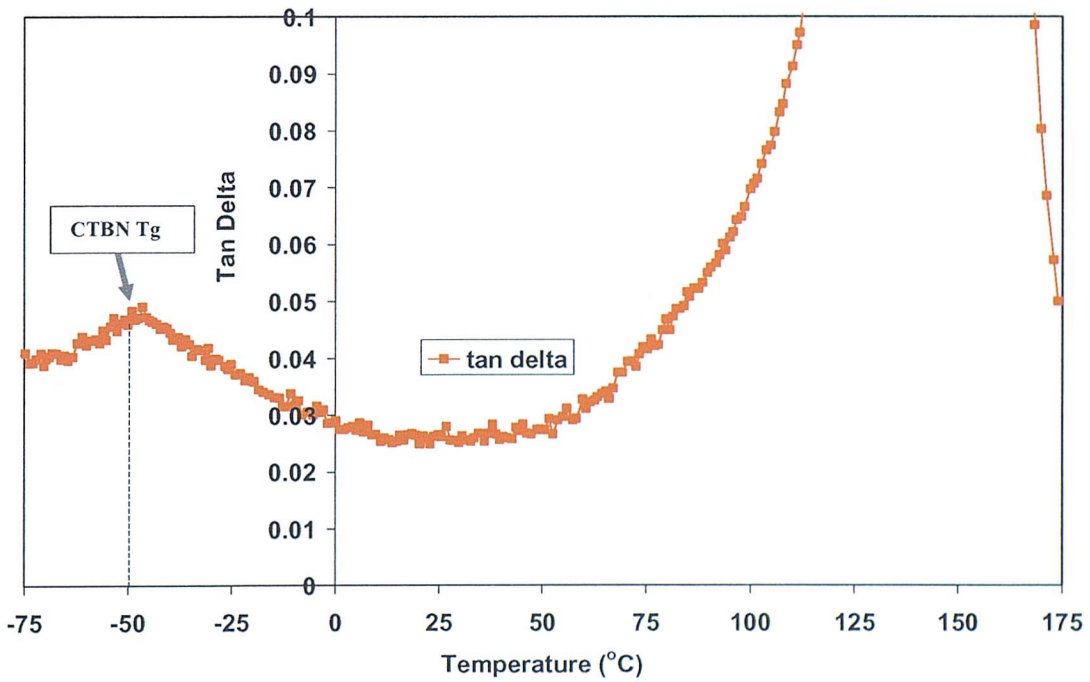


Figure 6.1.17. (a) Sample DMTA trace performed at 1Hz for a sample containing 9 wt. % CTBN and 10.5 wt. % nano-silica. (b) Trace of same sample with adjusted Y-axis showing the rubber peak more clearly.

It was found that the T_g of the CTBN was the same for all the samples (ie. ~ -50°C) and most of the samples containing CTBN showed a peak at around this temperature. This is a very similar glass transition temperature to what was reported in other publications on this grade of CTBN (ie. Hycar 1300x8) [134,135]. The epoxy glass transition results are shown in Figure 6.1.18, and the numerical values can be found in Table 6.1.3. Note that the error in each value is ±2°C.

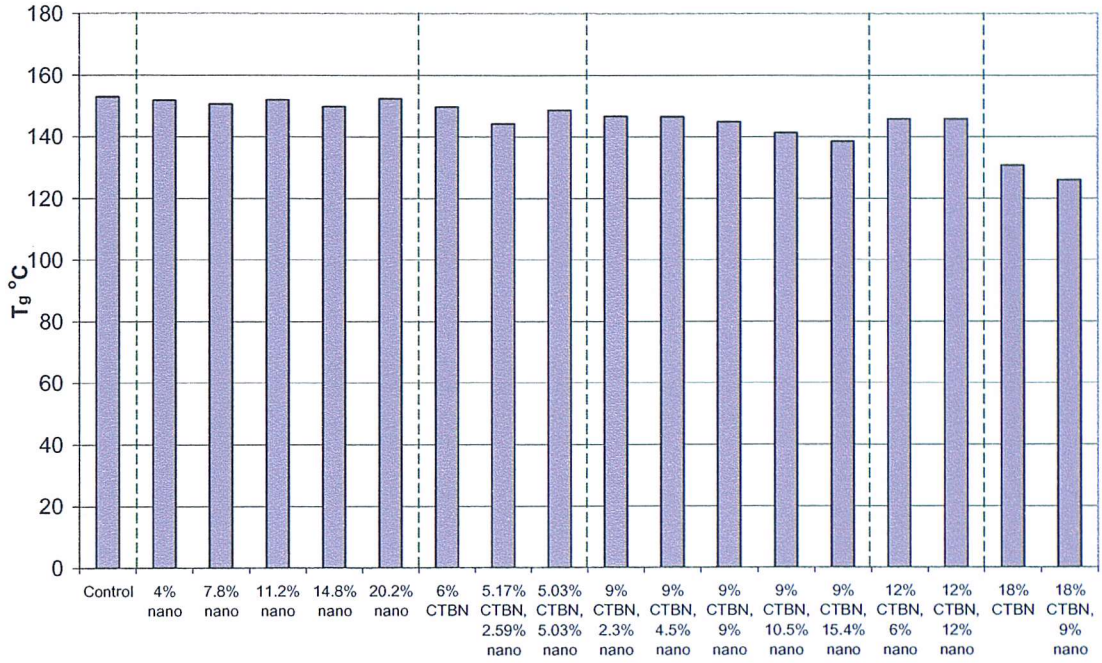


Figure 6.1.18. Glass transition temperatures for the anhydride-cured DGEBA-based bulk epoxy polymers at a test frequency of 1Hz. The dashed lines separate the samples into sub-systems of similar CTBN content.

Table 6.1.3. Summary of the glass transition temperatures of the epoxy for all the anhydride-cured DGEBA-based bulk epoxy polymers, tested at a frequency of 1Hz.

wt. % CTBN	wt. % nano-silica	T_g (°C)
0	0	153
0	4	152
0	7.8	154
0	11.1	151
0	14.8	152
0	20.2	150
6	0	152
5.03	5.03	144
5.17	2.59	150
9	2.3	149
9	4.5	147
9	9	147
9	10.5	145
9	15.4	141
12	6	139
12	12	146
18	0	146
18	9	131
18	18	126

Other work has shown varying glass transition temperatures for an unmodified DGEBA epoxy cured with an anhydride hardener. The work of Tcharkhtchi *et al.* [170] had a T_g of ~140°C, whereas the work of Brady *et al.* [171] showed a glass transition temperature of ~160°C. The value obtained in this study (153°C) correlates well with

the literature. Nano-silica particles alone do not change the glass transition temperature of the epoxy.

Only two formulations containing CTBN-only were tested (6 wt. % and 18 wt. % CTBN) and there was a slight decrease in glass transition temperature because some of the rubber remained in solution in the epoxy. Calculations using the Fox-Flory Equation (see Equation 2.23 in Chapter 2) showed that for the 18 wt. % CTBN sample, ~2.5 wt. % of rubber remained in solution in the epoxy phase to account for the small decrease in the glass transition temperature. Volume fraction analysis of the microstructure images however, suggests that ~13.5 wt. % remained in the epoxy phase. Although the Fox-Flory Equation is only intended as a guide, this large discrepancy is probably because the micrographs were obtained from a rubber-deficient region, or the staining of the TEM slices was not performed for a sufficient length of time to allow all the rubber particles to darken.

In the hybrid samples containing 9 wt. % CTBN, small amounts of nano-silica did not alter the epoxy T_g, but 15.4 wt. % nano-silica reduced the T_g slightly, possibly because it changed the cure kinetics of the sample and inhibited the phase separation of the rubber. At higher CTBN contents (ie. 18 wt. %) it can be seen that increasing nano-silica content caused a decrease in T_g by changing the cure kinetics. A detailed volume fraction analysis of at least twelve microstructure images could be done in the future to more accurately compare the microstructure to the glass transition temperatures. This would assist in explaining how nano-silica affects the phase separation of rubber particles.

6.1.2.2 Tensile test results

Tensile tests were performed using dumbbell specimens at a rate of 1mm/min at 20°C, to determine the Young's modulus of the different compositions. (Note that tensile results for formulations containing 12 and 18 wt. CTBN are not included, since there was insufficient plate to make tensile dumbbells.) The main results are summarised in Figure 6.1.19 and a summary of the numerical values of the Young's moduli for the different formulations can be found in Table 6.1.4.

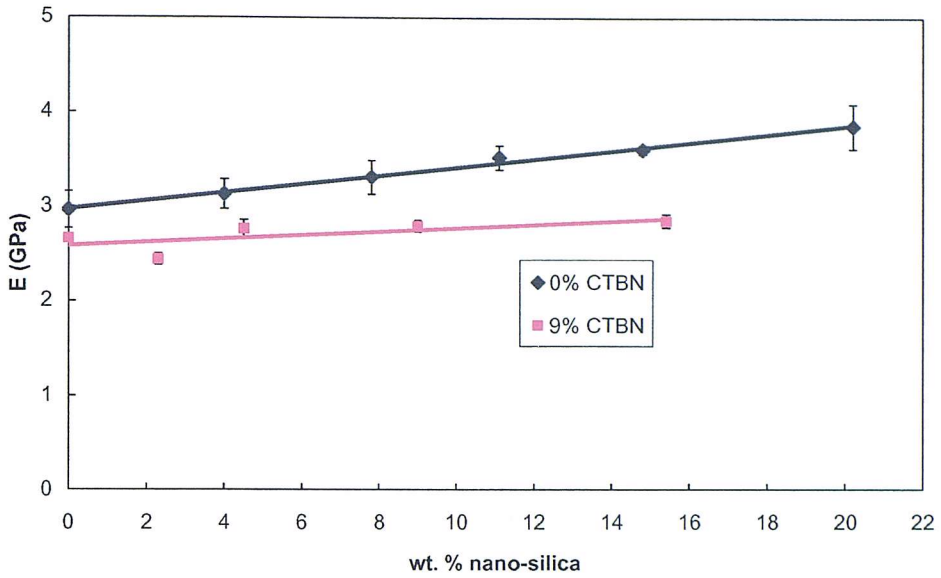


Figure 6.1.19. Young's moduli for samples containing 0% and 9% CTBN. (error bars are ± one standard deviation)

Table 6.1.4. Summary of Young's moduli for the anhydride-cured DGEBA-based bulk epoxy polymers (± one standard deviation).

wt. % CTBN	wt. % nano-silica	Young's Modulus, *E (GPa)*
0	0	2.96 ± 0.20
0	4	3.21 ± 0.15
0	7.8	3.43 ± 0.18
0	11.1	3.57 ± 0.13
0	14.8	3.60 ± 0.05
0	20.2	3.85 ± 0.24
5.03	5.03	2.85 ± 0.25
5.17	2.59	2.86 ± 0.06
9	0	2.44 ± 0.06
9	2.3	2.66 ± 0.04
9	4.5	2.77 ± 0.09
9	9	2.79 ± 0.06
9	15.4	2.85 ± 0.07

Mauri *et al.* [172] found that unmodified DGEBA cured with an anhydride hardener had a Young's modulus of 2.8GPa, which compares well with the modulus of 2.96GPa recorded in this work. The stiffness of the nano-only samples increases with increasing nano-silica content. This is expected, since silica particles are known to have a much higher modulus than the epoxy ie. (~70GPa) [137,138]. A comparison with analytical models predicting the Young's moduli can be found in Chapter 7.

All of the samples containing CTBN are less stiff than the unmodified epoxy. Indeed, an examination of the samples containing 9 wt. % CTBN shows that the rubber produces up to a 15% decrease in the Young's modulus compared to the unmodified epoxy. This is expected, since rubber has a much lower stiffness than the epoxy [129] and Pearson and Yee [7] showed an ~20% decrease in stiffness with a similar rubber content, which correlates well with this study.

6.1.2.3 Fracture Test Results

At least triplicate three-point bend tests were performed at a rate of 1mm/min at 20°C, to ascertain the critical mode I stress intensity factor (K_{Ic}). This fracture toughness value was then converted to the mode I critical fracture energy, using Equation 2.9 in Chapter 2. (Note that where there was no tensile data available, a value extrapolated from the 0 and 9 wt. % CTBN was used.) The pre-crack was formed by drawing a new razor blade through the notch tip.

Figure 6.1.20 shows graphs of the fracture energies for samples containing no rubber and 9 wt. % CTBN, with increasing nano-silica content. Figure 6.1.21 shows two graphs of fracture energies for samples containing no nano-silica, and ~9 wt. % nano-silica, with increasing CTBN content. Table 6.1.5 shows a summary of all the numerical values of the fracture tests results, and includes data for some samples not considered in the graphs. It should be noted that these values are all initiation values since there was no stable crack growth in the short height of the specimen.

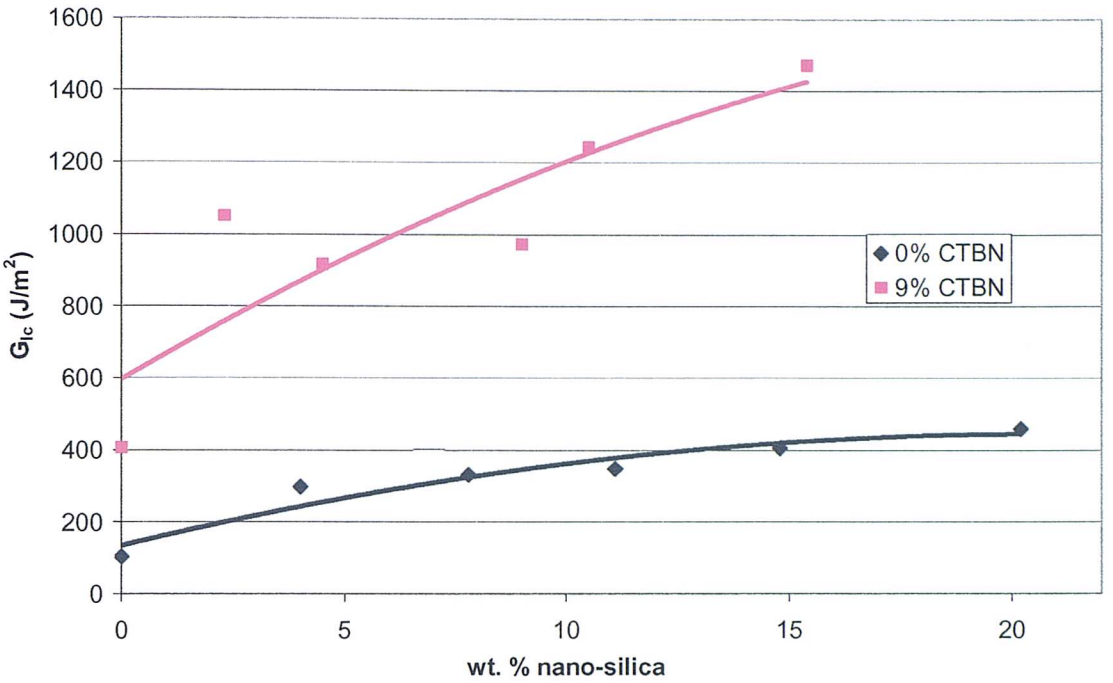


Figure 6.1.20. Fracture energy versus nano-silica content, for samples containing 0 and 9 wt. % CTBN.

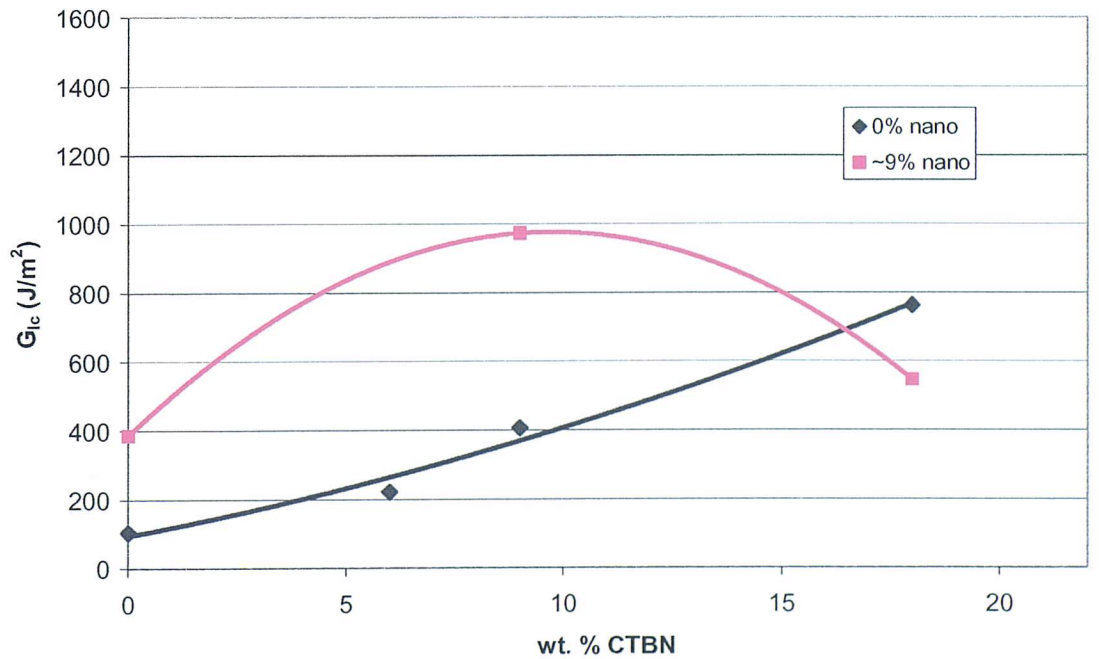


Figure 6.1.21. Fracture energy versus CTBN content for samples containing 0 and 9 wt. % nano-silica content.

Table 6.1.5. Summary of fracture toughness and fracture energies for the bulk anhydride-cured DGEBA-based epoxy polymers (± one standard deviation).

wt. % CTBN	wt. % nano-silica	K_{Ic} *(MPa $m^{1/2}$)*	G_{Ic} *(J/m^2)*
0	0	0.59 ± 0.03	103
0	4	1.03 ± 0.24	291
0	7.8	1.17 ± 0.14	352
0	11.1	1.18 ± 0.17	343
0	14.8	1.29 ± 0.20	406
0	20.2	1.42 ± 0.15	461
6	0	0.84 ± 0.11	221
5.03	5.03	1.86 ± 0.24	1068
5.17	2.59	1.70 ± 0.11	889
9	0	1.11 ± 0.17	444
9	2.3	1.71 ± 0.03	1050
9	4.5	1.7 ± 0.21	918
9	9	1.76 ± 0.11	977
9	10.5	1.99 ± 0.03	1240
9	15.4	2.19 ± 0.16	1480
12	6	1.83 ± 0.1	1050
12	12	1.75 ± 0.16	960
18	0	1.56 ± 0.18	763
18	9	1.32 ± 0.11	546
18	18	1.93 ± 0.05	1167

The work of Natarajan *et al.* [173] showed that unmodified DGEBA cured with an anhydride hardener can have a toughness of ~0.60MPa $m^{1/2}$, which agrees well with the results from this study (0.59MPa $m^{1/2}$).

Figure 6.1.20 shows that there is a steady increase in fracture energy for the 9 wt. % CTBN samples as the nano-silica content is increased, with the maximum fracture energy being 1480J/m^2 for a sample toughened with 15.4 wt. % nano-silica. Indeed, Moloney *et al.* [174] showed that CTBN can produce spectacular increases (up to five times) in toughness compared to unmodified anhydride-cured epoxy. There is also a steady increase in fracture energy for the 0 wt. % CTBN formulations, from 103J/m^2 for unmodified epoxy, to 461J/m^2 for a sample toughened with 20.2 wt. % nano-silica.

Figure 6.1.21 shows that there is a linear increase in fracture energy (as the percentage of CTBN is increased) for 0 wt. % nano-silica, from 103 J/m^2 for unmodified epoxy to 763 J/m^2 for a sample containing 18 wt. % CTBN. For samples containing 9 wt. % nano-silica, the fracture energy first increases, and then decreases as the percentage of CTBN increases. The maximum fracture energy is 977J/m^2 for a CTBN content of 9 wt. %.

It can be seen that the series of samples containing 9 wt. % CTBN gave the highest fracture energy values and best synergy between rubber and nano-silica, and the fracture mechanisms will be discussed in more detail in the next section (in conjunction with the fractography), as well as in Chapter 7. (For this reason, the 9 wt. % CTBN series of samples was chosen as the matrix for CFRP samples, as discussed later in this Chapter.) This agrees well with the work of Azimi *et al.* [96] who showed that the volume fraction of rubber should not be less than the rigid particle content to obtain good toughness in hybrid polymers.

6.1.2.4 Summary

The addition of nano-silica has no adverse effect on the glass transition temperature, whilst the CTBN reduces the T_g because some CTBN remains in solution in the epoxy phase. Nano-silica counteracts the reduction in epoxy stiffness caused by the CTBN, and at the same time it improves the toughness of the samples.

6.1.3 Bulk Fracture Surfaces

Scanning electron microscopy was performed on some of the fracture surfaces of the SENB samples to investigate the fracture mechanisms responsible for the change in

toughness that was observed. It should be noted that the pre-crack was formed by drawing a new razor blade through the notch tip, and this pre-crack is usually visible in the low magnification images as a vertical line to the far left of the micrograph.

6.1.3.1 Unmodified Epoxy

The fracture surface of the unmodified epoxy is shown in Figure 6.1.22, where the direction of crack propagation is from left to right. The fracture surface is relatively smooth and glassy, which is typical of a brittle thermosetting polymer [83], and shows that no large-scale plastic deformation has occurred during fracture. This agreed well with the low toughness of 0.59MPa $m^{1/2}$. In addition, there are apparent steps and changes of the level of the crack (feather markings), which are caused by the crack forking due to the excess of energy associated with the relatively fast crack growth. This repeated forking and the multi-planar nature of the surface are ways of absorbing this excess energy in a very brittle material [145]. The unmodified epoxy sample was then placed under the high resolution SEM with a field emission gun attached (FEG-SEM), giving the image in Figure 6.1.23. Even at very high magnification, the fracture surface is featureless.

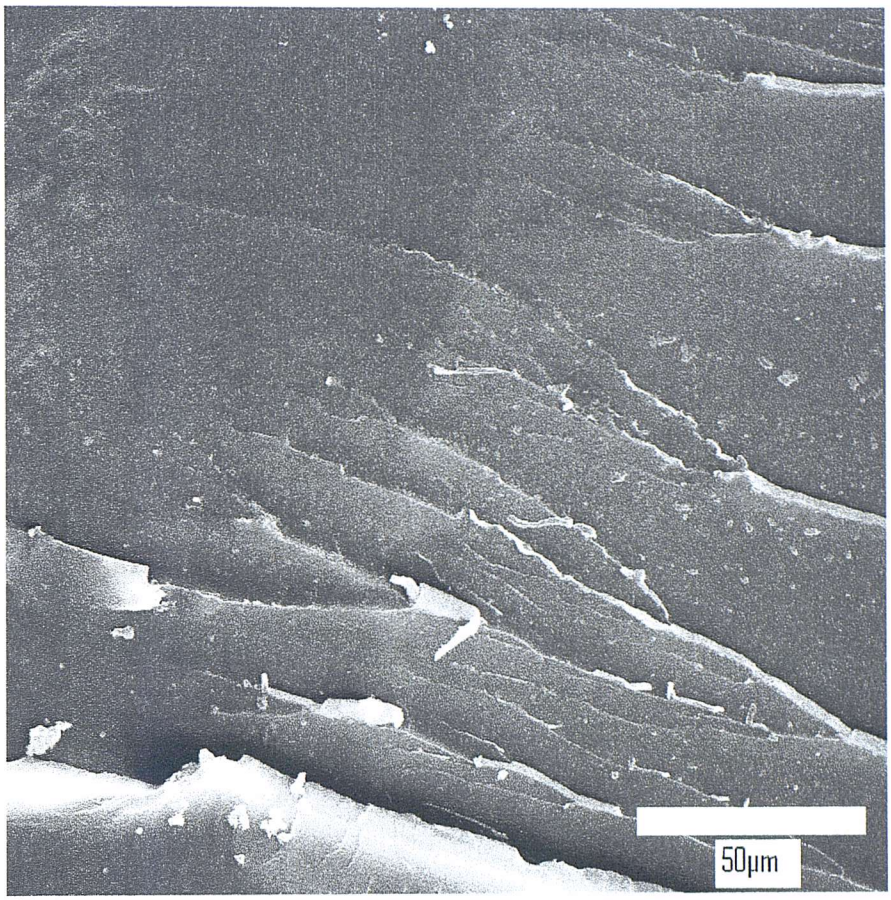


Figure 6.1.22. Fracture surface of unmodified epoxy (crack propagation from left to right).

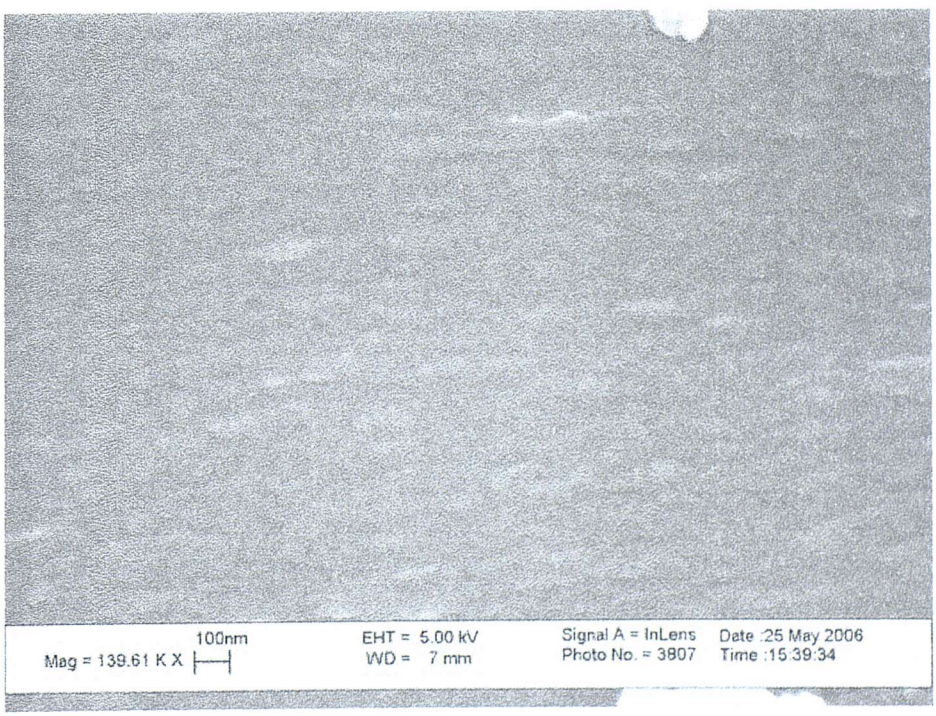


Figure 6.1.23. Fracture surface of a unmodified epoxy sample (crack propagation from *right* to *left*).

6.1.3.2 Nano-silica Modified Epoxies

The micrograph in Figure 6.1.24 is of the fracture surface of a sample containing 4.1 wt. % nano-silica with the crack propagating from left to right. The pre-crack from the razor blade can clearly be seen. The surface is very similar to that of the unmodified epoxy and is relatively flat, except for the feather markings. The nano-silica particles cannot be seen at this magnification because of their very small diameter.

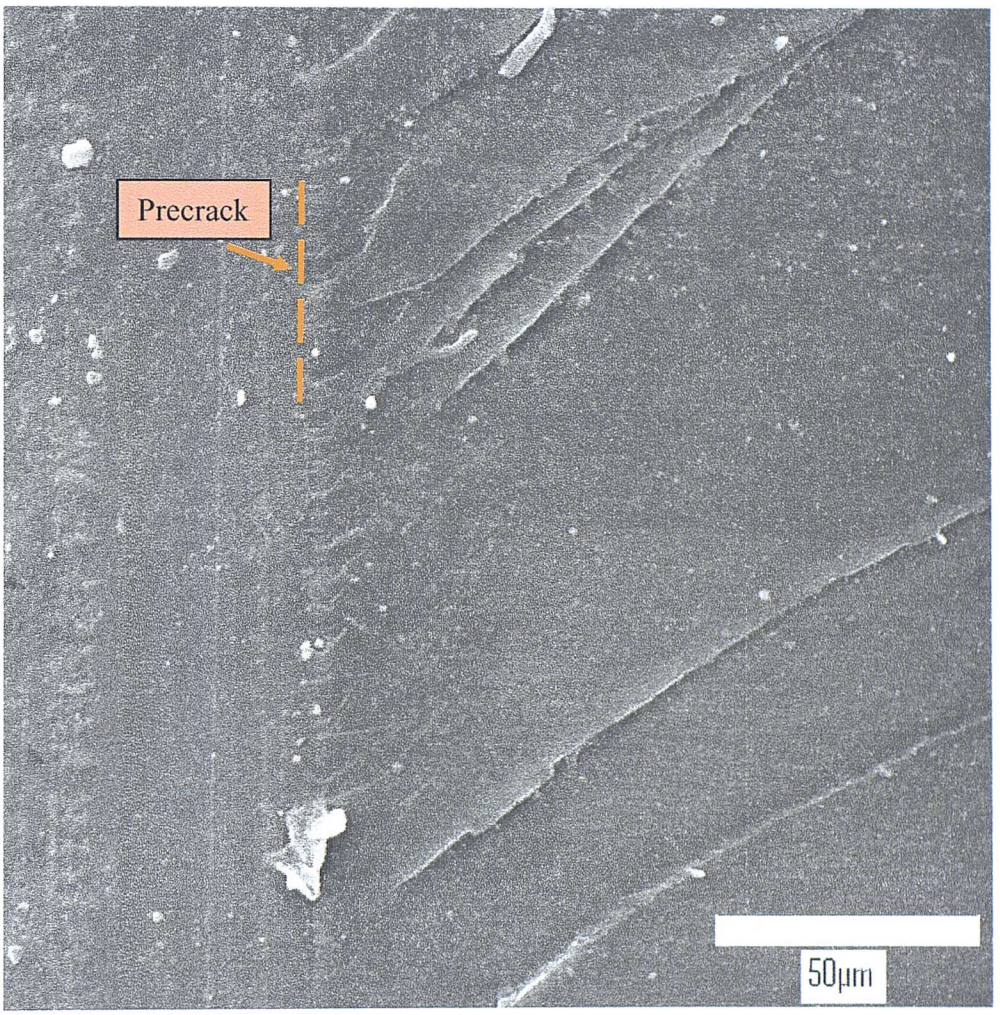


Figure 6.1.24. Fracture surface of a sample containing 4.1 wt. % nano-silica only (crack propagation from left to right).

The micrograph in Figure 6.1.25 shows the fracture surface of a sample containing 20.2 wt. % nano-silica. Its appearance shows no apparent increase in the roughness, unlike what is observed in epoxies with micron-sized particles (as reported by Kinloch and Taylor [175]), despite having a higher toughness than the previous samples. Thus at low magnifications, the fracture surfaces do not explain why the addition of nano-silica increases the toughness of the epoxy.

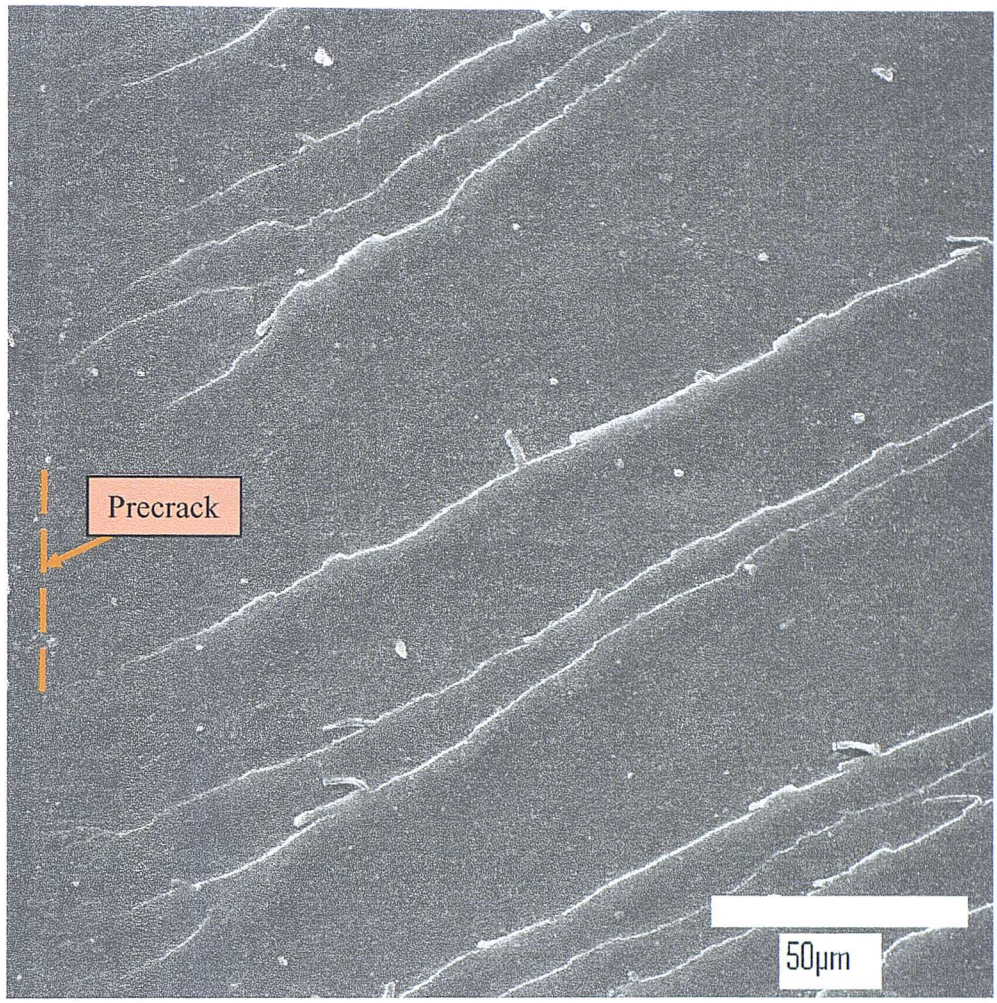


Figure 6.1.25. Fracture surface of a sample containing 20.2 wt. % nano-silica only (crack propagation from left to right).

When some of the samples were placed under the FEG-SEM, the micrographs in Figure 6.1.26 and Figure 6.1.27 were obtained. Figure 6.1.27 is an enlarged area indicated by the red box in Figure 6.1.26. Voids around the nano particles are clearly visible, suggesting that plastic void growth is one of the fracture mechanisms by which nano-silica increases toughness. The micrograph of the unmodified epoxy viewed at similar magnification and focus in Figure 6.1.23 (ie. in the previous section) showed no nano-silica-sized particles, or void-like features, confirming that the features seen in the sample containing nano-silica, are indeed voids. This possible fracture mechanism will be discussed in further detail in Chapter 7.

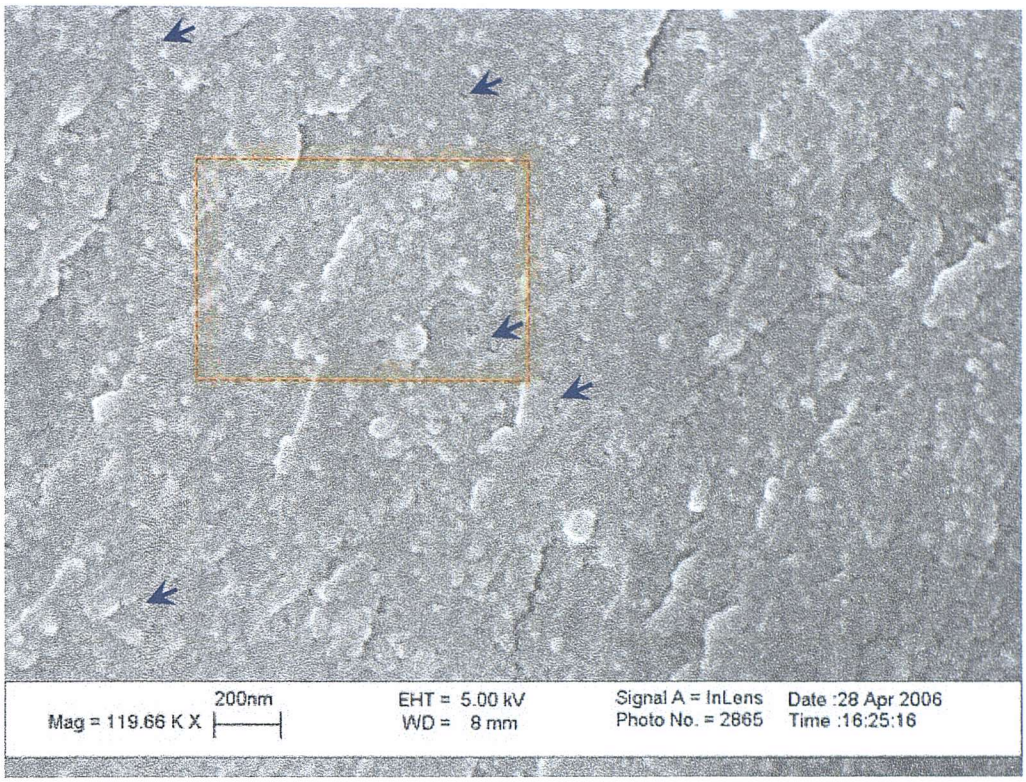


Figure 6.1.26. Fracture surface of a sample containing 14.8 wt. % nano-silica only. Blue arrows point to some nano particles. Box indicates area to be enlarged in the following figure. (crack propagation from *top right to bottom left*).

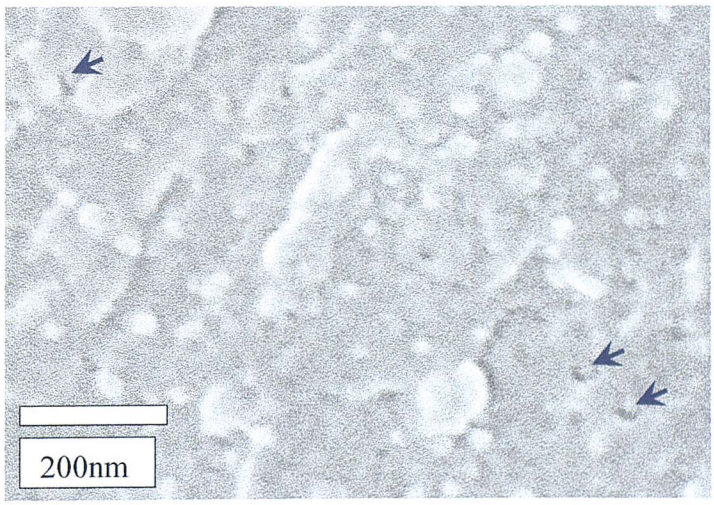


Figure 6.1.27. Enlargement of boxed area in previous Figure. Blue arrows point to some nano particles and voids around them.

6.1.3.3 Rubber Modified Epoxies

The micrographs in Figure 6.1.28 and Figure 6.1.29 are the fracture surfaces of a sample containing 6 wt. % CTBN. There is no large scale plastic deformation, but there is some

evidence of cavitated rubber particles in Figure 6.1.29. The cavitated rubber particles are ~1μm in diameter, which is comparable to the size of rubber particles observed in the microstructure images for other samples containing CTBN-only.

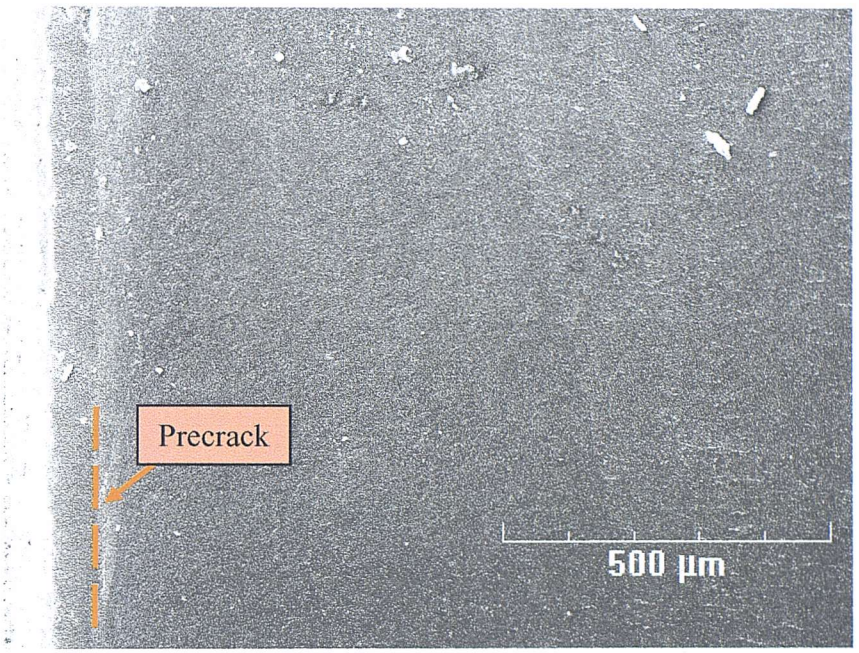


Figure 6.1.28. Fracture surface of a sample containing 6 wt. % CTBN. (crack propagation from left to right).

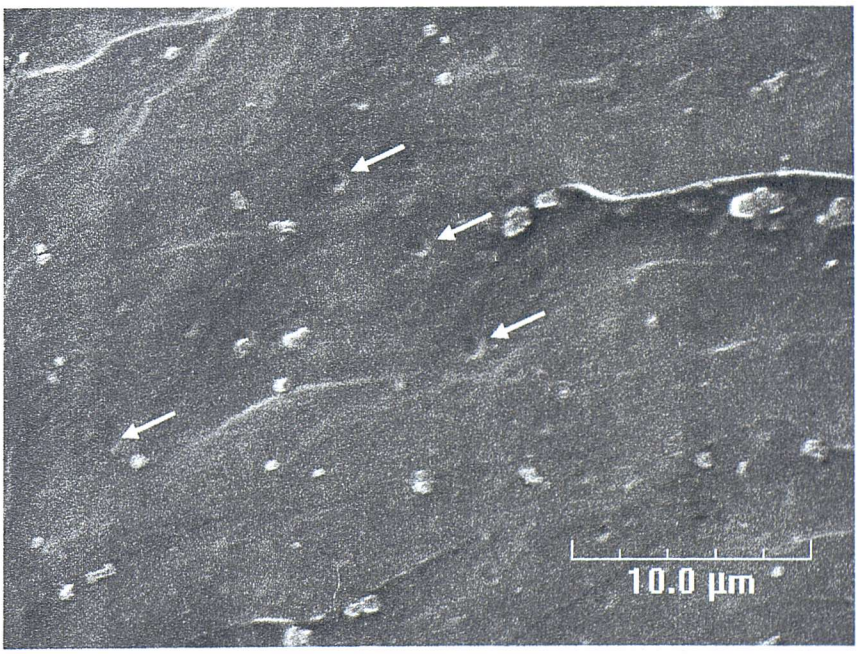


Figure 6.1.29. Fracture surface of a sample containing 6 wt. % CTBN. Cavitated rubber particles are indicated by white arrows (crack propagation from left to right).

The micrographs in Figure 6.1.30 and Figure 6.1.31 are of a sample containing 9 wt. % CTBN. There is more plastic deformation of the epoxy and cavitated rubber particles than in the previous sample. This explains why the toughness was higher than the sample with 6 wt. % CTBN.

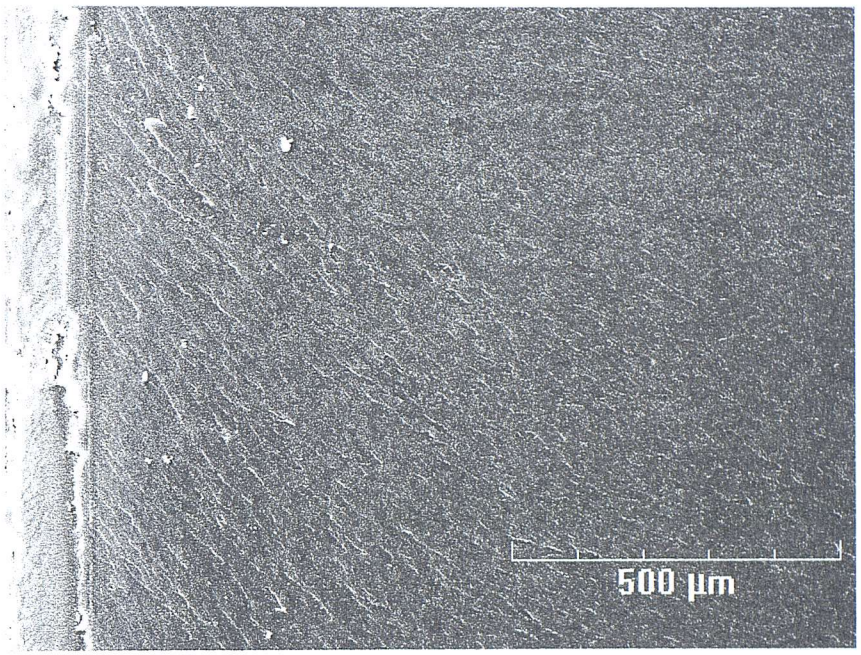


Figure 6.1.30. Fracture surface of a sample containing 9 wt. % CTBN. (crack propagation from left to right).

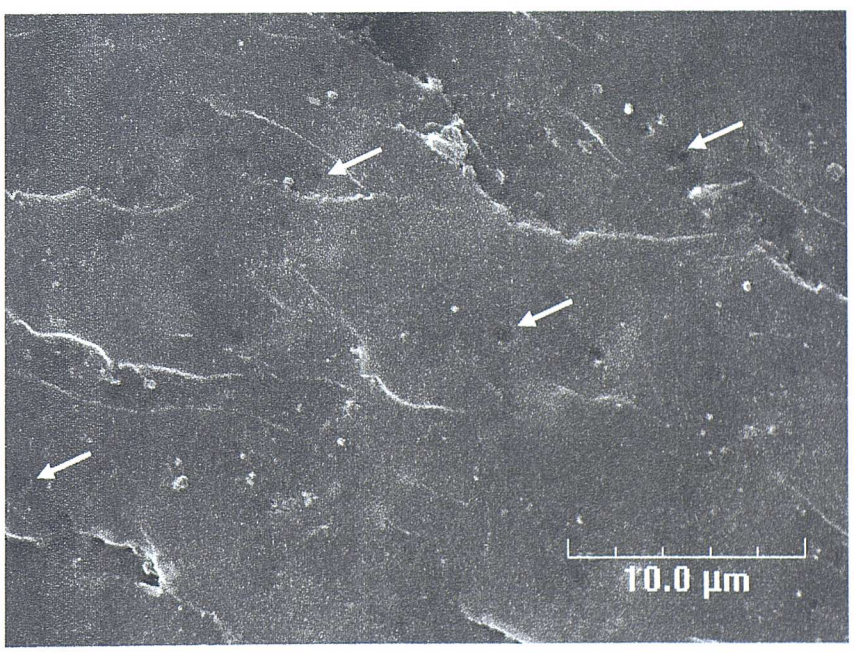


Figure 6.1.31. Fracture surface of a sample containing 9 wt. % CTBN. Cavitated rubber particles are indicated by white arrows (crack propagation from left to right).

The fracture surface of the sample with 18 wt. % CTBN is shown in Figure 6.1.32 and Figure 6.1.33. Although the microstructure images show that there were some phase separated rubber particles, there is no evidence in these micrographs of cavitation of the rubber particles having taken place. It is believed that this sample was more than twice the toughness of the unmodified epoxy because of shear yielding of the epoxy between the phase separated rubber particles, and the plasticisation of the epoxy by the rubber that remains in the epoxy phase [15,16]. This is confirmed by glass transition temperature reductions (see Section 6.1.2.1) which show that some rubber does indeed remain in solution in the epoxy phase.

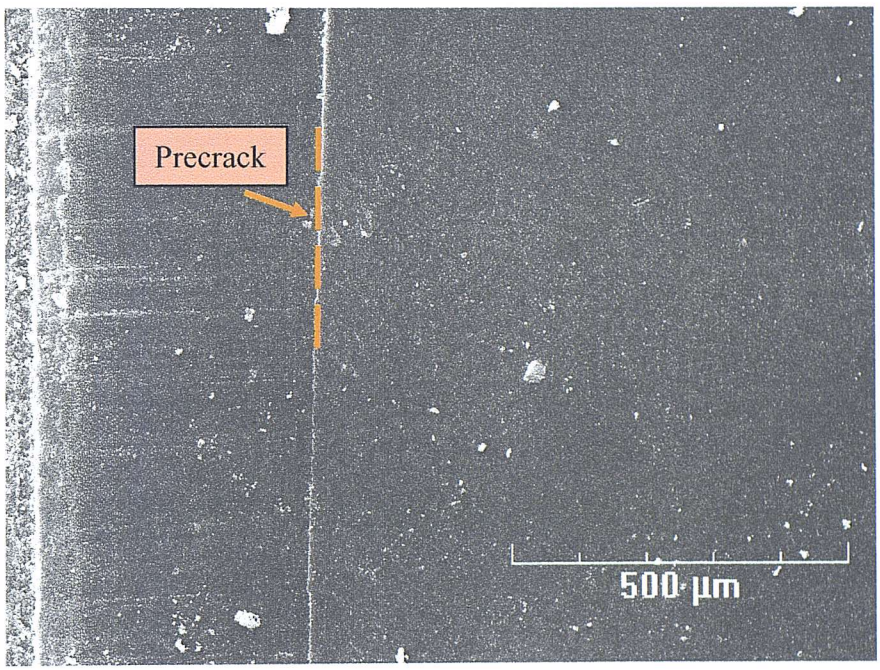


Figure 6.1.32. Fracture surface of a sample containing 18 wt. % CTBN. (crack propagation from left to right).

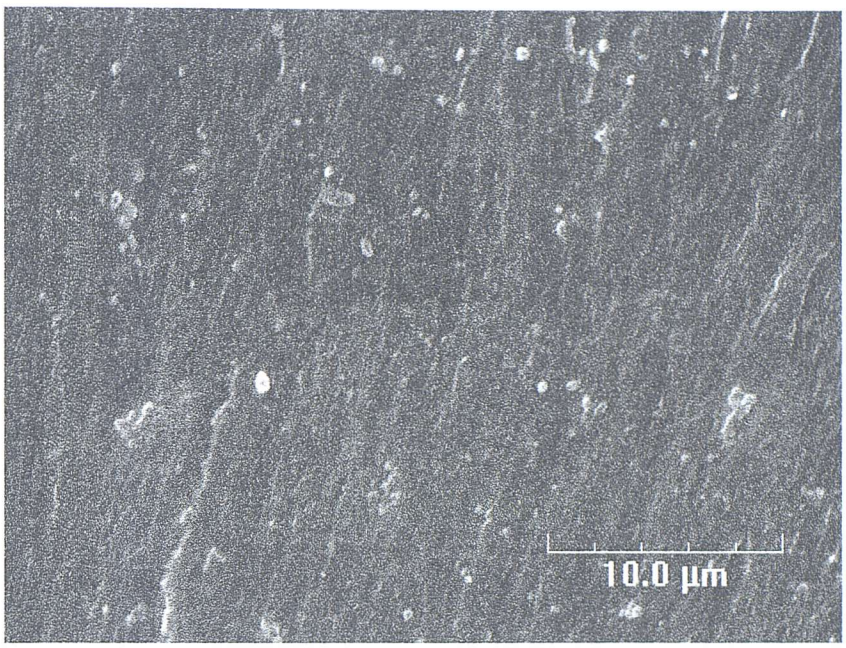


Figure 6.1.33. Fracture surface of a sample containing 18 wt. % CTBN at higher magnification. (crack propagation from left to right).

6.1.3.4 Hybrid Modified Epoxies

The micrograph in Figure 6.1.34 shows the fracture surface of a sample containing 9 wt. % CTBN and 2.3 wt. % nano-silica, taken near the precrack, with the crack front moving from left to right. The surface appears to be rougher than that of the previous samples and there are cavitated rubber particles, which account for an increase in fracture energy. The 20nm diameter nano particles, however, are not visible at this magnification.

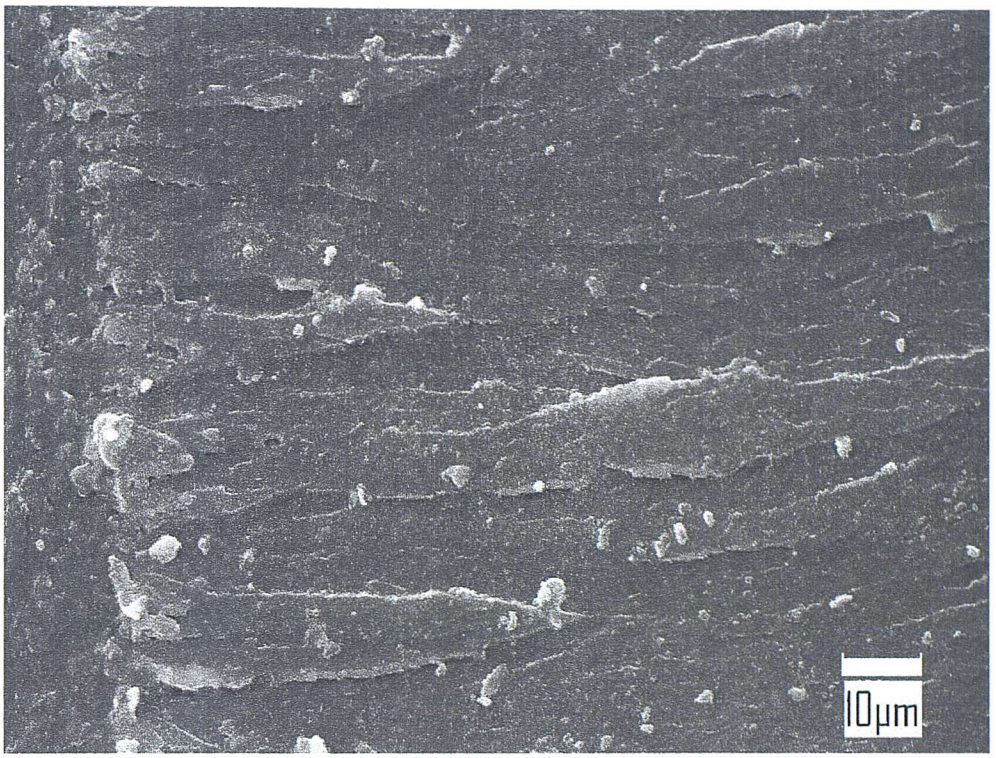


Figure 6.1.34. Fracture surface of a sample containing 9 wt. % CTBN and 2.3 wt. % nano-silica. (crack propagation from left to right).

The micrographs in Figure 6.1.35 and Figure 6.1.36 are for a sample containing 9 wt. % CTBN and 10.5 wt % nano-silica. The micrograph in Figure 6.1.35 is very similar in appearance to the previous sample (hence the inclusion of only a few micrographs, since all the hybrid samples had similar fracture surfaces). From the fracture surface, there is no apparent reason why the hybrid sample containing 10.5 wt. % nano-silica has a higher fracture energy than the one containing 2.3 wt. %. Figure 6.1.36 clearly shows the cavitation of the rubber particles but nano particles are still indiscernible.

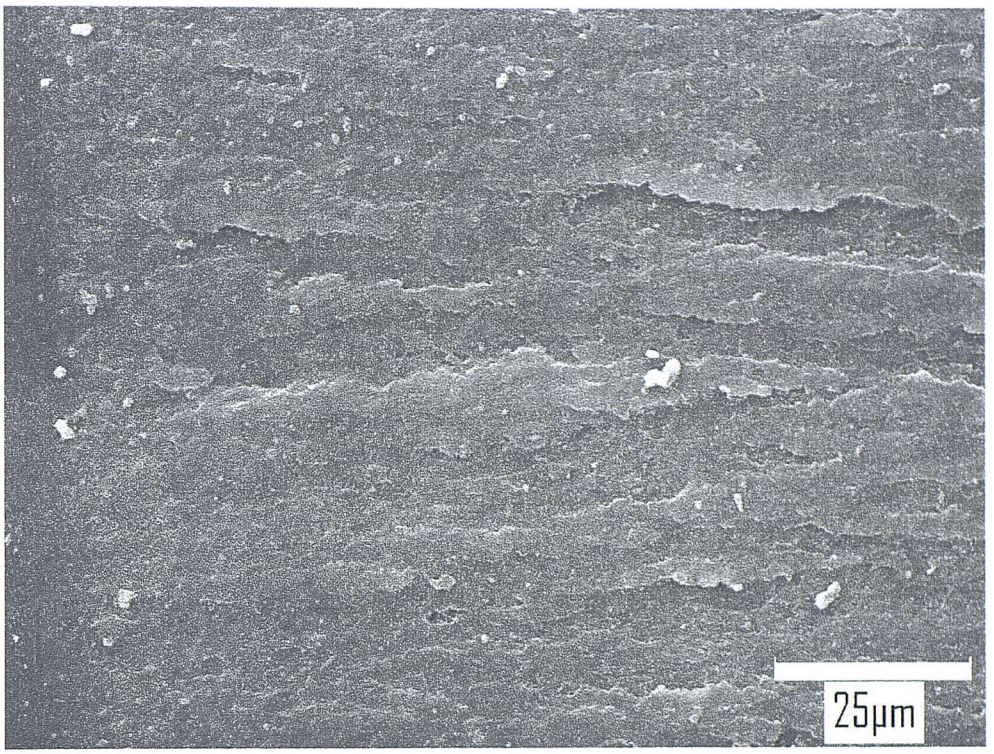


Figure 6.1.35. Fracture surface of a sample containing 9 wt. % CTBN and 10.5 wt. % nano-silica. (crack propagation from left to right).

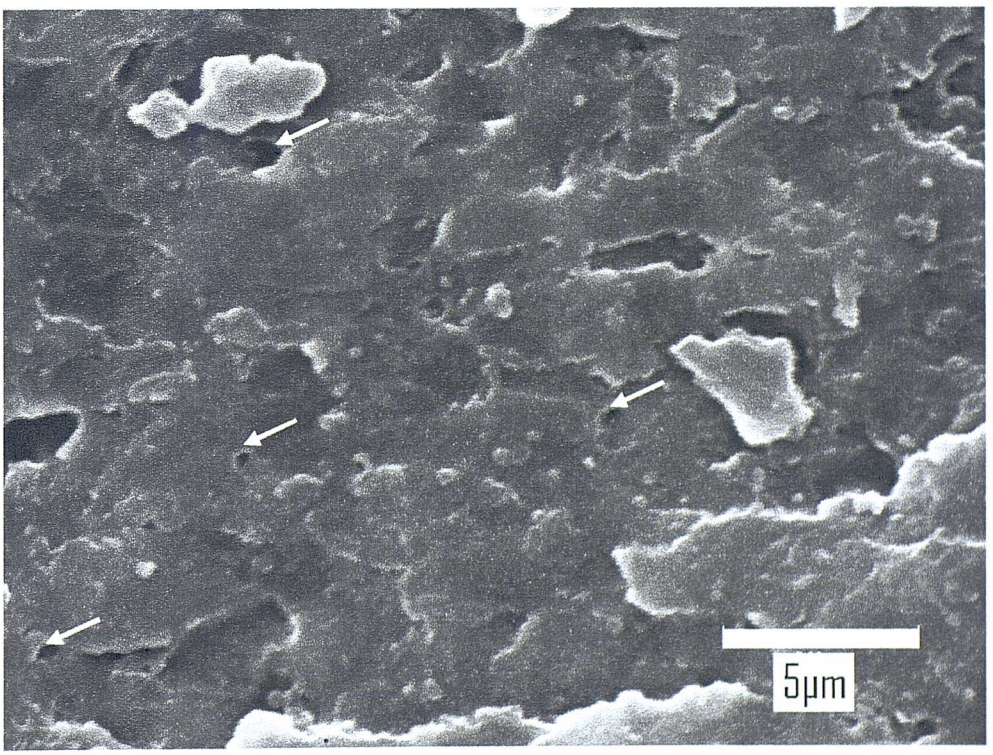


Figure 6.1.36. Fracture surface of a sample containing 9 wt. % CTBN and 10.5 wt. % nano-silica at higher magnification. Cavitated rubber particles are indicated by white arrows. (crack propagation from left to right).

When the sample containing 9 wt. % CTBN and 10.5 wt. % was examined using a FEG-SEM, the micrograph in Figure 6.1.37 was obtained. The nano particles are now clearly visible as both individual particles, and as agglomerates. Although not as clear as the FEG-SEM images of the nano-only samples, cavities around some nano particles are visible in this sample. Due to the roughness of the surface, and the angle of inclination of different regions of the fracture surface, voids are not visible for all particles. Indeed, it is believed that like the nano-only samples, not all the nano-silica particles debond from the epoxy matrix. The possible toughening mechanisms of the nano-silica particles will be discussed in greater detail in Chapter 7.

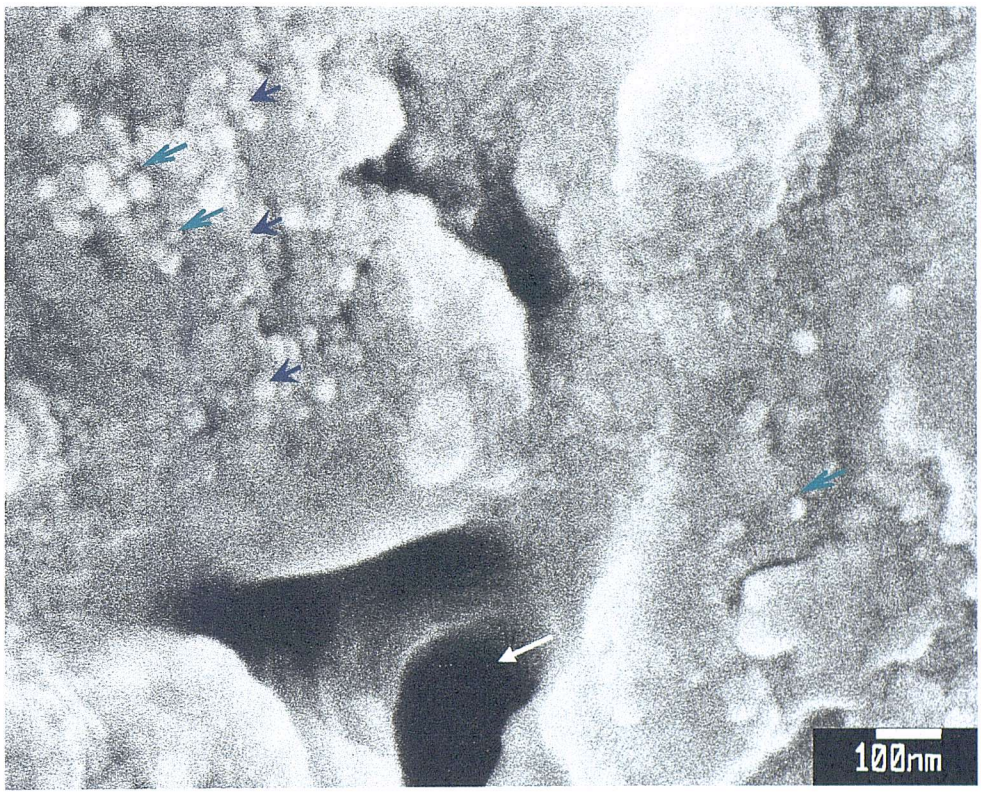


Figure 6.1.37. FEG-SEM image of the fracture surface of a sample containing 9 wt. % CTBN and 10.5 wt. % nano-silica. A possible rubber cavity is indicated by the white arrow. Agglomerates of nano-silica are indicated by the dark blue arrows, and voids by light blue arrows. (crack propagation from left to right).

The micrographs in Figure 6.1.38 are examples of the fracture surfaces of the other hybrid samples. The fracture surfaces at higher CTBN contents are similar, and there is almost no evidence of cavitated rubber particles. Indeed, it is believed that the dominant rubber toughening mechanisms are shear yielding, and the plasticisation of the epoxy by the rubber that remains in the epoxy phase [15,16]. This is confirmed by glass transition

temperature reductions which show that some rubber does indeed remain in solution in the epoxy phase. The mechanisms by which the nano-silica particles improve the toughness, cannot be ascertained at this magnification, but can be pursued in the future using FEG-SEM investigations.

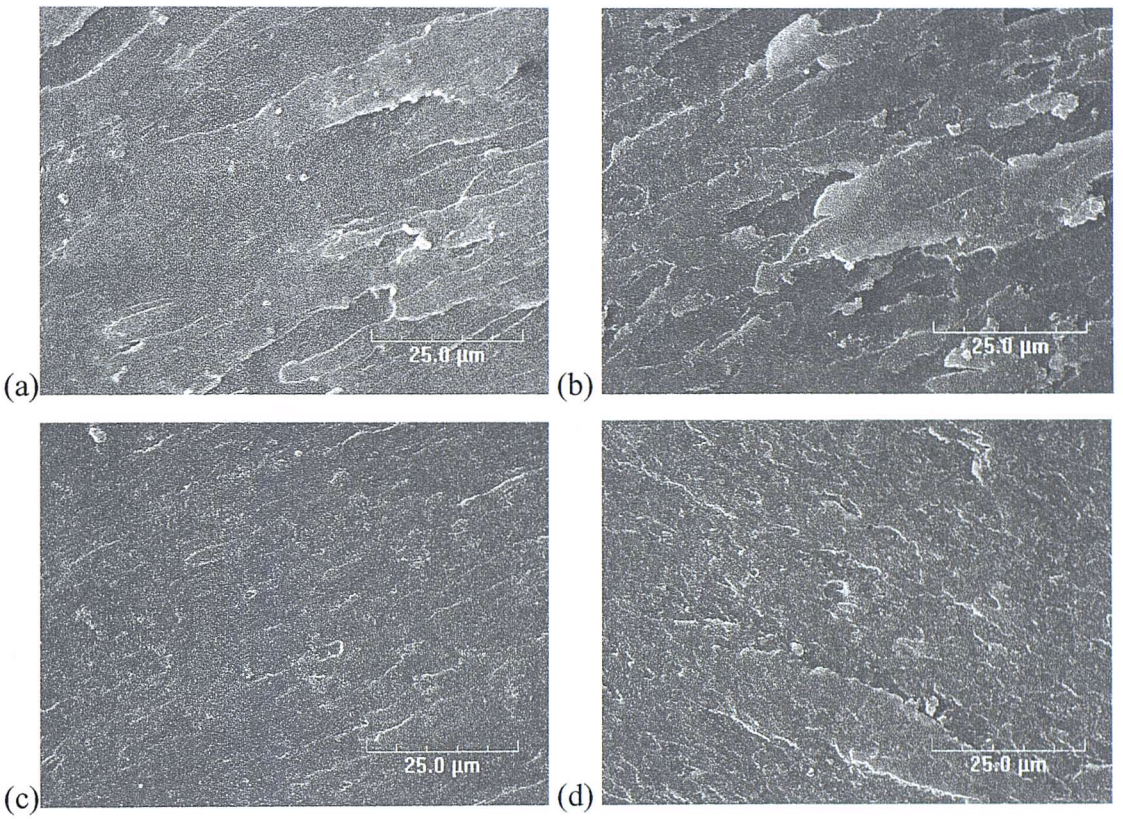


Figure 6.1.38. Fracture surfaces of hybrid samples containing: (a) 12 wt. % CTBN and 6 wt. % nano-silica, (b) 12 wt. % CTBN and 12 wt. % nano-silica, (c) 18 wt. % CTBN and 9 wt. % nano-silica, and (d) 18 wt. % CTBN and 18 wt. % nano-silica (crack propagation from left to right).

6.1.3.5 Summary

The feather marks and glassy appearance of the unmodified epoxy's fracture surface, as well as the surfaces of the samples containing only nano-silica, correlates well with the low toughness recorded (compared to the samples containing CTBN). At much higher magnifications it becomes apparent that the nano-silica increases the fracture toughness of the epoxy by the formation of plastically deformed voids around the particles. The cavitation of the rubber particles is visible in some of the hybrid samples, but the major toughening contributions are believed to be from shear yielding, and the plasticisation of the epoxy by the rubber that remains in the epoxy phase.

6.2 Carbon Fibre Reinforced Polymer Results

Laminates were manufactured by VARTM, using some of the bulk epoxy polymers (examined earlier in this Chapter) as their matrices. Mode I fracture tests, flexural modulus tests, and volume fraction analyses were performed on the laminates, and the results are presented in the following Sections.

6.2.1 Mode I Fracture Results

The double cantilever beam (DCB) CFRP specimens were loaded under uni-axial tension (Mode I) to determine their interlaminar fracture energies. At least three repeat tests were performed for each formulation. An example graph in Figure 6.2.1 shows that there was no major R-curve behaviour in any of the samples.

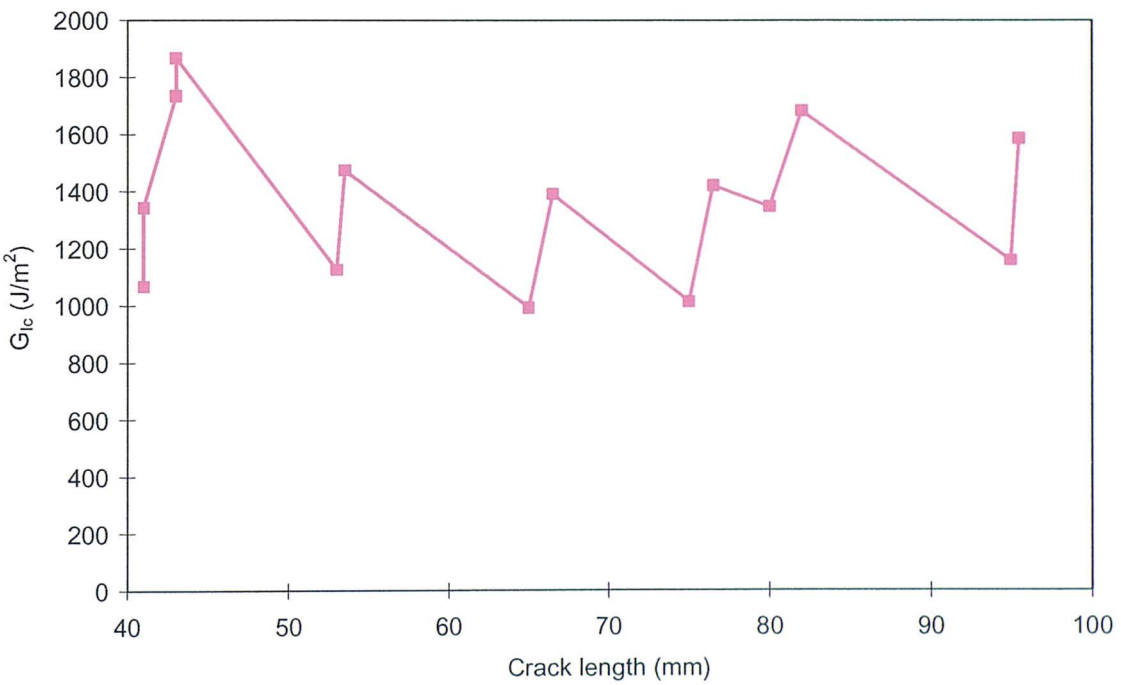


Figure 6.2.1. Sample graph showing the mode I interlaminar fracture energy (initiation and arrest) versus the crack length for a sample containing 9 wt. % CTBN and 10.5 wt. % nano-silica.

The graph in Figure 6.2.2, illustrates the initiation interlaminar fracture energies. Error bars of ± one standard deviation are included to show the variability of the results. Failure occurred in an unstable fashion (stick-slip) for these specimens. Table 6.2.1 contains the numerical values of the fracture energies for the different formulations.

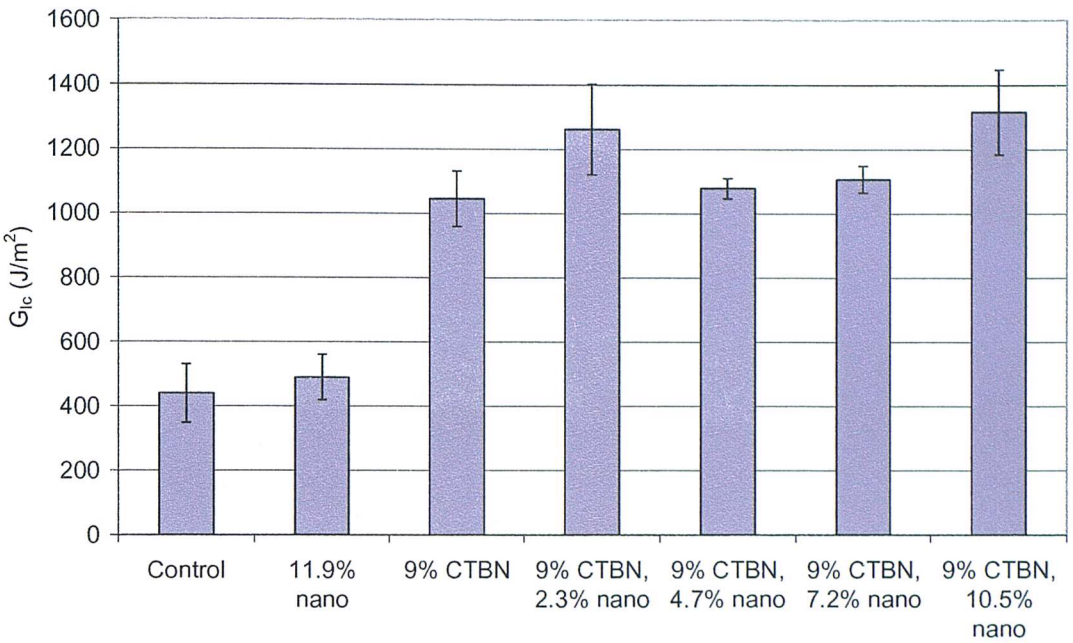


Figure 6.2.2. Mode I interlaminar fracture energy for CFRPs with an anhydride-cured DGEBA matrix. (error bars are ± one standard deviation)

Table 6.2.1. Summary of the mode I interlaminar fracture energy for CFRPs with an anhydride-cured DGEBA matrix. (± one standard deviation)

wt. % CTBN	wt. % nano-silica	G_{Ic} *(J/m^2)*
0	0	439 ± 91
0	11.9	489 ± 71
9	0	1044 ± 87
9	2.3	1261 ± 141
9	4.7	1078 ± 31
9	7.2	1106 ± 41
9	10.5	1316 ± 132

Compared to the control laminate, nano-silica on its own does not improve the interlaminar fracture energy, but CTBN on its own causes a doubling in interlaminar fracture energy. The improvement in fracture resistance when CTBN is present, has been seen in the other two systems discussed in Chapters 4 and 5. The hybrid CFRP sample with 9 wt. % CTBN and 2.3 wt. % nano-silica showed a 200% increase in

interlaminar fracture energy (to over 1200J/m^2), compared to the control CFRP. Laminates containing nano-silica and rubber particles are more fracture resistant than rubber-only or nano-only laminates. The possible reasons for this will be explored in the following Section which examines the fracture surfaces of the laminates.

6.2.2 Mode I CFRP Fracture Surfaces

Scanning electron microscopy was performed on some of the CFRP fracture surfaces to investigate the fracture mechanisms responsible for the changes in toughness that were observed.

6.2.2.1 Unmodified Epoxy Matrix

The micrographs in Figure 6.2.3 and Figure 6.2.4 are of a CFRP sample with an unmodified epoxy matrix. The lower magnification micrograph in Figure 6.2.3 shows large areas of cohesive failure [155] through the epoxy matrix. There is hardly any plastic deformation of the epoxy matrix, and the fracture surface is very similar to the fracture surface of the unmodified bulk epoxy polymer. The micrograph at higher magnification in Figure 6.2.4 shows evidence of good interfacial strength between the fibres and the matrix. Fibre debonding and pullout is also visible. The good fibre-matrix bonding, and the additional fibre toughening mechanisms account for the increase in interlaminar fracture energy of the laminate compared to the bulk epoxy [155].

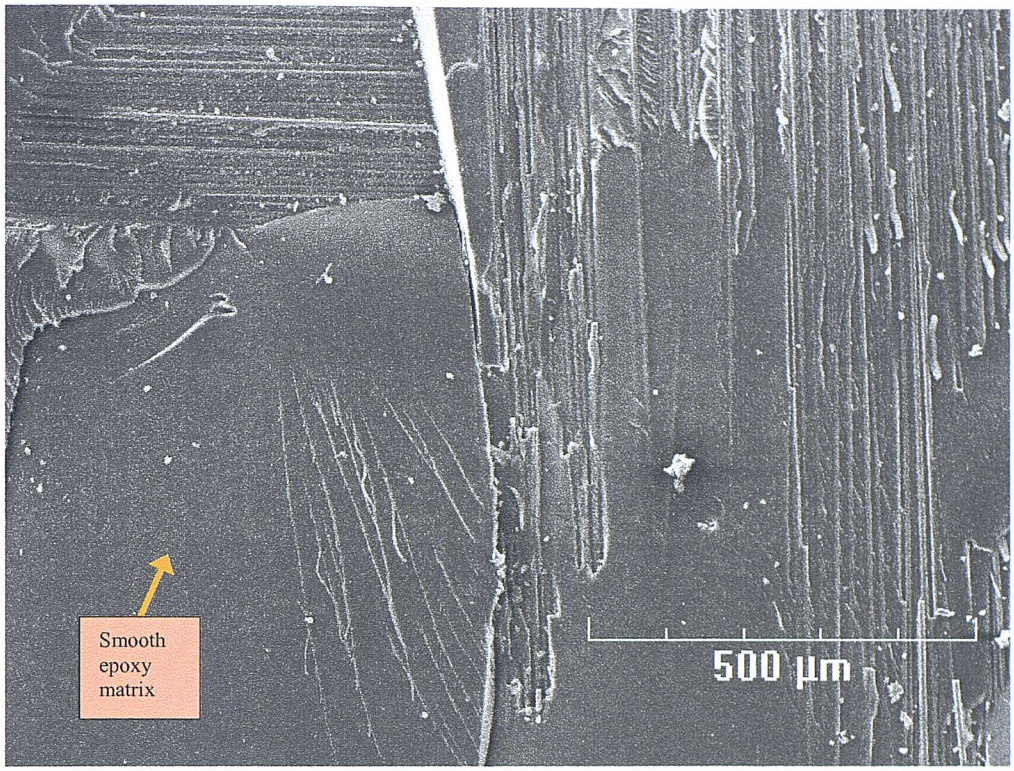


Figure 6.2.3. Fracture surface of a CFRP sample with an unmodified anhydride-cured epoxy matrix (crack propagation from right to left).

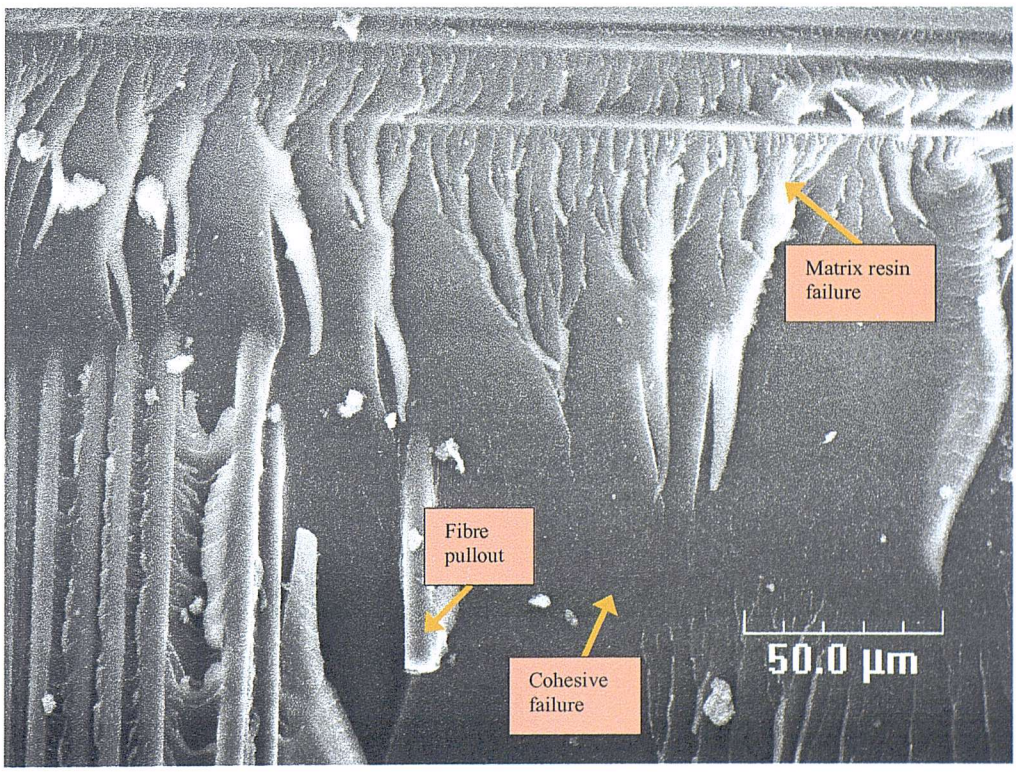


Figure 6.2.4. Fracture surface of a CFRP sample with an unmodified anhydride-cured epoxy matrix at higher magnification (crack propagation from right to left).

6.2.2.2 Nano-silica Modified Epoxy Matrix

The micrographs in Figure 6.2.5 and Figure 6.2.6 are the fracture surfaces of a laminate toughened with 11.9 wt. % nano-silica. The interlaminar fracture surface is similar to that of the control laminate because there are large areas of epoxy matrix indicating cohesive failure. There is also good interfacial strength between the fibres and the matrix, and the continuous channels [156] indicate that the fibres debonded and pulled out. Indeed, this sample had a similar interlaminar fracture energy to the control laminate, and a slightly higher fracture energy than its nano-only bulk epoxy polymer counterpart. (Note that the nano-silica particles are not visible at this magnification due to their small size.)

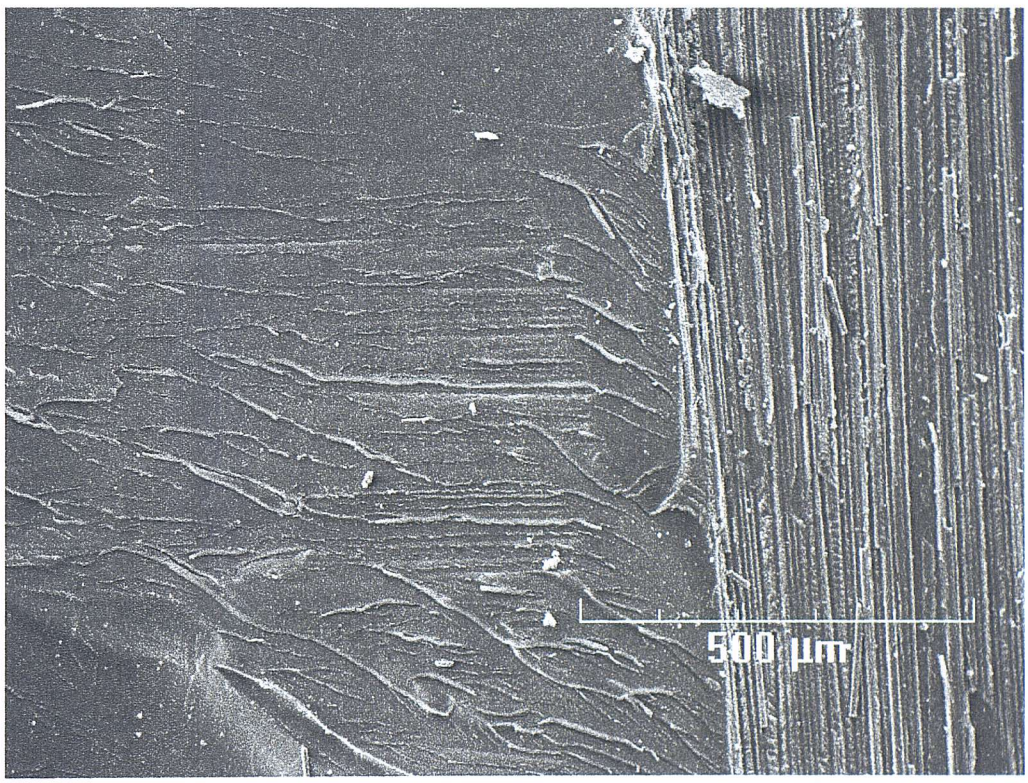


Figure 6.2.5. Fracture surface of a CFRP sample with an anhydride-cured epoxy matrix containing 11.9 wt. % nano-silica only (crack propagation from right to left).

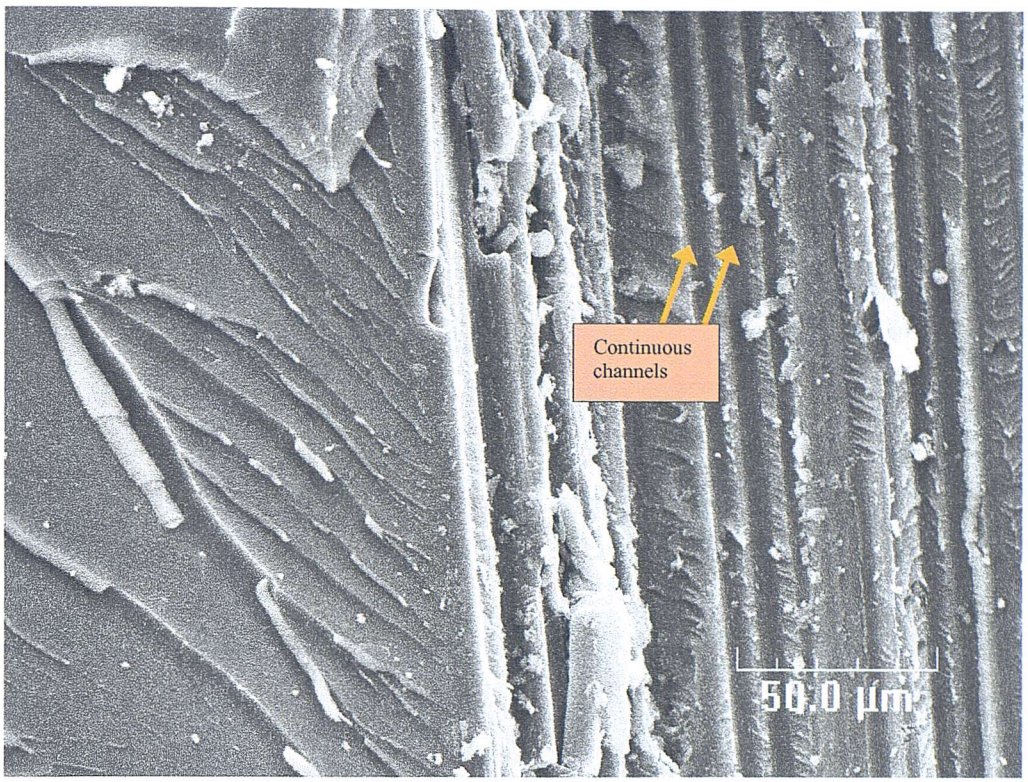


Figure 6.2.6. Fracture surface of a CFRP sample with an anhydride-cured epoxy matrix containing 11.9 wt. % nano-silica only at higher magnification (crack propagation from right to left).

6.2.2.3 Rubber Modified Epoxy Matrix

The micrograph in Figure 6.2.7 is a low magnification image of the fracture surface of a sample containing 9 wt. % CTBN. There is widespread evidence of cohesive failure, suggesting that failure occurred through the epoxy matrix. Indeed, the higher magnification micrographs in Figure 6.2.8 and Figure 6.2.9 show evidence of cavitated rubber particles. Compared to its bulk epoxy polymer fracture surface, there are more cavitated rubber particles in the laminate's matrix which would account for an increase in fracture energy compared to its bulk counterpart. It is possible that there was more rubber cavitation in the laminate because more rubber particles phase separated on curing. There was also evidence of fibre toughening mechanisms, like fibre debonding and pullout, as well as good fibre-matrix bonding, which increased the interlaminar fracture energy further.

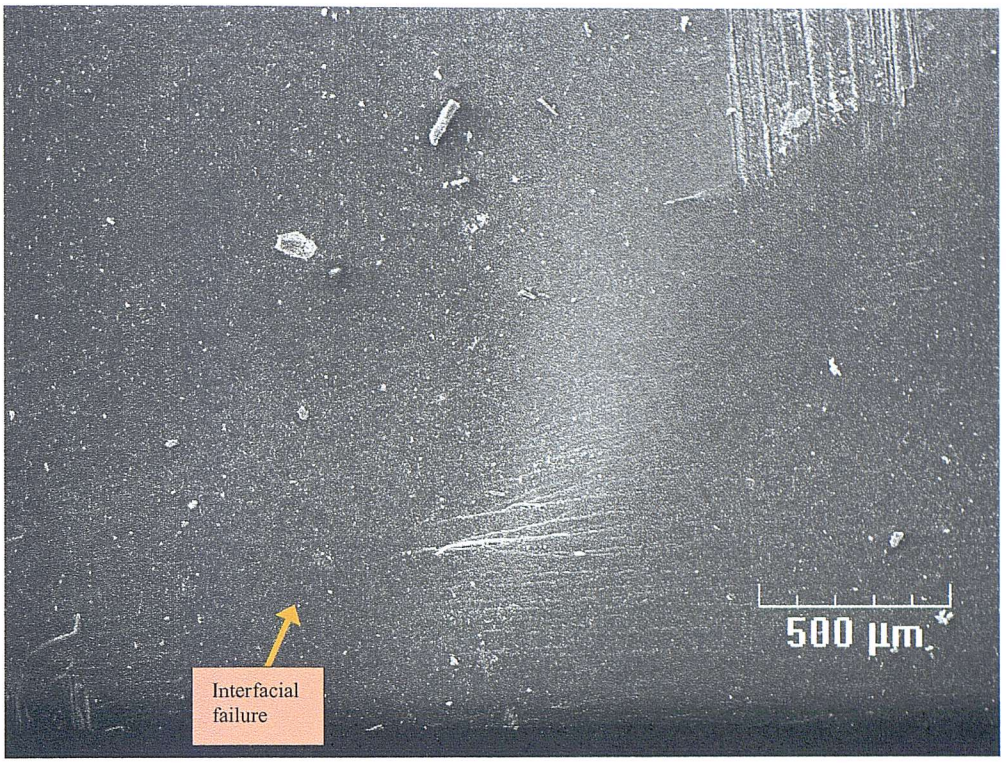


Figure 6.2.7. Fracture surface of a CFRP sample with an anhydride-cured epoxy matrix containing 9 wt. % CTBN (crack propagation from right to left).

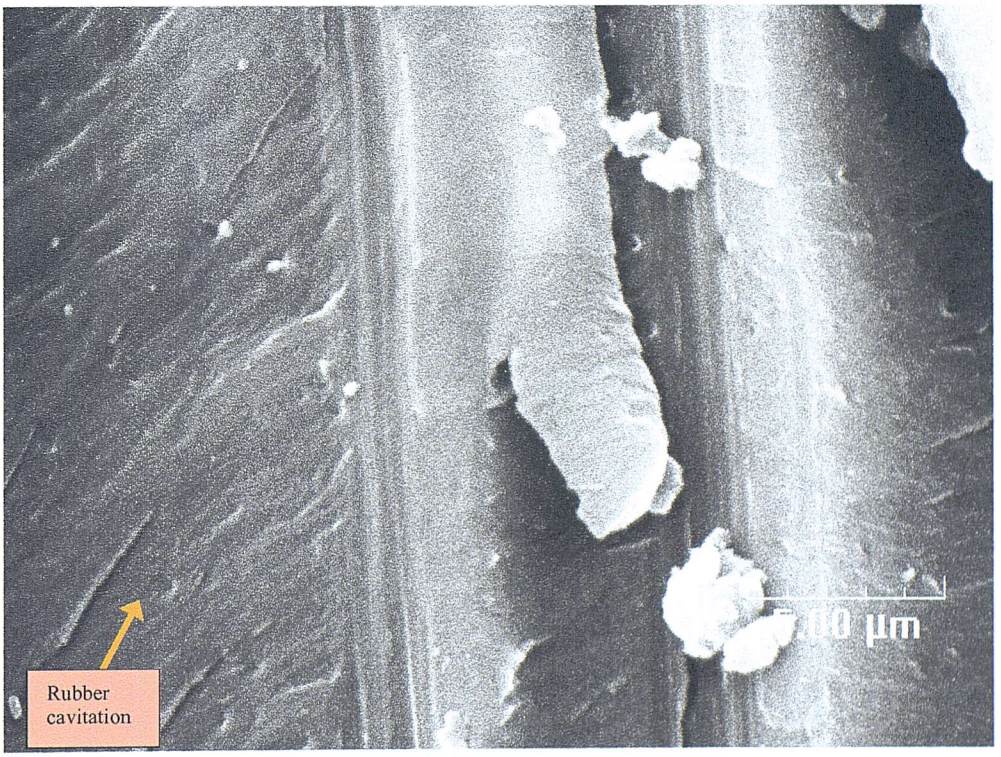


Figure 6.2.8. Fracture surface of a CFRP sample with an anhydride-cured epoxy matrix containing 9 wt. % CTBN at higher magnification (crack propagation from right to left).

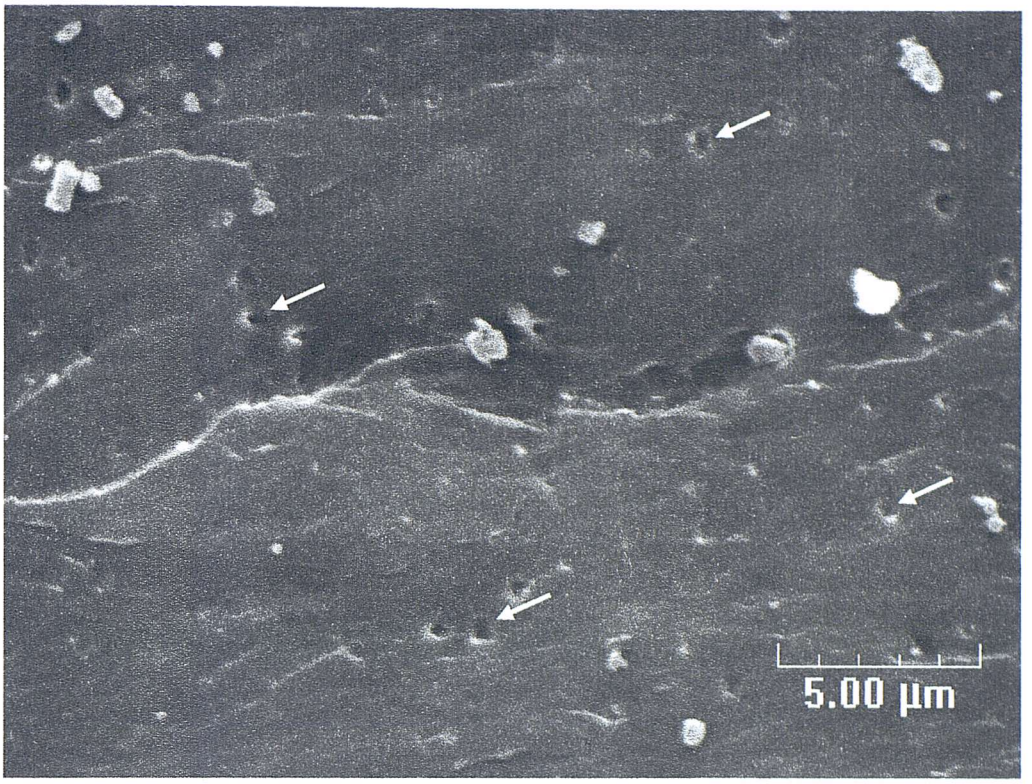


Figure 6.2.9. Fracture surface of a CFRP sample with an anhydride-cured epoxy matrix containing 9 wt. % CTBN only at higher magnification. White arrows point to some cavitated rubber particles (crack propagation from right to left).

6.2.2.4 Hybrid Modified Epoxy Matrices

The fracture surfaces of the laminates in this system all appeared quite similar. For this reason, only two of the hybrids are included in this Section since the fracture surfaces of the hybrids were indistinguishable compared to each other. It can be seen from the micrographs in Figure 6.2.10 and Figure 6.2.11 of a sample with 9 wt. % CTBN and 2.3 wt. % nano-silica, that there was widespread failure through the epoxy matrix, as well as good fibre-matrix bonding. There was also some fibre debonding and pullout, which accounted for the hybrids all having a slightly higher interlaminar fracture energy than their respective bulk epoxy polymers. Although the micrograph in Figure 6.2.12 is from the fast fracture region, there is evidence that rubber cavitation occurred.

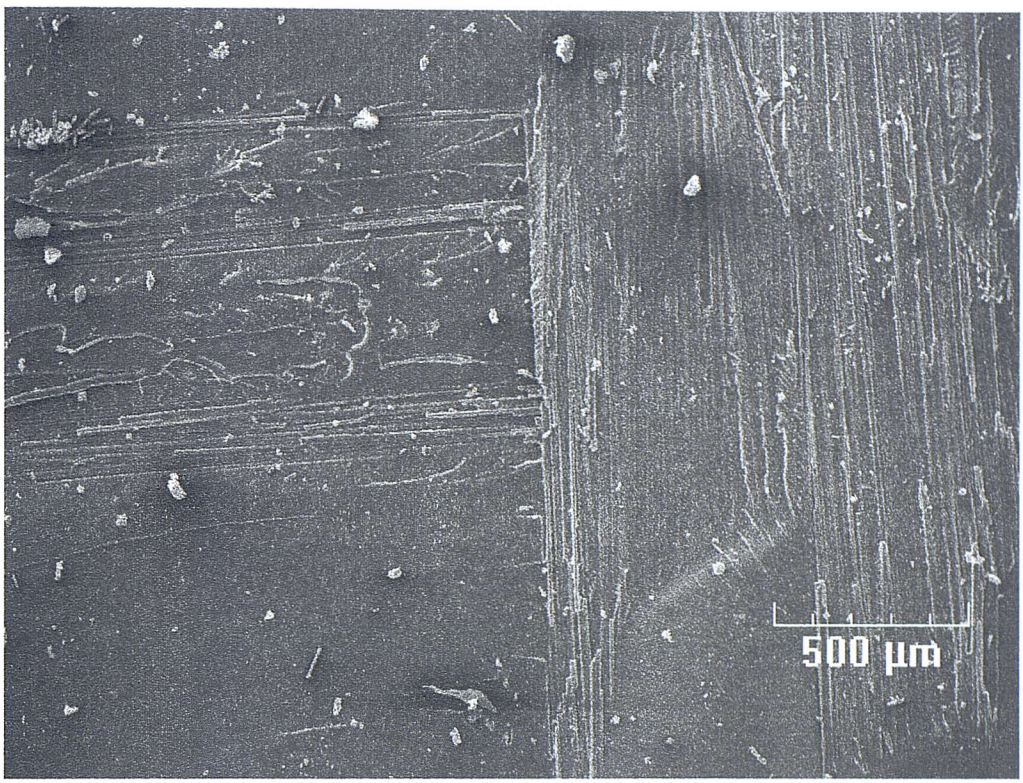


Figure 6.2.10. Fracture surface of a CFRP sample with an anhydride-cured epoxy matrix containing 9 wt. % CTBN and 2.3 wt. % nano-silica (crack propagation from right to left).

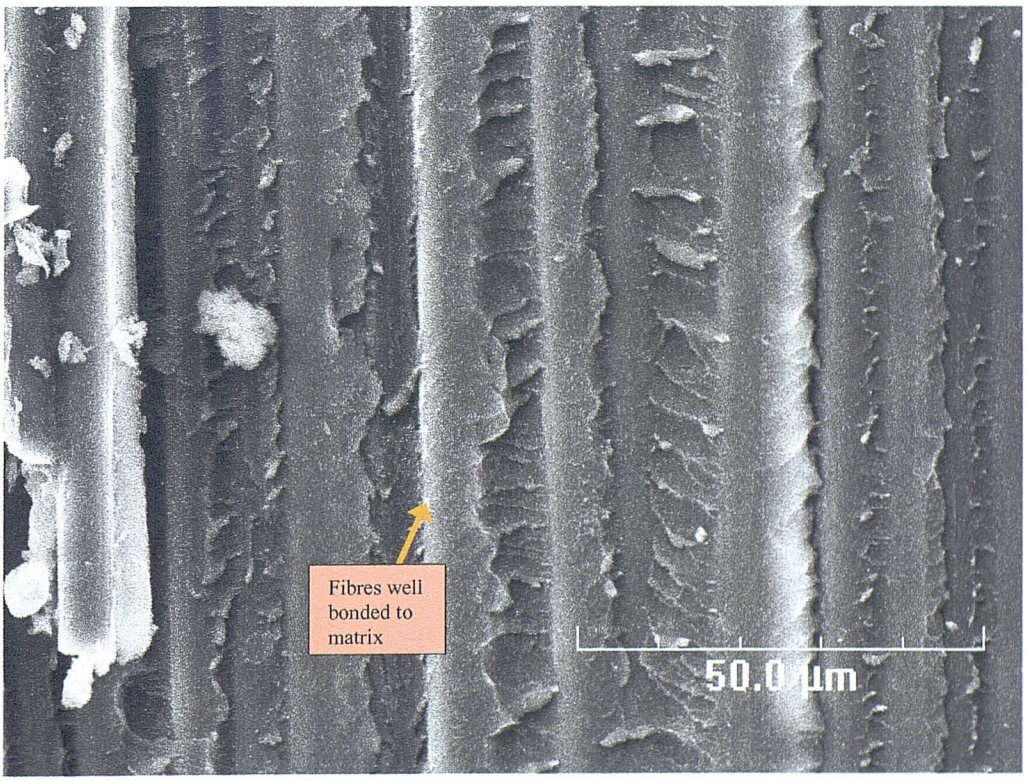


Figure 6.2.11. Fracture surface of a CFRP sample with an anhydride-cured epoxy matrix containing 9 wt. % CTBN and 2.3 wt. % nano-silica at higher magnification (crack propagation from right to left).

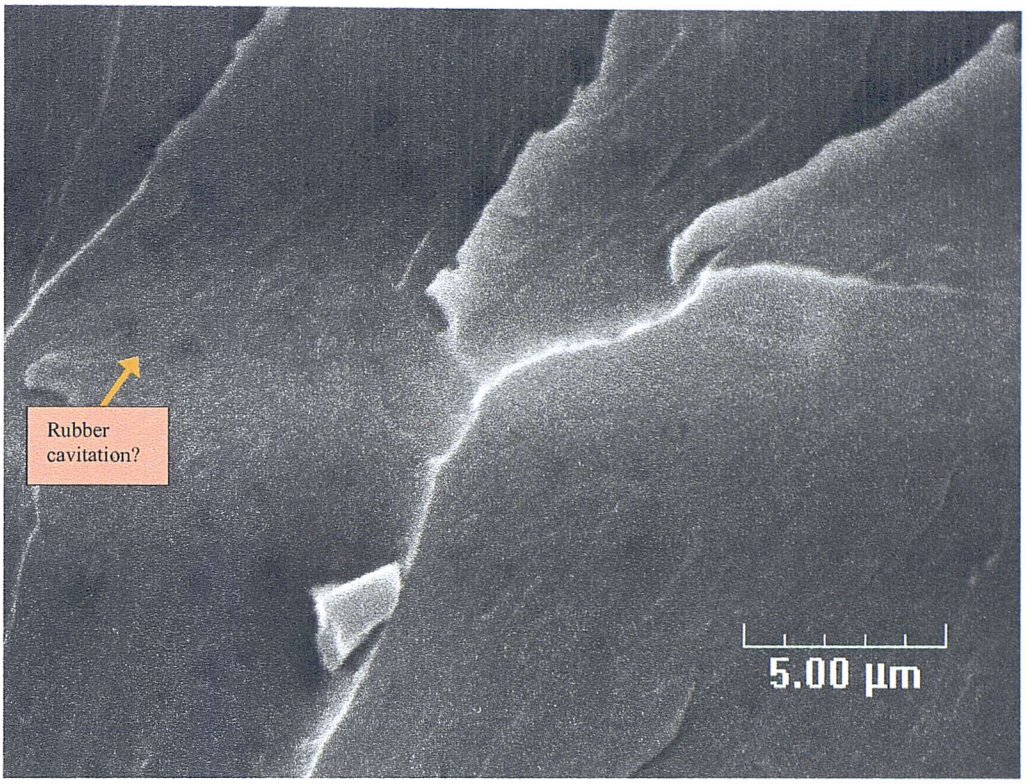


Figure 6.2.12. Fracture surface of a CFRP sample with an anhydride-cured epoxy matrix containing 9 wt. % CTBN and 2.3 wt. % nano-silica at higher magnification (crack propagation from right to left).

The micrographs in Figure 6.2.13 and Figure 6.2.14 are the fracture surfaces of a sample with 9 wt. % CTBN and 10.5 wt. % nano-silica. There is less cohesive failure in this sample, and more evidence of toughening from the fibres. Indeed, as in all the previous samples, there is good fibre-matrix bonding, fibre debonding and fibre pullout. In addition, evidence of fibre bridging is visible, which would have contributed to the small R-curve that was observed in this sample.

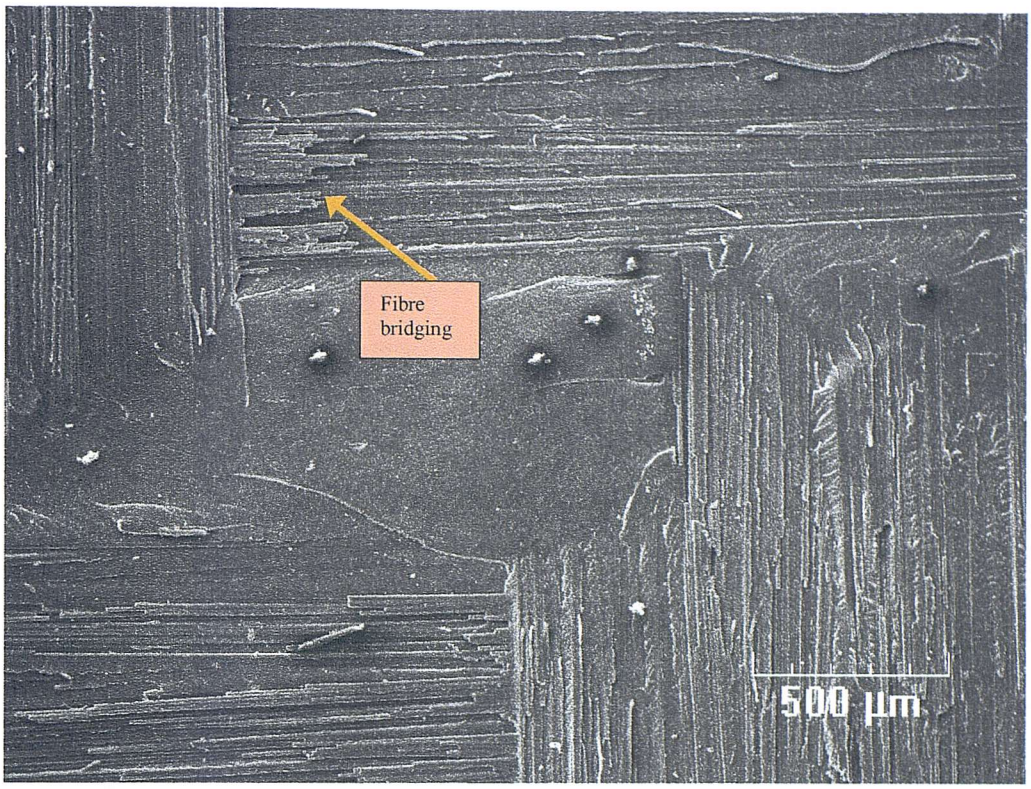


Figure 6.2.13. Fracture surface of a CFRP sample with an anhydride-cured epoxy matrix containing 9 wt. % CTBN and 10.5 wt. % nano-silica (crack propagation from right to left).

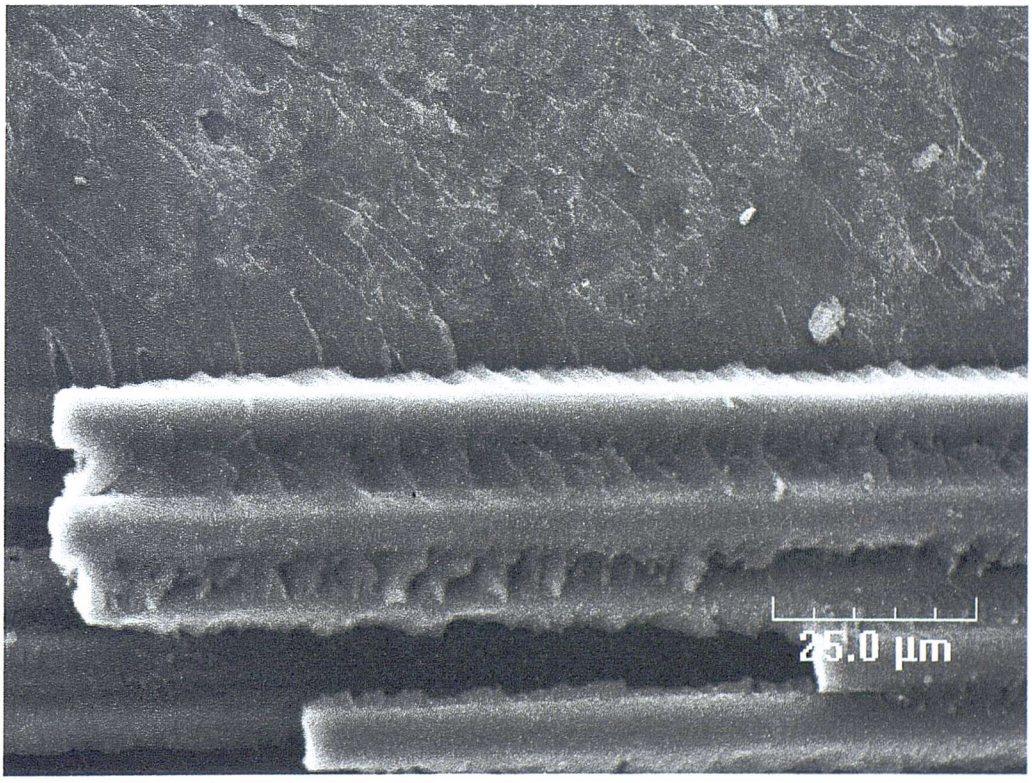


Figure 6.2.14. Fracture surface of a CFRP sample with an anhydride-cured epoxy matrix containing 9 wt. % CTBN and 10.5 wt. % nano-silica at higher magnification (crack propagation from right to left).

6.2.2.5 Summary

A common feature in all the laminates was the good fibre-matrix adhesion. There was also widespread evidence of cohesive failure of the epoxy matrix and rubber cavitation, but the nano-silica particles were not visible (due to their small size). Fibre debonding, pullout and bridging provided some extra interlaminar fracture energy, so that all the laminates had higher interlaminar fracture energies than their corresponding bulk epoxy polymer fracture energies.

6.2.3 Flexural Modulus

The laminates underwent three point elastic loading at a constant strain rate of 0.01/min. Load-displacement graphs were recorded and the flexural moduli were calculated. The results are shown in Figure 6.2.15 with error bars of ± one standard deviation.

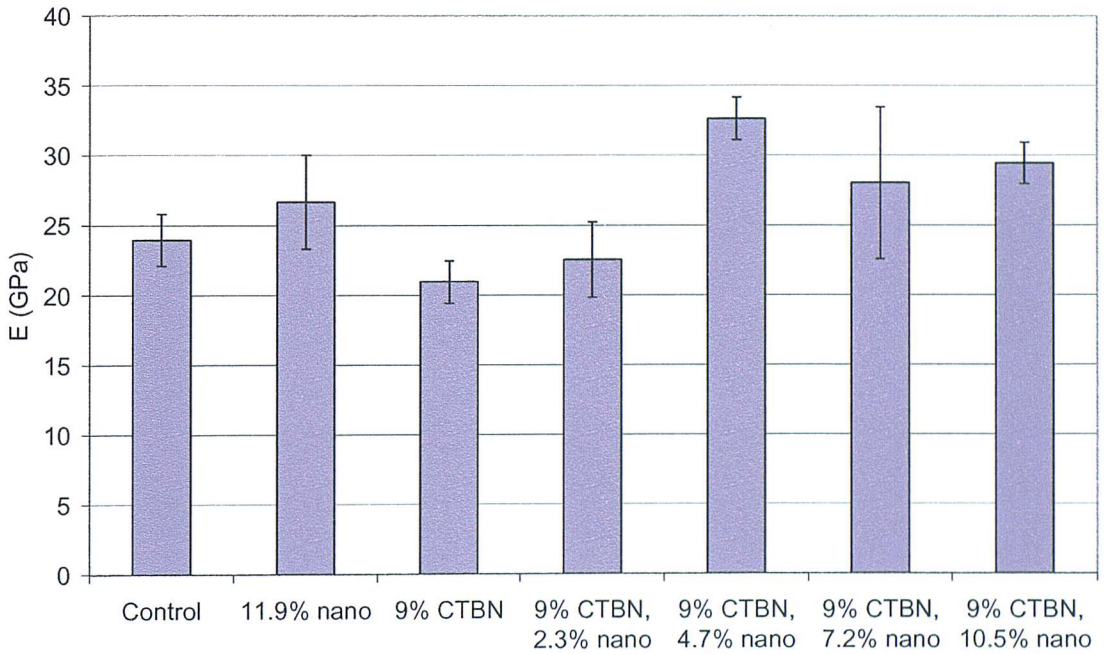


Figure 6.2.15. Flexural modulus results for CFRPs with an anhydride-cured DGEBA matrix. (error bars are ± one standard deviation)

The control had a flexural modulus of ~24GPa and adding nano-silica particles raised the modulus to 26GPa. Since rubber is much more compliant than epoxy, adding rubber lowered the modulus of the laminates to 21GPa. The hybrid samples had varying results which did not correlate to what was expected, since the moduli should have followed

the same trend (albeit less pronounced) than their corresponding bulk moduli (ie. rubber should have decreased the modulus, and nano-silica should have increased it). Indeed, the modulus of the epoxy was much lower than the fibre modulus, and there should not have been such a large fluctuation of results as observed.

6.2.3.1 Fibre Volume Fraction Analysis

After reviewing the fracture and modulus results (the large variation in modulus results was unexpected), it was decided to investigate the volume fraction of carbon-fibres in the specimens to see if this could have explained the results. Figure 6.2.16 shows that fibre volume percentages varied between formulations and repeats of each formulation. The mean fibre volume fraction for the specimens was 26.5%.

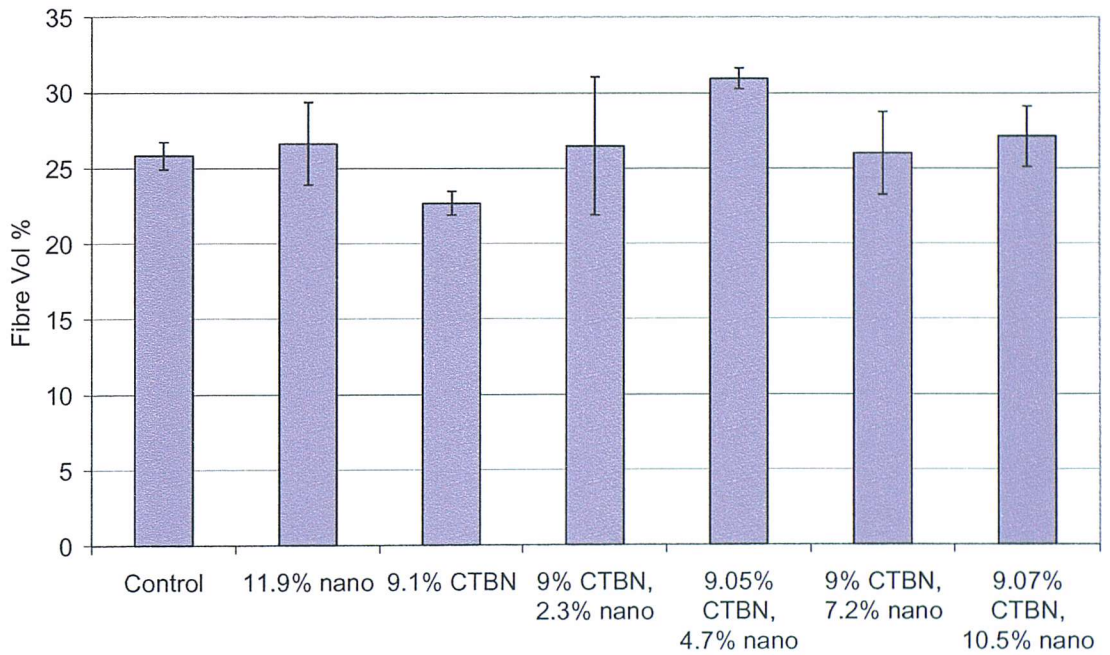


Figure 6.2.16. Fibre volume fraction for CFRPs with an anhydride-cured DGEBA based matrix. (error bars are ± one standard deviation)

There is a strong correlation between the measured fibre volume fraction and the modulus, showing that as the volume fraction of fibres increases, the modulus of the CFRP increases, as shown in Figure 6.2.17. This confirms that the flexural modulus of the CFRPs is dominated by the carbon fibres.

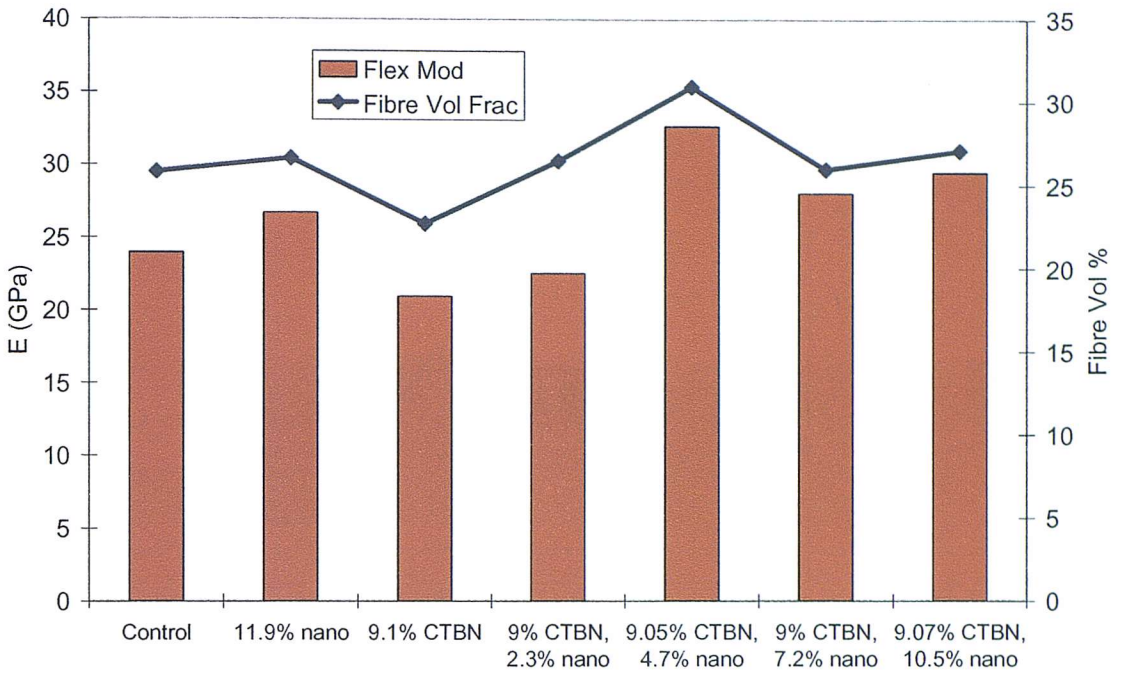


Figure 6.2.17. A comparison of the flexural moduli, with the fibre volume fractions for the CFRPs.

If the moduli of the specimens are calculated (using the Rule of Mixtures as given in Equation 2.15 in Chapter 2) assuming constant fibre modulus (91GPa [176]) and volume fraction (26.5%), then the results shown in Figure 6.2.18 are obtained.

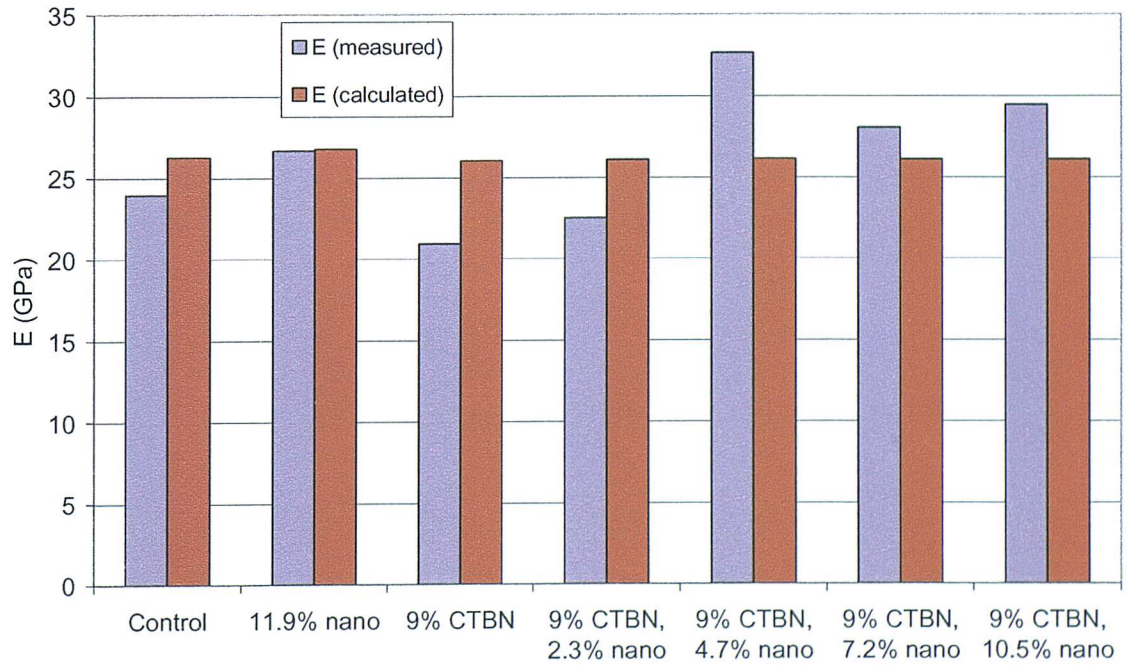


Figure 6.2.18. Comparison of calculated and measured moduli for the CFRPs.

Figure 6.2.18 (the calculated values) shows that the modulus increases slightly when only nano-silica is added (due to nano-silica having a higher modulus, but being present in low concentrations). The modulus decreases slightly when only rubber is added (due to rubber having a lower modulus, but being present in low concentrations), and remains relatively constant for hybrid formulations. All the laminates have a calculated flexural modulus of ~26.2GPa and the numerical values can be found in Table 6.2.2.

Table 6.2.2. Summary of the calculated flexural moduli of the CFRPs.

wt. % CTBN	wt. % nano-silica	E *(GPa)*
0	0	26.3
0	11.9	26.8
9	0	25.9
9	2.3	26.1
9	4.7	26.1
9	7.2	26.2
9	10.5	26.2

6.2.3.2 Summary

The trend of the measured flexural moduli did not correlate with what was expected, and fibre volume analyses were performed. It was found that there was a strong correlation between the fibre volume fraction and the flexural modulus: the modulus increased with increasing fibre volume fraction. When corrected (assuming constant fibre volume fraction and fibre modulus), it was found that the flexural modulus for all the laminates was ~26.2GPa.

6.3 Chapter Discussion

This chapter has investigated the microstructure, mechanical properties and fracture of an anhydride-cured DGEBA-based bulk epoxy polymer that was toughened with CTBN rubber and nano-silica particles. It has also explored the toughness and flexural modulus of laminates that were composed of carbon fibres. Both the bulk epoxy polymer and the CFRPs have commercial applications. Indeed, the bulk epoxy polymer is used to coat electrical transformers, and the CFRPs are being used in sporting equipment such as hockey sticks, ski poles and tennis racquets [150]. Accordingly, the results from the bulk epoxy polymer and the CFRPs will be discussed separately, and then the transfer of fracture energy from bulk epoxy polymer to CFRP will be examined.

6.3.1 Bulk Epoxy Polymers

Table 6.3.1 shows all the results (for easy reference) for the various samples tested.

Table 6.3.1. Summary of the mean values of the material properties for the anhydride-cured DGEBA-based bulk samples. ('ND' means No Data)

wt. % CTBN	wt. % nano-silica	T_g (°C)	Young's Modulus *E (GPa)*	K_{Ic} *(MPa $m^{1/2}$)*	G_{Ic} *(J/m^2)*
0	0	153	2.96	0.59	103
0	4	152	3.21	1.03	291
0	7.8	154	3.43	1.17	352
0	11.1	151	3.57	1.18	343
0	14.8	152	3.60	1.29	406
0	20.2	150	3.85	1.42	461
6	0	152	*ND*	0.84	221
5.03	5.03	144	2.85	1.86	1068
5.17	2.59	150	2.86	1.70	889
9	0	*ND*	*ND*	1.11	444
9	2.3	149	2.44	1.71	453
9	4.5	147	2.66	1.7	918
9	9	147	2.77	1.76	977
9	10.5	145	2.79	1.99	1240
9	15.4	141	2.85	2.19	1480
12	6	139	*ND*	1.83	1050
12	12	146	*ND*	1.75	960
18	0	146	*ND*	1.56	763
18	9	131	*ND*	1.32	546
18	18	126	*ND*	1.93	1167

TEM and AFM images of the nano-only bulk epoxies showed excellent dispersion of the nano-silica, even at higher concentrations. The presence of the nano-silica particles had no effect on varying the value of the glass transition temperature beyond that of the unmodified epoxy. However, the presence of the nano particles increases the Young's modulus of the polymer, with the value of E increasing steadily as the wt. % of the nano-silica is increased. The inclusion of only 4 wt. % nano-silica doubles the fracture energy of the bulk polymer and thereafter, further increases in the amount of nano-silica produce a small, but steady increase in the measured toughness. The fracture surfaces for the unmodified epoxy and samples containing nano-silica only, are glassy and show feather markings: classic brittle failure features. Micrographs at higher magnification suggest that the nano-silica toughens the epoxy by the particles debonding and relieves the constraint in the epoxy so that the epoxy plastically deformed around each particle, to form voids. This toughening mechanism shall be discussed in greater detail in Chapter 7.

The rubber particles that have phase separated are easily seen in the TEM micrographs and AFM images, as clearly defined spherical domains of up to 1μm in diameter. Where volume fraction analysis was performed, it was found that 50% and 25% of the rubber phase separated in the samples containing 9 and 18 wt. % CTBN respectively. When only CTBN is added to the epoxy, the glass transition temperature decreases because not all of the CTBN phase separates into rubber particles (which was confirmed by the volume fraction analysis). The CTBN has a much lower stiffness compared to the unmodified epoxy or nano-silica, so its inclusion decreased the Young's modulus of the samples but increased the fracture energy with increasing rubber content. The cavitation of the rubber particles is clearly visible in some of the micrographs, but it is believed that the dominant rubber toughening mechanisms are shear yielding and the plasticisation of the epoxy matrix, since volume fraction analysis and thermal analysis showed that some of the rubber remains in solution in the epoxy phase.

For hybrid samples, the TEM micrographs show that at low amounts of CTBN the nano-silica remains well dispersed. However, when 9 wt. % CTBN or more was incorporated into a sample, the nano-silica started to coalesce into necklace-like, three-dimensional structures. One hypothesis is that the rubber increases the surface energy of the particles, thereby causing the nano-silica particles to agglomerate [168]. These

agglomerates, however, are well dispersed throughout the samples. For a given CTBN content (except 12 wt. %) the glass transition temperature decreases as the nano-silica content increases. This suggests that increasing the amount of nano-silica causes more CTBN to remain in the epoxy phase. This phenomenon is most apparent in the samples containing 18 wt. % CTBN, but more TEM micrographs and AFM images would have to be obtained for volume fraction analysis to confirm this. The Young's modulus of the hybrids increases steadily as the wt. % of the nano-silica is increased, because the silica particles have a higher modulus than the unmodified DGEBA or CTBN. The sample with 9 wt. % CTBN and 15.4 wt. % nano-silica had a fracture energy that was fourteen times more than that of the unmodified epoxy, and three times more than that of its CTBN-only counterpart. Indeed, there is a good synergy between rubber and nano-silica in this system.

6.3.2 CFRP Laminates

The flexural modulus data had to be corrected because of the varying fibre volume fraction. It was found that when corrected, the average flexural modulus of all the samples was ~26.2GPa.

A comparison of the fracture energies of the bulk epoxy polymer and CFRPs is summarised in Figure 6.3.1. The graph shows that the CFRP fracture energies are higher than those of the bulk epoxy polymer, as discussed in Sections 6.1.2.3 and 6.2.1. However, there is a good correlation between the two, suggesting that the tougher the epoxy, the tougher the CFRP. Under mode I conditions, a nano-modified epoxy matrix gives similar fracture resistance but increases the modulus compared to the control laminate. A rubber-modified resin yields a very tough, but less stiff laminate. Combining both CTBN and nano-silica, gives a CFRP with a high toughness and stiffness, with an increase in toughness of almost 300% above that of a CFRP containing unmodified epoxy. The fracture surfaces of the laminates have shown that there is good deformation of the epoxy matrix (including some rubber cavitation), and that there is good adhesion between the fibres and the matrix. The extra fracture resistance is provided by fibre debonding, pullout and bridging.

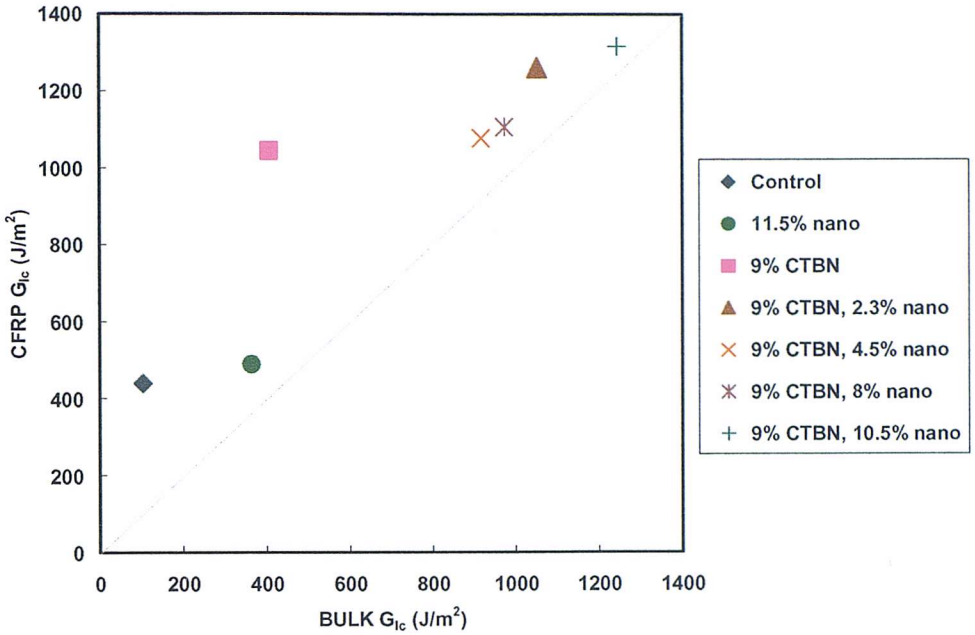


Figure 6.3.1. Comparison of bulk and CFRP fracture energies.

6.4 Conclusions

This chapter has investigated the microstructure, mechanical properties and fracture of an anhydride-cured DGEBA-based bulk epoxy polymer that was toughened with CTBN rubber and nano-silica particles. It has also explored the toughness of laminates that were composed of carbon fibres using these bulk epoxy polymers as the matrices.

It was found that for the bulk epoxy polymers, the addition of CTBN-only led to a decrease in stiffness and glass transition temperature, but an increase in fracture energy. Microstructural analysis showed that the rubber phase-separated in varying amounts as spherical particles, whilst some rubber remained in solution in the epoxy phase (which accounted for the decrease in glass transition temperature). Hybrid bulk epoxy polymers containing both rubber and nano-silica showed a small change in T_g (because in some cases the nano-silica suppressed the phase separation of the rubber), an increase in stiffness (due to the higher stiffness of silica particles). In the hybrids containing 9 wt. % CTBN, it was found that the fracture toughness increased with increasing nano-silica content, and there was a synergistic effect between the rubber and the nano-silica.

There was an enhancement of toughness from the bulk epoxy polymers to the CFRPs possibly because of the good adhesion at the fibre-matrix interface. The hybrid laminates were found to have the highest interlaminar fracture energies.

CHAPTER 7

SYSTEM COMPARISONS AND TOUGHENING MECHANISMS: BULK EPOXY POLYMERS

7 Introduction

During the course of this Thesis, the reader has been introduced to the theories which attempt to explain and model the material properties and fracture mechanisms of the bulk epoxy polymers, and FRPs which used these bulk epoxies as the matrices. The results from investigations of three different systems have been presented:

1. The amine-cured DGEBA-based system (see Chapter 4);
2. The amine-cured TGMDA-based system (see Chapter 5);
3. The anhydride-cured DGEBA based system (see Chapter 6).

This Chapter will review the results from the bulk epoxy polymers of all three systems and discuss them with respect to each other. The similarities and differences between the systems will be critically assessed and, in keeping with the main theme of this Thesis, emphasis will be placed on identifying and modelling the operative fracture mechanisms.

7.1 Microstructural Aspects

Atomic force and transmission electron microscopes (ie. an AFM and TEM) were used to ascertain the microstructure of the bulk epoxy polymers. It has been established that images from either technique can be used, since they showed similar features. All the figures presented in this Section can be found in the earlier Chapters. However, the main ones have been included again for ease of reference and to enable comparisons to be readily seen and reached between the three different systems. (Note that the arrows pinpointing various features have been omitted in many of the figures presented in this Chapter because of the reduced size of the images.)

7.1.1 Unmodified Epoxies

The TEM micrographs of ultra-thin slices in Figure 7.1.1 (a) and (c), and the AFM micrograph in Figure 7.1.1 (b), are of the unmodified epoxies of the three systems investigated in this study. It can be seen that the micrographs of these epoxies are all featureless, which is expected for unmodified homogenous thermosetting polymers. (Ignore the arc-like feature in Figure 7.1.1 (c), which was the copper grid that the microtomed slice was placed on.)

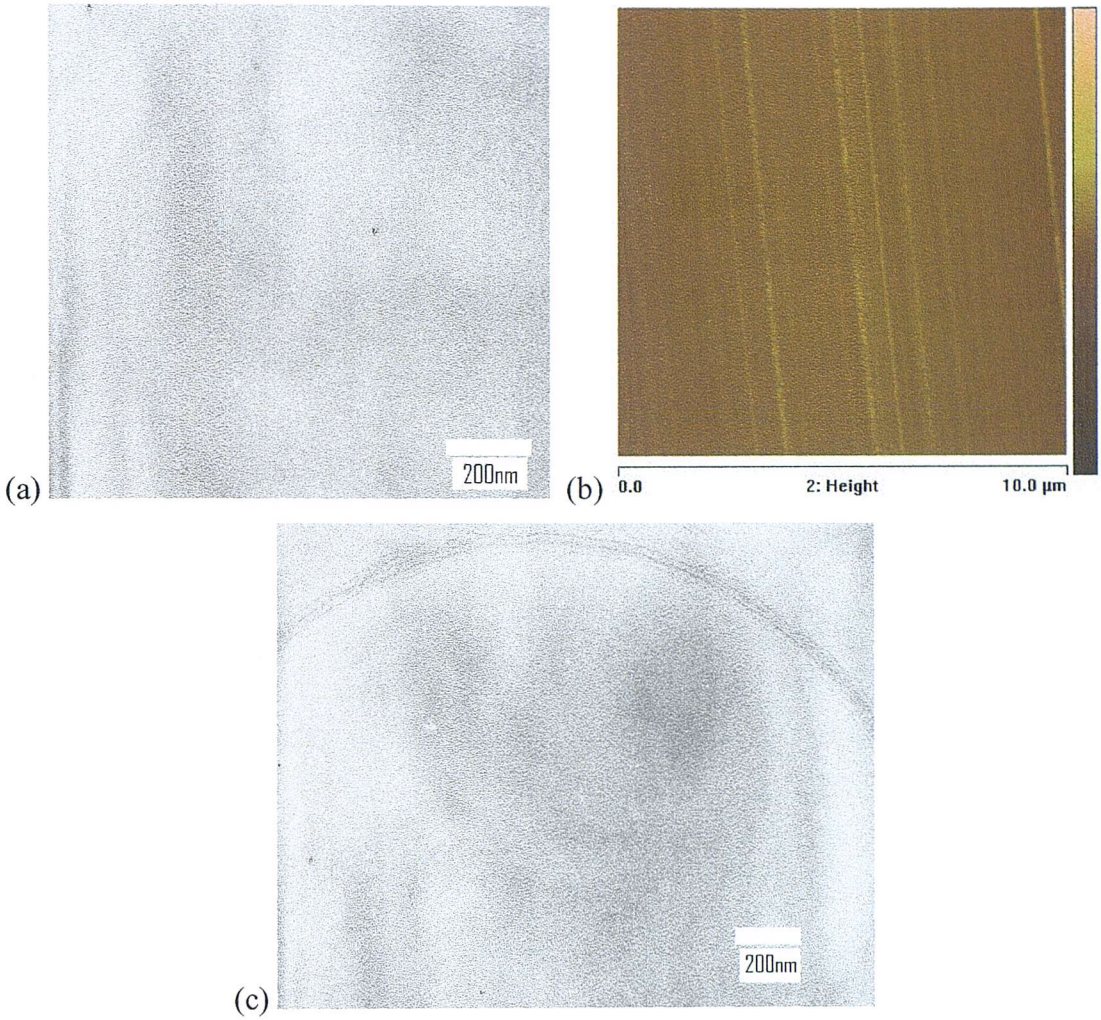


Figure 7.1.1. Microscopy images showing the microstructure of the unmodified epoxies of the: (a) amine-cured DGEBA-based system, (b) amine-cured TGMDA-based system and (c) anhydride-cured DGEBA-based system (ignore arc-like feature).

7.1.2 Rubber Modified Epoxies

All three systems showed some phase separation of the CTBN into spherical rubbery domains that can easily be discerned with the AFM and TEM (when stained with osmium tetroxide). However, the differences between the three systems in the size of the rubber particles and the degree of phase separation, can be seen from the samples containing a comparable amount of rubber (ie. ~ 8 wt. %) in Figure 7.1.2. Indeed, the rubber particles are up to 0.5µm in diameter in the amine-cured DGEBA-based system and about ~80% of the rubber phase (according to volume fraction analysis) separates, regardless of the CTBN content. The amine-cured TGMDA-based system shows particles up to 1µm in diameter, but only about ~25% of the CTBN phase separates. The

anhydride-cured DGEBA-based system also has particles up to 1μm in diameter, with up to about 50% of the CTBN phase separating.

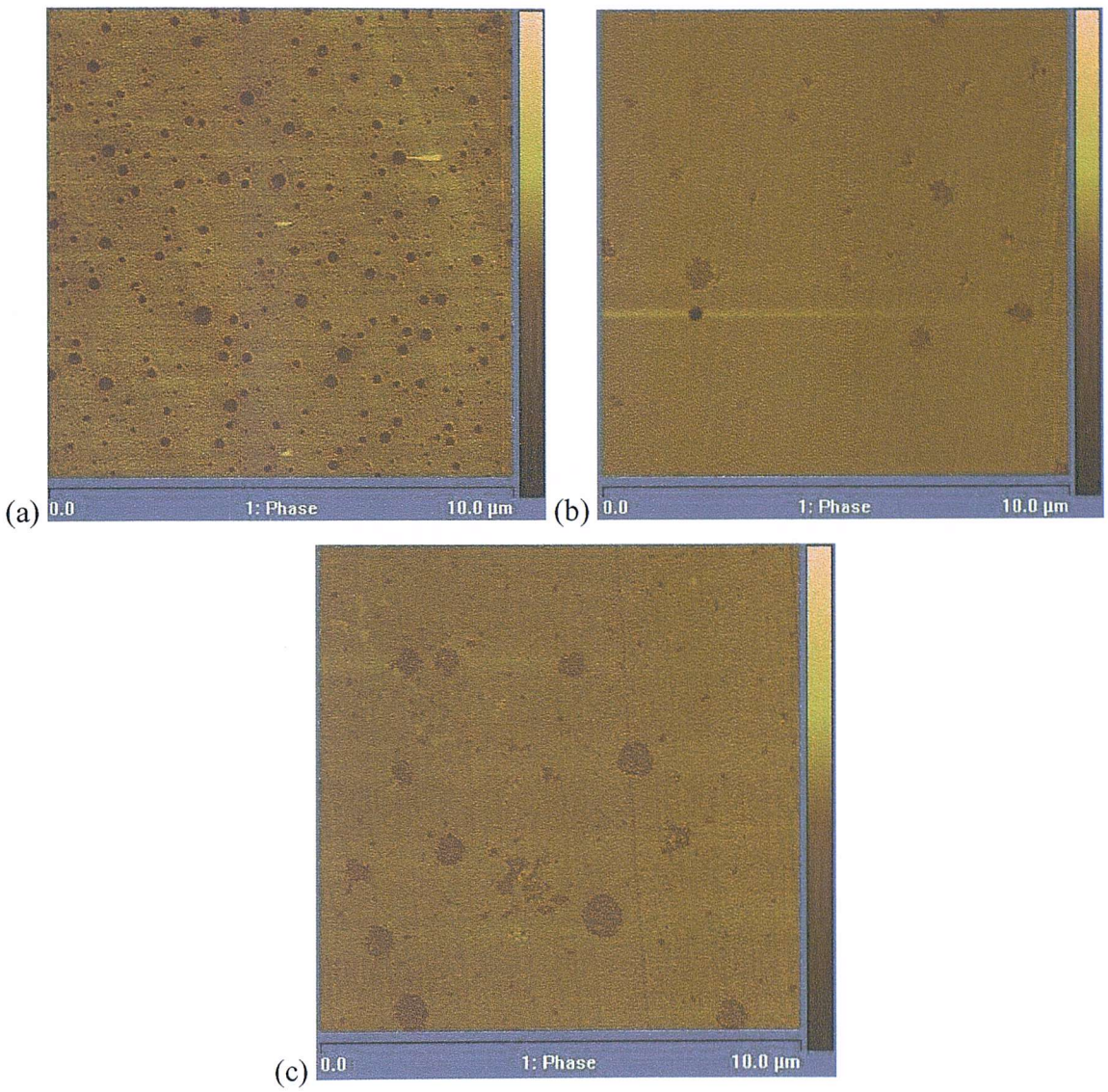


Figure 7.1.2. AFM images of (a) an amine-cured DGEBA-based sample with 6.9 wt. % CTBN, (b) an amine-cured TGMDA-based sample with 8 wt. % CTBN, and (c) an anhydride-cured DGEBA-based sample with 9 wt. % CTBN.

It is interesting to note that the volume fraction of rubber that phase separates in the amine-cured DGEBA-based system increases linearly with increasing rubber content (see Table 4.1.2 in Chapter 4), but remains relatively constant in the anhydride-cured DGEBA-based system. Overall, there seems to be a correlation between the degree of phase separation and particle size: small particles lead to more phase separation, and *vice versa*. Since both of these systems are DGEBA-based epoxies, and both are toughened with the same type of CTBN (Hycar 1300x8), it follows that the morphology

and phase distribution varies due to the different curing agents and curing regimes. The work of Russell and Chartoff [126] showed that the cure conditions change the morphology and phase distribution of rubber in a rubber-modified epoxy polymer, which is in agreement with the observations from the present work.

The rubber morphology for all three systems is summarised in Table 7.1.1. It shows the wt. % CTBN added to each system, the wt. % CTBN that phase separated according to volume fraction analysis, and the wt. % CTBN that phase separated calculated using the glass transition temperatures (see Section 7.2.1 for details). (It should be noted that volume fraction analysis was performed and then converted to wt. % values for ease of comparison.) It can be seen that the visually ascertained wt. % of CTBN that phase separated and the calculated values are only in good agreement in the amine-cured DGEBA-based system. (It is possible that the discrepancy for the other systems occurred because the images were taken from a rubber deficient area. Performing volume fraction analysis on at least a dozen images would be necessary to get a more accurate estimate of the amount of rubber that phase separates.)

Table 7.1.1. Summary of the rubber morphology. (*ND* – No Data)

System	wt. % CTBN added	Visual wt. % CTBN phase separated	Calculated wt. % CTBN phase separated	Particle diameter, μm
Amine-cured DGEBA-based system	4.6	3.5	2.1	0.1 – 0.5
	6.9	6	4.4	0.1 – 0.5
	10.9	9	8.4	0.1 – 0.5
Amine-cured TGMDA-based system	8	2	6	0.1 – 1
Anhydride-cured DGEBA based system	9	4.5	*ND*	0.4 – 1
	18	4.5	15.5	0.4 – 1

7.1.3 Nano-silica Modified Epoxies

No samples toughened with nano-silica only were supplied by *hanse chemie* for the amine-cured DGEBA-based system. However, there was a systematic range of nano-only epoxy polymers for the other two systems. The micrographs in Figure 7.1.3 are from these two systems containing similar concentrations of nano-silica particles.

In the amine-cured TGMDA-based system, the nano-silica particles coalesce into agglomerates containing larger numbers of particles with increasing nano-silica content. This observation is in good agreement with the work of Wu *et al.* [178] and Vladimirov *et al.* [179] who also showed an increase in the size of nano-silica agglomerates with increasing nano-silica content. A possible explanation for the agglomeration of nano-silica particles has been proposed by Vega-Baudrit *et al.* [158]. These authors suggested that the silanol content causes moisture adsorption on the silica surface and therefore the filler–filler interactions increase, which in turn leads to agglomeration of the nano-silica particles. Their work suggests why the nano-silica particles agglomerate, but does not explain why agglomeration increases with increasing nano-silica content. One possible reason is that the different epoxies, curing agents, and curing regimes used, affect the surface tension of the nano-silica particles and therefore cause them to agglomerate [168].

The nano-silica particles in the anhydride-cured DGEBA-based system are well dispersed regardless of the nano-silica content. It should be noted that the micrograph in Figure 7.1.3 (b) appears to have a relatively very high concentration of nano-silica particles. However, this is misleading, since the AFM image shows only the surface of the sample, whereas the TEM micrographs are transparent slices of ~100nm thickness; and three or four 20nm diameter particles that appear to be next to each other may indeed be below the surface - thus giving the impression of more particles. The morphology of the nano-silica particles in the nano-only bulk epoxy polymers for all three systems is summarised in Table 7.1.2.

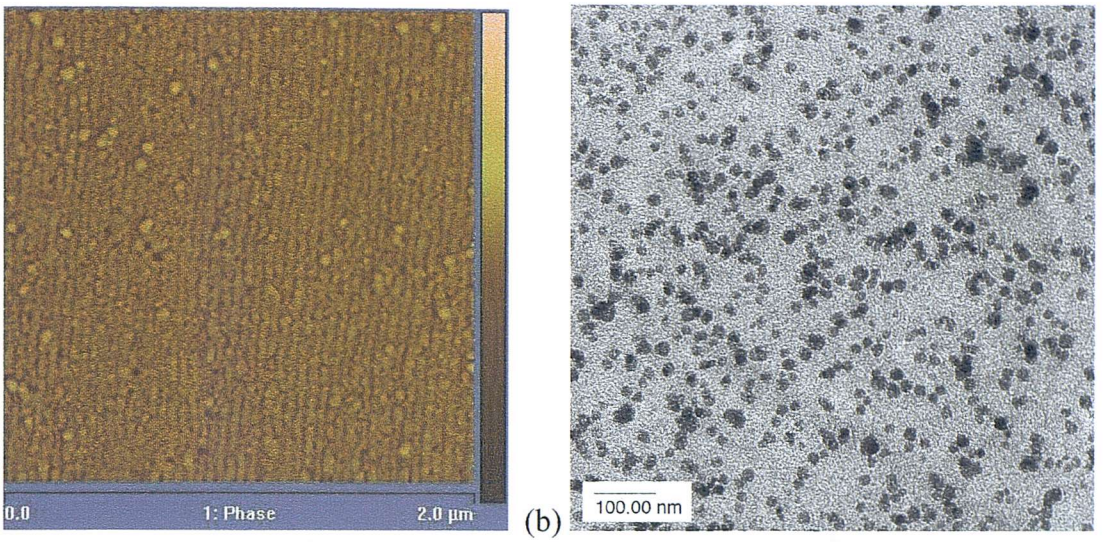


Figure 7.1.3. Micrographs of (a) an amine-cured TGMDA-based sample with 5 wt. % nano-silica, and (b) an anhydride-cured DGEBA-based sample with 5 wt. % nano-silica [116].

Table 7.1.2. Summary of the nano-silica morphology.

System	wt. % nano-silica	Nano-silica Microstructure	Typical formation size
Amine-cured TGMDA-based system	5	Single spherical particles, and small agglomerates consisting of up to *two* particles	Ø20nm, 20nm x 45nm
	10	Single spherical particles, and small agglomerates consisting of up to about *six* particles	Ø20nm, 60nm x 50nm
	19.5	Few single spherical particles. Mostly small agglomerates consisting of up to about *twelve* particles	Ø20nm. 80nm x 80nm
Anhydride-cured DGEBA based system	4	Well-dispersed single spherical particles	Ø20nm
	7.8	Well-dispersed spherical single particles	Ø20nm
	11.1	Well-dispersed spherical single particles	Ø20nm
	14.8	Well-dispersed spherical single particles	Ø20nm
	20.2	Well-dispersed spherical single particles	Ø20nm

7.1.4 Hybrid Modified Epoxies

The TEM micrographs in Figure 7.1.4 are of selected amine-cured DGEBA-based hybrid samples. The micrographs are of samples containing 4.1, 7 and ~11 wt. CTBN and it can be seen that the rubber particles are well dispersed and are less than 1μm in diameter. (They appear oval-shaped (instead of spherical) because of compression during microtoming.) Volume fraction analysis suggests that the presence of nano-silica does not affect the amount of phase separation of the CTBN that occurs, or the size of the rubber particles. It should be noted that this series of micrographs was chosen to show that the rubber morphology is not influenced by the nano-silica content, and more importantly, to also illustrate the different morphologies of the nano-silica particles, as discussed below.

Figure 7.1.4 (a) shows a sample with 2 wt. % nano-silica, and the nano-silica particles can be seen to be well dispersed. Figure 7.1.4 (b) shows a sample with 5.7 wt. % nano-silica, and they agglomerate into three dimensional 'necklace-like' chains. Figure 7.1.4 (c) is of a sample with 7 wt. % nano-silica, and the dominating features are the 5μm diameter agglomerates ('super-clumps'), in addition to the smaller necklace-like chains. Figure 7.1.4 (d) shows a sample with 11.6 wt. % nano-silica, and the super-clumps are very clearly visible. This shows that for this system the propensity for agglomeration, and the size of the agglomerates, are dependent on the nano-silica content but independent of the CTBN content. Thus, to summarise, the nano-silica remains well dispersed up to ~4.5 wt. %, and forms necklace-like chains up to ~6 wt. %. At higher nano-silica contents, regardless of the CTBN content, super-clumps form. (The difference between the necklace-like chains and the super-clumps, is that the former are smaller and not as 'approximately spherical' as the latter.)

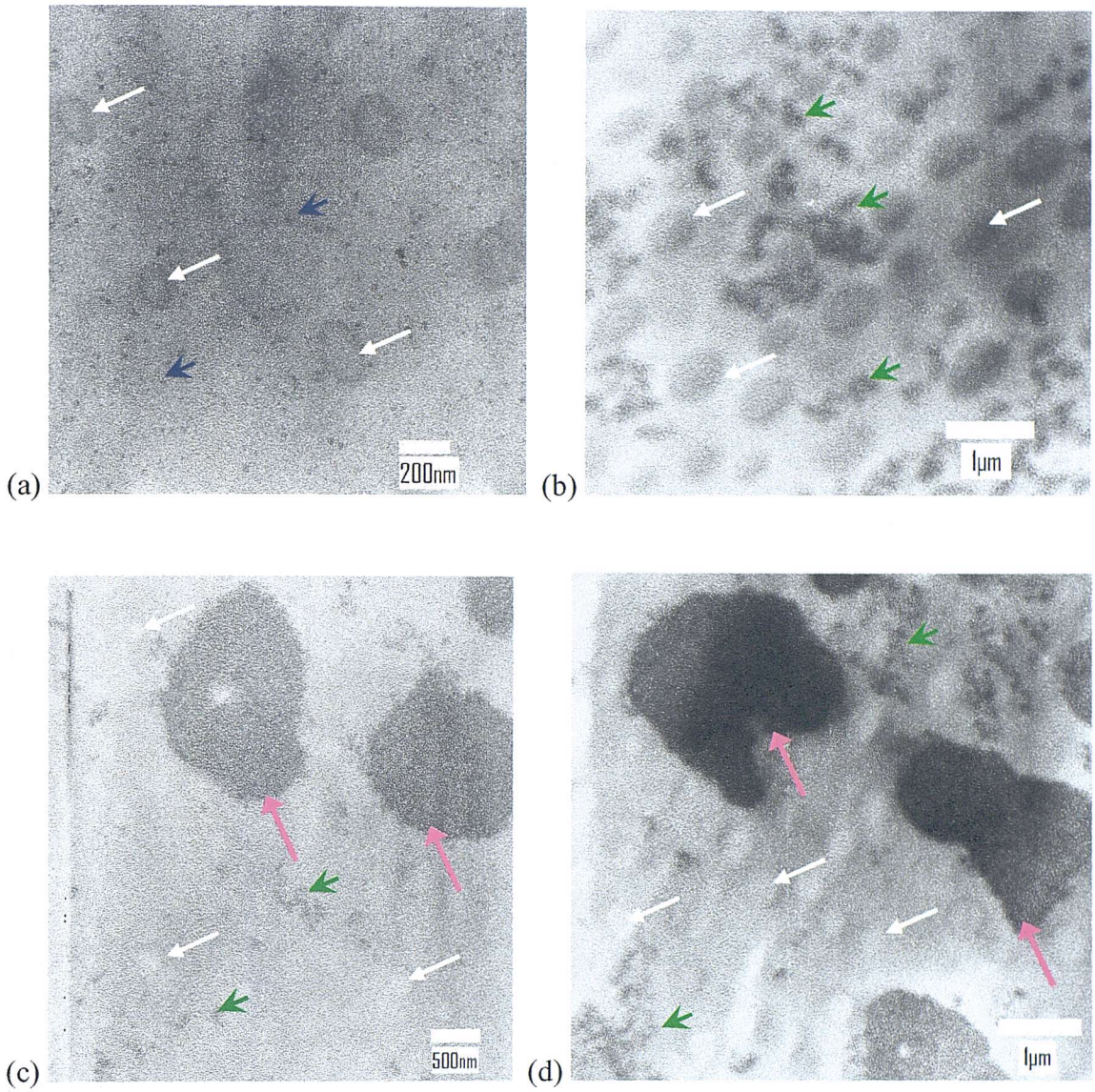


Figure 7.1.4. TEM images of amine-cured DGEBA-based samples containing: (a) 4.1 wt. % CTBN and 2 wt. % nano-silica, (b) 11.3 wt. % CTBN and 5.7 wt. % nano-silica, (c) 7 wt. % CTBN and 7 wt. % nano-silica, and (d) 11.6 wt. % CTBN and 11.6 wt. % nano-silica. (White arrow points to some rubber particles, blue arrows point to some nano particles, green arrows point to some three dimensional necklace-like structures and pink arrows point to super-clumps.)

The AFM image in Figure 7.1.5 (b) is of an amine-cured TGMDA-based sample with 8 wt. % CTBN and 10 wt. % nano-silica. The well dispersed rubber particles are ~1μm in diameter, and volume fraction analysis suggests that ~2 wt. % CTBN phase separates: both features are similar to the CTBN-only sample in Figure 7.1.5 (a). The nano-silica particles agglomerate into three-dimensional necklace-like structures of ~2μm in diameter. A comparison with the 10 wt. % nano-only sample in Figure 7.1.3 (b) shows

that the presence of rubber causes the nano-silica to coalesce into larger agglomerates containing many more particles.

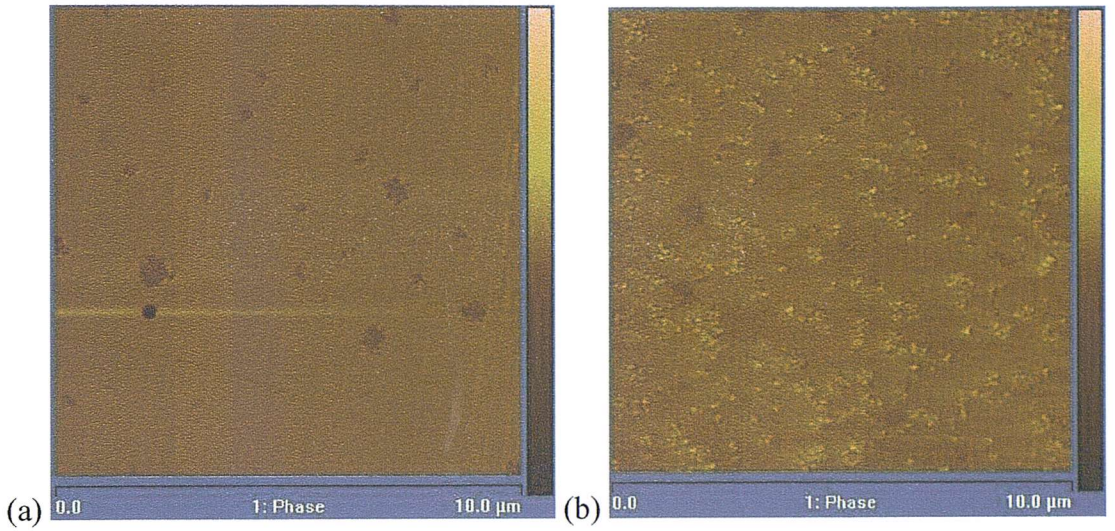


Figure 7.1.5. AFM image of an amine-cured TGMDA-based samples with (a) 8 wt. % CTBN-only, and (b) 8 wt. % CTBN and 10 wt. % nano-silica.

The TEM micrographs in Figure 7.1.6 are of hybrid anhydride-cured DGEBA-based samples. The phase-separated, well-dispersed, spherical rubber particles are up to 1µm in diameter, except in the hybrid sample with 18 wt. % CTBN and 18 wt. % nano-silica. Indeed, in this particular sample, no rubber particles are visible. This is because at high concentrations of CTBN, the nano-silica appears to suppress phase separation, and most of the rubber remains in the epoxy phase. Therefore, the nano-silica is affecting the cure-kinetics, which influences the phase separation of the rubber [126,112]. (It should be noted that the 18 wt. % CTBN-only sample clearly showed the presence of phase separated rubber particles (see Table 7.1.1).) Volume fraction analysis suggests that up to 9 wt. % CTBN, the nano-silica does not affect the propensity for phase separation and the nano-silica particles remain well dispersed at low CTBN contents, as is evident from Figure 7.1.6 (a). However, as the CTBN content increases to more than 9 wt. %, the nano particles agglomerate into necklace-like, three dimensional structures. Even at very high nano-silica contents, as in Figure 7.1.6 (d), necklace-like structures of up to 4µm in length persist. This is in direct contrast with the amine-cured DGEBA-based system, where agglomeration was dependent on nano-silica content (*not* CTBN content), and super-clumps were formed at ~7 wt. % nano-silica.

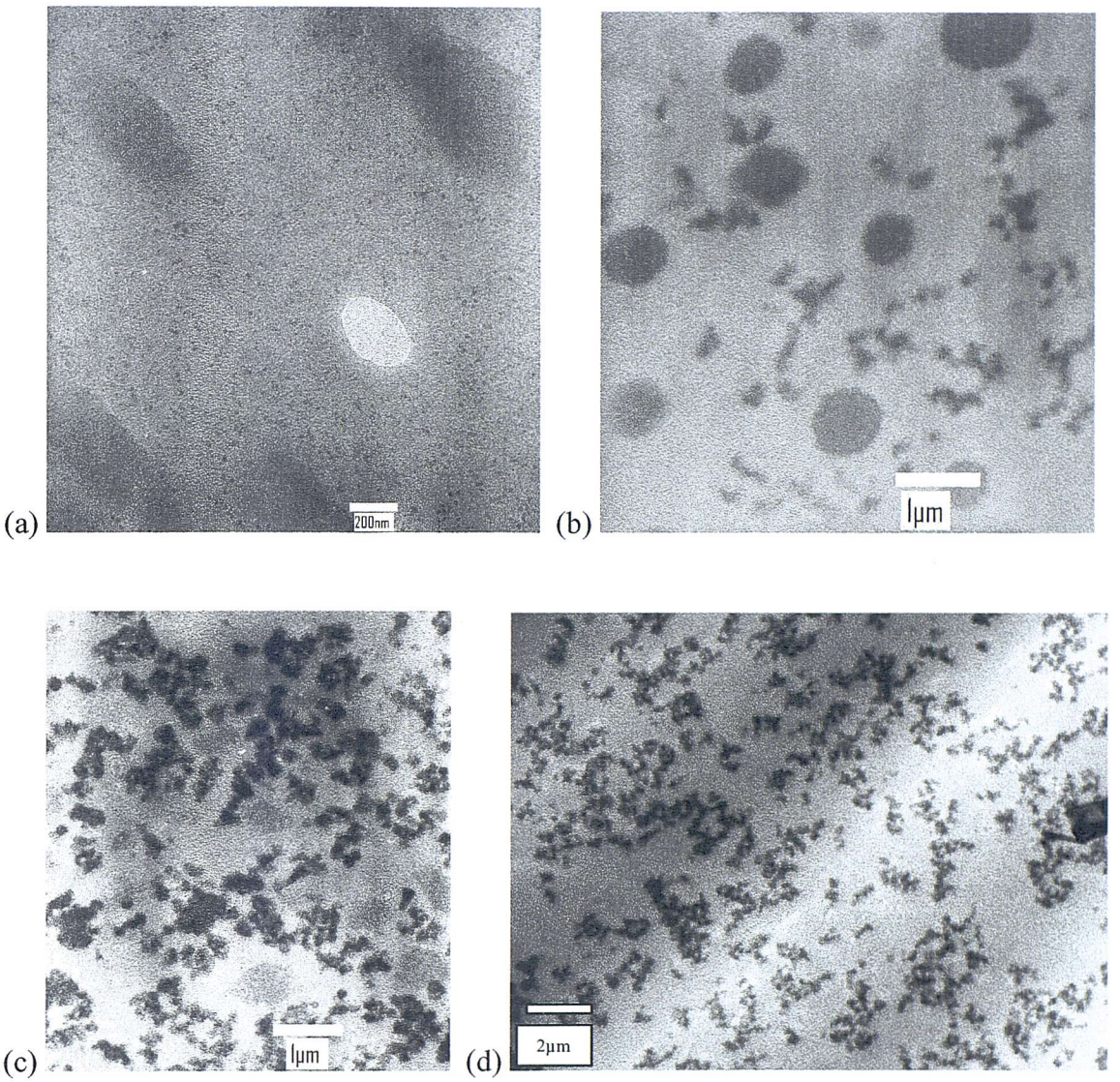


Figure 7.1.6. TEM micrographs of anhydride-cured DGEBA-based samples containing: (a) 5.03 wt. % CTBN and 5.03 wt. % nano-silica, (b) 9 wt. % CTBN and 2.3 wt. % nano-silica, (c) 9 wt. % CTBN and 15.4 wt. % nano-silica, and (d) 18 wt. % CTBN and 18 wt. % nano-silica.

The morphology of the CTBN rubber and the nano-silica particles is summarised in Table 7.1.3. The interaction between the rubber and nano-silica was different for each system. Firstly, in the amine-cured DGEBA-based system, the presence of nano-silica and rubber had no effect on each other's morphology. But, agglomerates of nano-silica of increasing size were formed with increasing nano-silica content. Secondly, in the amine-cured TGMDA-based system, the presence of CTBN rubber prompted the formation of larger agglomerates of nano-silica. Thirdly, images from the anhydride-cured DGEBA-based system show that the rubber content determines the particle distribution of the nano-silica, with agglomerates forming after a certain CTBN-content

threshold was exceeded. At very high CTBN concentrations in this system, the presence of nano-silica suppressed the phase separation of the rubber. (The reasons for the particular nano-silica/CTBN interactions observed, will form the basis of some very interesting future studies.)

Thus, these studies reveal that the nano-silica cannot simply be treated as a 'simple' filler, since the nano-silica phase affects the microstructure, depending on the type of epoxy and the nano-silica content. In addition, the nano-silica phase affects the phase separation of the CTBN rubber (and hence affects the glass transition temperature of the epoxy).

Table 7.1.3. Summary of the rubber and nano-silica morphology of the hybrid samples.

System	wt. % CTBN	wt. % nano-silica	Rubber microstructure	Nano-silica microstructure
Amine-cured DGEBA-based system	4.1	2	Well dispersed rubber spheres, 0.1-0.5μm diameter	Well dispersed 20nm spheres
	4.1	4.1	Well dispersed rubber spheres, 0.1-0.5μm diameter	Well dispersed 20nm spheres
	6.9	3.5	Well dispersed rubber spheres, 0.1-0.5μm diameter	Well dispersed 20nm spheres
	7	7	Well dispersed rubber spheres, 0.1-0.5μm diameter	Super-clumps 4μm in diameter, as well as chains
	11.3	5.7	Well dispersed rubber spheres, up to 1μm diameter	Chains 1μm in length, 0.2μm in width. Well dispersed
	11.6	11.6	Well dispersed rubber spheres, up to 1μm diameter	Super-clumps 4μm in diameter, as well as chains
Amine-cured TGMDA-based system	8	10	Well dispersed rubber spheres, up to 1μm diameter	Necklace-like chains of up to 1.5μm x 0.5μm in size
Anhydride-cured DGEBA based system	5.03	5.03	Well dispersed rubber spheres, up to 1μm diameter	Well dispersed 20nm spheres
	9	2.3	Well dispersed rubber spheres, up to 1μm diameter	Necklace-like chains of up to 2μm x 0.1μm in size
	9	10.5	Well dispersed rubber spheres, up to 1μm diameter	Necklace-like chains of up to 2μm x 0.1μm in size
	9	15.4	Well dispersed rubber spheres, up to 1μm diameter	Necklace-like chains of up to 3μm x 0.5μm in size
	12	12	Well dispersed rubber spheres, up to 1μm diameter	Necklace-like chains of up to 2μm x 0.4μm in size
	18	9	Rubber remained in solution in the epoxy phase	Necklace-like chains of up to 3μm x 0.5μm in size
	18	18	Rubber remained in solution in the epoxy phase	Necklace-like chains of up to 3μm x 0.5μm in size

7.1.5 Summary

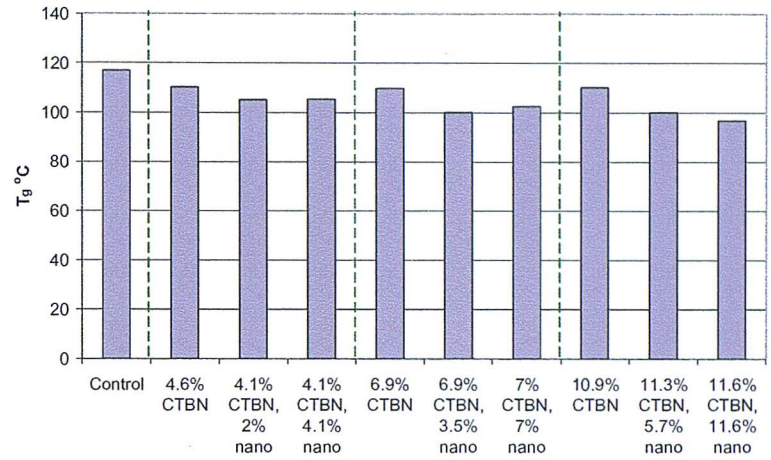
All the images for the unmodified epoxies (ie. the 'control' materials) of the three systems were featureless. No nano-only samples were available for the amine-cured DGEBA-based system, but the amine-cured TGMDA-based system showed increasing agglomeration with increasing nano-silica content, whilst the anhydride-cured DGEBA-based system showed good particle dispersion at all nano-silica contents. In the CTBN-only samples, about ~80% of the CTBN phase separated into comparatively small particles in the amine-cured DGEBA-based system. The amine-cured TGMDA-based system showed larger particles, but only ~25% phase separated. Samples from the anhydride-cured DGEBA-based system show slightly larger particles, but phase separation decreased with increasing CTBN content. The hybrid samples of the amine-cured DGEBA-based system showed large agglomerate formation with increasing nano-silica content, and beyond a threshold nano-silica content, super-clumps formed. The amine-cured TGMDA-based system showed that CTBN caused larger agglomerates of nano-silica to form than the nano-only sample. Images from the anhydride-cured DGEBA-based system suggest that agglomerates (similar in size and shape to that of the amine-cured TGMDA-based system) form after a certain CTBN-content threshold is passed, but no super-clumps form even at high nano-silica contents.

7.2 Thermal and Mechanical Properties

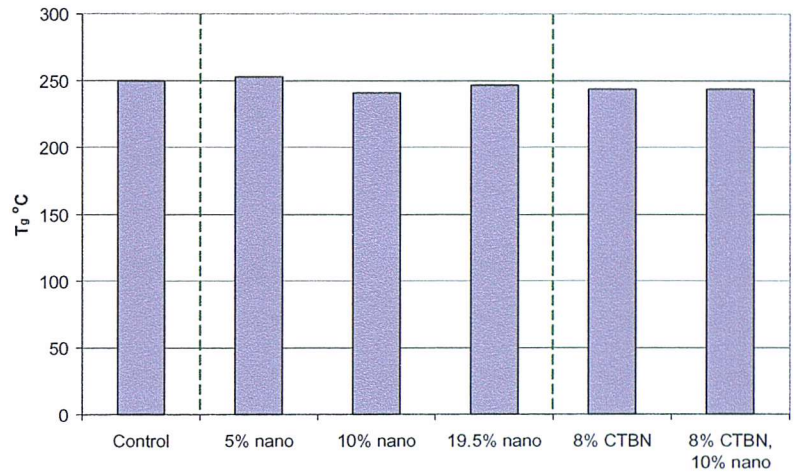
This Section will compare and contrast the glass transition temperatures, the Young's moduli, and the fracture toughness of the bulk epoxies of the three systems.

7.2.1 Glass Transition Temperature

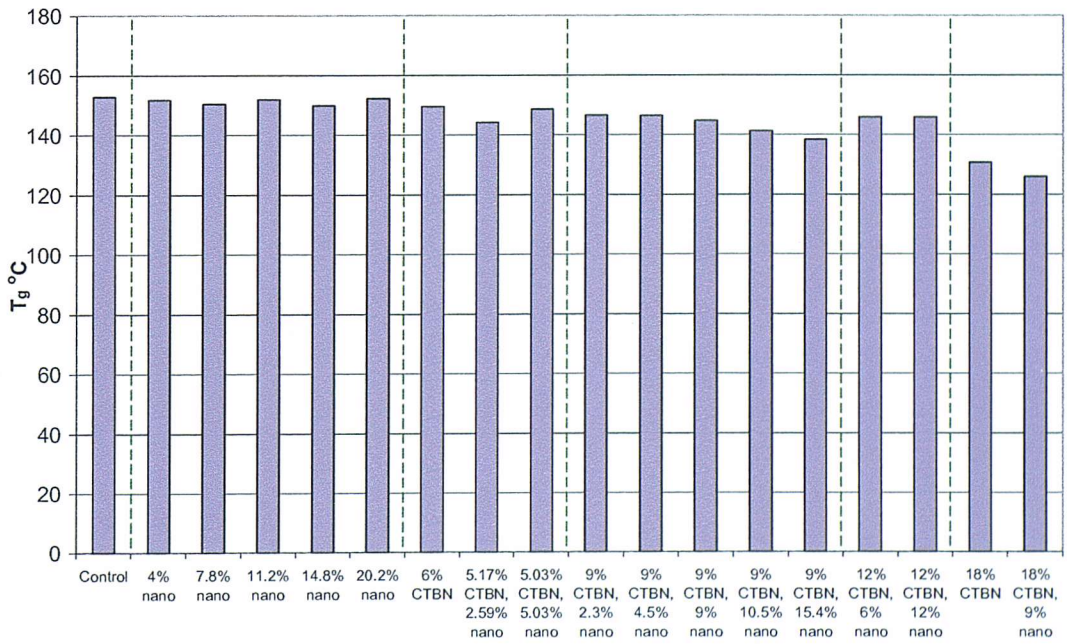
Figure 7.2.1 summarises the glass transition data for all three systems. On examining just the control T_g of each system, it can be seen that the glass transition temperature of the amine-cured DGEBA-based system is ~120°C and that of the anhydride-cured DGEBA-based system is ~150°C. However, the amine-cured TGMDA-based system has a T_g of ~250°C. This is expected for a TGMDA epoxy, since it is a tetrafunctional epoxy and is more highly crosslinked than DGEBA which is a difunctional epoxy [180].



(a)



(b)



(c)

Figure 7.2.1. Graphs showing the glass transition temperature at 1Hz for the: (a) amine-cured DGEBA-based system, (b) amine-cured TGMDA-based system, and (c) anhydride-cured DGEBA-based system.

The nano-only samples from both the amine-cured TGMDA-based system and anhydride-cured DGEBA-based system showed no changes in their glass transition temperatures, regardless of the nano-silica content. This shows that the addition of the nano-silica causes no change in the crosslink density [112].

In the amine-cured DGEBA-based system, the addition of CTBN produced a decrease in the glass transition temperature. Indeed, all the CTBN-only samples had the same mean T_g, which suggests that the same wt. % of CTBN remained dissolved in the epoxy phase. This was confirmed by volume fraction analysis of the microstructure images. (See Table 4.1.3 in Chapter 4 for T_g data, and Table 7.1.1 in Chapter 7 for volume fraction analysis.)

The amine-cured TGMDA-based system with 8 wt. % CTBN also showed a small decrease in T_g, since again some of the rubber remained in solution. The volume fraction analysis of the AFM images suggested that ~6 wt. % remained in solution. (See Table 5.1.3 in Chapter 5 for T_g data, and Table 7.1.1 in Chapter 7 for volume fraction analysis.) It should be noted that calculations performed using the Fox-Flory equation suggest that ~2 wt. % of the rubber should have remained in solution to produce the small decrease in T_g, but only one AFM image was investigated so this image may have been from a relatively rubber-deficient area.

For the anhydride-cured DGEBA-based system, results from the volume fraction analysis and the Fox-Flory equation agreed quite well. (See Table 7.1.1 for the details.) Indeed, with increasing amounts of CTBN, the glass transition temperature decreased, showing that more rubber remained in solution. (See Table 6.1.2 in Chapter 6 for the T_g data.) Thus, in all three epoxy systems, some rubber remains in solution, but the relative amounts are dependent on the exact details of the system (ie. they depend on the exact epoxy and curing agent used).

The hybrid samples of the amine-cured DGEBA-based system and the anhydride-cured DGEBA-based system show a lower glass transition temperature than their CTBN-only counterparts. This is because as more nano particles are added, more of the long, flexible rubber molecules are being crosslinked into the epoxy matrix instead of participating in domain formation. There is no change in T_g in the hybrid sample of the

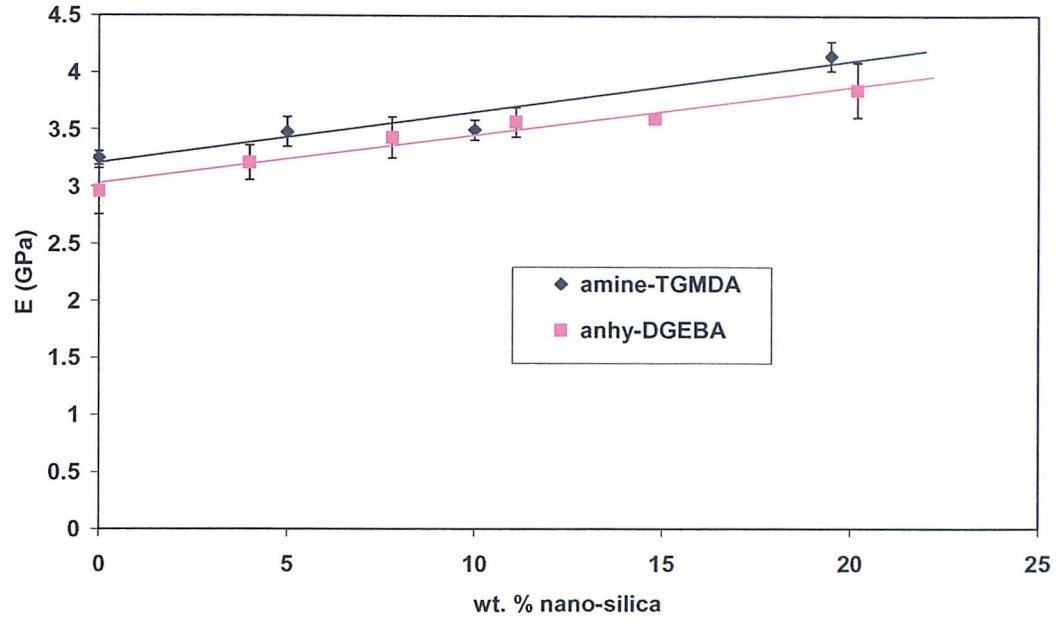
amine-cured TGMDA-system, compared to the CTBN-only sample; and this observation is confirmed by volume fraction analysis of the AFM images, when it was found that the same amount of rubber appeared to phase separate in the hybrid as in its CTBN-only counterpart.

Thus to summarise, in all three systems, some rubber remains in solution in the epoxy phase, but the relative amounts are system (ie. epoxy and curing agent) dependent. Furthermore, the nano-silica affects the phase separation of the CTBN rubber, and hence the glass transition temperatures of the amine and anhydride-cured DGEBA-based systems.

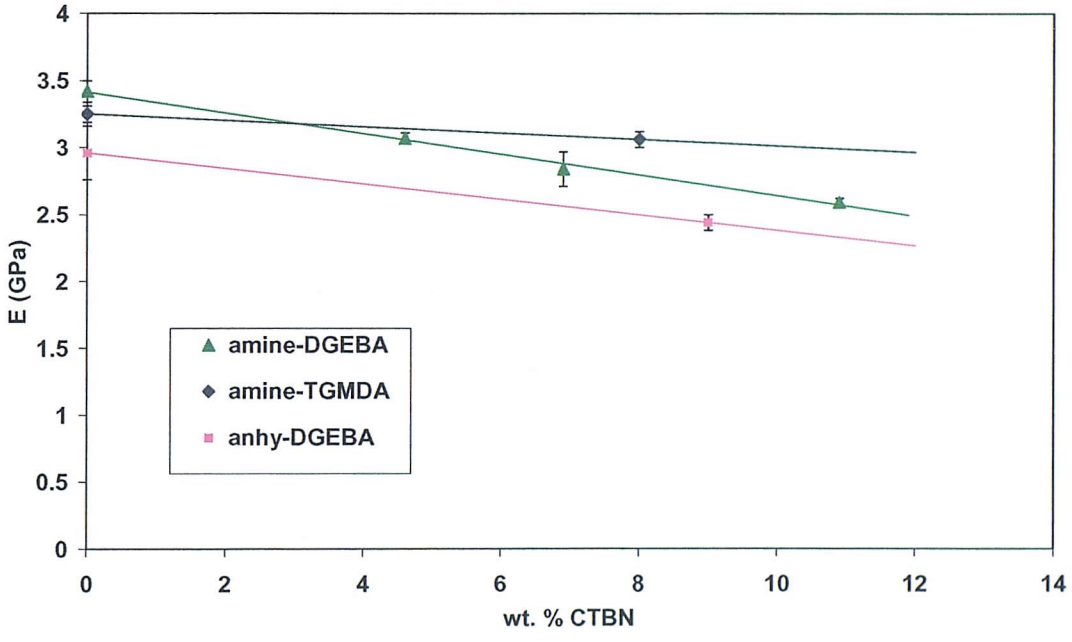
7.2.2 Young's Modulus

Figure 7.2.2 shows graphs of the tensile moduli of the three systems. There were no samples containing only nano-silica in the amine-cured DGEBA-based system, but the other two systems showed increasing moduli with increasing nano-silica content. This is expected [137,138], since silica has a very high modulus (ie. ~70GPa) compared to that of the epoxy. The gradients of the linear best-fit lines were similar, as would be expected, since it was the same type of nano-silica particles used in both systems. Figure 7.2.2 (b) shows the trends in the samples of the three systems containing CTBN only. It should be noted that there was only one CTBN-only result available for the amine-cured TGMDA-based and anhydride-cured DGEBA-based systems, and this is not sufficient for an in-depth discussion on the trends. However, it can be seen that the moduli for all three systems decrease with increasing amounts of CTBN. This was as expected, due to the low modulus of the CTBN. It was not possible to make a useful comparison of hybrid moduli for the three systems, due to the many different permutations of nano-silica and CTBN content. Nevertheless, in all the systems, increasing the nano-silica content increased the modulus, often recouping the stiffness lost due to the presence of the CTBN.

(It should be noted that for the analytical models, the Young's modulus of the silica and rubber were taken to be 70GPa [137,138] and 7MPa [126] respectively. $\zeta = 2/3$ [41] was used for the Halpin-Tsai model, and for the Lewis and Nielsen model $V_{max} = 0.632$ [2] and $k_E = 0.867$ [44] were used. See Section 2.3.2 for more details about the analytical models used in this study.)



(a)

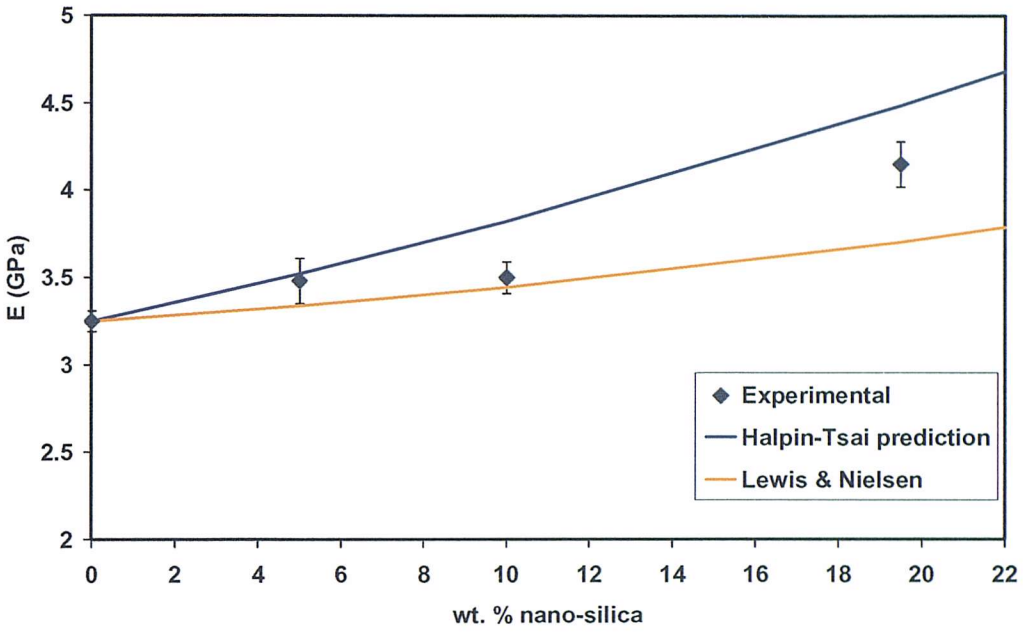


(b)

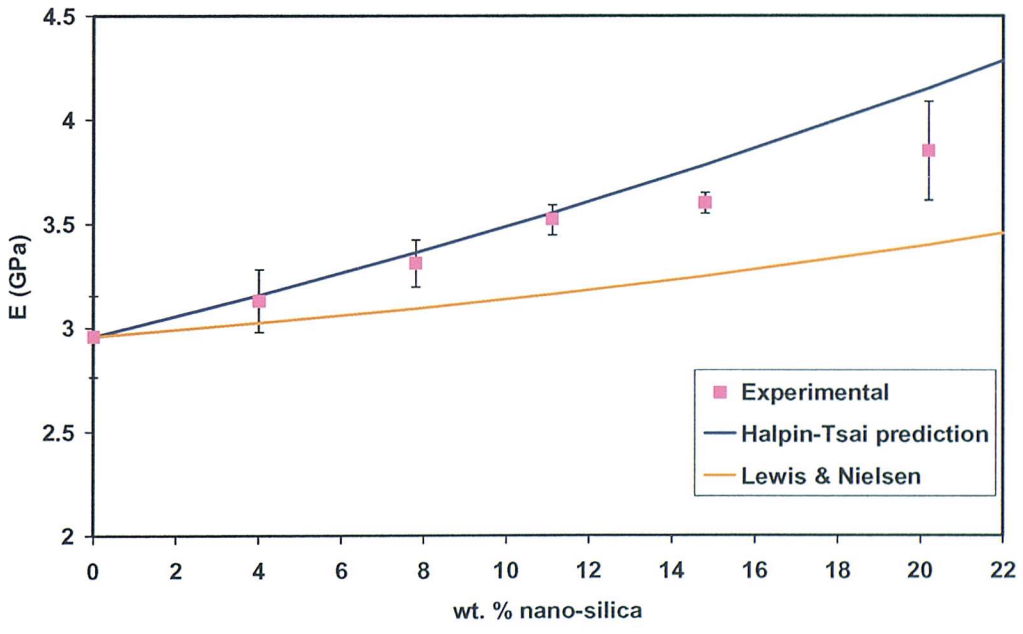
Figure 7.2.2. Graphs comparing the Young's moduli for all three systems containing: (a) nano-silica only, and (b) CTBN only. The points are the experimental data, and the lines are a linear best-fit to the data.

The tensile moduli for the nano-only samples for the amine-cured TGMDA-based and anhydride-cured DGEBA-based systems were compared to the predictions from the various analytical models (which were discussed in Section 2.3.2 in Chapter 2) and the comparison is shown in Figure 7.2.3. It can be seen that the trends in both systems are similar, in that the two models show increasing modulus with increasing nano-silica

content. The Halpin-Tsai model overpredicts the modulus, since it assumes that there is perfect bonding between the particles and the matrix which is normally not the case [108]. The Lewis & Nielsen model assumes that slippage occurs between the particles and the epoxy matrix, and tends to underpredict the modulus. For both systems, there is better correlation with the two models at lower concentrations of nano-silica.



(a)



(b)

Figure 7.2.3. Comparison of predicted tensile modulus with experimental results of samples with only nano-silica from the: (a) amine-cured TGMDA-based system, and (b) anhydride-cured DGEBA-based system.

Figure 7.2.4 shows a comparison between the experimental data and the theoretical predictions for the amine-cured DGEBA-based system containing only CTBN as the toughener. (Note that the other systems were not considered, since there was only one data point for each.) It can be seen that there is a relatively good agreement between the trend for the experimental data and the analytical models, since both show a decrease in modulus with increasing CTBN content. This decrease, as has been mentioned before, occurs because the rubber particles have a very low stiffness (~7MPa according to the work of Russell *et al.* [126]) compared to the epoxy polymer. However, again the Halpin-Tsai model overpredicts the modulus, and the Lewis & Nielsen model underpredicts the modulus.

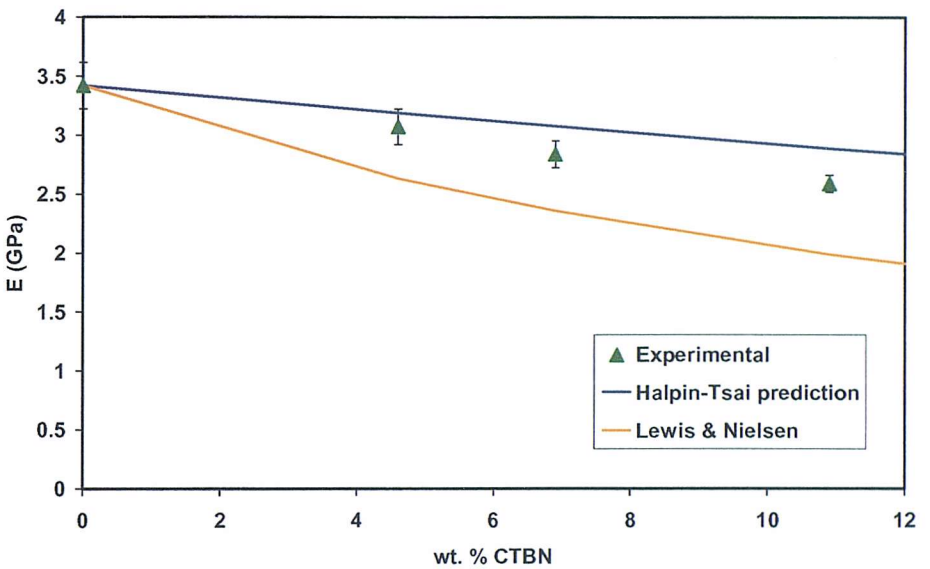


Figure 7.2.4. Comparison of predicted tensile modulus with experimental results of samples with CTBN-only from the amine-cured DGEBA-based system.

7.2.3 Fracture Toughness

It has been mentioned a number of times in the course of this Thesis that although thermosetting polymers have some attractive properties, their brittleness often limits their use. A focal point of the research has therefore been on the toughening of the epoxies using CTBN rubber and nano-silica. Each system investigated for this Thesis has a different application, thus it would be inappropriate to compare their absolute fracture energies. As a result, the fracture energies have been normalised relative to a control (unmodified) sample of the respective system. For graphical clarity, the error bars have been omitted, but the standard deviation of the results may be found in Chapters 4, 5 and 6.

7.2.3.1 Nano-silica Modified Epoxies

Figure 7.2.5 shows a comparison of the fracture energies of samples containing only nano-silica, from the amine-cured TGMDA-based system and the anhydride-cured DGEBA-based system. (In order to link the microstructure of the samples to their fracture toughness, it is very useful to review the summary of the microstructures of the nano-only samples, which can be found in Table 7.1.2.)

The amine-cured TGMDA-based system shows a slight increase in toughness with increasing nano-silica content, followed by a decrease to a value below that of the control at high concentrations of nano-silica. The initial increase is caused by the increase in the nano-silica content, which shows that small agglomerates do not have an adverse effect on toughness. The decrease is possibly caused by the increase in the number and size of agglomerates, due to the diminished amount of epoxy available for plastic deformation [85], and because of the increased difficulty in debonding of the individual nano-silica particles. In contrast, the anhydride-cured DGEBA-based system shows an increasing fracture resistance with increasing nano-silica content, with a plateau at a relatively high nano-silica content. Now, for this system, the results shown in Table 7.1.2 showed that the nano-silica particles remain well dispersed even at high amounts of nano-silica. The toughening mechanism responsible for this increase in toughness will be discussed later in this Chapter.

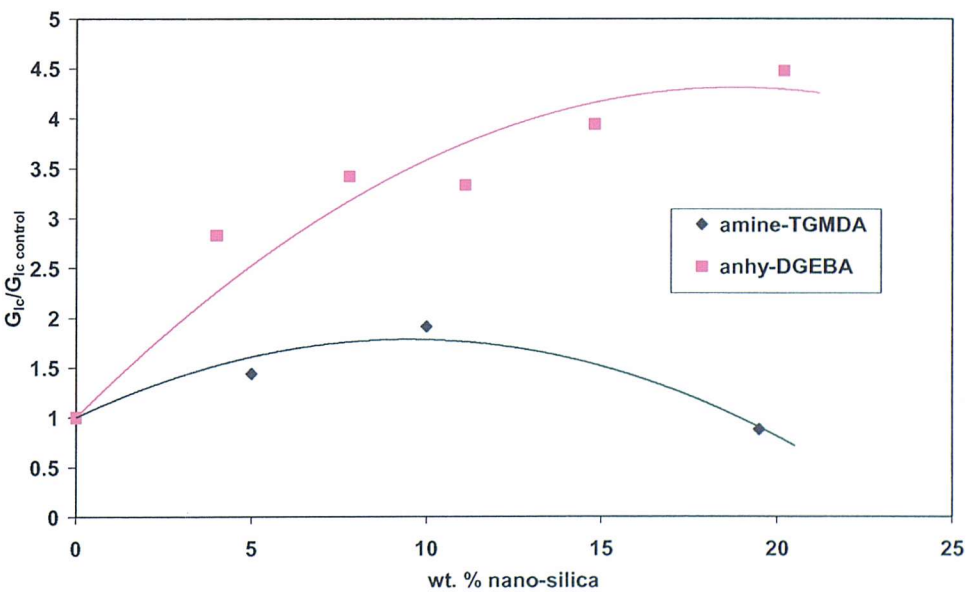


Figure 7.2.5. Graph showing the relative fracture energy results of the nano-only samples for the amine-cured TGMDA-based system and the anhydride-cured DGEBA-based system. The lines are the polynomial best-fit lines to the data.

7.2.3.2 Rubber Modified Epoxies

Figure 7.2.6 compares the normalised fracture energies of the CTBN-only samples for all three systems. In all three systems, there is an increase in fracture energy with increasing CTBN content, which is expected, and has been discussed in the respective Chapters on the experimental results. What is interesting to note, however, is that the amine-cured DGEBA-based system shows the smallest increase in fracture resistance with increasing CTBN content. Here, the phase-separated rubber particles were smaller than those of the other systems. (See Table 7.1.1 for a summary of the rubber morphology in the CTBN-only samples, and Figure 7.1.2 for AFM images which compare the general size of the rubber particles in the CTBN-only samples of the three systems.) Previous researchers, such as Kim *et al.* [76] and Lazzeri *et al.* [77], have commented that particles less than 0.3μm in diameter (as are many particles in this system) are more difficult to cavitate, and would therefore not give a very large increase in toughness. They also suggested that the optimal particle diameter is ~1μm, which is confirmed by the larger increases in fracture energy displayed by the amine-cured TGMDA-based and the anhydride-cured DGEBA-based systems, which had particle sizes in this range.

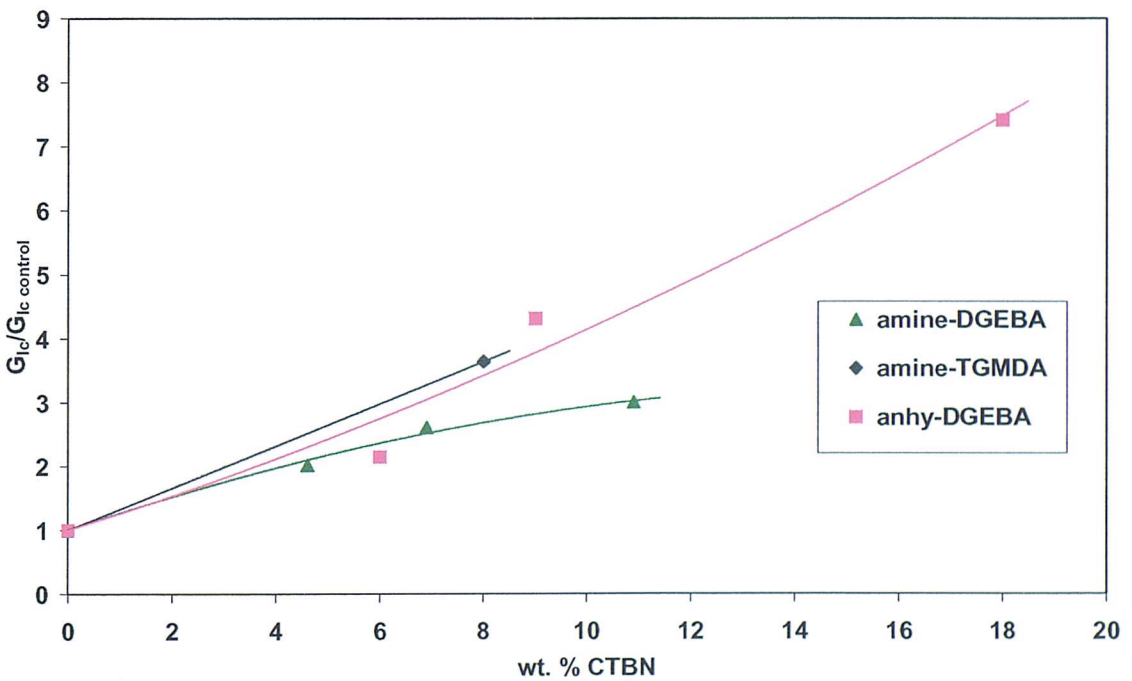


Figure 7.2.6. Graph showing the relative fracture energy results of the CTBN-only samples for all three systems. The lines are the polynomial best-fit lines to the data.

7.2.3.3 Hybrid Modified Epoxies

Due to the many permutations of the hybrid samples, it was not readily possible to compare 'like with like'. The most numerous hybrid samples of all three epoxy systems, were those with ~9 wt. % CTBN. (These were also of importance since the anhydride-cured DGEBA-based CFRPs were toughened with hybrids containing 9 wt. % CTBN.) It was therefore decided to compare the hybrid samples of the three systems that contained approximately 7-9 wt. % of CTBN. For the amine-cured DGEBA-based system, the hybrid samples containing ~7 wt. % CTBN were chosen, and were normalised relative to the sample with ~7 wt. % CTBN-only. A similar format was followed for the amine-cured TGMDA-based system (which contained 8 wt. % CTBN); and the samples containing 9 wt. % CTBN were chosen from the anhydride-cured DGEBA-based system. The results are presented in Figure 7.2.7. (A summary of the microstructure of the rubber and nano-silica particles in the hybrid systems can be found in Table 7.1.3.)

It may be seen that the best synergy between the CTBN and nano-silica occurs in the anhydride-cured DGEBA-based system, since for a given CTBN content, the fracture energy increases with increasing nano-silica content. A review of the microstructure (see Table 7.1.3) shows that the nano-silica particles in this system formed three-dimensional necklace-like chains. This suggests that this nano-silica morphology is desirable to produce increases in fracture toughness with increasing nano-silica content in this system.

The amine-cured TGMDA-based system shows a relatively small increase when nano-silica is added, but there was only one hybrid sample which is insufficient to discern a trend. It is interesting to note, however, that the nano-silica particles formed three-dimensional necklace-like chains (see Table 7.1.3), very similar in appearance to the anhydride-cured DGEBA-based system.

The amine-cured DGEBA-based system shows that small amounts of nano-silica do not improve the fracture energy, but higher concentrations have a detrimental effect on the fracture energy. The microstructure of the hybrid samples (see Table 7.1.3) suggests that three-dimensional necklace-like chains (as seen in the anhydride-cured DGEBA-based and the amine-cured TGMDA-based systems) slightly improve the fracture

energy. However, the formation of super-clumps at higher nano-silica contents has a detrimental effect on the fracture resistance. The next Section will explore the toughening mechanisms in the three systems in more detail.

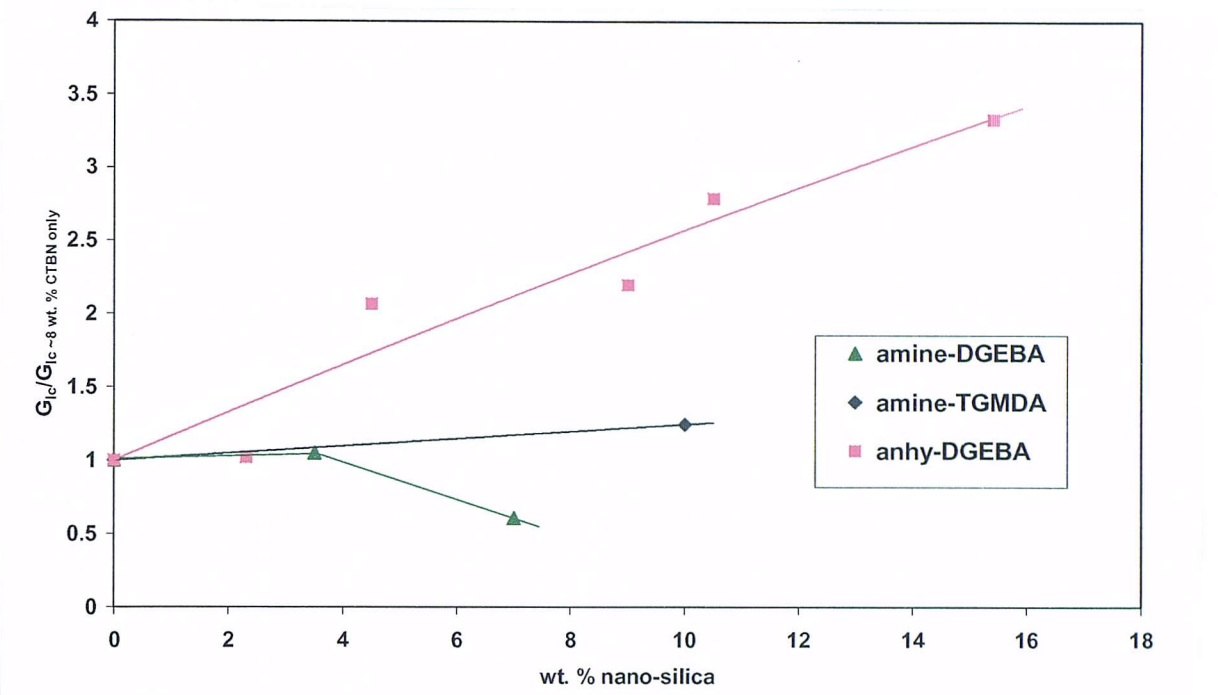


Figure 7.2.7. Graph showing the relative fracture energy results of the hybrid samples containing ~8 wt. % CTBN relative to their respective ~8 wt. % CTBN-only fracture energies for all three systems. The lines are the polynomial best-fit lines to the data.

7.3 Bulk Epoxy Toughening Mechanisms

This section will explore the evidence supporting the various means by which CTBN and nano-silica toughen the three epoxy-based systems. The rubber toughening effect will be discussed first since this has been well documented in the literature, and then the nano-silica toughening will be investigated.

7.3.1 Rubber Toughening

SEM micrographs are the best way of ascertaining the way in which rubber toughens the epoxy systems. Note that the micrographs in this section were chosen because the samples all contained ~7-9 wt. % of CTBN. These micrographs are typical and representative of the CTBN-only samples for their respective systems. The pre-cracks are the vertical lines at the far left of the low magnification micrographs, and the crack propagated from left to right.

Micrographs of samples from the amine-cured DGEBA-based system containing only CTBN, showed evidence of a stress-whitened region as can be seen in the micrograph in Figure 7.3.1 (a) (the stress-whitened region is indicated by the pink parenthesis). A visual inspection of the fracture surfaces prior to SEM analysis, confirmed the existence of the stress-whitening phenomena where the cavitated rubber particles interact with incident light to give the appearance of a white band near the crack tip. (See Section 2.5.2.1 in Chapter 2.) These regions increased in length ahead of the rack tip with increasing CTBN content, and led to an increase in fracture energy which agrees with the work of Kim *et al.* [148] who showed a strong correlation between the size of the stress-whitened region and toughness. It should be noted that rubber cavitation alone does not provide a significant amount of fracture resistance. According to researchers such as Kinloch *et al.* [4], Bagheri and Pearson [58], and Wang and Guild *et al.* [62] rubber cavitation allows the matrix to deform by plastic yielding, and this plastic yielding is one of the main contributors to fracture resistance. (See Section 2.5.2.3 in Chapter 2.)

Figure 7.3.1 (b) is a micrograph of the fracture surface of a sample from the amine-cured TGMDA-system with 8 wt. % CTBN and Figure 7.3.1 (c) is from the anhydride-cured DGEBA-based system containing 6 wt. % CTBN. There is no evidence of a stress-whitened region in either sample.

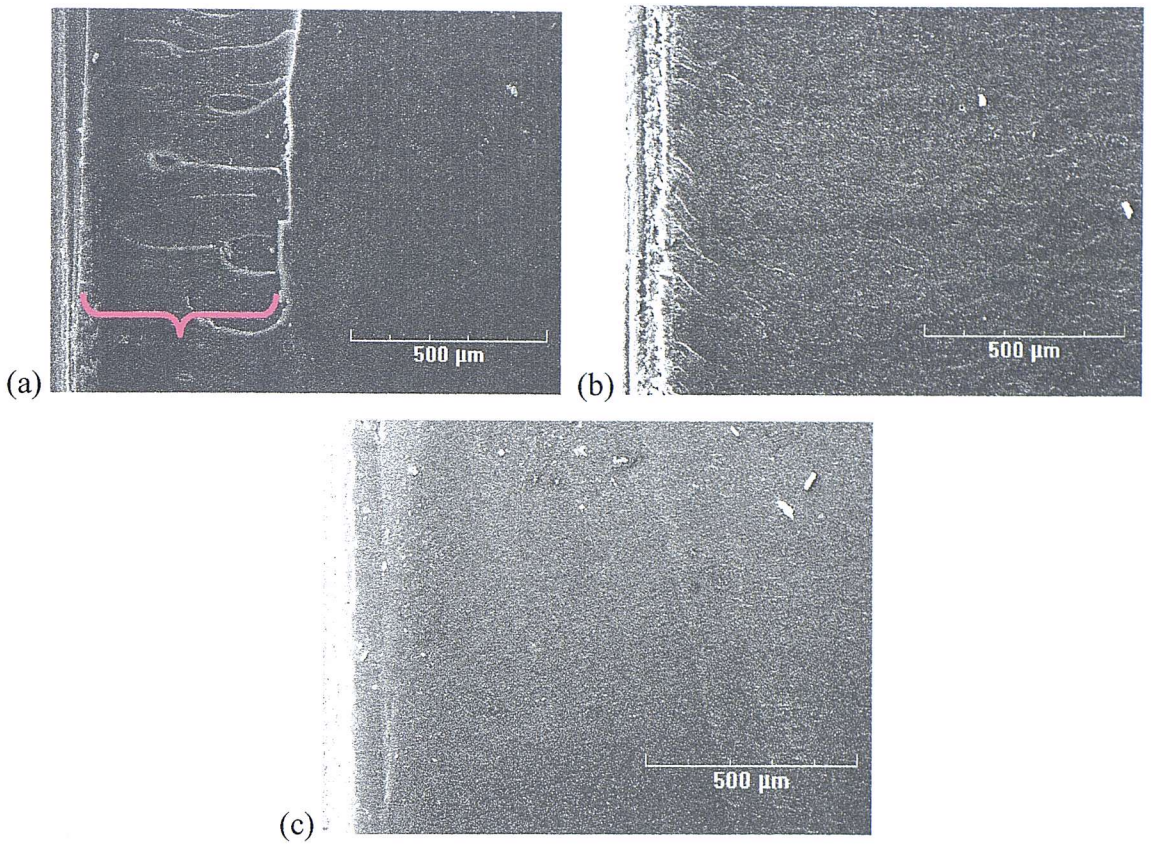


Figure 7.3.1. SEM micrographs of the fracture surfaces of samples from: (a) the amine-cured DGEBA-based system containing 6.9 wt. % CTBN (the stress-whitened region is indicated by the pink parenthesis), (b) the amine-cured TGMDA-based system containing 8 wt. % CTBN, and (c) the anhydride-cured DGEBA-based system containing 6 wt. % CTBN.

The micrographs in Figure 7.3.2 are of the same samples in the previous Figure, but at a higher magnification. It can be seen that there are many cavitated rubber particles in the first sample, but hardly any evidence in the other two samples. Since all micrographs were taken from near the crack-tip, it can be deduced that the visual evidence of the stress-whitening phenomenon is due to the cavitation of the rubber particles [4,7]. The reader may recall that the amine-cured DGEBA-based sample in Figure 7.3.2 had a fracture energy of ~1600J/m^2, whereas the amine-cured TGMDA-based and anhydride-cured DGEBA-based samples had fracture energies of 640J/m^2 and 221J/m^2 respectively. The series of micrographs suggests that the fracture energy increases because of the amount of cavitation that occurs (which allows plastic hole growth of the epoxy to occur, and thereby increases the fracture energy). However, a comparison with their respective unmodified (control) epoxy fracture energy paints a different picture. Compared to their respective control epoxies, the samples that are considered in this

Section (ie. samples containing similar amounts of CTBN) show a 2.5 times increase in fracture energy in the amine-cured DGEBA-based system, a 3.5 times increase in the amine-cured TGMDA-based system, and a doubling in the anhydride-cured DGEBA-based system. This shows that there is no direct correlation between the amount of cavitation observed, and the relative increase in fracture energy.

SEM micrographs can only conclusively show evidence of rubber cavitation, but the fracture energy results strongly suggest that other rubber toughening mechanisms may occur. Since little or no rubber cavitation was observed in the amine-cured TGMDA-based system and in the anhydride-cured DGEBA-based system, the dominant rubber toughening mechanisms in these systems would appear to be shear yielding of the epoxy between the phase-separated rubber particles [4,7]. Finally, the plasticisation of the epoxy caused by the rubber that remains in solution in the epoxy phase would probably assist these mechanisms by making the epoxy matrix more amenable to undergoing plastic deformation.

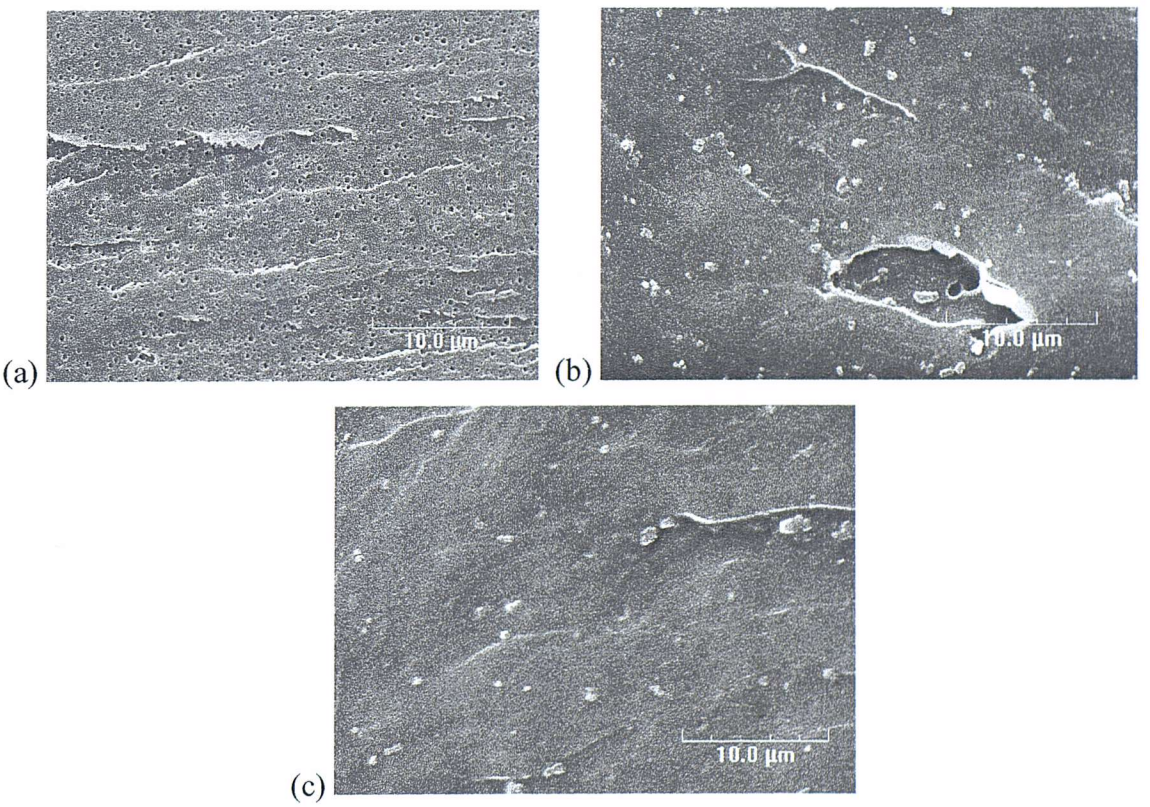


Figure 7.3.2. Higher magnification SEM micrographs of the fracture surfaces of samples from: (a) the amine-cured DGEBA-based system containing 6.9 wt. % CTBN, (b) the amine-cured TGMDA-based system containing 8 wt. % CTBN, and (c) the anhydride-cured DGEBA-based system containing 6 wt. % CTBN.

7.3.2 Nano-silica Toughening

In this section, the toughening mechanisms by which the nano-silica particles may increase the toughness of the epoxies will be considered. In particular, emphasis will be placed on the anhydride-cured DGEBA-based system, since only in this system was a good dispersion of nano-silica particles obtained (see Table 7.1.2), which led to significant increases in the toughness of the nano-silica modified epoxies (see Figure 7.2.5). Various toughening mechanisms have been proposed for the increases in the fracture energy, G_{Ic}, that may be observed when rigid, hard particles are added to thermosetting polymers (see Section 2.6 in Chapter 2). These mechanisms are discussed below with respect to the anhydride-cured DGEBA-based system.

7.3.2.1 Crack Pinning

As was discussed in Chapter 2, crack pinning is one possible method by which rigid particles can toughen an epoxy. However, in the previously reported work [63,88] crack pinning occurred when the particles were larger than the crack opening displacement. To see if a pinning argument is reasonable for nano-sized particles, the crack opening displacement, δ_{tc}, was calculated and compared to the particle size using Equation 2.14 (see Chapter 2).

For the unmodified epoxy the crack opening displacement is 1.7μm. For the maximum toughness measured in the present work (ie. the sample toughened with 20.2 wt. % nano-silica) a value of δ_{tc}=7.5μm may be calculated. The crack tip is shown schematically in Figure 7.3.3, which shows the relative size of the nano particles compared to the crack opening displacement. From this figure, it can be seen that such comparatively small particles are unlikely to cause crack pinning.

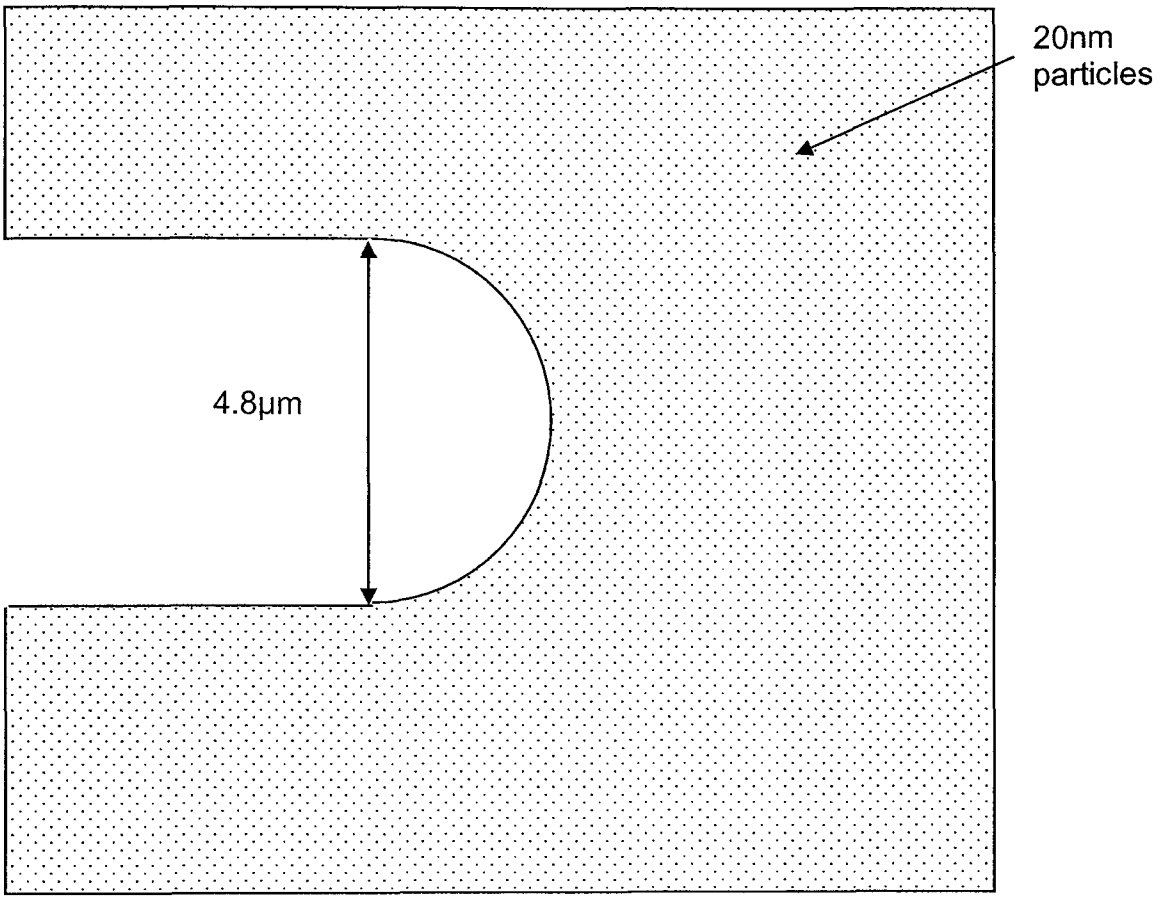


Figure 7.3.3. Schematic showing the crack tip, with the calculated crack opening displacement and nano particles for the epoxy polymer containing approximately 4.1 wt. % nano-silica.

As noted above, where crack pinning has been proposed as the main toughening mechanism, the particle diameter is much larger than the crack opening displacement. Kinloch *et al* [63] quoted δ_{tc}=1.8μm at room temperature while the mean particle diameter was 50μm, using an epoxy matrix with glass particles. Similarly, Green *et al* [88] demonstrated pinning with 132μm diameter glass particles, but δ_{tc}=0.3μm (a conservative estimate calculated assuming that the yield stress is equal to the quoted fracture stress).

Thus, since in the present materials the nano-silica particles are so much smaller than the crack opening displacement, then they are unlikely to cause crack pinning. Furthermore, the lack of direct experimental evidence, specifically the absence of bowed crack-front markings on the fracture surfaces in the present work, indicates that crack pinning is unlikely to be responsible for the observed increases in toughness.

7.3.2.2 Crack Deflection

The toughening effect could be due to crack deflection occurring, where the crack front tilts and twists when it encounters the particles and hence passes around them [81,83]. This causes firstly an increase in the total fracture surface area and secondly causes the crack to grow locally under mixed-mode I/II conditions. The former toughening effect can be evaluated by comparing the measured fracture toughness with the surface roughness, and the latter toughening effect can be evaluated using the analysis by Faber and Evans [81].

Work by Arakawa and Takahashi [181] showed that the toughening effect due to an increase in the true fracture surface area gives a *linear* relationship between the surface roughness and the overall toughening contribution, Ψ. The average surface roughness, R_a, of the fracture surfaces was therefore measured (see Section 3.2.1.1 in Chapter 3). For the unmodified epoxy polymer it was relatively low with R_a=0.04μm, which is typical for the fracture surface of an unmodified epoxy [175]. The fracture surface roughness generally increased with an increasing concentration of nano-silica, from a minimum of R_a=0.03μm at 4.1 wt. % nano-silica to a maximum of R_a=0.15μm at 20.2 wt. % nano-silica. The data are shown in Figure 7.3.4 where the measured roughness is plotted against the overall toughening contribution, Ψ, from the presence of the nano-silica. The data does *not* show a linear relationship, and hence it appears that the increases in the fracture surface area cannot be directly correlated to the increases in the toughness. Indeed, examination of the nano-only fracture surfaces in Chapter 6, confirmed that there are no discernible differences in their appearance compared to the fracture surface of the unmodified epoxy.

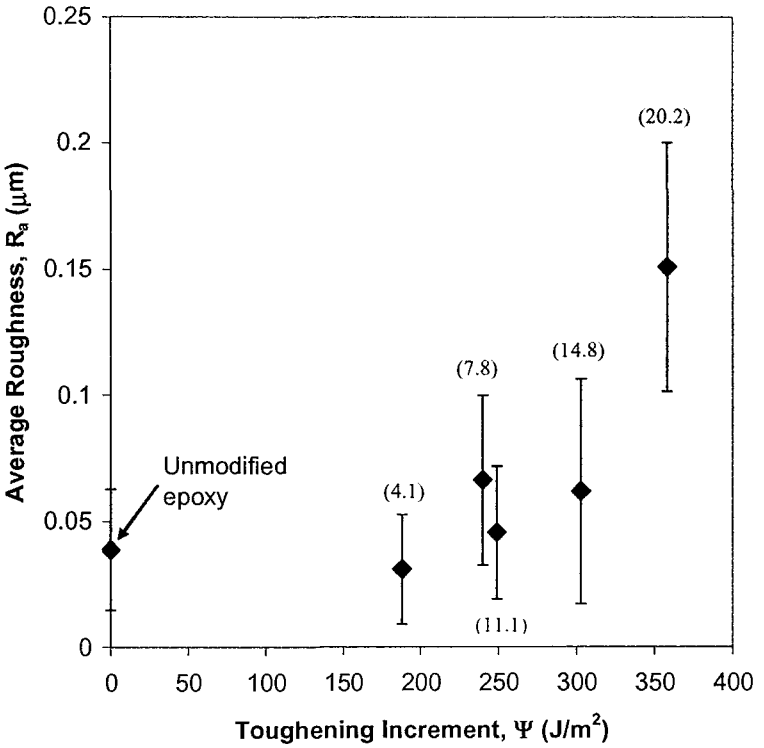


Figure 7.3.4. Mean roughness of the fracture surfaces versus measured toughening increment, Ψ. The wt. % of nano-silica is shown in brackets.

The measured fracture energies may also be compared to the model proposed by Faber and Evans [81], which considers that crack deflection causes the crack to grow locally under mixed-mode I/II conditions. This analysis uses the shape of the particles (spherical in this case) and their volume fraction in the prediction of toughness. For example, the Faber and Evans model predicts that the fracture energy for a volume fraction of 2.5% (ie. 4.1 wt. %) of silica spheres will be 1.2 times that of the unmodified epoxy. The G_{Ic} of the unmodified epoxy is 103J/m^2 and hence the predicted fracture energy from using the Faber and Evans model is 120J/m^2. However, the measured fracture energy of 291J/m^2 is more than twice this predicted value. Indeed the Faber and Evans model consistently under-predicts the fracture energy, and this suggests that this mechanism is unlikely to fully explain the increase in toughness.

In addition, as noted in Section 7.3.2.1 and Figure 7.3.3, the nano particles are so much smaller than the crack opening displacement that they are unlikely to cause the crack to deflect. This argument, and the relatively poor agreement with the crack deflection

models, indicates that crack deflection is unlikely to fully explain the observed toughening effects.

7.3.2.3 Plastic Void Growth

The toughening mechanisms associated with micrometre-sized particles have frequently been shown to be due to debonding of the particles followed by plastic void growth of the matrix [15,85]. Micrographs showing the plastic void growth phenomena can be seen in Figure 2.6.4 in Chapter 2. Further, Kinloch and Taylor [83] have demonstrated that the voids around the micrometre-sized glass spheres closed-up when the epoxy polymer was heated above its T_g and allowed to relax. This observation showed that prior to fracture, there was good adhesion between the glass spheres and the epoxy matrix, and hence the voids occurred as a result of fracture.

High resolution scanning electron microscopy (ie. using a field emission gun source (FEG-SEM)) of a fracture surface of a sample containing 14.8 wt. % nano-silica shown in Figure 7.3.5, reveals the presence of voids around several of the nano particles. This indicates that plastic void growth of the epoxy matrix, initiated by debonding of the nano particles, has occurred. The diameter of these voids is typically 30nm and the voids were also observed in the fracture surfaces of samples with different contents of nano-silica. (It should be noted that although the samples are coated to prevent charging in the electron microscope, the voids are not artefacts of the coating as they could not be observed on a coated fracture surface of the unmodified epoxy (see Figure 7.3.6). Also, the samples containing nano-silica appeared similar whether they were coated with either platinum or gold.)

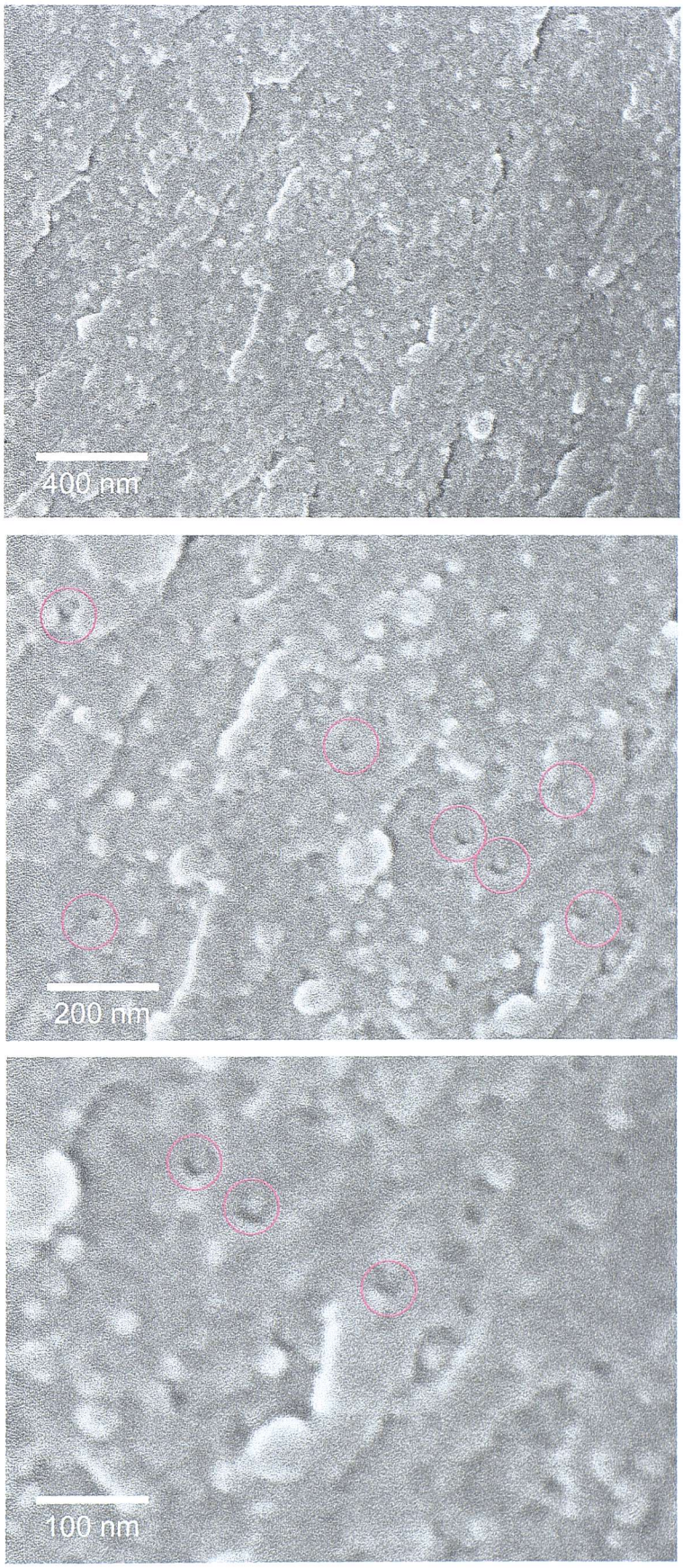


Figure 7.3.5. FEG-SEM micrographs of the fracture surface of a sample containing 14.8 wt. % nano-silica. (Voids with nano-silica particles are circled in the middle and last image.)

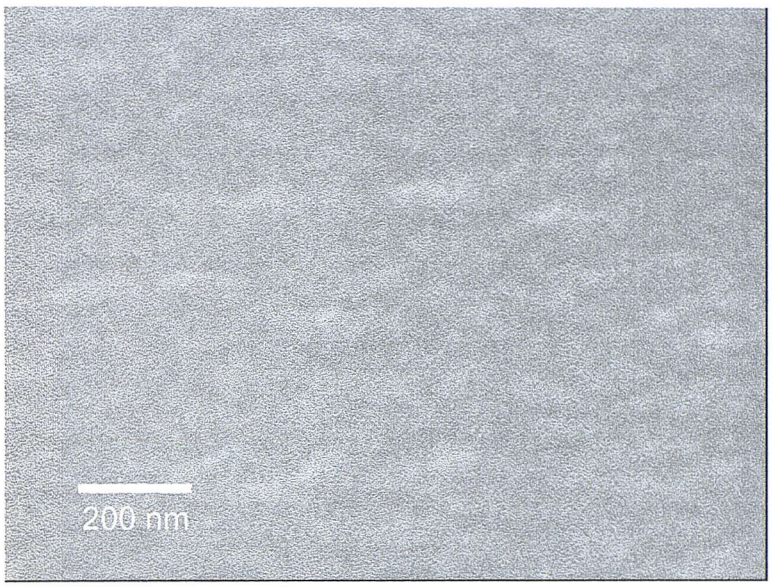


Figure 7.3.6. FEG-SEM micrograph of the fracture surface of the unmodified epoxy.

In addition, similar voids were observed from AFM micrographs of uncoated fracture surfaces of the nano-silica modified epoxies, as shown in Figure 7.3.7. (Note that this image is presented in black and white because of the better contrast.) However, the apparent diameter of the nano particle in the void highlighted in Figure 7.3.7 is 30nm, as shown in Figure 7.3.8; whereas transmission electron microscopy has shown that the mean particle size is actually ~20nm. This discrepancy is due to the 'tip-broadening effect' when the AFM is used to identify such small features. Namely, as the tip radius of the AFM probe is about 10nm, this makes features that are protruding out of a surface appear larger than their true size in the micrographs. Thus, the AFM can only be reliably used to quantitatively assess the size of relatively large voids.

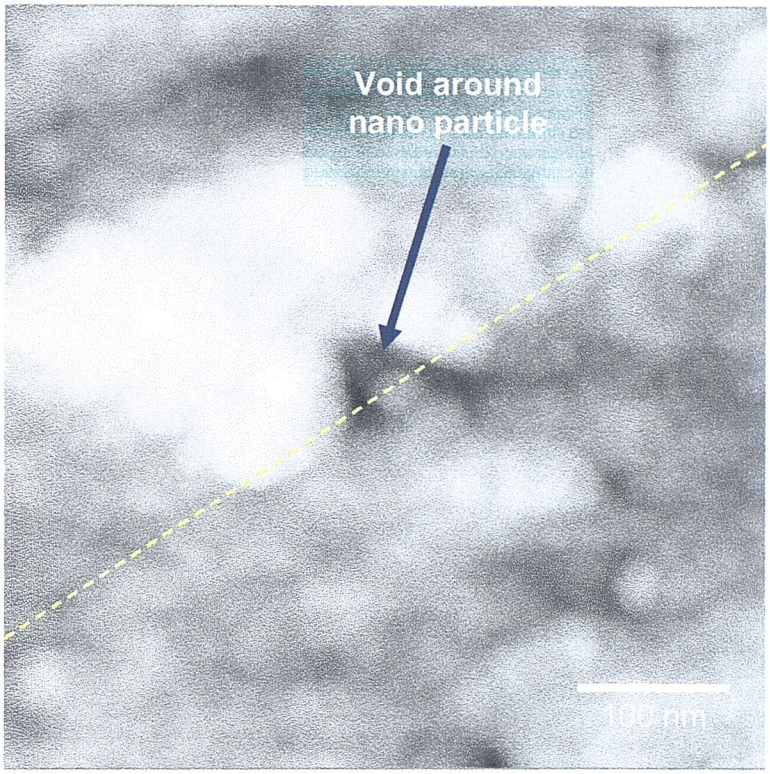


Figure 7.3.7. AFM height image of a fracture surface of the epoxy polymer containing 14.8 wt. % nano-silica.

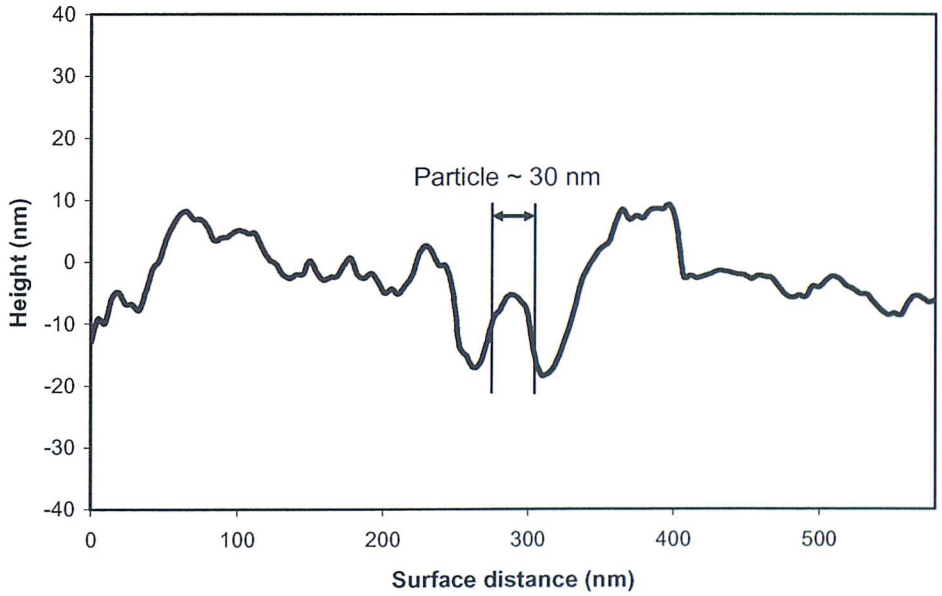


Figure 7.3.8. Surface profile of the dashed line drawn across the nano-silica particle and void in the previous Figure.

Voids with no nano-silica particles apparently present were also observed with the FEG-SEM. However, here the particles associated with these voids are either situated in the other half of the fracture surface, or are assumed to have fallen out of the surface

completely during fracture, as is commonly observed with micrometre-sized particles [83]. (It should be noted that the diameters of most of the holes are less than those discussed above, as the matrix is unlikely to fail across the widest point of the void. Additionally, the coating, which is 5nm thick, will partially fill the voids, and hence the observed size may be smaller than the true (uncoated) diameter.)

Thus, the FEG-SEM mirographs show voids around some of the nano-silica particles, and the subsequent AFM analysis of the height images confirm that plastic deformation of the epoxy around some of the nano-silica particles (ie. void growth) occurs.

7.3.2.4 Modelling the Contribution from Plastic Void Growth

To confirm whether the observed debonding and plastic void growth which occur for the nano-modified epoxy could be responsible for the toughening effect, the increase in toughness can be compared to the results predicted from a theoretical model. A suitable model for this has been proposed by Huang and Kinloch [56]. This model assumes that the fracture specimens behave in a bulk linear-elastic manner, and that the energy dissipation is localised to a small plastic zone at the crack tip, as observed in the present work. The theory and equations presented in the present Section have been discussed in Section 2.5.2.5 in Chapter 2, but will be briefly reviewed again to aid in the understanding of the arguments.

Huang and Kinloch [56] suggested that the overall toughening contribution, Ψ, was composed of contributions from particle bridging, localised shear banding in the epoxy matrix, and plastic void growth of the epoxy matrix which is initiated by cavitation or debonding of the particulate phase. Now, the plastic void growth mechanism has been reported [56,82] to be often the dominant toughening micromechanism, and thus the relationship may be written:

$$G_{Ic} \approx G_{Icu} + \Delta G_v \qquad \textbf{Equation 7.1}$$

Where ΔG_v is the contribution to the increase in fracture energy from plastic void growth of the epoxy matrix. For simplicity, it will be initially assumed that the adhesion between the silica and epoxy phases is relatively poor, and hence debonding will not

contribute to the toughening effect. The contribution to the increase in fracture energy from the plastic void growth mechanism, ΔG_v, is given [56] by:

$$\Delta G_v = (1-\mu_m^2/3)(V_v - V_f)\sigma_{yc} r_{yu} K_{vm}^2 \qquad \textbf{Equation 7.2}$$

Where μ_m is a material constant, V_v is the volume fraction of voids, V_f is the volume fraction of particles, σ_{yc} is the compressive yield stress of the unmodified epoxy polymer, r_{yu} is the radius of the plastic zone of the unmodified epoxy polymer, and K_{vm} is the maximum stress concentration factor of the von Mises stress in the plastic matrix. The value of μ_m, which describes the pressure sensitivity of the material in the von Mises yield criterion, has been reported [46] to be between 0.175 and 0.225, and is normally taken to be 0.2, as reported by Huang and Kinloch. The material properties for the calculation of ΔG_v are summarised in Table 7.3.1. The maximum stress concentration factor, K_{vm}, was found from a finite element analysis [56] to be 2.22 around a void in an epoxy matrix.

Table 7.3.1. Material properties of the unmodified epoxy, and constants used for calculation of the fracture energy, G_{Ic}, and for the contribution to the increase in fracture energy from the plastic void growth mechanism, ΔG_v. (Ref. 1 - measured in present work)

Property	Symbol	Ref.	Units	Value
Fracture toughness	K_{Ic}	1	$MNm^{-3/2}$	0.59
Modulus	E_m	1	GPa	2.96
Poisson's ratio	ν	[31]	-	0.35
Tensile yield stress	σ_y	1	MPa	61.1
Compressive yield stress	σ_{yc}	1	MPa	77.3
Von Mises pressure sensitivity	μ_m	[46]	-	0.2
Max. stress concentration factor	K_{vm}	[46]	-	2.22

The size of the plastic zone ahead of the crack tip can be calculated assuming linear-elastic fracture-mechanics (LEFM) behaviour using Equation 2.12 in Chapter 2 for plane strain conditions. This gave a plastic zone crack tip radius of 5μm.

Now, Equation 7.3 requires a knowledge of the volume fraction of voids and it is difficult to measure this parameter accurately from the micrographs, as it is difficult to identify all the voids due to the resolution of the microscopes used. Nevertheless, a mean void diameter can be calculated from the features which are clearly voids in the micrographs of Figure 7.3.5, which gave a mean void diameter of 30nm. (It should be noted that micrographs of the formulation containing 4.1 wt. % nano-silica indicated an average void diameter of just below 30nm. However, some voids up to 50nm in diameter are observed in all formulations, where micrographs from FEG-SEM analysis are available.)

The predicted toughening increment, Ψ, was calculated using Equations 7.1 and 7.2 and it was assumed that the measured toughening increment is entirely caused by plastic void growth (i.e. $\Psi = \Delta G_v$), and that all the particles initiated the growth of voids which have a final diameter of 30nm. For the epoxy with 14.8 wt. % of nano-silica, the measured toughening increment is 303J/m^2 and the predicted toughening increment is 394J/m^2. The toughening increment can also be predicted for the other formulations, for which FEG-SEM images are not available, assuming that the average void diameter is constant and that all of the particles initiate void growth. The results are shown in Table 7.3.2.

Table 7.3.2. Measured and predicted toughening increments. Predicted values calculated assuming that $\Psi = \Delta G_v$. (Note $G_{Icu} = 103$J/m^2.)

Nano-silica content	**Nano-silica content**	**Toughening increment, Ψ (J/m^2)**	
(wt. %)	(vol. %)	Measured	Predicted
4.1	2.5	188	107
7.8	4.9	249	209
11.1	7.1	240	297
14.8	9.6	303	394
20.2	13.4	358	540

Considering the assumptions made in the above quantitative modelling calculations, then firstly, it is highly unlikely that all of the particles will debond and initiate void

growth. Indeed, from the FEG-SEM images of the fracture surfaces in Figure 7.3.5 it can be seen that not all of the nano-silica particles seem to initiate void growth. The difficulty of quantifying the number of debonded particles, when considering the present nano-silica particles, has been discussed above and has been reported by van Hartingsveldt and van Aartsen [182] who studied the debonding of glass particles with a diameter of 20 to 50μm in a polyamide matrix. They clearly demonstrated that only a fraction of the particles debonded, but that this fraction could be as high as about 0.8 to 0.9. Furthermore, such a value was attained at levels of applied strain which are relatively low compared to those which exist in the region of the crack tip, as is being considered in the present work. Also, the present nano-silica particles have a very narrow distribution of particle size. Thus, they would be expected to possess an almost constant value of the applied stress needed to debond them [182, 183], and hence might be expected to exhibit a relatively high fraction of particles which show a similar behaviour. (Although, previous work [182, 183] has suggested that, for a given level of interfacial adhesion, the nano-silica particles should require a relatively high level of debonding stress compared to glass particles which are many micrometres in diameter.) Thus, on balance, it is reasonable to assume that most of the nano-silica particles will debond and initiate plastic void growth in the epoxy matrix. However, clearly, if only a fraction of the particles initiate void growth, or if only partial debonding occurs, then the predicted toughening increments would be reduced compared to the values shown in Table 7.3.2.

Secondly, for simplicity, it has been assumed that the adhesion between the silica and epoxy phases was poor. If this is not the case, then the energy absorbed by the debonding process will also contribute to the toughening effect. Thirdly, the presence of nano particles in the ligaments between the debonded nano particles will increase the stiffness of the plastically-deforming ligaments and the failure strain, and hence might be expected to increase the strain-energy density absorbed by the ligaments during their plastic deformation. Indeed, the data from tensile tests showed that the modulus (and the failure strain) increased with increasing nano-silica content (see Figure 7.2.2 (a)), and that the strain-energy density at fracture of the nano-silica-modified epoxy is greater than that of the unmodified epoxy. Clearly, both of these effects would tend to lead to the experimentally measured values of G_{Ic} being greater than the predicted values. Hence, these effects would offset the above effect of not all of the particles debonding.

Nevertheless, there is no direct evidence for these effects being of significance and, for the present, will not be considered further.

In summary, considering the simplifying assumptions made, the agreement between the measured and the predicted toughening increments is very reasonable. The predicted values are somewhat larger than the measured values for the high nano-silica contents, but the predicted values agree very well with the experimental data for the lower nano-silica contents. This confirms that plastic void growth of the epoxy matrix, initiated by a void being formed by debonding of the nano-silica, can indeed produce the major increases in the values of the fracture energy, G_{Ic}, recorded for the nano-only samples from the anhydride-cured DGEBA-based system.

7.3.3 Hybrid Toughening

In the preceding Sections, the toughening micromechanisms of the rubber-only and nano-silica only materials were investigated. This Section will briefly consider the toughening mechanisms and synergy that occur in the hybrid samples from the three epoxy-based systems.

7.3.3.1 Hybrid Toughening - Rubber

The toughening mechanisms of the CTBN rubber remain the same in the hybrids of the three systems as they were in their CTBN rubber-only counterparts (see Sections 7.1.4 and 7.3.1). That is to say, that when shear yielding was the major toughening mechanism in a rubber-only sample in a particular system, shear yielding was *also* the major rubber toughening mechanism in the hybrid sample of that particular system.

7.3.3.2 Hybrid Toughening – Nano-silica

In the amine-cured DGEBA-based system, no nano-only samples were examined due to time constraints. Microscopy (see Table 7.1.3) showed that for the hybrid samples at low nano-silica contents, the nano-silica remained well dispersed, but there was no statistical increase in the fracture toughness compared to a CTBN-only sample. This suggests that if debonding of the nano-silica particles and subsequent void growth in the epoxy occurred, it did so on a very limited scale. What is clear, however, is that when

large amounts of nano-silica are present, super-clumps form which reduce the fracture toughness to a similar level to that of the unmodified epoxy. This is because the large agglomerates act like very brittle defects, and also reduce the amount of epoxy available for deformation [85]. Other work has shown a similar reduction in toughness because of large agglomerates [178,179]. This would suggest that the toughness should be less than that of the unmodified epoxy, but some fracture resistance is still provided by the CTBN rubber (see Section 7.3.1 for more details on the rubber toughening mechanisms).

For the amine-cured TGMDA-based system, it is imperative to consider the nano-only samples before considering the hybrid sample. The nano-only samples showed an increasing degree of agglomeration with increasing nano-silica content. There was no statistical increase in the fracture energies from the addition of nano-silica, which suggests that the void growth observed in the anhydride-cured DGEBA-based system (see Section 7.3.2.3), was not present in the amine-cured TGMDA-based system. Indeed, the FEG-SEM images of the nano-only latter system with 10 wt. % nano-silica did not show any evidence of void growth around the nano-silica particles, as may be seen in Figure 7.3.9.

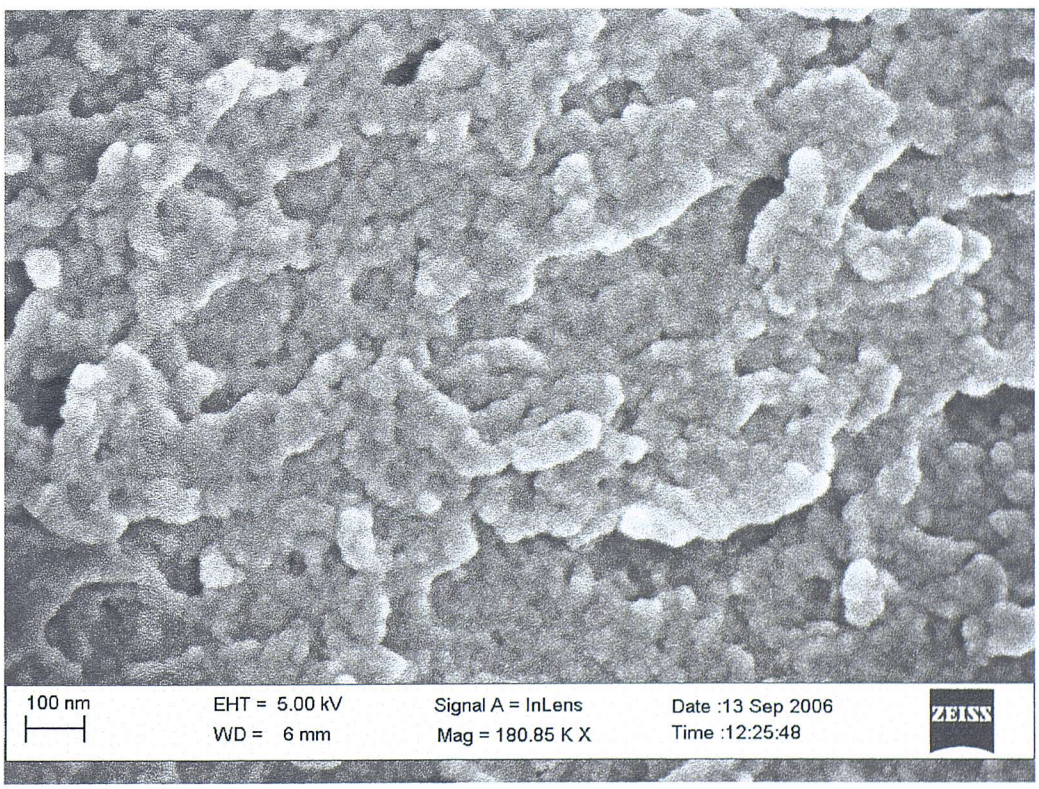


Figure 7.3.9. FEG-SEM micrograph of the fracture surface of an amine-cured TGMDA-based sample with 10 wt. % nano-silica.

7.3.3.3 Hybrid Toughening – Synergy

Synergy may be defined as the change in toughness of a hybrid sample (relative to the unmodified epoxy) being numerically greater than the sum of the changes in toughness of the rubber-only sample and the nano-only sample. Synergy may therefore be expressed mathematically as follows:

$$\Delta G_{hybrid} > (\Delta G_{rubber} + \Delta G_{nano-silica}) \qquad \textbf{Equation 7.3}$$

Where ΔG is the difference in fracture energy between a toughened sample and the unmodified epoxy, and the subscripts *hybrid*, *rubber* and *nano-silica* denote the type of toughening.

This synergistic effect was only observed in the anhydride-cured DGEBA-based system and the relevant calculations are shown in Table 7.3.3. (It should be noted that where a hybrid sample has no exact rubber-only or nano-only counterpart, the fracture energy of the sample with the closest wt. % is used. For example, the hybrid sample containing 5.03 wt. % CTBN and 5.03 wt. % nano-silica is compared to the rubber-only sample containing 6 wt. % CTBN and the nano-only sample containing 4 wt. % nano-silica.) The table shows that all the hybrid samples based upon this epoxy system show synergy (ie. the ΔG_{hybrid} in the fourth column is larger than the sum of ΔG_{rubber} and $\Delta G_{nano\text{-}silica}$ in the fifth column), except for the sample containing 18 wt. % CTBN and 9 wt. % nano-silica. (Whilst this sample may be an anomaly, it should still be the source of future research to ascertain why there was no synergy for this particular formulation.)

Table 7.3.3. Summary of the fracture energy results to show synergy for epoxy polymers based upon the anhydride-cured DGEBA-based system. The blue cells denote the hybrids. The fourth column, ΔG, denotes the difference in the measured fracture energy for the rubber-only, nano-only and hybrid samples compared to the unmodified epoxy. (*NA* – Not applicable)

wt. % CTBN	wt. % nano-silica	G_{Ic} (J/m^2)	ΔG (J/m^2)	$\Delta G_{rubber} + \Delta G_{nano\text{-}silica}$ (J/m^2)
0	0	103	0	*NA*
0	4	291	188	*NA*
0	7.8	352	249	*NA*
0	11.1	343	240	*NA*
0	14.8	406	303	*NA*
0	20.2	461	358	*NA*
6	0	221	118	*NA*
5.03	5.03	1068	***965***	118+188 = ***306***
5.17	2.59	889	***786***	118+188 = ***306***
9	0	444	341	*NA*
9	2.3	1050	***947***	341+188 = ***529***
9	4.5	918	***815***	341+188 = ***590***
9	9	977	***874***	341+249 = ***590***
9	10.5	1240	***1137***	341+240 = ***581***
9	15.4	1480	***1377***	341+303 = ***644***
18	0	763	660	*NA*
18	9	546	***443***	660+249 = ***909***
18	18	1167	***1064***	660+358 = ***1018***

Whilst future work will investigate the toughening micromechanisms for the synergy observed in this system (ie. from having both rubber and nano-silica particles present) in more detail, one possible explanation will be suggested below.

Using Equation 2.12 in Chapter 2 to calculate the plastic zone size ahead of the crack tip, it was found that for the unmodified epoxy $r_p \approx 5\mu m$, for a nano-only sample $r_p \approx 10\mu m$, and for a rubber-only sample $r_p \approx 20\mu m$. Thus, compared to the unmodified epoxy and nano-modified epoxy, the triaxial stresses are large for a greater distance ahead of the crack tip in the rubber-modified epoxy. It follows that in the hybrid samples (because of the presence of the rubber particles, and the subsequent larger plastic zone), more nano-silica particles would have a sufficiently higher triaxial stress acting on them to cause debonding and subsequent plastic void growth of the epoxy (compared to a nano-only sample). In addition, the debonding and subsequent plastic void growth in the hybrid modified epoxy would further increase the plastic zone size, and the stresses would be relatively larger for an even greater distance ahead of the crack tip (and even more nano-silica particles would debond), which would lead to an increase in toughness.

7.4 Chapter Summary

This Chapter has compared and contrasted the microstructure, material properties and fracture of bulk epoxy polymers from an amine-cured DGEBA-based system, an amine-cured TGMDA-based system, and an anhydride-cured DGEBA-based system. The rubber, nano-silica, and hybrid fracture mechanisms were also investigated.

It was found that the major rubber toughening mechanisms were shear yielding, plasticisation of the epoxy, rubber cavitation and plastic void growth of the epoxy. The dominant nano-silica toughening mechanism in the anhydride-cured DGEBA-based system was found to be due to the debonding of the nano-silica particles and the subsequent plastic void growth in the epoxy around the nano particles. In the anhydride-cured DGEBA-based system's hybrid samples, a synergistic effect was observed. This was possibly caused by the rubber enabling higher triaxial stresses in a relatively large plastic zone ahead of the crack tip, leading to more nano-silica particles debonding (and more plastic void growth in the epoxy) than in its nano-only counterpart.

The next Chapter will compare and contrast the material properties, fracture and toughening mechanisms in fibre reinforced polymers (FRPs) that use the bulk epoxy polymers discussed in this Chapter, as their matrices.

CHAPTER 8

SYSTEM COMPARISONS AND TOUGHENING MECHANISMS: FRPS

8 Introduction

This Chapter will compare and contrast the mode 1 interlaminar fracture energies, the flexural moduli and discuss possible toughening mechanisms of the FRPs of the three epoxy-based systems. Thus, three sets of laminates were manufactured by vacuum-assisted resin transfer moulding (VARTM) and were supplied using the formulations and systems discussed in the previous Chapter as the matrices. These were therefore:

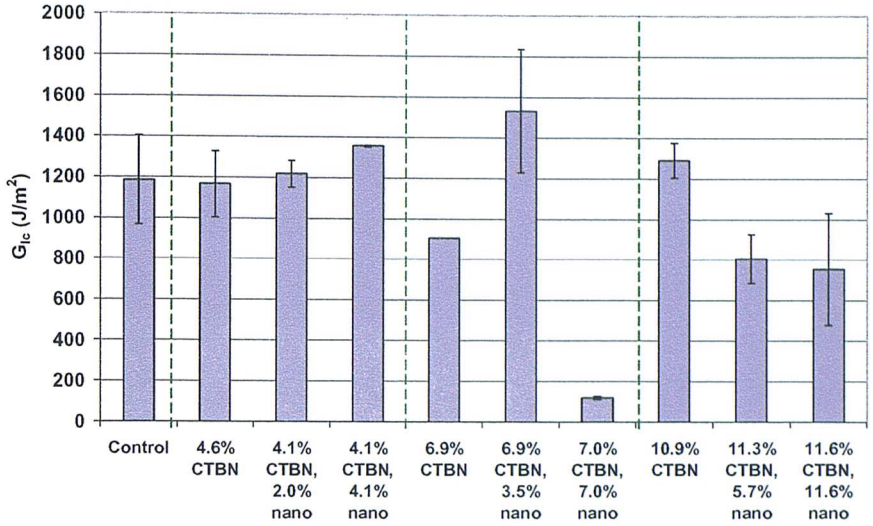
1. The amine-cured DGEBA-based system reinforced with glass fibres. Eight plies of isotropic linen-weave glass fibre fabric with a density of 200g/m^2, arranged in a 0/90° pattern, were used.
2. The amine-cured TGMDA-based system reinforced with carbon fibres. Eight plies of isotropic linen-weave carbon fibre fabric with a density of 370g/m^2, arranged in a 0/90° pattern, were used.
3. The anhydride-cured DGEBA-based system reinforced with carbon fibres. Six plies of isotropic linen-weave carbon fibre fabric with a density of 168g/m^2, arranged in a 0/90° pattern, were used.

It should be reiterated that nano-silica particles do not adversely affect manufacturing processes such as VARTM, since the particles are not 'strained out' (which limits the use of micron-sized glass particles in FRPs), nor is the viscosity of the resin significantly increased.

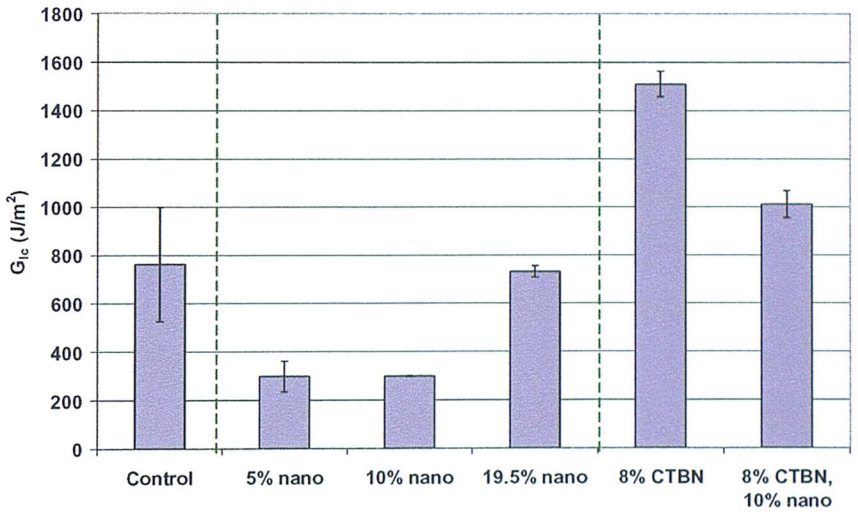
8.1 Mode I Fracture Energy

Figure 8.1.1 shows bar charts of the mode I (initiation) interlaminar fracture energies calculated using the CBT method (see Equations 3.6-8 in Chapter 3) for all three systems. As discussed in Section 3.1 in Chapter 3, the three laminates have different applications and are therefore reinforced with different types of fibres, so it may be inappropriate to make a direct comparison of the values of the absolute fracture energies.

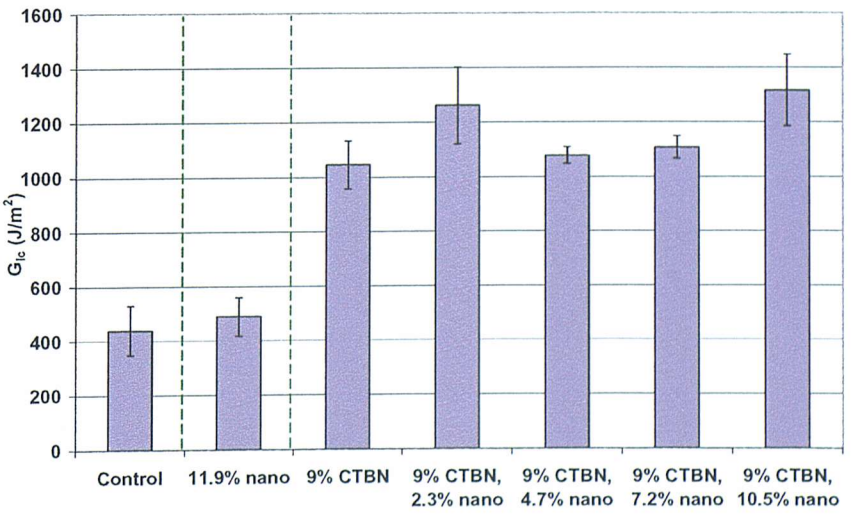
What is apparent, however, is that compared to the respective control (ie. the laminate with an unmodified epoxy matrix) even the most apparent fracture-resistant laminate based on the amine-cured DGEBA-based system is not actually statistically tougher than the control (see Figure 8.1.1 (a)). Nevertheless, the amine-cured TGMDA-based system demonstrates a 1.5 times increase in the interlaminar fracture energy. The anhydride-cured DGEBA-based system demonstrates a 2.5 times increase in the interlaminar fracture energy using the best modified epoxy compared to the corresponding unmodified epoxy matrix. Clearly the biggest improvement due to the inclusion of nano-silica and CTBN rubber as the matrix toughening comes from the FRPs employing an anhydride-cured DGEBA matrix. Now, a better comparison of the results may be between the bulk fracture energies and the FRP fracture energies for a given system, as will be discussed below.



(a)



(b)



(c)

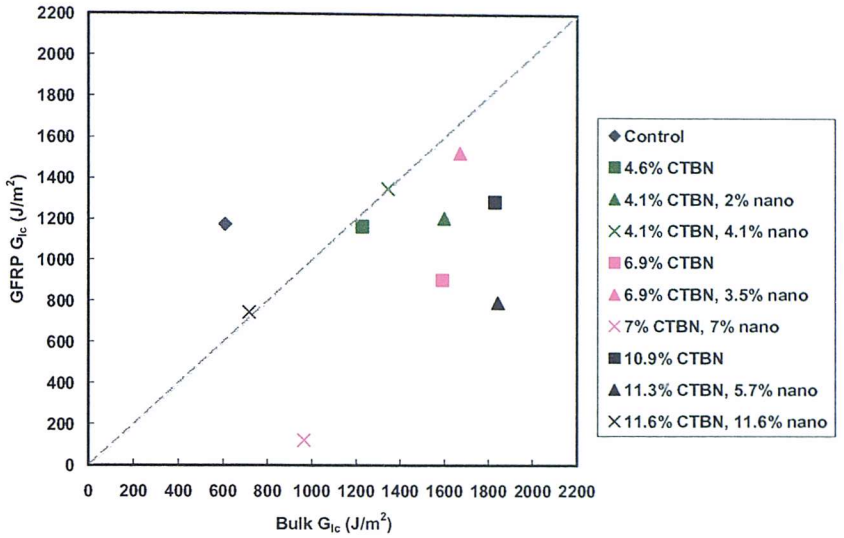
Figure 8.1.1. Mode I (initiation) interlaminar fracture energies calculated using the CBT method for laminates with matrices of: (a) amine-cured DGEBA, (b) amine-cured TGMDA, and (c) anhydride-cured DGEBA. (The 'control' employs the appropriate unmodified epoxy as the matrix for the FRP.)

Therefore, Figure 8.1.2 shows a comparison between the interlaminar fracture energies of the FRPs and the corresponding bulk fracture energies for the three systems investigated. These graphs illustrate the transfer (or lack thereof) of fracture resistance from the bulk epoxy systems to the corresponding FRPs.

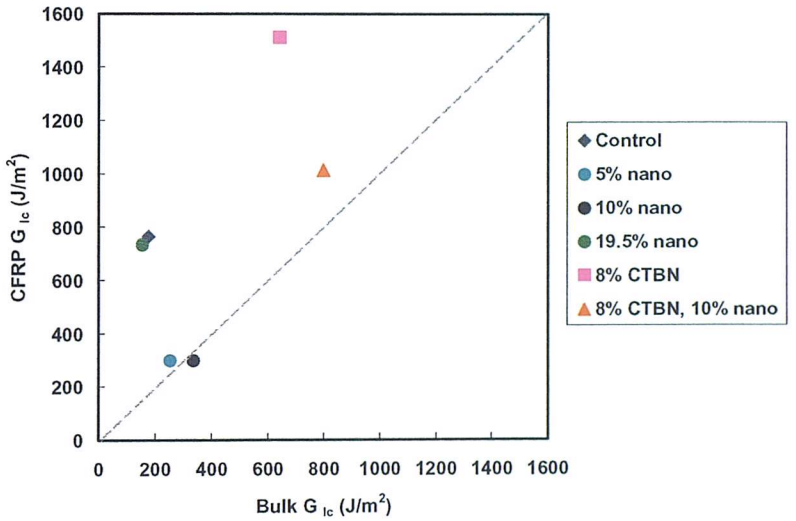
It can be seen from Figure 8.1.2 (a) that the fracture resistance of the control (ie. the unmodified) FRP for the amine-cured DGEBA-based system is enhanced compared to the bulk epoxy, since $G_{Ic(FRP)} > G_{Ic(Bulk)}$. The fracture resistance is transferred from the bulk epoxy to the FRP in two of the hybrids and the CTBN-only sample (ie. $G_{Ic(FRP)} \approx G_{Ic(Bulk)}$). However, in the five remaining hybrid epoxy systems, there is no transfer of toughness (ie. $G_{Ic(FRP)} < G_{Ic(Bulk)}$).

All the laminates manufactured using the amine-cured TGMDA-based system (see Figure 8.1.2 (b)) and the anhydride-cured DGEBA-based system (see Figure 8.1.2 (c)) show a transfer or enhancement of fracture resistance from the bulk epoxy polymer to the FRPs, since $G_{Ic(FRP)} \geq G_{Ic(Bulk)}$. Indeed, only the two nano-only samples in the amine-cured TGMDA-based system showed merely a transfer of toughness, whereas all other samples in that system, as well as all the samples in the anhydride-cured DGEBA-based system, showed an enhancement of toughness. The laminates with the largest increase in fracture energy, compared to their bulk counterparts, were the CTBN-only samples in both systems: both of which had an approximate CTBN concentration of 8.5 wt. %.

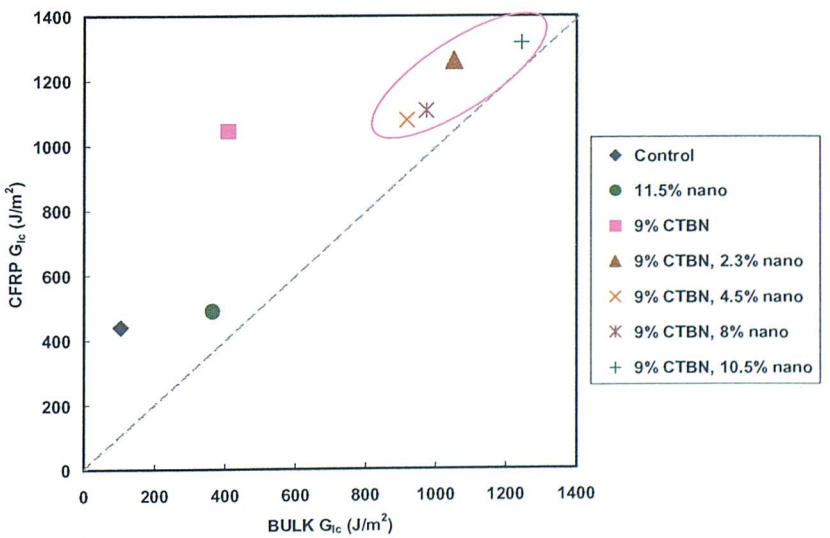
Overall, therefore, the anhydride-cured DGEBA-based system demonstrated the best enhancement of bulk toughness to the corresponding FRP. In addition, the hybrid laminates from this system had the highest fracture energies of this system, and these results are circled in pink in Figure 8.1.2 (c). A more in-depth discussion on the toughening mechanisms in the FRPs can be found in the next Sections.



(a)



(b)



(c)

Figure 8.1.2. Comparison between the interlaminar FRP and bulk epoxy fracture energies for the: (a) amine-cured DGEBA-based system, (b) amine-cured TGMDA-based system, and (c) anhydride-cured DGEBA-based system (Note: the hybrid toughened systems are circled in pink in Figure 8.1.2 (c)).

8.2 FRP Fracture Comparisons and Toughening Mechanisms

Micrographs of the fracture surfaces of the mode I FRP samples were obtained in order to ascertain the toughening mechanisms that occur during fracture. Such micrographs are considered below to help explain the results shown in Figure 8.1.2.

8.2.1 Unmodified Epoxy Matrices

Figure 8.2.1 shows a comparison of laminates from the three systems, each having unmodified matrices, and crack propagation from right to left. Firstly, the micrograph in Figure 8.2.1 (a) is from the amine-cured DGEBA-based system and shows poor adhesion between the fibres and the matrix. Indeed, this FRP was only ~2 times more fracture resistant than its bulk epoxy counterpart. Secondly, the FRPs shown in Figure 8.2.1 (b) and (c) (from the amine-cured TGMDA-based system and the anhydride-cured DGEBA-based system respectively) show a relatively high degree of deformation of the matrix compared to the laminate from the amine-cured DGEBA-based system. Indeed, these two laminates also show better adhesion between the fibres and matrix, than the laminate from the amine-cured DGEBA-based system. This good adhesion between fibres and matrix undoubtedly contributes to these laminates having ~3.5 times the fracture energy of the corresponding bulk epoxy (see Figure 8.1.2 (b) and (c)).

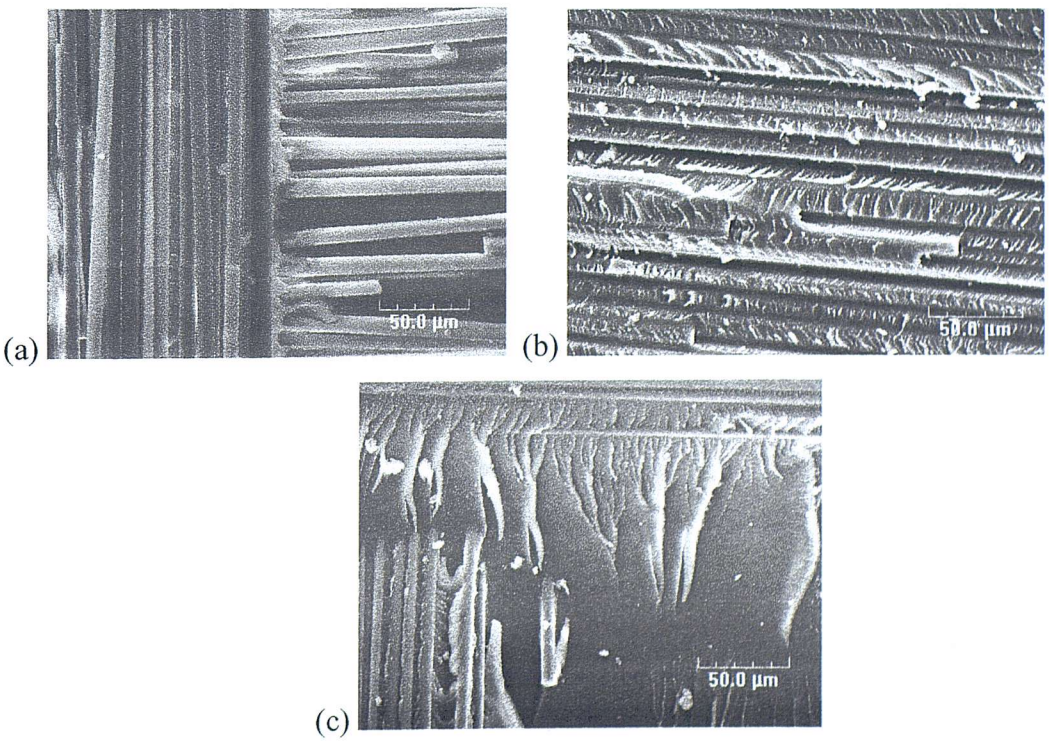


Figure 8.2.1. Micrographs of the fracture surface of laminates with unmodified matrices from the: (a) amine-cured DGEBA-based system, (b) amine-cured TGMDA-based system, and (c) anhydride-cured DGEBA-based system.

8.2.2 Nano-silica Modified Matrices

No laminates from the amine-cured DGEBA-based system that were toughened with only nano-silica were examined, due to time constraints. However, FRP laminates were manufactured using nano-silica modified epoxy matrices based on the other two systems. Micrographs of the fracture surfaces of these FRPs are shown in Figure 8.2.2, where the crack growth is from right to left. There appears to be good adhesion between the matrix and fibres in all of the samples, as well as some deformation of the epoxy matrix. This suggests that the fracture energy of the laminates should at least be of a similar magnitude to that of the corresponding bulk epoxy system, which is exactly what was observed as shown in Figure 8.1.2 (b) and (c).

The fracture surfaces of the FRPs in Figure 8.2.2 (a) and (b) containing 5 and 10 wt. % nano-silica respectively, from the amine-cured TGMDA-based system, have similar fracture energies compared to that of their corresponding bulk epoxy (see Figure 8.1.2 (b)). There is evidence of fibre pull-out, debonding, and good fibre-matrix adhesion, so this might suggest a higher fracture energy than that of the bulk epoxy. However, in the absence of AFM or TEM images, it can only be postulated that agglomeration of the nano-silica occurred during manufacture of the laminates, and hence had a detrimental effect on their interlaminar fracture energies. It is noteworthy that these two FRPs also possessed a much lower interlaminar fracture energy than the control laminate, which again suggests a change in the morphology of the matrix during FRP manufacture.

From Figure 8.1.2 (b) and (c) it can be seen that the only nano-only FRP laminates that showed an improvement in their fracture energies compared to their corresponding bulk epoxy, were those from the amine-cured TGMDA-based system containing 19.5 wt. % nano-silica (see Figure 8.2.2 (c)), and from the anhydride-cured DGEBA-based system containing 11.5 wt. % nano-silica (see Figure 8.2.2 (d)). However, neither FRP showed a significant improvement in their interlaminar fracture energy compared to their respective control FRP laminate. This reveals that nano-silica particles alone do not enhance the interlaminar fracture energy of either the amine-cured TGMDA-based system or the anhydride-cured DGEBA-based system, compared to the fracture energy of the respective bulk epoxy. This implies that the debonding of the nano-silica particles and subsequent epoxy void growth that was observed and discussed in Chapter 7,

probably does not occur in this FRP laminate based upon the anhydride-cured DGEBA-based system.

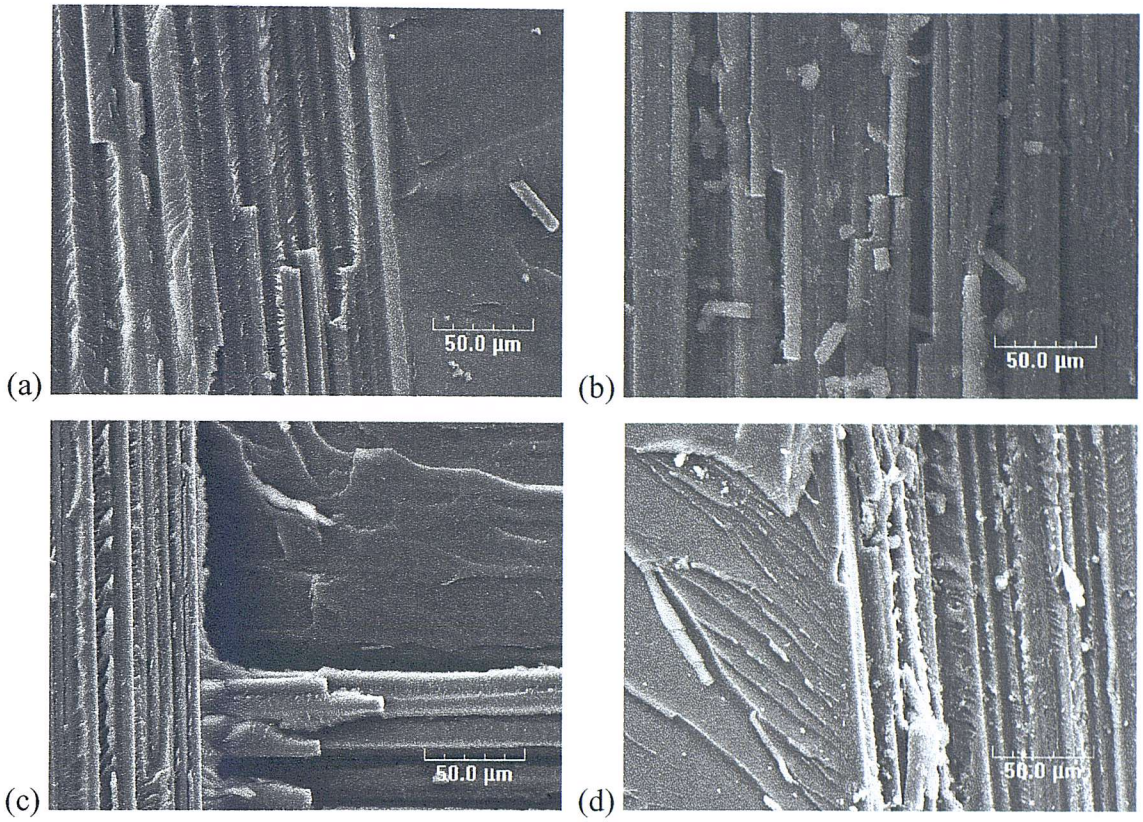


Figure 8.2.2. Micrographs of the fracture surface of laminates with the following matrices: (a) 5 wt. % nano-silica in an amine-cured TGMDA-based system, (b) 10 wt. % nano-silica in an amine-cured TGMDA-based system, (c) 19.5 wt. % nano-silica in an amine-cured TGMDA-based system, and (d) 11.5 wt. % nano-silica in an anhydride-cured DGEBA-based system.

8.2.3 Rubber Modified Matrices

The CTBN-only laminates based upon the amine-cured DGEBA-based system were the only CTBN-only laminates that showed no enhancement in fracture energy compared to their respective bulk epoxy system (see Figure 8.1.2). Indeed, an examination of the fracture surface (a representative example of which is shown in Figure 8.2.3 (a), where the crack growth is from right to left), shows that although there was evidence of cavitated rubber particles, failure occurred due to poor adhesion between the fibre and matrix (as suggested by the 'clean' fibres). As a result, the epoxy matrix was not allowed to deform to its full potential, since the crack propagated between the fibres and matrix and not exclusively through the epoxy. It should also be noted that the addition

of only CTBN to the epoxy matrices did not improve the interlaminar fracture energy of the amine-cured DGEBA-based FRP compared to the control FRP.

The fracture energies of the CTBN-only laminates based upon the amine-cured TGMDA-based system and the anhydride-cured DGEBA-based system were higher than that of their corresponding bulk epoxies and control laminates (see Figure 8.1.2 (b) and (c)). This is assumed to arise from the observation that in both systems (as shown in Figure 8.2.3 (b) and (c), where the crack growth is from right to left) there was good adhesion between the fibres and the matrix, and there was extensive plastic deformation of the matrix as well as rubber cavitation. However, the cavitation was not extensive, and indeed appeared to be as infrequent, and of the same size, as was observed for the respective bulk epoxies.

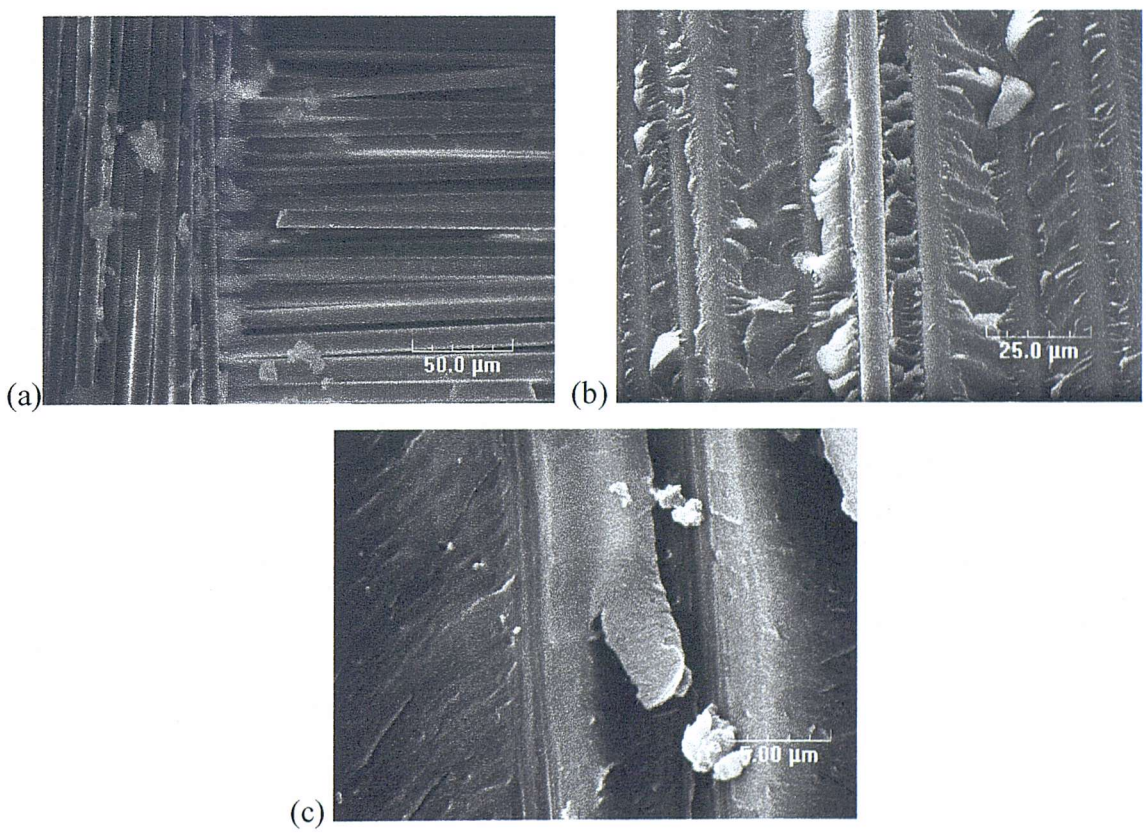
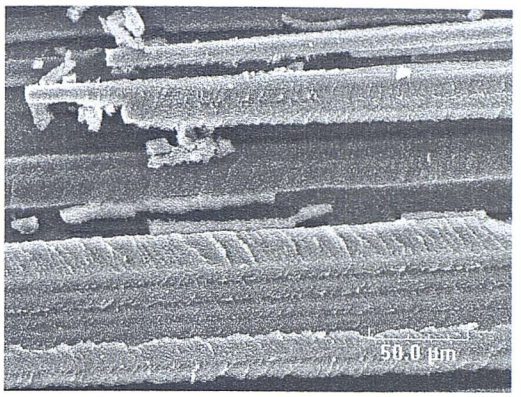


Figure 8.2.3. Micrographs of the fracture surface of laminates with the following matrices: (a) 6.9 wt. % CTBN in an amine-cured DGEBA-based system, (b) 8 wt. % CTBN in an amine-cured TGMDA-based system, and (c) 9 wt. % CTBN in an anhydride-cured DGEBA-based system.

8.2.4 Hybrid Modified Matrices

The hybrid laminates of the three systems are a complex group to discuss: indeed, the hybrid FRP laminates of the amine-cured DGEBA-based system had relatively low fracture energies compared to both the bulk epoxy and the control FRP laminate (see Figure 8.1.2 (a)). Although there was not sufficient time to investigate the microstructure of the laminates, it is reasonable to assume that the formations of super-clumps of nano-silica (ie. at high nano-silica contents) observed in the bulk epoxy polymer (see the summary of the hybrid microstructures in Table 7.1.3 in Chapter 7), was also present in the matrix of the laminates. This would be likely to have caused a sharp decrease in the fracture resistance of the matrix. In addition, micrographs of the fracture surfaces showed that there was poor adhesion between the fibres and the matrix, which would also contribute to the lack of fracture resistance. This poor adhesion was a common feature of the laminates with an amine-cured DGEBA-based matrix (see Section 4.2.2 in Chapter 4 for all the SEM micrographs), and one way to improve the adhesion between the fibres and matrix, might be to surface-treat the fibres [32] with an organofunctional alkoxysilane [31].

The micrographs shown in Figure 8.2.4 (a) and (b) are of hybrid laminates from the amine-cured TGMDA-based system and the anhydride-cured DGEBA-based system respectively, with comparable CTBN contents (~8.5 wt. % CTBN). Both have higher interlaminar fracture energies than their respective bulk epoxy polymers (see Figure 8.1.2 (b) and (c)). However, compared to their control laminates, the interlaminar fracture energy of the FRP based upon the amine-cured TGMDA-based system is comparable, and the FRP from the anhydride-cured DGEBA-based system is twice as fracture resistant. Compared to their CTBN-only FRP counterparts, the further addition of nano-silica to the amine-cured TGMDA-based system decreases its interlaminar fracture energy; whereas the hybrids based upon the anhydride-cured DGEBA-based system have comparable interlaminar fracture energies.

(a) 

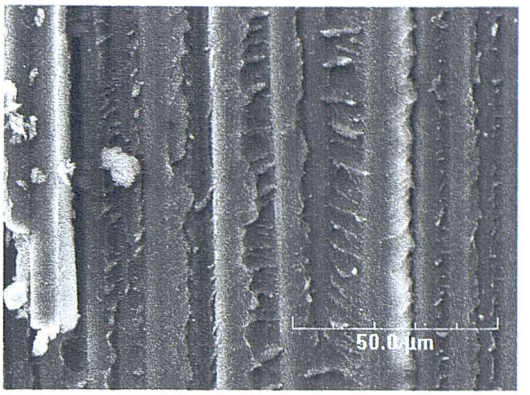
(b) 

Figure 8.2.4. Micrographs of the fracture surface of laminates with the following matrices: (a) 8 wt. % CTBN and 10 wt. % nano-silica in an amine-cured TGMDA-based system, and (b) 9 wt. % CTBN and 2.3 wt. % nano-silica in an anhydride-cured DGEBA-based system.

In the amine-cured DGEBA-based system, a common observation was the poor adhesion between the fibres and matrix, which may have led to a poor transfer of fracture energy from the bulk epoxy to the corresponding FRP. Kinloch and Taylor [20] showed that if there was perfect adhesion between the fibres and the matrix, then the FRP laminate would fail through the epoxy, and the fracture energy would simply be the same as that of the bulk matrix. If there was zero interfacial adhesion, the fracture energy would be slightly lower than that of the polymer, since the woven mat only covers a fraction of the bonded surface. However, in this amine-cured DGEBA-based system, the fracture surface showed a large surface area occupied by the woven mat, which might explain why the FRP interlaminar fracture energy was so much lower in some cases than the bulk epoxy.

Indeed, it has also been noted [20] that intermediate levels of fibre-matrix adhesion would give the highest fracture energy. This might explain what was observed in the FRPs based upon the amine-cured TGMDA-based system and the anhydride-cured DGEBA-based system, since additional toughening was contributed by the fibres. Evidence of fibre debonding, pull-out and bridging was observed. It should be noted, however, that because of the woven nature of the fibres, they would only be able to bridge a short distance (unlike a unidirectional laminate) and would give small R-curves [11,20]. Indeed, the R-curves for all three epoxy based systems were either very small, or non-existent, which agrees well with the literature.

8.2.5 Summary

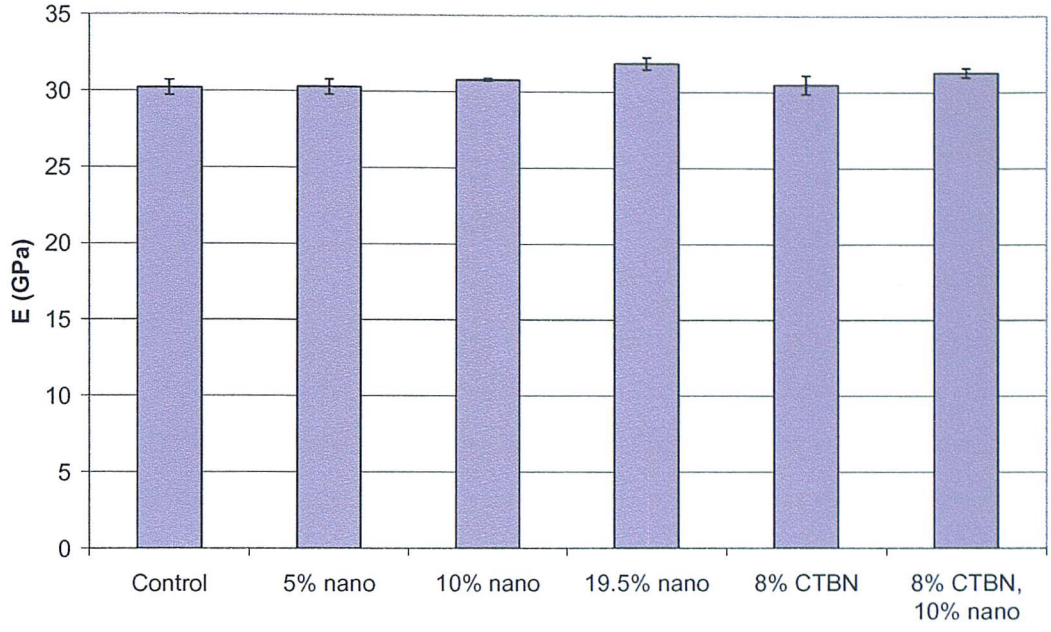
In general, the toughness values were not transferred from the bulk epoxy to the laminates in the amine-cured DGEBA-based system. The main reason for this is suggested to be the poor interfacial bonding between the fibres and matrix. In the case of the amine-cured TGMDA-based system there was possibly also agglomeration of the nano-silica particles during the manufacture of the FRP laminates which helped lead to relatively low fracture energies. However, for this latter system the CTBN-only and hybrid FRP laminates possessed relatively high values of interlaminar toughness. The best laminates were from the anhydride-cured DGEBA-based system. These showed an enhancement of fracture energy from bulk to laminate, and the hybrid FRPs in particular had excellent interlaminar fracture resistance compared to the FRP control laminate. The dominant toughening mechanisms in these hybrid laminates were plastic deformation of the polymer matrix, cavitation of the rubber particles as well as some additional contributions from fibre debonding, pull-out and bridging.

8.3 Flexural Modulus

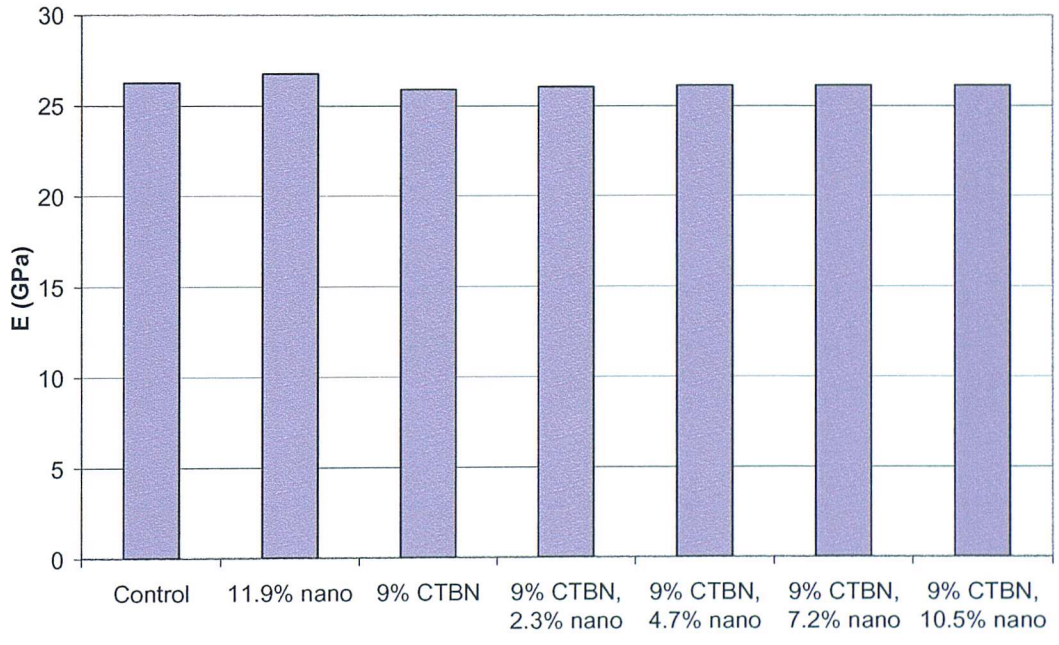
No flexural modulus tests were performed on the laminates manufactured using the amine-cured DGEBA-based system because of their relatively poor standard of manufacture and surface finish. Indeed, many of these samples were 'epoxy-rich' and any values of laminate modulus would have been very misleading.

However, flexural modulus tests were performed on FRP laminates manufactured using the amine-cured TGMDA-based system and the anhydride-cured DGEBA-based system. The laminates from the amine-cured TGMDA-based system were manufactured to a good standard. The laminates appeared to have a good surface-finish, were relatively uniformly thick, and the cracks during interlaminar fracture tests generally propagated through the mid-plane of the laminate, and gave a small scatter of results. This suggests that FRPs from this latter system had a relatively consistent fibre:epoxy ratio. However, the results from the anhydride-cured DGEBA-based system had to be adjusted after detailed fibre volume analysis showed the inconsistency of the fibre:epoxy ratio in that system's FRPs.

The modulus results are presented in Figure 8.3.1, and similar trends can be observed in both systems. Both systems show that the addition of nano-silica (which has a much higher modulus than the epoxy matrix [137,138]) produces a small increase in the flexural modulus. Conversely, the addition of CTBN (with a much lower modulus than the epoxy matrix [126]) causes a slight decrease. Hybrid FRP laminates had similar, or even higher moduli, than their respective control samples. Both sets of laminate moduli are fibre-dominated, with the amine-cured TGMDA-based system having a modulus of ~30GPa, and the anhydride-cured DGEBA-based system having a modulus of ~26GPa. (It should be noted that the main reason that the FRPs based upon the amine-cured TGMDA-based system have a higher flexural modulus is because more carbon fibre plies of a higher fibre density were used than in the anhydride-cured DGEBA-based system.) Mouritz [37] performed flexural modulus tests on a wide variety of FRPs with different fibres, including woven glass and carbon fibres. He showed results of between 25 and 30GPa which agree well with the values obtained in this study. Thus, in both systems it has been shown that the addition of nano-silica makes the laminates stiffer, and such addition can retrieve some of the stiffness lost when CTBN is added. The latter point is especially important for the amine-cured TGMDA-based system, since CTBN is not traditionally used in high performance applications [33]. However, the present study has shown that laminates from this system can be both fracture resistant and stiff if nano-silica is added.



(a)



(b)

Figure 8.3.1. Flexural modulus results for laminates with the following matrices: (a) amine-cured TGMDA, and (b) anhydride-cured DGEBA.

8.4 Chapter Summary

This Chapter has compared and contrasted the properties of the bulk epoxy materials and the corresponding FRP laminates of the three epoxy systems. The FRP laminates based upon the amine-cured DGEBA-based system showed a poor transfer of toughness from the bulk epoxy to the FRPs. This was suggested to arise from the relatively poor

adhesion between the fibres and the matrix. However, there was a good transfer of toughness, and even a significant enhancement of toughness in some instances, observed for FRPs based upon the amine-cured TGMDA-based system and the anhydride-cured DGEBA-based system. It was suggested that the major reason for this, was the good adhesion between the fibres and these matrices leading to the toughening mechanisms of the bulk epoxy being able to operate; and also enabling other additional toughening mechanisms from the presence of the fibres to function. Overall, the nano-silica particles had the most significant, positive effect on the toughness of the FRP laminates manufactured using the anhydride-cured DGEBA-based system. In addition, it was found that the nano-silica particles can reinstate any stiffness that was lost due to the CTBN rubber being present: an exciting development that might permit CTBN to be used in FRP laminates based upon the amine-cured TGMDA-based, and other similar, systems.

CHAPTER 9

CONCLUSIONS AND FUTURE WORK

9 Background

Over the course of this Thesis, the reader has been introduced to the use of nano-silica particles and carboxyl-terminated butadiene acrylonitrile (CTBN) rubber as toughening agents in three epoxy-based systems, namely two different epoxies cured with three different hardeners. The present Chapter will firstly summarise the main findings and conclusions regarding the microstructure and the material properties of each epoxy-based system. Secondly, it will compare and contrast the microstructure, material properties and fracture of the three epoxy-based systems. Thirdly, it will discuss and summarise the main toughening mechanisms in both the epoxy polymers and the fibre-reinforced polymer (FRP) laminates, which have been manufactured using the three epoxy-based systems as the matrices. Finally, several areas of future work will be suggested to answer some of the questions arising from the present work, and to assist in further understanding the material properties and fracture of these nano-toughened epoxy systems.

9.1 Material Properties of the Epoxy-Based Systems

This Section will summarise the main findings from the research performed on the three epoxy-based systems to ascertain their microstructure and material properties.

9.1.1 Amine-cured DGEBA-based System

This system was discussed in detail in Chapter 4. No samples with only nano-silica were provided for this system due to time constraints. The CTBN-only bulk epoxy

polymers had a microstructure where up to about 80% of the CTBN rubber had phase-separated into well-dispersed, spherical rubber particles of up to 0.5μm in diameter. Compared to the unmodified epoxy, increasing amounts of CTBN caused a 5% decrease in the glass transition temperature and up to a 30% decrease in the tensile modulus, but an increase in the fracture energy up to 200%. The value of G_{Ic} of the untoughened (ie. unmodified) epoxy being 612J/m^2, whilst that for the epoxy toughened with 10.9 wt. % of CTBN, which showed the maximum toughness, was 1835J/m^2.

Considering the 'hybrid' materials (ie. where both the nano-silica particles and the CTBN rubber were present), the nano-silica remained well-dispersed in the epoxy at low wt. % concentrations but formed large agglomerates of up to 4μm in diameter (ie. 'super-clumps') at higher concentrations of nano-silica. The morphology of the nano-silica particles was independent of the CTBN content; and the size and shape of the rubber particles were unaffected by the presence of the nano-silica particles. However, the presence of nano-silica particles in the hybrids did suppress the degree of phase separation of the rubber particles, and hence lowered the glass transition temperature of the epoxy. The tensile modulus of these hybrids increased with increasing amounts of nano-silica and the stiffness that was lost by the presence of the CTBN was restored. It should be noted that the measured tensile moduli of all the bulk epoxy polymers agreed well with the predictive analytical models. Compared to the CTBN-only samples, the additional presence of the nano-silica did not increase the fracture energy of the epoxy at low wt. % concentrations and, the fracture energy actually decreased compared to that of the unmodified epoxy due to the formation of super-clumps at high nano-silica contents. It may therefore be concluded that, in the hybrids, the additional presence of the nano-silica in relatively low concentrations (eg. less than 5 wt. %) results in a similar value of the fracture energy shown by its CTBN-only counterpart, but increases the stiffness. For example, the value of G_{Ic} of the epoxy toughened with 6.9 wt. % of CTBN was 1595J/m^2, whilst that for the hybrid material containing 6.9 wt. % CTBN and 3.5 wt. % nano-silica, was 1674J/m^2. The values of the moduli, E, were 2.84GPa and 3.09GPa, respectively.

There was a poor transfer of the fracture energy from the variously toughened amine-cured DGEBA-based polymers to the FRP laminates, which used this system as the

matrix material. Indeed, disappointingly, none of the modified laminates were more fracture resistant than the control laminate based upon the untoughened epoxy system.

9.1.2 Amine-cured TGMDA-based System

This system was discussed in detail in Chapter 5. For the bulk epoxy polymers containing nano-silica only, the nano-silica particles formed increasingly large agglomerates with increasing nano-silica content. (It should be noted that the agglomerates formed in the nano-only bulk epoxy polymers consisted of up to about twelve nano-silica particles, and were much smaller than the 'super-clumps' observed in the amine-cured DGEBA-based system.) As the concentration of nano-silica was increased no significant changes in the glass transition temperature or the fracture energy were observed, but the tensile moduli of these epoxy polymers which contained only the nano-silica particles did increase.

Only 25% of the rubber phase-separated into spherical particles of up to 1μm in diameter in the CTBN-only and hybrid bulk epoxy polymers. It was found that the nano-silica particles in the hybrid formed three-dimensional necklace-like chains of up to 1.5μm in length and 0.5μm in width. Rubber on its own caused a decrease in the tensile modulus, but the addition of the nano-silica (ie. to form a hybrid) restored this lost stiffness. It should be noted that, again, the measured tensile moduli of all the bulk epoxy polymers agreed well with the predictive analytical models. Compared to the unmodified epoxy polymer, the addition of only CTBN caused the fracture energy to triple, and the further addition of nano-silica (ie. to form a hybrid bulk polymer) caused a further increase in G_{Ic}. For example, the value G_{Ic} of the untoughened epoxy was 176J/m^2, whilst that of the 8 wt. % CTBN-only polymer was 640J/m^2; and that of the hybrid containing 8 wt. % CTBN and 10 wt. % nano-silica, which demonstrated the maximum toughness, was 798J/m^2.

Considering the FRP laminates toughened with only nano-silica, it was found that, compared to the control laminate, which employed the unmodified epoxy matrix, the addition of 19.5 wt. % nano-silica produced a laminate that was slightly stiffer than the control laminate, but had a similar interlaminar fracture energy to that of the control laminate, (ie. the values of G_{Ic} being about 750J/m^2). However, lower concentrations of

nano-silica in the epoxy matrix produced laminates that were more brittle than the control laminate, but were of a similar fracture energy to that of their corresponding bulk epoxy polymers, (ie. the values of G_{Ic} being about 300J/m^2).

The FRP laminate with the CTBN-only modified matrix had the highest interlaminar fracture energy of these various laminates, (ie. more than twice that of the untoughened G_{Ic} value of 764J/m^2), but the lowest flexural modulus. The addition of nano-silica (ie. to form a hybrid matrix) reinstated the lost stiffness, but reduced the interlaminar fracture energy to a level that was slightly higher than that of the control laminate, (ie. ~1000J/m^2). Now, relatively high concentrations of CTBN are not normally used for high performance laminates based upon TGMDA, due to the presence of the CTBN causing a reduction in the stiffness. Nevertheless, it can be concluded that using a hybrid matrix (ie. one containing both CTBN rubber and nano-silica) based upon this epoxy system can lead to FRP laminates with good stiffness and good fracture resistance, which represents a combination of highly desirable properties for laminates destined for use in the aerospace industry.

9.1.3 Anhydride-cured DGEBA-based System

This system was discussed in detail in Chapter 6. Considering the bulk epoxy polymers containing only nano-silica, it was found that even at relatively high nano-silica contents, the nano-silica particles remained well dispersed in the bulk epoxy. Compared to the unmodified epoxy, increasing the nano-silica content produced a steady increase in the tensile modulus (of up to 30%), up to a 300% increase in the fracture energy, and no change in the glass transition temperature of the epoxy. Thus, for example the value of G_{Ic} increased from 103J/m^2 for the unmodified epoxy, to 461J/m^2 for the epoxy polymer containing 20.2 wt. % of nano-silica particles.

Compared to the unmodified bulk epoxy polymer, the addition of CTBN produced decreases in the tensile modulus and the glass transition temperature of the epoxy. However, the fracture energy increased up to 600% at relatively high amounts of CTBN (ie. to a value of 763J/m^2 when 18wt. % of CTBN was present) but only a fraction of the CTBN phase separated into spherical rubber particles of up to 1μm in diameter.

Microstructural investigation of the hybrid epoxy polymers showed that the nano-silica particles formed three-dimensional necklace-like structures of up to 3μm in length and 0.5μm in width at high CTBN contents (eg. more than 9 wt. %), but remained well dispersed at lower CTBN contents (ie. the nano-silica microstructure was dependent on the CTBN content). The nano-silica particles increased the tensile modulus but reduced the glass transition temperature of the epoxy, since they appear to suppress the phase separation of the rubber particles. It should be noted that the measured tensile moduli of all the bulk epoxy polymers again agreed well with the predictive analytical models. In general, the fracture energy of the hybrid modified epoxies (ie. for a given CTBN content) increased with increasing nano-silica content, and a synergistic toughening effect between the CTBN and the nano-silica was observed. Thus, for example the value of G_{Ic} increased from 103J/m^2 for the unmodified epoxy to 1480J/m^2 for the hybrid epoxy polymer containing 9 wt. % of CTBN rubber and 15.4 wt. % of nano-silica particles.

Compared to the control laminate, the presence of nano-silica particles in the epoxy matrix improved the flexural modulus of the laminate, but produced no significant change in the interlaminar fracture energy. However, the addition of only CTBN reduced the flexural modulus, but doubled the interlaminar fracture energy compared to the control laminate, (ie. from 439 to 1044J/m^2). When nano-silica was added (ie. to form a hybrid matrix), the flexural modulus increased and the interlaminar fracture energy either remained the same, or increased relatively slightly compared to the laminate toughened with only CTBN. It may be concluded that when this epoxy-based system is used as the matrix for FRPs, a hybrid modified laminate (ie. containing both CTBN and nano-silica in the epoxy matrix) can have a relatively high fracture energy, as well as stiffness. The laminates using anhydride-cured DGEBA-based matrices, together with woven carbon-fibres, are employed in sporting equipment, such as tennis racquets and ski poles, and for such laminates, this combination of properties is highly desirable.

9.2 Toughening Micromechanisms

This Section will summarise the main toughening micromechanisms in the bulk epoxies and the FRPs, which were discussed in detail in Chapters 7 and 8 respectively.

9.2.1 Toughening Micromechanisms in the Bulk Epoxy Polymers

Detailed investigations into the nano-silica toughening mechanisms were only performed on the bulk epoxy polymers based upon the anhydride-cured DGEBA-based system due to time constraints. It was concluded that there was very little evidence to suggest that the nano-silica particles toughen the epoxy by means of crack pinning or crack deflection. Indeed, the fractographical evidence suggested that the toughening effect was caused by the debonding of the nano-silica particles, and the subsequent plastic void growth of the epoxy in the immediate vicinity around the particle. A comparison of the fracture energies measured experimentally to the theoretical values obtained from an analytical model suggested that plastic hole growth in the epoxy polymer, following the debonding of the nano-silica particles, can indeed produce the major increases in toughness that were observed in this epoxy system from the presence of well-dispersed nano-silica particles.

The fracture surfaces of the bulk epoxy polymers toughened with only CTBN rubber in the amine-cured DGEBA-based system, showed increasing amounts of cavitated rubber particles with increasing rubber concentrations. It may be concluded that, in the amine-cured DGEBA-based system, the cavitated rubber particles facilitate plastic hole growth of the epoxy, which increases the toughness of the rubber modified epoxy polymers. This is in contrast to the amine-cured TGMDA-based system and the anhydride-cured DGEBA-based system, where there was very little evidence of rubber cavitation on the fracture surfaces. Indeed, the major rubber toughening mechanisms in these two systems are believed to be from (a) the shear yielding of the epoxy between the phase separated rubber particles, and (b) the plasticisation of the epoxy by the rubber that remained in solution in the epoxy phase.

9.2.2 Toughening Micromechanisms in the FRPs

There was very little transfer of toughness from the bulk epoxies to the FRPs for the amine-cured DGEBA-based system. However, there was a good transfer, and in many cases an enhancement, of toughness in the amine-cured TGMDA-based and the anhydride-cured DGEBA-based systems, upon comparing the interlaminar fracture energies of the FRP laminates to the fracture energies of the corresponding bulk epoxy polymers.

It is believed that the lack of transfer of toughness in the amine-cured DGEBA-based system may have been due to the poor adhesion between the fibres and the matrix. This would have suppressed the deformation of the epoxy matrix. Hence, the bulk toughening mechanisms, that were discussed in the previous Section, would not have been able to operate.

There was much better adhesion between the fibres and the matrix in the FRPs based upon the amine-cured TGMDA-based and the anhydride-cured DGEBA-based systems. This is suggested to have led to the bulk toughening mechanisms being able to operate, which led to the transfer of toughness that was observed in many of the laminates. Where an enhancement of toughness was recorded in these two systems, it is believed that this extra toughness was provided by fibre toughening mechanisms such as fibre debonding, fibre pullout and a limited amount of fibre bridging.

9.3 Concluding Remarks

Whilst CTBN rubber and micron-sized glass particles have been used in previous studies as tougheners for epoxies, and the material properties and fracture of such toughened epoxies have been studied in great detail, the present work has examined a novel toughening agent: silica spheres of approximately 20nm in diameter which are formed in-situ in the epoxy resin to give the potential for an excellent dispersion of the nano particles in the cured epoxy polymer.

The present work has shown that in three different epoxy-based systems, the addition of nano-silica has had no effect on the glass transition temperature of the epoxy, except where its presence influences the phase separation of the CTBN rubber, if present, to form a 'hybrid' toughened polymer. Nano-silica particles can increase the stiffness of the bulk epoxy polymer, and restore any decrease in the stiffness caused by the presence of rubber in the hybrid bulk epoxy polymers. The most significant increases in toughness were observed in the hybrid bulk epoxy polymers, where both CTBN rubber and nano-silica were employed. When the nano-silica particles are well-dispersed, or form three-dimensional necklace-like chains, as in the hybrids, significant increases in toughness were observed. Indeed, a strong synergistic toughening effect between the

nano-silica particles and the CTBN rubber was observed in many of the hybrid bulk epoxy polymers.

Considering the FRP laminates which were manufactured employing the above epoxy polymers as the matrices, nano-silica particles do not cause an increase in resin viscosity (by virtue of their small size) and so can readily be used as tougheners for epoxy matrices where transfer moulding manufacture methods are to be used. The laminates with the highest interlaminar fracture energy, employed a hybrid toughened epoxy-based matrix, and there was the added benefit of the nano-silica particles reinstating the loss in stiffness caused by the presence of the CTBN rubber. This study has shown that in many cases the toughness of the bulk epoxy can be transferred to the corresponding FRP laminate, or can even be enhanced, when both nano-silica and CTBN rubber are used as toughening agents.

9.4 Future Work

As in any type of research, although many questions have been answered in the course of the present Thesis, some areas of possible future work have surfaced. These areas are outlined below.

1. **Microstructure of the FRPs** – Although the initial efforts to microtome the surface of an FRP were unsuccessful, future attempts could be made at lower temperatures and using a sharper knife. The resulting TEM and AFM micrographs would be able to shed some light as to why nano-silica increases the toughness in some FRP systems, but not in others. They would also reveal whether there really was a difference in morphology between the bulk epoxy polymers and when they are used as the matrices for FRP laminates.

2. **Additional FRP tests** – Mode II and mixed-mode (I/II) fracture tests could be performed on laminate samples from all three systems. This would compliment the mode I tests performed in this study and further the knowledge of the fracture properties of these systems.

3. **Better manufactured materials** – This would be especially useful in systems where there were large variations in results, and the overlapping error bars suggested that there were no significant changes in the properties. In addition, the laminates of the amine-cured DGEBA-based system were poorly manufactured. They had a poor surface finish and had poor interfacial strength between the fibres and the matrix. It is suggested that a new batch of laminates could be manufactured, with an emphasis on improving the laminate quality.

4. **Additional formulations** - It would be beneficial to perform all of the tests discussed in this thesis on some nano-only samples from the amine-cured DGEBA-based system for comparison, and to test the claim that agglomeration occurs solely because of the nano-silica content. More tests could be performed on the amine-cured TGMDA-based system with different combinations of CTBN and nano-silica, in a similar way that it was ascertained that 9 wt. % CTBN was the optimum rubber content in the anhydride-cured DGEBA-based system.

5. **Toughening mechanisms** – The toughening mechanisms (or lack thereof) of the nano-silica in the amine-cured DGEBA-based system and the amine-cured TGMDA-based system, could be investigated to a similar degree as that of the anhydride-cured DGEBA-based system. This would involve high magnification investigation (eg. AFM and FEG-SEM) of the fracture surfaces.

6. **Volume fraction analysis** – An in-depth study could be undertaken on all three systems to ascertain how much rubber remains in solution after curing. This would involve taking at least a dozen random micrographs of each sample, and then subsequent image analysis. Thus, there would be a better understanding of the phase distribution and morphology relative to the CTBN and nano-silica contents.

7. **Dynamic properties** – This Thesis has investigated the static properties of the three bulk epoxy systems. The bulk epoxies of the amine-cured DGEBA-based system and the anhydride-cured DGEBA-based system are used as adhesives and protective coatings. Therefore, the cyclic fatigue properties would be useful

to measure, so as to determine how these systems behave under cyclic loading. In addition, it would show whether nano-silica has any effect on the fatigue life of these systems, and it would compliment the static data in characterising these materials fully.

8. **Modelling** – Future research could be undertaken into developing an analytical model to accurately predict the fracture resistance of epoxies with nano-silica particles. Emphasis could be placed on taking into account the fact that not all the nano particles debond, and the particles are not always fully dispersed. It would be useful to model the hybrid systems to understand why the fracture energy of some hybrid samples is more than the sum of its CTBN-only and nano-silica-only fracture energies (ie. to explain why the 'toughening synergy' occurs).

REFERENCES

[1] Personal Communication with Stephan Shaw, *Technology Chief in Polymeric Materials, Structural Materials Centre, Defence Research Agency, Farnborough, UK*, (2004).

[2] Nielsen L.E., Landel R.F., *Mechanical Properties of Polymers and Composites*, 2nd ed. New York: Marcel Dekker, (1994).

[3] Drake R.S., Siebert A.R., *SAMPE Quarterly*, **6(4)**, 11-21, (1975).

[4] Kinloch A.J., Shaw S.J., Tod D.A., Hunston D.L., *Polymer*, **24**, 1341-1354, (1983).

[5] Kinloch A.J., *MRS Bulletin*, **28(6)**, 445-448, (2003).

[6] Rowe E.H., Siebert A.R., Drake R.S., *Modern Plastics*, **47**, 110-117, (1970).

[7] Pearson R.A., Yee A.F., *Journal of Materials Science*, **21(7)**, 2475-2488, (1986).

[8] Pascault J.P., Williams R.J.J., *Formulation and Characterization of Thermoset - Thermoplastic Blends. In: Paul D.R., Bucknall C.B., editors. Polymer Blends Volume 1: Formulation.* New York, USA: John Wiley & Sons, (1999).

[9] Bucknall C.B., Partridge I.K., *Polymer*, **24**, 639-644, (1983).

[10] Kinloch A.J., Yuen M.L., Jenkins S.D., *Journal of Materials Science*, **29**, 3781-3790, (1994).

[11] Young R.J., Beaumont P.W.R., *Journal of Materials Science*, **10**, 1343-1350, (1975).

[12] Spanoudakis J., Young R.J., *Journal of Materials Science*, **19(2)**, 473-486, (1984).

[13] Amdouni N., Sautereau H., Gerard J.F., *Journal of Applied Polymer Science*, **46(10)**, 1723-1735, (1992).

[14] Lee J., Yee A.F., *Polymer*, **41**, 8363-8373, (2000).

[15] Kawaguchi T., Pearson R.A., *Polymer*, **44(15)**, 4239-4247, (2003).

[16] Kitey R., Tippur H.V., *Acta Materiala*, **53(4)**, 1167-1178, (2005).

[17] Kinloch A.J., Taylor A.C., Lee J.H., Sprenger S., Eger C., Egan D., *Journal of Adhesion*, **79(8-9)**, 867-873, (2003).

[18] Kinloch A.J., Mohammed R.D., Taylor A.C., Eger C., Sprenger S., Egan D., J *Journal of Materials Science*, **40(18)**, 5083-5086, (2005).

[19] Ragosta G., Abbate M., Musto P., Scarinzi G., Mascia L., *Polymer*, **46(23)**, 10506-10516, (2005).

[20] Zhang H., Zhang Z., Friedrich K., Eger C., *Acta Materiala*, **54(7)**, 1833-1842 (2006).

[21] Kinloch A.J and R. J. Young R.J., *Fracture Behaviour of Polymers*, Applied Science Publishers Limited, (1983).

[22] Young R.J., *Introduction to Polymers*, Chapman and Hall, (1991).

[23] Mills N.J., *Plastics: microstructure, properties and applications*, Edward Arnold, (1986).

[24] www.specialchem4polymers.com, (2006).

[25] Brydson J.A., *Plastic Materials*, Butterworth – Heinemann, (1999).

[26] Pearce P.J., Morris C.E.M. and Ennis B.C., *Polymer*, **37(7)**, 1137-1150, (1996).

[27] Hayes B.S., Seferis J.C., Chen J.S., *Polymer Composites*, **17(5)**, 730 – 742, (1996).

[28] Callister, W.D., *Materials Science and Engineering – An Introduction*, John Wiley and Sons, (2000).

[29] Kinloch A.J., *Structural adhesives: development in resins and primers*, Elsevier Applied Science Publishers, (1983).

[30] Ashby M.F., Jones D.R.H., *Engineering Materials: An Introduction to Properties, Applications and Design: Volume 1*, Butterworth-Heinemann Ltd, (2005).

[31] Kinloch A.J., *Adhesion and Adhesives: Science and Technology*, Chapman and Hall, (1987).

[32] Griffith A.A., *Philosophical Transactions of the Royal Society of London*, **A221**, 163, (1920).

[33] Orowan E., *Reports on Progress in Physics*, **12**, 185, (1948).

[34] Irwin G.R., *Applied Materials Research*, **3**, 65 (1964).

[35] Westergaard H.M., *Journal of Applied Mechanics*, **A6**, 49, (1939).

[36] Knott J.F., *Fundamentals of Fracture Mechanics*, Butterworth, (1973).

[37] Dugdale D.S., *Journal of the Mechanics and Physics of Solids*, **8**, 100, (1960).

[38] Brown N., *Failure of Plastics, Edited by W. Brostow and R. D. Corneliussen*, Hanser Publishers, (1983).

[39] Haward R.N., *The Physics of Glassy Polymers*, Applied Science Publishers, (1975).

[40] Fornes T.D., Paul D.R., *Polymer*, **44(17)**, 4993-5013, (2003).

[41] van Es M., *Nanocomposites 2000 Conference*, Brussels, Belgium, (2000).

[42] Lewis T.B., Nielsen L.E., *Journal of Applied Polymer Science*, **14(6)**, 1449-1471, (1970).

[43] McGee S., McCullough R.L., *Polymer Composites*, **2(4)**, 149-161, (1981).

[44] Nielsen L.E., *Journal of Composite Materials*, **2(1)**, 120-123, (1968).

[45] McGarry F.J., *Proceedings of the Royal Society of London*, **A319**, 59, (1970).

[46] Sultan J.N., McGarry F.J., *Polymer Engineering and Science*, **13**, 29, (1973).

[47] Garg A.C., Mai Y.M., *Composites Science and Technology*, **31**, 179, (1988).

[48] Sankaran S., Chanda M., *Journal of Applied Polymer Science*, **39**, 1635, (1990).

[49] Hwang J.F., Manson J.A., Hertzberg R.W., Miller G.A., Sperling L.H., *Polymer Engineering and Science*, **29**, 1477, (1989).

[50] Sayre J.A., Assink R.A., Lagasse R.R., Polymer, **22**, 87, (1981).

[51] Chan L.C., Gillham J.C., Kinloch A.J., Shaw S.J., *Rubber-Modified Thermoset Resins, Edited by K. Riew and J. C. Gillham*, American Chemical Society Advances in Chemical Series, **208**, 235, (1984).

[52] Kinloch A.J., *Rubber-Toughened Plastics, Edited by K. Riew*, American Chemical Society Advances in Chemical Series, **222**, 67, (1989).

[53] Kunz-Douglass S., Beaumont P.W.R., Ashby M.F., *Journal of Materials Science*, **15**, 1109, (1980).

[54] Yee A.F., Li D., Li X., *Journal of Materials Science*, **28**, 6392, (1993).

[55] Li D., Yee A.F., Chen I.W., Chang S.C., Takahashi K., *Journal of Materials Science*, **29**, 2205, (1994).

[56] Huang Y., Kinloch A.J., *Journal of Materials Science*, **27**, 2753, (1992).

[57] Huang Y., *Imperial College London, University of London, London, Ph.D. thesis*, (1991).

[58] Bagheri R., Pearson R.A., *Polymer*, **37**, 4529, (1996).

[59] Morgan R.J., Mones E.T., Steele W.J., *Polymer*, **23**, 295, (1982).

[60] Lilley J., Holloway D.G., *Philosophical Magazine*, **28**, 215, (1973).

[61] Bucknall C.B., *Toughened Plastics*, Applied Science Publishers, (1977).

[62] Wang X., Guild F.J, Kinloch A.J., Taylor A.C., Hadavinia H., *Proceedings of the 28th annual meeting of the Adhesion Society*, Alabama, USA, (2005).

[63] Kinloch A.J., Maxwell D.A., Young R.J., *Journal of Materials Science*, **4**, 1276, (1985).

[64] Kaiser T., *Progress in Polymer Science*, **14**, 373, (1989).

[65] Kinloch A.J., Finch C.A., Hashemi S., *Polymer Communications*, **28**, 322, (1987).

[66] Hwang J.F., Manson J.A., Hertzberg R.W., Miller G.A., Sperling L.H., *Polymer Engineering and Science*, **29**, 1466, (1989).

[67] Bauer R.S., *Polymeric Materials Science and Engineering*, **59**, 820, (1988).

[68] Pearson R.A., Yee A.F., *Journal of Materials Science*, **24**, 2571, (1989).

[69] Bucknall C.B., Yoshii T., *British Polymer Journal*, **10**, 53, (1978).

[70] Karger-Kocsis J., Friedrich K., *Composites Science and Technology*, **48**, 263, (1993).

[71] Kinloch A.J., Hunston D.L., *Journal of Materials Science*, **6**, 137, (1987).

[72] Bascom W.D., Cottington R.L., Jones R.L., Peyser P., *Journal of Applied Polymer Science*, **19**, 2545, (1975).

[73] Wu S., *Polymer*, **26**, 643, (1985).

[74] Margolina A., Wu S., *Polymer*, **29**, 2170, (1988).

[75] Pearson R.A., Yee A.F., *Journal of Materials Science*, **26**, 3828, (1991).

[76] Kim D.S., Cho K., Kim J.K., Park C.E., *Polymer Engineering and Science*, **36**, 755, (1996).

[77] Lazzeri A., Bucknall C.B., *Journal of Materials Science*, **28**, 6799, (1993).

[78] Huang Y., Kinloch A.J., Bertsch R.J., Siebert A.R., *Toughened Plastics I, Edited by C. K. Riew and A. J. Kinloch*, Advances in Chemistry Series, **233**, 189, (1993).

[79] Y. Huang Y., Kinloch A.J., *Polymer*, **33**, 1331, (1992).

[80] Lange F.F., *Philosophical Magazine*, **22**, 983, (1970).

[81] Faber K.T., Evans A.G., *Acta Metallurgica*, **31**, 565, (1983).

[82] Johnsen B.B., Kinloch A.J., Taylor A.C., *Polymer*, **46**, 7352, (2005).

[83] Kinloch A.J., Taylor A.C., *Journal of Materials Science*, **37**, 433, (2002).

[84] Evans A.G., Williams S., Beaumont P.W.R., *Journal of Materials Science*, **20**, 3668, (1985).

[85] Lee J., Yee A.F., *Polymer*, **41**, 8375, (2000).

[86] Lee J., Yee A.F., *Polymer*, **42**, 577, (2001).

[87] Evans A.G., *Philosophical Magazine*, **26**, 1327, (1972).

[88] Green D.J., Nicholson P.S., Embery J.D., *Journal of Materials Science*, **14**, 1657, (1979).

[89] Kawaguchi T., Pearson R.A., *Composites Science and Technology*, **64**, 1991, (2004).

[90] Lange F.F., Radford K.C., *Journal of Materials Science*, **6**, 1197, (1971).

[91] Young R.J., Beaumont P.W.R., *Journal of Materials Science*, **12**, 684, (1977).

[92] Mallick P.K., Broutman L.J., *Materials Science and Engineering*, **18**, 63, (1975).

[93] Spanoudakis J., *Queen Mary College, University of London, London, Ph.D. thesis*, (1981).

[94] Vallo C.I., Hu L., Frontini P.M., Williams J.J., *Journal of Materials Science*, **29**, 2481, (1994).

[95] Low I.M., Bandyopadhyay S., Mai Y.M., *Polymer International*, **27**, 131, (1992).

[96] Azimi H.R., Pearson R.A., Hertzberg R.W., *Journal of Applied Polymer Science*, **58**, 449, (1995).

[97] Tarrant A.E., *Imperial College London, University of London, London, Ph.D. thesis*, (2004).

[98] Lee J.H., *Imperial College London, University of London, London, Ph.D. thesis*, (2006).

[99] Lan T., Pinnavaia T.J., *Chemistry of Materials*, **6**, 2216, (1994).

[100] Messersmith P.B., Giannelis E.P., *Chemistry of Materials*, **6**, 1719, (1994).

[101] Ahmadi S.J., Huang Y.D., Li W., *Journal of Materials Science*, **39**, 1919, (2004).

[102] Sprenger S., Eger C., Kinloch A., Taylor A., Mohammed R., *JEC Composites Magazine*, **19**, 73, (2005).

[103] Sprenger S., Eger C., Kinloch A., Taylor A., Mohammed R., *JEC Composites Magazine*, **21**, 66, (2005).

[104] Sprenger S., Eger C., Kinloch A., Taylor A., Mohammed R., *JEC Composites Magazine*, **30**, 54, (2007).

[105] Kinloch A.J., Mohammed R.D., Taylor A.C., Eger C., Sprenger S., Egan D., *Journal of Materials Science*, **40**, 5083, (2005).

[106] Kinloch A.J., Mohammed R.D., Taylor A.C., Eger C., Sprenger S., Egan D., *Journal of Materials Science*, **41**, 5043, (2006).

[107] Kinloch A.J., Mohammed R.D., Taylor A.C., Eger C., Sprenger S., Egan D., "The Bulk and Interlaminar Composite Toughness of 'Hybrid-Toughened' Temperature-Resistant Epoxy Polymers", *Journal of Materials Science*, **In-Press**, (2006).

[108] Johnsen, B.B., Kinloch A.J., Mohammed R.D., Taylor A.C., Sprenger S., *Polymer*, **48**, 530, (2007).

[109] Hull D., Clyne T.W., An Introduction to Composite Materials, Cambridge University Press, (1996).

[110] http://www.engr.ku.edu, (2006).

[111] Schmachtenberg E., Schulte zur Heide J., Töpker J., *Polymer Testing*, **24**, 330, (2005).

[112] Personal Communication with Ambrose Taylor, *Lecturer, Department of Mechanical Engineering, Imperial College London, UK*, (2006).

[113] Matthews F.L., Rawlings R.D., *Composite Materials: Engineering and Science*, Chapman and Hall, (1994).

[114] Pagano N.J., *Composites PartB*, **29B**, 93, (1998).

[115] Lee W., Howard S.J., Clegg W.J., *Acta Materiala*, **44**, 3905, (1996).

[116] www.hanse-chemie.com, (2006).

[117] ISO-527-1: *Plastics - Determination of Tensile Properties - Part 1: General Principles*, Geneva: ISO, (1993).

[118] ISO-527-2: *Plastics - Determination of Tensile Properties - Part 2: Test Conditions for Moulding and Extrusion Plastics*, Geneva: ISO, (1996).

[119] ISO-13586: *Plastics-Determination of Fracture Toughness (G_{Ic} and K_{Ic}) - Linear Elastic Fracture Mechanics (LEFM) Approach*, Geneva: ISO, (2000).

[120] ISO-15024: *Determination of the Mode I delamination resistance of unidirectional fiber-reinforced polymer laminates using the double cantilever beam (DCB).* Geneva: ISO, (1999).

[121] Blackman B.R.K., Dear J.P., Kinloch A.J., Osiyemi S., *Journal of Materials Science*, **10**, 253, (1991).

[122] ASTM-D790M-93: *Test methods for flexural properties of unreinforced and reinforced plastics and electrical insulating materials [metric]*. Philadelphia: ASTM, (1999).

[123] BS-EN-2564: *Carbon Fibre Laminates – Determination of the fibre, resin and void contents*, (1998).

[124] Airline Division (Woodford), on behalf of British Aerospace, BAER 3014: *Test Method for the Fibre and Void Content of Cured Carbon and Glass Fibre Composites*, (1990).

[125] Arias M.L., Frontini P.M., Williams J.J., *Polymer*, **44(5)**, 1537, (2003).

[126] Russell B., Chartoff R., *Polymer*, **46(3)**, 785, (2005).

[127] Meng, F., Zheng S., Liu T., *Polymer*, **47(21)**, 7590, (2006).

[128] Karger-Kocsis J., Gryshchuk O., Fröhlich J., Mülhaupt R., *Composites Science and Technology*, **63(14)**, (2003).

[129] Thomas R., Abraham J., Thomas S.P., Thomas S., *Journal of Polymer Science Part B: Polymer Physics*, **42(13)**, 2531, (2004).

[130] Mafi R., Mirabedini S.M., Moradian S., *Progress in Organic Coatings*, **54(3)**, 164, (2005).

[131] Barral L., Cano J., López J., López-Bueno I., Nogueira P., Ramírez C., Torres A., Abad M.J, *Thermochimica Acta*, **344(1-2)**, 137, (2000).

[132] Zhang, Y., Vyazovkin S., *Polymer*, **47(19)**, 6659, (2006).

[133] Chen W., Wang Y., Kuo S., Huang C., Tung P., Chang F., *Polymer*, **45(20)**, 6897, (2004).

[134] Wise C.W., Cook W.D., Goodwin A.A., *Polymer*, **41(12)**, 4625, (2000).

[135] www.emeraldmaterials.com, (2006).

[136] Qi B., Zhang M., Mai Y., *Composite Structures*, **75(1-4)**, 514, (2006).

[137] Goodfellow Product Catalogue, Huntingdon: Goodfellow, (2005).

[138] Pascoe K.J., *An Introduction to the Properties of Engineering Materials*, Van Nostrand Reinhold, London, (1978).

[139] Zhang, D., Jia D., *Journal of Applied Polymer Science*, **101(4)**, 2504, (2006).

[140] Park S., Jin F., Shin J., *Materials Science and Engineering A*, **390(1-2)**, 240, (2005).

[141] Jin F., Han M., Park S., *Polymer International*, **55(11)**, 1265, (2006).

[142] Mezzenga R., Manson J.E., *Polymeric Materials: Science & Engineering*, **84** (2001).

[145] Andrews E.H., *Fracture in Polymers*, Oliver & Boyd, Edinburgh, (1968).

[146] Harada M., Morimoto M., Ochi M., *Journal of Polymer Science Part B: Polymer Physics*, **41(11)**, 1198, (2003).

[147] Kim H.R., Myung B.Y., Yoon T.H., Song K.H., *Journal of Applied Polymer Science*, **84(8)**, 1556, (2002).

[148] Kim H.S., Ma P., *Journal of Applied Polymer Science*, **61(4)**, 659, (1996).

[149] Han J.T., Cho K., *Journal of Materials Science*, **41**, 4239, (2006).

[150] Personal Communication with Stephan Sprenger, *BU Manager, Adhesives & Composites Materials, nanoresins, Geesthacht, Germany*, (2006).

[151] Personal Communication with Anthony J. Kinloch, *Professor, Department of Mechanical Engineering, Imperial College London, UK*, (2006).

[152] Velmurugan R., Solaimurugan S., *Composites Science and Technology*, **67(1)**, 61, (2007).

[153] Suppakul P., Bandyopadhyay S., *Composites Science and Technology*, **62**, 709, (2002).

[154] Shindo Y., Inamoto A., Narita F., Horiguchi K., *Engineering Fracture Mechanics*, **73(14)**, 2080, (2006).

[155] Ashcroft I.A., D. J. Hughes D.J., Shaw S.J., *International Journal of Adhesion and Adhesives*, **21(2)**, 87, (2001).

[156] Lee C.S., Hwang W., Park H.C., Han K.S., *Composites Science and Technology*, **59(12)**, 1789, (1999).

[157] Bucknall C.B., Ayre D.S., Dijkstra D.J., *Polymer*, **41(15)**, 4625, (2000).

[158] Vega-Baudrit J., Navarro-Bañón V., Vázquez P., Martín-Martínez J.M., *International Journal of Adhesion and Adhesives*, **26(5)**, 378, (2006).

[159] Pascal T., Bonneau J.L., Biolley N., Mercier R., Sillion B., *Polymers for Advanced Technologies*, 6(4), 219, (1995).

[160] Song X., Zheng S., Huang J., Zhu P., Guo Q., *Journal of Applied Polymer Science Volume*, 79(4), 598, (2001).

[161] Park S., Jin F., Lee J., *Materials Science and Engineering A*, **374(1-2)**, 109, (2004).

[162] Becker O., Varley R., Simon G., *Polymer*, **43(16)**, 4365, (2002).

[163] Scott J.M., Phillips D.C., *Journal of Materials Science*, **10(4)**, 551, (1975).

[164] Mouritz, A.P., *Materials Science and Engineering A*, **359(1-2)**, 237, (2003).

[165] Hojo M., Ando T., Tanaka M., Adachi T., Ochiai S., Endo Y., *International Journal of Fatigue*, **28(10)**, 1154, (2006).

[166] Kim J., Mai Y., *Journal of Materials Science*, **26(17)**, 4702, (1991).

[167] Zhang H., Zhang Z., Friedrich K., Eger C., *Acta Materialia*, **54(7)**, 1833, (2006).

[168] Personal Communication with Bernt B. Johnsen, *Research Associate, Department of Mechanical Engineering, Imperial College London, UK*, (2006).

[169] Lin K., Chung U., *Journal of Materials Science*, **29(5)**, 1198, (1994).

[170] Tcharkhtchi A., Faivre S., Roy L.E., Trotignon J.P., Verdu J., *Journal of Materials Science*, **31(10)**, 2687, (1996).

[171] Brady R.F., Sikes A.M., *Polymer Bulletin*, **22(5-6)**, 521, (1989).

[172] Mauri A.N., Riccardi C.C., Williams R.J.J., *Polymer Bulletin*, **45(6)**, 523, (2003).

[173] Natarajan K., Kumar R.P., Reddy P.V., Gowda N.M.N., Rao R.M.V.G.K., *Polymer International*, **49(11)**, 1321, (2000).

[174] Moloney A.C., Kausch H.H., Kaiser T., Beer H.R., *Journal of Materials Science*, **22(2)**, 381, (1987).

[175] Kinloch A.J., Taylor A.C., *Journal of Materials Science*, **41(11)**, 3271, (2006).

[176] www.lange-ritter.de, (2005).

[177] Couchman P.R., *Journal of Materials Science*, **15(7)**, 3271, 1680, (1980).

[178] Wu C.L., Zhang M.Q., Rong M.Z., Friedrich K., *Composites Science and Technology*, **62**, 1327, (2002).

[179] Vladimirov V., Betchev C., Vassiliou A., Papageorgiou G., Bikiaris D., *Composites Science and Technology*, **66**, 2935, (2006).

[180] Karad S.K., Attwood D., Jones F.R., *Composites Part A: Applied Science and Manufacturing*, **36(6)**, 764, (2005).

[181] Arakawa K., Takahashi K., *International Journal of Fracture*, **48**, 103, (1995).

[182] van Hartingsveldt E.A.A., van Aartsen J.J., *Polymer*, **30(11)**, 1984, (1989).

[183] Vollenberg P., Heikens D., Ladan H.C.B., *Polymer Composites*, **9(6)**, 382, (1988).

[184] Guild F.J., Kinloch A.J., *Journal of Materials Science Letters*, **13**, 629, (1994).

[185] Chen X., Mai Y., *Journal of Materials Science*, **33**, 3529, (1998).

[186] Guild F.J., Young R.J., *Journal of Materials Science*, **24**, 298, (1989).

[187] Wu W., Sadeghipour K., Boberick K., Baran G., *Materials Science and Engineering A*, **332**, 362, (2002).

[188] Chawla N., Chawla K.K., *Journal of Materials Science*, **41**, 913, (2006).

APPENDIX – PUBLICATIONS FROM THE WORK CONDUCTED FOR THIS STUDY

[1] Sprenger S., Eger C., Kinloch A., Taylor A., Mohammed R., "Rubber-toughened FRCs optimised by nanoparticles", *JEC Composites Magazine*, **19**, 73, (2005).

[2] Sprenger S., Eger C., Kinloch A., Taylor A., Mohammed R., "Rubber-toughened GFRCs optimised by nanoparticles", *JEC Composites Magazine*, **21**, 66, (2005).

[3] Sprenger S., Eger C., Kinloch A., Taylor A., Mohammed R., "Rubber-toughened CFRCs for high performance applications optimised by nanoparticles – Part III", *JEC Composites Magazine*, **30**, 54 (2007).

[4] Kinloch A.J., Mohammed R.D., Taylor A.C., Eger C., Sprenger S., Egan D., "The effect of silica nano particles and rubber particles on the toughness of multiphase thermosetting epoxy polymers", *Journal of Materials Science*, **40**, 5083, (2005).

[5] Kinloch A.J., Mohammed R.D., Taylor A.C., Eger C., Sprenger S., Egan D., "The interlaminar toughness of carbon-fibre reinforced plastic composites using 'hybrid-toughened' matrices", *Journal of Materials Science*, **41**, 5043, (2006).

[6] Kinloch A.J., Mohammed R.D., Taylor A.C., Eger C., Sprenger S., Egan D., "The Bulk and Interlaminar Composite Toughness of 'Hybrid-Toughened' Temperature-Resistant Epoxy Polymers", *Journal of Materials Science*, **In-Press**, (2006).

[7] Johnsen, B.B., Kinloch A.J., Mohammed R.D., Taylor A.C., Sprenger S., "Toughening mechanisms of nanoparticle-modified epoxy", *Polymer*, **48**, 530, (2007).